NUREG/CR-5098
SAND88-7018

An Analytical Study of Seismic Threat to Containment Integrity

Prepared by M. Amin, P. K. Agrawal, S&L
T. J. Ahl, CBI

Sargent & Lundy
CBI Na-Con, Inc.

Sandia National Laboratories

Prepared for
U.S. Nuclear Regulatory
Commission

AVAILABILITY NOTICE

Availability of Reference Materials Cited in NRC Publications

Most documents cited in NRC publications will be available from one of the following sources:

1. The NRC Public Document Room, 2120 L Street, NW, Lower Level, Washington, DC 20555
2. The Superintendent of Documents, U.S. Government Printing Office, P.O. Box 37082, Washington, DC 20013-7082
3. The National Technical Information Service, Springfield, VA 22161

Although the listing that follows represents the majority of documents cited in NRC publications, it is not intended to be exhaustive.

Referenced documents available for inspection and copying for a fee from the NRC Public Document Room include NRC correspondence and internal NRC memoranda; NRC Office of Inspection and Enforcement bulletins, circulars, information notices, inspection and investigation notices; Licensee Event Reports; vendor reports and correspondence; Commission papers; and applicant and licensee documents and correspondence.

The following documents in the NUREG series are available for purchase from the GPO Sales Program: formal NRC staff and contractor reports, NRC-sponsored conference proceedings, and NRC booklets and brochures. Also available are Regulatory Guides, NRC regulations in the *Code of Federal Regulations*, and *Nuclear Regulatory Commission Issuances*.

Documents available from the National Technical Information Service include NUREG series reports and technical reports prepared by other federal agencies and reports prepared by the Atomic Energy Commission, forerunner agency to the Nuclear Regulatory Commission.

Documents available from public and special technical libraries include all open literature items, such as books, journal and periodical articles, and transactions. *Federal Register* notices, federal and state legislation, and congressional reports can usually be obtained from these libraries.

Documents such as theses, dissertations, foreign reports and translations, and non-NRC conference proceedings are available for purchase from the organization sponsoring the publication cited.

Single copies of NRC draft reports are available free, to the extent of supply, upon written request to the Office of Information Resources Management, Distribution Section, U.S. Nuclear Regulatory Commission, Washington, DC 20555.

Copies of industry codes and standards used in a substantive manner in the NRC regulatory process are maintained at the NRC Library, 7920 Norfolk Avenue, Bethesda, Maryland, and are available there for reference use by the public. Codes and standards are usually copyrighted and may be purchased from the originating organization or, if they are American National Standards, from the American National Standards Institute, 1430 Broadway, New York, NY 10018.

DISCLAIMER NOTICE

This report was prepared as an account of work sponsored by an agency of the United States Government. Neither the United States Government nor any agency thereof, or any of their employees, makes any warranty, expressed or implied, or assumes any legal liability of responsibility for any third party's use, or the results of such use, of any information, apparatus, product or process disclosed in this report, or represents that its use by such third party would not infringe privately owned rights.

NUREG/CR-5098
SAND88-7018
R1, RD

An Analytical Study of Seismic Threat to Containment Integrity

Manuscript Completed: May 1989
Date Published: July 1989

Prepared by
M. Amin, P. K. Agrawal, Sargent & Lundy
T. J. Ahl, CBI Na-Con, Inc.

Sargent & Lundy
55 East Monroe
Chicago, IL 60603

CBI Na-Con, Inc.
800 Jorie Boulevard
Oak Brook, IL 60522

under Contract to:
Sandia National Laboratories
Albuquerque, NM 87185

Prepared for
Division of Engineering
Office of Nuclear Regulatory Research
U.S. Nuclear Regulatory Commission
Washington, DC 20555
NRC FIN A1401

For sale by the Superintendent of Documents, U.S. Government Printing Office
Washington, D.C. 20402

ABSTRACT

The methodology used and the results of an analytical scoping study of the seismic capacity of four containment buildings located in the Eastern United States are described in this report. The study was undertaken to provide quantitative information of containment seismic capacity considering a rather complete list of limit states. This type of information was not available previously.

The four containments represent a cross-section of containment, reactor, and foundation types. Evaluations included time history analyses, four combinations of seismic with pressure and temperature loading to consider different severe accident conditions, and seismic aftershocks. Containments were evaluated for applicable limit states from a list of sixteen limit states that included structural, penetration, and foundation failures.

The results are presented in terms of capacity margin factors at a prescribed value of peak horizontal ground acceleration, or by stating the seismic capacity in the governing limit states when the capacity is smaller than the acceleration value at which margin factors are listed. For certain critical limit states, curves showing the variation of capacity margin factor with peak horizontal ground acceleration are presented. The report also includes a discussion of factors that are significant for determining seismic capacity and provides recommendations for future work.

TABLE OF CONTENTS

TABLE OF CONTENTS (Cont'd.)

TABLE OF CONTENTS (Cont'd.)

TABLE OF CONTENTS (Cont'd.)

TABLE OF CONTENTS (Cont'd.)

LIST OF FIGURES

LIST OF FIGURES (Cont'd.)

LIST OF FIGURES (Cont'd.)

LIST OF FIGURES (Cont'd.)

LIST OF FIGURES (Cont'd.)

LIST OF FIGURES (Cont'd.)

LIST OF FIGURES (Cont'd.)

LIST OF FIGURES (Cont'd.)

LIST OF FIGURES (Cont'd.)

LIST OF FIGURES (Cont'd.)

LIST OF FIGURES (Cont'd.)

LIST OF FIGURES (Cont'd.)

LIST OF FIGURES (Cont'd.)

LIST OF FIGURES (Cont'd.)

LIST OF FIGURES (Cont'd.)

LIST OF FIGURES (Cont'd.)

LIST OF FIGURES (Cont'd.)

LIST OF FIGURES (Cont'd.)

LIST OF FIGURES (Cont'd.)

LIST OF FIGURES (Cont'd.)

LIST OF FIGURES (Cont'd.)

LIST OF FIGURES (Cont'd.)

LIST OF FIGURES (Cont'd.)

LIST OF TABLES

LIST OF TABLES (Cont'd.)

LIST OF TABLES (Cont'd.)

LIST OF TABLES (Cont'd.)

LIST OF TABLES (Cont'd.)

ACKNOWLEDGMENT

The Sandia Technical Representative for the project was D. B. Clauss. His continuing interest in the project and the timely comments and clarifications he provided helped plan and conduct the project work. His input and cooperation is gratefully acknowledged. J. F. Costello as NRC Program Manager and W. A. von Riesemann of Sandia participated in the review meetings held for the project and provided helpful comments. Their help and support is deeply appreciated.

At Sargent & Lundy the work on the project progressed under technical consultation with the following individuals:

B. A. Erler	A. K. Singh
A. Walser	C. N. Krishnaswamy

During the course of the investigation, the project team was guided by their individual comments and their group review of the interim and final results. This advice and cooperation is gratefully acknowledged.

The following engineers at S&L and CBI made major contributions to the evaluations described in this report

At S&L	At CBI
A. M. Al-Dabbagh	P. Morgan
J. Pop, Jr.	
N. C. Bhatia	

We are grateful for their contributions and assistance.

EXECUTIVE SUMMARY

The containment in a nuclear power plant is an important engineered safeguard feature. It provides the last barrier to the occurrence of an uncontrolled radiological release in case of an accident. The earthquake loading is considered in the design of the containment using the provisions of the American Society of Mechanical Engineers (ASME) Code and the Nuclear Regulatory Commission (NRC) requirements. However, not much work has been done on the subject of the ultimate seismic capacity of containments. Seismic events much beyond the design-basis earthquake could initiate a severe accident in a nuclear plant resulting in high pressure and temperature. The containment, which may have been weakened by the main seismic shock, may then be challenged by the combination of elevated pressure and temperature and an earthquake aftershock. Therefore, a study of containment behavior under earthquake loading beyond the design-basis earthquake is important.

This report provides the results of a scoping study performed to determine the seismic capacity of four different containments: Fermi, Clinton, Zion, and Sequoyah. The four containments studied represent a cross section of containment, reactor, and foundation types. Specifically, Fermi has a BWR of the Mark I type with a steel containment on a rock foundation; Clinton has a BWR of the Mark III type with a reinforced concrete containment on a soil foundation; Zion has a PWR with a dry prestressed concrete containment on a soil foundation; and Sequoyah has a PWR with a steel ice-condenser type of containment on a rock foundation.

It is recognized that the seismic capacity of a particular containment depends significantly upon its unique design features and site characteristics. However, in order to gain some perspective on the problem, this scoping study examined four representative containments that may illustrate typical values for seismic capacity.

The objectives of the study were to identify governing seismic limit states, to gain an understanding of the containment behavior under strong seismic loading by estimating the seismic capacities of containments through a quantitative evaluation, and to identify areas of uncertainty that should be further studied using more detailed analysis or testing.

Four different combinations of pressure and temperature loading were considered in the study. First, the effect of an initial main earthquake shock on the containments was studied based on operating conditions of the plant. This is referred to as Task 3 loading in the report. (Tasks 1 and 2 formulated methodology and evaluation criteria for this study.) The other three load combinations addressed the behavior of the containments assuming that the containments did not fail under the initial main shock and that a severe accident was initiated through some component failure. An aftershock was then postulated to occur at various stages of the severe accident progression, and seismic capacities of the containments were calculated for three different

pressure and temperature combinations corresponding to different stages of the severe accident. One of these combinations, referred to as Task 4 in the report, represented the case of an aftershock occurring early in the accident progression, when the pressure and temperature were assumed to be equal to the design accident pressure and temperature for each containment. The next combination, referred to as Task 5, represented the case of an aftershock occurring late in the accident progression when high pressure and temperature conditions exist in the containment.

The temperature values for the Task 5 condition were specified by Sandia National Laboratories based on severe accident profiles for different reactors and containments. The pressure values represented those pressures at which yielding in the containment would initiate for the given temperatures. The last combination, referred to as Task 6, represented a condition in-between Tasks 4 and 5, and pressure and temperature values chosen were the average values of these two tasks.

It is noted that in the load combinations discussed above, it has been assumed that the main seismic shock does start an accident leading to a severe accident scenerio. In addition, it has been assumed that a strong aftershock occurs during the severe accident. These are clearly conservative assumptions.

Before starting the actual calculations for estimating the seismic capacity, various limit states for each of the four containments were postulated and explicit failure criteria for each of the limit states were established. Then the seismic capacity of the containments was calculated for each applicable limit state and the governing limit states were identified.

The limit states identified include both direct and indirect limit states. Direct limit states are those that are directly related to the containment pressure boundary. Tensile or buckling failure of a steel containment shell, failure of a liner, failure of reinforcing bars or prestressing tendons in a concrete containment wall or basemat, and transverse shear failure of a concrete containment wall or basemat are examples of direct limit states. Indirect limit states are not directly related to the containment pressure boundary; however, their realization may lead to conditions under which assurance of containment integrity without further detailed studies or testing cannot be established. Basemat or biological shield wall failure in Fermi, shield building failure in Sequoyah, or foundation failures in bearing, sliding, or liquefaction in any of the containments are examples of indirect limit states.

The use of a three-dimensional nonlinear model of containment and adjacent structures that would consider all pertinent nonlinearities in one time-history analysis model was not practical because of analysis cost and because definitive information was unavailable on the significance of various nonlinearities that could potentially affect the results. Instead, a simplified time history analysis procedure that included nonlinearities at various stages of evaluation was used.

The analysis, briefly, consisted of (1) determining the strain-compatible soil shear modulus and damping values for various levels of earthquake, using a one-dimensional vertical shear wave propagation model; (2) constructing a seismic beam model of the containment and adjacent structures, including the impedance functions of the soil or rock foundation to account for the soil-structure interaction effects, and one-way soil springs to account for the basemat uplift; (3) constructing moment-curvature diagrams of the beam elements in the seismic model to predict the nonlinear behavior of the containment after appropriately considering the effect of non-seismic loads, i.e., gravity, pressure, temperature and prestressing loads; (4) performing a nonlinear seismic time-history analysis of the model and obtaining responses of interest; (5) performing an elastic axisymmetric static shell analysis of the containment with the peak responses obtained from seismic analysis; (6) performing a cracked section, element-level analysis for critical concrete containment sections, including material nonlinearity for liner and reinforcing bars, using the shell forces obtained from the elastic shell analysis of the previous step; (7) obtaining the maximum stress, strain, or displacements, as needed, at the critical locations; and (8) calculating margins at a specified earthquake level by comparing the maximum stress, strain, or displacements obtained in the previous step with the failure criteria established for each limit state.

In addition, a three-dimensional, finite element model of the Clinton containment was also analyzed statically using peak seismic accelerations to verify the results of Steps 5 through 7 of the simplified analysis described above. In this three-dimensional model, the effects of concrete cracking and the yielding of the liner and reinforcing bars on the containment responses were included at the structural system level as opposed to the simplified analysis where these effects were included only on an element level.

Horizontal and vertical acceleration time histories used as input to the seismic analysis model were derived such that their response spectra enveloped the Regulatory Guide 1.60 response spectra for a specified maximum horizontal ground acceleration. Use of the Regulatory Guide 1.60 response spectral shapes allowed linear scaling of time histories with the maximum horizontal ground accelerations. Thus, margins and capacities of the containments are stated in terms of maximum horizontal ground accelerations (A_H) only.

Overall Conclusions

This study has developed a conservative estimate of seismic capacity of the four containments. In the analyses performed to determine the seismic load effects and parameters defining containment limit states, conservative parameters and approaches were selected. The conservative approach taken is consistent with other studies of the seismic margin of nuclear power plant structures and components. Indeed, the approach taken in this study can be viewed as the Conservative Deterministic Failure Margin (CDFM) method of determining High Confidence of Low Probability of Failure (HCLPF) seismic capacity of containments.

The following overall conclusions were developed:

1. Even given the conservatism, results of the calculations suggest that the four containments evaluated in this study have seismic capacities at least three times higher than their design-basis safe shutdown earthquake (SSE). Table ES.1 lists the first few governing limit states for each containment and their associated capacities for Tasks 3 and 5. The table also lists the design-basis SSE peak horizontal ground acceleration and its specified spectral shape. For earlier vintage containments, the design spectral shape is in terms of Housner's spectra, which is less intense than the Regulatory Guide 1.60 spectra by a factor of about two in the frequency range of interest for containments. Considering this factor, calculated margins from capacities in Table ES.1 are three or more for the four containments evaluated.

2. Many of the governing limit states in Table ES.1 for the Fermi, Clinton, and Sequoyah containments are indirect limit states, i.e., they are not directly related to the containment pressure boundary. The calculated seismic capacities in these instances are not affected by the presence of accident pressure and temperature in the containment. Of course, for direct limit states, the interaction of thermal and pressure effects with seismic influences the aftershock seismic capacity. In some instances the aftershock seismic capacity is increased, and in some cases the capacity is decreased. The instance of capacity decrease is quantified in Table ES.1 for the Zion containment where pressure-induced tension has overcome wall prestressing and for Clinton where pressure induced tension has decreased available seismic capacity in the wall reinforcing bars. The example of aftershock seismic capacity increase occurs for basemat shear failure in Sequoyah because of the beneficial effect of thermal compression in the basemat.

3. None of the governing limit states for Task 3 in Table ES.1 are associated with a significant straining of containment concrete elements in compression that could cause partial crushing, or with significant beyond-yield straining of steel elements that could cause a reduction of the ductility limit. Consequently, effects of such initial shock weakening of containments are not considered important. For the Fermi and Sequoyah containments, the failure of the biological shield wall or the shield building due to an initial shock could cause additional loading on steel containments. In this report the effect of interaction of failed buildings with containments during aftershock seismic evaluation has not been studied.

4. Table ES.1 also shows that basemat failure in transverse shear is an important limit state for the Fermi and Sequoyah containments.

5. Another major conclusion from the study relates to the effect of basemat uplift. Basemat uplift initiates somewhere after A_H = 0.25g at Fermi, Zion, and Sequoyah. Due to its large extent, the Clinton basemat does not uplift even at A_H = 1.0g. The effect of

basemat uplift is significant for Fermi and Sequoyah containments because of a hard impact condition between the basemat and rock foundation. For the Zion containment, the effects of uplift are relatively small because of absence of hard impact conditions at the basemat-soil interface. The in-structure response spectra calculated for the Fermi and Sequoyah containments after basemat uplift are very high in the high frequency region (8 Hz and above). It is conceivable that some critical components in the containment may be affected by the high spectral accelerations, thus having potential for altering the severe accident scenario.

While foundation uplift does not affect the response of containment walls significantly, its effect on the basemat response, particularly on rock foundation, is important.

6. From a comparison of the results of simplified methodology and three-dimensional Clinton containment analysis, it is concluded that the simplified methodology used here for concrete containments provides conservative estimates for reinforcing bar and liner strains. The estimates for transverse shear in the wall from this simplified procedure are also conservative. Basemat shear and moment predictions are reasonably close.

7. Finally, a review of parameters having significant effect on containment seismic response shows that in addition to seismic input, the following items are important: soil spring and dashpot constants, parameters defining initiation of uplift phenomenon, reduction in concrete shear stiffness due to cracking, and definition of evaluation criteria for shear failure in concrete plate and shell structures. It is important to properly define the variability in these parameters in any further study of containment seismic capacity.

Recommendations for Future Work

To perform the scoping study several simplifying assumptions and approximations were made. The study concentrated on considering the structural and foundation limit states. To confirm some of the assumptions made and to investigate critical equipment failures, the following studies are recommended.

1. The failure of the biological shield wall in Fermi and shield building in Sequoyah yielded the lowest seismic capacities for these containments. The evaluations made are considered conservative based on the ACI Code capacities used. A three-dimensional, quasi-static, materially nonlinear analysis is recommended to better predict the capacity of these shield walls, which may significantly improve the capacities reported herein. If such an evaluation does not improve the seismic capacity and if additional capacity needs to be investigated, the effect of potential interactions of these failed buildings with containment in determining seismic aftershock capacity should be considered.

2. The occurrence of uplift for containments founded on rock significantly affects the in-structure response spectra for frequencies beyond 8 Hz. An investigation is necessary to show whether high frequency excitations of the type calculated can affect the functionality of critical components. In case these conditions exist, it is important to establish through analytical studies and/or testing whether initiation of basemat uplift would occur in containments embedded in a rock foundation as is assumed in this report. The study should include a proper representation of actual construction practices used and their effect on the foundation uplift.

3. Since for steel containments the effect of biaxial stress states on the containment shell was derived through an approximate procedure based on reduced yield stress and a beam analysis, the confirmation of this simplified analysis procedure through a quasi-static, nonlinear, three-dimensional shell analysis is recommended.

4. The basemat evaluations performed in this study are considered approximate; where uplift of the basemat occurs, the prediction of basemat forces is complex. The source of the complexity is in providing appropriate definition of simultaneous wall reactions, mat inertia, and soil reaction including damping that act on the basemat. A time-history analysis using an elastic, three-dimensional model of containment and basemat with consideration of uplifting foundation is recommended to improve the prediction of forces. This improved basemat force distribution should be used to investigate basemat seismic capacity.

Report Organization

The report is organized into nine chapters and several appendixes. Background information and scope of work, including the design parameters of the four containments analyzed, the 16 limit states investigated, and the pressure and temperature values for the four loading combinations studied are described in Chapter 1. Chapter 2 describes the methodology and the criteria for evaluating the 16 limit states that were identified. Chapters 3, 4, 5, and 6 contain descriptions of the containment, the application of methodology, and the results for the Fermi, Clinton, Zion, and Sequoyah containments, respectively. Chapter 7 describes the three-dimensional, quasi-static, nonlinear analysis of the Clinton containment. Chapter 8 describes the uncertainties in the analytical modeling and procedures, and their potential impact on the results. Chapter 9 gives overall conclusions of the study. Appendixes A and B describe certain referenced items in the text in more detail. Appendix C contains a summary of seismic responses for various containments. Appendix D contains a flow chart of the analyses performed for each containment, and identifies computer programs that are used. Appendix E contains a brief description of various computer programs that were utilized in this study.

Table ES.1 - Governing Limit States and Conservative Estimates of Capacities[1]

Containment	Design SSE and Spectra	Task 3[2] Limit State	Task 3[2] Capacity	Task 5[2] Limit State	Task 5[2] Capacity
Fermi	0.15g Housner[3]	Failure of biological shield wall	0.39g	Failure of biological shield wall	0.39g
		Failure of basemat in shear and bending	0.45g	Failure of basemat in shear and bending	0.45g
Clinton	0.25g RG 1.60	Liquefaction of soil under basemat	0.83g	Liquefaction of soil under basemat	0.83g
				Failure of wall reinforcing bars and liner	1.0g
Zion	0.17g Housner[3]	Failure by interference between containment and auxiliary buildings	0.75g	Failure of wall reinforcing bars	0.34g
				Failure of wall in transverse shear	0.39g
				Failure by interference between containment and auxiliary buildings	0.75g
				Shear failure at buttress plates	0.75g
Sequoyah	0.18g Housner[3]	Failure of shield building	0.30g	Failure of shield building	0.30g
		Failure of basemat in transverse shear	0.52g	Failure of basemat in transverse shear	>1.0g[4]

1. Capacities are given in terms of peak horizontal ground acceleration, A_H, and time histories consistent with Regulatory Guide 1.60 spectra.
2. The loads considered in Task 3 include dead load, prestress (if applicable), and seismic load. The loads considered in Task 5 include the same loads in Task 3 plus high pressure and temperature corresponding to a severe accident (see Table 1.4).
3. In the frequency range of interest to containment structural response, the Regulatory Guide 1.60 spectra are about a factor of two higher than the Housner spectra (see Figure 2.2). This difference must be accounted for when calculating margins to failure relative to the original design basis.
4. The basemat shear capacity is higher in Task 5 than in Task 3 due to the beneficial effect of compression resulting from thermal loads in Task 5.

1. INTRODUCTION

1.1 Background

The importance of containment structures in minimizing the risk of radiological exposure of the public from a severe accident in a nuclear power plant is well recognized. Especially since the Three Mile Island and Chernobyl accidents, the capacity of containment structures to withstand the loadings beyond the design basis has been a subject of extensive research. However, most of the work to date has focused on the effects of static overpressurization. Integrity of a containment may also be threatened by seismic loads. The general scenario may be one in which the main shock of an earthquake, probably with seismic loads at least 2-3 times that of the Safe Shutdown Earthquake (SSE), damages the containment. Seismic loads from aftershocks could act on the damaged containment, possibly in combination with internal pressure and elevated temperature.

Given these hypothetical conditions, there are at least two ways in which containment performance might be affected by a seismic event.

1. A strong main shock may damage the containment structure causing loss of integrity of the pressure boundary.

2. The containment does not fail under the main shock, but a severe accident progression is initiated due to a component failure. Then an aftershock may occur after the main shock and the combination of pressure and temperature loads with seismic loads could exceed the capability of the pressure boundary. Depending upon the timing of the aftershock, the pressure and temperature caused by a severe accident may be quite different, which could affect the containment seismic capability. Thus consideration of aftershocks in combination with high pressure and temperature becomes important.

In recent years there has been a more concerted effort to understand the response of nuclear facilities, including containment buildings, due to a seismic event. As part of the Systematic Evaluation Program, seismic reviews of a number of older containments were conducted (Reference 1.1-1.4). These investigations only considered earthquakes with peak accelerations at about the SSE level and used very simple models to represent the containment. Under the Seismic Safety Margins Research Program (SSMRP), which included some seismic probabilistic risk assessments, peak accelerations beyond the SSE level were considered, and a number of containment failure modes were conceptualized (References 1.5-1.7). However, the possibility of aftershocks acting in combination with internal pressure and elevated temperature were not considered. Many potentially important failure modes, for instance, penetration failures, were not considered. A number of studies have suggested that the dominant failure modes for containments subject to seismic loads could be associated with soil failures or soil liquefaction (References 1.5, 1.6, 1.8). There is a need for further investigation in this area. This study is a step in that direction.

1.2 Scope of Work

There are a multitude of scenarios involving seismic excitation that could potentially threaten a containment. In addition, every containment building in the U.S. has unique site characteristics and design features. However, in order to gain perspective on the problem, four reference containments, each subject to four different load combinations, have been analyzed. These four containments are Fermi, Clinton, Zion, and Sequoyah, all of which are located in the Eastern United States. The Fermi, Zion and Sequoyah containments are of older design; Clinton is more recent.

Table 1.1 lists the type of these containments, their foundation material, the design SSE level, design response spectra type, and design accident pressure and temperature conditions.

As can be seen from this table, the four containments studied include two steel and two concrete containments, one of reinforced concrete construction and another of post-tensioned construction. The reactor types include BWR Mark I, BWR Mark III, a dry PWR, and a PWR with ice condenser. Two containments are founded on rock and two are on soil foundation. Thus a cross-section of containment, reactor, foundation types is included in the study.

The study was performed under six tasks as follows:

Task 1, Identification of Limit States:

Under this Task the list of limit states to be evaluated for each selected containment was developed. The limit states selected are either directly related to the containment integrity or their realization may lead to conditions under which assurance of containment integrity without further detailed studies or testing cannot be established. Table 1.2 lists the limit states considered and their applicability to the four containments.

Task 2, Development of Methodology and Evaluation Criteria:

Under this Task analytical models and procedures for seismic analysis of the containment were identified. For example, methods for (1) characterizing ground motion, (2) evaluating soil-structure interaction, (3) modeling containment building, (4) evaluating nonlinear response of soil and structure were developed. In addition, explicit criteria for evaluating the identified limit states were also delineated.

Tasks 3 through 6, Containment Evaluations

These four Tasks identified different combinations of pressure and temperature loading for which the seismic capacity of reference containments were evaluated for the defined limit states. These load combinations are summarized in Table 1.3 and they are described as follows:

Task 3. Under this task ambient conditions are assumed in the containment when the main seismic excitation E_m occurs. This represents the occurrence of main shock during the normal operation of the plant.

Task 4. In this Task the design-basis pressure and temperature (P_d, T_d) are assumed acting when the aftershock seismic load E_a occurs. This represents a condition for which the containment does not fail under the main shock, but due to some component failure, an accident is initiated and followed by an aftershock.

Task 5. For this task the aftershock, E_a, is assumed to occur when the pressure and temperature conditions have become more severe due to the progression of the severe accident. Values of T_y for Task 5 were specified by Sandia based on severe accident profiles for different reactors and containments. The values of P_y for Task 5 were determined by analysis of each containment. As specified by Sandia, P_y corresponds to the pressure at which yielding of the containments is imminent for the given value of T_y. The detailed determination of P_y are discussed in Chapters 3, 4, 5, and 6 for separate containments.

Task 6. The pressure and temperature values of Task 6 (P_{AVE}, T_{AVE}) are the average values of those used in Tasks 4 and 5 for each containment. Due to the proximity of P_d and P_y values, Task 6 calculations for Fermi and Sequoyah containments were not conducted.

Table 1.4 summarizes the pressure and temperature values for the four tasks for each of the four containments studied.

1.3 Report Organization

Chapter 2 describes the methodology and criteria for evaluating limit states. Chapters 3, 4, 5, and 6, contain description of containment, application of methodology and the results for Fermi, Clinton, Zion, and Sequoyah containments, respectively. For Task 3 the Clinton containment has additionally been evaluated using a 3-D finite element model that considers cracking and crushing of concrete and yielding of reinforcement as quasi-static loading is applied to the system. This information is summarized in Chapter 7.

It should be noted that this is a scoping study to gain a better perspective on the subject of containment seismic capacity. Of necessity, many assumptions and engineering judgments were made throughout the study. Bases for such judgment and assumptions are generally stated throughout the report. These assumptions and uncertainties in the analytical modeling and procedures and their potential impact on the results are further discussed in Chapter 8. Chapter 9 contains overall conclusions of the study and recommendations for future work.

Appendices A and B describe certain referenced items in the text in more detail. Appendix C contains a summary of seismic responses for various containments. Appendix D contains flow charts of various analyses performed for each containment, and identifies computer programs that were used. Appendix E contains a brief description of various computer programs that were utilized in this study.

1.4 REFERENCES

1.1 Murray, R. C., Nelson, T. A., Ng, D. S., Liaw, C. Y., and Stevenson, J. D., "Seismic Review of Robert E. Ginna Nuclear Power Plant as Part of the Systematic Evaluation Program," NUREG/CR-1821, UCRL-53014, Lawrence Livermore Laboratory, Livermore, CA, December 1980.

1.2 Nelson, T. A., Murray, R. C., Wesley, D. A., and Stevenson, J. D., "Seismic Review of Palisades Nuclear Power Plant Unit 1 as Part of the Systematic Evaluation Program," NUREG/CR-1833, UCRL-53015, Lawrence Livermore Laboratory, Livermore, CA, January 1981.

1.3 Murray, R. C., Nelson, T. A., Ma, S. M., and Stevenson, J. D., "Seismic Review of Oyster Creek Nuclear Power Plant as Part of the Systematic Evaluation Program," NUREG/CR-1981, UCRL-53018, Lawrence Livermore Laboratory, Livermore, CA, April 1981.

1.4 Nelson, T. A., Murray, R. C., Liaw, C. Y., Wesley, D. A., and Stevenson, J. D., "Seismic Review of Millstone 1 Nuclear Power Plant as Part of the Systematic Evaluation Program," NUREG/CR-2024, UCRL-53022, Lawrence Livermore Laboratory, Livermore, CA, July 1981.

1.5 Campbell, R D. and Wesley, D. A., "Potential Seismic Structural Failure Modes Associated with the Zion Nuclear Plant," NUREG/CR-1704, UCRL-15140, Lawrence Livermore Laboratory, Livermore, CA, March 1981.

1.6 Shieh, L. C., Johnson, J. J., Wells, J. E., Chen, J. C., and Smith, P. D., "Simplified Seismic Probabilistic Risk Assessment: Procedures and Limitations," NUREG/CR-4331, UCRL-20468, Lawrence Livermore Laboratory, Livermore, CA, August 1985.

1.7 Budnitz, R. J., et al., "An Approach to the Quantification of Seismic Margins in Nuclear Power Plants," NUREG/CR-4334, UCRL-20444, Lawrence Livermore Laboratory, Livermore, CA, August 1985.

1.8 Proceedings: EPRI/NRC Workshop of Nuclear Power Plant Reevaluation to Quantify Seismic Margins, EPRI NP-4101-SR, Electric Power Research Institute, Palo Alto, CA, August 1985.

Table 1.1
List of Containments Evaluated

Containment	Type	Design Parameters SSE Foundation	Spectra (g)	Type	Pressure (psig)	Temp. (^{o}F)
Fermi	BWR, Mark I, Steel	Rock	0.15	Housner	56.0	281
Clinton	BWR, Mark III, Reinforced Concrete	Soil	0.25	RG 1.60	15.0	185
Zion	PWR, Dry, Prestressed Concrete	Soil	0.17	Housner	47.0	271
Sequoyah	PWR, Ice Condenser, Steel	Rock	0.18	Housner	10.8	220

Table 1.2
Limit States Considered and Their
Applicability to Containments

Code	Description	Containment			
		Fermi	Clinton	Zion	Sequoyah
1	Tensile Failure of Steel Liner	NA*	Yes	Yes	Yes**
2	Failure of Reinforcing Bars	Yes	Yes	Yes	Yes
3	Failure of Prestressing Tendons	NA	NA	Yes	NA
4	Tensile Failure of Steel Containment Shell	Yes	NA	NA	Yes
5	Buckling of Steel Containment Shell	Yes	NA	NA	Yes
6	Transverse Shear Failure in Wall/ Basemat	Yes	Yes	Yes	Yes
7	Through-Wall Crushing of Concrete	NA	Yes	Yes	NA
8	Penetration Failure in Concrete Containment	NA	Yes	Yes	NA
9	Failure of Pretensioned Bolted Connections at Equipment Hatch and Drywell Head	Yes	Yes	Yes	Yes
10	Shear Failure at Buttress Plate	NA	NA	Yes	NA
11	Failure of Containment Shell at Beam Seats or Ice Chest Supports	Yes	NA	NA	Yes
12	Failure of Suppression Chamber Supports	Yes	NA	NA	NA

Table 1.2
Limit States Considered and Their
Applicability to Containments (cont'd)

Code	Description	Containment			
		Fermi	Clinton	Zion	Sequoyah
13	Bearing Failure of Foundations	Yes	Yes	Yes	Yes
14	Failure Due to Sliding of Containment	No***	No	Yes	No
15	Liquefaction of Foundation Soil	No	Yes	No	No
16	In-Plane Shear Failure of Walls Adjacent to Containment	Yes	No	No	Yes

* NA = Condition does not exist; therefore, not applicable.
** Applies to basemat and other concrete structures
*** No = Limit state ruled out from general considerations.

Table 1.3
Load Combinations

Task	Combination
3	$0 + E_m$
4	$0 + P_d + T_d + E_a$
5	$0 + P_y + T_y + E_a$
6	$0 + P_{AVE} + T_{AVE} + E_a$

E_m = main shock seismic load

E_a = aftershock seismic load

0 = gravity and other static loads based on containment type, e.g., prestressing load in Zion

P_d, T_d = Design accident pressure and temperature, respectively

P_y, T_y = Yield pressure and temperature, respectively

P_{AVE} = $1/2\ (P_d + P_y)$; $T_{AVE} = 1/2\ (T_d + T_y)$

Table 1.4
Pressure and Temperature Values Used for Four Tasks

Containment	Task 3 Pressure (PSIG)	Task 3 Temp (°F)	Task 4 Pressure (PSIG)	Task 4 Temp (°F)	Task 5 Pressure (PSIG)	Task 5 Temp (°F)	Task 6 Pressure (PSIG)	Task 6 Temp (°F)
FERMI	0	150	56.0	281	74	550	NA	NA
CLINTON	0	104	15.0	185	45	400	30	300
ZION	0	120	47.0	271	93	360	70	316
SEQUOYAH	0	120	10.8	220	24.8	360	NA	NA

NA = not evaluated because of proximity of Tasks 4 and 5 pressure values

2. METHODOLOGY

2.0 General

The evaluation of seismic capacity when the containment is under pressure and thermal loads involved a number of basic steps. These steps are described in Section 2.1 for the general condition of a containment founded on soil. Section 2.2 summarizes the evaluation criteria for the sixteen limit states that are given in Table 1.2.

2.1 Basic Steps in Seismic Capacity Evaluation

Six basic steps were utilized in determining, by iteration, the peak horizontal ground acceleration, A_H, that causes failure in one of the limit states for a given containment under specified pressure and thermal loads (P, T). These steps are summarized in Figure 2.1 and they are described in Sections 2.1.1 through 2.1.6.

2.1.1 Characterization of Ground Motion for a Prescribed A_H (Step 1)

The nonlinear analyses performed in this study for the containment seismic capacity evaluation require an acceleration time history to represent earthquake input to the seismic models. While there are many recorded acceleration time histories available from strong motion earthquake databank, each of these time histories has different frequency content, as shown by their response spectra. Use of time histories recorded from one earthquake would not be representative of other earthquakes, and use of an ensemble of time histories for all the analyses would be cost-prohibitive. Therefore, use of a synthetic time history, which yields an acceptable and representative response spectrum, was considered as appropriate. Synthetic time histories are commonly used in the seismic analysis of nuclear power plants for the same reasons as explained here.

The next question is the choice of an appropriate response spectrum. Since its issue in 1973, NRC Regulatory Guide 1.60 spectra for horizontal and vertical ground motions have been widely used for nuclear power plant design. The use of ground motions derived from NRC Regulatory Guide 1.60 spectra was seen as a convenient means to extend the results obtained from the present study to other plants. Primarily based on this consideration, and also due to the fact that there is a lack of generally accepted data to consider different frequency characteristics other than the broad-band spectra of Regulatory Guide 1.60 for the high magnitude earthquakes being considered in this study, the ground motions used in this study are based on Regulatory Guide 1.60 spectra.

It should be noted that Regulatory Guide 1.60 response spectra for both horizontal and vertical directions are anchored to the peak horizontal ground acceleration. Thus, the peak horizontal ground acceleration, A_H, and use of Regulatory Guide 1.60 completely define the horizontal and vertical response spectra. Thus, it is possible to define the containment seismic capacities in terms of A_H only.

It is also recognized here that the duration of a high magnitude earthquake may be much longer than a smaller earthquake, but since the evaluations were done using peak responses without considering stiffness degradation, durations longer than 10 seconds were not of concern except for liquefaction evaluation, where it was appropriately considered by using proper number of stress cycles. Evaluations with the generated records of 10 second duration showed that maximum responses occur within the first 6 seconds of the records; therefore, most results have been obtained using the first 6 seconds of the records.

As shown in Table 1.1, Regulatory Guide 1.60 response spectra were used as design-basis only for the Clinton containment. The other three containments in this study, i.e., Fermi, Zion, and Sequoyah, because of their earlier vintage of construction, used Housner response spectra as the design-basis. A comparison of Housner and Regulatory Guide 1.60 horizontal response spectra is shown in Figure 2.2 for a reference ground acceleration of 0.15g at 5% damping. It can be seen from this figure that the use of Regulatory Guide 1.60 spectrum provides a significant conservatism over the design-basis for Fermi, Zion and Sequoyah.

In the analysis of the seismic models of containments, three components of earthquake motion, i.e., two horizontal and one vertical, must be considered to act simultaneously. For the axisymmetric containment structures being analyzed in this study, however, the maximum responses due to the two equal horizontal components are the same in magnitude, but they occur at different locations. Based on this, the containments were analyzed for simultaneous action of one horizontal and one vertical time-history. The effect of the other horizontal component was factored into the containment evaluation, as explained in Section 2.1.6.

The following procedure was used to obtain the two acceleration time histories required for making containment evaluations. Two statistically independent ground motion time histories, $\ddot{x}_o(t)$ for horizontal and $\ddot{y}_o$ for vertical, were generated such that their 5% damped spectra are consistent with the 5% damped spectra of Regulatory Guide 1.60. Sargent & Lundy's proprietary computer program RSG was used for this purpose. Figures 2.3 and 2.4 show the time histories for $\ddot{x}_o(t)$ and $\ddot{y}_o(t)$. The corresponding 5% damped spectra are compared to the Regulatory Guide 1.60 spectra in Figures 2.5 and 2.6, respectively. The comparison in Figures 2.5 and 2.6 is for an A_H value of 0.25g. As can be seen from these comparisons, the time histories used give conservative response spectra with respect to the Regulatory Guide 1.60 spectra for frequencies higher than 1 Hz. To obtain motions for other values of A_H, the motions $\ddot{x}_o(t)$ and $\ddot{y}_o$ are modified as follows:

$$\ddot{x}(t, A_H) = \frac{A_H}{0.25} \ddot{x}_o(t) \qquad (2.1a)$$

$$\ddot{y}(t, A_H) = \frac{A_H}{0.25} \ddot{y}_o(t) \qquad (2.1b)$$

The use of Equations (2.1) implies that seismic capacity, when stated in terms of A_H, refers to ground motions having free field peak surface acceleration of A_H and frequency characteristics of spectra in Regulatory Guide 1.60.

2.1.2 Generation of Foundation Spring and Dashpot Constants for A_H (Step 2)

The dynamic response of the containment buildings is computed using a time-history analysis in order to consider nonlinear effects such as foundation uplift and/or material yielding. Because nonlinear structural responses were evaluated, the foundation spring and dashpot constants used were considered not to depend on frequency; considering frequency dependent foundation parameters requires a linear system response. The analysis, however, considered the dependency of soil parameters (shear modulus and damping) on the maximum soil strain level that, in turn, depends on the A_H value being considered in the analysis. To include the effect of this strain dependency of soil, a soil column was first subjected to a deconvolution study using the horizontal time history in Equation (2.1a) and appropriate shear moduli of soil layers were thus determined. The computer program SHAKE was used for this evaluation.

After computing the strain-compatible shear moduli and damping values in various soil layers, the next step was to determine frequency independent foundation spring and dashpot constants. These constants could have been determined using elastic half-space equations, or by developing frequency-dependent impedance functions and choosing the constants at appropriate frequencies from there. For simplicity, elastic half space equations were used in this study, with weighted average values of soil shear moduli in various layers representing the shear modulus of the half-space. This approach is described below. A discussion on the uncertainty introduced due to the use of this method to account for soil-structure interaction is included in Chapter 8.

Let $G_i\ (A_H)$ denote the strain-compatible shear modulus of layer i which is of thickness h_i. The weighted average of shear moduli with respect to thickness was used to define an effective shear modulus for all soil layers. Therefore,

$$\bar{G}\ (A_H) = \frac{\Sigma G_i\ (A_H)\ h_i}{\Sigma_i\ h_i} \qquad (2.2)$$

Results from Equation (2.2) were used in elastic half-space equations, Reference 2.1, to determine the horizontal, vertical, and rocking soil spring and dashpot constants as follows:

$$K_x\ (A_H) = \frac{32\ (1 - \bar{\nu})\ \bar{G}\ R}{7 - 8\ \bar{\nu}} \qquad (2.3)$$

$$C_x (A_H) = 0.576 K_x R \sqrt{\frac{\bar{\rho}}{\bar{G}}} \quad (2.4)$$

$$K_y (A_H) = \frac{4 \bar{G} R}{1-\bar{\nu}} \quad (2.5)$$

$$C_y (A_H) = 0.85 K_y R \sqrt{\frac{\bar{\rho}}{\bar{G}}} \quad (2.6)$$

$$K_\phi (A_H) = \frac{8\bar{G} R^3}{3(1-\bar{\nu})} \quad (2.7)$$

$$C_\phi (A_H) = \frac{0.30}{1 + B_\phi} K_\phi R \sqrt{\frac{\bar{\rho}}{\bar{G}}} \quad (2.8)$$

where

$$B_\phi = \frac{3 (1 - \bar{\nu}) I_o}{8 \bar{\rho} R^5} \quad (2.9)$$

In these equations

K_x, K_y, K_ϕ = foundation spring constants in horizontal, vertical, and rocking directions, respectively.

$C_x, C_y, C\phi$ = foundation dashpot constants in horizontal, vertical, and rocking direction, respectively.

R = $\sqrt{\frac{A_f}{\pi}}$ = Equivalent radius of foundation with A_f denoting the area of the foundation in seismic analytical model.

I_o = total mass moment of inertia of structure and basemat, in the seismic model, about the rocking axis at the base.

$\bar{\nu}$ = average Poisson's ratio, averaged with respect to thickness of soil layers.

$\bar{\rho}$ = average mass density, averaged with respect to thickness of soil layers.

If a containment is directly built on rock, the foundation shear modulus does not depend on A_H and the strain independent shear modulus of the rock was used in Equations (2.3) through (2.8) to obtain the relevant values of foundation spring and dashpot constants.

2.1.3 Factoring Effects of Pressure, Temperature, and Initial Earthquake on Subsequent Dynamic Analysis (Step 3)

In the dynamic analysis model, the containment shell was represented as a vertical beam with lumped masses. Idealization of containment shell structures, which typically have height to radius ratios greater than one, as a beam for seismic analysis purposes is considered reasonable (Reference 2.2). The beam element between adjacent mass points was assumed to be elastic. Hysteretic yielding was allowed to occur only at the ends of these beams. For each beam element a bilinear moment-curvature (M-Ø) diagram, which applies to both ends of the beam, was derived.

The effects of pressure, temperature, and other loads were considered in the analysis by appropriately modifying the construction of M-Ø diagrams. In concrete containments, the liner is the only steel element in a biaxial state of stress. However, when the meridional tensile strain at the wall exceeds the yielding point of reinforcing bars, the contribution of liner to the total meridional tensile force is typically less than 15% for the concrete containments studied. Therefore, the construction of the M-Ø diagrams for concrete containments did not consider the effects of biaxial stress. However, the effect of biaxiality was considered for steel containments. For this reason, the factoring of pressure and temperature loads is discussed separately for concrete and steel containments in this subsection.

Factoring the effect of initial earthquake on subsequent dynamic analysis is also separately discussed for concrete and steel containments.

Effect of Pressure and Temperature

a. Concrete Containments

Effects of P and T were considered in the dynamic analysis by factoring the meridional strain induced by these loads, ε_{p+T}, into the moment-curvature (M-Ø) diagram of a typical containment beam element. Figure 2.7 illustrates this aspect of the analysis for a containment beam element ij of length l.

For appropriate values of P and T, first an axisymmetric shell analysis of the containment was made to determine values of meridional strain ε_{p+T} at various elevations in the containment. This analysis was done with S&L Program DYNAX or by hand calculations. The evaluation includes effects of cracking in concrete.

Continuing with the description of the M-Ø calculation, the beam element in Figure 2.7a was assumed to have, at both ends, the same bilinear-hysteretic moment curvature diagram shown in Figure 2.7f. Consider a reinforced concrete containment. The beam ij, was assumed to have a tubular section of constant thickness t and mean diameter d_m, Figure 2.7b. Several types of meridional steel, having

area per length of circumference A_{sk}, k = 1, 2, 3 are shown in Figure 2.7b. The stress-strain diagram of each of these steels is elasto-plastic with yield strength f_{yk} for steel type k, Figure 2.7d. The moment curvature diagram was constructed by assuming a linear strain distribution across the diameter of the tubular section, Figure 2.7c and using stress-strain diagrams of the steel elements and concrete to determine value of moment at the section for an assumed curvature $\emptyset = 1/x$ in Figure 2.7c. The resulting M-$\emptyset$ diagram was then approximated by a bilinear curve, Figure 2.7f. In the M-$\emptyset$ calculations, the stress-strain diagram used for concrete (Figure 2.7e) assumes a zero tension capacity in meridional direction. It also assumes that concrete compressive strength is the same as the strength in uniaxial compression. The reason for making these assumptions was as follows: If peak ground acceleration is such that overall seismic moment on the containment is not expected to exceed the cracking moment of concrete, gross concrete section properties can be used and no consideration of cracking is then necessary for M-$\emptyset$ calculations, i.e., relations for an uncracked tube of concrete is used. For values of A_H that could cause concrete cracking, during the entire time history, concrete is assumed to have zero tension capacity and the M-$\emptyset$ diagram constructed on the basis of Figure 2.7 applies. The reason for not reducing concrete crushing strength below f_c' is the level of hoop strains that are expected to occur for the studies of this report. Based on data in Reference 2.9, when hoop tension strain is of the order of yield strain of hoop rebars, reduction in crushing strength from f_c' is 15% or less. Even in Task 5 condition, the level of hoop strain, primarily caused by pressure, will be limited to yield strain in this report. Therefore, assuming no reduction in f_c' is reasonable.

When P=T=0 (Task 3), in stress-strain diagram of Figure 2.7d, $\varepsilon_{p+T} = 0$ and the values of f_{yk} are used in the M-$\emptyset$ calculations. When ε_{p+T} is greater than zero (Tasks 4, 5, and 6), the origin of stress-strain diagram is shifted to the position marked ε_{p+T} in Figure 2.7d and the applicable yield strength for M-$\emptyset$ calculations becomes f^*_{yk} rather than f_{yk}.

For a post-tensioned concrete containment, the effect of post-tensioning is also considered in the construction of the M-$\emptyset$ diagram. When prestressing is not expected to be overcome by seismic load, elastic concrete properties are used in defining the M-$\emptyset$ diagram, i.e. procedure of Figure 2.7 is not required. If prestressing is expected to be overcome at least once during the excitation, construction of Figure 2.7 is used with ε_{p+T} which also includes effect of prestressing.

b. Steel Containments

For a steel containment, construction of the M-$\emptyset$ diagrams is similar to Figure 2.7 except that concrete is absent and only one type of steel exists. The construction of the stress-strain diagram of Figure 2.7d for this steel, however, must consider the effect of

temperature on reducing the material yield strength, the effect of stresses produced by axisymmetric loads, and the effect of the biaxial stress condition in the shell due to seismic loads. Figure 2.8 shows the process of modifying the stress-strain diagram to consider the effect of biaxiality.

Generally, shear stresses produced by seismic loads in steel containments are small. For example, for the Fermi containment when $A_H = 0.6g$, the maximum shear stress is about 5.5 ksi. Accordingly, it is assumed that meridional stress, σ_m, and hoop stress, σ_h, are the principal stresses. The first step towards constructing stress-strain diagram is then to determine the ratios of σ_h/σ_m along the height of the containment shell. For simplicity, this is done by applying a constant static lateral loading, representing the seismic loads along the height of the containment, and determining σ_h and σ_m due to this loading. Through a study of ratio $\alpha = \sigma_h/\sigma_m$ along the height of the containment shell, the containment is divided into several elevation zones. Each zone is identified by a constant value of α that applies to that zone.

Figure 2.8 shows the procedure for determining the steel stress-strain diagram for each zone. Figure 2.8a shows the Tresca yield condition and the way this is used to define effective meridional yield stresses σ_y^+ and σ_y^- in tension and compression, respectively. In Figure 2.8a f_y (T) is the material yield strength applicable at temperature T. Point A with stress coordinates σ_m (P+T) and σ_h(P+T) shows state of stress at the zone caused by pressure and temperature load in meridional and hoop directions, respectively. To obtain values of σ_y^+ and σ_y^-, a linear seismic load path with slope α, passing through point A is constructed. The intersection points of this line with the yield criteria define values of σ_y^+ and σ_y^-.

The stress-strain diagram, to be used in place of that shown in Figure 2.7d, is shown in Figure 2.8b. In Figure 2.8b the center of stress-strain diagram for M-Ø construction is at σ_m(P+T) and effective yield values in tension and compression are $f_y^+ = [\sigma_y^+ - \sigma_m(P+T)]$ and $f_y^- = [\sigma_y^- (P+T) - \sigma_m(P+T)]$. The modulus of elasticity remains the value applicable to steel at the temperature being considered, i.e., E(T). The M-Ø diagram for the circular cross-section is thus constructed for each containment beam element.

The procedure described above considers the occurrence of yielding in the containment beams appropriately. The deformation in the plastic zone is, however, approximated because flow rules are not employed and two-dimensional stress state is approximated by a one-dimensional stress situation. While the approximation is considered reasonable for the purposes of the scoping study being conducted here, some future confirmatory studies--even under quasistatic loading--may be appropriate.

Effect of Damage from Initial Earthquake

In Tasks 4 through 6, the effect of damage from the initial earthquake is to be factored in. The initial earthquake level to be considered for this purpose has been set, by judgment, to be the average value of the seismic capacity of Task 3 and the seismic level at which yielding in the containment occurs. The damage caused by this initial earthquake is factored into the analysis using the following considerations:

a. Concrete Containment Wall

If the intensity of the initial earthquake is such that diagonal cracks are expected in certain portions along the height of the wall, shear modulus appropriate to cracked sections is used for these heights in the analysis for any level of aftershock. Cracked shear modulus values used for various containments are discussed in Appendix A.

Additionally, the effect of any concrete spalling that results from the initial earthquake is also included. This step proceeds as follows. The depth of the region of spalling in the wall is calculated by determining the zone in the wall in which compressive concrete strain exceeds 0.2%, assuming a linear distribution of strain through the wall thickness. For subsequent analyses, the spalled portion of concrete, which is assumed to exist in a ring along the circumference of the containment, is ignored in stiffness and strength evaluations. However, the rebars in this region are assumed to provide resistance in tension. The basis for 0.2% strain above is that in tests of concrete cylinders or columns under concentric compression, load begins to drop at a strain of about 0.2%; see, for example, Reference 2.11.

b. Steel Elements

The effect of initial earthquake on the stiffness properties of steel elements is considered small and it is ignored. The depletion of ductility limit, however, may be significant. For steel elements where strains go beyond yield strain, the maximum permanent set is estimated and deducted from limiting strain values given in Sections 2.2.1, 2.2.2 and 2.2.4.

2.1.4 Overall Seismic Analysis Model (Step 4)

Figures 2.9 and 2.10 show typical seismic analysis models. The principal features of these models are described below:

a. Different vertical beams are used to represent the containment building, containment internal structures and other buildings which, with containment, rest on a common basemat. In Figure 2.9 for Fermi, for example, there are five vertical beam branches representing the reactor building, the concrete biological shield wall, the steel containment, the reactor pressure vessel, and the sacrificial shield. Horizontal truss type members are used to

connect beam elements where positive connection between vertical beam nodes exists. If nodes of two beams at the same elevation are not physically connected but their relative motion is of interest, a very soft horizontal truss element is used to conveniently monitor such interferences; the element from node 10 to 17 in Figure 2.10, is an example.

b. The basemat is modeled by horizontal beam elements to which foundation springs and dashpots are attached; see horizontal beam elements from node 7 to 8 in Figure 2.9 and from node 38 to 64 in Figure 2.10, as examples.

c. In the containment building vertical walls stiffen the basemat against bending. This effect is simulated by considering fictitious horizontal girders, such as the girders connecting nodes 1-9-16-13-4 in Figure 2.9. In this situation, the total base moment of the reactor building in the beam element 21 - 16 is transferred to the stiff horizontal girder at node 16 and the vertical truss members 1-7. 9-14, 13-15 and 4-8 transfer the moment load to the basemat nodes. These vertical truss members are selected at locations of major shear walls and column lines in the reactor building.

d. The horizontal shear load of buildings is transferred to the basemat by fictitious inclined truss members connecting the base of the vertical beams at horizontal girder to the basemat nodes; see elements 16-7, 16-14, 16-15, and 16-8 in Figure 2.9.

e. Masses are concentrated at vertical beam building nodes and on the horizontal beam nodes which represent the basemat. The horizontal fictitious girder(s) are massless.

f. As discussed in Section 2.1.3, at the ends of beam elements representing the containment building, bilinear-hysteretic hinges have been provided to consider the effects of yielding in the vertical direction due to seismic moments. The effect of pressure on these elements is also included. The beam section between the end plastic hinge locations, as well as beam elements in other vertical beams representing various concrete buildings and the basemat beams, are treated as elastic with moment of inertia equal to the average of cracked and uncracked section properties. Normal area used for these elements varies from about 0.7 to 1.0 times the uncracked concrete area. In the stiffness calculation the parameters $E_c I$ or $E_c A$ are calculated using above values of moment of inertia I, or area A, and the modulus of elasticity E_c computed from Equation (2.10).

$$E_c = 57000 \sqrt{f'_c} \qquad (2.10)$$

in which

E_c = modulus of elasticity of concrete, psi

f'_c = 28-day cylinder strength of concrete modified for 5-year aging, psi

The concrete shear modulus G_c is calculated from

$$G_c = \frac{E_c}{2(1 + \nu_c)} \qquad (2.11)$$

where

ν_c = Poisson's ratio for concrete = 0.17

For shear stiffness calculation of the vertical beam elements representing the containment wall, the effect of cracking on reducing the shear modulus is considered by appropriately reducing the shear area as discussed in Appendix A.

For other concrete beam elements in the seismic model, the effect of reduction in shear stiffness is considered similarly; however, the reduction factors vary from those listed for the containment wall in Appendix A. These factors differ for different parts of the model and were determined using the approach in Appendix A and the analyst's best judgment on the nature of tension or compression which should be considered acting in the vertical direction. A discussion on the uncertainties related to the choice of these parameters is included in Chapter 8.

g. In the seismic models springs and dashpots are attached to the basemat nodes; see Figure 2.9 (the dashpots are not explicitly shown in this figure for clarity) for example. The constants for these elements were determined using Equations (2.3) through (2.8); a uniform distribution of parameters with respect to basemat area was assumed.

For all containments, the effect of foundation uplift during seismic excitation is considered. This consideration requires using one-way vertical springs and dashpots. Figure 2.11 shows the behavior of spring and dashpot forces that are attached in the vertical direction to a basemat node. When a basemat node moves upward relative to ground beyond a certain value v_{t1}, herein referred to as limiting tensile displacement, the tensile spring force remains constant at F_{t1}, see Figure 2.11. During unloading, the spring force is again constant at F_{t1} until relative displacement becomes less than v_{t1}. For relative displacements less than v_{t1}, a linear behavior is assumed. The value of v_{t1} is determined for each spring from

$$v_{t1} = \frac{F_{t1}}{k} \qquad (2.12)$$

where

k = spring constant of vertical spring

F_{tl} = tensile limit for a spring

Within the values of F_{tl} specified for a nodal spring, the effect of downward friction forces acting on basement walls as well as adhesion between basemat and rock are considered. The highest value used for this adhesion is 20 psi for rock foundations and only 1 psi for soil foundations. The tensile strength across concrete construction joints well exceeds 100 psi (References 2.12 and 2.13). The adhesion of concrete to rock is similar to the adhesion of concrete to concrete; therefore, the use of 20 psi adhesion for rock foundations is conservative. For values of A_H greater than the value for which adhesion is overcome, the contribution of adhesion to F_{tl} is considered negligibly small.

The vertical dashpot force acting in parallel with a one-way spring is calculated as

$$F_{Dashpot} = \begin{cases} c\dot{v}, & v \leq v_{tl} \\ 0, & v > v_{tl} \end{cases} \qquad (2.13)$$

in which c is the dashpot constant and v and $\dot{v}$ are the vertical basemat node displacement and velocity relative to the ground.

2.1.5 Calculation of Dynamic Response (Step 5)

Time history analysis of the seismic models is conducted using a step-by-step integration procedure. For a selected value of A_H, time histories of horizontal and vertical acceleration are applied at the support points of boundary springs and dashpots simultaneously. The solution is calculated using S&L Program NONLIN 2. This program uses an incremental approach to integrate the equations of motion. In addition to the foundation dashpots, a damping matrix,

$$[C] = \alpha[M] + \beta[K] \qquad (2.14)$$

is included in the analysis to represent the structural damping. The constants α and β were chosen in such a manner that, for elastic response, an equivalent modal damping of 4% to 10% resulted for the predominant structural modes.

2.1.6 Assessment of Containment at A_H (Step 6)

For the containment and load combination under consideration, the applicable limit states of Table 1.2 are evaluated using the peak seismic forces determined from peak accelerations of the analysis of Section 2.1.5 and the effects of other forces in the load combination. The evaluation criteria are described in Section 2.2.

For each limit state under consideration, the capacity margin factor is the ratio

$$m = \frac{\text{Capacity according to failure criterion applicable to limit state}}{\text{Load effect for load combination applicable to the task}} \qquad (2.15)$$

Details of evaluating limit states and calculating capacity margin factors are described in Chapters 3 through 6 for the four containments. It should be noted that basically these evaluations require combining effects from dead load, prestressing, pressure, temperature and peak seismic loads. For limit states which require shell analysis, the analyses are performed for each load separately and then results are combined. For concrete containments, these analyses were performed using program DYNAX. In this application of DYNAX, however, the effect of concrete cracking was not considered because DYNAX can consider cracking only for axisymmetric loads and seismic loads are not axisymmetric. The shell element forces thus derived were combined in the S&L program TEMCO. TEMCO considers effects of concrete cracking and steel yielding at the element level for the combined element shell forces. In this manner, strains in liner, reinforcing steel, and concrete were evaluated.

The TEMCO evaluation also considered the effect of the hc tal earthquake component not included in the plane-frame seismi- sis. This effect was considered by including in the shell an orthogonal horizontal load with intensity equal to 0. the horizontal load determined through time history analysis. se of 0.4 factor represents a good approximation of the square ro ne sum of squares rule; see Reference 2.2.

The approximation of linearly combining different load effects to obtain total response for nonlinear systems considered in this report is recognized. In order to assess the effect of this approximation, further studies were made on the Clinton containment only. For this containment, effects of concrete cracking and rebar and liner yielding were considered on the system level by applying peak seismic loads in sequence with dead load to a finite element model of the containment. This quasi-static incremental analysis utilized Program ADINA. Results of this evaluation are discussed in Chapter 7.

For steel containments, peak seismic and other loads were applied to an axisymmetric model of the containment vessel using CBI program E0778A.

Finally, at the conclusion of assessment of Step 6, if for the value of A_H being evaluated, sufficient margin is demonstrated against the limit states of interest, capacity at this A_H is not reached. Seismic level is then increased by increasing A_H and repeating the six-step evaluation until the margin at some A_H becomes 1.0, which defines realization of the limit state being evaluated.

2.2 Criteria for Evaluation of Limit States

In establishing the criteria for evaluation of limit states listed in Table 1.2, the prevailing philosophy was that the analysis being performed should predict, with a reasonable degree of confidence, the levels of A_H up to which the containment, although approaching its limits, would not actually fail. Obviously, this study being a scoping study to evaluate containment seismic capacity, containment behavior in the nonlinear range is evaluated. However, no attempt has been made to extensively probe the actual limits of containment capacity before actual failure. In general, somewhat conservative evaluation criteria have been established for various limit states. Since the basic purpose of this study is to get a perspective on containment behavior under strong seismic loading and to identify any potential weak links, this somewhat conservative approach is considered appropriate. Thus it is important to note that the seismic capacities reported from this study should not really be taken as the earthquake level at which containments will actually fail. Our collective judgment is that there is still margin left beyond the capacities identified in this report. Some of the reasons for this judgment are discussed in Chapter 8. Probing the limits of this additional margin will take more extensive analysis and/or testing, which is beyond the scope of this study. The conservative approach described in this paragraph is consistent with other studies of seismic margin of nuclear power plant structures and components. Indeed, the approach taken in this study can be viewed as the Conservative Deterministic Failure Margin (CDFM) method of determining High Confidence of Low Probability of Failure (HCLPF) seismic capacity of containments.

Table 2.1 lists the strain-, stress-, or force-based evaluation criteria used to define realization of the sixteen limit states shown in Table 1.2. The use of word "failure" in these two tables should be understood in the context of the discussion provided in the above paragraph. A discussion of the criteria given in Table 2.1 is provided in the following subsections.

2.2.1 Failure of Steel Liner

The criterion shown in Table 2.1 for evaluating failure of a steel liner is based on the results of a post-test analysis of 1:8 scale steel containment model pressurized to failure (Reference 2.3). This analysis showed surface principal strain of 3% at locations away from the point of discontinuity at which failure occurred. Also, at these locations, bending strains were insignificant. Therefore, the surface strain can be interpreted as membrane strains. At failure point, calculated failure strain was about 15%. Since within the scope of our analysis it is not possible to account for non-axisymmetric features and local strain intensifications and our evaluated strains will be overall strains, it is reasonable to use 3% as the limit for mid-thickness strain. However, because of additional uncertainties, a slightly more conservative limit of 2% for mid-thickness strain for this study was selected. Since selection of this failure criterion, preliminary results from the high pressure test on 1:6 scale reinforced concrete

containment model have become available (Reference 2.10). In this model, the liner is attached to concrete with studs. The free-field liner strains at failure varied from about 1.1% to 2.3%. Based on this information the failure criterion of 2% for membrane strain in liner in Table 2.1 is described as being close rather than as conservative.

The ratio of allowable combined strain to allowable membrane strain in ASME Section III, Division 2, Table CC-3720-1 is about 3. Using this information and the selected mid-thickness strain limit of 2%, the limit for surface strain is determined as 6%.

These criteria are intended for checking a containment liner at regions of high containment shell forces including tangential shear.

2.2.2 Failure of Reinforcing Bars

The limit of 10 for the ratio of rebar strain to its yield strain, shown in Table 2.1, can be inferred from the maximum limit permitted for plastic hinge rotation in reinforced concrete beams and slabs. Based on the interpretation of test results, the limit of plastic hinge rotation, in radians, can be expressed as (References 2.4 and 2.5)

$$\phi l_p \leq 0.0065 \left(\frac{d}{c}\right) \text{ but not more than } 0.07 \qquad (2.16)$$

where

ϕ = curvature ductility
l_p = plastic hinge length
d = distance from compression face to tensile reinforcement
c = distance from compression face to neutral axis considering tension and compression reinforcements

Using crushing strain value of 0.003 for concrete in reinforced concrete beams, and $\ell_p = 2d$, it can be shown that for the walls of concrete containments in this study the ratio of rebar strain to its yield strain exceeds 10. Therefore, it is reasonable to use a limit of 10 for this ratio. Since the upper limits for plastic hinge rotation noted above are regarded as conservative, it is our judgment that use of 10 X yield strain in Table 2.1 is also conservative.

This criterion is intended for checking containment at regions of high tangential shear, bending, membrane plus bending, and also for checking local effects at points of interference with adjacent structures.

2.2.3 Failure of Prestressing Tendons

For tendons, the difference between yield and ultimate strains, based on applicable stress-strain diagrams, is relatively small compared to similar differences for reinforcing bars and liner steel. Therefore, limiting the tendon strain to the yield strain is reasonable, as shown in Table 2.1.

2.2.4 Tensile Failure of Steel Containment Shell

The criterion for the tensile failure of the steel containment shell is the same as the criterion for steel liner. Based on the discussion of the 1:8 scale steel containment tests given in Section 2.2.1, the selected limits are considered as conservative. This criterion is intended for checking the containment shell for high membrane tension and bending plus tension at points of embedment to concrete, cylinder to bottom liner transition, or at penetrations.

2.2.5 Buckling of Steel Containment Shell

The use of ASME Code Case N-284 in Table 2.1 is conservative even when a factor of safety of 1.0 is used. This conservatism results from the fact that the knockdown factors used are based on the maximum imperfections which are permitted in the ASME code. The stiffening effect of orthogonal tension, and a modification in the theoretical elastic buckling stress using BOSOR computer program was included for Fermi containment evaluation, as discussed in Chapter 3 and Appendix B.

2.2.6 Transverse Shear Failure in Containment Wall/Basemat

For a wall, if shear capacity is exceeded, subsequent cycles of seismic loading could lead to rebar and liner buckling. The criterion shown in Table 2.1 is to guard against this potential for loss of containment integrity. Even though our evaluations using Section 11.3 of ACI Code employ a capacity reduction factor of unity, the evaluation is considered to be conservative in view of inherent conservatism of shear failure criteria in the ACI Code.

For basemat, the transverse shear capacity from the ACI code is compared to the average, rather than the peak, shear force calculated across a section through the width of the basemat. The average shear force is considered because it is intended to evaluate a gross shear failure, rather than a local shear failure at the basemat. Because of averaging, this application of the criterion is classified by judgment as close rather than conservative in Table 2.1.

2.2.7 Through-Wall Crushing of Concrete

The criterion of a strain of 0.002 shown in Table 2.1 corresponds to the strain at which load begins to drop in concrete test cylinders (Reference 2.11). This strain at ultimate stress is assumed to correspond to commencement of crushing as would be the case for a short tied column under concentric loading. Partial crushing of concrete in the wall by itself does not constitute failure. However, through-wall crushing of concrete resulting from compression on both faces may cause buckling of liner and rebar which upon cycling during seismic event can potentially cause loss of containment integrity.

The criterion shown in Table 2.1 is classified as close based on the results of concrete column testing.

2.2.8 Penetration Failure in Concrete Containments

The penetration capacity used for the evaluation of this limit state is the calculated capacity of the anchorage of the penetration, determined using provisions of paragraph CC-3421.6 of the ASME Code, Section III, Division 2.

In lieu of a detailed study to evaluate the failure of attachment welds between the penetrating pipe, the pipe sleeve and the liner, failure of the penetration anchorage per this criterion is considered to be the structural weak link in the penetration assembly and anchorage. The evaluation is conservative in view of inherent conservatisms of code capacities as demonstrated by recent tests discussed in Section 4.4.4.

The failure of a penetration in steel containments is addressed by the strain criterion for steel containment shells given in Section 2.2.4.

The penetration evaluation was made for large, representative penetrations.

2.2.9 Failure of Pretensioned Bolted Connections at Equipment Hatch and Drywell Head

The shear resistance at the bolted connection of equipment hatch or drywell is mobilized by frictional resistance resulting from bolt preload and by tongue and groove engagement, as applicable. When frictional resistance from bolt preload is considered, the value of preload was determined from drawings or Operating Manual. If this information was not specified on the drawing or Operating Manual, a fraction of bolt allowable load using ASME Code for operating conditions was employed. This fraction, based on design assumptions, was 75% for pressure seated, and 100% for pressure unseated construction. The value of preload used in the evaluation was reduced from the specified value by 10% to consider the effects of bolt torque relaxation.

The above evaluation criterion for the bolted connections is classified as close, since the contribution from friction, as well as the tongue and groove engagement are utilized at their best estimate values.

2.2.10 Shear Failure at Buttress Plate

In computing the frictional resistance at the buttress plate for the evaluation of this limit state, a coefficient of friction, = 0.40, is used based on Reference 2.6. The shear contribution of reinforcing bars and monolithic concrete is also included according to ACI 318 Section 11.3. The evaluation is judged to be conservative because of the inherent conservatism of the Code shear evaluation.

2.2.11 Failure of Steel Containment Shell at Beam Seats and Ice Chest Supports

As shown in Table 2.1, evaluation for this limit state is based on initiation of yielding and therefore is considered conservative. A non-

linear evaluation of the local strains developed at the support points in the containment shell was too expensive for this scoping study, therefore a conservative criterion was used.

2.2.12 Failure of Suppression Chamber Supports

Again, as shown in Table 2.1, the criterion for this limit state is based on elastic evaluations due to cost considerations, and therefore it is considered conservative.

2.2.13 Bearing Failure of Foundation

This limit state is an indirect limit state since failure of foundation is not directly related to the loss of containment integrity. However, since large soil displacements and strains are likely to occur after a bearing failure of foundation, which could indirectly affect containment integrity, it is identified as one of the limit states. For evaluation of bearing failure in presence of rocking and uplift, the average pressure on contact area, rather than the maximum pressure, is compared to the bearing pressure because exceeding the bearing pressure at a point may not precipitate bearing failure. This application of criterion is classified, by judgment, as close in Table 2.1.

2.2.14 Failure Due to Sliding of Containment

For the evaluation of this limit state, as shown in Table 2.1, the frictional resistance at the basemat-soil interface is determined from available contact area and shear resistance at time t, considering effects of both horizontal and vertical seismic motions. The side pressure differential is determined from the integrated resistance obtained from the difference between passive and active pressures acting on the projected area of the buried part of the structure at time t.

Like the bearing failure of foundation, this limit state is an indirect limit state. When containment has a separate basemat, differential movements between containment and adjacent buildings resulting from sliding may produce a potential for loss of containment integrity due to potential ripping of pipings attached to two buildings. Any more detailed analysis of the displacement effects after sliding is beyond the scope of this study. Therefore sliding itself is considered an indirect limit state. When containment and adjacent structures are on a common basemat, sliding of basemat is not considered to cause a similar loss of containment integrity.

2.2.15 Liquefaction of Foundation Soil

Similar to the bearing failure of foundations, this limit state also has potential for causing large soil displacements and therefore is considered an indirect limit state. The evaluation for this limit state is based on References 2.7 and 2.8. A factor of safety of 1.0 against initiation of liquefaction is used as the criterion. Since initiation of liquefaction is used as the criterion, this evaluation is considered conservative.

2.2.16 In-Plane Shear Failure of Walls Adjacent to Containment

At Fermi and Sequoyah the failure of shield walls outside the containment could indirectly affect the structural integrity of the containment. Therefore, failure of shield wall itself is considered an indirect limit state. The overall shear failure of walls is evaluated using the ACI Code criteria as shown in Table 2.1. Due to the inherent conservatisms of the Code provisions, this criterion is considered conservative.

2.3 References

2.1 Ad Hoc Group on Soil-Structure Interaction, "Analyses for Soil-Structure Interaction Effects for Nuclear Power Plants," American Society of Civil Engineers, May 1979.

2.2 ASCE Standard 4-86, "Seismic Analysis of Safety Related Nuclear Structures and Commentary On Standards for Seismic Analysis of Safety Related Nuclear Structures," American Society of Civil Engineers, September 1986.

2.3 Clauss, D. B., "Comparison of Analytical Predictions and Experimental Results for a 1:8 - Scale Steel Containment Model Pressurized to Failure," NUREG/CR-4209, SAND 85-0679, Sandia National Laboratories, Albuquerque, NM, June 1985.

2.4 ACI 349-76, "Code Requirements for Nuclear Safety Related Concrete Structures, Appendix C-Special Provisions for Impulsive and Impactive Loads," American Concrete Institute 1976.

2.5 Kennedy, R. P., "A Review of Procedures for the Analysis and Design of Concrete Structures to Resist Missile Impact Effects," Journal of Nuclear Engineering and Design, Vol. 37, No. 2, May 1976.

2.6 Prestressed Concrete Institute, "PCI Design Handbook, Precast and Prestress Concrete," Third Edition, PCI, Chicago, Illinois, 1985.

2.7 Seed, H. B., and Idriss, I.M., "Simplified Procedure for Evaluating Soil Liquefaction Potential," Proc. ASCE, Vol. 98, No. SM9, September 1971, pp. 1249-73.

2.8 Seed, H. B., Arango, I. and Chan, C., "Evaluation of Soil Liquefaction Potential During Earthquakes," Report No. EERC 75-81, Earthquake Engineering Research center, University of California, Berkeley, California, October 1975.

2.9 Vecchio, R. J., and Collins, M. P., "Modified Compression-Field Theory of Reinforced Concrete Elements Subjected to Shear," ACI Journal, March-April 1986, pp. 219-231.

2.10 Horschel, D. S., "High Pressure Test Briefing", Sandia National Laboratories, August 2, 1987.

2.11 Winter, G., and Nilson, A. H., Design of Concrete Structures, (McGraw-Hill Book Co., 1972), pp. 15-18.

2.12 Waters, T., "A Study of the Tensile Strength of Concrete Across Construction Joints", Magazine of Concrete Research, V.6, No. 18, Dec. 1954, pp. 151-153.

2.13 Ruffert, G., "Bond and Load Transfer in Reinforced Concrete," Beton, Herstellung Verwendung, May 1979, pp. 171-194 (in German).

Table 2.1
Criteria For Evaluation Of Limit States

	Limit State Description	Evaluation Criteria (Note 1)	Remark
1.	Tensile failure of steel liner	Mid-thickness strain > 0.02 Surface strain > 0.06	Close
2.	Failure of reinforcing	Strain > 10 x yield strain	Conservative
3.	Failure of prestressing tendons	Strain > yield strain	Close
4.	Tensile failure of steel containment shell	Mid-thickness strain > 0.02 Surface Strain > 0.06	Conservative
5.	Buckling of steel containment shell	Membrane compression > buckling stress determined from ASME Code Case N-284 for factor of safety of 1.0	Conservative
6.	Transverse shear failure in wall/basemat	Nominal shear stress > capacity per ACI 318-83 Section 11.3	Conservative (for wall) Close (for basemat)
7.	Through-wall crushing of concrete	Average through-wall compressive strain > 0.002	Close
8.	Penetration failure in concrete containment	Force on penetration anchorage > capacity of penetration	Conservative
9.	Failure of pretensioned bolted connections	Shear at connection > shear resistance at equipment hatch and drywell head	Close
10.	Shear failure at buttress plate	Longitudinal shear flow > frictional plus shear resistances including rebars	Conservative
11.	Failure of containment shell at beam seats or ice chests supports	Initiation of yielding according to Tresca yield criterion	Conservative
12.	Failure of suppression chamber supports	Stress > 1.60 AISC allowables or 1.0 stress limits, whichever is less	Conservative

Table 2.1
Criteria For Evaluation Of Limit States (cont'd)

	Limit State Description	Evaluation Criteria (Note 1)	Remark
13.	Bearing failure of foundation	Average pressure on contact area > ultimate bearing capacity of foundation material	Close
14.	Failure due to sliding of containment	Horizontal force > frictionsl resistance plus side pressure differential	Close
15.	Liquefaction of foundation soil	Average cyclic shear > average cyclic shear capacity	Conservative
16.	In-plane shear failure of walls adjacent to containment	Total shear force > strength per ACI 318.83, Section A-7.3	Conservative

NOTE (1) Provided reasonable numerical procedures for calculation of nonlinear response are used, an inability to load the model further is also considered a failure criterion, even if the limits stated here are not exceeded.

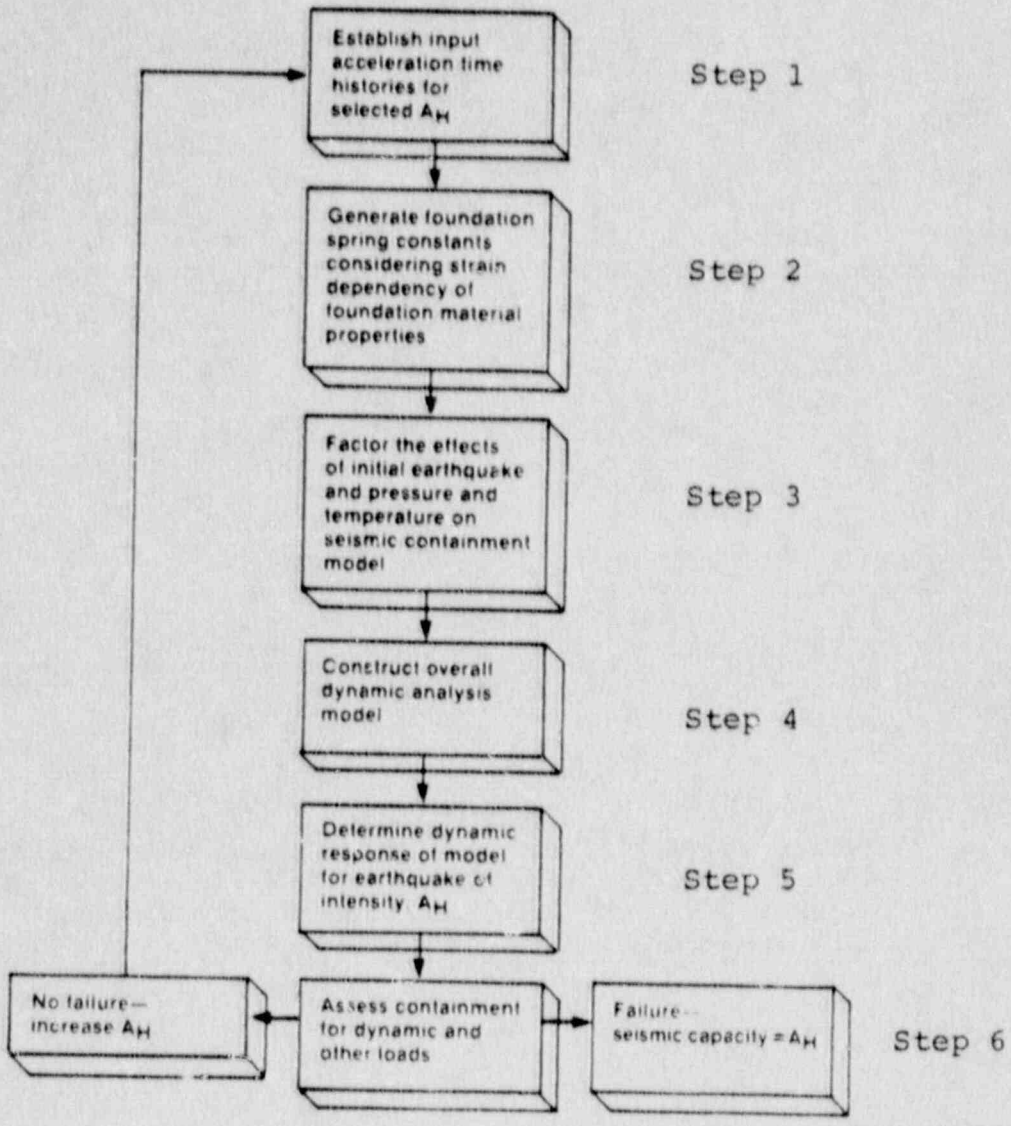

Note A_H = peak horizontal input acceleration

Figure 2.1 Steps to Determine Containment Seismic Capacity

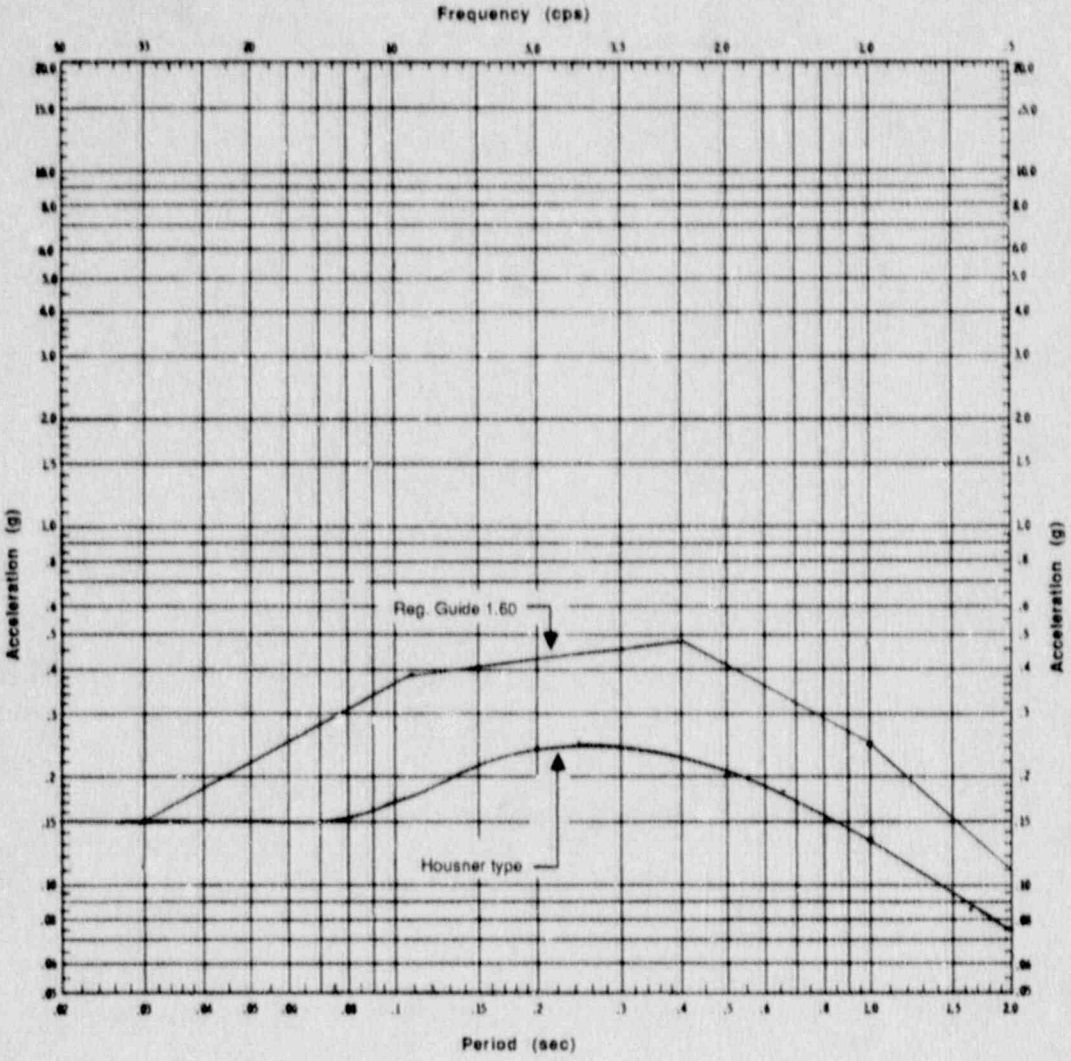

Figure 2.2 Comparison of Housner and Reg. Guide 1.60 Horizontal Response Spectra, A_H = 0.15 g, Damping = 5%

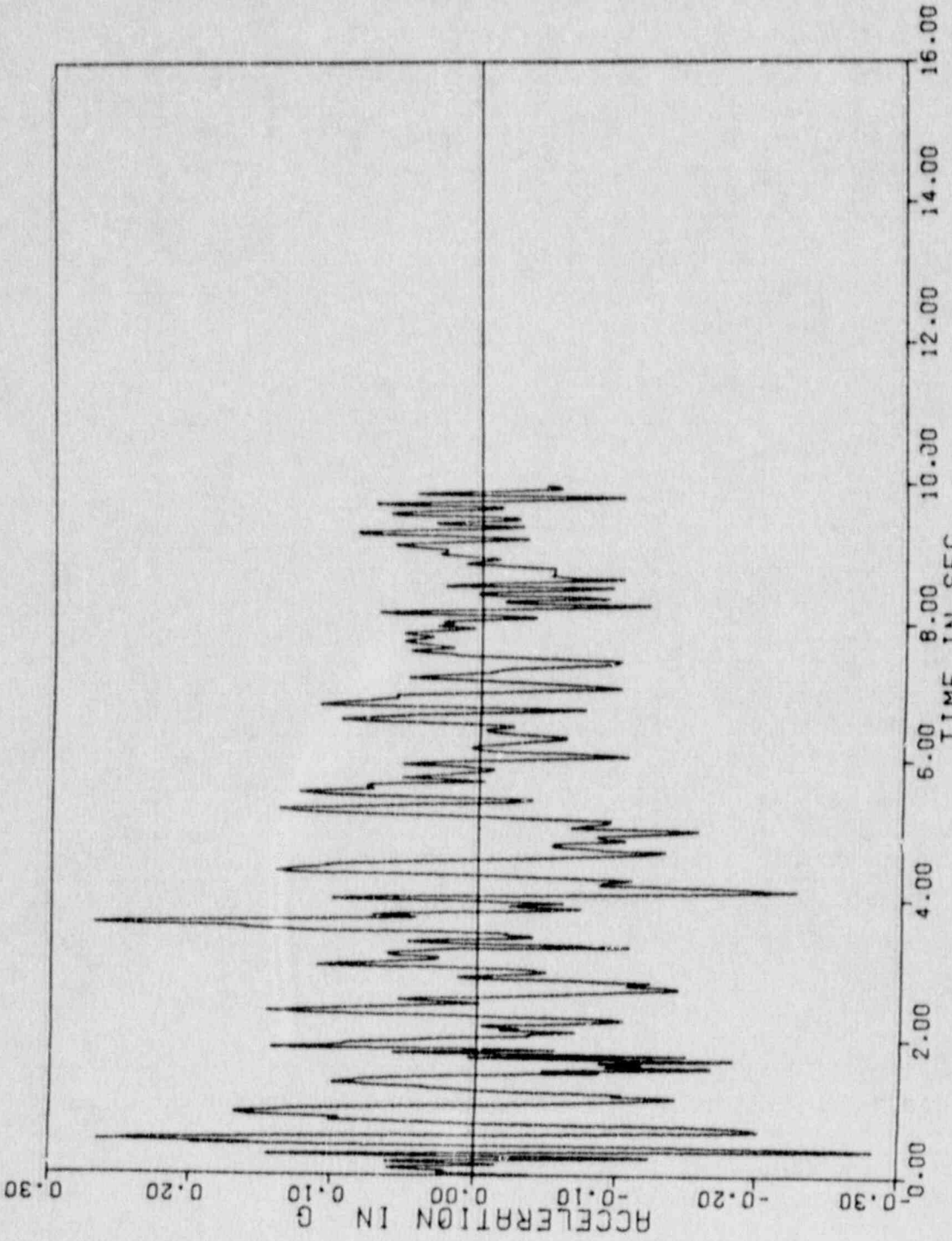

Figure 2.3 Ground Horizontal Acceleration Time History, $\ddot{x}_0(t)$, $A_H = 0.25g$

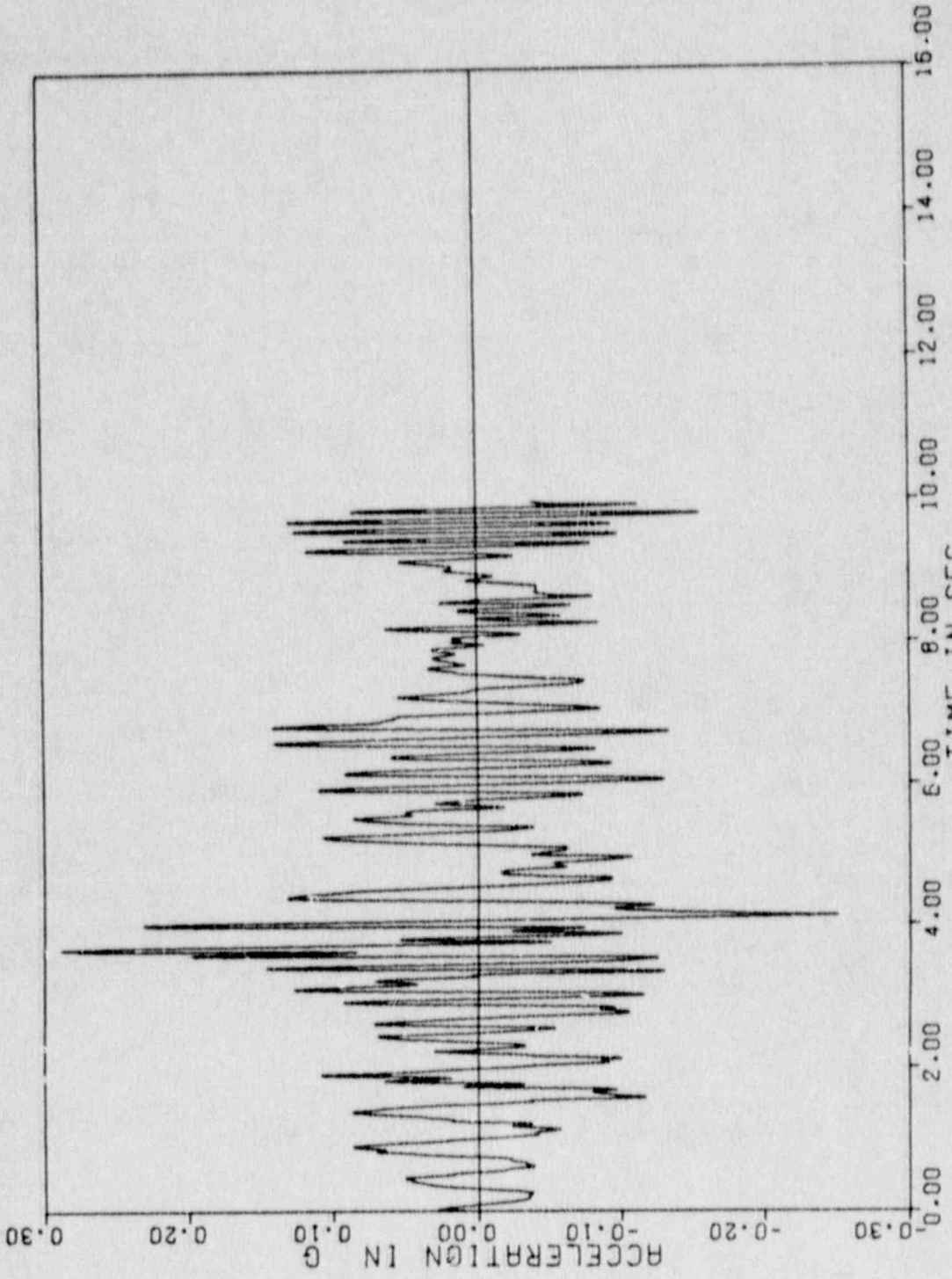

Figure 2.4 Ground Vertical Acceleration Time History, $\ddot{Y}_0(t)$, $A_H = 0.25g$

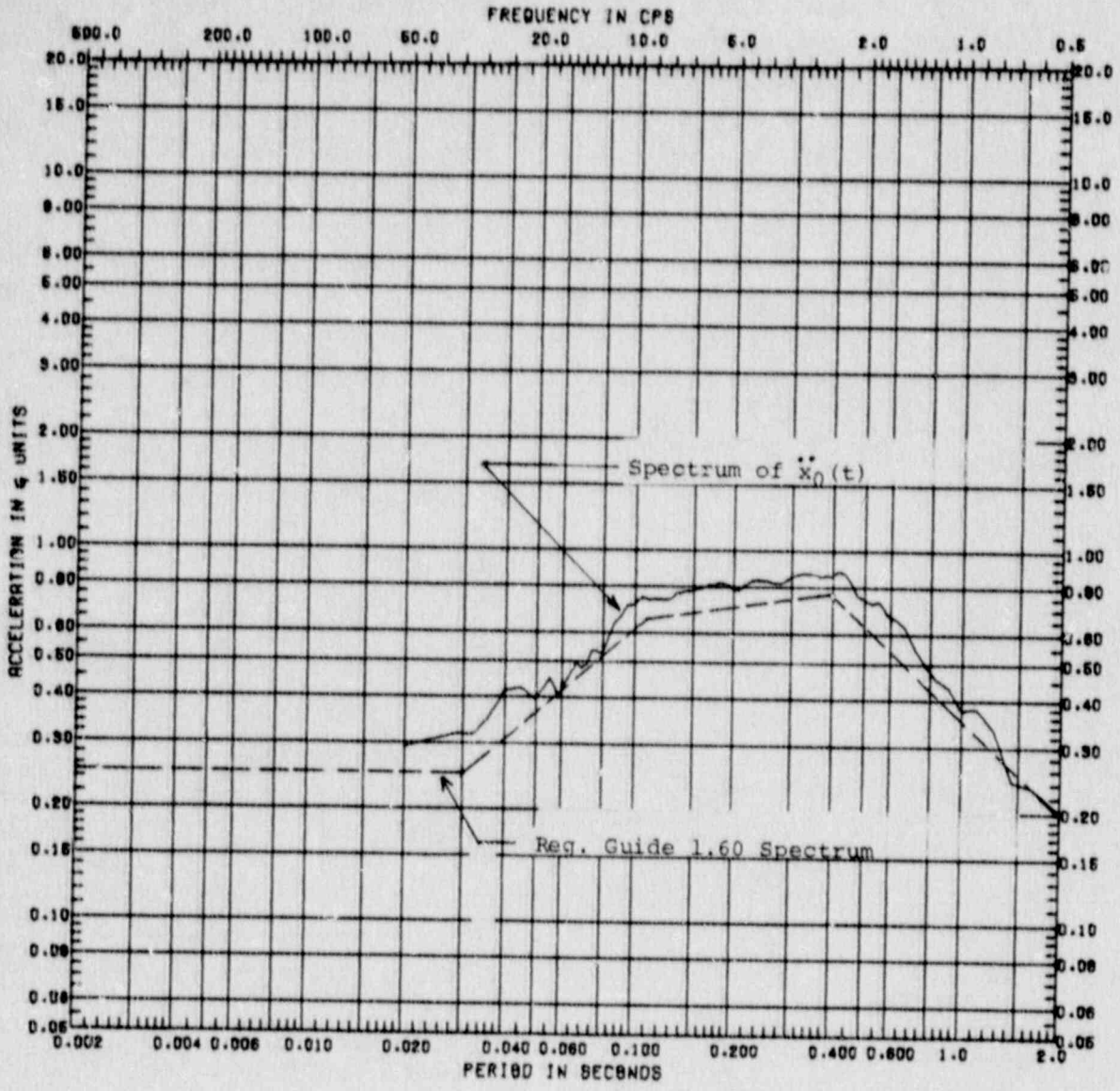

Figure 2.5 Comparison of Spectrum of $\ddot{x}_0$ (t), Time History to Reg. Guide 1.60 Horizontal Spectrum, A_H = 0.25 g, Damping = 5%

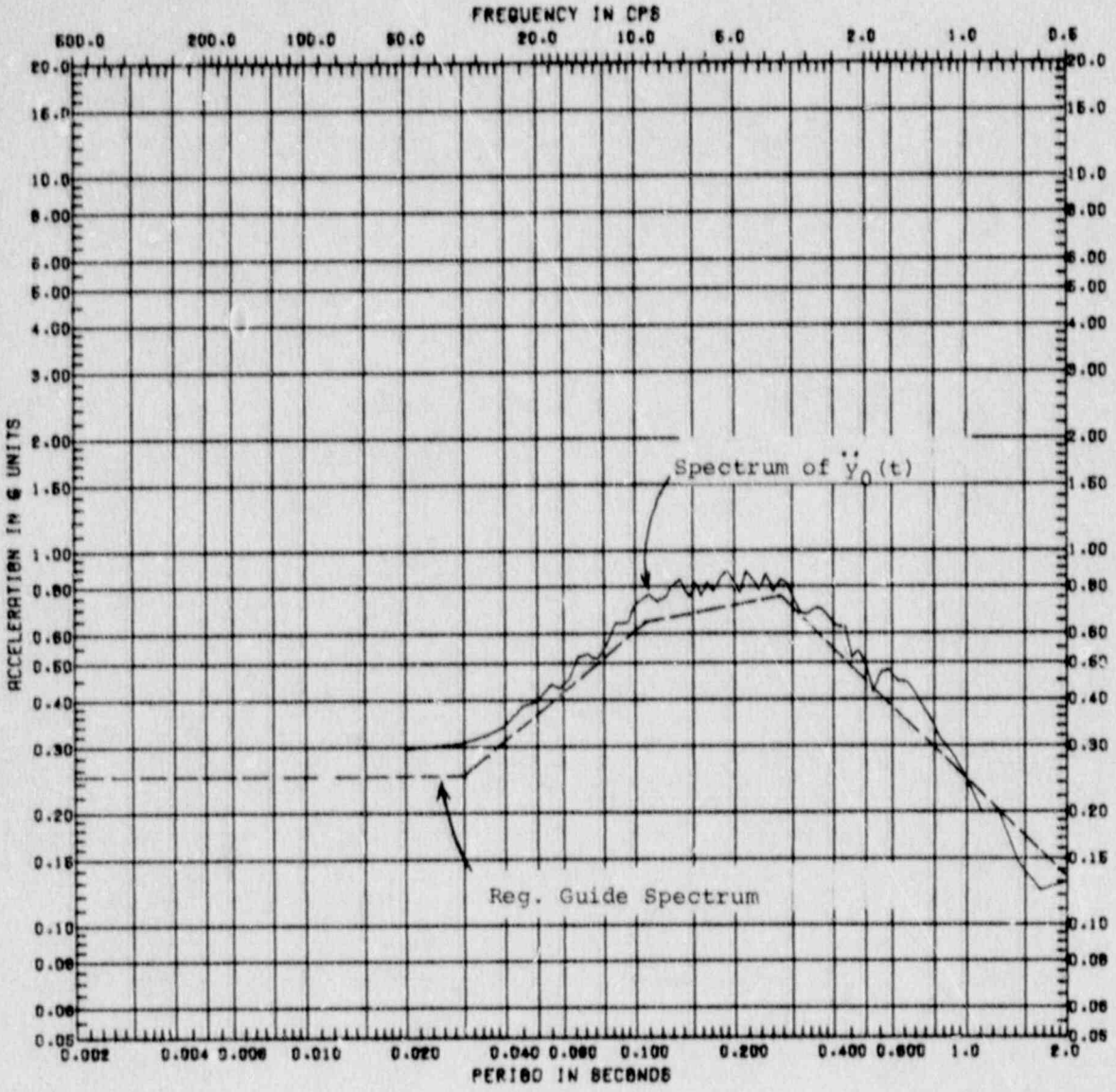

Figure 2.6 Comparison of Spectrum of $\ddot{y}_0$ (t), Time History to Reg. Guide 1.60 Vertical Spectrum, A_H = 0.25 g, Damping = 5%

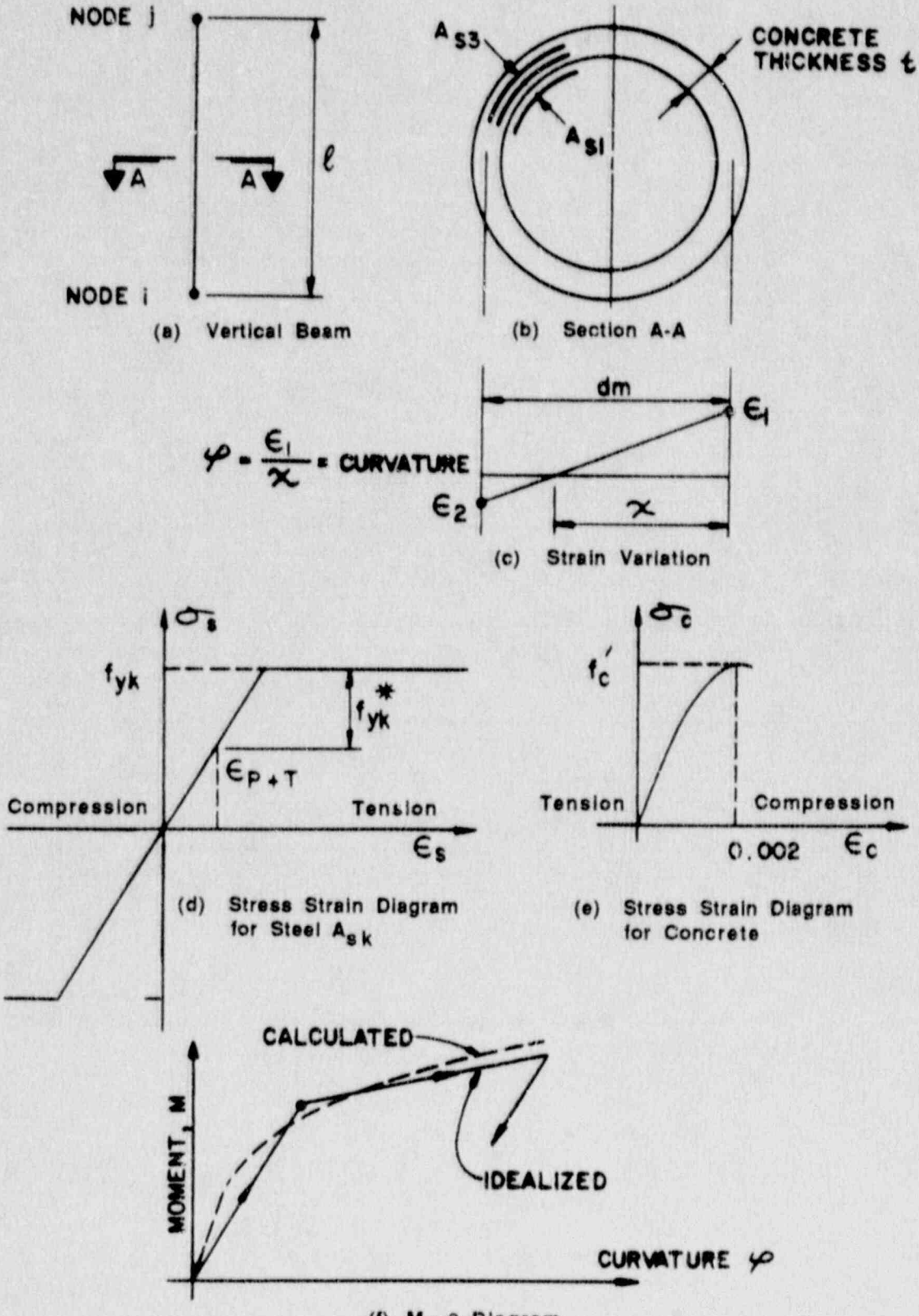

Figure 2.7 Assumptions and Information for Moment-Curvature (M-ϕ) Diagram of Vertical Beam Elements

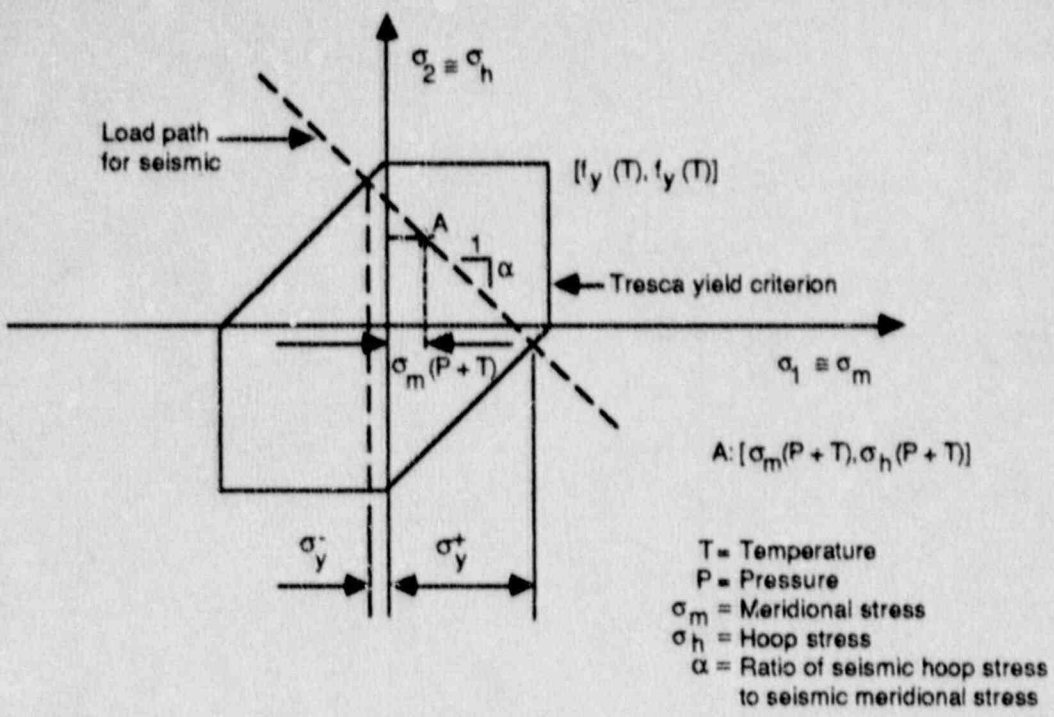

(a) Determination of σ_y^+ and σ_y^- for a seismic shell zone with specified α

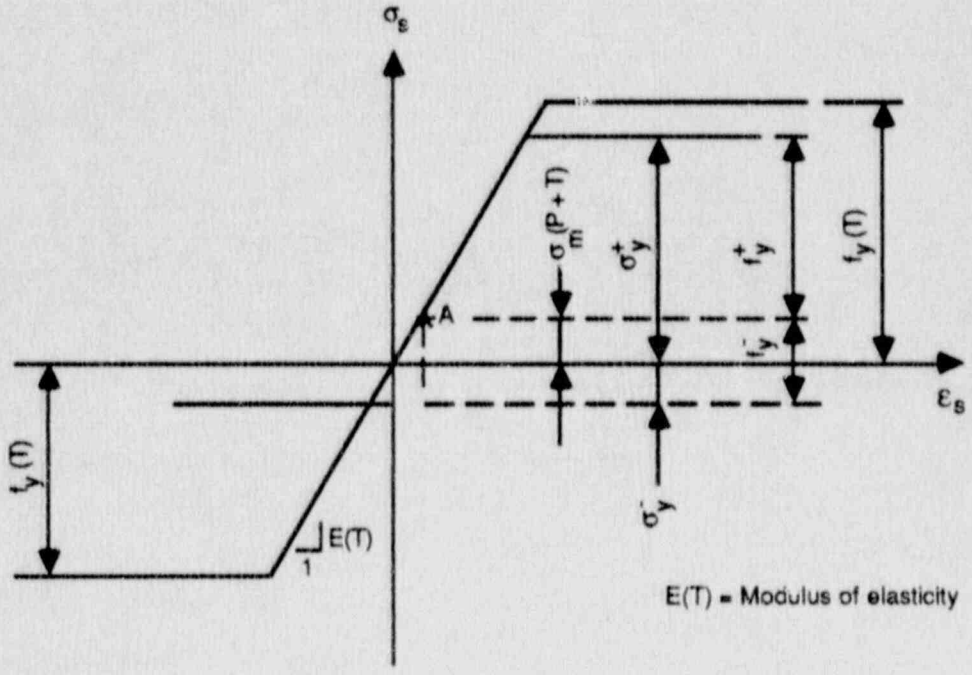

(b) Modified stress-strain diagram for meridional shell direction

Figure 2.8 Modification of Stress-Strain Diagram to Consider Biaxiality in Steel Containments

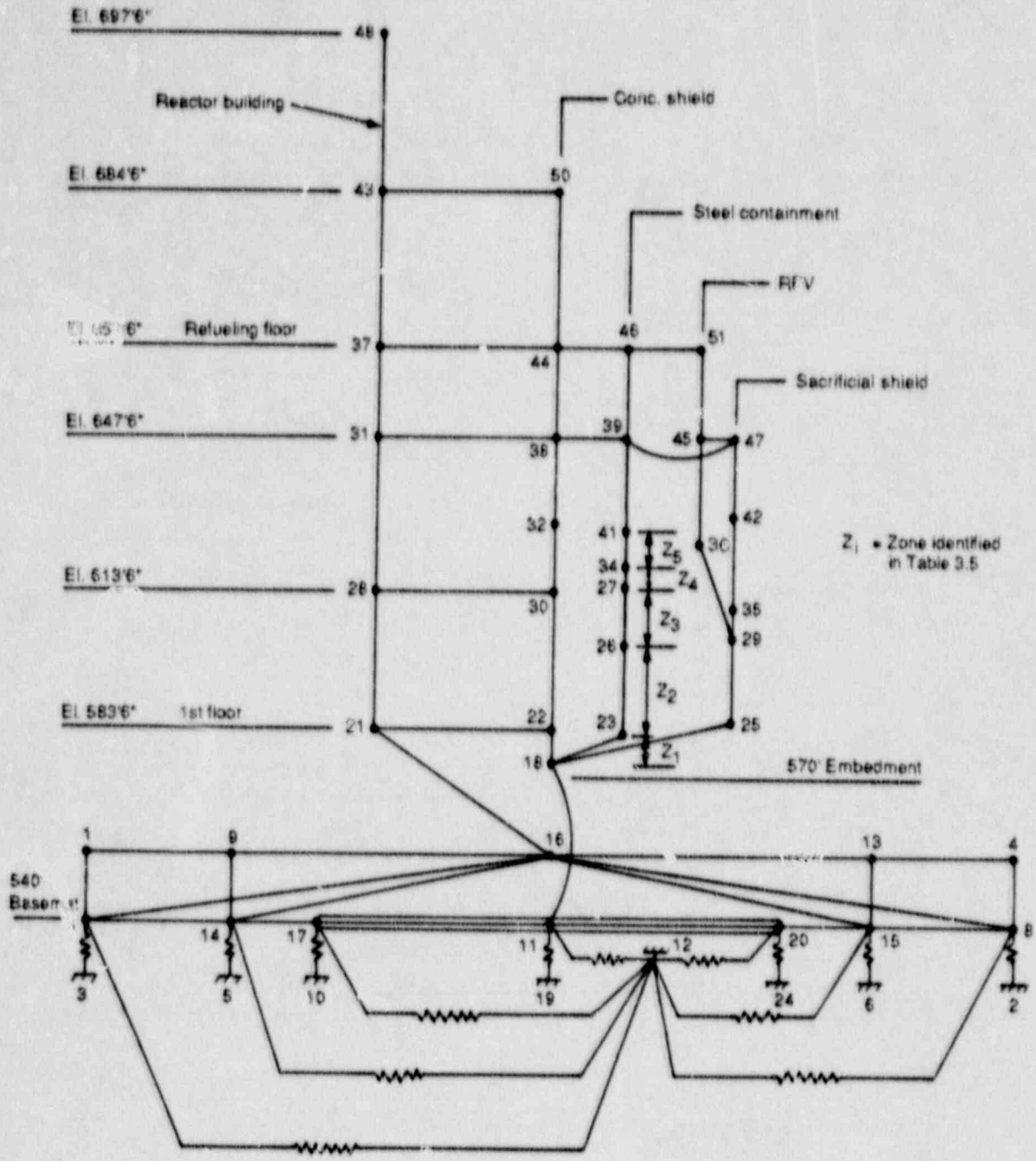

Figure 2.9 Fermi Seismic Analysis Model

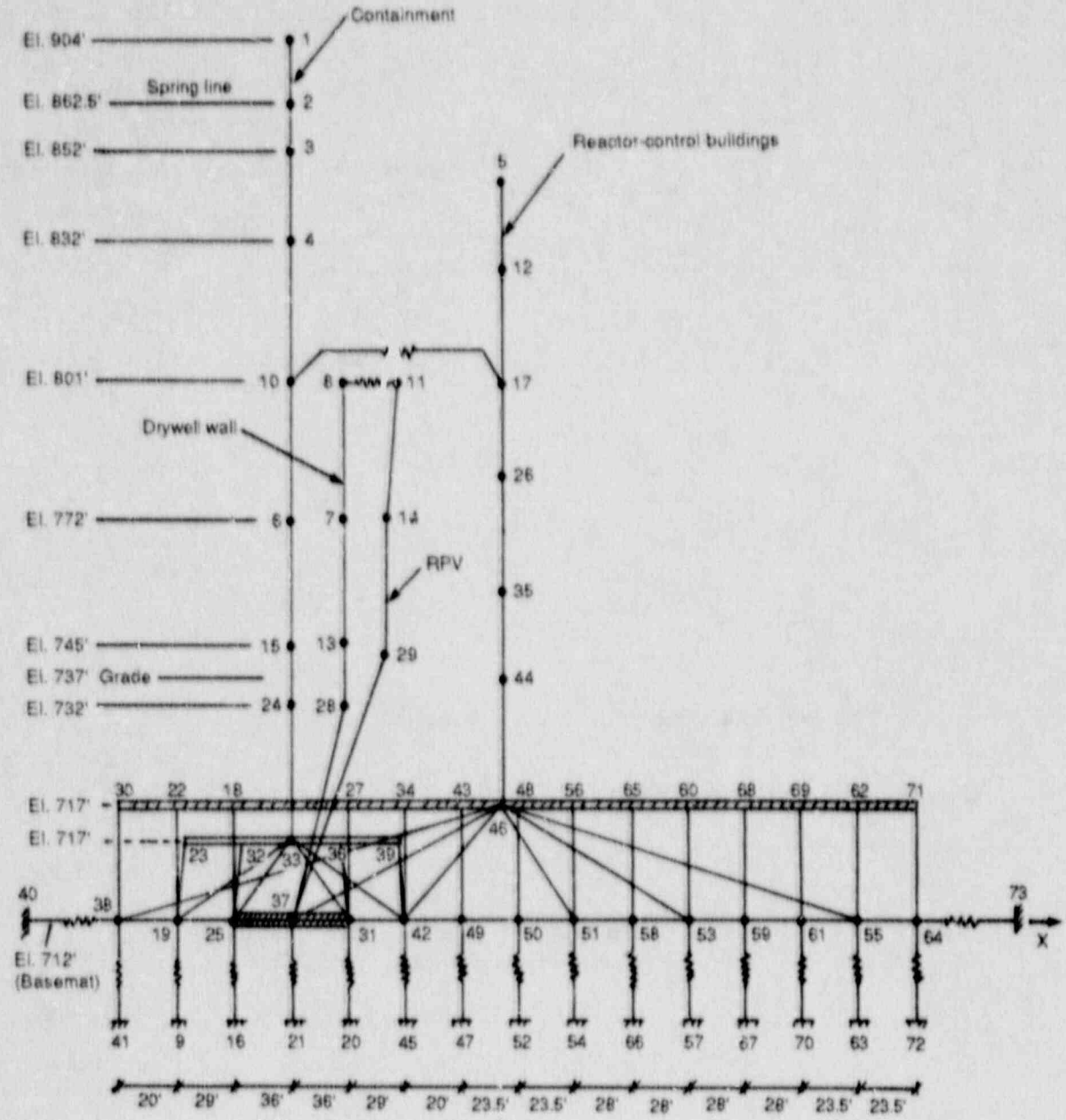

Figure 2.10 Clinton Seismic Analysis Model

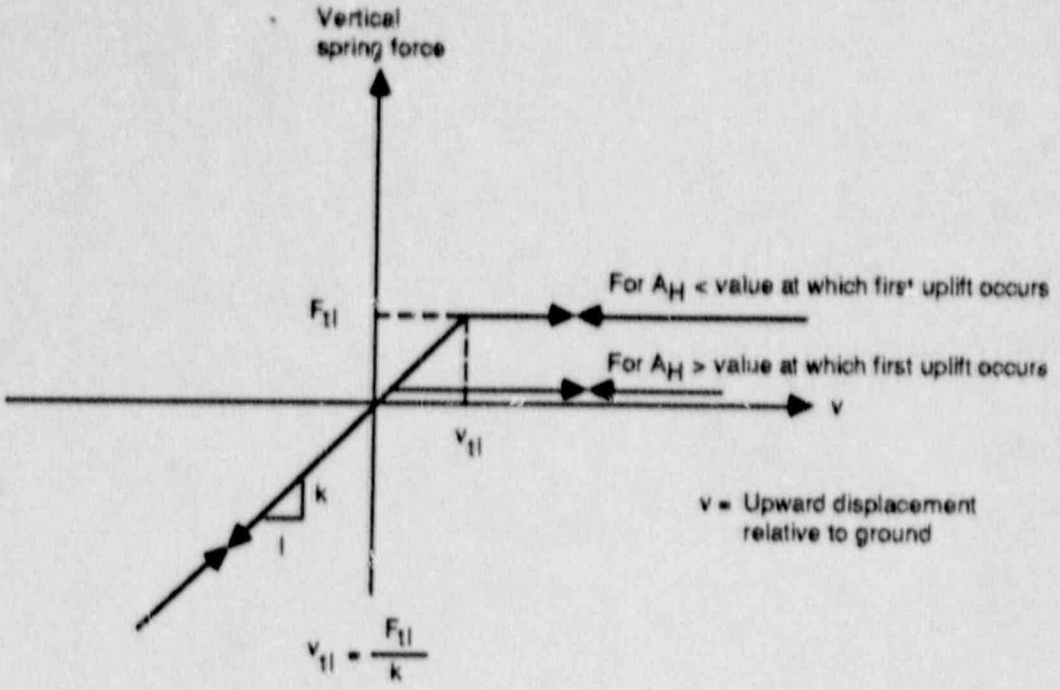

$$F_{damper} = \begin{cases} C\dot{v}, & v \le v_{tl} \\ 0, & v > v_{tl} \end{cases}$$

F_{tl} = Tensile limit force
k = Spring constant
C = Dashpot constant

Figure 2.11 Behavior of Vertical Foundation Spring and Dashpot Connected to Basemat Nodes

3. EVALUATION OF FERMI CONTAINMENT

3.1 Description of Fermi Containment

Figure 3.1 shows a general arrangement plan of major structures in Fermi. Only the reactor and auxiliary buildings are included in the seismic analysis model. These buildings and the direction assumed for horizontal acceleration in the analysis are indicated in Figure 3.1. Figure 3.2 shows an East-West section through the reactor building. Because of the continuity of the reactor building basemat with auxiliary building shown in Figure 3.2, tendency for uplift is greater in the North-South direction. For this reason analysis is made along the shorter plan dimension of the reactor and auxiliary buildings.

As shown in Figure 3.2, the reactor building is founded on a square (154' x 154'), rock supported, four feet thick, reinforced concrete basemat at elevation 540'-0". A circular concrete pedestal, centrally located on the base slab, extends upward to the first floor; and concrete walls extend upward from the basemat to the first floor.

The primary containment system's pressure suppression chamber, a steel pressure vessel shaped as a torus with a 112 ft.-6 in. major diameter and a 30 ft.-6 in. cross-sectional diameter, encircles the circular pedestal and is supported on the concrete basemat. Figures 3.3 and 3.4 show the suppression chamber plan and its supports.

The bulb shaped steel drywell, shown in Figure 3.5, is housed within the drywell cavity in the reactor building. The spherical surface of the bottom of the drywell is embedded in the top of the concrete pedestal from elevation 570'-1", marked embedment in Figure 3.5, to the lowest point of sphere which occurs at elevation 563'-0". As shown in Figure 3.5, a 68 feet diameter spherical section forms the lower portion of the drywell, and a 38 ft.-10 in. diameter cylindrical section forms the upper portion of the 115 ft.-0 5/32 in. high steel drywell. The drywell houses the reactor pressure vessel, the reactor coolant recirculation loops, and other branch connections of the reactor primary system. Eight 6'-0" diameter circular vent pipes, equally spaced around the spherical portion of the drywell, radiate downward to form the connection between the drywell and the pressure suppression chamber; see Figure 3.3.

Immediately above the embedment elevation, the drywell is backed by compacted sand to provide a transition from full embedment to an unrestrained condition. This is marked as sand pocket in Figure 3.5.

A reinforced concrete biological shield wall, monolithic with the floor slabs of the reactor building, surrounds the drywell (see Figure 3.2). The drywell is separated from the concrete shield wall by a two inch gap, except for its lower portion which is embedded in the concrete drywell pedestal.

As indicated in Figure 3.5, at elevation 647'-6", where the sacrificial shield stops, the reactor pressure vessel is connected to the sacrificial shield, and the sacrificial shield, in turn, is connected to the drywell by a stabilizer truss arrangement. At this same elevation, the drywell is also connected to the reinforced concrete biological shield wall by eight shear lug connections. These shear lugs permit some radial and vertical movement but inhibit any tangential movement of the drywell at this elevation.

There are further horizontal connecting elements between reactor pressure vessel, drywell, and the biological shield wall. These occur near the flanges of reactor pressure vessel and drywell head between elevations 659'to 662'-6"; see Figure 3.5. At these levels, the reactor pressure vessel is connected to drywell by refueling bellows and the drywell is connected to biological shield wall by drywell bellows.

Containment Internal Structures

The main structural elements within the drywell, marked in Figure 3.5, are as follows:

a. Drywell floor: This is a reinforced concrete pad poured on the bottom of the drywell. It is connected to the basemat concrete pedestal with special shear keys that transfer lateral forces to the mat.

b. Reactor Pedestal: This is a reinforced concrete cylindrical shell with an outer radius of 14'-6 1/2" and a height of approximately 26 feet. The thickness of this shell varies from four feet at its base to 5'-6 1/2" at its top. The shell is reinforced on both faces by hoop and meridional steel and is integral with the drywell floor. The reactor pedestal supports the reactor vessel sacrificial shield, and pipe whip restraints either directly or indirectly

c. Sacrificial shield: This is a composite structural steel structure which is filled with grout. The sacrificial shield wall has outside diameter of 29'-1", height of 48'-11 3/4", and wall thickness of 1'-9 1/4". The sacrificial shield acts as a radiation and heat barrier. It also laterally supports the reactor vessel, and drywell stabilizers, and pipe whip restraints.

d. Platforms: There are two gallery floor levels within the drywell at elevations 607'-0" and at 585'-3 7/8". Upper gallery beams span from the sacrificial shield to upper beam seats on the drywell. Lower gallery beams span from the reactor pedestal to the lower beam seats on the drywell.

Access to Drywell and Suppression Chamber

Drywell access is provided by one personnel lock at elevation 588'-11 1/2", two equipment hatches of 12' and 13' diameters, both at elevation 590'-4", and the drywell head at elevation 662'-6". The personnel lock has two gasketed doors in series and is cantilevered from the drywell.

The lock is welded in the drywell to a 160 inch diameter three inch thick insert plate. The 12' diameter door is pressure seated; the 13' diameter door and the drywell head are both pressure unseated.

The suppression chamber is equipped with two 48 inch inside diameter access manways. Each cover is bolted with 28 5/8" diameter bolts.

3.2 Analysis of Drywell for Gravity, Pressure, and Temperature Loads

Analyses to determine the effects of gravity, pressure, and temperature loads were made using CBI program E0778A. The shell membrane stresses are calculated at 10 selected locations above the embedment point (see Figure 3.6) for the gravity and pressure loading by this program. For areas of the shell removed from geometric and thermal discontinuities, the membrane stress is essentially the same as the surface stress. This is true for points 1 thru 8 shown in Figure 3.6. Points 9 and 10 are in regions of geometric and thermal discontinuities and therefore are subject to local membrane effects and surface stress evaluations. The output loads from CBI program E0778A at point 8 are used as boundary loads of a local analysis of the shell in the sand pocket zone, i.e., between points 9 and 10. This analysis is performed using CBI program E0781A-Kalnins Shells of Revolution Program. The local membrane values in this zone of geometric and thermal discontinuities are thus determined.

Although surface stresses as well as membrane stresses have been calculated, only membrane stresses have been used in the construction of M-Ø diagram for seismic analysis model. The use of membrane stresses is justified in that gross yielding or buckling will occur if and only if, the membrane stress reaches the critical level.

Table 3.1 summarizes meridional and circumferential stresses at design pressure of P_d = 56 psig and design temperature of T_d = 281°F. For thermal evaluations a construction temperature of 70°F was assumed.

At Task 5 temperature of 550°F, the circumferential stress at the upper cone to cylinder junction elevation 658.7 ft. in Figure 3.6 reaches 29.4 ksi when the pressure is 74 psig. Since the specified minimum yield stress of the drywell steel, which is SA-516 Grade 70, is 29.4 ksi at 550°F, this value of 74 psig is used as P_y for Task 5. Table 3.2 lists values of meridional and circumferential stresses at 9 nodes for this temperature and pressure.

Because of the small difference between Task 4 pressure of 56 psig and Task 5 pressure of 74 psig, no separate calculations for Task 6 were made.

3.3 Seismic Analysis

3.3.1 Overall Seismic Model

Figure 3.7 shows the overall seismic model used for the Fermi containment analysis. The details of constructing this model are

discussed in Section 2.1.4. Additional information specific to this model is discussed in this section.

Since Fermi containment is founded on rock, which has a minimum shear wave velocity of 6500 ft./sec., foundation properties are considered independent of strain. A shear modulus value for rock equal to 72,000 ksf, Poisson's ratio of 0.24, unit weight of 150 lb./ft.^{3}, and an equivalent basemat radius of 102 ft. were used to compute the foundation spring and dashpot constants based on equations given in Section 2.1.2. Table 3.3 lists the values of the spring and dashpot constants.

The concrete compressive strength, f'_c, used relative to the design value in the Fermi analysis is 4680 psi, which includes an increase of 17% relative to the design value due to aging (Reference 2.11). The minimum specified yield stress of reinforcing bars is 60 ksi. The drywell steel properties are given in Table 3.4. These material properties are based on the minimum specified values, and therfore are considered convervative.

In order to construct M-Ø diagrams for the drywell beams, as discussed in Section 2.1.3, first the Fermi drywell model was loaded with a uniform horizontal loading, and ratios of hoop to meridional stresses, α, were determined at various elevations. Then the drywell was divided in five zones and one M-Ø diagram was constructed for each of these zones for each task based on the calculated values of α, the existing stresses due to pressure and temperature shown in Table 3.1 and 3.2, and the steel properties shown in Table 3.4. The elevations of the five zones, the corresponding α values, and the membrane stresses used for yield stress calculations using the procedure of Figure 2.8 are listed in Table 3.5. The yield stresses for tension and compression loading, f_y^+ and f_y^- obtained from this application are summarized in Table 3.6.

It can be seen from Table 3.6 that the effective yield stress is significantly reduced due to the effect of biaxility. The more significant reduction in Zone 5 is due to the high α value of 8.29. It is noted that this α value represents an average of the calculated α values over the zone, whereas in other zones, maximum α values have been used to represent the zone. The choice of average α in Zone 5 was dictated by the fact that the use of maximum α value, which occurs at the knuckle, would mean a hoop stress very close to yield during seismic excitation in the zone.

For Tasks 4 and 5, the circumferential stress values shown at point 9 in Tables 3.1 and 3.2 show significant compression due to the thermal load effect near the embedment into the concrete. Because of a significant tensile hoop stress at Point 8, which is approximately 4.5 feet above Point 9, see Figure 3.6, stress states of Points 8 and 9 were averaged to determine the parameters used for determining the reported values of f_y^+ and f_y^- in Table 3.5 for Tasks 4 and 5.

The M-Ø diagrams for the five zones are shown in Figures 3.8 and 3.9 for Tasks 3 and 5, respectively. It should be noted that in Zone 1 the yield moment of the section is reduced by a factor of 1.86 in going from

Task 3 to Task 5 because of the effect of pre-existing pressure stresses and the reduction in yield stress due to elevated temperature. In Zone 5, this reduction is by a factor of 3.08, because of higher pressure stresses and higher a factor.

The lowest point of the drywell included in the seismic model is at the concrete drywell floor El. 572'-1". Because of the presence of concrete, shell evaluation below this point was not considered necessary.

The stiffnesses of element 44-46 (drywell bellows), element 46-51 (refueling bellows), element 38-39 (shear lug connection between drywell and containment shield), element 39-47 (stabilizer truss), and element 45-47 (reactor stabilizer) were obtained from Reference 3.1.

In the evaluation of the tensile limit force of the vertical rock springs, F_{t1} shown in Figure 2.11, a value of 20 psi was used for adhesion when A_H is less than or equal to 0.45g. The basis for 20 psi is given in the discussion that follows Equation (2.12). For higher values of A_H, because of occurrence of uplift, a minimal value of 1 psi was used for adhesion.

The first six modal frequencies of the structures included in the Fermi seismic model, assuming linear behavior are shown in Table 3.7. This table also includes the frequencies of the fixed base model, i.e., one without the foundation springs representing the rock half space. It can be seen that the difference between the frequencies of the two models is small because of the stiff rock foundation condition.

3.3.2 Seismic Analysis Results

Figures 3.10 and 3.11 show the vertical displacement time histories of the ends of the basemat, i.e., nodes 7 and 8 in Figure 3.7, for A_H = 0.45g. As can be seen from these figures, the tension limit of one way rock springs is just exceeded at this acceleration level. Figures 3.12 and 3.13 show the same results at A_H = 0.60g. As can be seen from these figures, significant basemat uplift takes place at this acceleration level. As regards to the extent of the basemat affected by uplift, at A_H = 0.60 g, 75% of the basemat uplifts, i.e., in Figure 3.7 the nodes 8 through 17 of the basemat uplift, and the length of contact reduces from the original of 157 feet to 40 feet.

Figures 3.14 and 3.15 show the horizontal and vertical response spectra, respectively, at node 46, which is top of the drywell, for A_H = 0.60g, when significant uplift has occurred. These spectra are compared with the spectra corresponding to A_H = 0.45g, multiplied by a factor of 1.33, which represents the same level of excitation, but a condition of no uplift. It can be seen that the high frequency portion of the response, in both horizontal and vertical directions, increases significantly due to uplift. In the horizontal direction, a slight effect of softening of the structure due to uplift is also evident at the fundamental frequency of the structure, i.e., around 2.6 cps, where the peak response decreases slightly and a small frequency shift in the peak occurs.

Table 3.8 shows the comparison of base shear and moment for the steel drywell shell, when it is considered elastic. It can be seen that the uplift reduces the structural responses somewhat in this case. The effect of uplift on the structural response depends upon the structural frequencies, as is further discussed under Sequoyah containment in Section 6.3.2.

The effect of uplift on basemat transverse shear and moment is not presented here, but it is discussed in Sections 5.3.2 and 6.3.2 for Zion and Sequoyah containments, respectively.

3.4 Capacity Margin Factors

The capacity margin factors, calculated using Equation (2.15), for the Fermi containment are listed in Tables 3.9 and 3.10. Table 3.9 contains margins for limit states that are directly related to the containment pressure boundary. Table 3.10 contains margins for those limit states whose realization may indirectly affect the containment performance; containment integrity beyond these limit states cannot be determined within the scope of the present study.

In Tables 3.9 and 3.10 the direct and indirect limit states, respectively, are arranged in decreasing order of criticality. the calculated margins are used, with some judgment, to arrive at this rank ordering. Further comments on the relative criticality of limit states are included in Section 3.5. The margins given in Tables 3.9 and 3.10 were generated by using time history analysis results at A_H = 0.15g, 0.30g, 0.45g, and 0.60g. The containment was evaluated for peak seismic loads using the failure criteria which are stated in Section 2.2. These tables also contain a statement of the criteria used for ready reference.

The tables list the limit state code for correlation with Table 1.2 which describes limit states to be evaluated. It will be noted that all limit states cited in Table 1.2 have been addressed.

Note that margin factors given in Tables 3.9 and 3.10 generally refer to the seismic excitations associated with A_H = 0.60g, unless the margin for a limit state becomes 1.0 at a smaller value of A_H.

Specific comments about the capacity margin factors in Tables 3.8 and 3.9 are given below in Sections 3.4.1 through 3.4.9; concluding comments are given in Section 3.5.

3.4.1 Buckling of Steel Containment Shell

The buckling evaluation of the drywell was performed using the theoretical buckling strength obtained from ASME Code Case N-284, and reducing this strength by a knockdown factor to account for fabrication/construction imperfections. The knockdown factor was computed, as discussed in Appendix B, by modifying the Code recommended knockdown factor to account for the stiffening effect of the orthogonal tension.

If the capacity margin factor thus calculated was less than one, a more detailed analysis of the theoretical buckling strength was performed using BOSOR computer program, as discussed in Appendix B.

The critical region of the shell for buckling evaluation is near the embedment, on the compression side, at node point 9 in Figure 3.6. The capacity margin factors for meridional buckling, using the Code Case buckling strength values and the modified knockdown factor, are 1.22, 1.46, and 0.99, for Tasks 3, 4, and 5, respectively. Since the margin was less than one for Task 5, BOSOR analysis for the theoretical buckling strength was made, which yielded a capacity margin factor of 1.96, as reported in Table 3.9.

Figure 3.16 shows the change in the capacity margin factor with the increase in A_H for meridional buckling in Task 3, the case where margin factor is the smallest. It can be seen that the margin reduces quite slowly after A_H = 0.45g, showing non-critical nature of this limit state even if A_H is increased beyond 0.60g.

In the circumferential direction use of Code Case buckling strength and the modified knockdown factor gave the capacity margins of 1.37, 0.84, and 0.68 for Tasks 3, 4, and 5, respectively. The BOSOR analysis yielded higher theoretical buckling strength values which resulted in capacity margin factors of 1.74 and 1.45 for Tasks 4 and 5, respectively, as reported in Table 3.9. The lower margin in Task 5 is due to a high compressive stress produced due to thermal effect, as shown in Table 3.2.

3.4.2 Tensile Failure of Steel Containment Shell

This limit state was evaluated by calculating maximum strain determined from the time history analysis. During the time history, yielding occurs both in the containment beams and in the beams which represent the biological shield wall. Yielding in the biological shield wall reduced calculated plastic strains in the containment beams.

For Task 3 condition yielding occurs only in element 18-23 of Figure 3.7 which represents the zone just above the dyrwell embedment. For Tasks 4 and 5 yielding occurs in element 34-41 of Figure 3.7 which corresponds to the knuckle area of the drywell. This difference in the behavior under Task 3 and Tasks 4 and 5 is a result of the changes in the yield moment capacities of these elements in the three tasks, see for example Figures 3.8 and 3.9. In Tasks 4 and 5 no yielding in the element near the embedment occurred. The calculated margin factors are 6.60, 9.91, and 8.85 for Tasks 3, 4 and 5, respectively. The reason for higher margin in Tasks 4 and 5 than in Task 3 is that different zones of the drywell shell are yielding in these tasks.

For element 34-41, which is the yielding element in Tasks 4 and 5, the reduction in yield moment from Task 4 to Task 5 condition is about 31%. The associated margin factors in Table 3.9 are 9.91 for Task 4 and 8.85 for Task 5. Therefore, the fluctuation in the seismic response is such that a significant reduction in yield moment is accompanied with only a

minor reduction in the margin factor. This observation is well known from the study of elasto plastic and associated elastic systems in seismic analysis, i.e., it is not unusual to find the elasto-plastic spring distortions to be comparable to that of the associated elastic system. This observation leads to the conclusion that the failure due to the membrane yielding of containment under seismic load is not a likely event.

Figure 3.17 shows the change in the capacity margin factor with increase in A_H for Task 3 condition when yielding occurs in element 18-23 of the seismic model. A smooth variation in the margin shows the non-critical nature of this limit state even beyond A_H = 0.60g.

3.4.3 Tensile Failure of Containment Shell at Beam Seats

This limit state refers to the occurrence of yielding in the drywell shell due to the superimposed local effects produced by beam seats. The localized effects of beam seats were evaluated using CBI programs E0854 and E0857.

CBI Program E0854 considers the stiffened region of the shell at the upper beam seats as a ring girder and evaluates the effect of seismically increased beam reaction loads on this girder.

CBI Program E0857 consists of an analysis of a spherical shell subjected to a local radial and tangential load. The locally stressed portion of the shell is analyzed in accordance with procedures described in Welding Research Council Bulletin Number 107, Reference 3.2. This analysis evaluates the effect of seismically increased beam reactions as well as the initial stress states in the shell.

In both programs, initial shell stresses and additional vertical seismic beam seat loads are included as input. The vertical seismic beam seat loads incorporate the peak vertical acceleration from the response spectrum curve at the elevation closest to the beam seat elevation. It should be noted that the choice of peak spectral acceleration in lieu of a detailed beam frequency calculations, and then calculation of beam reactions on the beam seats by using this peak spectral acceleration introduces a conservatism to the analysis.

The capacity margin factors for this limit state were calculated by comparing the material yield stress to the calculated stress intensity. The capacity margin factors given in Table 3.9 show that yielding does not occur in Tasks 3 and 4 at either of the beam seats. Local yielding does occur for Task 5 condition at A_H = 0.55g at the upper beam seats, and at A_H = 0.49 g at the lower beam seats.

Considering the fact that the failure criterion for this limit state is based on initiation of yielding, and the discussion given in Section 3.4.2 for yielding under seismic loading, the realization of this limit state is not considered critical for containment integrity.

Figures 3.18 and 3.19 show the capacity margin curves at upper and lower beam seats, respectively for Task 5 loading.

3.4.4 Failure of Pretensioned Bolted Connections

The drywell head is bolted with 72-2 1/2" diameter SA 193-B7 bolts. For the evaluation under this limit state, the bolt preload was based on 100% of ASME bolt allowable stress, which is 25 ksi. A 10% reduction for torque relaxation was then applied. For Task 3 condition, since no flange separation occurs, shear capacity is provided by friction between flanges, plus tongue and groove engagement. The tongue and groove engagement was based on a predetermined arc length using relations for contacting cylinders. A friction coefficient of 0.4 between mating faces of flange was assumed. This is based on steel to steel contact and grease-free in air condition (Reference 3.4). For seismic loading, the zero-period acceleration values of node point 46 (elevation 659'-6"0 in Figure 3.7) were used. For Tasks 4 and 5, flange separation occurs, due to pressure, therefore the calculated margins are smaller than Task 3. The margin curve for Task 5 condition is shown in Figure 3.20. Note that as A_H is increased from 0.45 to 0.60g, the margin factor drops only from 1.98 to 1.71, showing the relative insensitivity of this margin to increases in A_H.

The margin factors for the 12' diameter pressure-seated equipment hatch are based on 20-1 1/4" diameter bolts with assumed preload of 75% of ASME allowables. The margin factors for the 13' diameter pressure-unseated equipment hatch are based on 36-1 3/4" diameter bolts and assumed preload equal to 100% of ASME allowables. Other aspects of evaluation are the same as that for the drywell head.

Although not listed in Table 3.9, the manway covers of the suppression chamber were evaluated and found to have conservative margin even for A_H values higher than 0.6g for all tasks.

3.4.5 Failure of Containment Shell at Penetrations

This limit state refers to the tensile failure of containment vessel at penetrations. The capacity margins were evaluated by dividing the mid-thickness and surface strain limits of 0.02 and 0.06, respectively, by the calculated strains determined from a generic evaluation of the shell response at the nozzle for an imposed displacement along the nozzle.

The generic evaluation was done by considering a typical penetration geometry and analyzing the penetration using ADINA computer program NO. E1824 installed at CBI. Figure 3.21 shows the penetration and local shell thicknesses considered. Figure 3.22 shows the finite element model of this nozzle which has been analyzed. In Figure 3.22, a concentrated force is applied at point a, the end of the nozzle. Boundary points a and b move together and their common displacement is traced through the static incremental analysis. The boundary points c of the sphere are permitted to move only normal to the surface of the sphere. The only effect of temperature considered in the analysis is the reduction in yield stress and modulus of elasticity. Table 3.4

lists the values of these parameters used in the analysis for Tasks 3, 4, and 5.

The penetration/containment shell model was loaded with the appropriate pressure for Tasks 3, 4, and 5 and an incremental seismic loading. Figures 3.23, 3.24, and 3.25 show the plots for surface and mid-thickness strains as function of displacement of node point a in Figure 3.22 for Tasks 3, 4, and 5, respectively. Since outward movement of sphere more than 2 inches brings the drywell and concrete into contact, these figures show that for the outward movements, limits of 0.02 for membrane strain and 0.06 for surface strain will not be exceeded. Margin factors given in Table 3.9, were evaluated from the inward movements of the shell shown in Figures 3.23 - 3.25 using a conservative value for horizontal seismic displacement. This displacement is the maximum relative displacement of node point 46 in Figure 3.7 relative to the basemat node 11. For A_H = 0.6g the value of displacement used is 2.38 inches. The margin evaluation assumes that all the relative displacement will be absorbed in the local deformation of the shell. Even this conservative evaluation shows margin factors from 2.1 to 4.0 for this limit state.

3.4.6 Failure of Suppression Chamber Supports

Because of the pool dynamic loads, the support system for the suppression chamber was modified from a column support system to a 180° saddle support system which adds significant stability to the suppression chamber. The suppression chamber was analyzed as a horizontal vessel supported on saddle type supports using the methods described in Reference 3.3. This technique is an industry accepted standard for the assessment of stresses in a cylindrical vessel supported on saddles for various loading conditions and stiffening systems.

The total saddle load, Q, used in the analysis of the saddle support system was determined by summing the dead load, water load, live load, horizontal and vertical earthquake loads, the vent thrust due to pressure and the vent thrust due to temperature loads. The horizontal seismic shear load was absorbed in the suppression chamber seismic ties whereas, the horizontal seismic overturning moment was resolved into a system of vertical saddle loads times their distance to the neutral axis. All vertical loads were divided by the number of saddles to obtain the load per saddle.

The effect of the radial thermal gradient in the saddle was not readily available from this analysis. The portion of the saddle immediately adjacent to the torus shell was assumed to be at the same temperature as the torus shell. This temperature was assumed to extend far enough into the saddle to eliminate any restraining effect of the saddle on the saddle ring girders. A detailed heat transfer and thermal analysis was not performed.

The capacity margin factors for this limit state were calculated by comparing the material yield stress to the calculated stresses at

support locations. Because of this elastic consideration, this evaluation is considered conservative.

The minimum calculated capacity margin for A_H = .60g at point A, as shown in Figure 3.4, is 1.45 for Task 5, as given in Table 3.9. Figure 3.26 shows the capacity margin curve for Task 5 condition. The margin factor reduces from 1.59 to 1.46 as the A_H increases from 0.45g to 0.60g. The absence of any known phenomenon to produce a sharp drop in the margin curve in the neighborhood of A_H = 0.60g leads us to conclude that this limit state is relatively insensitive to the increase in A_H value.

3.4.7 Failure of Biological Shield Wall

The biological shield wall in Fermi is not part of the containment pressure boundary, therefore its failure is not considered a direct limit state. However, failure of the biological shield wall could introduce additional mass and seismic forces on the steel drywell, which may indirectly affect the drywell structural integrity. A detailed evaluation of the effects of biological shield wall failure on the drywell integrity is beyond the scope of this study, however, the failure of biological shield wall itself is identified as an indirect limit state.

The critical element for biological shield wall evaluation is judged to be the element from node 22 to node 30 in Figure 3.7. Review of plan drawings shows that above elevation 614'-4" in Figure 3.7, the seismic lateral forces are shared between the biological shield wall and another shear wall in the reactor building. In the time history analysis, yielding occurred in the vertical beam representing the shield wall in the seismic model at element 22-30.

The biological shield wall failure was evaluated on an overall basis using provisions of ACI-318-83, Section A.7. In applying the provisions of the ACI code the equivalent length of the shield wall, which is physically circular, needs to be hypothesized in the evaluation. Figure 3.27 shows the idealization of the region of the shield wall that has been treated as shear wall. More than 80% of a total horizontal shear would be carried by the central portion shown in Figure 3.27, if a sinusoidal distribution of tangential shear is assumed on the circumference. For this reason the central portion in the figure was used to define the equivalent shear walls. In this evaluation the tension and compression caused by the concurrently acting orthogonal horizontal component were also considered. The seismic capacity calculated using this approach is A_H = 0.39g.

The biological shield wall could also be evaluated using provisions of ACI Sections 11.10 (Special Provisions for Walls) and 11.7 (Shear Friction). The capacities determined from the application of Section 11.10 was also 0.39g; Section 11.7 yielded a capacity of 0.31g. Since shear friction concept assumes a fully and horizontally cracked section, it is our judgment that provisions of Section A.7 are more applicable. For this reason Table 3.10 lists the capacity of this limit state as

0.39g. It should be noted that this margin remains the same in Tasks 3, 4, and 5, since the shield wall is not subjected to pressure and temperature loads.

3.4.8 Failure of Basemat Due to Shear or Moment

These two limit states are indirect because the basemat is not part of the containment pressure boundary. However, since suppression chamber supports are connected to the basemat, a major failure in the basemat could introduce differential motion into the suppression chamber supports. A detailed evaluation of this phenomenon is beyond the scope of this study, however, failure of basemat itself has been evaluated as indirect limit state.

To evaluate the basemat, a quasi-static finite element analysis using the ADINA program was performed. The finite element model was used to represent the basemat, circular pedestal, and orthogonal and diagonal walls between the first floor at elevation 583'-6" and the basemat. Four- noded elastic shell elements were used to model the mat and the walls. The circular pedestal and the mat directly below it were treated as rigid. The finite element model also included one-way vertical foundation springs.

The dead load, followed by tension and compression forces resulting from peak values of bending moment and axial force calculated in elements 21-16 (reactor building) and 11-18 (circular pedestal) of seismic model in Figure 3.7 were applied to the finite element model.

Figures 3.28 and 3.29 show the critical sections and associated capacities in terms of A_H determined through this finite element analysis. The capacities are determined on the basis of average moment and average transverse shear forces. The lengths over which averaging was done are also shown in these figures. The minimum capacity thus determined for rebar strain exceeding 10 ε_y is A_H = 0.22g. For transverse shear capacity, the corresponding value is A_H = 0.26g.

As discussed in Section 3.3.2, basemat uplift is expected to occur for values of A_H higher than 0.45g. The finite element studies discussed in this Section confirmed that when basemat uplift occurs, the maximum mat moment and shears still occur in the part of the mat which is in contact with the rock. Since large differential movements are not expected to be introduced into suppression chamber supports prior to the occurrence of any uplift, the capacities reported for both of these limit states in Table 3.10 are A_H = 0.45g.

3.4.9 Bearing Failure of Foundation

The value of ultimate bearing capacity, based on design information, equals 300 ksf. The peak vertical force resulting from maximum load during the earthquake time history divided by the minimum contact area, is used to determine the average foundation pressure. The calculated margin in Table 3.9 for this limit state is 3.9 for Tasks 3, 4, and 5.

3.5 Conclusions

The following conclusions are drawn from the results discussed for Fermi containment in this chapter:

1. The evaluations performed for the biological shield wall and the basemat show that these structural elements could become governing for the seismic capacity of Fermi containment. The minimum capacity is A_H = 0.39g associated with the failure of biological shield wall. It is strongly felt that further evaluations of these two items using quasi-static finite element analysis with material nonlinearity could improve the reported capacities.

2. It should be noted that a capacity of 0.39g, calculated using time history consistent with Regulatory Guide 1.60 spectra, is over five times greater than the design safe shutdown earthquake of Fermi, which is 0.15g using Housner spectrum. This conclusion is based on the comparison of 0.15g Fermi SSE with seismic capacity of 0.39g and the fact that Regulatory Guide spectral accelerations at Fermi containment frequencies are about twice in comparison to the Housner spectrum, see Figure 2.2 and frequencies in Table 3.7.

3. Of the six direct limit states evaluated for Fermi containment, the tensile failure of the drywell shell and the failure of the shell at penetrations are not considered critical in view of high calculated margins at A_H = 0.60g, and the absence of any known phenomenon to produce a sharp drop in the margin in the vicinity of A_H = 0.60g. Because of the approximate manner in which the effect of biaxial stress condition is considered in the drywell evaluation for yielding, a confirmatory elastic-plastic shell analysis under quasi-static seismic loading may be appropriate to verify the conclusion of this report for this limit state.

   Of the four remaining direct limit states, the failure at beam seats and the failure of suppression chamber supports are also considered as not critical based on the conservative evaluation criteria employing initiation of yielding. It is our judgment that if a strain criterion in the nonlinear range is used, the capacities in these limit states would be much higher, as demonstrated by the behavior of the steel shell evaluated for the tensile failure condition and reported in the paragraph above.

   The direct limit states associated with the shell buckling and the bolted connection failure for the drywell head are considered as controlling limit states for seismic capacity of the Fermi containment. It should be noted, however, that the reported margin factor of 1.22 against meridional buckling for Task 3 condition could be improved by a more detailed BOSOR analysis, as demonstrated by the improvement obtained, for example, for Task 5 condition. As far as the drywell head is concerned, the factor of safety of 1.7 at A_H = 0.60g is considered comfortable, especially in view of the smooth margin curve shown in Figure 3.25.

4. The increased pressure and temperature values, caused by severe accident, decrease the margins in some limit states, e.g., tensile failure at beam seats and bolted connection failure at drywell head and pressure-unseated equipment hatch. However, since these limit states are not found to be critical, it can be concluded that the minimum seismic capacity of Fermi containment is not influenced by increases in pressure and temperature.

5. Time history analysis shows that uplifting of foundation starts to occur at about A_H = 0.45g. This nonlinearity significantly increases the responses in the high frequency region of horizontal and vertical response spectra. This effect, which is atrributed to the hard impact condition between the basemat and rock foundation, occurs for frequencies higher than 8 Hz for horizontal spectra and for frequencies higher than 16 Hz for vertical spectra. The structural responses in the containment shell are somewhat reduced due to the basemat uplift; the response of basemat, however, is sensitive to the initiation of uplift.

6. The effect of initial main shock, upto a level of A_H = 0.60g, on the subsequent seismic capacity of Fermi containment appears to be minimal. This effect is accounted for by reducing the ductility limit of the drywell shell by the amount of maximum plastic strain caused by the initial shock. However, as discussed in Section 3.4.2, the element which is critical in Tasks 4 and 5, i.e., the element near the knuckle area, does not yield in Task 3. Thus, there is no depletion in its ductility limit due to the initial shock.

3.6 References

3.1 Sargent & Lundy Report SL-2682, "Seismic Analysis of the Reactor Auxiliary Building Complex Enrico Fermi Atomic Power Plant Unit 2," September 1, 1982.

3.2 Wichman, K. R., Hooper, A. G. and Mershon, J. L., "Local Stresses in Spherical and Cylindrical Shells Due to External Loadings," Welding Research Council Bulletin Number 107, August 1965.

3.3 Zick, L. P., "Stresses in Large Horizontal Cylindrical Pressure Vessels on Two Saddle Supports," Welding Journal Research Supplement, September 1951.

3.4 Fuller, D. D., "Friction", in Mark's Standard Hardbook for Mechanical Engineers, McGraw-Hill Book Co., Eighth Edition, 1978, p. 3-25.

Table 3.1
Stresses Due To Pressure and Temperature (Task 4)

(Design Basis Accident Condition - 56 psig, 281°F)

Node Point In Fig. 3.6	Elevation (Ft.)	Meridional Stress (psi)	Circumferential Stress (psi)
1	627.9	2269	9438
2	624.8	2785	16636
3	623.3	3974	13977
4	622.3	13056	13056
5	606.0	13056	13056
6	587.6	13056	13056
7	582.2	7616	7616
8	576.5	7624	7949
9	572.1	8183	-15330

Table 3.2
Stresses Due To Pressure and Temperature (Task 5)
(P_y = 74 psig, T_y = 550°F)

Node Point in Fig. 3.6	Elevation (Ft.)	Meridional Stress (psi)	Circumferential Stress (psi)
1	627.9	2987	13960
2	624.8	3793	21070
3	623.3	4750	17680
4	622.3	17300	15840
5	606.0	17180	17190
6	587.6	17160	15730
7	582.2	10020	10060
8	576.5	9980	10487
9	572.1	10720	-25966

Table 3.3
Total Foundation Spring and Dashpot Constants

A_H (g)	K_H (KIP/FT.)	K_V (KIP/FT.)	C_H ($\frac{KIP.\ SEC.}{FT.}$)	C_V ($\frac{KIP.\ SEC.}{FT.}$)
All Values	3.53×10^5	3.88×10^7	5.3×10^5	8.6×10^5

Note: Individual spring and dashpot constants in Figure 3.7 were obtained using the total values and the applicable tributary area for each element.

Table 3.4
Values of Yield Stress and Modulus of Elasticity For Drywell Shell

Task	Temperature (°F)	Yield Stress (ksi)	Modulus of Elasticity (ksi)
3	150	36.4	29,100
4	281	33.9	28,400
5	550	29.4	27,000

Table 3.5

Values of α, σ_m and σ_h Used in Construction of M-Ø Diagrams

Zone Elevation (ft.)	α	σ_m (ksi) Task 3	Task 4	Task 5	σ_h (ksi) Task 3	Task 4	Task 5
1 (Drywell floor, 572.0 to 583.5)	-0.87	0	8.18	10.72	0	3.65	0.34
2 (583.5 to 598.0)	-1.14	0	7.62	10.02	0	7.62	10.06
3 (598.0 to 614.3)	-1.20	0	13.06	17.18	0	13.06	17.19
4 (614.3 to 622.3)	-0.83	0	13.06	17.30	0	13.06	15.84
5 (622.3 to 627.9)	+8.29	0	3.01	3.84	0	13.35	17.57

α = ratio of hoop to meridional stress due to seismic load

σ_m, σ_h = meridional and hoop stress, respectively

Table 3.6

Values Of Effective Yield Stress Used In Constructing M-Ø Diagram

Zone and Elevation (ft.)	f_y^+ (ksi)			f_y^- (ksi)		
	Task 3	Task 4	Task 5	Task 3	Task 4	Task 5
1 (Drywell floor) 572.0 to 583.5	19.5	15.7	10.4	-19.5	-20.6	-21.0
2 583.5 to 598.0	17.0	17.5	13.7	-17.0	-16.4	-13.7
3 598.0 to 614.3	16.5	15.4	12.2	-16.5	-15.4	-10.2
4 614.3 to 622.3	19.9	18.5	12.1	-19.9	-18.5	-16.3
5 622.3 to 627.9	4.39	2.48	1.43	-4.39	-5.7	-5.66

f_y^+, f_y^- = yield stress values for tension and comparison, respectively

Table 3.7

Modal Frequences For Fermi Seismic Model

Mode Number	Frequency (cps) Fixed Base	With Foundation Springs
1	2.97	2.60
2	9.04	7.84
3	10.6	8.56
4	10.8	10.7
5	13.6	13.3
6	16.8	14.9

Table 3.8

Effect Of Uplift On Base Shear and Moment
for an Elastic Drywell Model, A_H = 0.60g

Parameter	With Uplift	Without Uplift
V (kips)	6960	7680
M (k-ft)	506,000	557,000

Table 3.9

Capacity Margin Factors For Fermi Containment at A_H = 0.60g
(Except As Noted)
(Direct Limit States)
(See Note 1)

Code*	Description	Criterion	Tasks 3	4	5
5	Buckling of Steel Containment Shell				
	a. Meridional Buckling	$f_{cr}(m)/f$	1.22	1.46	1.96**
	b. Circumferential Buckling	$f_{cr}(c)/f$	1.37	1.74**	1.45**
4	Tensile Failure of Steel Containment Shell	$0.02/\varepsilon$	6.60	9.91	8.85
11	Tensile Failure of Containment Shell at Beam Seats				
	a. Upper	$\frac{f_y}{\text{Stress Intensity}}$	1.42	1.16	1.0 at A_H = 0.55g
	b. Lower		1.42	1.26	1.0 at A_H = 0.49g
9	Failure of Pretensioned Bolted Connection at				
	a. Drywell Head		>10	2.0	1.71
	b. 12'Ø Equip. Hatch (Pressure seated)	$\frac{\text{Shear Cap.}}{\text{Max. Shear}}$	7.0	>10	>10
	c. 13'Ø Equip. Hatch (Pressure unseated)		>10	5.9	3.1
4	Failure of Containment Shell at Penetration	$0.02/\varepsilon_m$ $0.06/\varepsilon_{total}$	2.1 2.5	4.0 4.0	4.0 3.5
12	Failure of Suppression Chamber Supports	f_y/f	2.22	1.58	1.45

* Refers to limit state identification number in Table 1.2.

** These values were determined using BOSOR analysis, other margin factors for buckling were determined using modified Code Case N-284, See Section 3.4.1 for further discussion.

(Note 1 of next page)

Table 3.9 (Cont'd.)

Note 1: It should be noted that the capacity margin factors reported in this table are based on the expressions shown under the 'criterion' column of this table. Since ultimate capacity evaluation of the containment involves nonlinear considerations, and since seismic load is only part of the total load on the containment, the margin factors do not imply that an A_H = 0.60g x Factor is the seismic capacity of the containment. For example, for the second item in this table, the capacity margin for Task 3 is reported as 6.6. This does not mean that the tensile failure of containment, i.e., 2% strain in the shell, will occur at A_H = 0.60g x 6.6 = 3.96g; due to nonlinear behavior it may occur sooner or later than that. For further understanding of the behavior of containment, margin curves provided should be considered.

Table 3.10

Capacity Margin Factors for Fermi Containment at A_H = 0.6g
(Except As Noted)
(Indirect Limit States)
(See Note 1)

Code*	Description	Criterion	Tasks 3	Tasks 4	Tasks 5
16	Failure of Biological Shield Wall	Shear strength per ACI 318 Section A7.3 / Lateral shear force	1.0 at A_H = 0.39g	1.0 at A_H = 0.39g	1.0 at A_H = 0.39g
2	Failure of Reinforcing Bars in Basemat	$\frac{10\varepsilon_y}{\varepsilon \text{ after uplift}}$	1.0 at A_H = 0.45g	1.0 at A_H = 0.45g	1.0 at A_H = 0.45g
6	Transverse Shear Failure in Basemat	Equiv. beam shear cap. / Max. beam shear after uplift	1.0 at A_H = 0.45g	1.0 at A_H = 0.45g	1.0 at A_H = 0.45g
13	Bearing Failure of Foundation	Ult. bearing capacity / Peak average pressure	3.9	3.9	3.9

* Refers to limit state identification number in Table 1.2

Note 1: A comment similar to Note 1 of Table 3.9 applies to this table also.

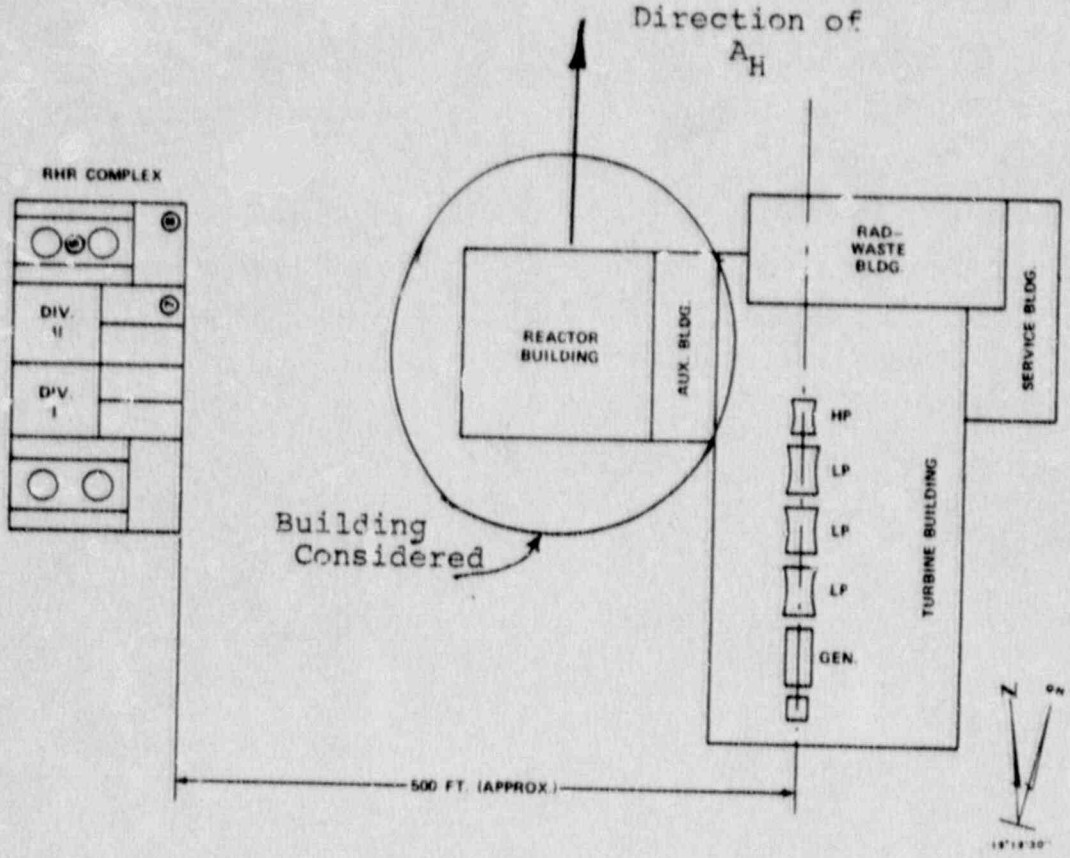

Figure 3.1 General Arrangement Plan of Major Structures at Fermi

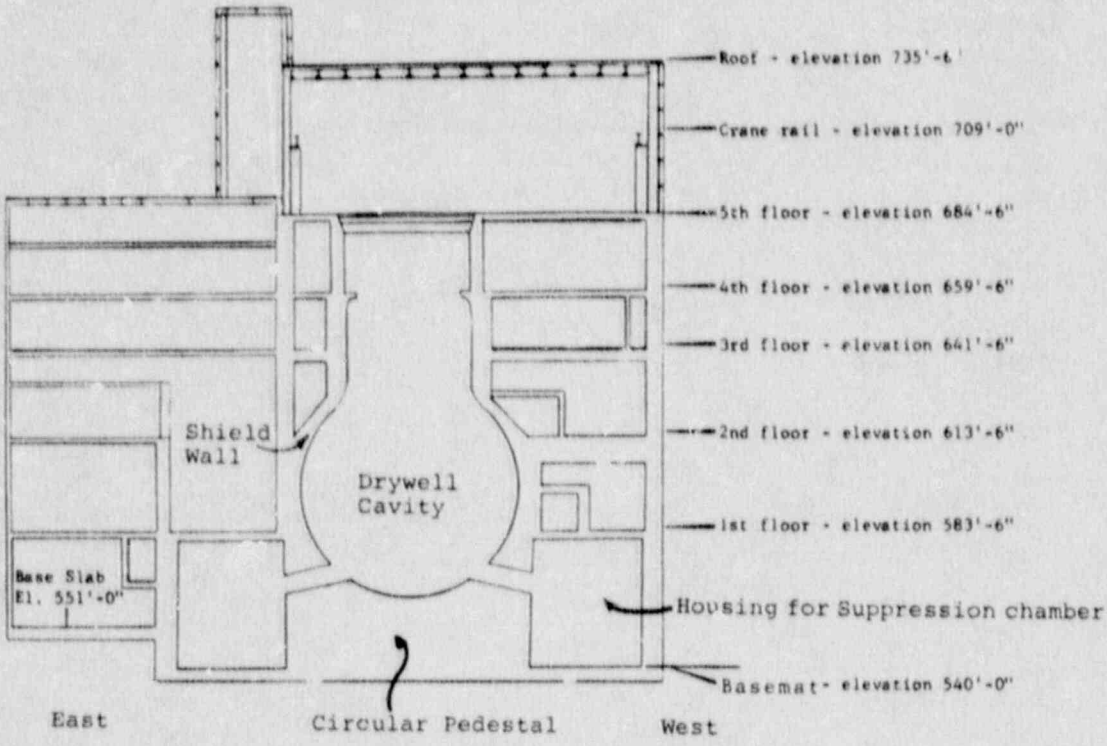

Fig. 3.2 **FERMI 2 REACTOR BUILDING (EAST–WEST SECTION THROUGH REACTOR CENTER LINE LOOKING SOUTH)**

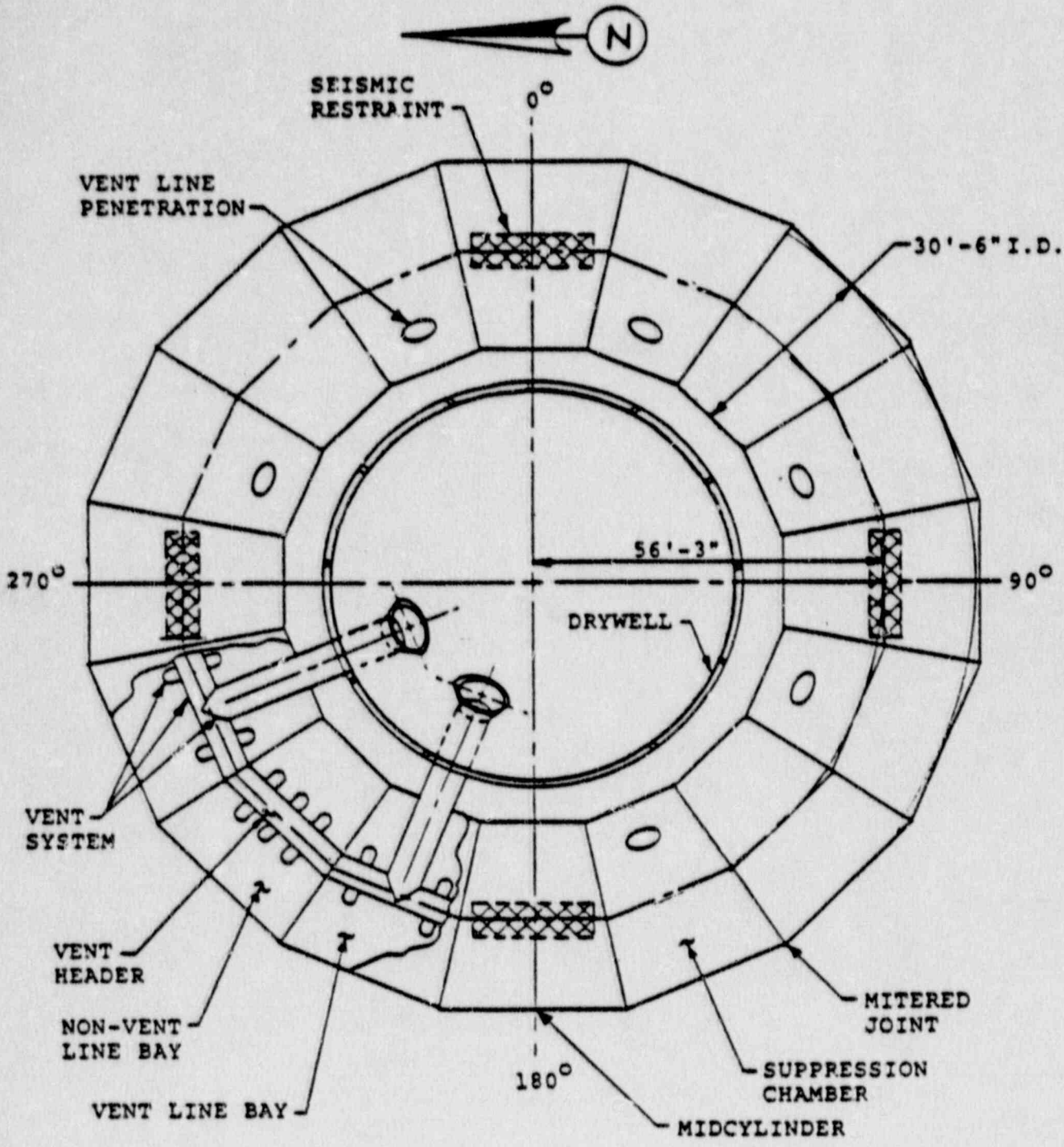

Figure 3.3 Suppression Chamber Plan

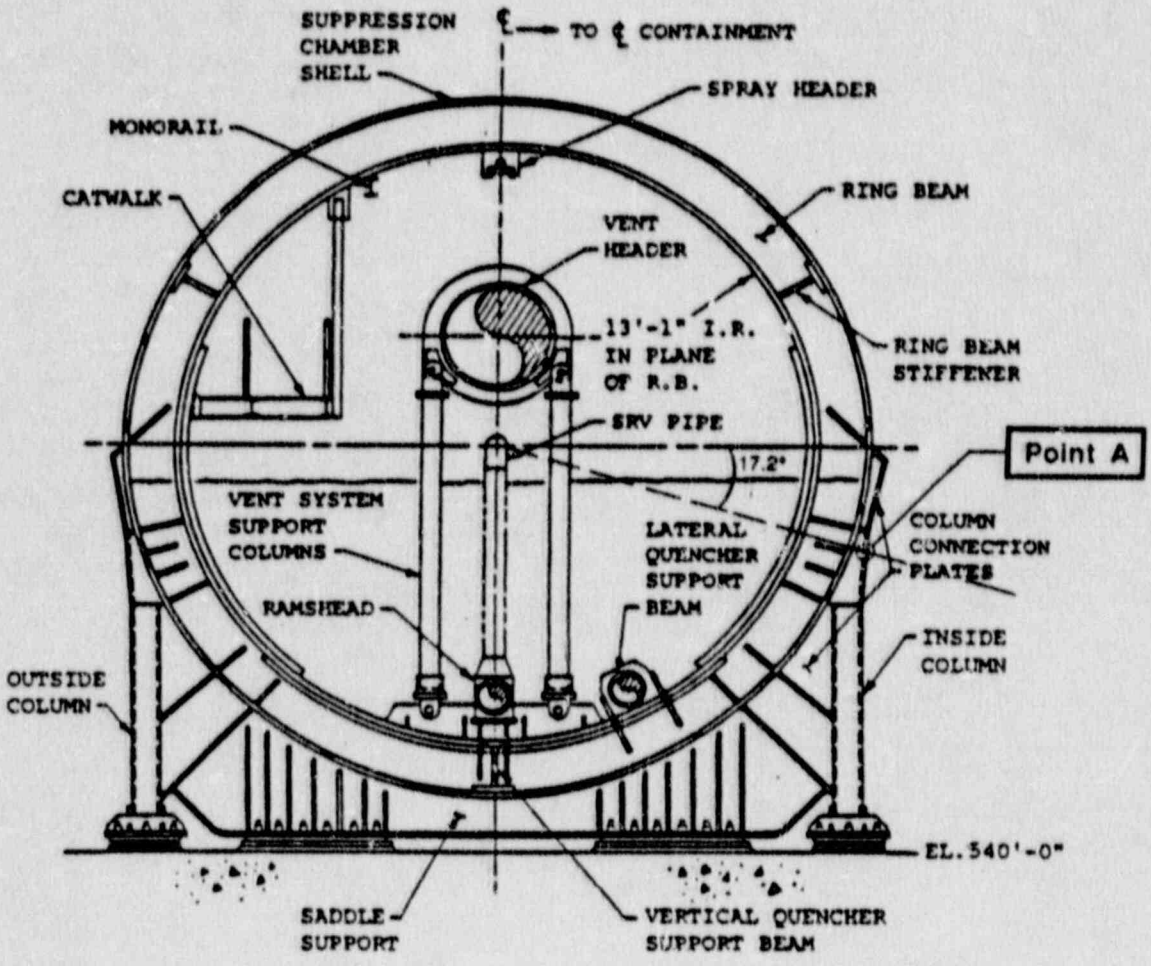

Figure 3.4 Suppression Chamber Support Details

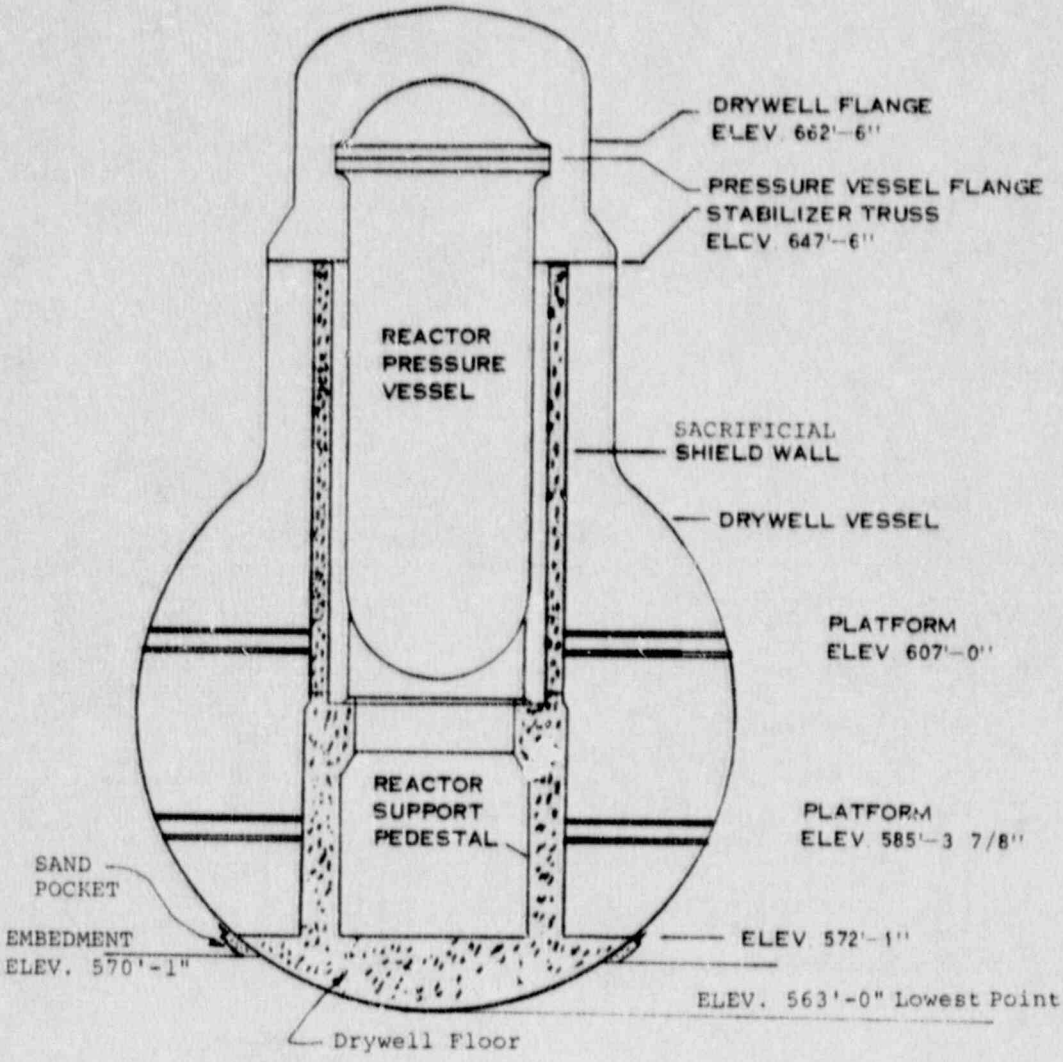

Fig. 3.5 SECTION THROUGH CENTER LINE OF DRYWELL

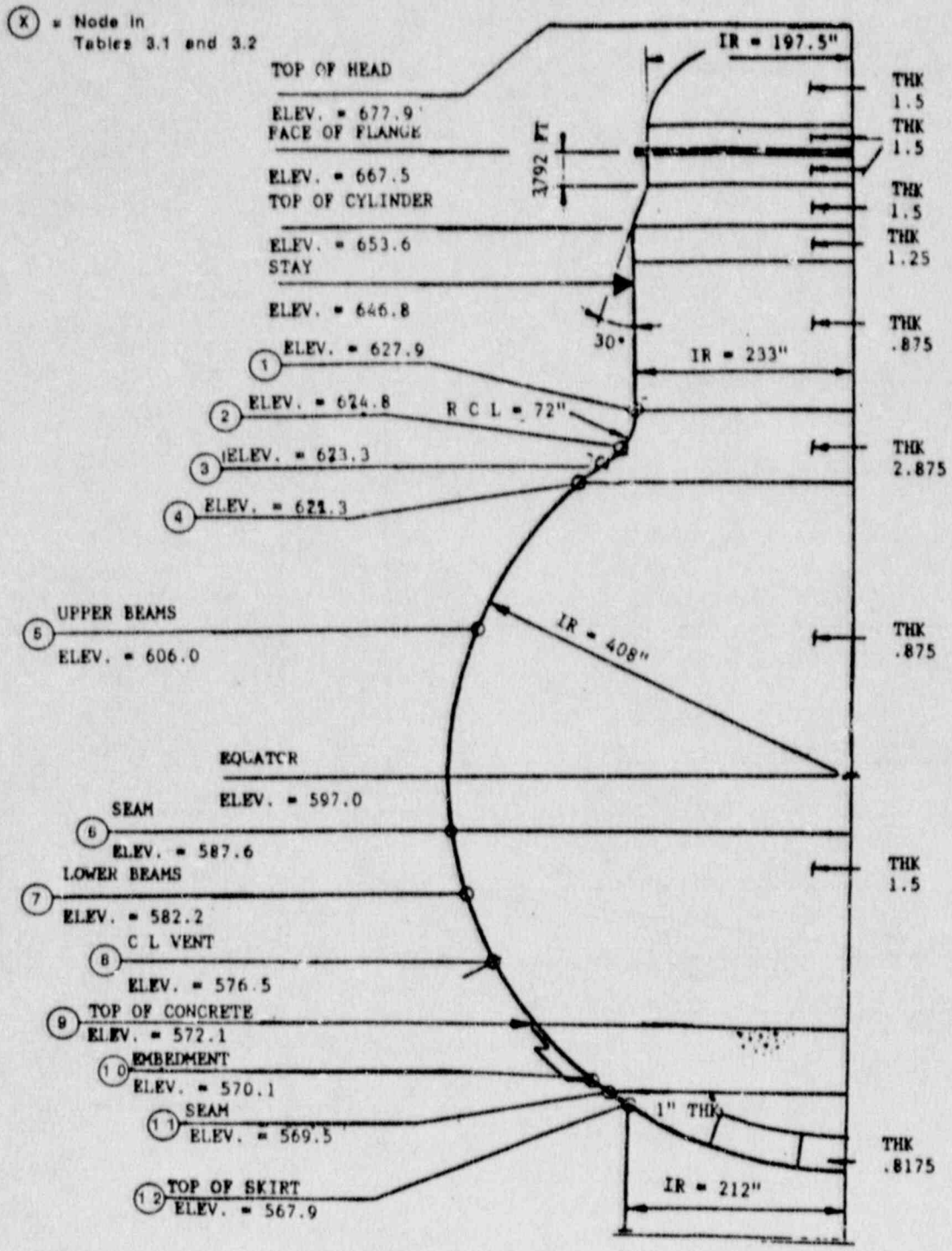

Figure 3.6 Analytical Model of Drywell Shell

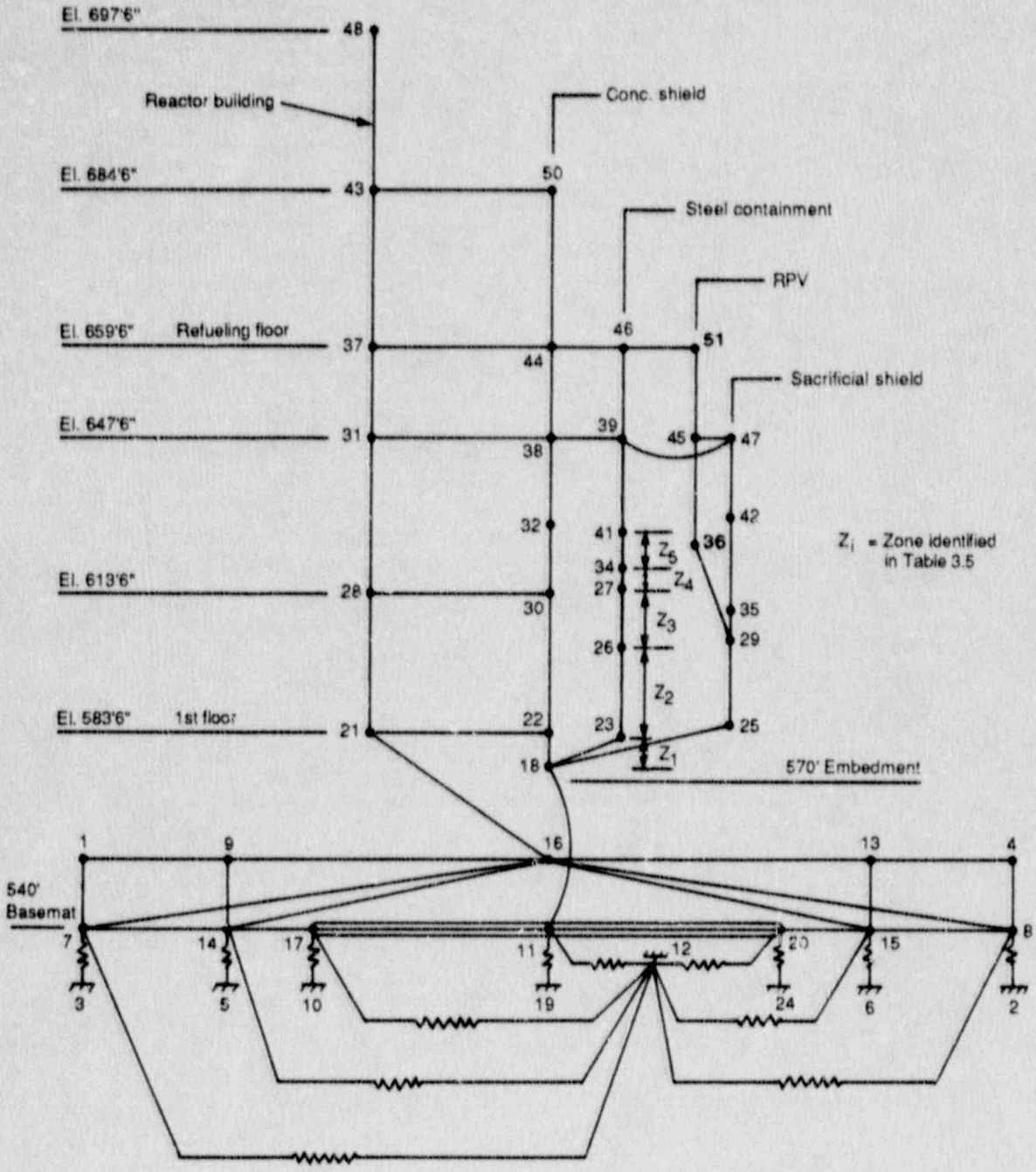

Figure 3.7 Seismic Analysis Model for Fermi Containment

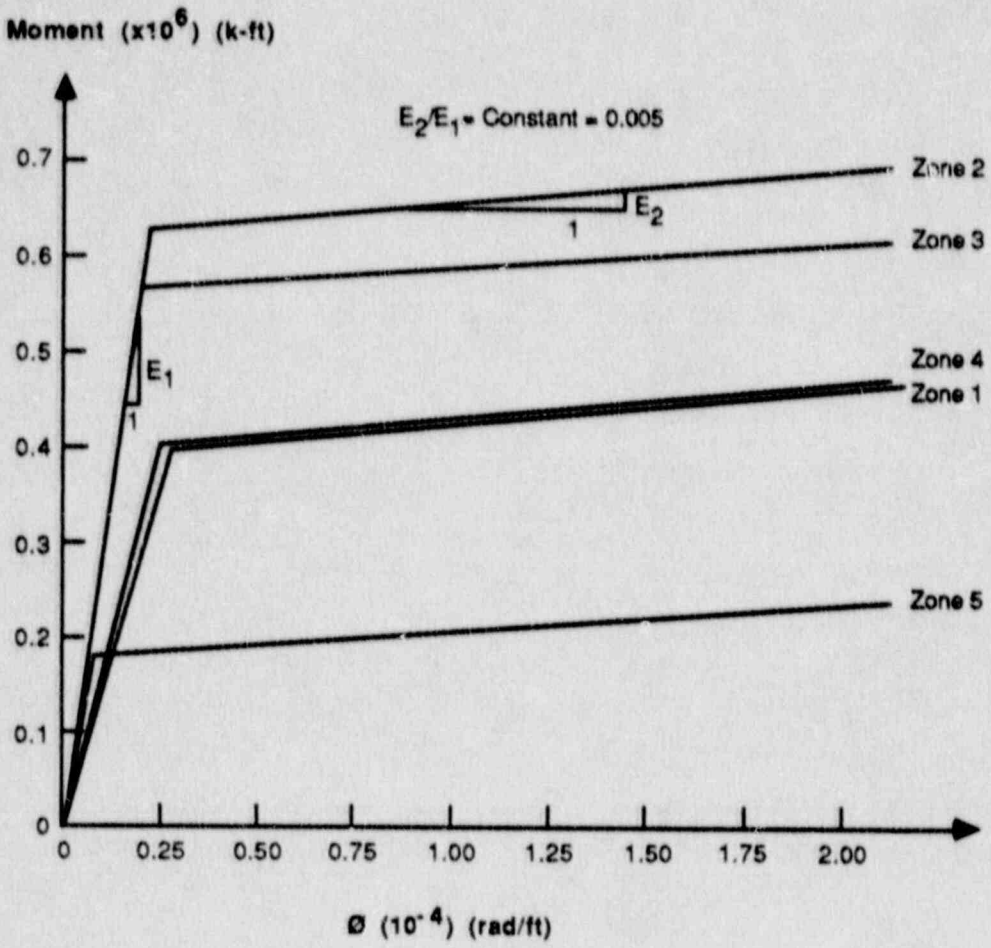

Figure 3.8 M-Ø Diagrams for Task 3

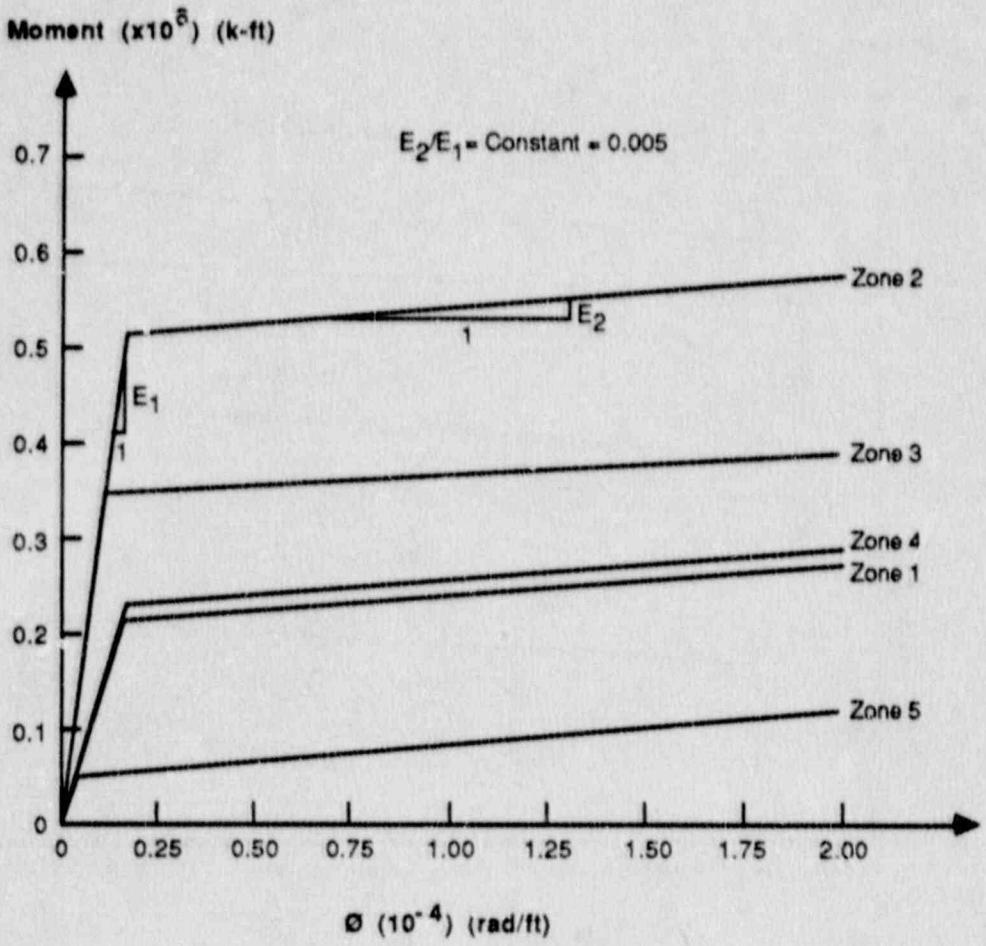

Figure 3.9 M-Ø Diagrams for Task 5

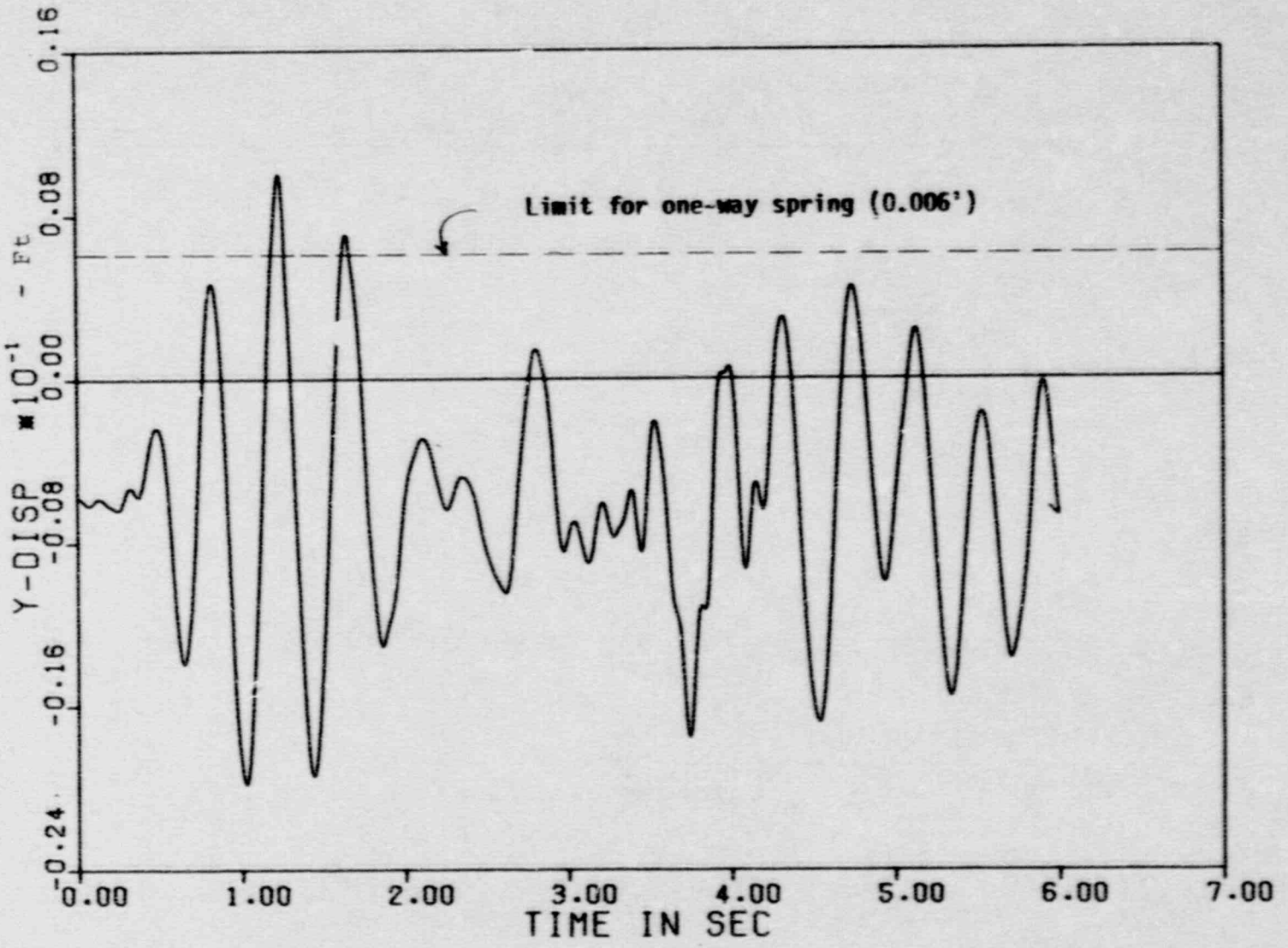

Figure 3.10 Vertical Displacement Time History at the End of Basemat, Node 7, A_H = 0.45g

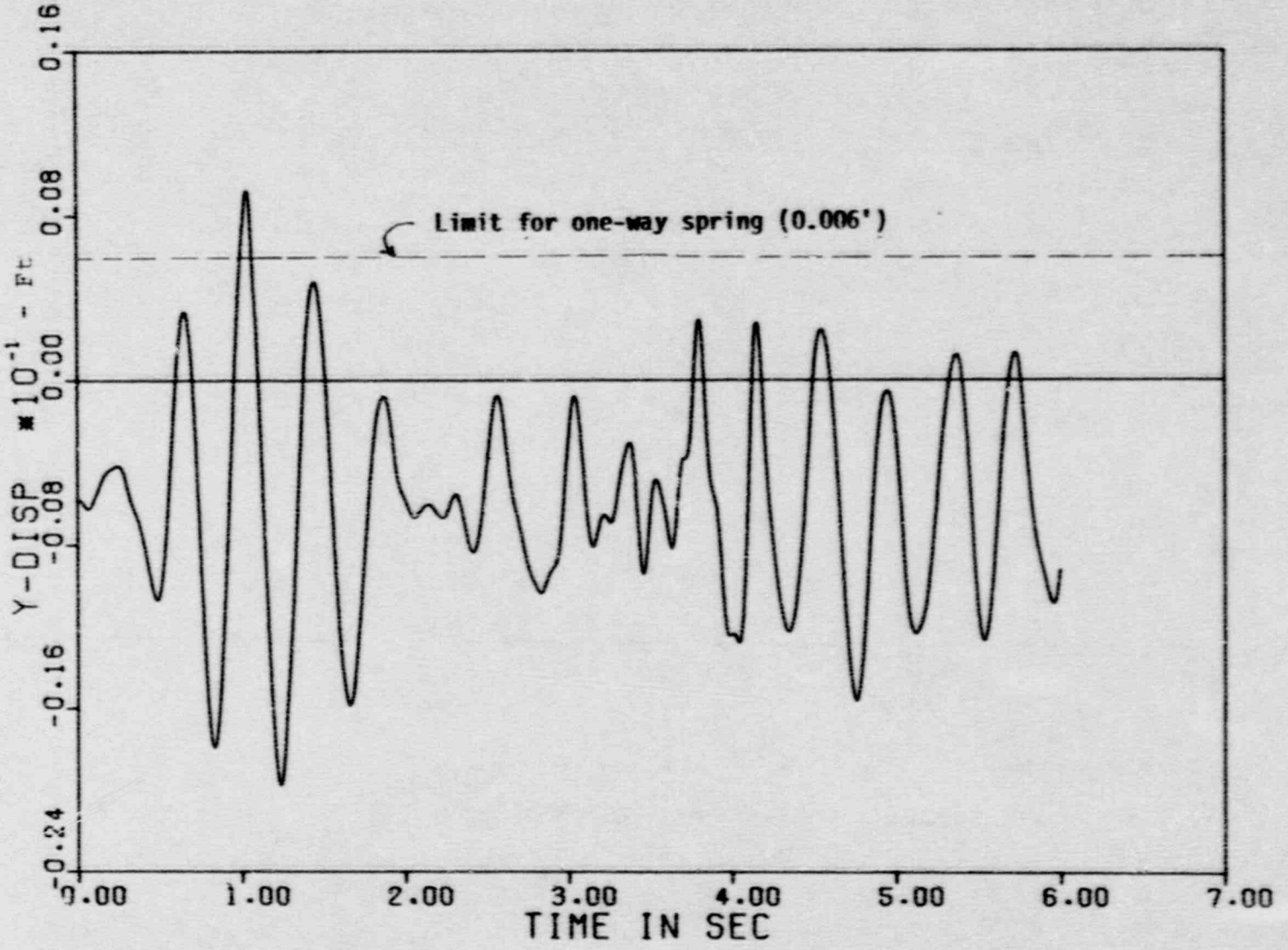

Figure 3.11 Vertical Displacement Time History at the End of Basemat, Node 8, A_H = 0.45g

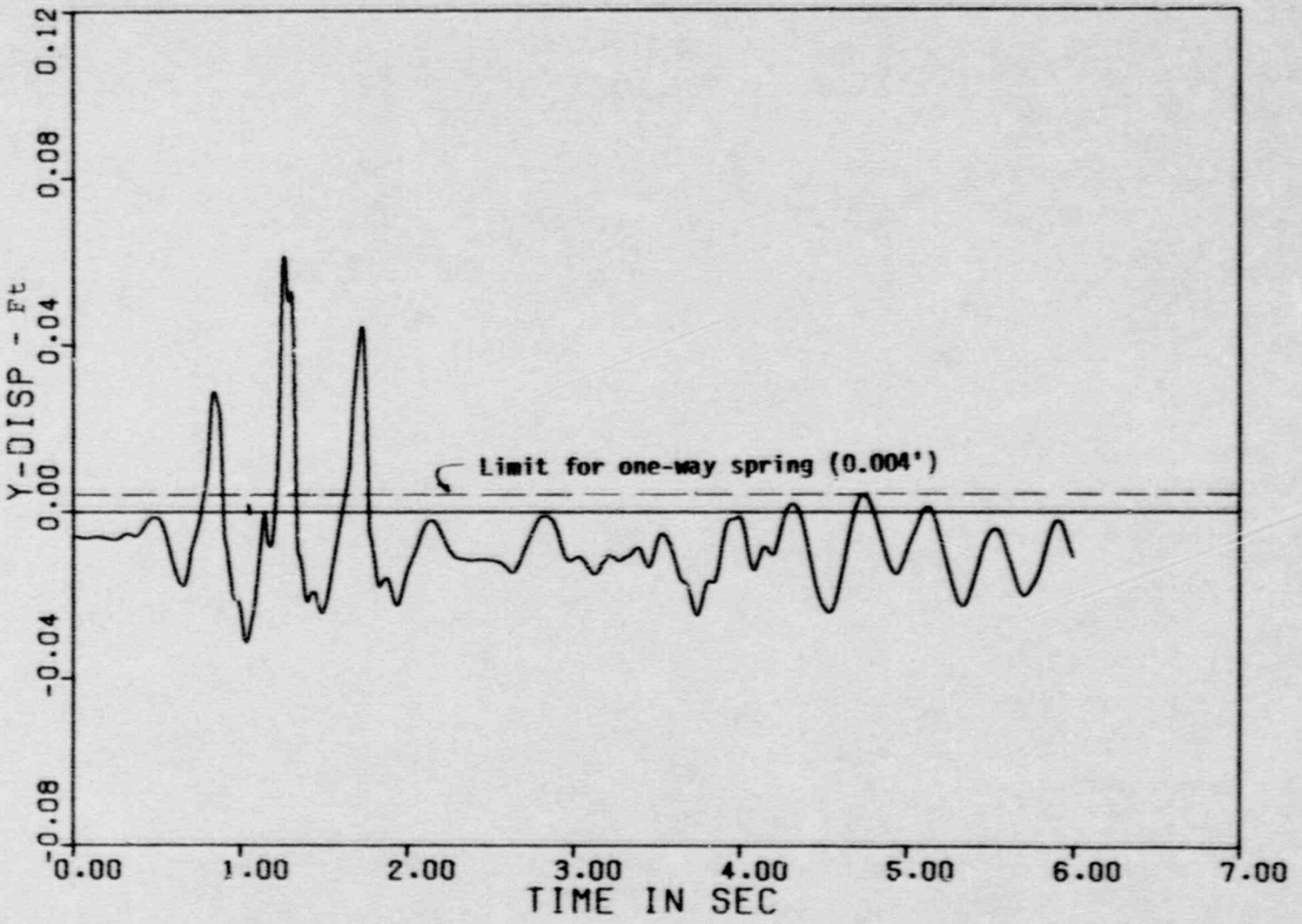

Figure 3.12 Vertical Displacement Time History at the End of Basemat, Node 7, A_H = 0.60g

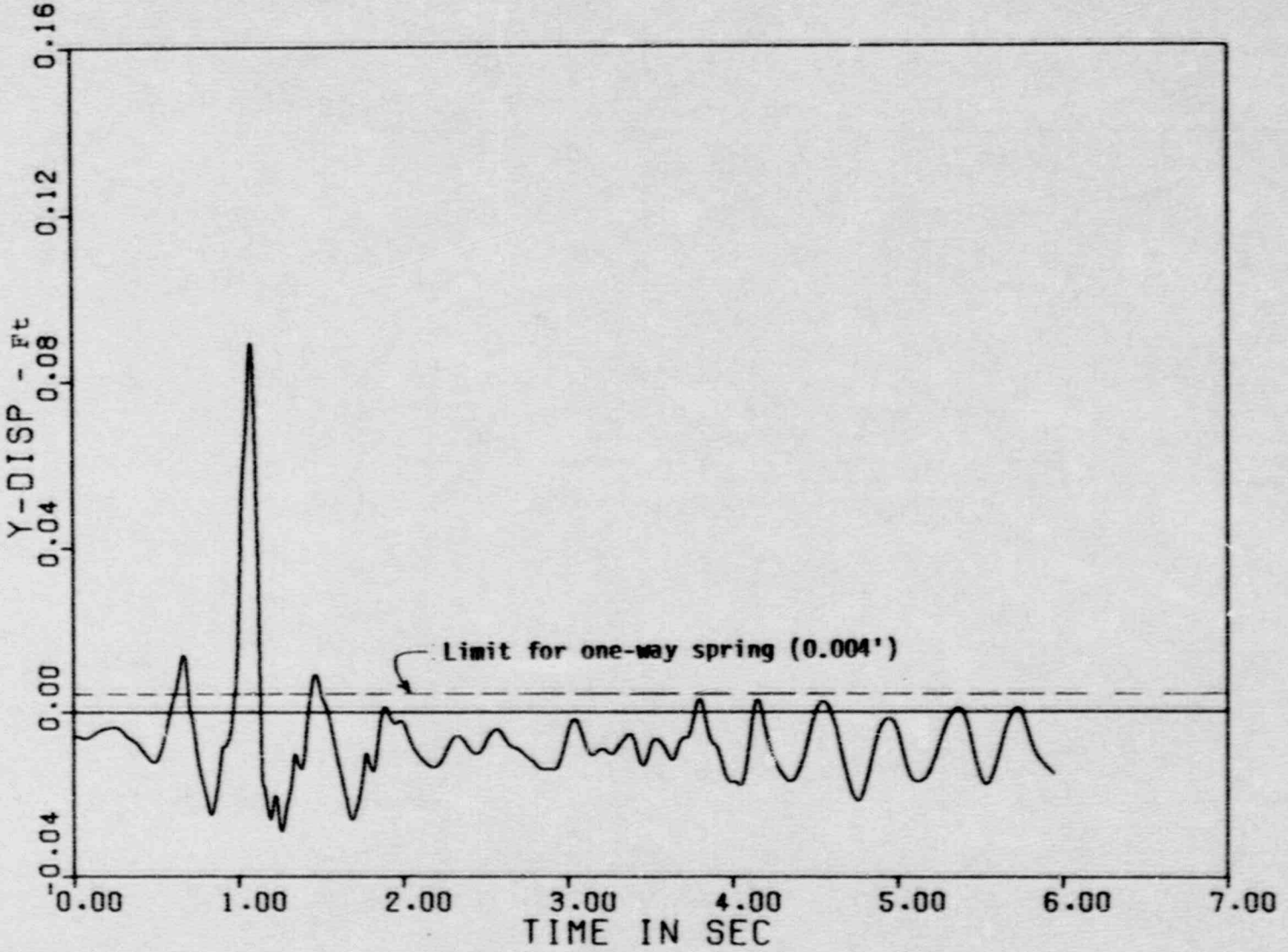

Figure 3.13 Vertical Displacement Time History at the End of Basemat, Node 8, A_H = 0.60g

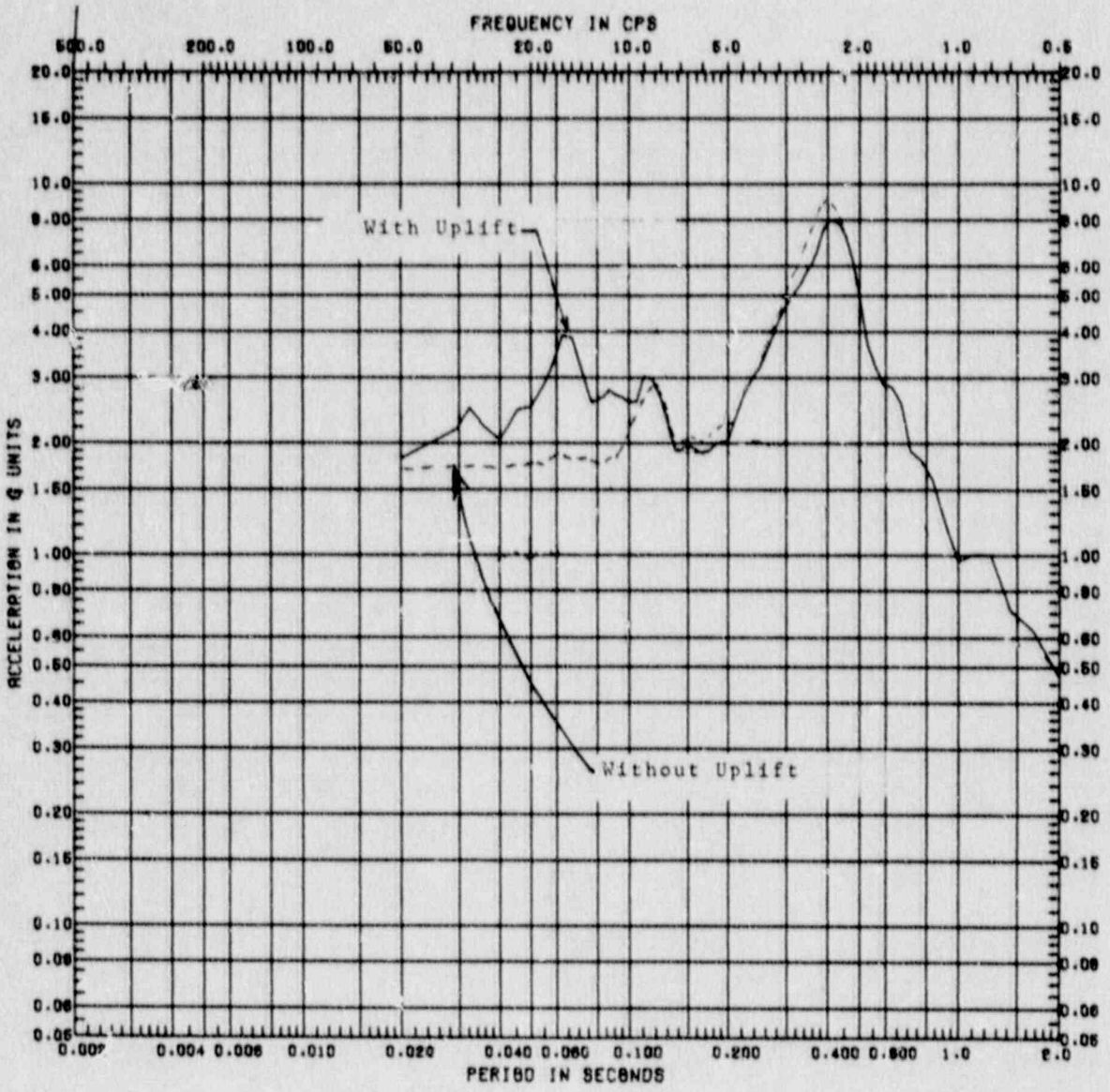

Figure 3.14 Horizontal Response Spectrum at the Top of Drywell, Node 46, A_H = 0.60g, Damping = 5%, With and Without Uplift

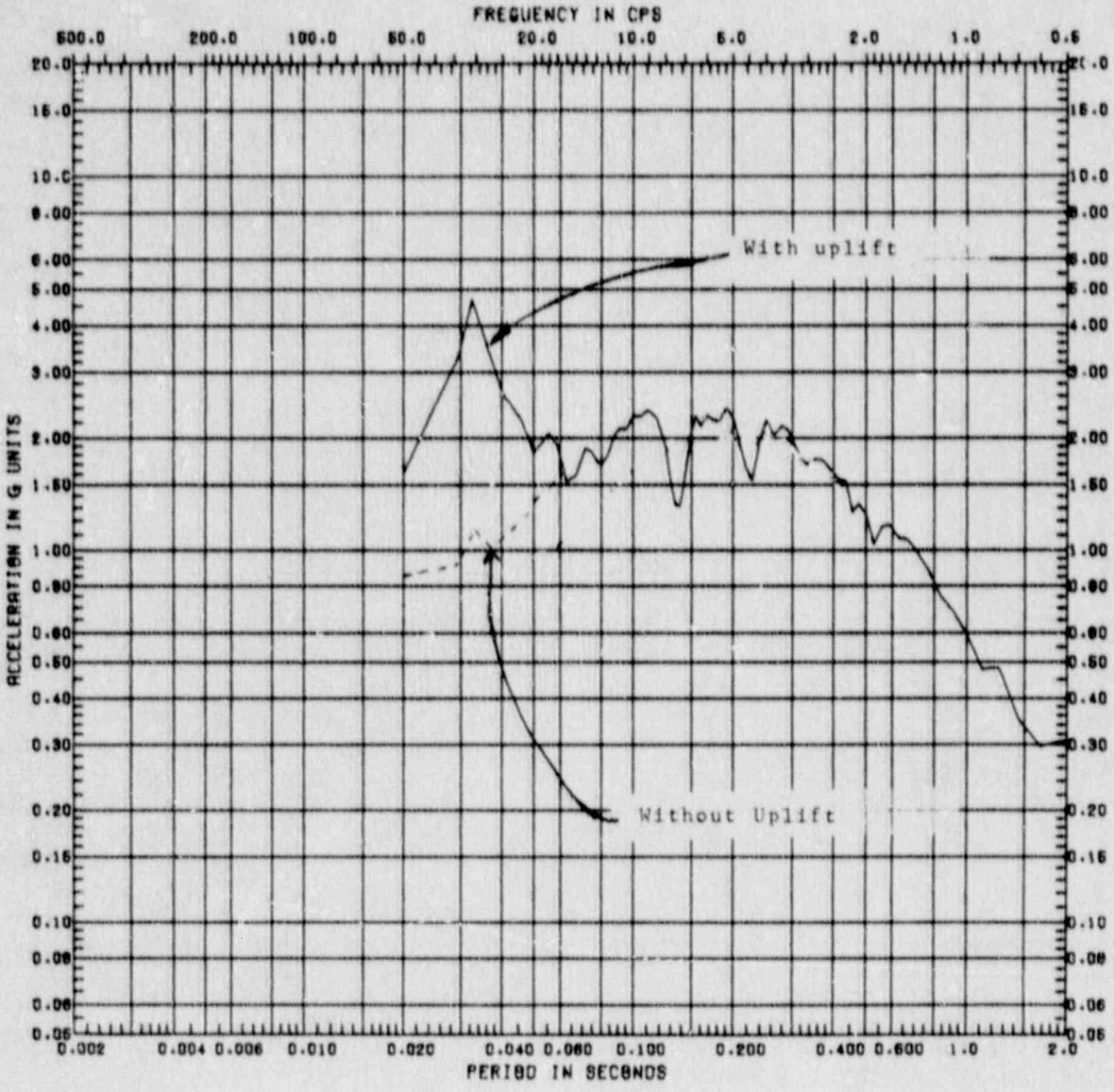

Figure 3.15 Vertical Response Spectrum at the Top of Drywell, Node 46, A_H = 0.60g, Damping = 5%, With and Without Uplift

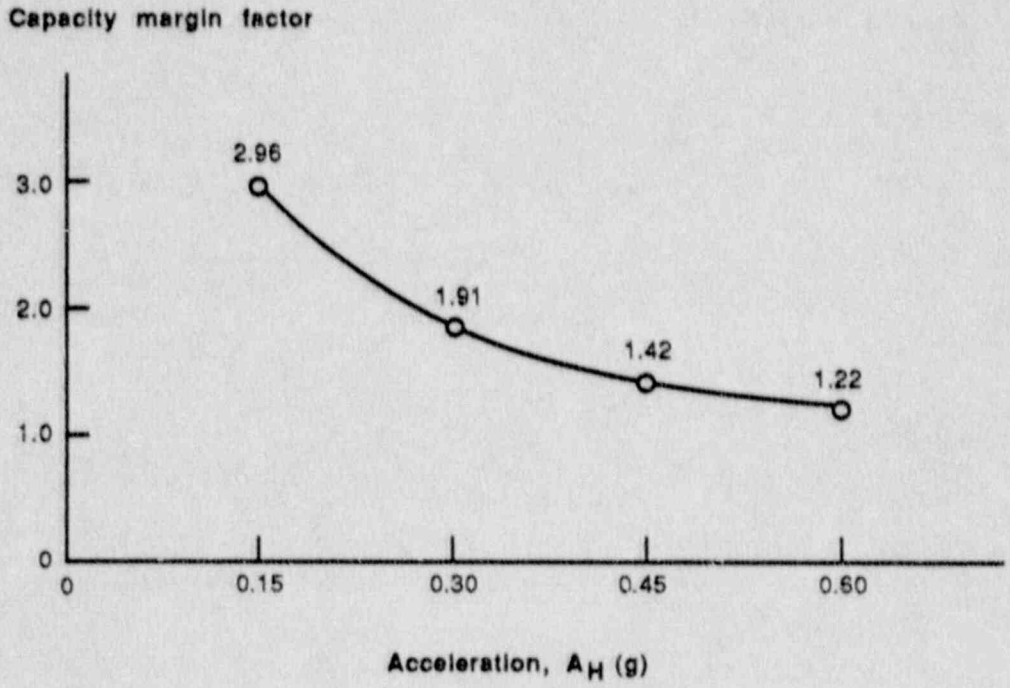

Figure 3.16 Variation of Margin with A_H for Meridional Buckling Under Task 3 Loading

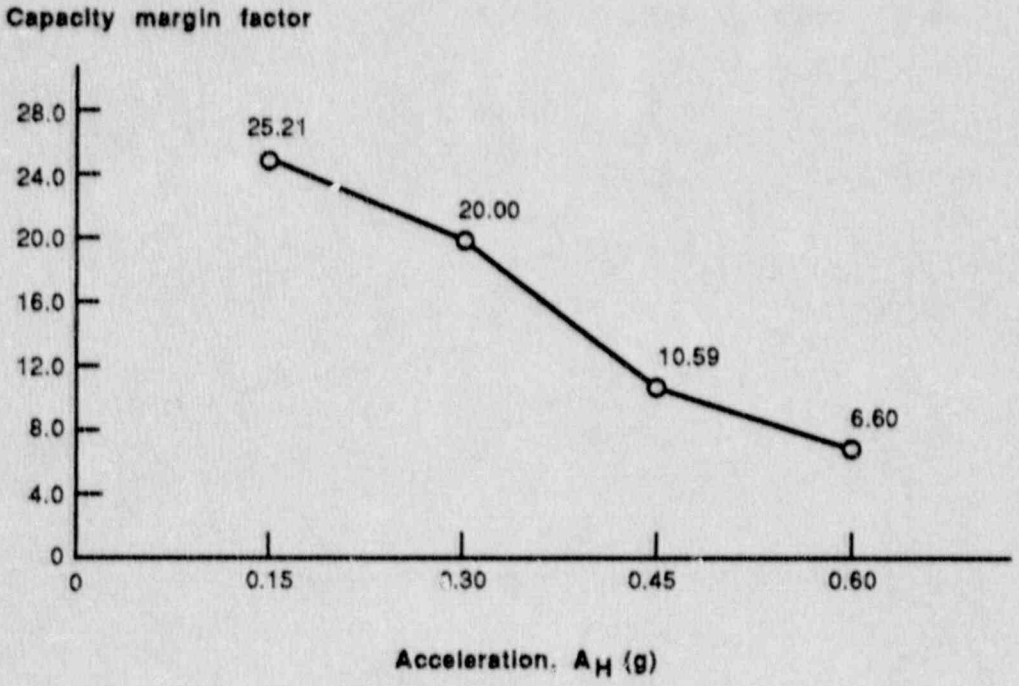

Figure 3.17 Variation of Margin with A_H for Tensile Failure of Containment Under Task 3 Loading

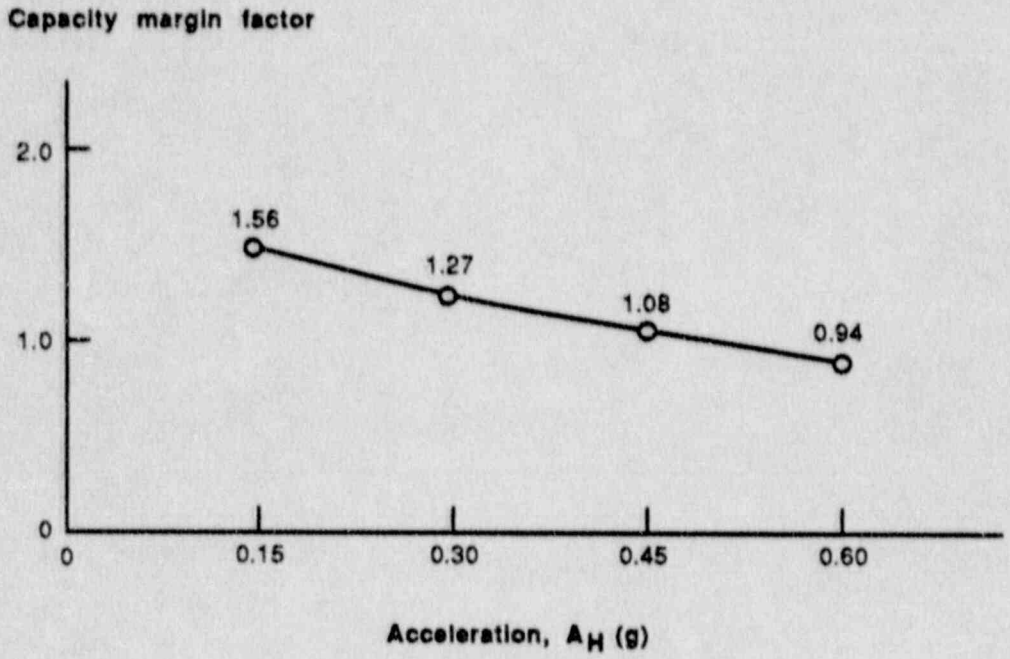

Figure 3.18 Variation of Margin with A_H at Upper Beam Seats Under Task 5 Loading

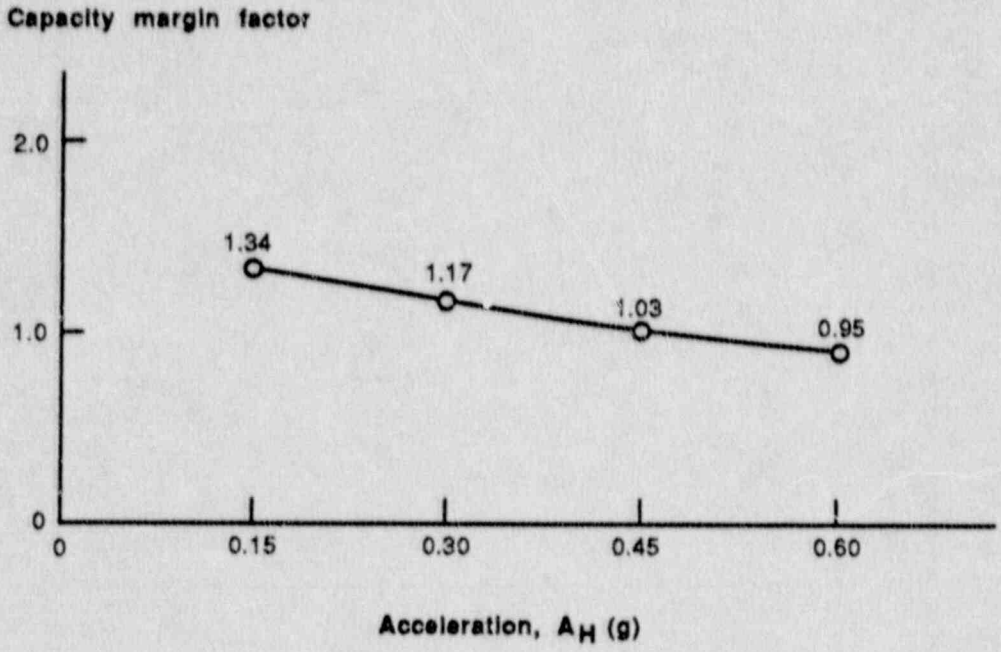

Figure 3.19 Variation of Margin with A_H at Lower Beam Seats Under Task 5 Loading

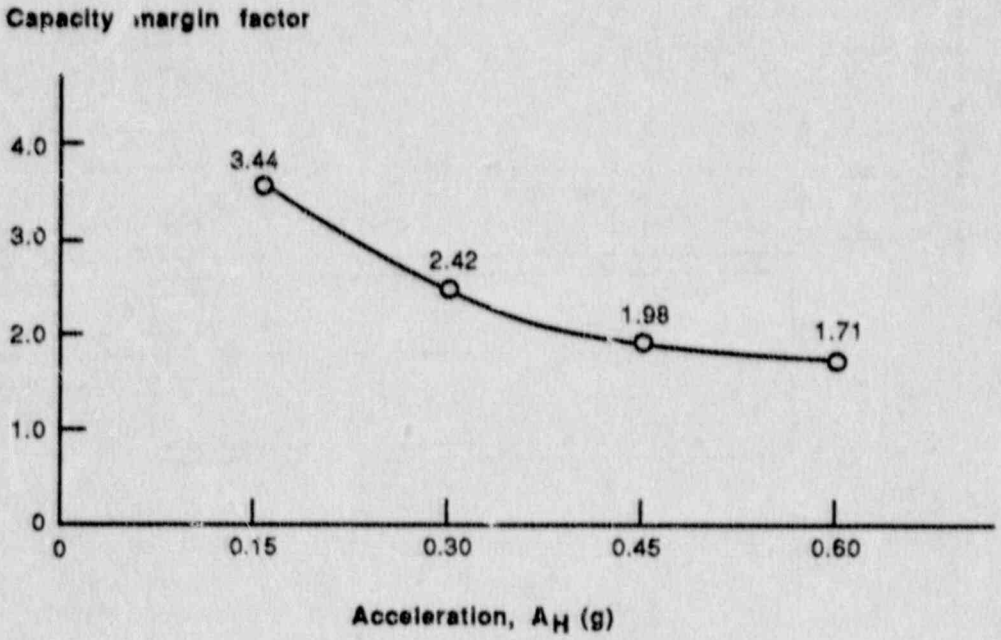

Figure 3.20 Variation of Margin with A_H for Drywell Head Bolted Connections Under Task 5 Loading

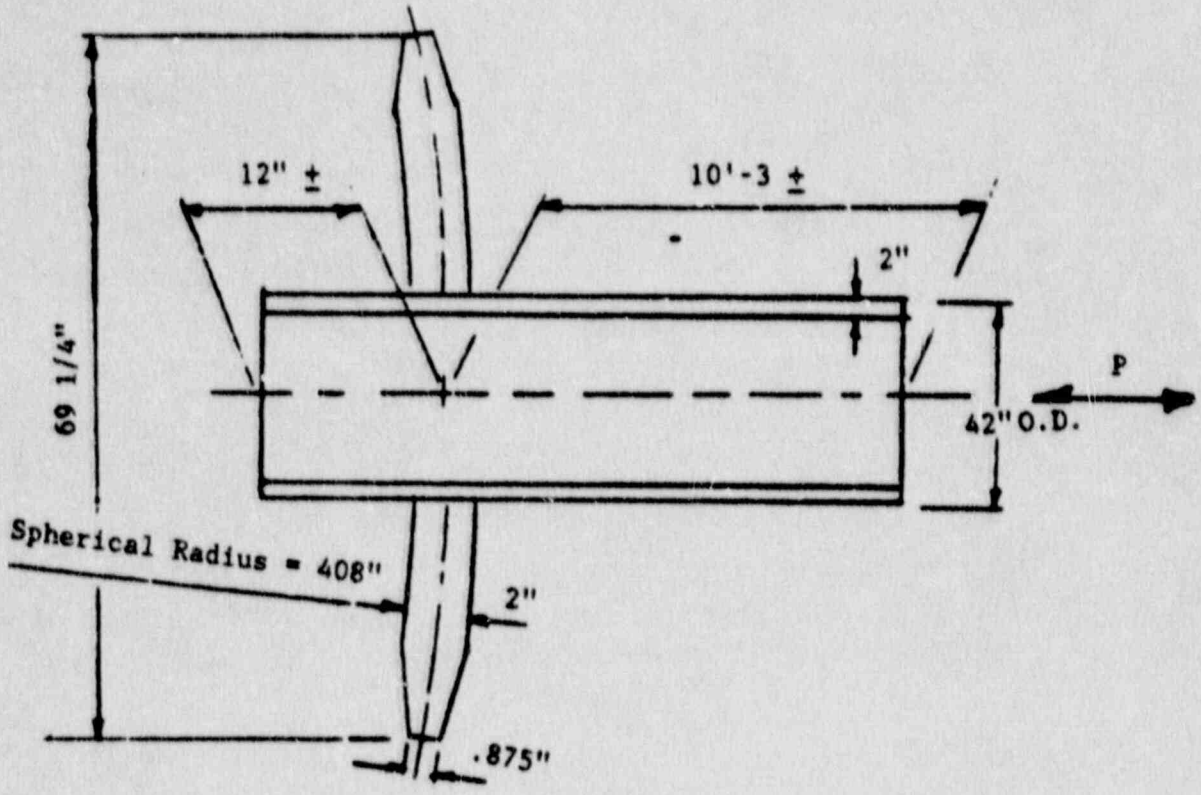

Figure 3.21 Details of Typical Main Steam or Feedwater Penetration Used in ADINA Analysis

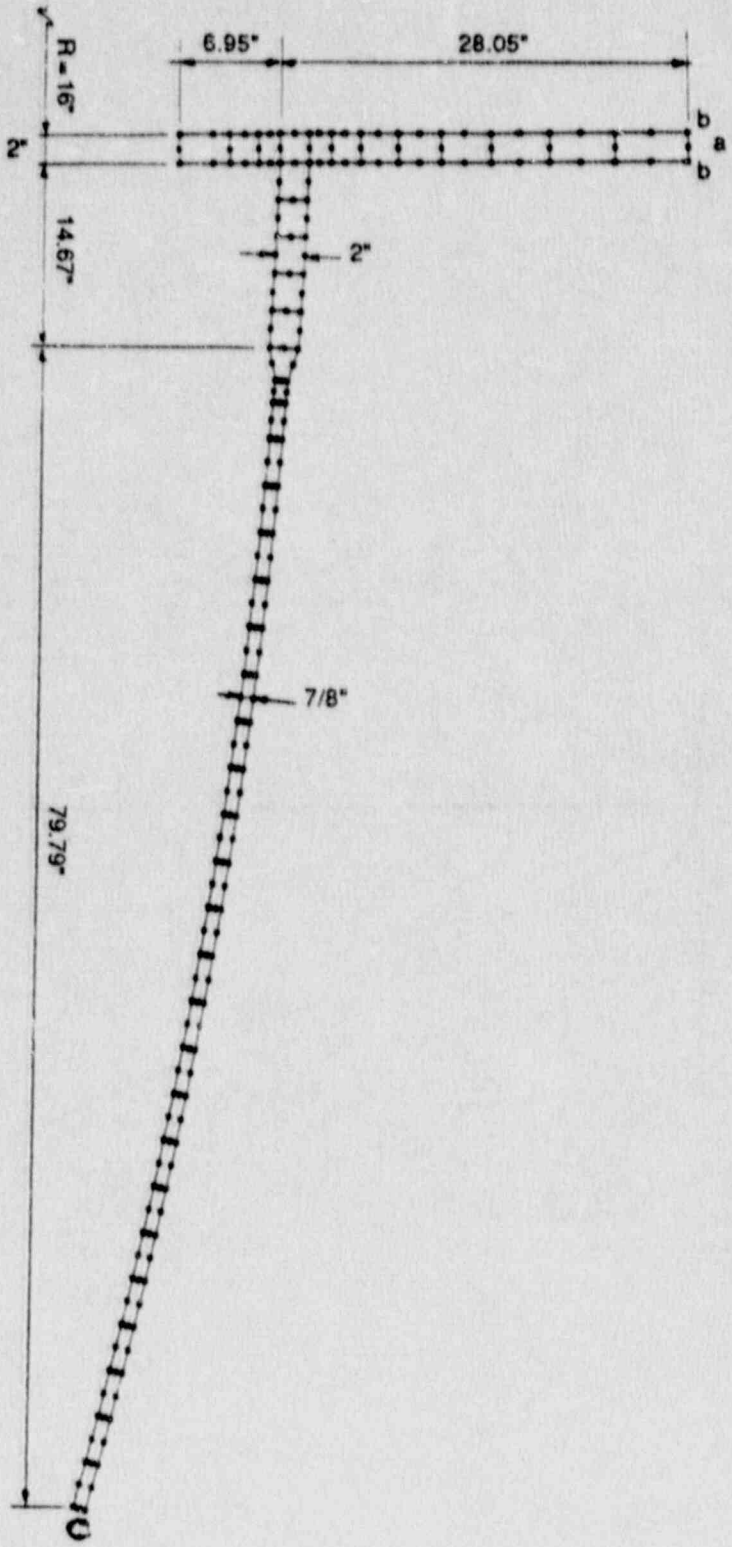

Figure 3.22 ADINA Finite Element Model of the Penetration

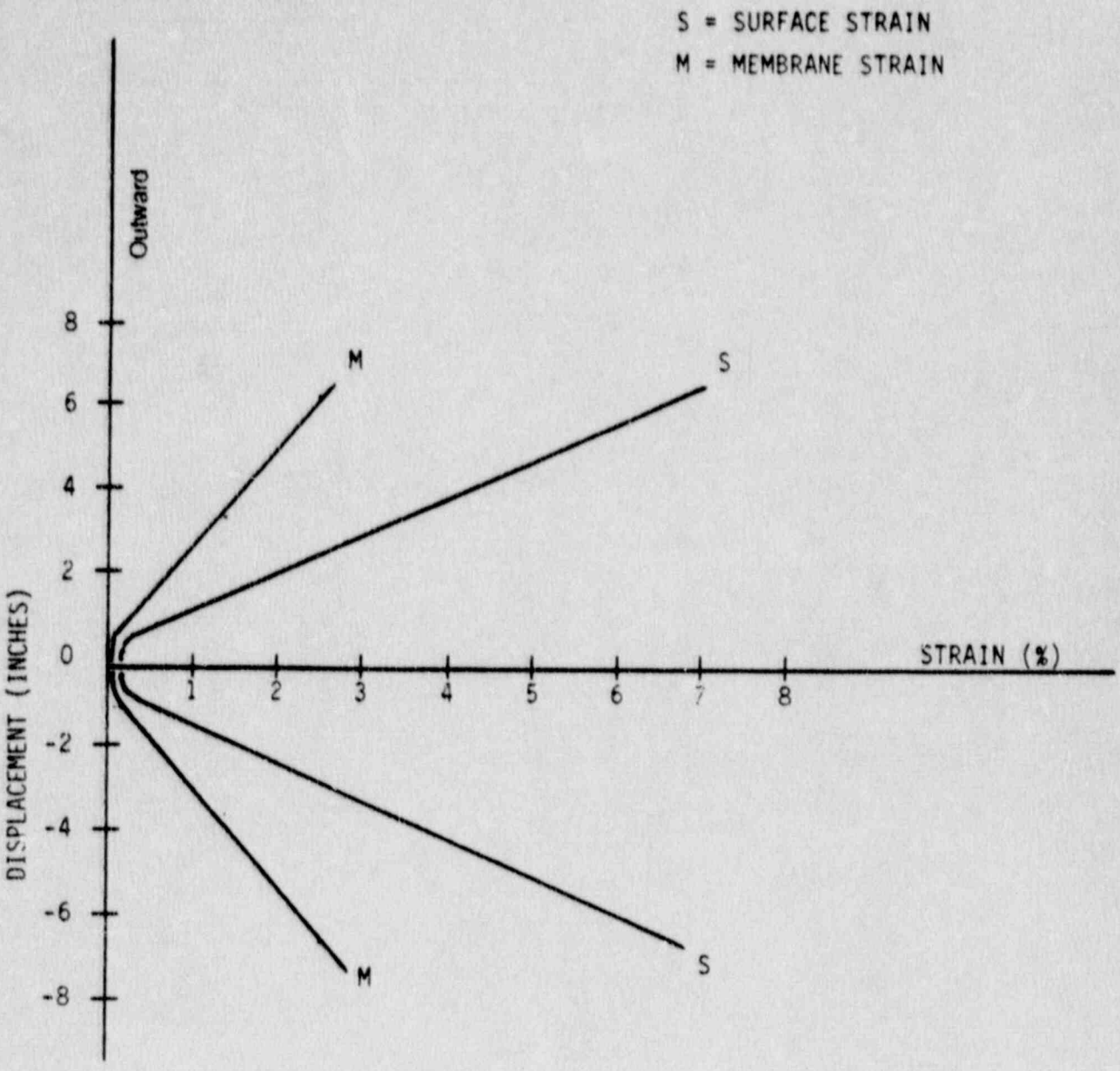

Figure 3.23 Results of ADINA for Penetrations (Task 3, Pressure = 0 psig, Temperature = 150°F)

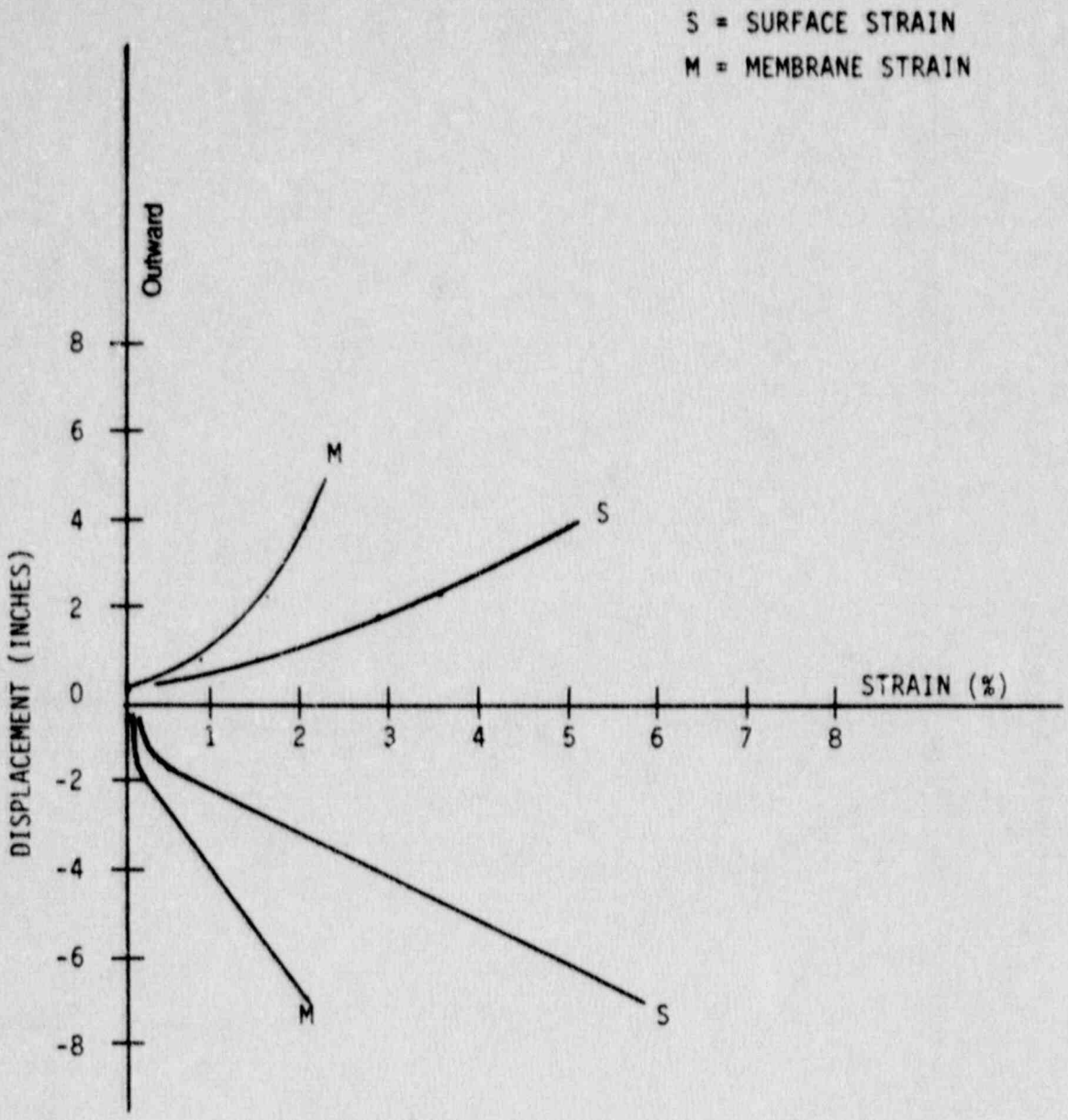

Figure 3.24 Results of ADINA Analysis for Penetrations (Task 4, Pressure = 56 psig, Temperature = 281°F)

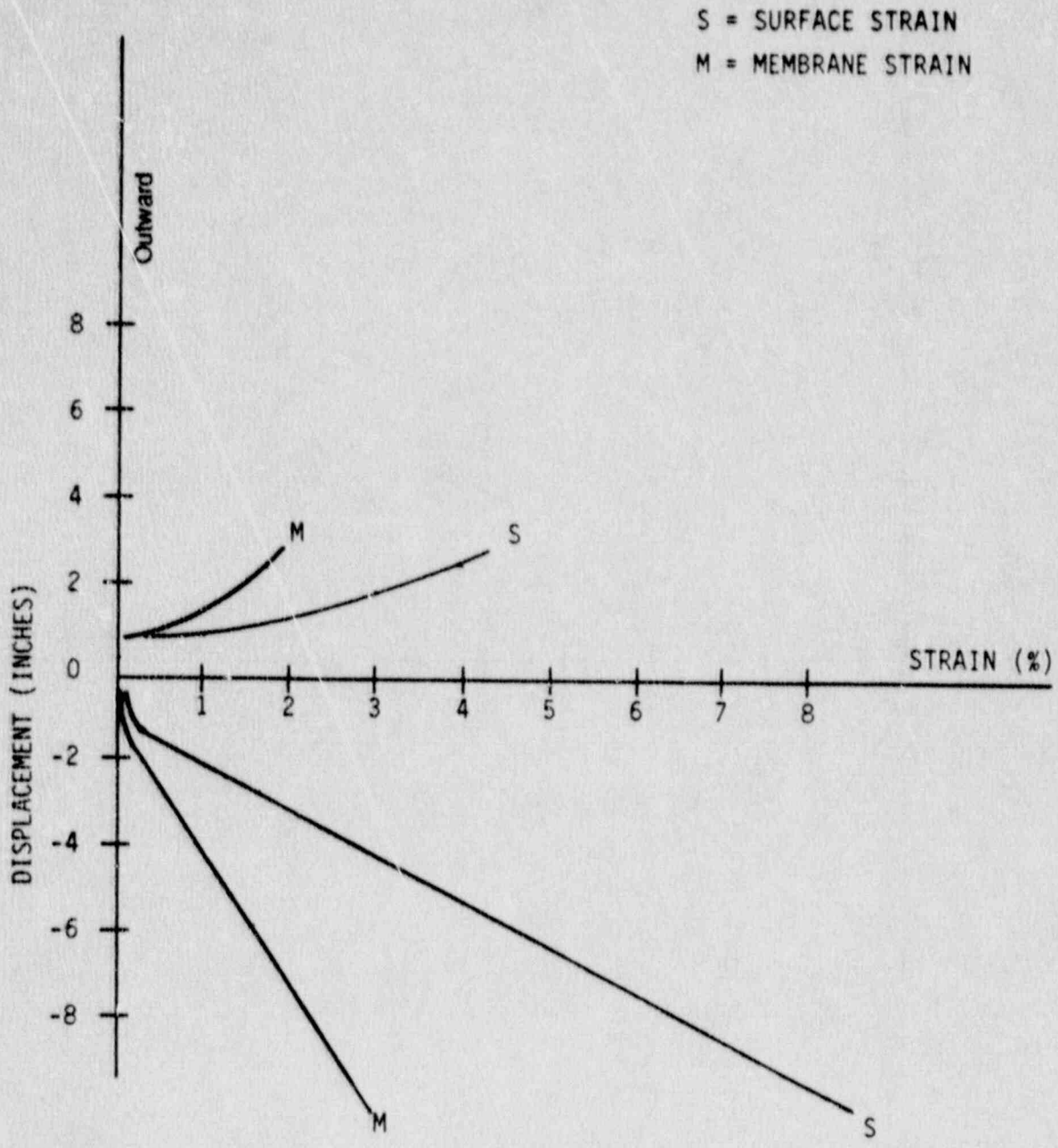

Figure 3.25 **Results of ADINA Analysis for Penetrations (Task 5, Pressure = 74 psig, Temperature = 550°F)**

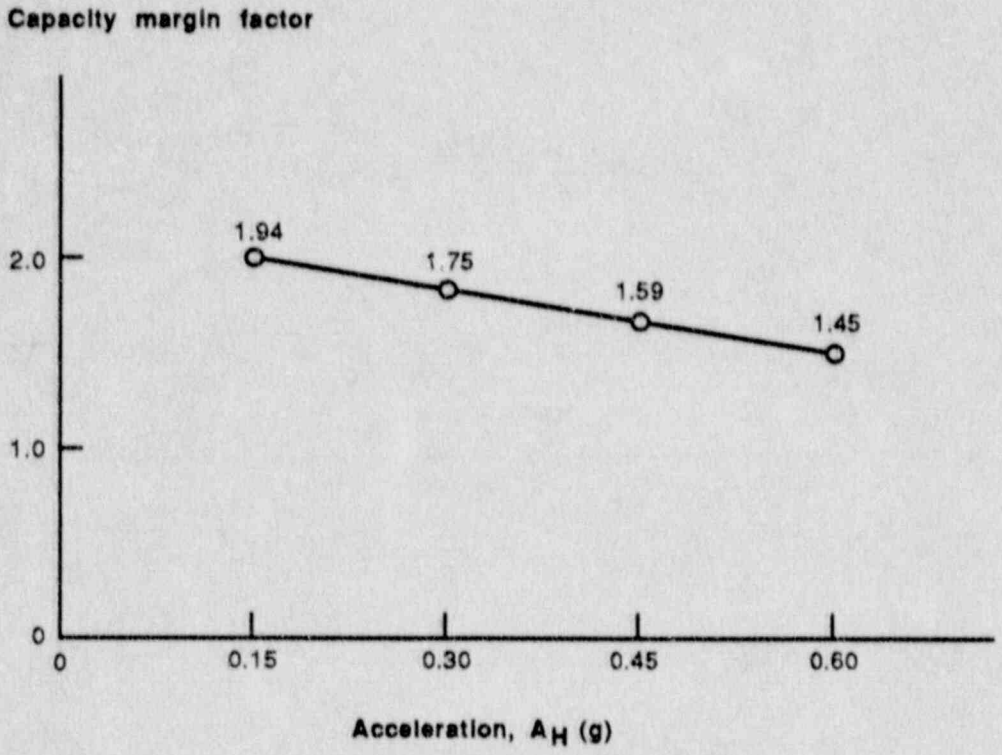

Figure 3.26 Variation of Margin with A_H for Suppression Chamber Supports for Task 5 Loading

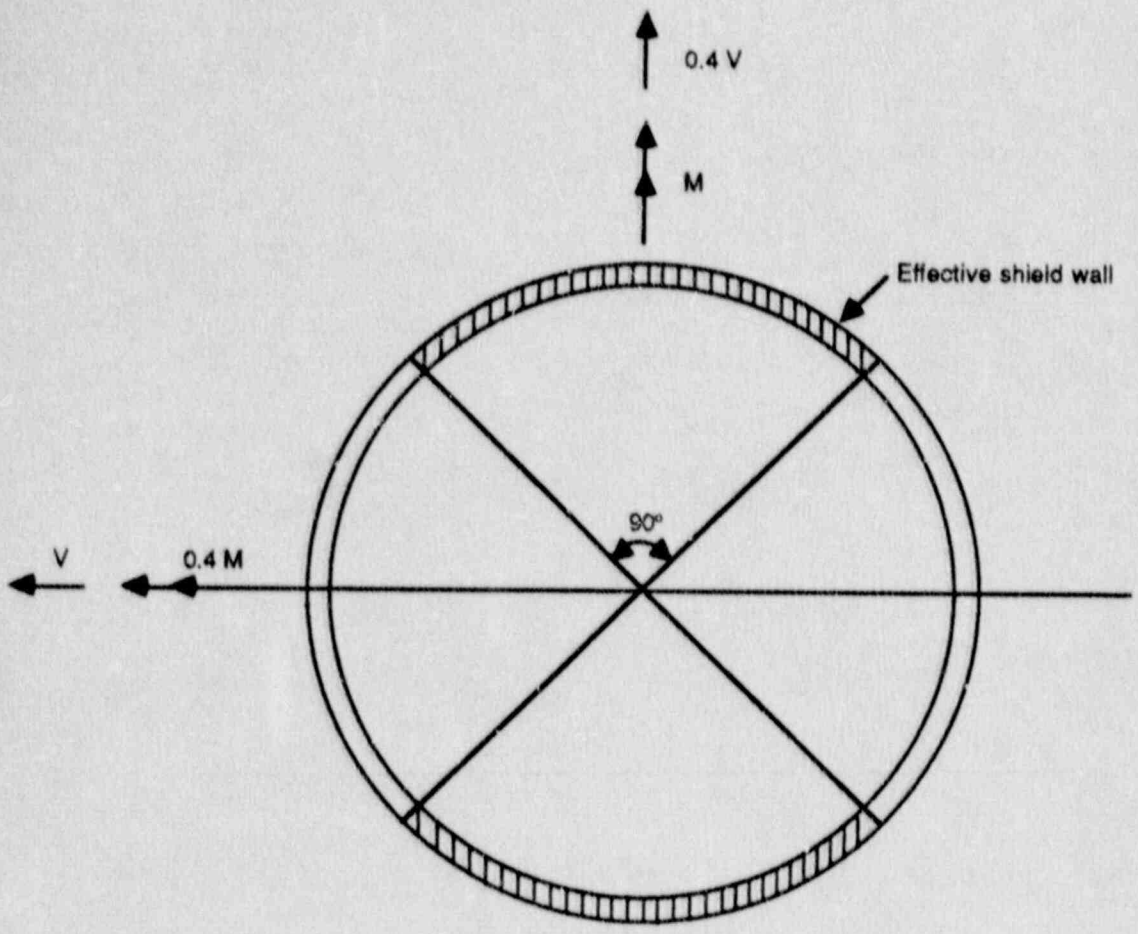

Figure 3.27 Portion of Circular Wall Section Considered to Resist Major Seismic Shear

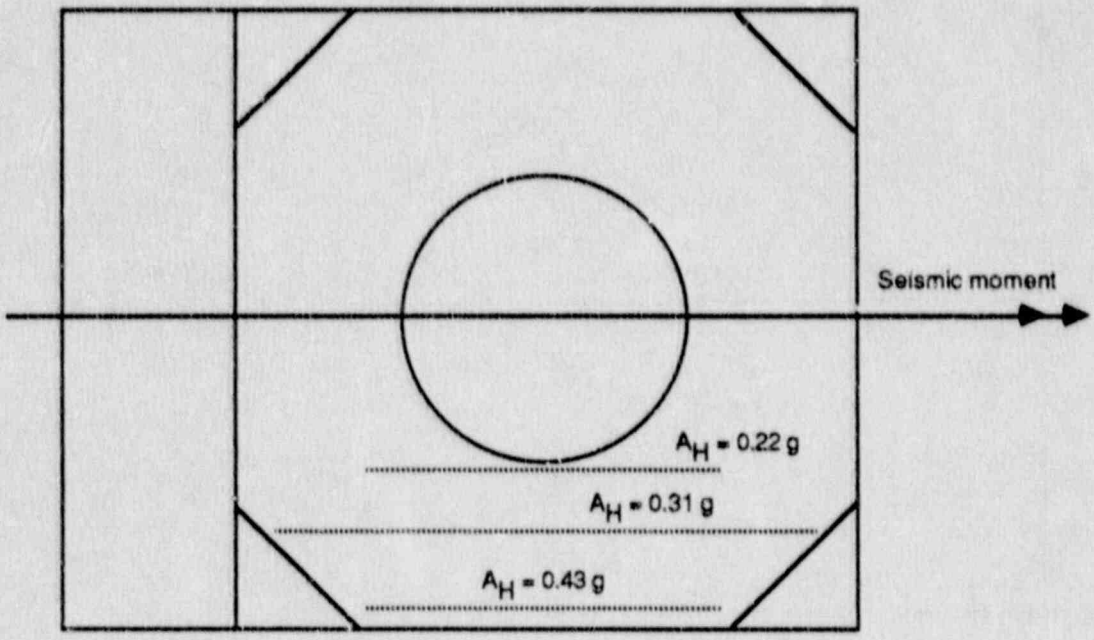

Figure 3.28 Critical Sections in Basemat for Moment Evaluation and Corresponding Seismic Capacities

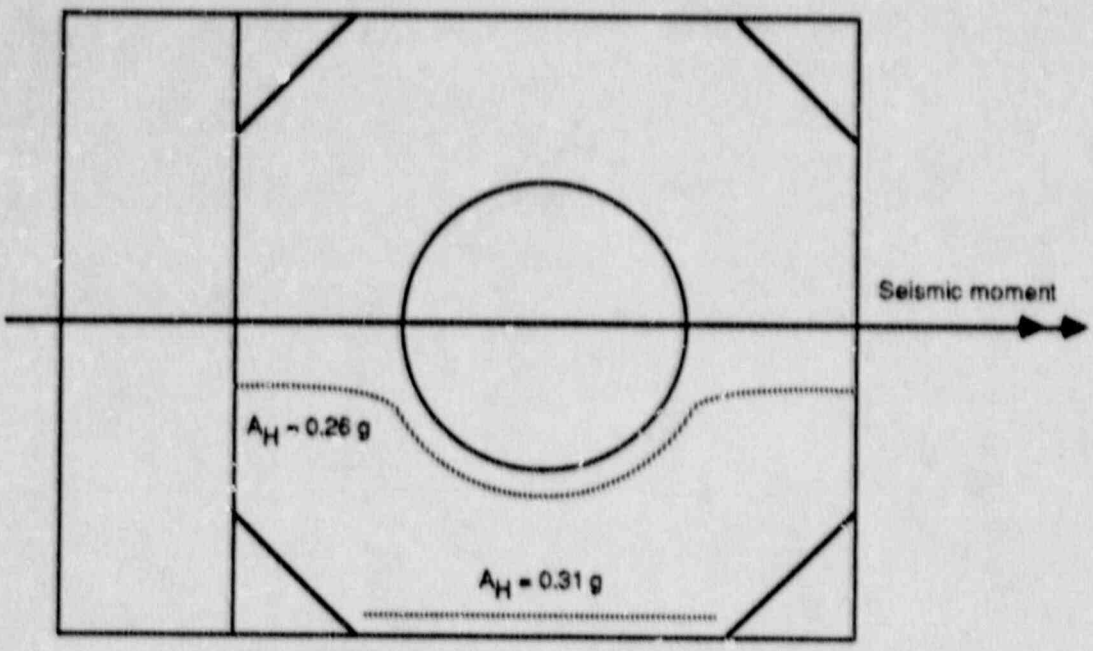

Figure 3.29 **Critical Sections in Basemat for Transverse Shear Evaluation and Corresponding Seismic Capacities**

4. EVALUATION OF CLINTON CONTAINMENT

4.1 Description of Clinton Containment Building

Figure 4.1 shows a general arrangement plan of major structures at Clinton Power Station. The structures included in the seismic model include the containment building, auxiliary/fuel building and control/diesel generator building. The buildings and the direction considered for horizontal seismic excitation are indicated on Figure 4.1. The orientation chosen for analysis is along the shorter plan dimension to maximize the potential for uplift. Turbine and radwaste buildings were not included in the seismic model to economize the analysis; their exclusion does not significantly affect the containment seismic responses.

The Clinton Power Station structures are founded on a well compacted, granular structural fill underlain by competent Illinoian and Pre-Illinoian glacial till deposits. A section through the foundation is shown in Figure 4.2.

A section through the containment building is shown in Figure 4.3. The containment consists of a right circular cylinder with a hemispherical domed roof and a flat basemat. It is constructed of reinforced concrete and is completely lined on the inside with 1/4-inch stainless steel plate below elevation 735 feet and with carbon steel plate of at least 1/4-inch thickness above elevation 735 feet.

The principal dimensions of the containment are:

a. Height above top of basemat: 215 feet;

b. Inside diameter: 124 feet;

c. Cylinder wall thickness: 3 feet;

d. Dome thickness: 2 feet 6 inches; and

e. Mat thickness: 9 feet 8 inches.

The containment structure supports the polar crane, galleries, and the access ramp to the refueling floor. The lower section of the containment acts as the outer boundary of the suppression pool. Two double-door personnel locks, one located at the refueling floor El. 803'-3" and the other located at the grade floor, El. 712'-0", permit access to the containment. An equipment hatch is located at the grade floor. The equipment hatch is sealed during normal operation, or at other times when primary containment is required.

The containment wall is reinforced in the hoop, diagonal and meridional directions. Wall reinforcement is deflected around small penetration sleeves to account for localized stress concentrations. The wall around the equipment hatch and personnel locks is thickened to 6 feet, and

additional reinforcement is provided. Tangential and transverse shear reinforcements are provided where necessary.

The dome is reinforced in two directions. Orthogonal grid type reinforcement is provided within a radius of 45 feet from the apex of the dome. The remaining portion of the dome is reinforced in the hoop and meridional directions.

The containment basemat is continuous with the adjacent auxiliary and fuel building basemats and is reinforced at top and bottom with reinforcing steel.

The major internal structures of the containment include the drywell structure, reactor shield wall, and reactor pedestal. The drywell is a cylindrical reinforced concrete structure which surrounds the reactor pressure vessel and its support structure.

The inside diameter of the drywell cylinder is 69 feet, and the wall thickness is 5 feet. The top of the drywell consists of a flat annular slab 6 feet thick at elevation 803 feet 3 inches. The drywell wall is rigidly attached to the basemat at elevation 712 feet. A steel head which can be removed to allow access to the reactor is located over the opening in the annular slab.

The reactor shield wall is an open-ended cylindrical shell 2 feet thick placed around the reactor pressure vessel. The primary function of the shield wall is to act as a radiation and heat barrier between the reactor pressure vessel and the drywell wall.

The shield wall consists of two concentric steel cylindrical shells, stiffened with radially placed diaphragms and filled with concrete in between the two shells. It is supported on top of the reactor pedestal ring girder.

The reactor pedestal supports the reactor pressure vessel (RPV) and reactor shield wall. The pedestal shell is a steel structure consisting of two concentric cylindrical shells connected by radially placed steel diaphragms for the entire height of the cylinders. The top of the pedestal consists of a ring girder to which the reactor shield wall is welded. The RPV base is anchored to the ring girder by pretensioned bolts which are designed to carry the loads through friction. To increase the stability of the structure, the annulus between the steel cylinders is filled with concrete. The concrete is not considered to act compositely with the steel plates.

The base of the pedestal is welded to embedded plates anchored in the sump floor with reinforcing bars attached to the plates.

4.2 Analysis of Containment for Gravity, Pressure, and Temperature Loads

A nonlinear laminated shell finite element model is used to determine the state of stress and strain in the containment and basemat under

gravity loads combined with internal pressure and temperature. Computer program DYNAX is used for this analysis. The containment and the basemat are divided into 57 thin shell finite elements, as shown in Figure 4.4. Each element is represented by multiple concrete and steel layers as shown in Figure 4.5. The concrete is divided into a number of layers and the reinforcing steel and the liner are included as separate layers placed at their actual positions in the section. The reinforcing steel layer thickness is determined by smearing the rebar area into an equivalent continuous layer, effective only in the direction of the rebars. Each layer is assumed to be in a state of plane stress. The layering of the elements allows the program to trace the extent of concrete cracking and the state of stress and strain in the liner and rebars as the structural system is incrementally loaded.

The soil is represented by a series of continuous springs supporting the basemat. The spring constant used is 518 K/ft^3 which is based on elastic soil deformation. Note that this spring constant is different from those applicable to seismic analysis which are presented in Section 4.3.

Table 4.1 summarizes the material properties used for rebars, liner, and concrete as a function of temperature.

Results of the analysis for gravity loads combined with the design accident pressure (15 PSIG) and temperature (185°F) are summarized in Table 4.2. In these finite element analyses the design temperature was assumed to exist at the inside face of the containment wall, a 70°F temperature was assumed to exist at the outside face of the wall, and a linear gradient through the wall was used. Along the height of the containment wall no temperature variation was used.

Analysis using the above finite element model and a temperature value of 400°F at various pressures indicated that the hoop rebar yielding is imminent at pressure of 45 psig. On this basis, the Task 5 pressure was selected as P_y = 45 psig. Results for this case are summarized in Table 4.3.

Task 6 pressure and temperature values are 30 psig and 300°F, which are the average of Tasks 4 and 5. Results for this case are summarized in Table 4.4.

4.3 Seismic Analysis

4.3.1 Overall Seismic Model

Figure 4.6 shows the overall seismic model used for the Clinton containment analysis. The details of constructing this model are discussed in Section 2.1.4. The additional information specific to this model is provided in this section.

The properties of the foundation soil are given in Table 4.5. The spring constant and dashpot values were obtained using the procedure

described in Section 2.1.2. These values for various ground acceleration levels are shown in Table 4.6.

The concrete compressive strength, f_c', used in the Clinton analysis is 4680 psi, which includes an increase of 17% for aging. The yield stresses of the reinforcing bars and the liner are 60 ksi and 32 ksi, respectively. All these material properties are based on the minimum specified values, and therfore are considered conservative, since actual properties are usually somewhat higher than the minimum specified; see Section 8.3.

Figure 4.7 shows the M-Ø diagrams used for the containment beam element 33-24 of Figure 4.6 for Tasks 3 through 5. Similar information was obtained and used for other containment elements.

In the evaluation of the tensile limit force of the vertical soil springs, F_{t1}, shown in Figure 2.11, a minimal adhesion of 1 psi between the basemat and soil was assumed.

For the time history analysis at A_H = 0.25g, which represents Clinton SSE level, the effect of cracking in the concrete element properties was not considered in order to be consistent with the original design basis, and therefore to benchmark the calculations. For higher acceleration levels the effect of cracking has been considered as described in Section 2.1.4.

4.3.2 Seismic Analysis Results

Figures 4.8 and 4.9 show the vertical displacement time histories at the ends of the basemat, i.e., nodes 38 and 64 in Figure 4.6, for A_H = 1.0g. Since the displacement remains negative at all times (indicating that the seismic displacement is less than settlement due to dead load), these time histories show that because of the large size of the basemat no uplift occurs up to this acceleration level.

Figures 4.10 and 4.11 show the comparison of horizontal response spectra at the basemat and the input ground spectra in the free field at A_H = 0.45g and 1.0g. The significant effect of soil-structure interaction is evident from this comparison. Due to softening of the soil at higher strains, the high frequency input is attenuated due to soil-structure interaction. As the level of ground shaking increases, the softening of soil also increases, and this attenuation becomes even more significant. Similar comparison for vertical shaking is shown in Figures 4.12 and 4.13, from which the same conclusions as for the horizontal shaking can be made.

Figures 4.14 through 4.16 show the horizontal response spectra for node point 4 on the containment model of Figure 4.6, at elevation 832 feet, i.e., 120 feet above the basemat, for A_H values of 0.25g, 0.75g, and 1.0g. To illustrate the amplification effects, the ground spectra are also shown on these figures.

The two notable features of the response spectra are the effects of concrete cracking and soil non-linearity. Comparison of horizontal response spectra at A_H = 0.25g (Figure 4.14) and A_H = 0.75g (Figure 4.15) shows the significant shift in the frequency of the peak response due to the effect of concrete cracking in the containment. A comparison of the horizontal peak spectral accelerations at A_H = 0.75g (Figure 4.15) and A_H = 1.0g (Figure 4.16) shows that the peak magnitude does not increase linearly with the increase in A_H due to the effect of soil nonlinearity.

Figure 4.17 shows a comparison of the vertical response spectrum at the node point 4 with the basemat spectrum at A_H = 1.0g. As can be seen, due to very high stiffness of the containment shell in the vertical direction, structural amplification is limited to high frequencies.

4.4 Capacity Margin Factors

The capacity margin factors for each limit state were defined in the same manner as in Equation (2.15). These margins for Clinton containment are listed in Tables 4.7 and 4.8. Table 4.7 contains margins for limit states which are directly related to the containment pressure boundary. Table 4.8 lists the margins for those limit states whose realization may indirectly affect the containment performance; integrity of the containment beyond these limit states cannot be determined within the scope of this study.

Tables 4.7 and 4.8 list the direct and indirect limit states, respectively, in their decreasing order of criticality. The calculated margin factors are used, with engineering judgment, to arrive at this rank ordering. Further comments on the relative criticality of various limit states are included in Section 4.5.

The margins listed in Tables 4.7 and 4.8 have been calculated for the A_H = 1.0g, unless the capacity in a limit state was reached prior to A_H = 1.0g. Tables 4.7 and 4.8 also contain a statement of the failure criteria used for the evaluation of the margins. These criteria are the same as stated in Table 2.1 and discussed in Section 2.2. The margin evaluations are made using the peak seismic responses. For shell responses the DYNAX model shown in Figure 4.18 was used. This model also includes the drywell and reactor pedestal walls. The vertical soil spring constants used are consistent with those used for seismic analysis, listed in Table 4.6. The analysis of this model and processing of data for reinforced concrete elements using computer program TEMCO were performed as discussed in Section 2.1.6.

4.4.1 Failure of the Reinforcing Bars

This limit state was investigated for the reinforcing bars in the containment wall and basemat. For the containment wall, the critical section for this limit state occurred in element 12 of Figure 4.18, i.e., three feet above the basemat. The critical reinforcement is the outside meridional reinforcement at zero degree azimuth on the tension side of the containment. The maximum strains are however not localized;

they extend circumferentially over at least 30 degrees. As shown in Table 4.7, a capacity, based on the strain criterion of 10 ε_y of A_H = 1.0g is calculated for Task 5.

Figure 4.20 shows the variation of margin with increases in A_H for failure of wall reinforcing bar for Task 5 loading condition. As can be seen from this figure, very high margins at lower A_H values exist for this limit state. Even at A_H = 1.0g, the calculated margin from TEMCO analysis is about seven. However, when the seismic load is slightly increased beyond A_H = 1.0g, the section analyzed in TEMCO cannot take this load. This behavior occurs because in the laminated reinforced concrete element, most concrete laminas crack and already yielded rebar elements cannot pick up the increased tension, causing a sharp drop in the margin. Because of this behavior, the capacity for this limit state has been reported as A_H = 1.0g in Table 4.7. It should be noted, however, that TEMCO analysis being an element-level analysis does not provide for the load redistribution in the meridional and circumferential directions in the containment. Therefore, calculated capacities should be considered somewhat conservative. This conservatism is demonstrated by a comparison of TEMCO analysis results and three-dimensional ADINA analysis results in Chapter 7. It should also be noted that similar phenomenon for containment wall rebar capacity was found in the Zion containment, after the internal pressure overcomes the effect of prestressing. This result is discussed in Section 5.4.1. The high margins reported for other tasks, in Table 4.7, will also undergo a similar sharp drop at some seismic level soon after A_H = 1.0g.

Evaluation of the basemat reinforcing bars was performed using the critical section near the drywell wall, as shown in Figure 4.19. Although the calculated margins in all tasks are greater than ten, a sharp drop is expected to occur in the margins soon after an estimated seismic level of A_H = 1.15g. This behavior is similar to the behavior of reinforcing bars in the wall, as explained in the above paragraph.

4.4.2 Tensile Failure of Liner

Like the reinforcing bar evaluation discussed in the above subsection both the basemat and wall liner sections were evaluated for this limit state. The critical sections for the liner are the same as for the reinforcing bars, discussed in the above subsection. The behavior of the liner is also very similar to the reinforcing bar behavior at these sections, except that a less critical situation exists in Tasks 4, 5, and 6 for the basemat liner due to temperature-induced compression. The comments regarding conversative nature of TEMCO analysis, made in the above subsection for reinforcing bars, are also applicable to the liner evaluation.

4.4.3 Transverse Shear Failure

This limit state was investigated for the basemat and also for the wall near the basemat junction. The critical section for the basemat shear is at element 6 in Figure 4.18, which is located between the drywell wall and the containment wall. Figure 4.19 shows the plan of the base-

mat where the section through which the total transverse shear was calculated for use in the margin calculation is identified. The lowest margin for basemat in this limit state was calculated as 1.6 at A_H = 1.0g, for Task 4 condition. The higher margins shown in Table 4.6, in Tasks 5 and 6, than in Tasks 3 and 4, are because of the significant compression provided by the high temperature.

For the containment wall, the maximum transverse shear was directly obtained from the DYNAX analysis. The lowest margin for the wall in this limit state was calculated to be 1.1 for Task 5. Figure 4.21 shows the variation in the margin factor for transverse shear failure in the wall with increase in A_H for Task 5 condition.

4.4.4 Failure of Containment Wall at Penetration

The penetration used for this evaluation was the main steam penetration at El. 770 ft., about 58' above the basemat. To calculate margin for this limit state, the penetration pull-out capacity is divided by the total piping stiffness at the wall to determine a displacement capacity. This displacement capacity is then divided by the maximum displacement from seismic plus pressure and temperature analysis to determine the margin; therefore, using a higher piping stiffness will provide conservative result.

In order to estimate the stiffness of the piping system, several piping analyses from existing projects were reviewed. The thermal reactions at the containment wall, and the thermal movement of the piping in the vicinity of the wall were obtained from this review. From this data, piping system stiffnesses of 10 k/in. to 100 k/in. were computed. A total stiffness of 160 k/in. was used for the margin evaluation at penetrations to account for both inside and outside stiffnesses. Note that the stiffness used is about 80% of the maximum of the stiffness determined from the review of piping stress reports; therefore, it is a relatively conservative stiffness value. The lowest margin thus obtained for this limit state is 2.5 for Task 5.

The pull-out capacity used in the evaluation of this limit state was based on ASME Code provisions. This is considered quite conservative in view of the test results obtained on the panel testing at Construction Technology Lab of Portland Cement Association, Reference 4.1. A comparison of the pull-out capacity obtained in the test, and the one calculated, using ASME Code provisions for the test panel showed that the test capacity is 2 to 2.5 times greater than the capacity obtained using Code provisions. This further demonstrates the conservatism inherent in the evaluation of this limit state.

4.4.5 Failure of Equipment Hatch and Personnel Locks

The critical item for these large penetrations was considered to be the pretensioned bolted connection at the equipment hatch. These connections have twenty 1-1/2 inch diameter SA 193 B7 bolts. The equipment hatch is a pressure seated type. The shear capacity of the bolted connection was computed using a pretension equivalent to the 75% value

of ASME bolt allowable stresses and a reduction of 10% for the effect of torque relaxation. A coefficient of friction 0.4 was used to obtain the available shear friction capacity. This is based on steel to steel contact and frease-free in air condition (Reference 3.4). The capacity margin was obtained using this capacity and a shear load computed using the zero-period acceleration of the applicable vertical response spectra. The zero-period acceleration is used here because of the rigidity of the component in the response mode being considered, which is the sliding between flanges. The minimum margin thus computed is 4.9 for Task 3. Due to the pressure-seated construction, the margins for other Tasks are higher.

In addition to the bolted connections, buckling of the equipment hatch and seismic capacity of the latching mechanism of the personnel locks were also evaluated and very significant capacity margins were computed, showing the noncritical nature of these items.

4.4.6 Through Wall Crushing of Concrete

The critical zone for this limit state is element 14 of Figure 4.18. The location of maximum membrane compression is at 180^{0} azimuth. The capacity margin of greater than 10 at A_H = 1.0g was computed for Task 3. For other Tasks, the existence of pressure increases this margin even further.

4.4.7 Liquefaction of Structural Fill

The liquefaction potential of the granular structural fill was evaluated by using 65% of the peak shear stresses transferred to the soil. An equivalent number of uniform shear stress cycles, with the above magnitude of the shear stress, was considered based on Reference 4.2. At A_H = 0.75g, 20 cycles and at A_H = 1.0g, 25 cycles of uniform stress were used. The cyclic shear strength data, corresponding to initial liquefaction, obtained from laboratory tests, shown in Figure 4.22, were reduced to their 70% value to represent the in-situ conditions. These reduced strength values were used to compute the factor of safety against initial liquefaction. A margin factor of one was obtained for A_H = 0.83g. Figure 4.23 shows the variation in capacity margin factor with increase in A_H for this limit state. These margins, obviously, are independent of tasks, since pressure and temperature have no significant effect on the soil stresses.

The structural fill below the Clinton containment basemat consists of well compacted granular soil. The minimum specified compaction was a relative density of 85%. Occurrence of liquefaction for such well compacted soils is not considered likely. However, for such high acceleration levels, as A_H = 0.75g and higher, the calculated stresses also become high, and calculational approach used shows likelihood of initiation of liquefaction. It is felt that a more detailed evaluation of this phenomenon may show that liquefaction of such well compacted soil is not very likely.

4.4.8 Bearing Failure of Foundation

The capacity margin factor for this limit state is based on the ultimate bearing capacity of 80 ksf, obtained from design information. The maximum bearing pressure during the seismic event was used for this evaluation. A high capacity margin of 8.0 was computed for this limit state for all tasks.

4.4.9 Failure of Bolted Connections at Drywell Head and Drywell Equipment Hatch

Although the drywell in the Clinton containment is not part of the containment pressure boundary, failure of the large penetrations, i.e., drywell head and equipment hatch, was evaluated to see if drywell can be prematurely breached. For this evaluation, it was assumed that the pressure between the drywell and containment will be equalized. There are 72, 2-3/4 inch diameter SA 193 Gr B6 bolts in the drywell head. A preload of 55.5 k/bolt was used based on the Operating and Maintenance Manual. The drywell equipment hatch has the same bolting as the containment equipment hatch discussed in Section 4.4.5.

Both the drywell head and drywell equipment hatch bolted connections were evaluated using the same method as discussed in Section 4.4.5. Capacity margin factors of 7.6 for drywell head and 5.9 for equipment hatch were calculated for all tasks.

4.5 Conclusions

The following conclusions are drawn from the results presented for Clinton containment in this chapter:

1. The calculated seismic capacity for Clinton containment is associated with the indirect limit state of the liquefaction of structural fill under the containment basemat. This capacity is A_H = 0.83g. However, as discussed in Section 4.4.7, it is felt that the occurrence of liquefaction in well compacted soils is not very likely. A more detailed evaluation of this phenomenon may improve the margins further. Compared to the design-basis SSE, even this conservative capacity shows a margin greater than three.

   Because the calculated capacity is associated with an indirect limit state, it is not affected by the presence of accident pressure and temperature in the containment.

2. Of the six direct limit states evaluated, the through-wall crushing of concrete, failure of bolted connections at containment equipment hatch, and failure of containment wall at penetrations are of no concern based on high margins calculated in all tasks at A_H = 1.0g.

   Of the remaining three direct limit states, the smallest capacity of A_H = 1.0g was calculated for failure of reinforcing bars and liner in the containment wall. Based on the element-level TEMCO analysis the capacity drops sharply when most concrete laminas crack and

yielded reinforcing bars cannot pick up the added seismic loads. A three-dimensional analysis, allowing for meridional and circumferential load redistribution, could significantly improve the margin, as discussed in Chapter 7.

The reinforcing bars in the basemat exhibit behavior similar to the rebar in the wall. Although the calculated margins at A_H = 1.0g are high, the estimated capacity is A_H = 1.15g.

3. The transverse shear failure in basemat is found to be less critical than in the containment wall due to thick Clinton basemat and liberal use of shear ties. The margin against transverse shear failure in basemat, at A_H = 1.0g, ranges from 1.6 to 2.1 in various tasks, whereas for the containment wall it ranges from 1.1 to 1.6. Again, comparisons shown in Chapter 7 demonstrates the conservative nature of results obtained from the simplified analysis.

4. The effect of increased pressure and temperature on Clinton containment is to reduce the margins against some of the limit states, e.g., failure of wall reinforcing bars or liner and failure due to transverse shear in wall. However, for basemat reinforcing bars and liner, the margin is not reduced because of temperature induced compression.

5. The initial main shock upto a level of A_H = 1.0g, is considered not to have any effect on the subsequent seismic capacity of Clinton containment, since no portion of the concrete wall is crushed in compression, thus allowing continued use of the full cross-section for evaluations in Tasks 4, 5 and 6.

6. Because of large basemat, no uplift of basemat occurs at A_H = 1.0g.

7. There is a significant soil-structure interaction effect, which reduces the responses in high frequency range, and this effect increases with increasing values of A_H due to the softening of soil.

4.6 References

4.1 Hansen, N. W., et al "Concrete Containment Structural Element Tests, Phase 2, Vol. I - Tests of Containment Structural Elements With Liner Plates, Description and Results," Draft Final Report to Electric Power Research Institute by Construction Technology Laboratory, Skokie, IL., September 1986.

4.2 Seed, H.B. "Soil Liquefaction and Cyclic Mobility Evaluation for Level Ground During Earthquakes," Proc. ASCE, Vol. 105, No. GT2, Feb. 1979.

Table 4.1
Summary of Material Properties for Rebar, Liner, and Concrete

1. Stainless steel liner - SA-240 Type 304

Property	100 ≤ (°F)	200(°F)	300(°F)	400°F)
Yield strength, F_y (ksi)	30.0	25.0	22.5	20.7
Young's modulus E (ksi)	28300	27600	27000	26500
Coef. of expansion x 10^{-6}	8.54	8.76	8.97	9.21

2. Carbon steel liner SA-516 Gr. 60

	100 ≤ (°F)	200(°F)	300(°F)	400°F)
Yield strength (ksi)	32	29.2	28.3	27.4
Young's modulus E (ksi)	29300	28600	28100	27500
Coef. of expansion x 10^{-6}	6.5	6.67	6.87	7.07

3. Reinforcing steel - ASTM A615 Gr. 60

	100 ≤ (°F)	200(°F)	300(°F)	400°F)
Yield strength (ksi)	60	57	57	57
Young's modulus E (ksi)	29000	29000	29000	29000
Coef. of expansion x 10^{-6}	6.5	6.5	6.5	6.5

4. Concrete

	100 ≤ (°F)	200(°F)	300(°F)	400°F)
Compressive strength (ksi)	4.68	4.68	4.68	4.68
Young's modulus E (ksi)	3900	3510	3510	3510
Coef. of expansion x 10^{-6}	5.5	5.5	5.5	5.5
Tensile Strength (ksi)	0.41	0.41	0.41	0.41

Table 4.2
Stresses Due To Dead Load, Pressure and Temperature
(Task 4, Pressure = 15 psig, Temperature = 185°F)

Element No. in Fig 4.4	Elevation	Liner Stresses (ksi) Meridional	Liner Stresses (ksi) Hoop	Inner Rebar Stresses (ksi) Meridional	Inner Rebar Stresses (ksi) Hoop	Outer Rebar Stresses (ksi) Meridional	Outer Rebar Stresses (ksi) Hoop
10	713'-7"	-12.37	-15.28	0.57	-3.72	-2.34	8.01
17	740'-0"	-10.02	-6.26	-4.50	8.08	9.31	19.82
24	776'-3"	-8.46	0.27	-3.73	8.48	8.55	20.22
30	805'-9"	-7.63	0.42	-3.15	8.42	8.54	20.17
38	844'-5"	-5.80	1.02	1.46	8.56	10.28	20.31
42	860-10"	-5.74	1.21	0.54	9.29	11.36	20.13
43	864'-4"	-6.15	0.85	0.10	9.25	11.96	19.45
50	907'-1"	-6.00	-4.47	0.58	3.85	10.60	14.00

Table 4.3
Stresses Due To Dead Load, Pressure and Temperature
(Task 5, Pressure = 45 psig, Temperature = 400^{0}F)

Element No. in Fig 4.4	Elevation	Liner Stresses (ksi) Meridional	Liner Stresses (ksi) Hoop	Inner Rebar Stresses (ksi) Meridional	Inner Rebar Stresses (ksi) Hoop	Outer Rebar Stresses (ksi) Meridional	Outer Rebar Stresses (ksi) Hoop
10	713'-7"	13.96	-3.36	12.28	-13.40	-0.04	20.29
17	740'-0"	-4.09	9.41	-4.50	21.21	35.31	54.90
24	776'-3"	0.06	12.01	-2.36	22.57	32.11	56.26
30	805'-9"	0.26	12.47	-1.29	29.96	32.92	56.65
38	844'-5"	1.54	13.83	0.20	22.92	33.89	56.62
42	860-10"	-0.40	11.60	2.82	23.22	37.42	59.30
43	864'-4"	2.40	10.67	4.10	22.47	38.56	51.74
50	907'-1"	4.27	8.79	8.79	11.56	36.63	40.75

Table 4.4
Stresses Due To Dead Load, Pressure and Temperature
(Task 6, Pressure = 30 psig, Temperature = 300°F)

Element No. in Fig 4.4	Elevation	Liner Stresses (ksi) Meridional	Liner Stresses (ksi) Hoop	Inner Rebar Stresses (ksi) Meridional	Inner Rebar Stresses (ksi) Hoop	Outer Rebar Stresses (ksi) Meridional	Outer Rebar Stresses (ksi) Hoop
10	713'-7"	2.94	-8.46	7.06	-8.84	-0.94	14.65
17	740'-0"	-12.04	-0.61	-4.64	15.49	23.05	38.97
24	776'-3"	-9.56	1.37	-3.40	16.72	21.15	40.21
30	805'-9"	-7.61	2.19	-1.01	16.83	22.65	40.31
38	844'-5"	-6.49	2.51	0.11	16.82	23.93	40.30
42	860-10"	-7.28	2.26	2.36	17.55	25.89	39.21
43	864'-4"	-5.24	1.27	3.33	17.31	27.03	37.71
50	907'-1"	-3.63	-4.45	7.13	9.21	26.38	29.50

Table 4.5
Foundation Soil Properties At Clinton

	Compacted Illinoian Structural Fill	Illinian Glacial Till	Lacustrine Deposits	Pre-Illinoian Glacial Till
Density (pcf)	132	150	134	145
Poisson's Ratio:	0.40	0.46	0.47	0.47
Dynamic Shear Modulus (psf)				
Single amplitude Shear strain				
= 1.0%	$8{,}000(f\sigma_m')^{1/2}$	8×10^5	8×10^5	8×10^5
= 0.1%	$32{,}000(\sigma_m')^{1/2}$	30×10^5	26×10^5	26×10^5
= 0.01%	$74{,}000(\sigma_m')^{1/2}$	100×10^5	77×10^5	77×10^5
= 0.001%	$97{,}000(\sigma_m')^{1/2}$	170×10^5	115×10^5	115×10^5
= 0.0001%	$100{,}000(\sigma_m')^{1/2}$	200×10^5	140×10^5	140×10^5
Damping (Percent of critical)				
Single amplitude Shear strain				
= 1.0%	16	22	20	20
= 0.1%	14	16	9	12
= 0.01%	6	8	5	8
= 0.001%	2	4	3	4
= 0.0001%	1	3	2	3

NOTE: σ_m' = mean effective stress (psf).

Table 4.6

Total Foundation Spring and Dashpot Constants

A_H (g)	K_H (KIP/FT.)	K_V (KIP/FT.)	C_H $(\frac{KIP.\ SEC.}{FT.})$	C_V $(\frac{KIP.\ SEC.}{FT.})$
0.25	5.10×10^6	7.24×10^6	4.31×10^5	9.04×10^5
0.45	3.30×10^6	4.69×10^6	3.47×10^5	7.27×10^5
0.75	1.98×10^6	2.82×10^6	2.69×10^5	5.64×10^5
1.0	1.43×10^6	2.03×10^6	2.28×10^5	4.78×10^5

Note: Individual spring and dashpot constants in Figure 4.6 were obtained using the total values and the applicable tributary area for each element.

Table 4.7

Capacity Margin Factors For Clinton Containment At A_H=1.0g
(Except as noted)
(Direct Limit States)
(See Note 1)

Code*	Description	Criterion	Tasks 3	4	5	6
2	Failure of Reinforcing Bars in					
	a. Containment Wall	$10\ \epsilon_y/\epsilon_s$	>10	>10	1.0	8.4
	b. Basemat	$10\ \epsilon_y/\epsilon_s$	>10	>10	>10	>10
1	Tensile Failure of Steel Liner					
	a. Containment Wall	$\frac{0.02}{\epsilon_{principal}}$	>10	>10	>10	>10
	b. Basemat		>10	In comp	In comp	In comp
6	Transverse Shear Failure					
	a. Containment Wall	Flexural shear cap. / Section shear	1.6	1.3	1.1	1.2
	b. Basemat		1.8	1.6	2.0	2.1
8	Failure of Containment Wall at Pentration	Pull-out cap. per ASME Code $K(\delta_S + \delta P + T)$ Based on K=160 kip/in. Elev. 770' Mainsteam	7.0	4.3	2.5	3.1
9	Failure of Pretensioned Bolted Connection at Containment Equipment Hatch	Shear cap. / Max. shear	4.9	>10	>10	>10
7	Through-Wall Crushing of Concrete	0.002 / Average comp. strain when wall thickness in compression	10	Not critical because of pressure		

*Refers to limit state identification number in Table 1.2.

Note 1: A comment similar to Note 1 of Table 3.9 applies to this table also.

Table 4.8
Capacity Margin Factors for Clinton Containment at A_H=1.0g
(Except As Noted)
(Indirect Limit States)
(See Note 1)

Code*	Description	Criterion	Tasks 3	4	5	6
15	Liquefaction of Structural Fill Under Basemat	Cyclic shear capacity / Ave. cyclic shear	1.0 at A_H=0.83g	1.0 at A_H=0.83g	1.0 at A_H=0.83g	1.0 at A_H=0.83g
13	Bearing Failure of Foundation	Ult. bearing capacity / Peak ave. pressure	8.0	8.0	8.0	8.0
9	Failure of bolted connections					
	a. Drywell Head	Shear capacity / Max. shear	7.6	7.6	7.6	7.6
	b. Equipment Hatch at Drywell Wall		5.9	5.9	5.9	5.9

*Refers to limit state identification number in Table 1.2.

Note 1: A comment similar to Note 1 of Table 3.9 applies to this table also.

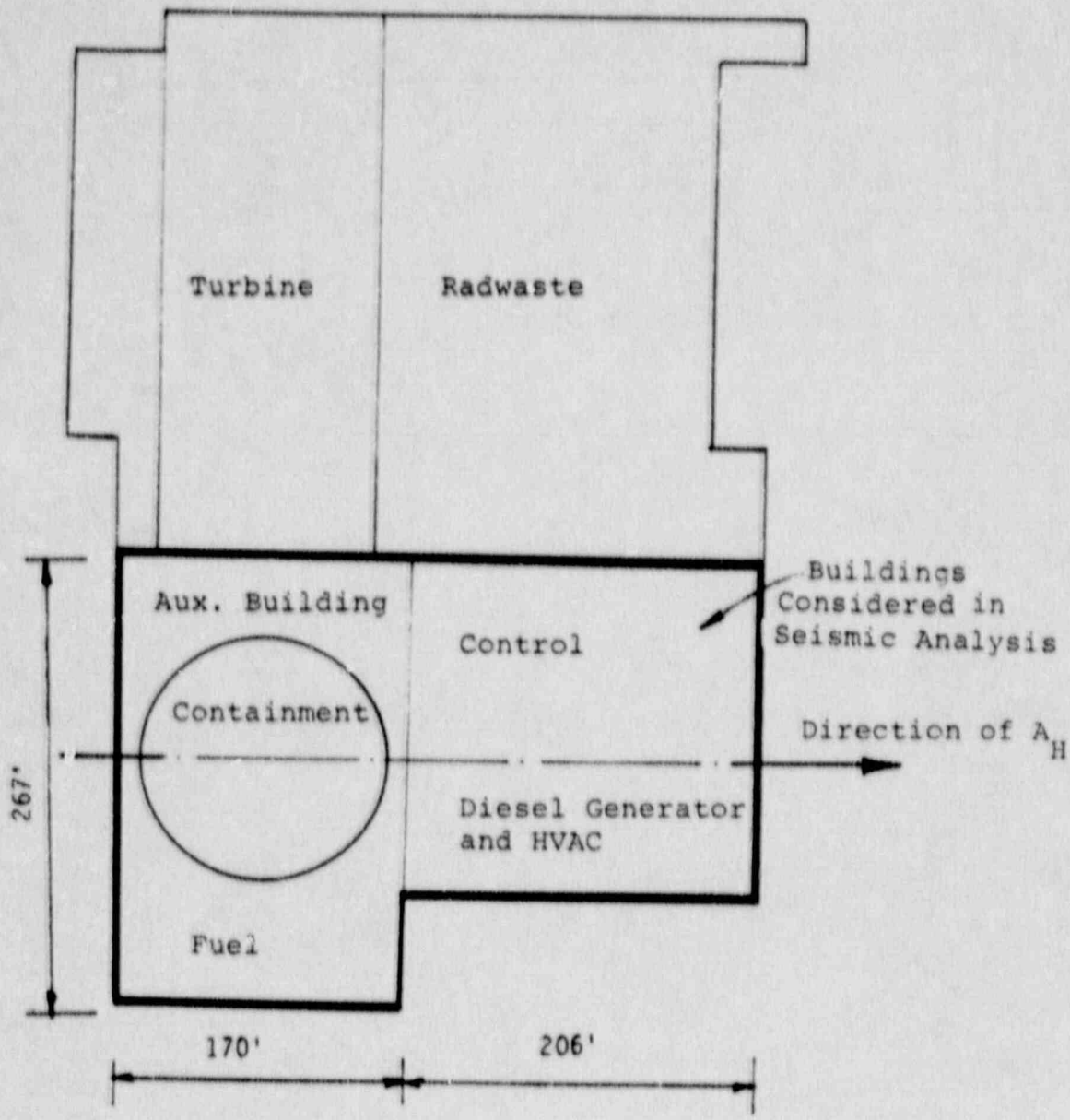

Figure 4.1 General Arrangement Plan of Major Structures at Clinton

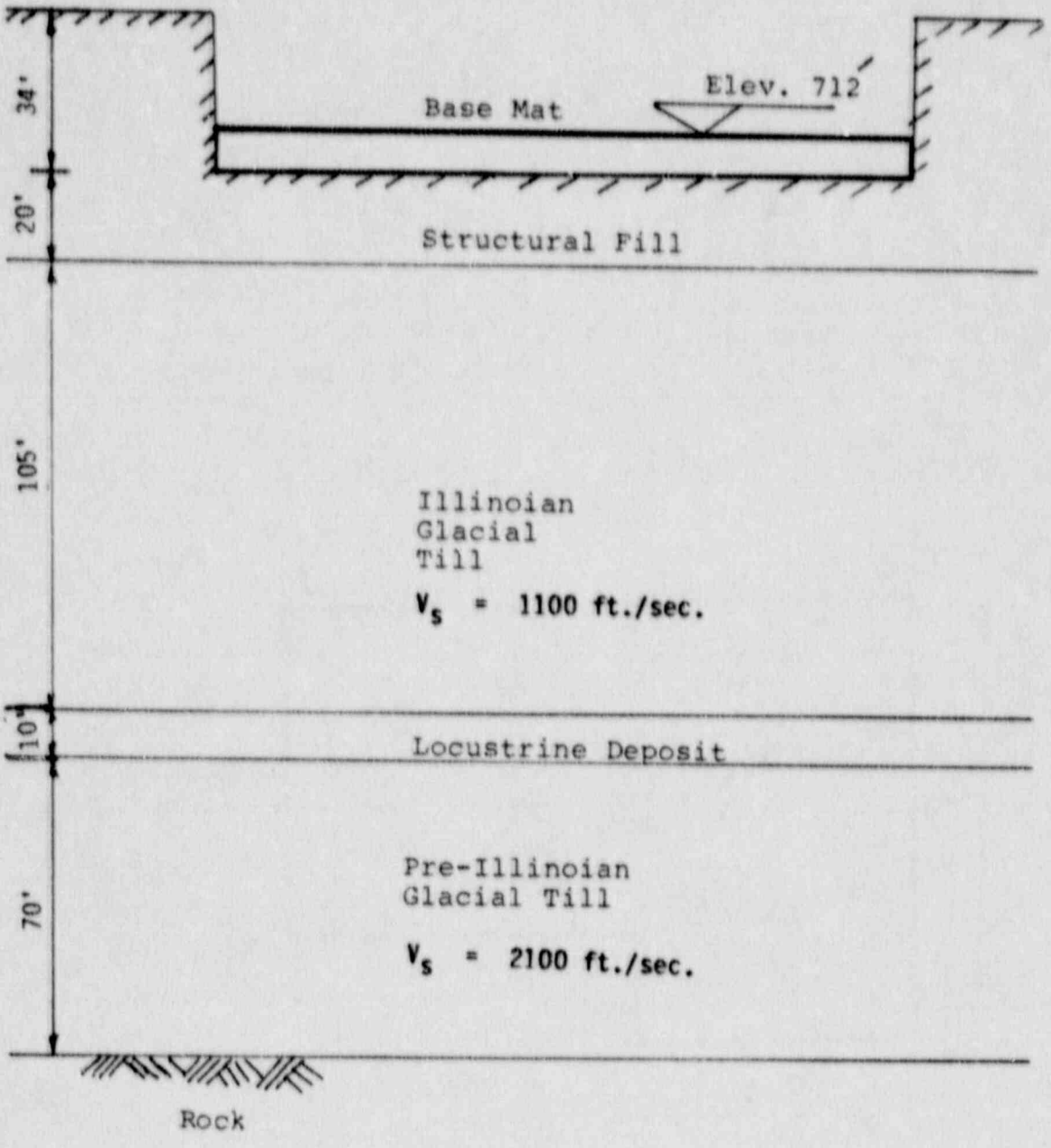

Note: V_s = shearwave velocity

Figure 4.2 Foundation Material Under Clinton Containment

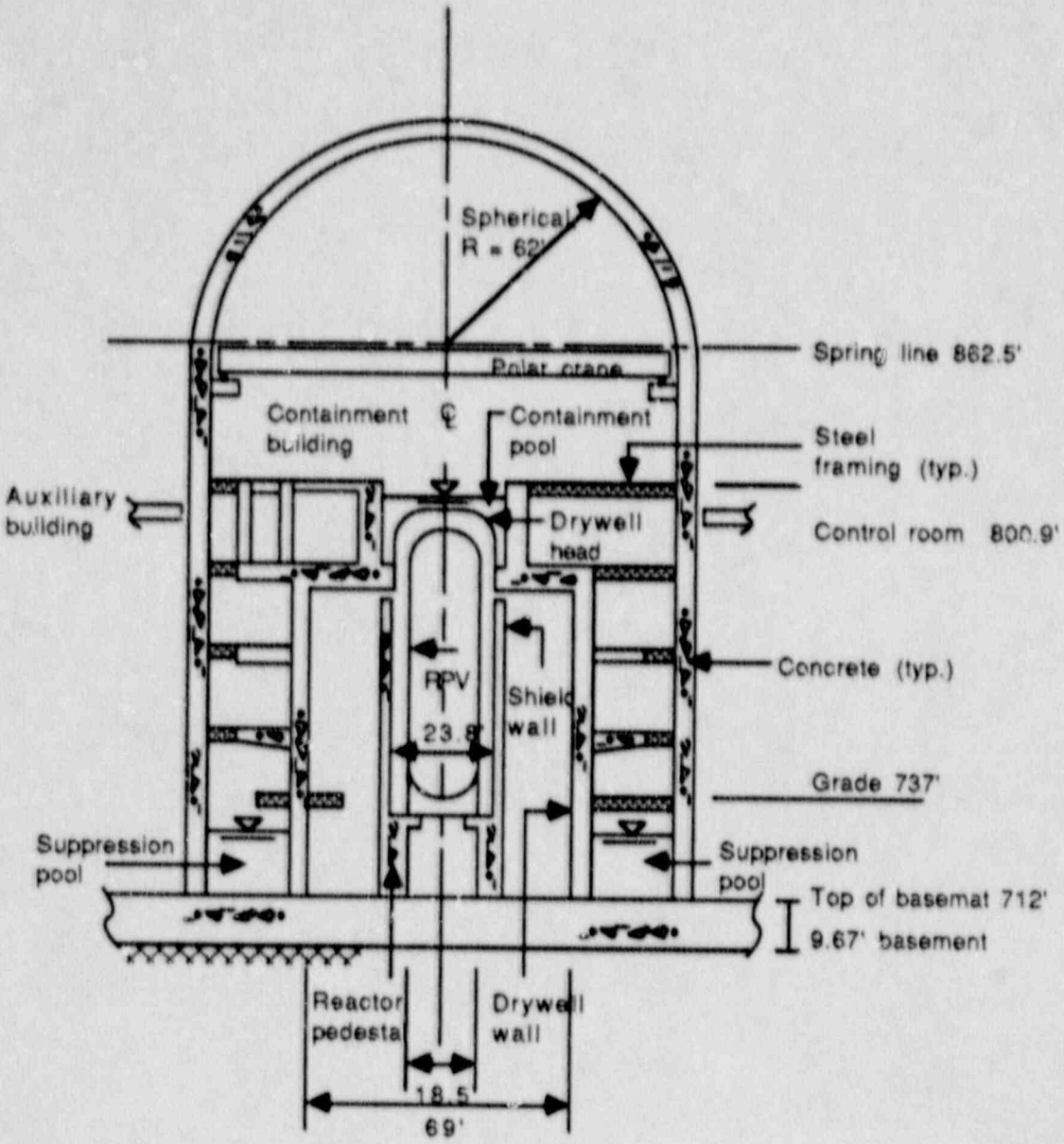

Figure 4.3 Section Through Containment Building

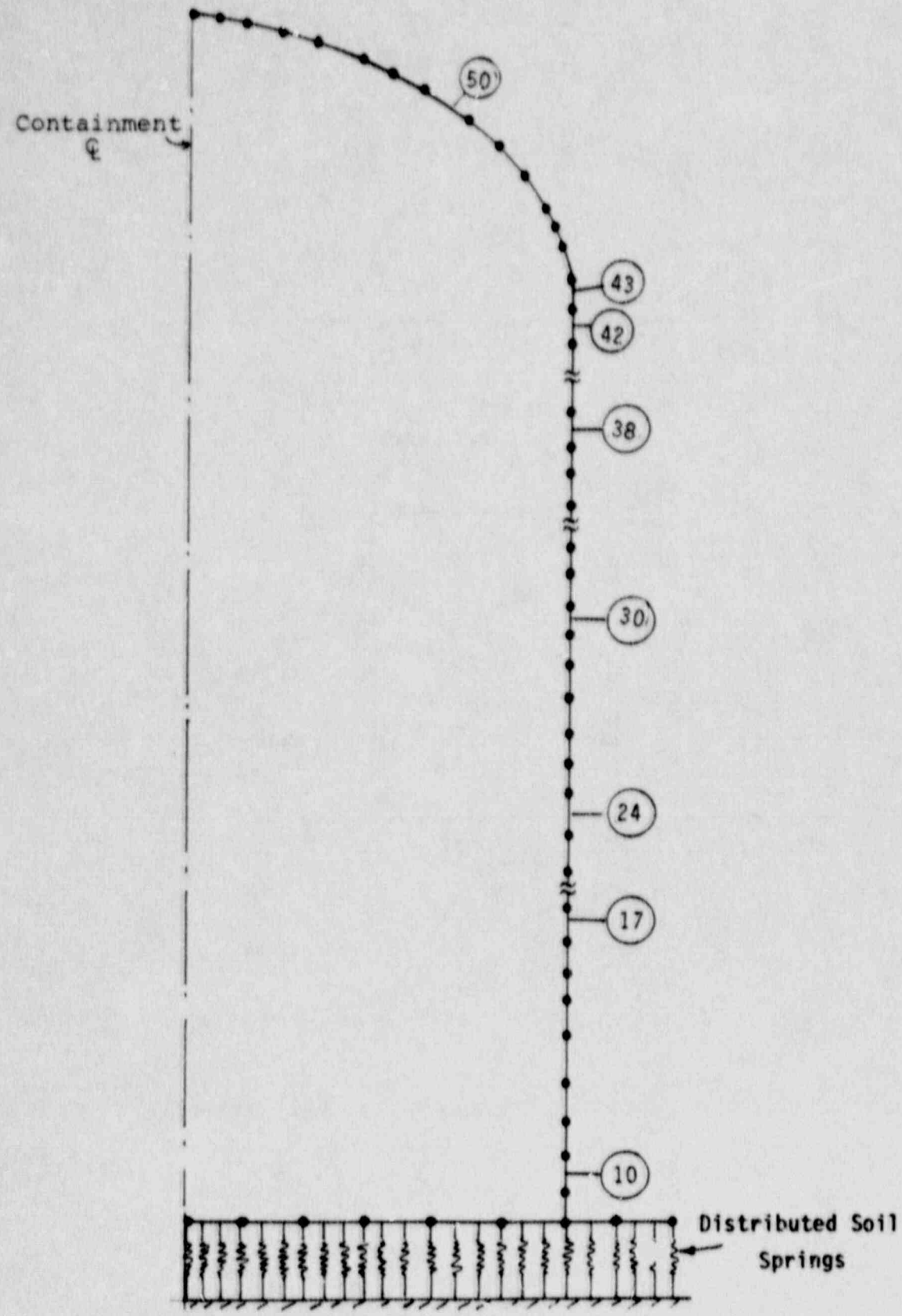

Figure 4.4 Clinton Containment Finite Element Model Used For Gravity and Pressure Plus Temperature Analysis

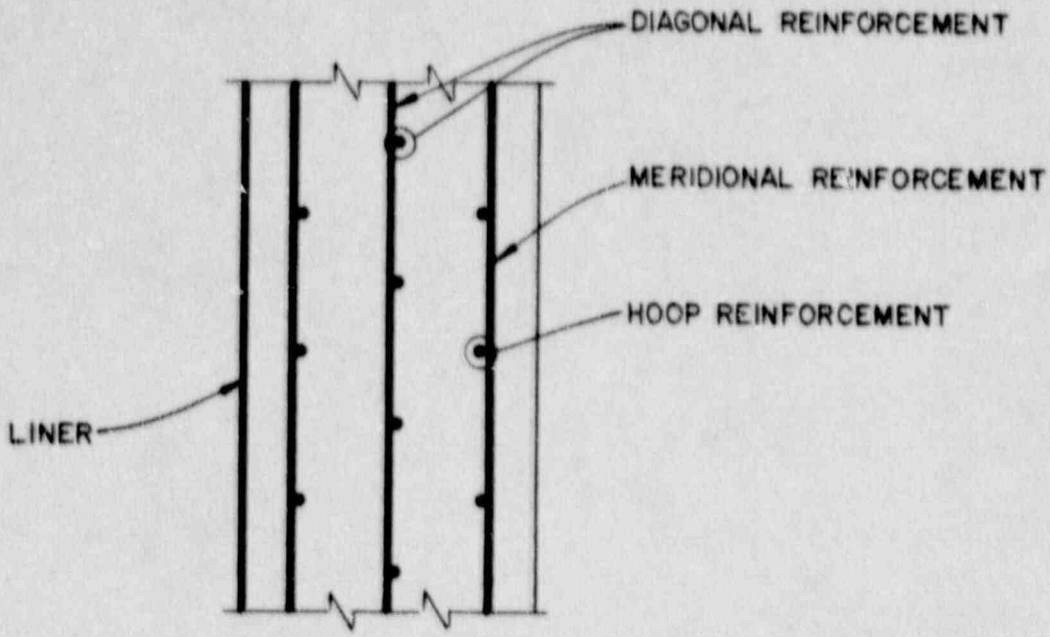

REINFORCED CONCRETE SHELL ELEMENT

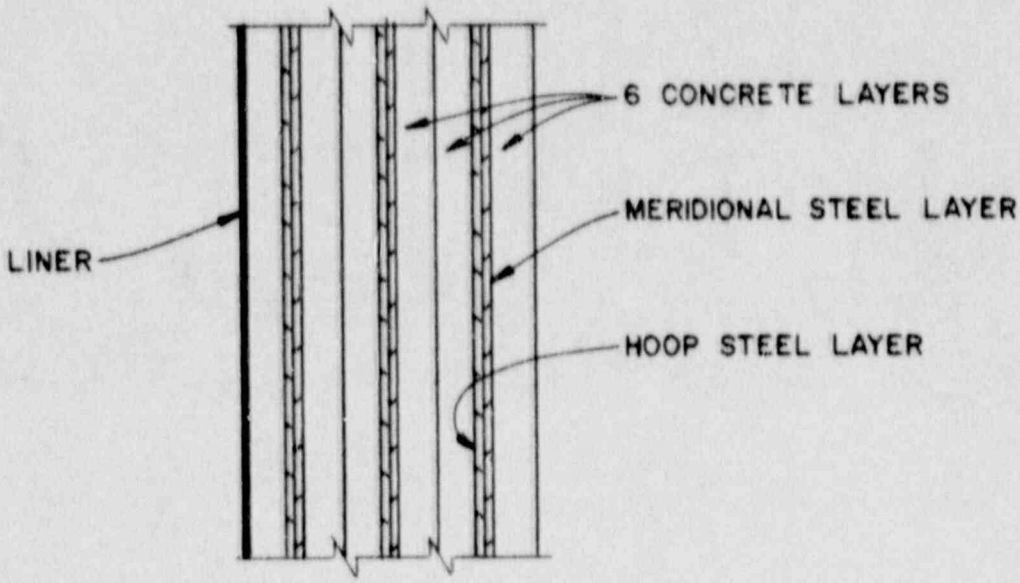

Figure 4.5 Idealized Shell Element For Cracked Analysis

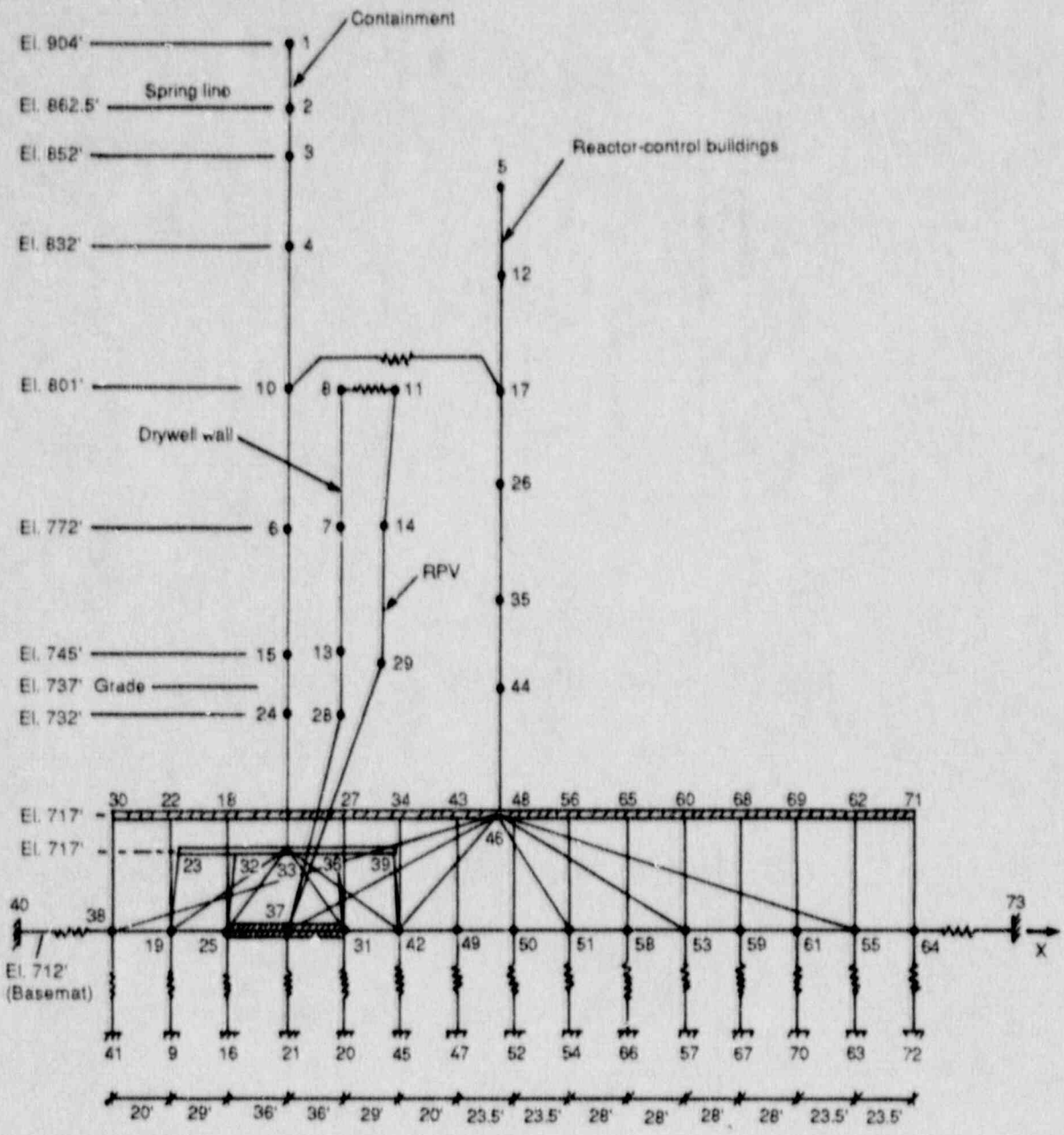

Figure 4.6 Seismic Analysis Model for Clinton Containment

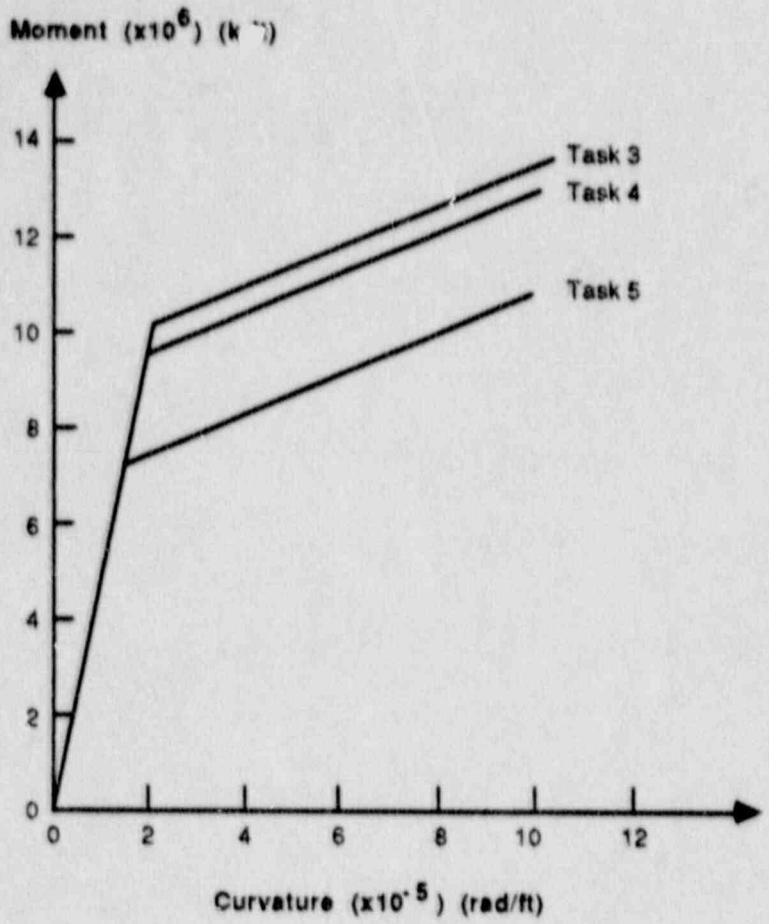

Figure 4.7 Idealized Moment-Curvature Diagrams for Containment Element (33-24) in Figure 4.6

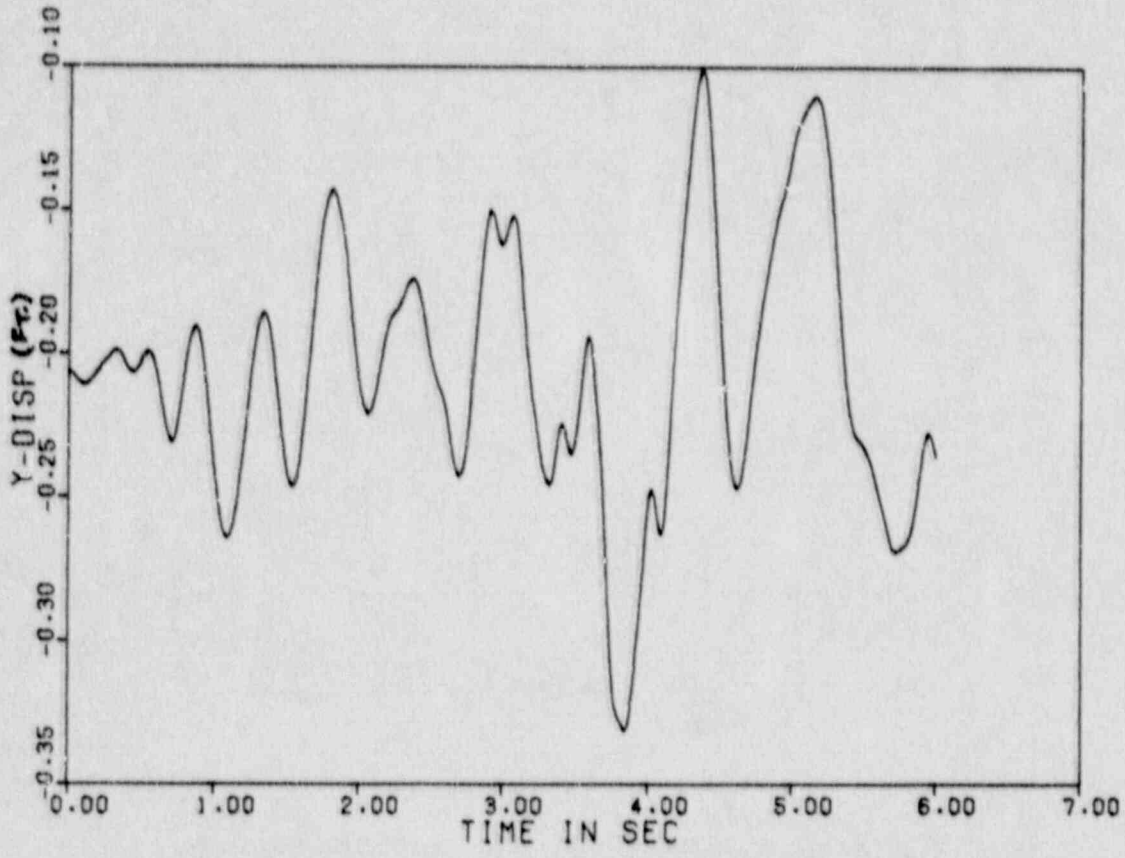

Figure 4.8 Vertical Displacement Time History at the End of Basemat, Node 38, A_H = 1.0g

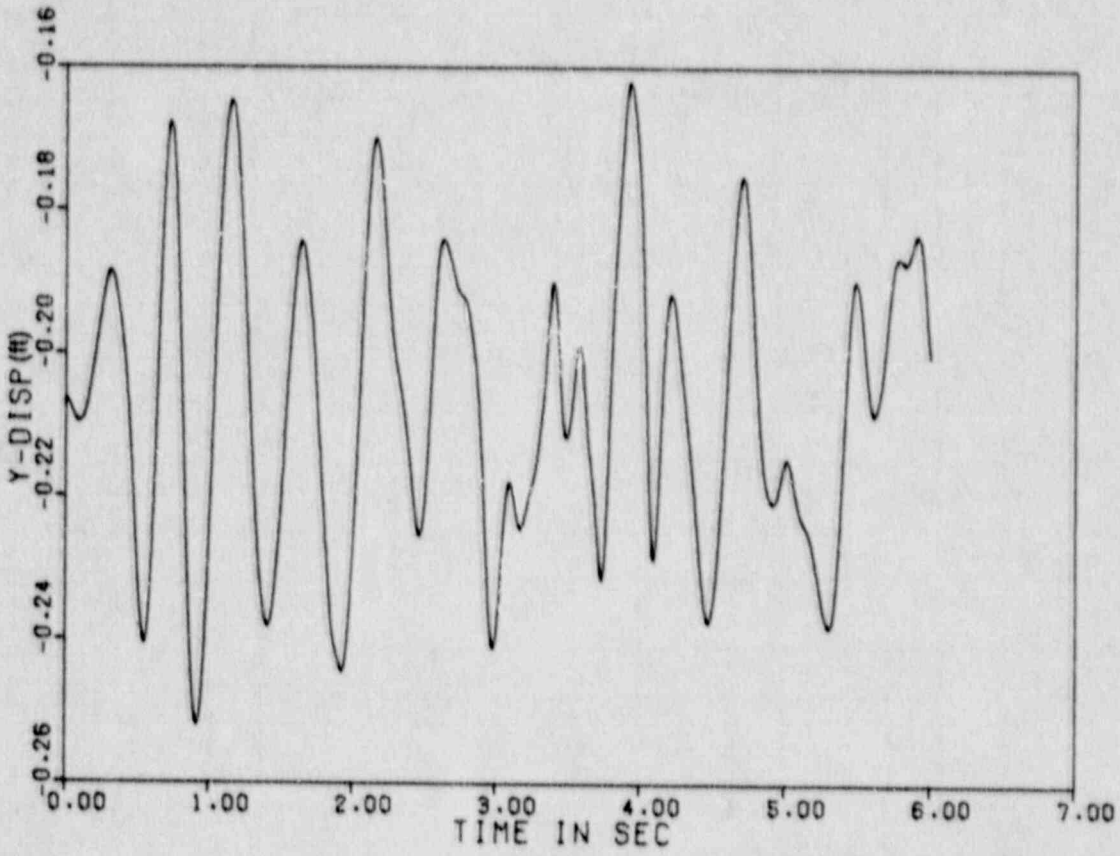

Figure 4.9 Vertical Displacement Time History at the End of Basemat, Node 64, A_H = 1.0g

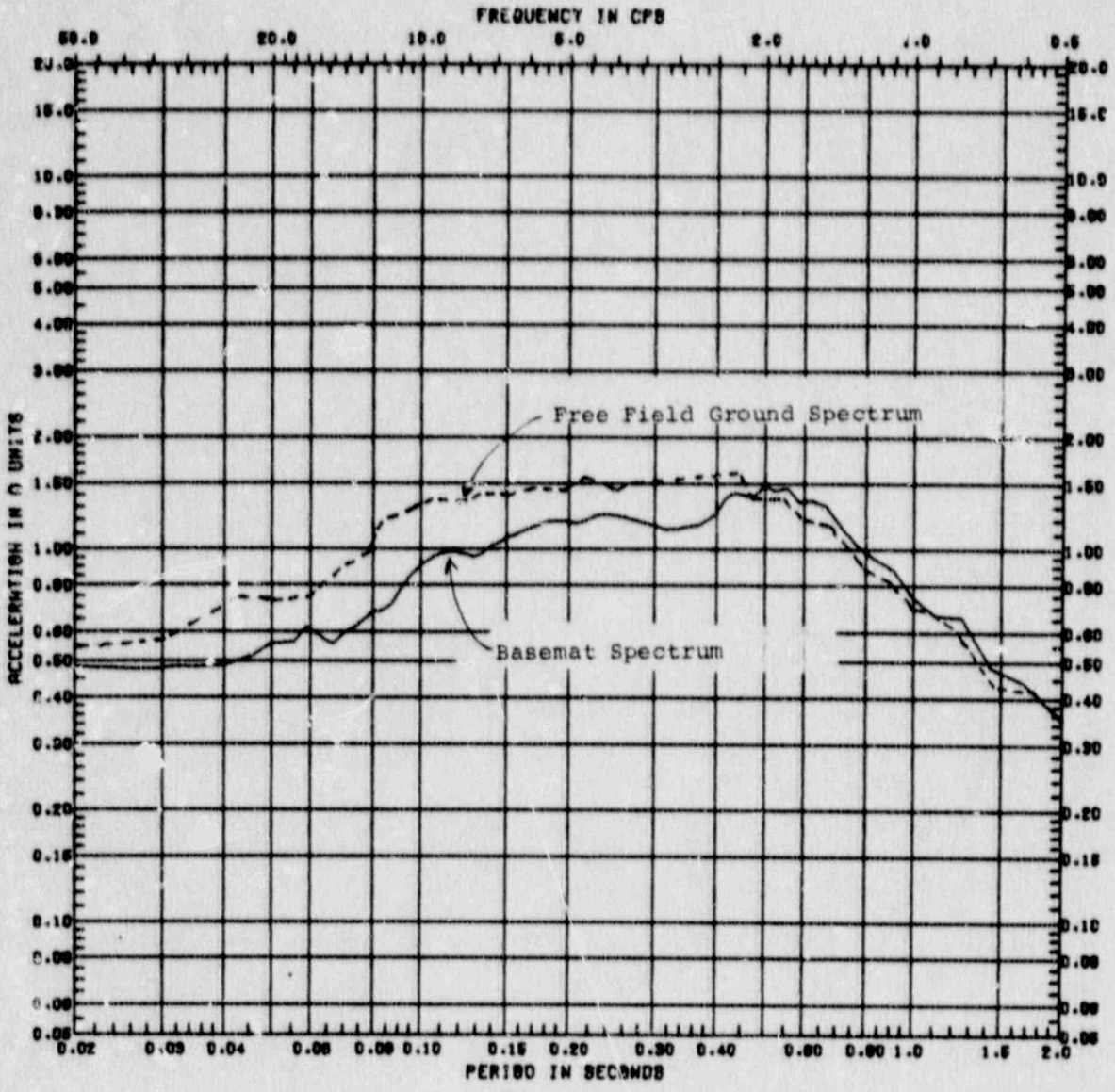

Figure 4.10 Comparison of Basemat and Free Field Ground Horizontal Response Spectra, A_H = 0.45g, Damping = 5%

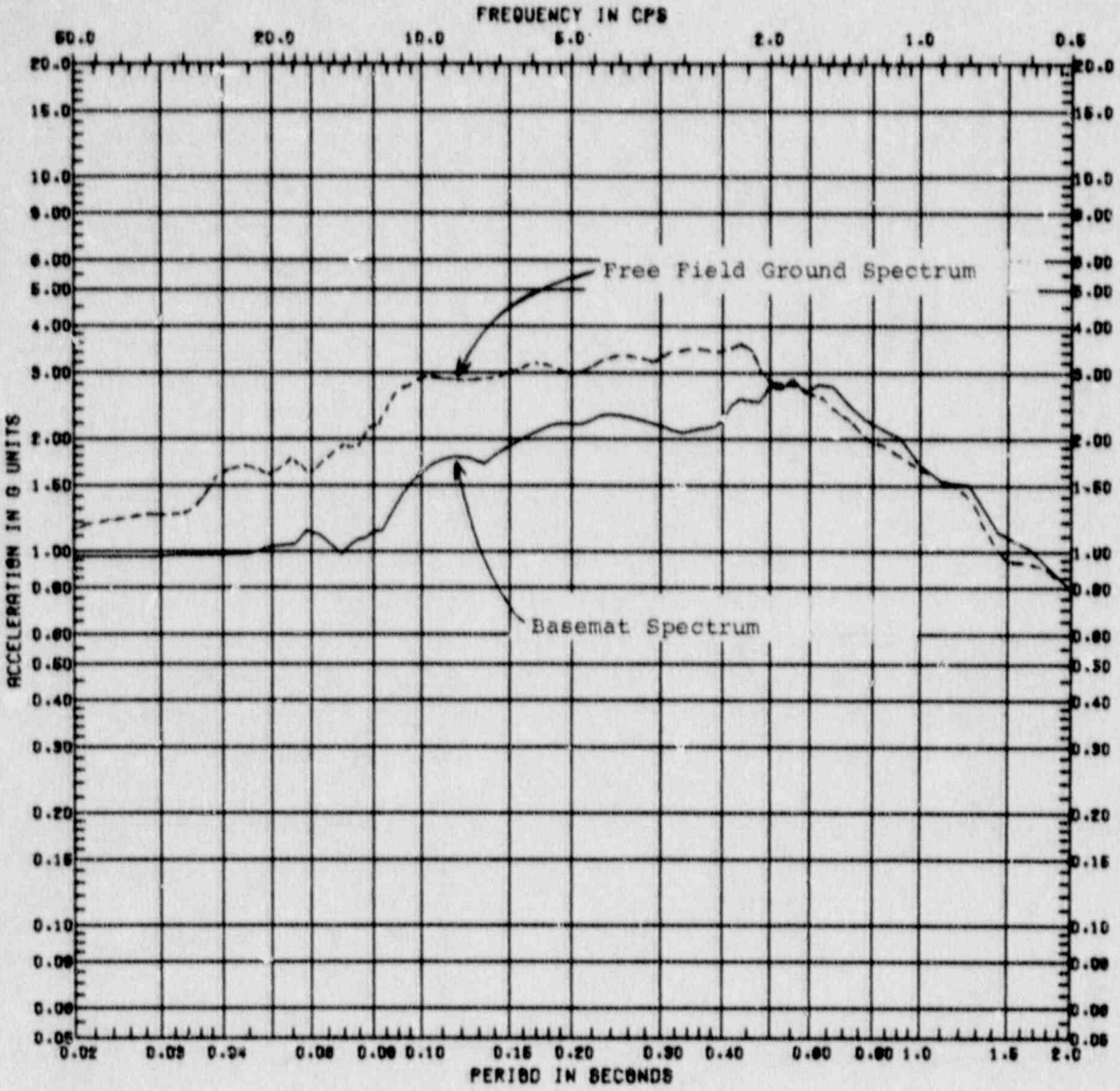

Figure 4.11 Comparison of Basemat and Free Field Ground Horizontal Response Spectra, A_H = 1.0g, Damping = 5%

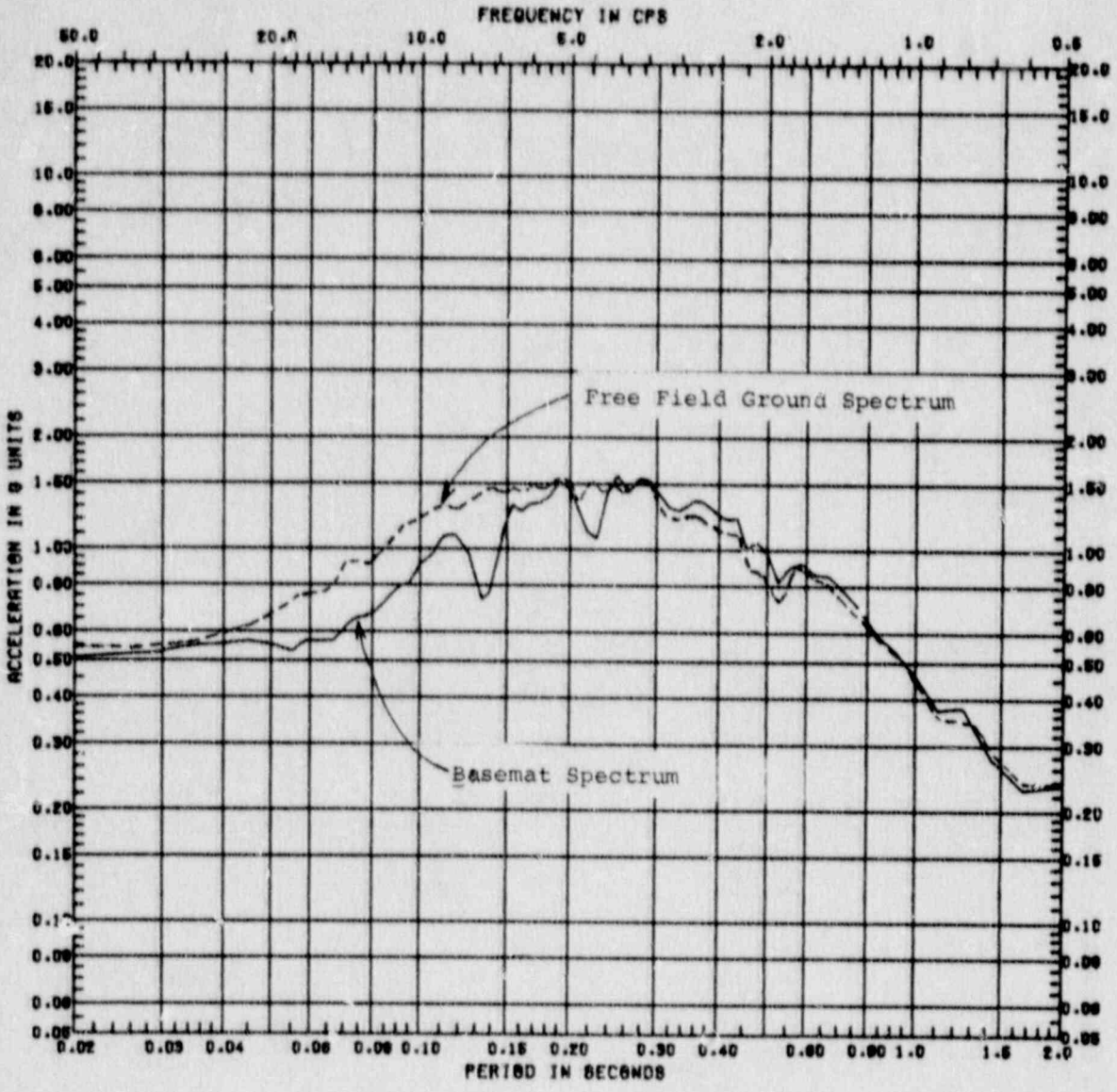

Figure 4.12 Comparison of Basemat and Free Field Ground Vertical Response Spectra, A_H = 0.45g, Damping = 5%

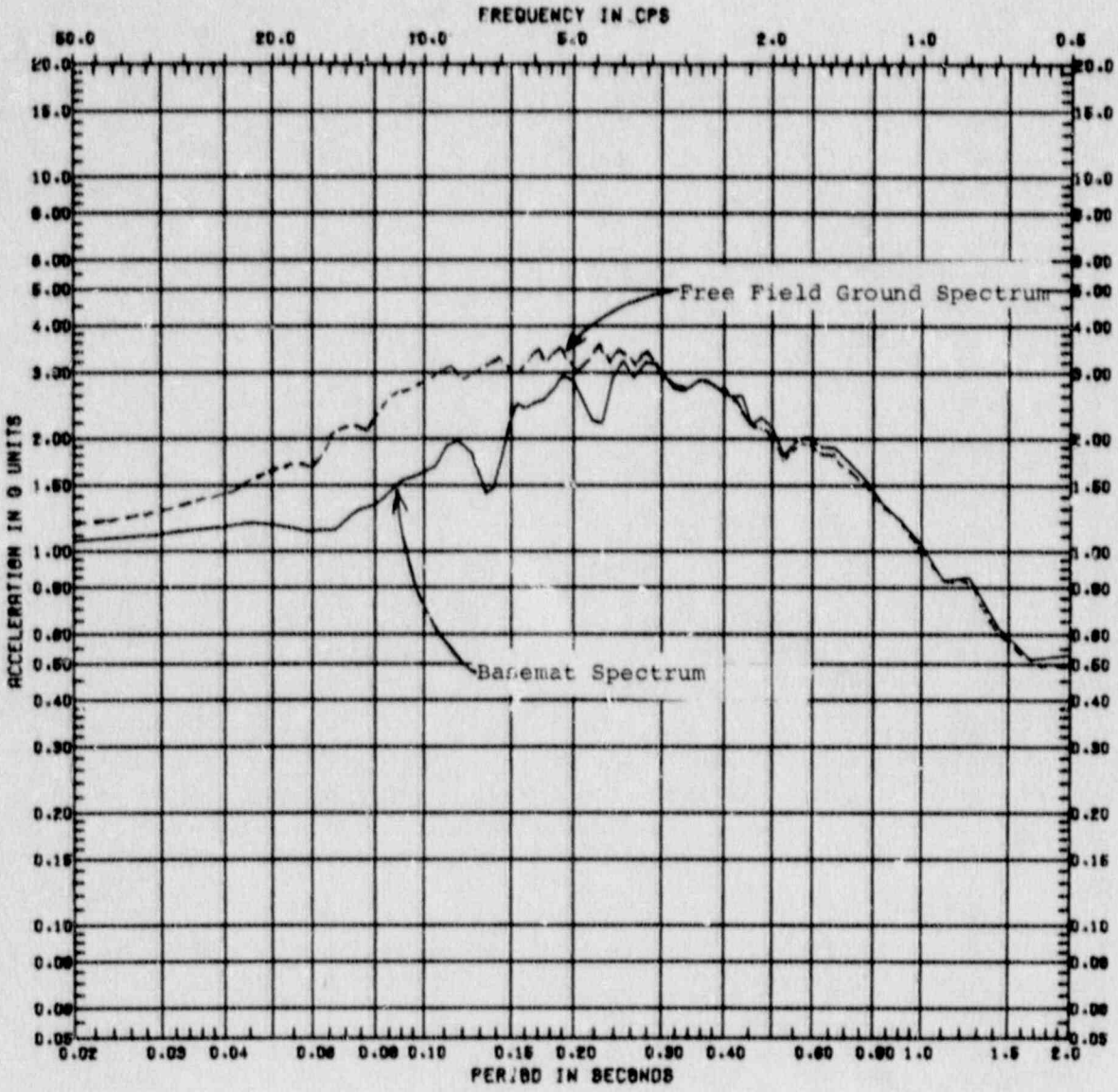

Figure 4.13 Comparison of Basemat and Free Field Ground Vertical Response Spectra, A_H = 1.0g, Damping = 5%

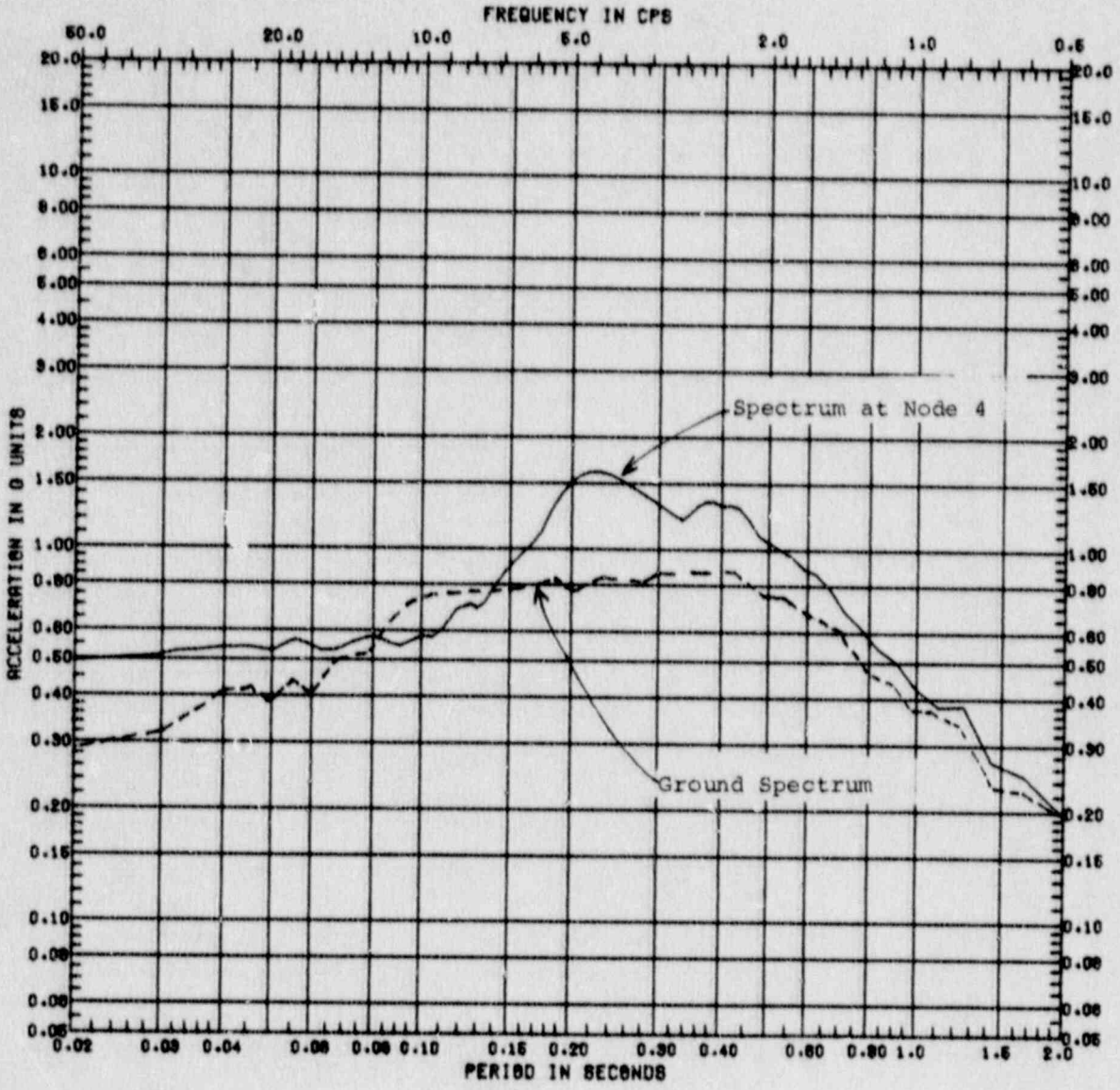

Figure 4.14 Horizontal Response Spectrum at Containment Elevation 832 ft., Node 4, A_H = 0.25g, Damping = 5%

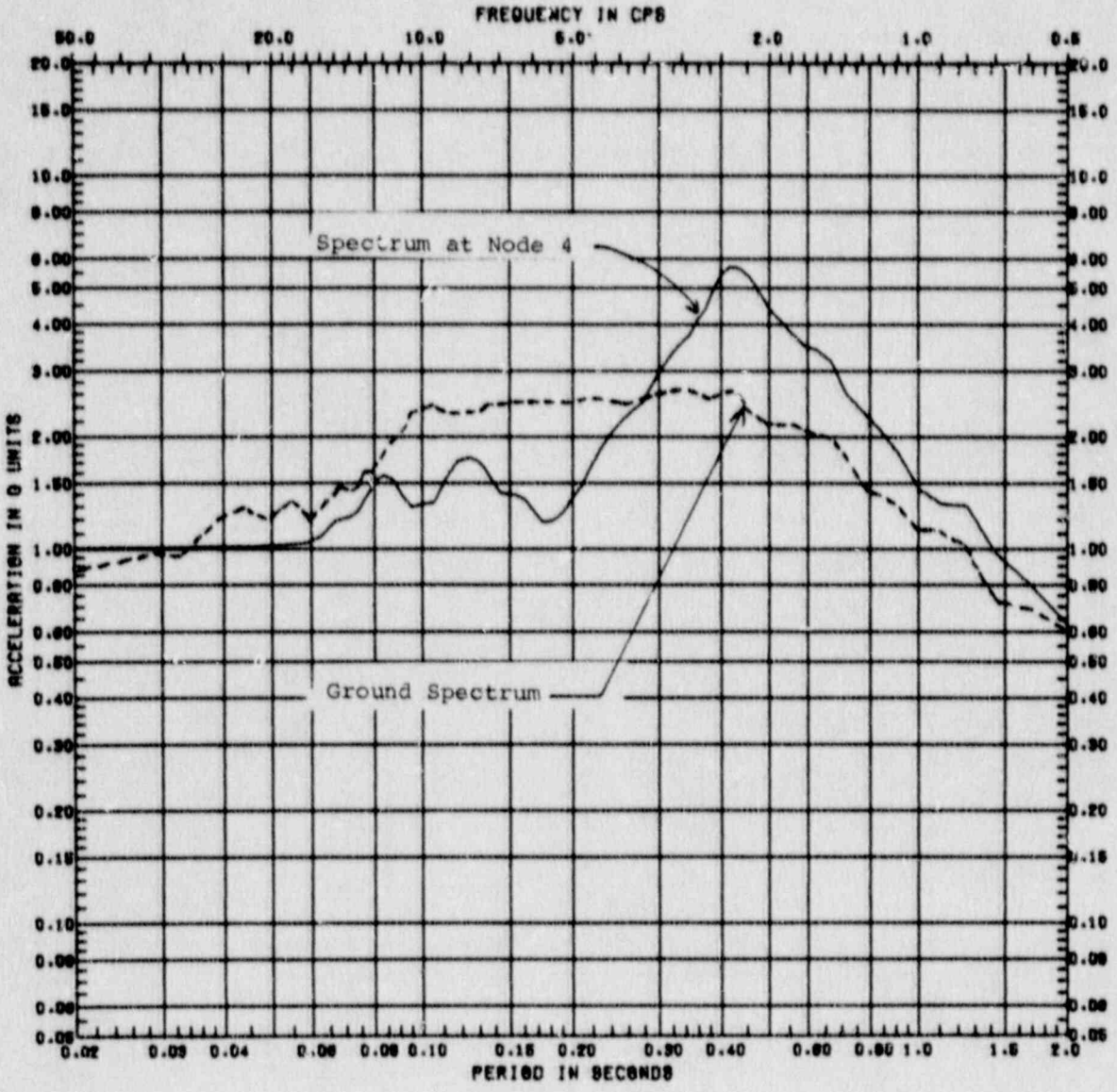

Figure 4.15 Horizontal Response Spectrum at Containment Elevation 832 ft., Node 4, A_H = 0.75g, Damping = 5%

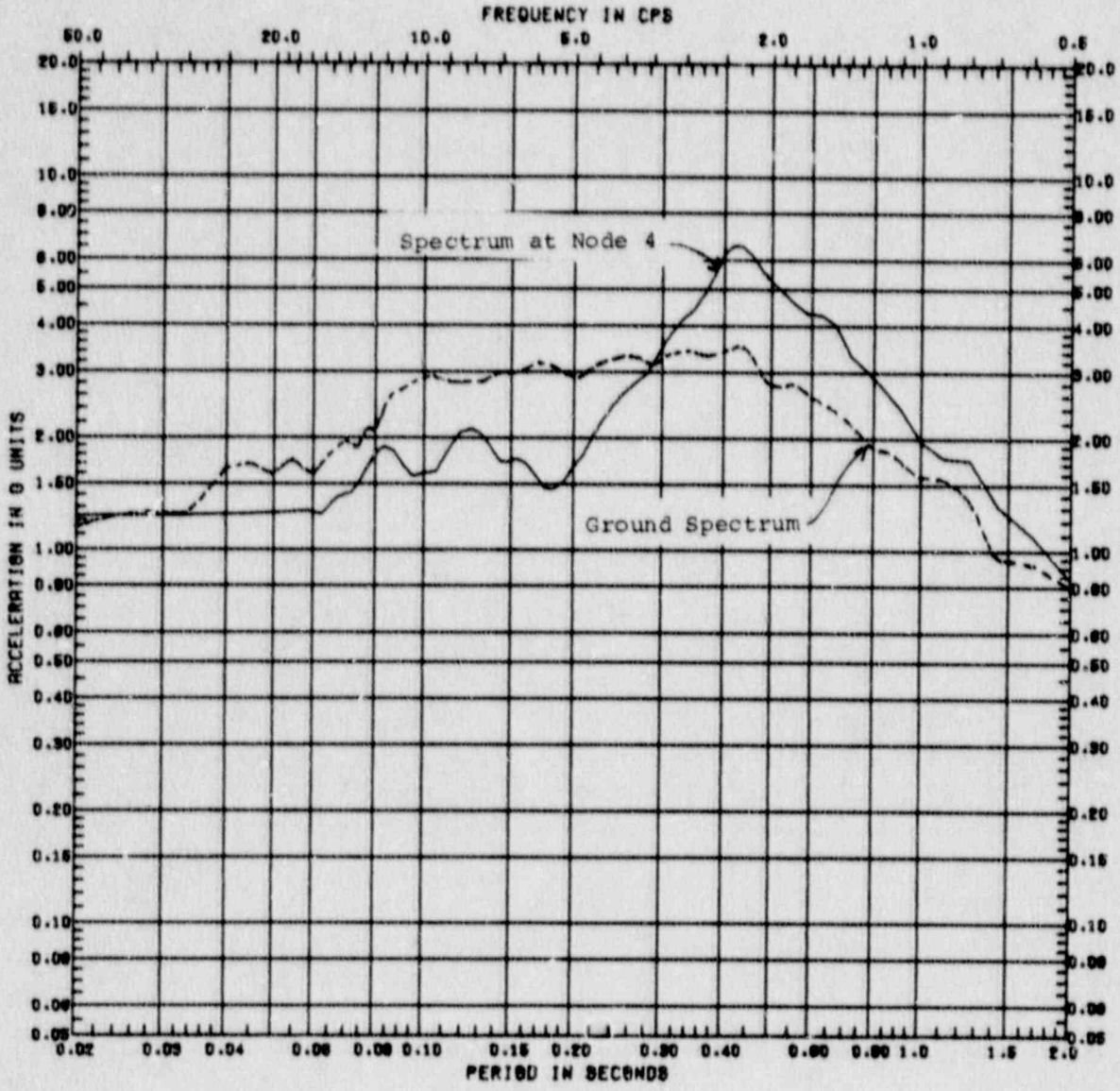

Figure 4.16 Horizontal Response Spectrum at Containment Elevation 832 ft., Node 4, A_H = 1.0g, Damping = 5%

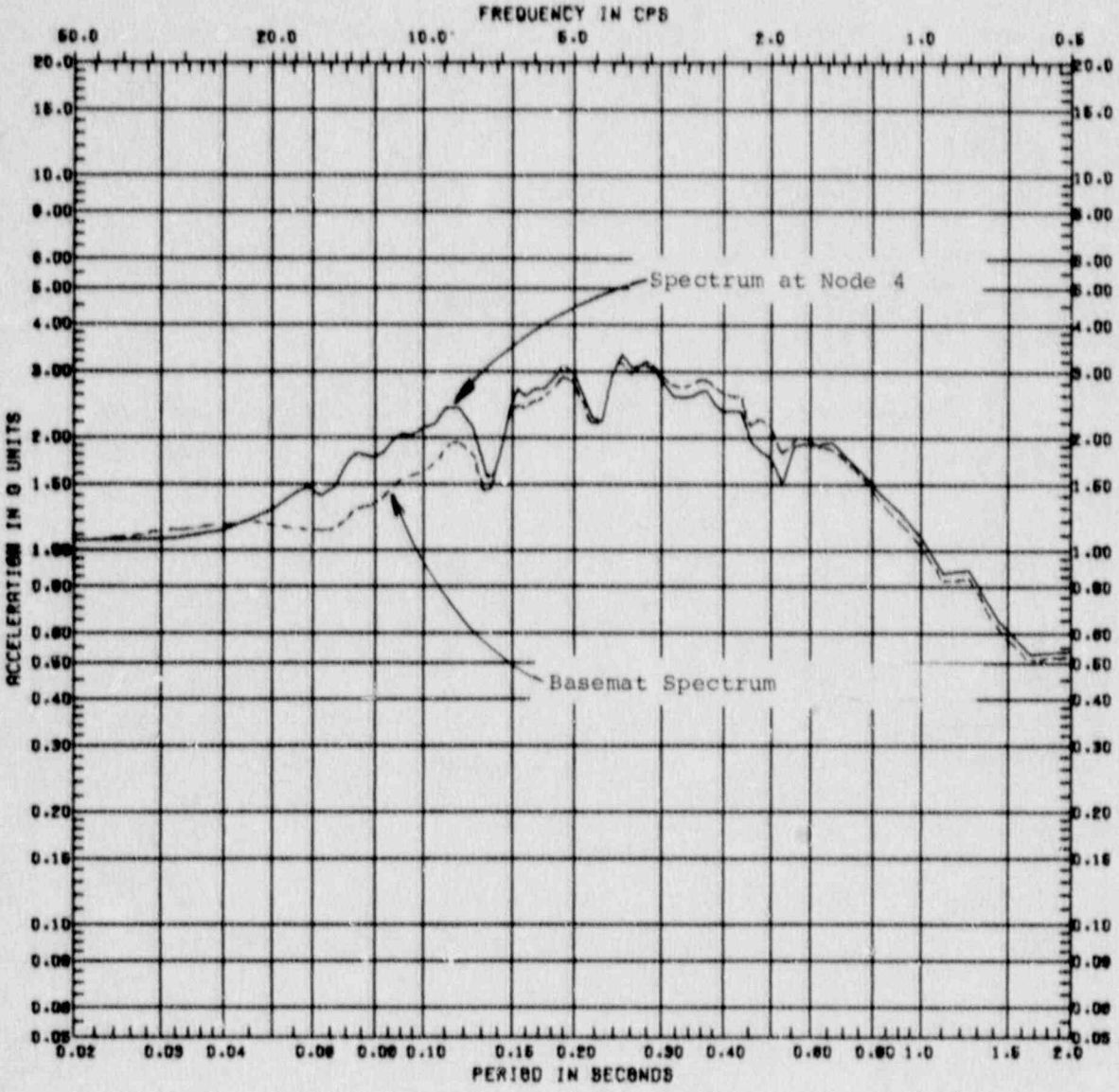

Figure 4.17 Vertical Response Spectrum at Containment Elevation 832 ft., Node 4, A_H = 1.0g, Damping = 5%

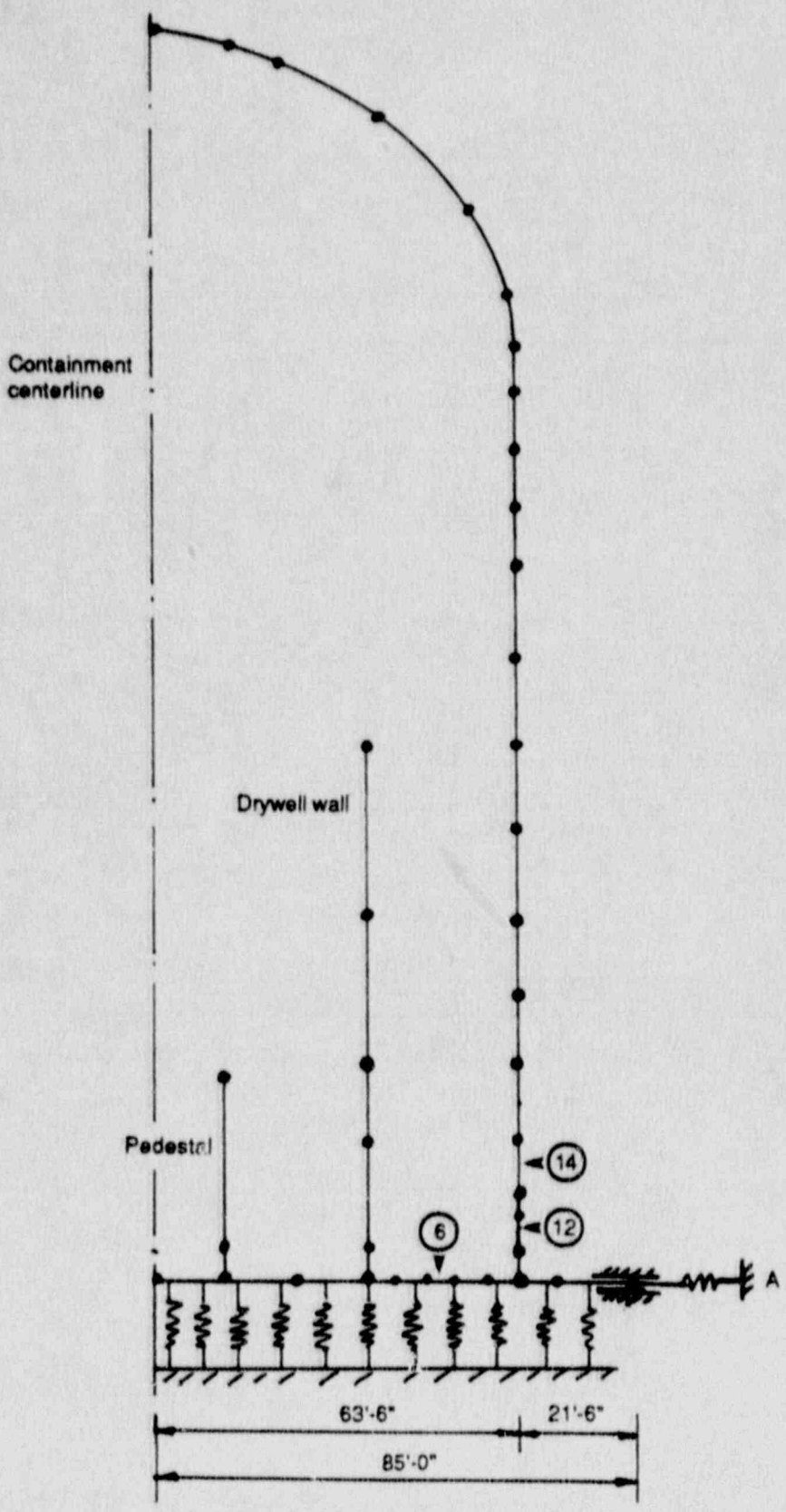

Figure 4.18 DYNAX Model for Obtaining Shell Responses

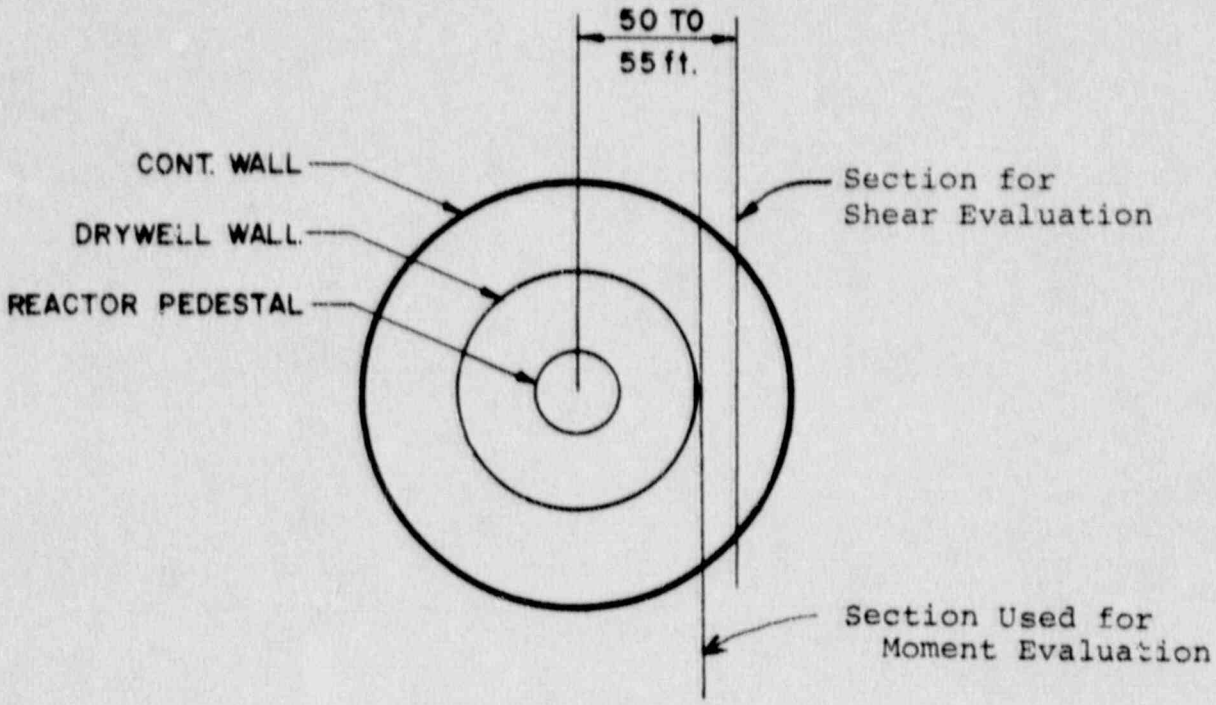

Figure 4.19 Sections Used in Basemat Capacity Evaluation

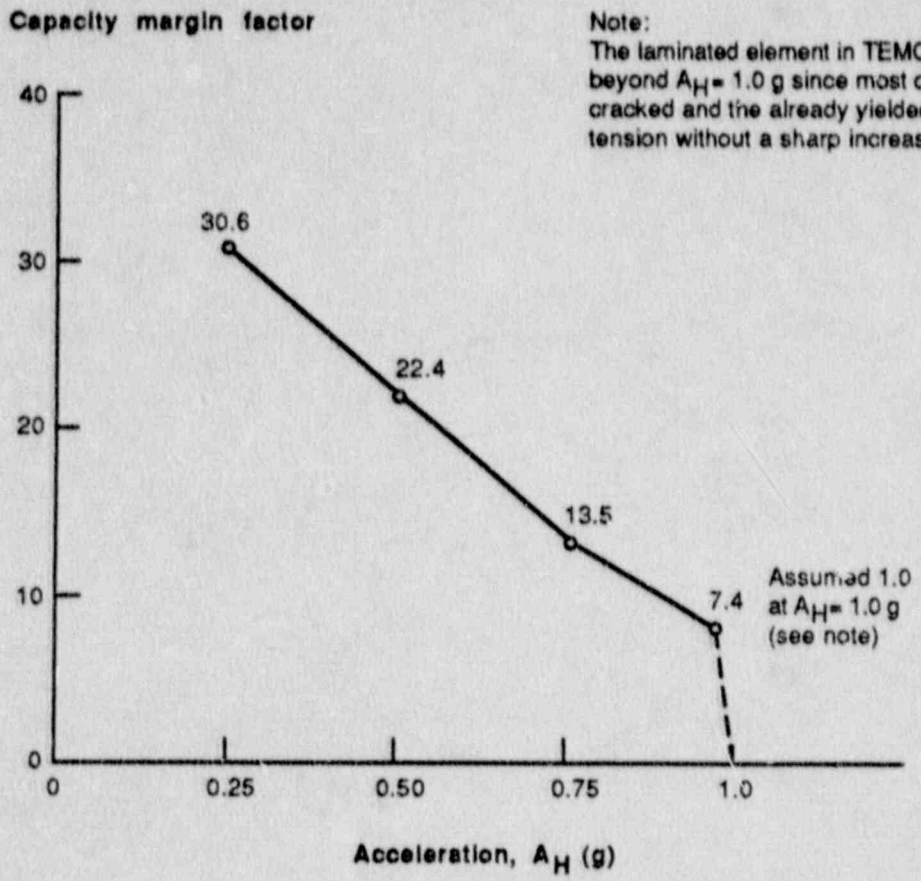

Figure 4.20 Variation of Margin with A_H for Wall Reinforcing Bars for Task 5 Loading Condition

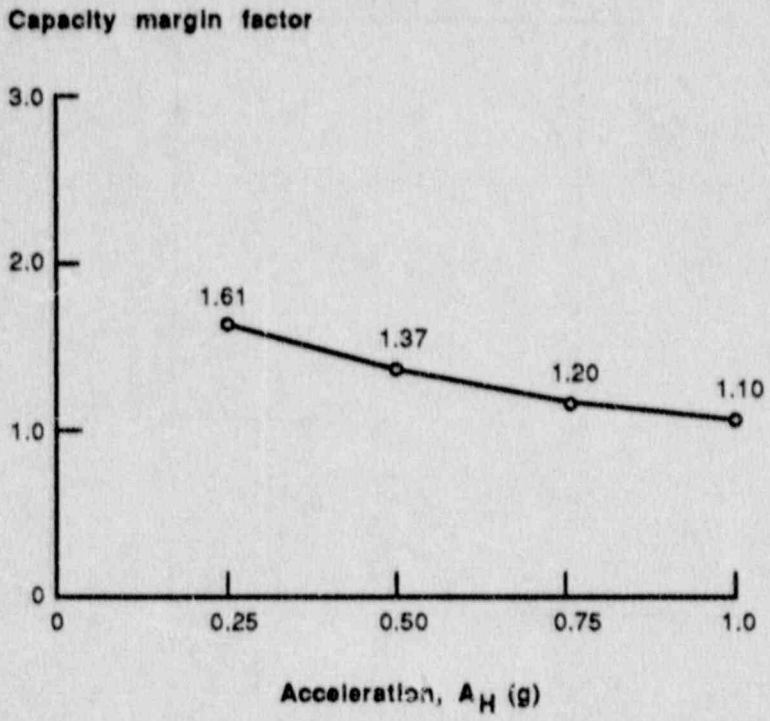

Figure 4.21 Variation of Margin with A_H for Transverse Shear Failure in Containment Wall Under Task 5 Loading

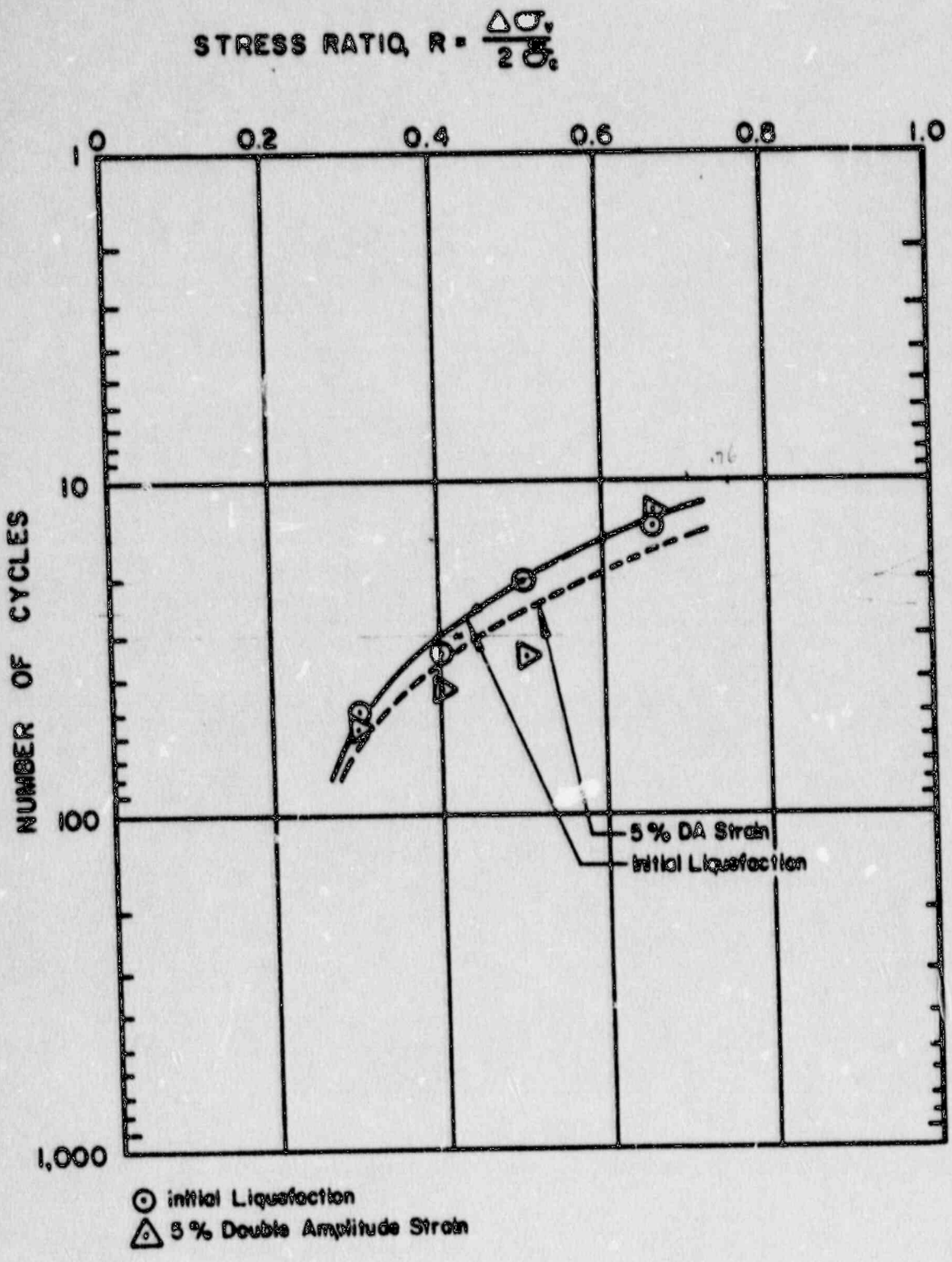

Figure 4.22 Results of Liquefaction Tests on Structural Fill

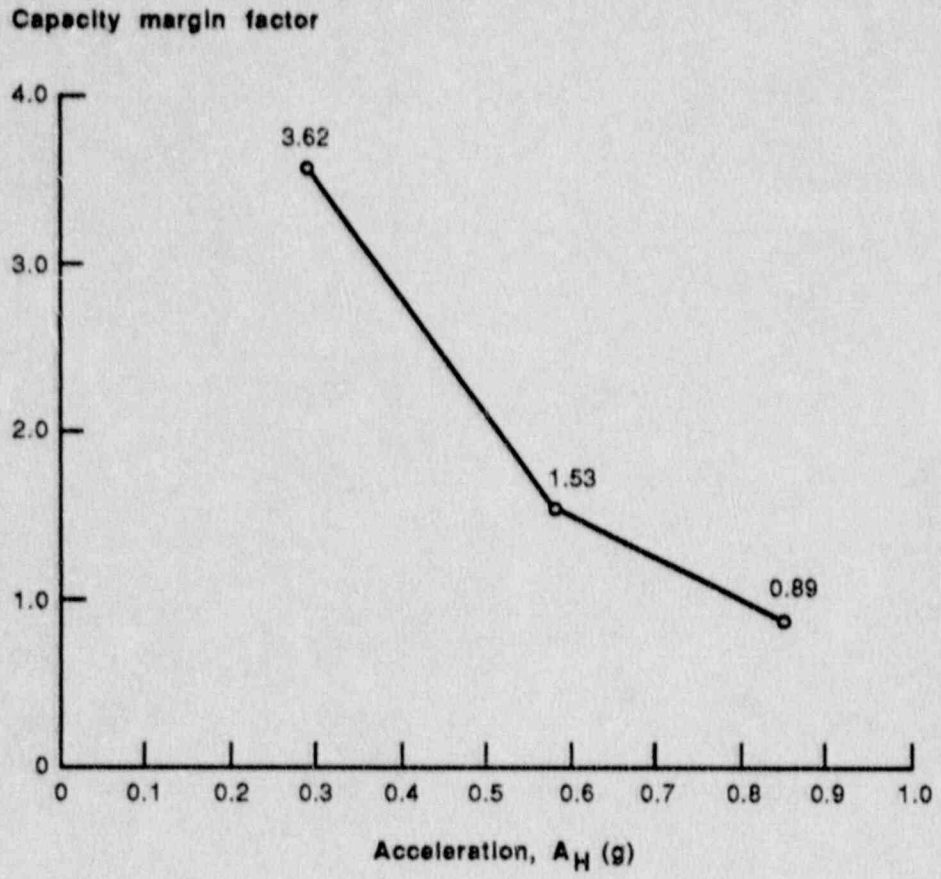

Figure 4.23 Variation of Margin with A_H for Initiation of Liquefaction in Soil, All Tasks

5. EVALUATION OF ZION CONTAINMENT

5.1 Description of Zion Containment

Figure 5.1 shows a schematic of the Zion containment. The containment is in the shape of a cylinder with a shallow domed roof and a flat foundation slab. The cylindrical portion is prestressed by a post-tensioning system consisting of horizontal and vertical tendons. The dome has a three-way post-tensioning system. The basemat, which is separated from the foundation slab of adjacent structures, is conventionally reinforced with reinforcing steel. The entire structure is lined with 0.25 inch welded steel plate to provide leak tightness.

The approximate dimensions of the reactor containment are: inside diameter, 140 feet; inside height, 212 feet; vertical wall thickness, 3-1/2 feet; dome thickness, 2 feet 8 inches; and the foundation slab thickness 9 feet. The subsurface condition consists of a granular deposit to a depth of 35 feet, followed by a glacial deposit to a depth of 72 feet, underlain by dolomite bedrock.

Nominal bonded reinforcing steel, in addition to prestressing steel, is provided in the cylinder and dome to distribute strains due to shrinkage and creep. Additional bonded reinforcing steel is used at penetration and discontinuities to resist local moments and shears.

The basemat is a reinforced concrete structure, 157 feet in diameter and 9 feet thick. A cylindrical reactor pit with a wall thickness of 16 feet and an internal diameter of 21 feet is at the center of the basemat. Both the basemat and the base slab of the reactor pit are provided with the top and bottom reinforcement. Shear reinforcement is also provided in the basemat from the radius of 50 ft. to 65 ft.

The post-tensioning system consists of:

1. Three groups of 63 dome tendons oriented at 120^{o} to each other for a total of 189 tendons anchored at the vertical face of the dome ring girder.

2. A total of 216 vertical tendons anchored at the top surface of the ring girder and at the bottom of the base slab.

3. A total of 555 hoop tendons anchored at six vertical buttresses.

Personnel and equipment access to the containment is provided by a double door lock and by a 18'-6" clear diameter double gasketed single door. A double door emergency personnel escape lock is also provided.

5.2 Analysis for Non-Seismic Loads

To establish the yield pressure for Task 5, P_y, a membrane analysis of containment was performed for gravity, pressure, and prestressing loads. This analysis was performed using a hand calculation. The analysis showed that at a pressure of 115 psig, hoop tendons yield and meridional

tendons reach 96% of yield point. The reinforcing bars begin yielding at a significantly lower pressure. Based on this the Task 5 pressure was selected as 93 psig which is about 80% of the pressure at which membrane yielding in the containment occurs. At this pressure level, some inelasticity has occurred in the reinforcing bars but there is still some remaining strength in the tendons to carry seismic loading. Since the design pressure for Zion is 47 psig, the pressure for Task 6 was established as 70 psig, i.e., the average of design and Task 5 pressures. The values of pressure and temperature for various tasks are summarized in Table 1.4.

To combine the non-seismic load effects with the effect caused by seismic loads, an elastic analysis of containment shell and internal structures was made using the computer program DYNAX. Results from this analysis were combined with seismic loads as discussed in Section 2.1.6.

5.3 Seismic Analysis

5.3.1 Overall Seismic Model

Figure 5.2 shows the overall seismic model used for the Zion containment analysis. The details of constructing this model are discussed in Section 2.1.4. The additional information specific to this model is provided in this section.

The properties of the foundation soil are given in Table 5.1. The spring constant and dashpot values were obtained using the procedure described in Section 2.1.2, except that effects of embedment and proximity to the rock were included based on procedure given in Reference 5.1. The total spring constant and dashpot values for various ground acceleration levels are shown in Table 5.2. The note in the table also describes the distribution of constants among the elements shown in Figure 5.2. This procedure was followed to obtain the same total spring and dashpot constants for horizontal and vertical translation and rocking as the total values listed in Table 5.2.

The concrete compressive strength, f_c', used in the Zion containment analysis is 5850 psi for basemat and 6435 psi for the cylinder and dome; these values include an increase of 17% from the specified desing values for aging. The yield stresses of the reinforcing bars, prestressing tendons and the liner are 60 ksi, 204 ksi, and 32 ksi, respectively. These properties are based on the minimum specified material properties, and therefore considered conservative; see Section 8.3.

Figure 5.3 shows the M-Ø diagrams used for the containment beam element (9-10) of Figure 5.2 for Tasks 3 through 6. Similar information was obtained and used for other containment beam elements.

In the evaluation of the tensile limit force of the vertical soil springs, F_{t1}, shown in Figure 2.11, a minimal adhesion of 1 psi between the basemat and soil was assumed.

Modal frequencies of the Zion model, assuming linear behavior, are summarized in Table 5.3. This table includes information for fixed base model and models which consider soil-structure interaction.

5.3.2 Seismic Analysis Results

The Zion seismic model was analyzed for A_H = 0.25g, 0.50g, 0.75g and 1.0g for Tasks 3,4,5 and 6 using appropriate M-Ø diagrams. For Tasks 3 and 4 containment remains uncracked up to A_H = 1.0g. Therefore solid concrete section moment of inertia was used in modeling the beam elements. For Tasks 5 and 6, at A_H values of 0.5g and higher, the concrete cracks. However, the beam members do not reach their yield moment, as determined from the applicable M-Ø diagrams. Consequently, the containment response is obtained from elastic beam members having moment of inertia equal to the average of solid section and cracked section moment of inertia for these two tasks. The values of the average moment of inertia are approximately 35% lower than the solid section moment of inertia. This much difference in the flexural section property does not have much effect on the seismic responses which are primarily governed by shear. For this reason the seismic responses for all the four tasks are approximately the same. Therefore, in the evaluation of the containment the same seismic responses were used for all four tasks.

Figures 5.4 and 5.5 show the comparison of horizontal response spectra at the basemat and the input ground spectra in the free field, at A_H = 0.25g and 1.0g. The significant effect of soil-structure interaction is evident from the comparison in Figure 5.4. Due to softening of the soil at higher strains, the high frequency input is attenuated due to soil-structure interaction. As the level of ground shaking increases, the softening of soil also increases, and this attenuation becomes even more significant as seen in Figure 5.5. Similar comparison for vertical shaking is shown in Figures 5.6 and 5.7, from which the same conclusions as for the horizontal shaking can be made. These conclusions are very similar to those drawn for the Clinton containment in Section 4.3.2.

Basemat uplift does not occur at A_H = 0.25g. At A_H = 0.5g, the uplift has occurred, as seen from Figure 5.8, which shows the vertical displacement time history of the end of the basemat, i.e., node 20 in Figure 5.2. As can be seen from this figure, the tension limit of the one-way soil spring has been exceeded at this acceleration level. Figure 5.9 shows the same results at A_H = 1.0g, significant basemat uplift takes place at this acceleration level. The extent of maximum basemat uplift is shown in Table 5.4 for various A_H values. The following paragraph discusses the effect of uplift on the seismic responses.

As A_H increases, the seismic responses are affected by both the soil softening and the effect of uplift. In order to study these two effects separately, a seismic run for A_H = 1.0g was made using soil properties corresponding to A_H = 0.25g. The results of this run would have the effect of uplift, but would not have any effect due to soil-softening in comparison to A_H = 0.25g analysis. A comparison of base shear and

moment obtained from this run and those obtained from A_H = 0.25g (after linearly scaling by a factor of 4 to account for the difference in A_H values), is given in Table 5.5. This comparison shows that a reduction of approximately 20% to 30% occurs in these responses due to uplift. This is apparently the effect of softening introduced in the dynamic model due to uplift of the basemat, and is consistent with the results reported in Reference 5.2.

The effect of uplift on the basemat response has also been investigated by comparing the transverse shear and bending moment obtained from a companion ADINA analysis with one-way soil spring and a two-way soil spring. This companion analysis is discussed in the next Section 5.4. The resulting ratios at A_H = 1.0g, from this comparison are presented in Table 5.6. It can be seen that, for Zion condition, the transverse shear and bending moment in the basemat are not significantly affected on the compression side; however, on the tension side a change of 15% to 40% occurs.

The effect of uplift on horizontal and vertical response spectra is shown in Figures 5.10 and 5.11. At high frequencies, the responses are much less affected by uplift at Zion than they are at Fermi (See Section 3.3.2, Figures 3.14 and 3.15). The reason for smaller effect at high frequencies in Zion is that at Zion a soft impact occurs between soil and basemat. On the other hand the rock foundation in Fermi causes a hard impact. Note that soft and hard impacts refer to the relative stiffness of the vertical springs. Figures 5.10 and 5.11 also show that at lower frequencies, uplift reduces the horizontal and vertical spectra.

Figure 5.12 shows the horizontal response spectrum for A_H = 0.25g at node 1, the highest point on the containment. The corresponding basemat spectrum is also shown on the figure to illustrate the structural amplification. As can be seen from this figure, the maximum amplification occurs near the fundamental frequency (1.49 CPS) of the coupled soil-structure model. The vertical spectrum at this node is shown in Figure 5.13. As can be seen, due to high stiffness of the containment shell in the vertical direction, structural amplification is limited to higher frequency range.

Figure 5.14 shows the comparison of the horizontal spectrum at node 1, for A_H = 1.0g, to the basemat spectrum. The significant point to note from Figure 5.14 and its comparison with Figure 5.12 is the effects of soil softening, due to:

(i) the peak magnitude does not increase linearly with the increase in A_H (compare 2.6g peak acceleration at A_H = 0.25g from Figure 5.12 to 4.7g peak at A_H = 1.0g in this figure)

(ii) the peak occurs at a lower frequency of 1.2 CPS now, in comparison to 1.49 CPS for A_H = 0.25g in Figure 5.12, and

(iii) a significant deamplification occurs in the higher frequency range.

5.4 Capacity Margin Factors

Tables 5.7 and 5.8 contain the margin factors for direct and indirect limit states, respectively, for Zion containment. The margins listed in these tables have been calculated for A_H = 1.0g, except as noted.

Tables 5.7 and 5.8 list the direct and indirect limit states, respectively, in their decreasing order of criticality. Calculated margin factors, along with engineering judgment, are used to arrive at this rank ordering. Further comments on the relative criticality of various limit states are included in Section 5.5.

The margin evaluations were made using the peak seismic responses. For shell evaluations the DYNAX model shown in Figure 5.15 was used. Since DYNAX program does not consider one-way spring, the effect of foundation uplift could not be directly considered using DYNAX. To consider this effect a companion study was performed using an elastic model of the basemat in ADINA program. This model represented the basemat by 4-node elastic plate elements and considered one-way action of the spring. Results of this companion analysis provided factors, which were used to modify the basemat responses obtained from the DYNAX analysis. The modified DYNAX results were used in the final evaluations instead of the results from ADINA because of the finer mesh used in the DYNAX model which was considered more representative of the basemat. Processing of the DYNAX results to obtain strains in the reinforcing bars using TEMCO program was the same as discussed in Section 2.1.6.

5.4.1 Failure of Reinforcing Bars

This limit state was investigated for the basemat and containment wall. The critical section for the basemat is the region between the crane wall and containment wall in Figure 5.15. The critical region for wall evaluation is approximately 30 ft. above the basemat. From this elevation to the spring line the meridional and hoop reinforcing bars are provided at outside face of the wall only. At lower elevations the reinforcing is on both faces of the wall.

As shown in Table 5.7, the strain in the basemat reinforcing bars is not limiting for any task. For Tasks 3 and 4, where compression due to post-tensioning has not been overcome, the reinforcing bar strains in the wall are also not limiting. For Tasks 5 and 6, however, the pre-stressing effect has been overcome due to the pressure. Therefore, the strain in the wall reinforcing bars governs the containment capacity. The estimated capacities are 0.34g for Task 5 and 0.63g for Task 6. Figures 5.16 and 5.17 show the variation of margin factors with increasing A_H for Tasks 5 and 6, respectively. As noted on these figures, the laminated reinforced concrete element analyzed in TEMCO program can not be further loaded, since most concrete laminas crack and already yielded rebar elements cannot pick up the increased tension, causing a sharp drop in the margins calculated. It should be noted that, TEMCO analysis being an element-level analysis does not provide for the load redistribution in the meridional and circumferential directions in the containment. Therefore, the calculated capacities

should be considered conservative. A similar behavior of containment wall reinforcing was noted in Clinton containment, as discussed in Section 4.4.1.

5.4.2 Transverse Shear Failure

This limit state was investigated for the basemat and containment wall. Transverse shear reinforcement is provided in the containment wall up to an elevation of approximately 11 ft. above the basemat. Therefore, it would appear that element 30-31 in Figure 5.15 is the critical element for this limit state. However, the transverse shear force in element 29-30 may be significantly higher than in element 30-31. Therefore, both elements were investigated. For Task 3, the critical region is element 29-30, with a margin factor of 3.46. For Tasks 4, 5 and 6, however, the critical region is element 30-31. The margin in Task 4 is 3.15. For Tasks 5 and 6, where prestressing effect is overcome by the pressure, the margins drop to below unity at A_H = 1.0g, giving capacity of 0.39g for Task 5, and 0.77g for Task 6. The variation of margin factors with A_H for Tasks 5 and 6 is shown in Figure 5.18.

For the basemat evaluations, the critical region is the compression side for Task 3, and tension side for Tasks 4, 5, and 6. This difference in behavior in various tasks is because of the fact that the dead load shear and seismic shear act in the same direction on the compression side; however, the shear due to pressure loading acts against the seismic shear on the compression side and with the seismic shear on the tension side. The smallest margin as shown in Table 5.7, is 1.29 at A_H = 1.0g in Task 5. The margin curve for the basemat transverse shear for Task 5 is shown in Figure 5.19.

5.4.3 Failure Due to Interference With Auxiliary Building

Due to the arrangement of buildings at Zion station, as shown in Figure 5.20, potential exists for interference between the containment and auxiliary buildings during a seismic event. The highest elevation for this potential interference is 642 ft., approximately 77 ft. above the containment basemat. At this elevation the interference could occur on a 90° arc length. The gap between the two buildings is 1.0 inch.

To evaluate the containment capacity for this limit state, it was assumed that the amount of interference equals the horizontal displacement of the containment building at elevation 642 feet. This means that the existing gap between buildings, local deformation of the auxiliary building slab involved in the impact, and the lateral deflection of the auxiliary building are not considered. The ignoring of the existing gap is clearly conservative. Because the auxiliary building slab has high in-plane stiffness and since the auxiliary building is a stiff shear wall structure, the ignoring of displacement due to these deformations is reasonable.

All of the interference was, therefore, assumed to be absorbed by the local deformation of the containment wall. To evaluate a limit for this local deformation the following analysis was made: a ring load around

the circumference was applied to an axisymmetric model of the containment in DYNAX program. The analysis considered the effects of concrete cracking and yielding in the reinforcing bar and liner in the vicinity of the ring load. Figure 5.21 shows the progressive deflection of the containment wall near the ring load as the intensity of the load is increased.
At the step just prior to the maximum load, only 6" of uncracked concrete remained in the vicinity of the ring load. Figure 5.22 shows the load- deflection curve of the containment wall for Tasks 3 and 5. It is concluded from Figure 5.22 that the maximum deformation that can be, conservatively, absorbed in the containment wall is approximately 0.295 feet. This displacement corresponds to A_H = 0.75g from the seismic analysis. This is the capacity listed in Table 5.7 for this limit state.

Additional factor to be noted in this evaluation is the following: for the same load intensity, the assumed ring load is expected to cause smaller deflections under the load than the corresponding deflections under a loading which covers only part of the circumference. Therefore, for a given deflection from seismic analysis, the ring load application yields a lower margin and it is conservative.

5.4.4 Shear Failure at Buttress Plate

Figure 5.23 shows the details of the tendon, buttress plate, reinforcing bar, and the concrete outline at the buttress. There are six buttresses in the containment. The buttress plate stops 6" short of the concrete outline. Shear resistance is provided by the friction between the plate and concrete, and the reinforcing bar passing through 6" of concrete at the termination of the plate, as shown in Figure 5.23. In Tasks 3, 4 and 6, a hoop compression exists in the containment wall, therefore, frictional resistance can be mobilized. In Task 5, containment wall is in tension, therefore, the only shear resistance which can be mobilized is that due to the reinforcing bars and 6" of concrete. Based on these considerations, the capacity margin factors for this limit state were calculated to be 2.4 and 1.4, at A_H = 1.0g, for Tasks 3 and 4, respectively. For Tasks 5 and 6, the capacities are A_H = 0.75g and 0.85g, respectively. The variation in margin for Task 5 for this limit state is shown in Figure 5.24. As can be seen, the margin gradually drops from 1.7 at 0.25g to 1.0 at 0.75g.

5.4.5 Failure of Prestressing Tendons

This limit state was evaluated by computing the strains in the meridional and hoop tendons due to seismic and non-seismic loads including post-tensioning stress, pressure and temperature. The contribution of the seismic load to the total strain in the tendons is very small in comparison to the other loads. Therefore, although the margins reported in Table 5.7 are not very high, they are quite insensitive to the increases in the seismic load. Figure 5.25, which shows the margin curve for Task 5, demonstrates this fact.

5.4.6 Failure in Containment Wall at Penetration

Penetrations of cold piping have more potential to cause failure of containment during a seismic event, because of absence of bellows or thermal loops which are provided on hot lines. Based on this consideration the large diameter cold pipes which penetrate containment at higher elevations were considered for the evaluation of this limit state. Figure 5.26 shows the penetration detail for 14" diameter service water line that penetrates the containment at elevation 604'5" (approximately 38 feet above the basemat). The penetration diameter is 28" and it is anchored into the wall by eight strap anchors.

For Tasks 3 and 4, when the wall at the vicinity of penetration is in compression, pull out capacity is provided by friction between concrete and steel. Based on Table 6.6.1 of Reference 5.3 a coefficient of friction of 0.4 was used to evaluate the penetration pull out capacity for these tasks. For Tasks 5 and 6, the containment wall is in tension around the penetration. The penetration pull out capacity in this case was evaluated from the capacity of the welds connecting the flange of the penetration to the strap anchors, which are the weakest elements in the connection.

In order to calculate margin factors for this limit state, penetration pull-out capacity was divided by the piping stiffness to determine the limiting displacement capacity at the penetration. This displacement capacity was divided by the combined seismic and pressure induced displacements to obtain the margin factors shown in Table 5.7. A value of 14.3 K/inch was used for piping stiffness in these evaluations. This stiffness was determined by reviewing the existing piping analysis results. The variation in margin for Task 5 is shown in Figure 5.27.

5.4.7 Through-Wall Crushing of Concrete

Critical zone for this limit state is element 32-33 in Figure 5.15. The calculated margin factor at A_H = 1.0g for Task 3 is 6.8. The presence of pressure load in other tasks increases this margin even further.

5.4.8 Failure of Steel Liner

The strain in the liner is not a controlling factor in any of the tasks. Tasks 3 and 4, the margins exceed 10 at A_H = 1.0g. In Tasks 5 and 6, the shell element capacity is governed by the strains in the reinforcing bars. The liner strains at the calculated capacity of reinforcing bars, i.e., 0.34g for Task 5 and 0.63g for Task 6, are such that the margins are greater than 10 at these A_H values, as reported in Table 5.7.

5.4.9 Failure of Bolted Connections at Equipment Hatch

The connections at the equipment hatch have twelve 1-1/2" diameter SA 19387 bolts. The equipment hatch is of pressure-seated type. The bolted connection capacity was evaluated as described in Section 4.4.5 for the Clinton containment equipment hatch. The minimum margin computed at A_H = 1.0g, is 3.6 for Task 3, and greater than 10 for all other tasks.

The buckling of the equipment hatch, and the seismic capacity of the latching mechanism of the personnel locks were also reviewed, and were found not to be critical.

5.4.10 Bearing Failure of Foundation

The capacity margin factor for this limit state is based on the ultimate bearing capacity of 45 ksf, obtained from design information. The maximum vertical pressure during seismic event, combined with the minimum contact area remaining after considering uplift, was used in the evaluation. The calculated margin at 1.0g is 1.8, as reported in Table 5.8. The margin curve for this limit state is shown in Figure 5.28.

5.4.11 Failure Due to Sliding of Containment

Since Zion containment is built on a basemat which is separate from the adjacent structures, sliding of containment could potentially cause large relative movements of the pipings connected to the containment and adjacent buildings. Based on this consideration, margin for sliding was computed for Zion containment.

The total sliding force was computed at the time when maximum base shear occurs. This sliding force was used along with the frictional resistance available from the remaining contact area of the basemat at this time, and the differential side pressure obtained from the pit area to compute the capacity margin factor. The resistance calculations used a value of soil cohesion of 7.3 ksf based on design information. A margin of 2.2 was calculated at A_H = 1.0g for this limit state.

5.5 Conclusions

The following conclusions are drawn from the results discussed for Zion containment in this chapter.

1. The governing limit state in Task 3 for Zion containment is the failure due to interference of the containment with the auxiliary building; and in Task 5 it is the failure of wall reinforcing bar, closely followed by transverse shear failure of the wall. The conservative estimates of capacity are 0.75g and 0.34g for Tasks 3 and 5, respectively.

2. It should be noted that a capacity of 0.34g, calculated using time history consistent with Regulatory Guide 1.60 spectra, is almost four times the design safe shutdown earthquake (SSE) of Zion, which is A_H = 0.17g using Housner spectrum. This conclusion is based on a comparison of 0.34g capacity vs. 0.17g design SSE, and the fact that Regulatory Guide spectral accelerations at Zion containment frequencies are about twice in comparison to the Housner spectrum, see Figure 2.2 and frequencies in Table 5.3.

3. Nine direct and two indirect limit states were evaluated for Zion containment. Of these, the prestressing tendons, steel liner, penetrations, and equipment hatch connections appear to be of no

concern. Even at the high acceleration, i.e., A_H = 1.0g, these items have ample margin against failure in all tasks. Similarly, crushing of concrete, and the failure of foundation due to bearing pressure, or sliding are of no concern based on a similarly high margin of safety.

Of the remaining four limit states, none is considered critical for Tasks 3 and 4. Although, the calculated capacity for the impact between the containment and the auxiliary building is 0.75g, this evaluation is considered conservative.

Seismic ruggedness of Zion containment is somewhat reduced in Tasks 5 and 6 because pressure loading overcomes the effect of prestress. This is observed in limit states associated with the straining of the wall reinforcing bar, the transverse shear loading on the wall, and slippage at buttress plates. Of these three, the slippage at the buttress plates is considered less critical than the straining of reinforcing bars and transverse shear on the wall.

Even the straining of reinforcing bars and the wall shear show capacities well above 0.5g for Task 6. Corresponding Task 5 capacities are 0.34g and 0.39g, respectively. It should be noted that evaluation of reinforcing bars, done on an element level, does not consider redistribution of forces which could take place due to the continuity of the structure. Similarly, the evaluation of the transverse shear capacity using provisions of ACI Code for shear strength is considered a lower bound.

4. The initial shock, up to a level of A_H = 1.0g does not affect the subsequent seismic capacity of the Zion containment, since the effect of prestressing is not overcome and escessive compression does not develop in the containment wall. This statement ignores the effect of local damage from interference with auxiliary building because of potential softening that may take place due to the initial interference.

5. Because of separate basemat and soil foundation, the Zion containment experiences relatively larger lateral displacements due to rocking than in Clinton which is on soil with continuous mat, and in Fermi which is founded on rock.

6. For values of A_H greater than 0.5g, significant uplift occurs. At A_H = 1g, 40% of basemat uplifts. However, this uplift is associated with reduction in structural forces in the containment wall. Some of the basemat responses are moderately increased. Moreover, because uplift occurs on soil foundation, the hard impact condition seen in the in-structure spectra of Fermi and Sequoyah containments is almost absent in the Zion containment.

7. Similar to the observation made on the Clinton containment, soil-structure interaction attenuates the responses at high frequency range and this effect increases with increasing values of A_H because soil softens.

5.6 References

5.1 Johnson, G. R., Christian P., and Epstein, H. I., "Stiffness Coefficient for Embedded Footings," Proc. ASCE, Journal of the Geotechnical Engineering Division, Vol. 101, No. GT8, August, 1975.

5.2 Chopra, A. K., and Yim, C. S., "Simplified Earthquake Analysis of Structures With Foundation Uplift," Proc ASCE, Journal of the Structural Division, Vol. 111, No. ST4, 1985, pp. 906-930.

5.3 Prestressed Concrete Institute, PCI Design Handbook: Precast and Prestressed Concrete, Chicago, IL. Third Edition, 1985.

Table 5.1

Foundation Material Properties at Zion

Material Property	Granular Deposits	Glacial Deposits	Dolomite
Density (PCF)	122	142	160
Poisson's Ratio	0.39	0.40	0.30
Dynamic Modulus of Elasticity E (PSF)			
Single Amplitude Shear Strain			
1.0% 8,300 $(\bar{\sigma}_m)^{1/2}$		12×10^5	
0.1% 41,700 $(\bar{\sigma}_m)^{1/2}$		34×10^5	
0.01% 111,200 $(\bar{\sigma}_m)^{1/2}$		101×10^5	
0.001%	158,500 $(\bar{\sigma}_m)^{1/2}$	232×10^5	
0.0001%	169,600 $(\bar{\sigma}_m)^{1/2}$	336×10^5	110×10^7
Dynamic Modulus of Rigidity G (PSF)			
Single Amplitude Shear Strain			
1.0% 3,000 $(\bar{\sigma}_m)^{1/2}$		4×10^5	
0.1% 15,000 $(\bar{\sigma}_m)^{1/2}$		12×10^5	
0.01% 40,000 $(\bar{\sigma}_m)^{1/2}$		36×10^5	
0.001%	57,000 $(\bar{\sigma}_m)^{1/2}$	83×10^5	
0.0001%	61,000 $(\bar{\sigma}_m)^{1/2}$	120×10^5	45×10^7
Damping (Percent of Critical)			
Single Amplitude Shear Strain			
1.0% 24	20		
0.1% 16	9		
0.01% 6	5		
0.001%	1.5	3	
0.0001%	0.5	2.5	1 to 2

$\bar{\sigma}_m$ = mean effective stress

Table 5.2

Total Foundation Spring and Dashpot Constants

A_H	K_H (k/ft)	K_V (k/ft)	K (k-ft/Rd)	C_H (k-s/ft)	C_V (K-s/ft)	C (k-ft-s/Rd)
0.25g	1.64×10^6	3.52×10^6	6.19×10^9	1.06×10^5	3.35×10^5	1.16×10^8
0.50g	0.93×10^6	2.01×10^6	3.52×10^9	0.80×10^5	2.52×10^5	0.87×10^8
0.75g	0.71×10^6	1.54×10^6	2.70×10^9	0.70×10^5	2.21×10^5	0.77×10^8
1.0g	0.62×10^6	1.35×10^6	2.37×10^9	0.65×10^5	2.07×10^5	0.72×10^8

Note: The two horizontal springs and dashpots in Figure 5.2 have values equal to one-half of the total values given in this table. The interior vertical springs and dashpots in Figure 5.2 have the same values; the end elements have higher values. In the vertical direction this discrete system has the total vertical and rocking constants equal to the values listed in the table.

Table 5.3

Model Frequencies For Zion Seismic Model

Mode Number	Frequency (cps) Fixed Base	SSI - Model Figure 5.2 A_H = 0.25g	A_H = 1.0g
1	3.05	1.55	1.06
2	5.42	3.78	2.54
3	10.57	4.28	2.71
4	10.61	5.97	5.62
5	10.69	10.66	10.65

Table 5.4

Maximum Extent of Basemat Uplift

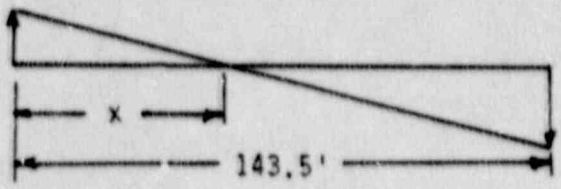

Node 20 Node 27

A_H	x
0.25g	0'
0.50g	35.6'
0.75g	52.1'
1.00g	59.8'

Table 5.5

Effect of Uplift on Containment Base Shear and Moment (A_H = 1.0g)

Response	No Uplift	With Uplift
V (Kips)	7.42 X 10^4	5.77 X 10^4
M (Ft. Kips)	10.8 x 10^6	8.94 x 10^6

Table 5.6

Effect of Uplift on Transverse Shear And Bending Moment In the Basemat (A_H = 1.0g)

$$\text{Ratio} = \frac{\text{Response With Uplift}}{\text{Response Without Uplift}}$$

	Shear	Positive Moment	Negative Moment
Compression Side	0.92	0.90	0.98
Tension Side	1.18	1.39	0.85

Table 5.7
Capacity Margin Factors for Zion Containment at A_H = 1.0g (Except As Noted)
(Direct Limit States)
(See Note 1)

Code*	Description	Criterion	Tasks			
			3	4	5	6
2	Failure of reinforcing bars					
	a. Containment wall	$10\ \varepsilon_y/\varepsilon$	>10	>10	1.0 at A_H=0.34g	1.0 at A_H=0.63g
	b. Basemat		>10	>10	>10	>10
6	Transverse shear failure in					
	a. Wall	Flexural shear cap per ACI 11.3 / Average nominal shear	3.46	3.15	1.0 at A_H=0.39g	1.0 at A_H=0.77g
	b. Basemat		4.15	2.36	1.29	1.66
2	Failure of containment wall due to interference with auxiliary building	Radial displ. cap. = 0.295 ft. / Max horiz. displ.	1.0 at A_H=0.75g	1.0 at A_H=0.75g	1.0 at A_H=0.75g	1.0 at A_H=0.75g
10	Shear failure at buttress plate	Long. shear cap. based on friction and reinforcement / Max. long. shear	2.40	1.40	1.0 at A_H=0.75g	1.0 at A_H=0.85g

Table 5.7 (Cont'd)
Capacity Margin Factors for Zion Containment at A_H = 1.0g (Except As Noted)
(Direct Limit States)
(See Note 1)

Code*	Description	Criterion	Tasks 3	4	5	6
3	Failure of prestressing tendons					
	a. Circumferenctial	$\varepsilon_y/\varepsilon$	2.05	1.78	1.48	1.72
	b. Meridional		1.94	1.73	1.62	1.69
8	Failure in containment wall at penetration	Pull-out capacity per ASME / Axial force from disp.	>10	5.70	NA	NA
		Strength of strap anchor weld / Effective weld force from disp.	NA	NA	1.90	2.30
7	Through wall crushing of concrete	0.002 / Average comp. strain when wall thickness in comp.	6.8	Not critical because of pressure		
1	Failure of steel liner	$0.02/\varepsilon_{principal}$	>10	>10	>10 at A_H=0.34g	>10 at A_H=0.63g
9	Failure of pretensioned bolted connections at equipment hatch	Shear capacity / Max. shear	3.60	>10	>10	>10

*Refer to limit state identification number in Table 1.2
Note 1: A comment similar to Note 1 of Table 3.9 applies to this table also.
NA = Not applicable

Table 5.8

Capacity Margin Factors for Zion Containment at A_H = 1.0g
(Indirect Limit States)
(See Note 1)

Code*	Description	Criterion	Tasks			
			3	4	5	6
13	Bearing failure of foundation	Ult. bearing capacity / Peak average pressure	1.80	1.80	1.80	1.80
14	Failure due to sliding	Frictional resistance plus side pressure differential / Peak horizontal force	2.20	2.20	2.20	2.20

*Refer to limit state identification number in Table 1.2

Note 1: A comment similar to Note 1 of Table 3.9 applies to this table also.

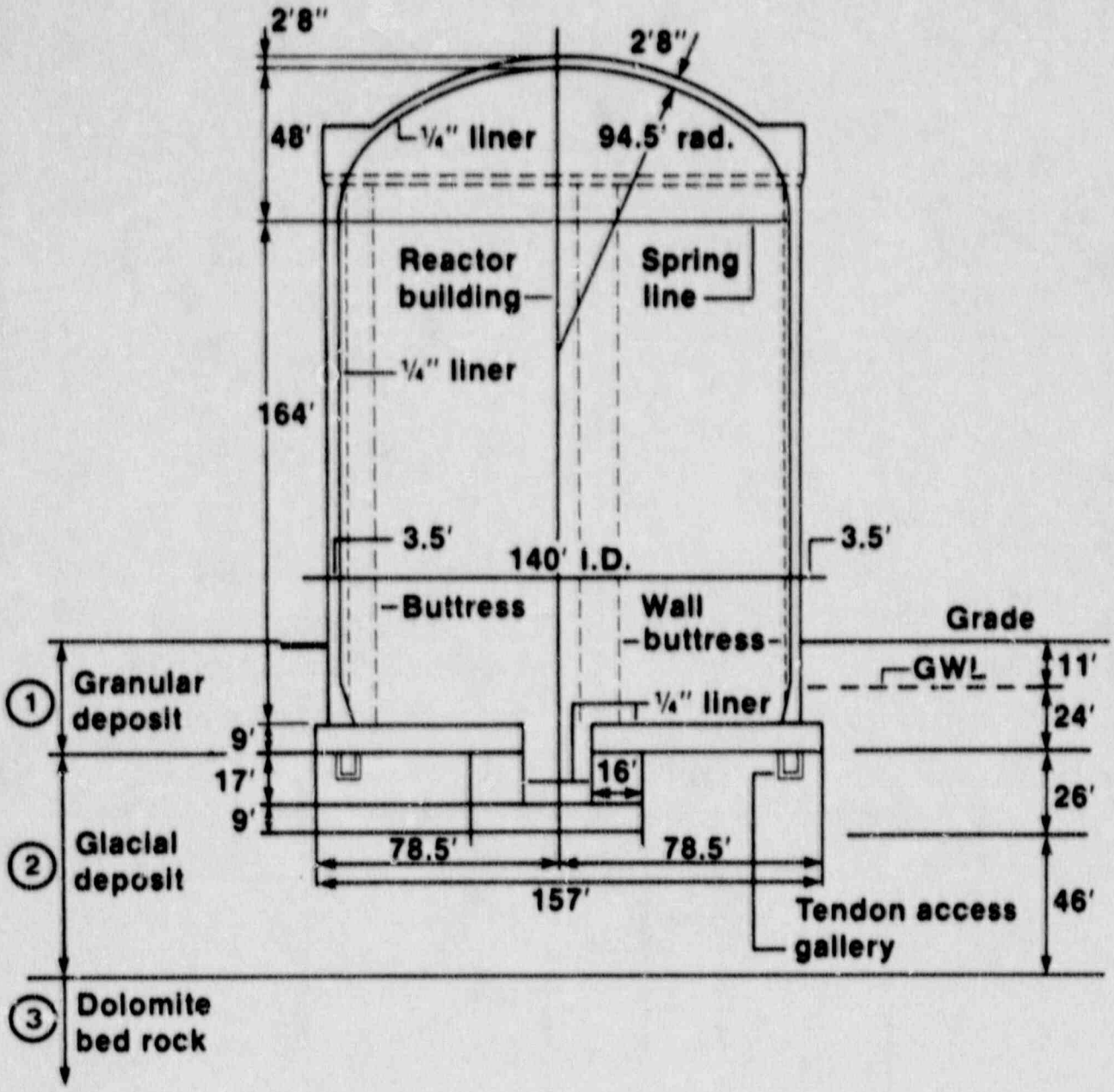

Figure 5.1 Schematic of Zion Containment and Its Foundation

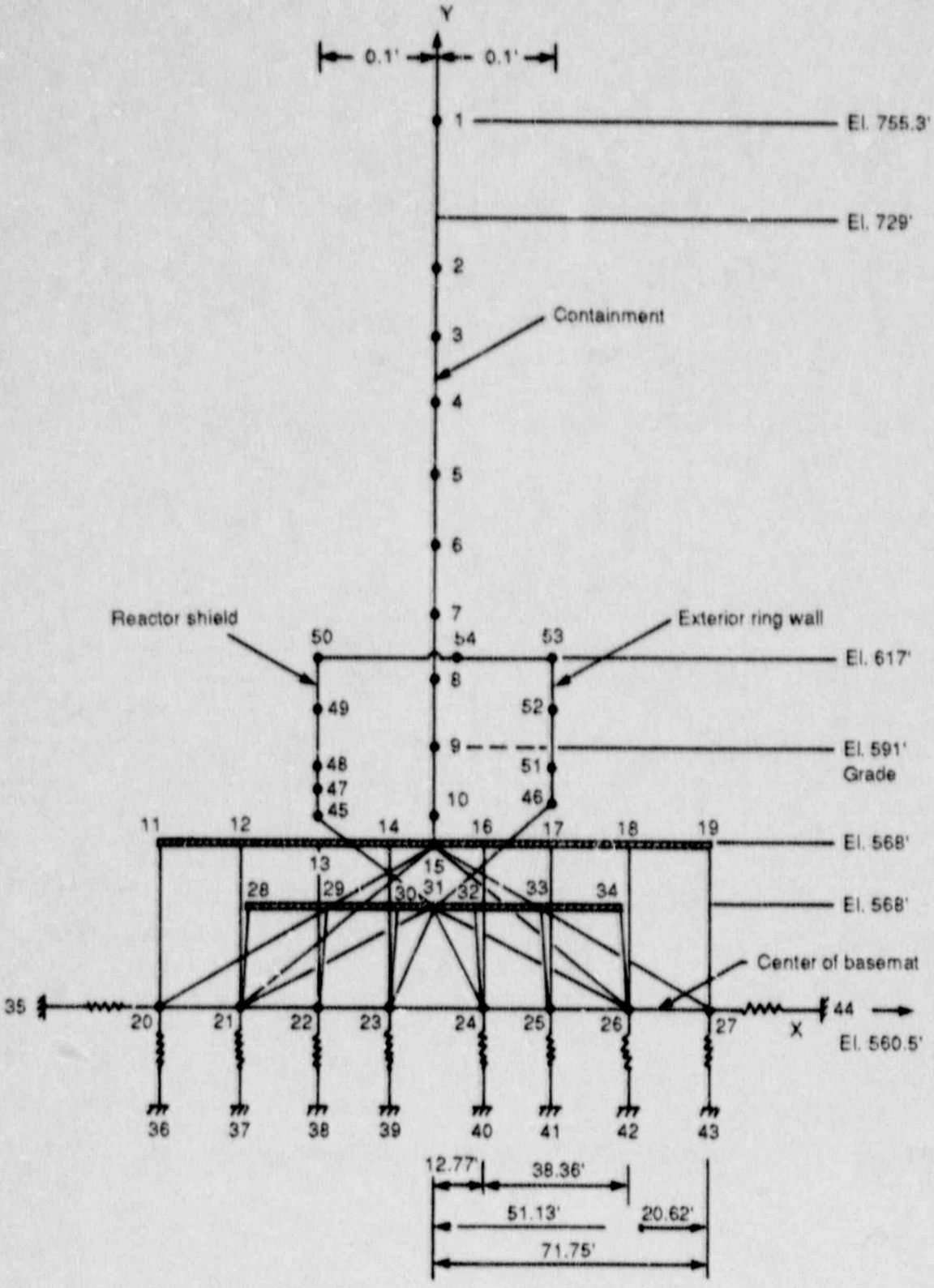

Figure 5.2 Seismic Model of Zion Containment

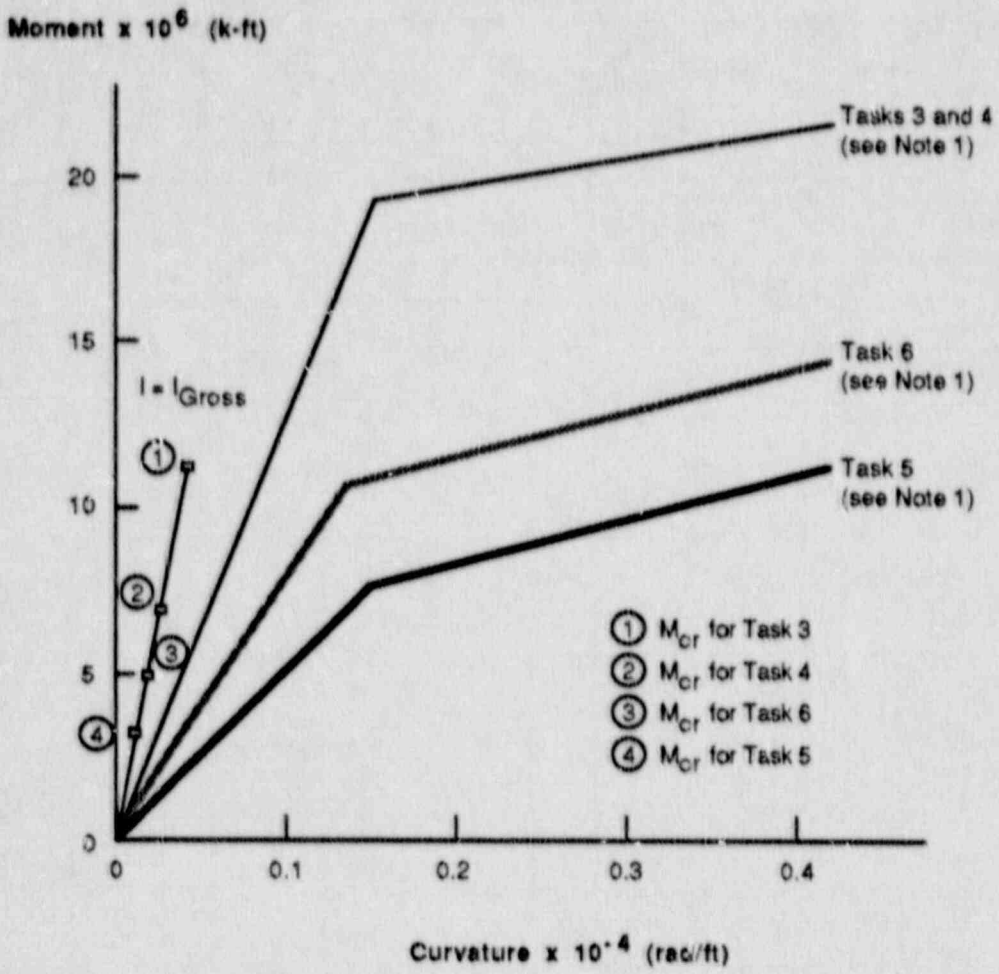

Notes:

1. The indicated diagram applies when A_H is high enough to cause circumferential cracking in concrete.
2. M_{cr} = Moment when concrete is on the verge of cracking.

Figure 5.3 Moment-Curvature Diagrams Used for Element Number (9-10) of Zion Seismic Model for Tasks 3 through 6

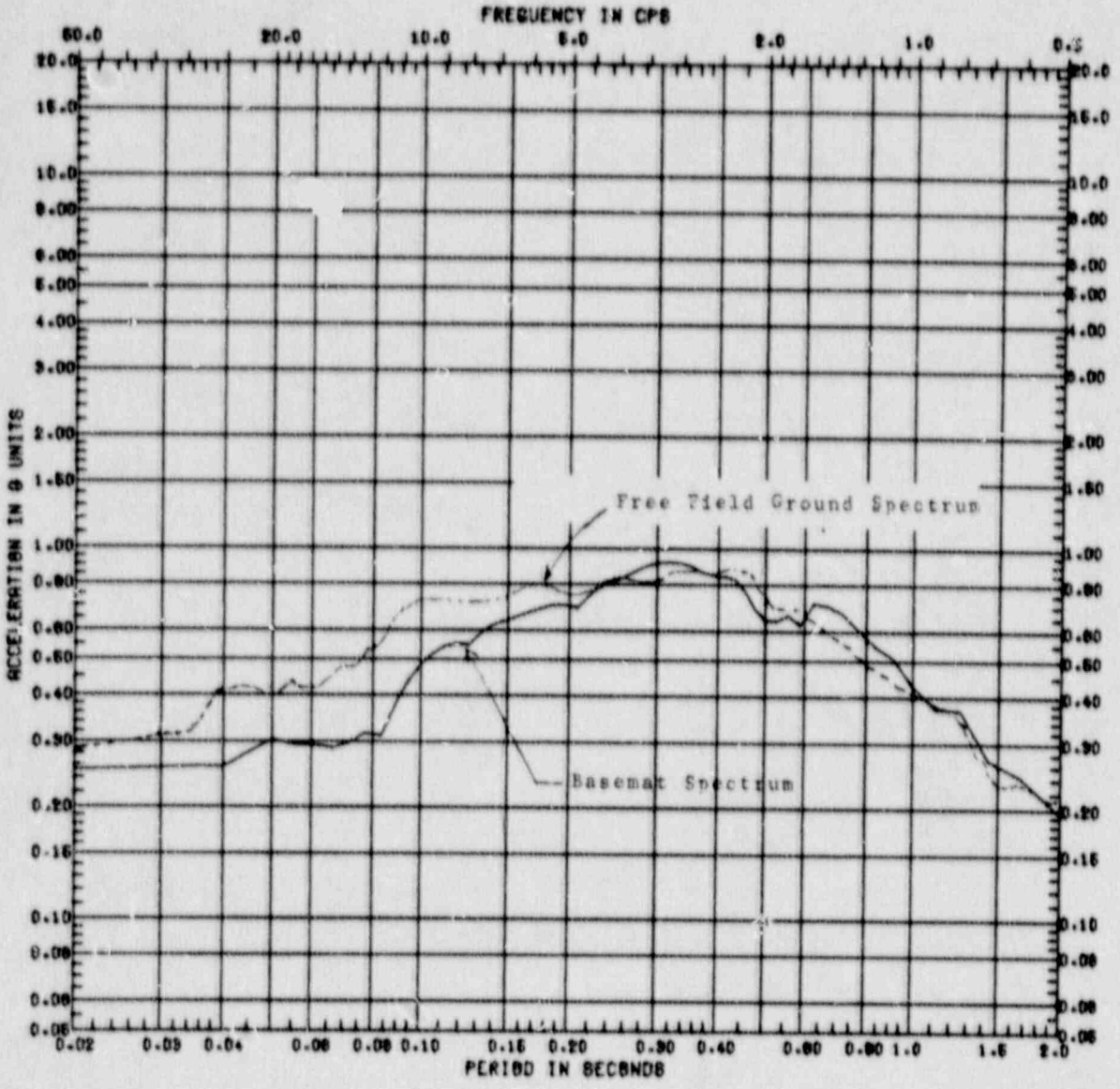

Figure 5.4 Comparison of Horizontal Response Spectrum at the Basemat at A_H = 0.25 g and the Input Ground Spectrum, Damping = 5%

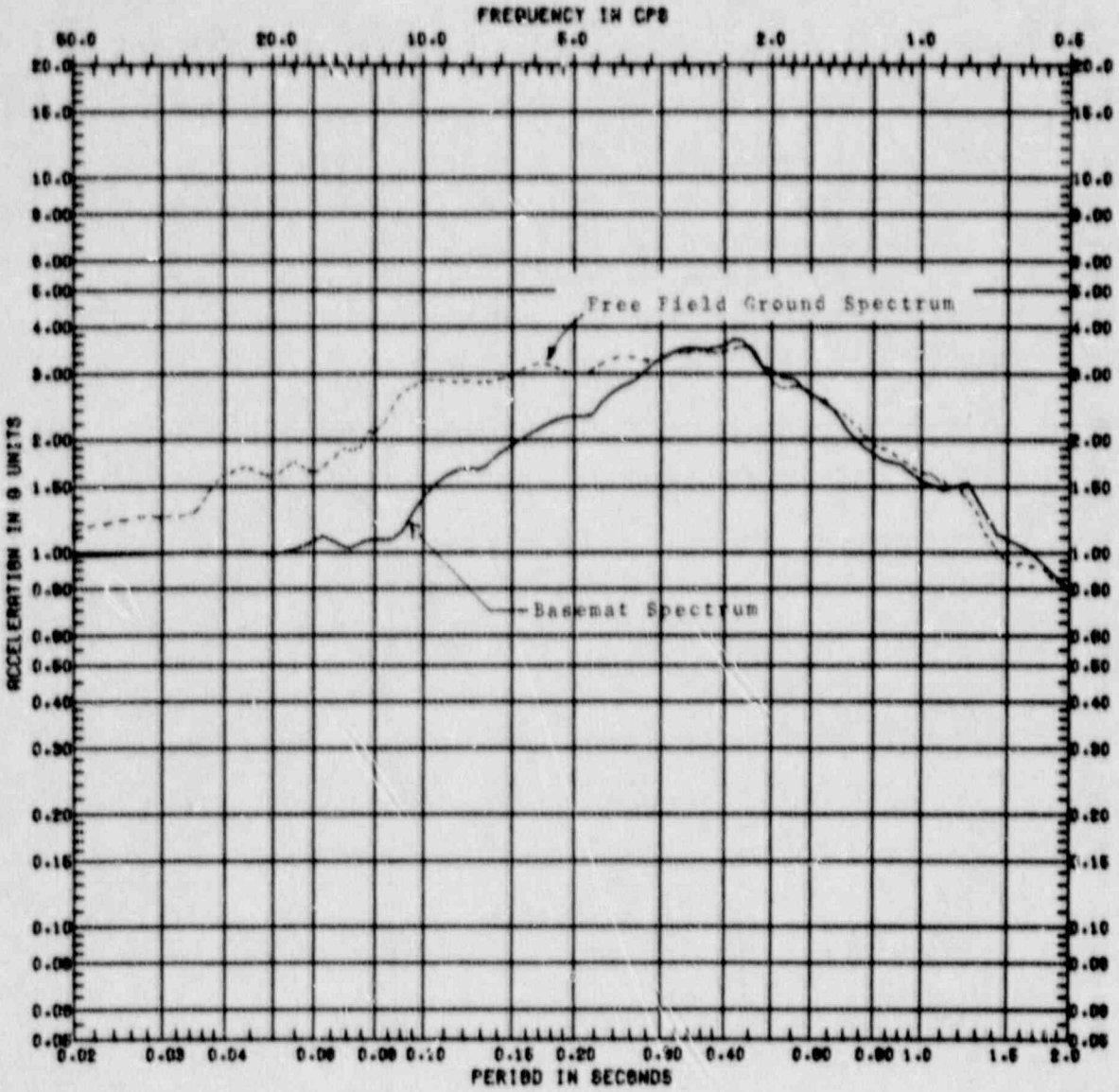

Figure 5.5 Comparison of Horizontal Response Spectrum at the Basemat at A_H = 1.0 g and the Input Ground Spectrum, Damping = 5%

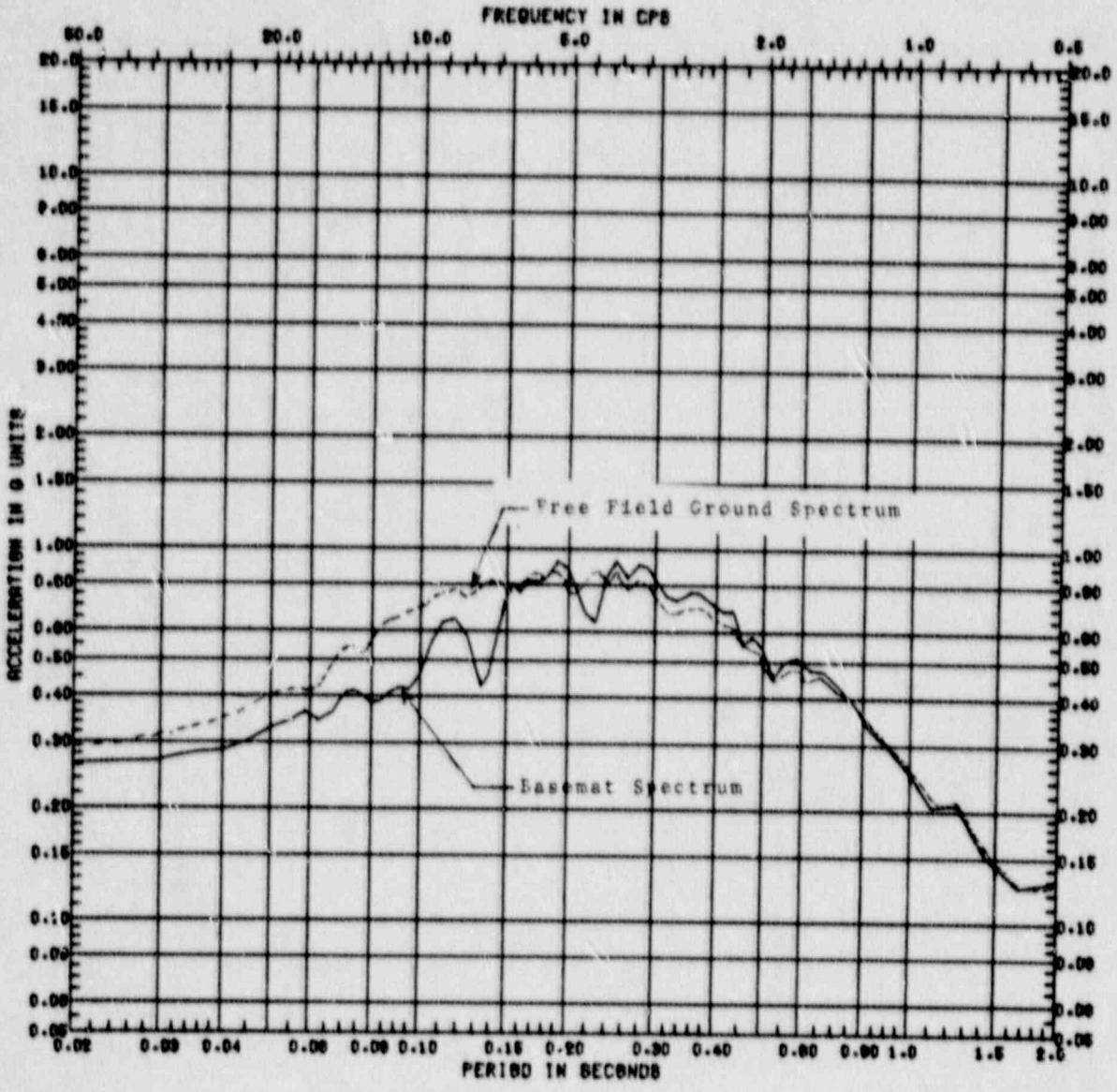

Figure 5.6 Comparison of Vertical Response Spectrum at the Basemat at A_H = 0.25g and the Input Ground Spectrum, Damping = 5%

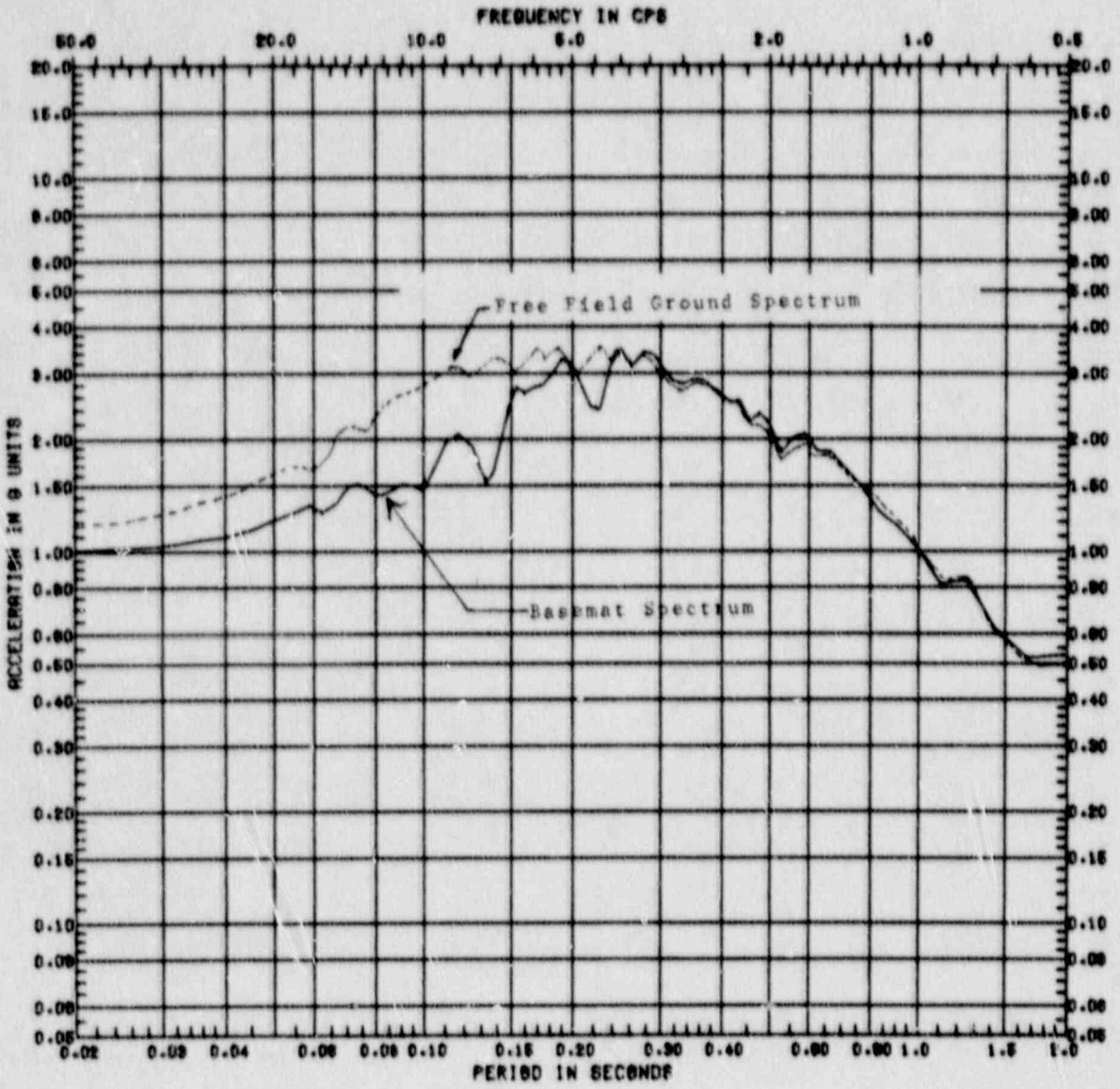

Figure 5.7 Comparison of Vertical Response Spectrum at the Basemat at A_H = 1.0g and the Input Ground Spectrum, Damping = 5%

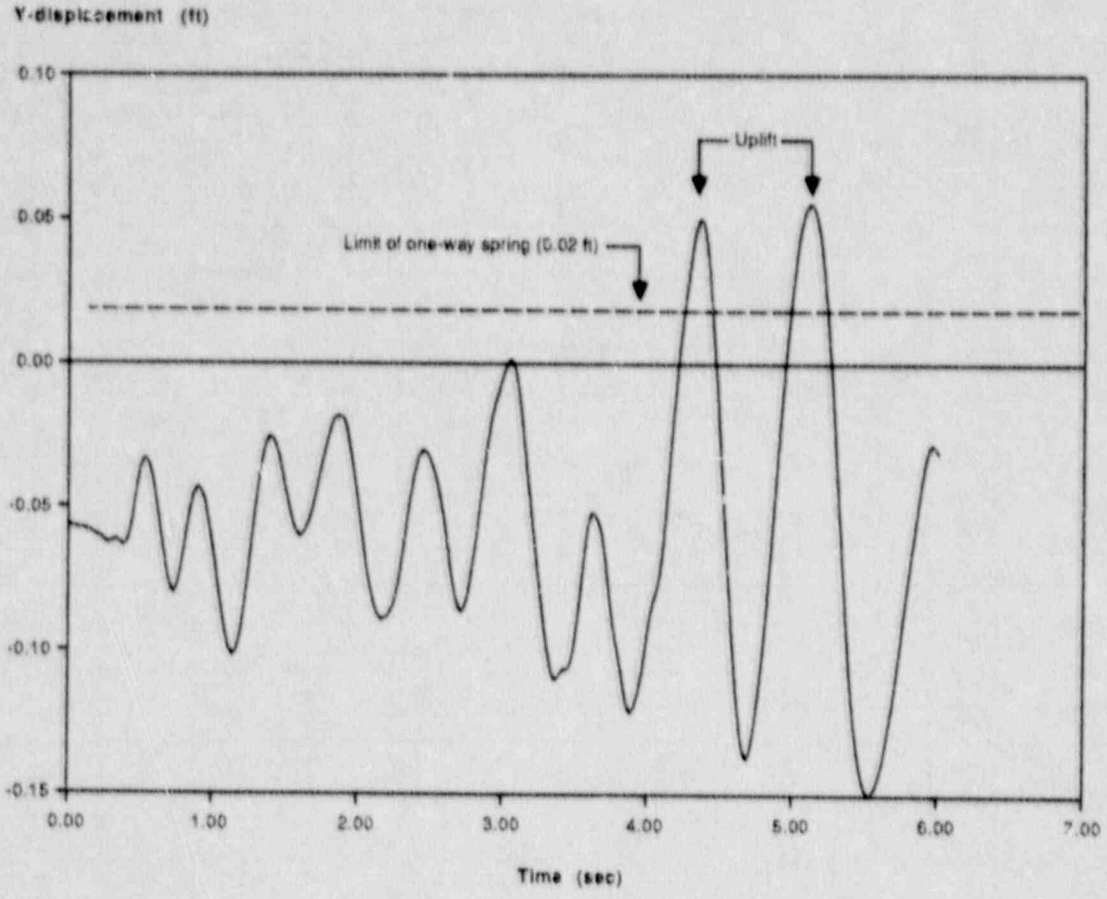

Figure 5.8 Vertical Displacement Time-History of Node 20 of the Seismic Model at A_H = 0.5 g, Showing Basemat Uplift

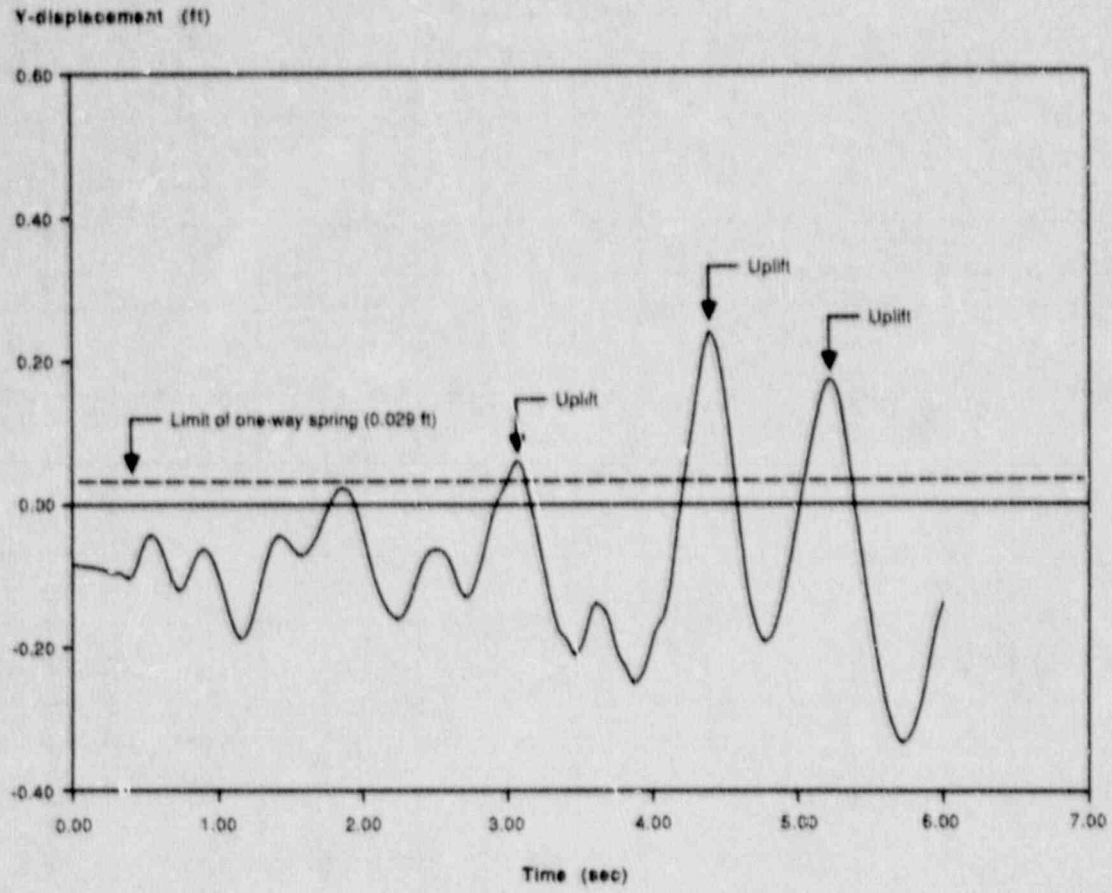

Figure 5.9 **Vertical Displacement Time-History of Node 20 of the Seismic Model at A_H = 1.0 g, Showing Significant Basemat Uplift**

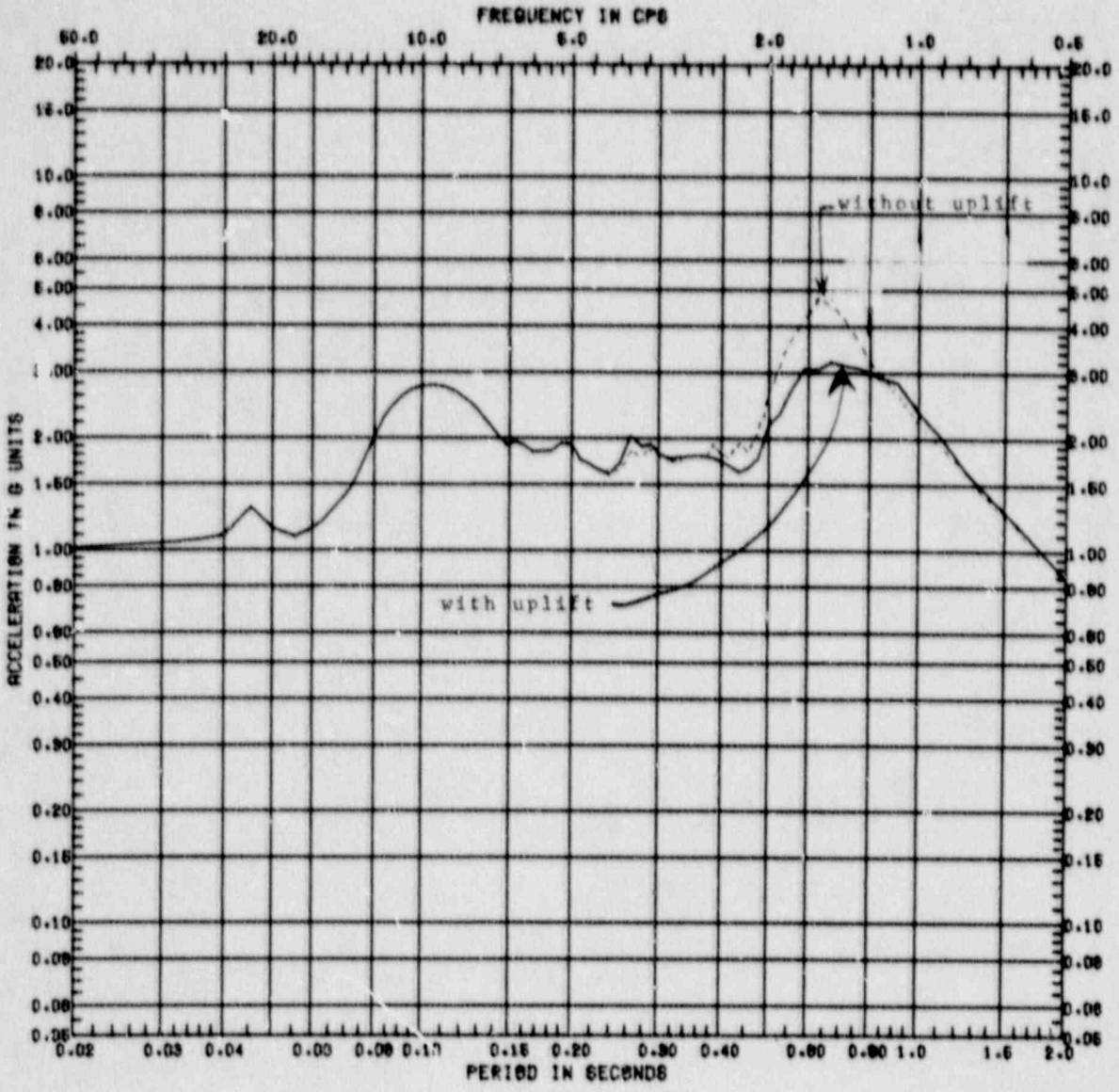

Figure 5.10 Comparison of Horizontal Response Spectra at Node 7 of the Seismic Model at A_H = 1.0g Showing Effect of Uplift, Damping = 5%

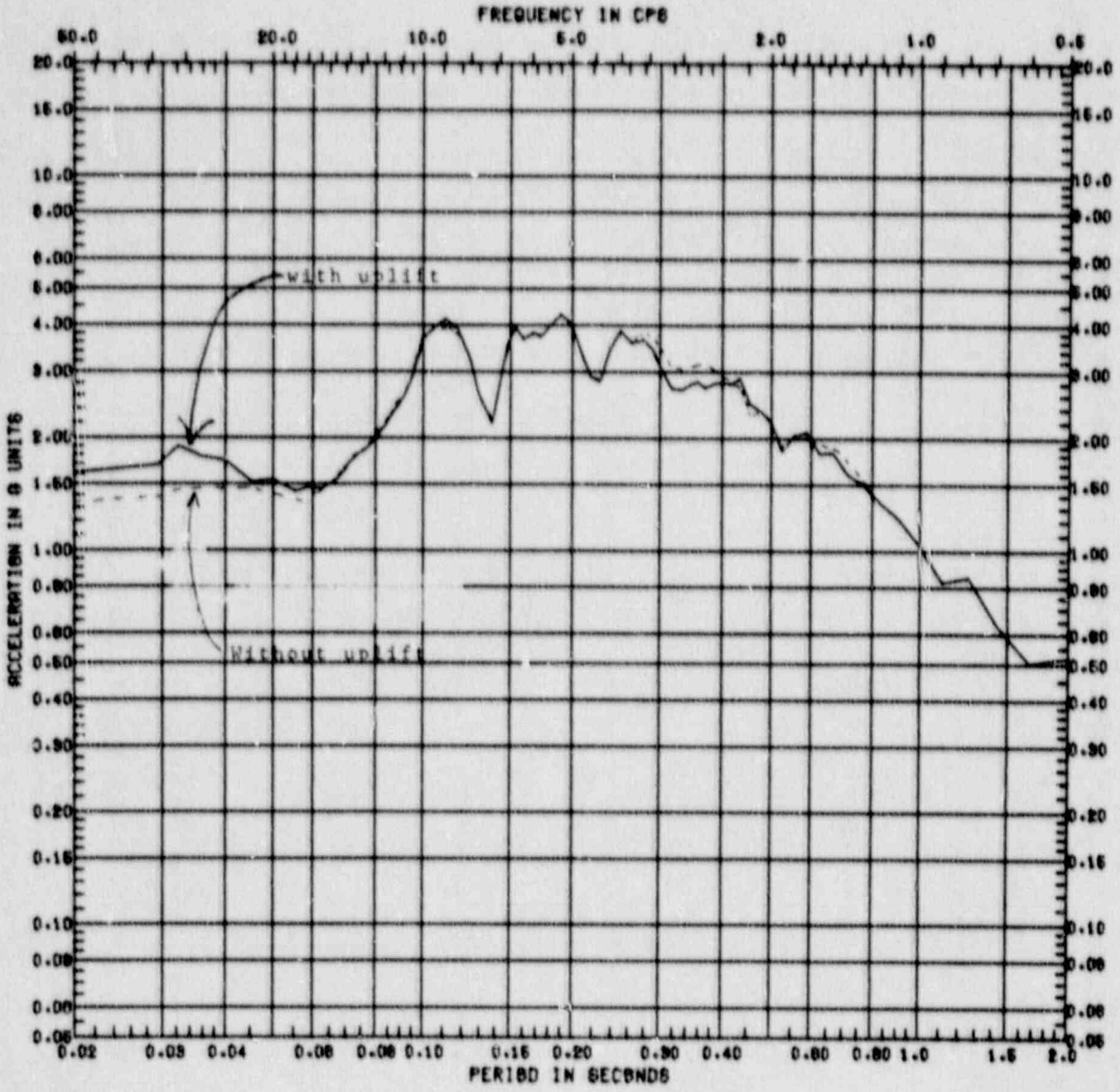

Figure 5.11 Comparison of Vertical Response Spectra at Node 7 of the Seismic Model at A_H = 1.0g Showing Effect of Uplift, Damping = 5%

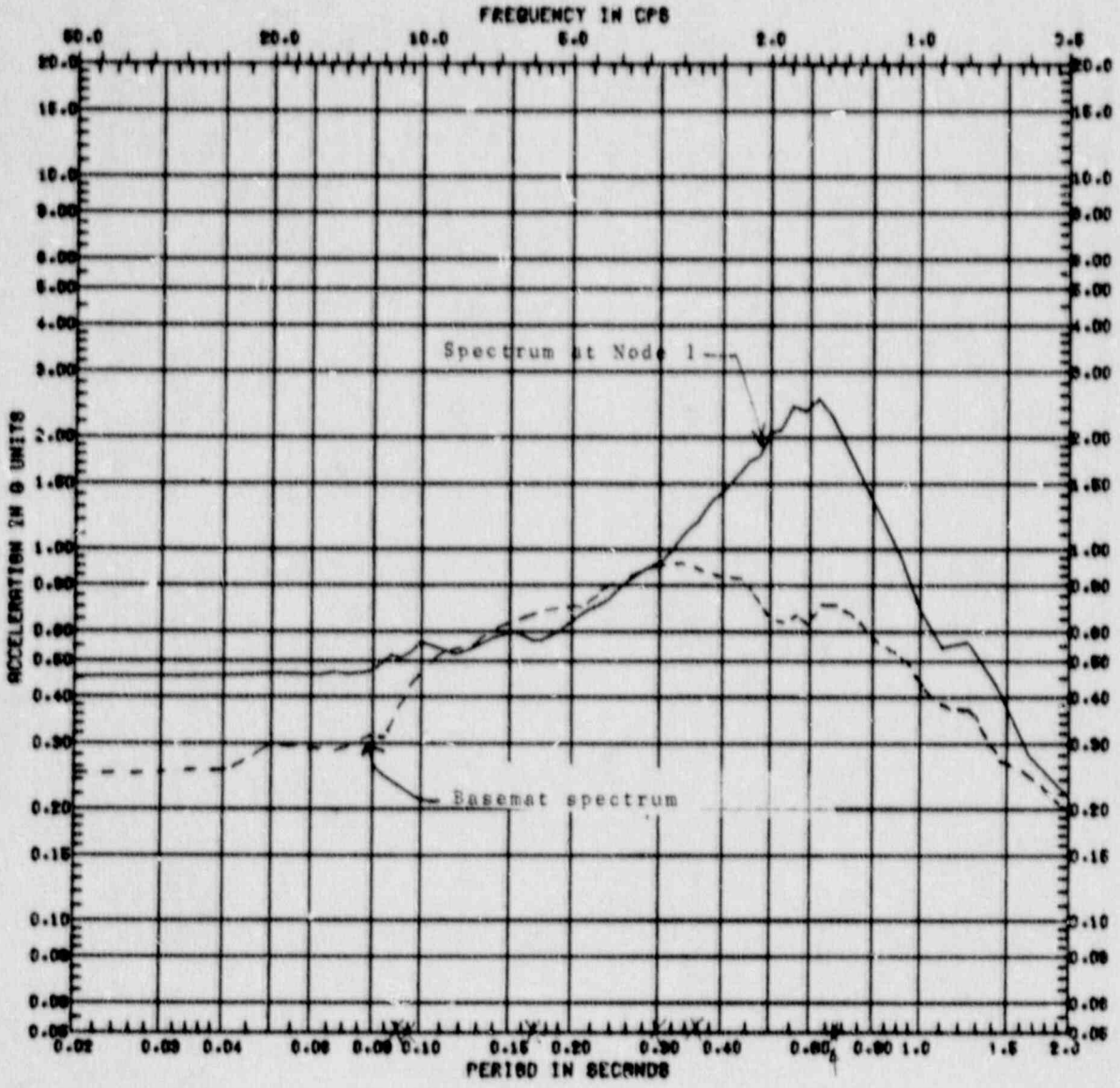

Figure 5.12 Comparison of Horizontal Response Spectra at Node 1 of the Seismic Model and Basemat at A_H = 0.25g, Damping = 5%

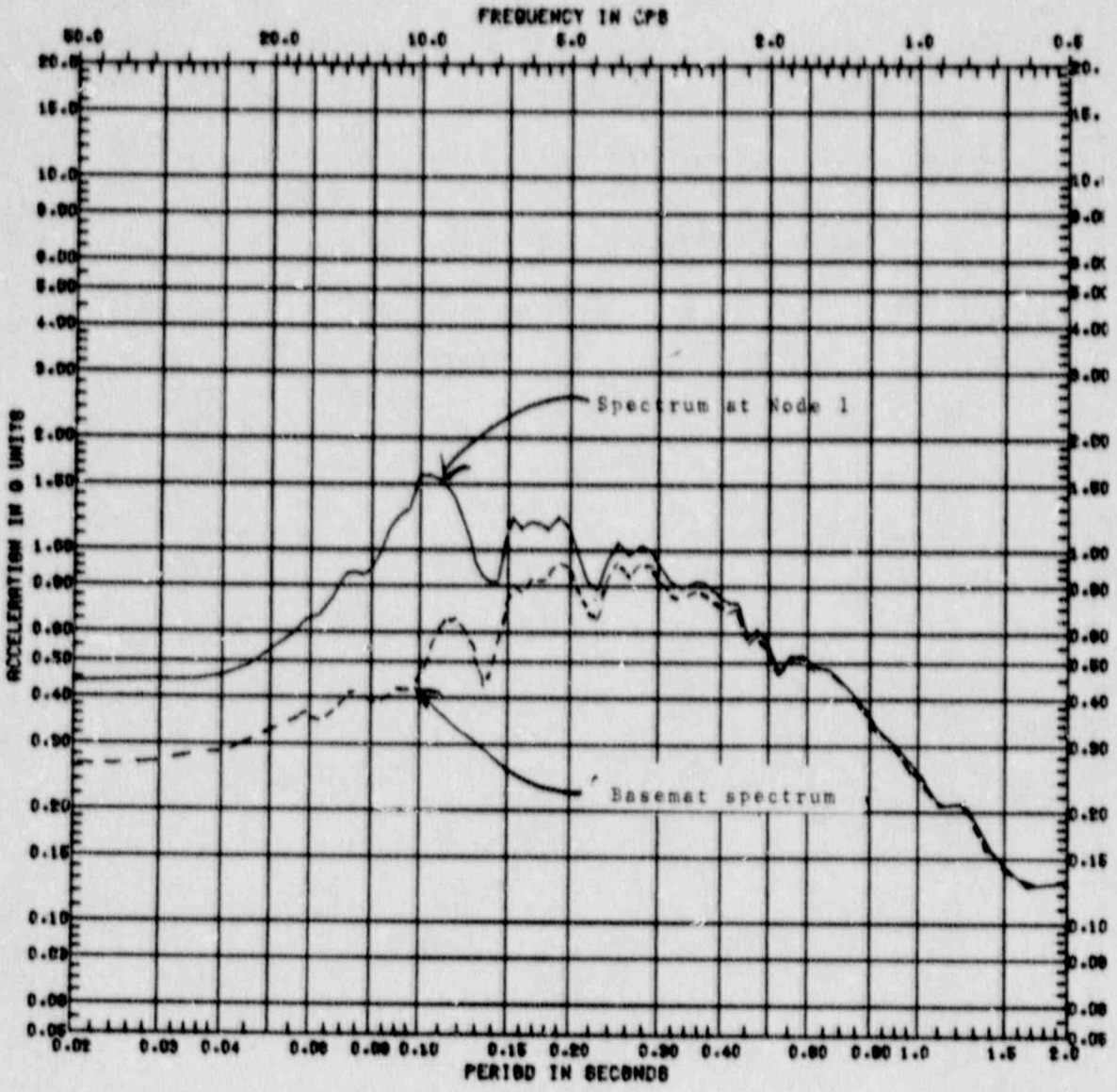

Figure 5.13 Comparison of Vertical Response Spectra at Node 1 of the Seismic Model and Basemat at A_H = 0.25g

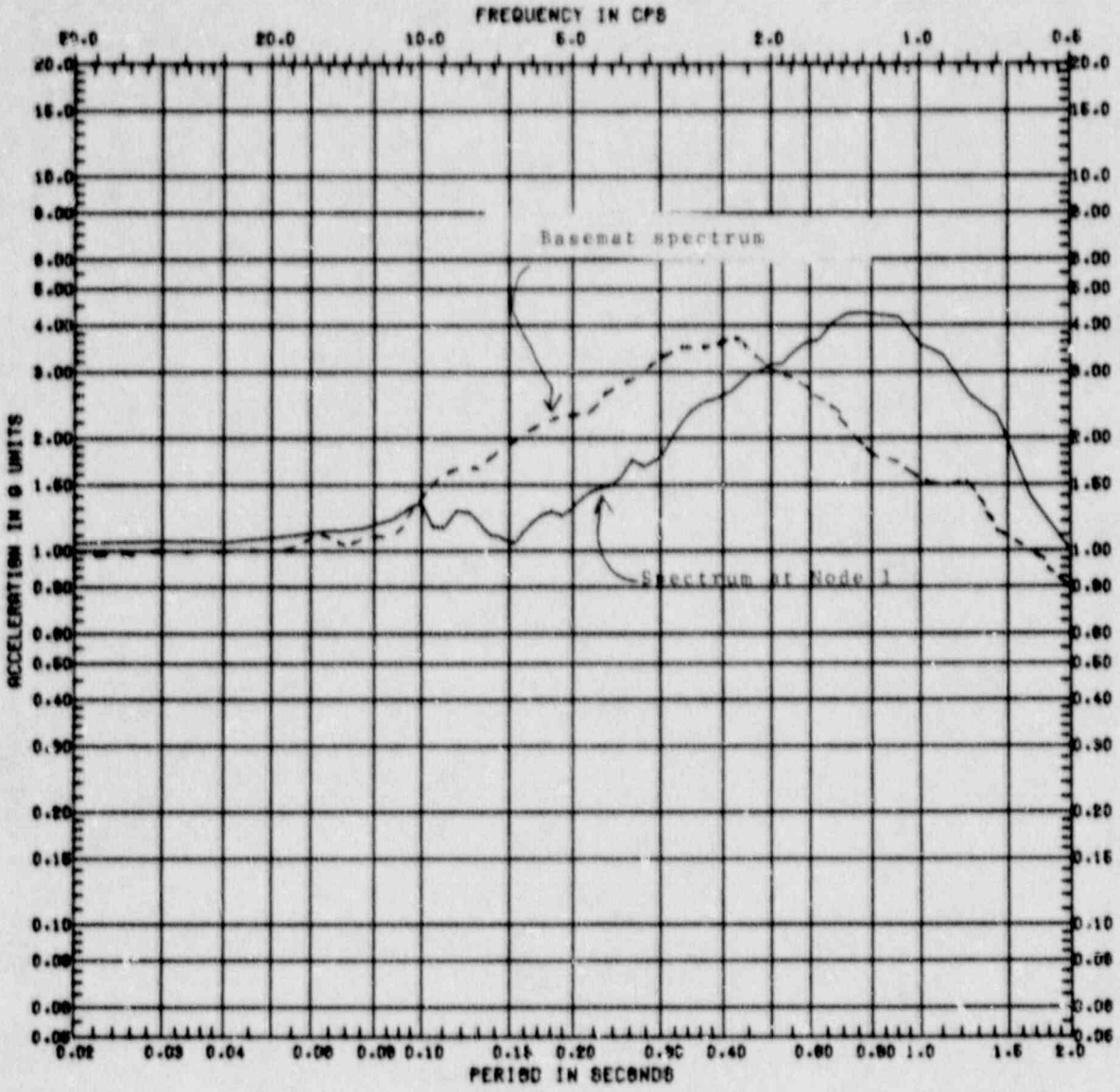

Figure 5.14 Comparison of Horizontal Response Spectra at Node 1 of the Seismic Model and Basemat at A_H = 1.0g

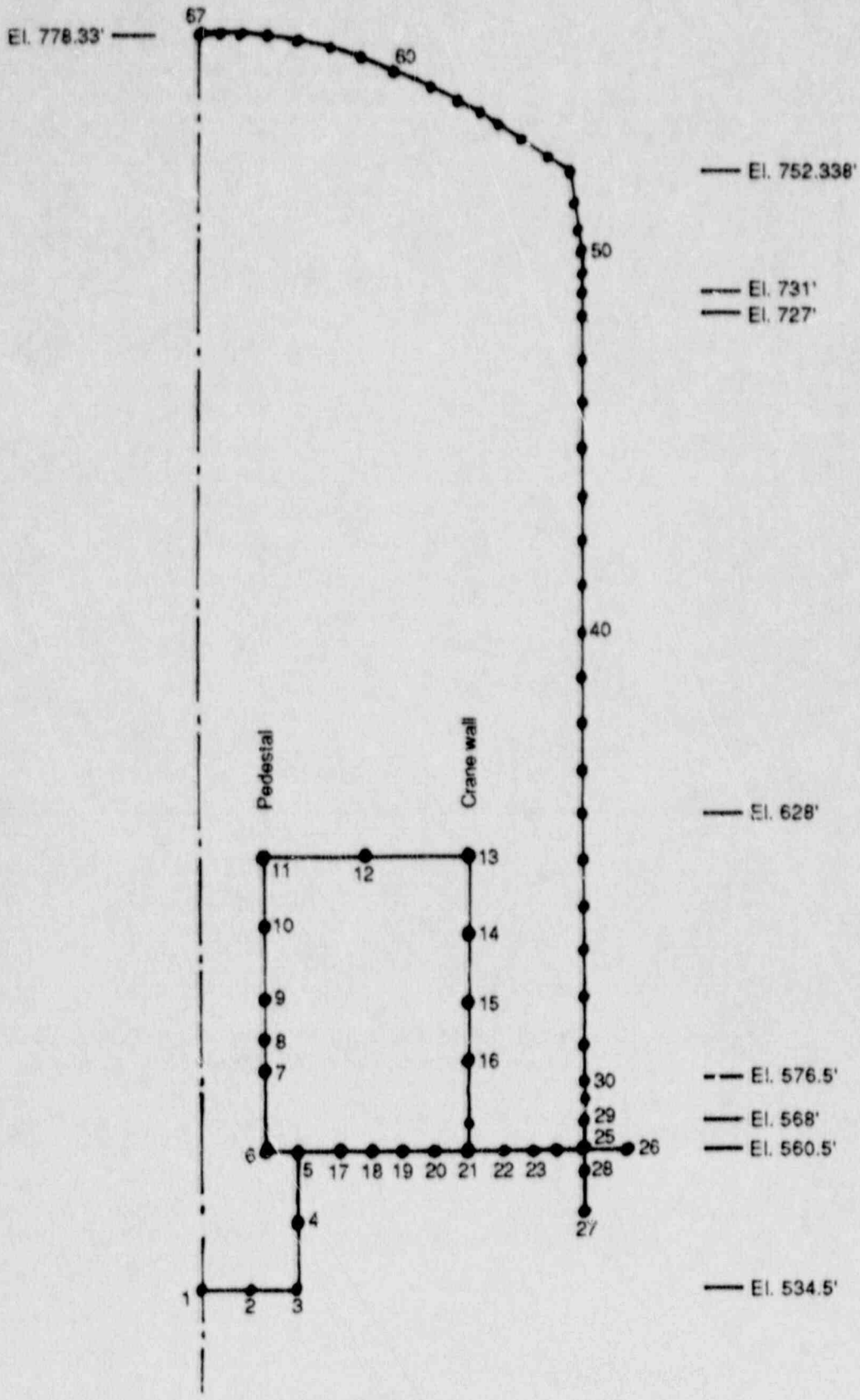

Figure 5.15 Axisymmetric DYNAX Model of the Zion Containment

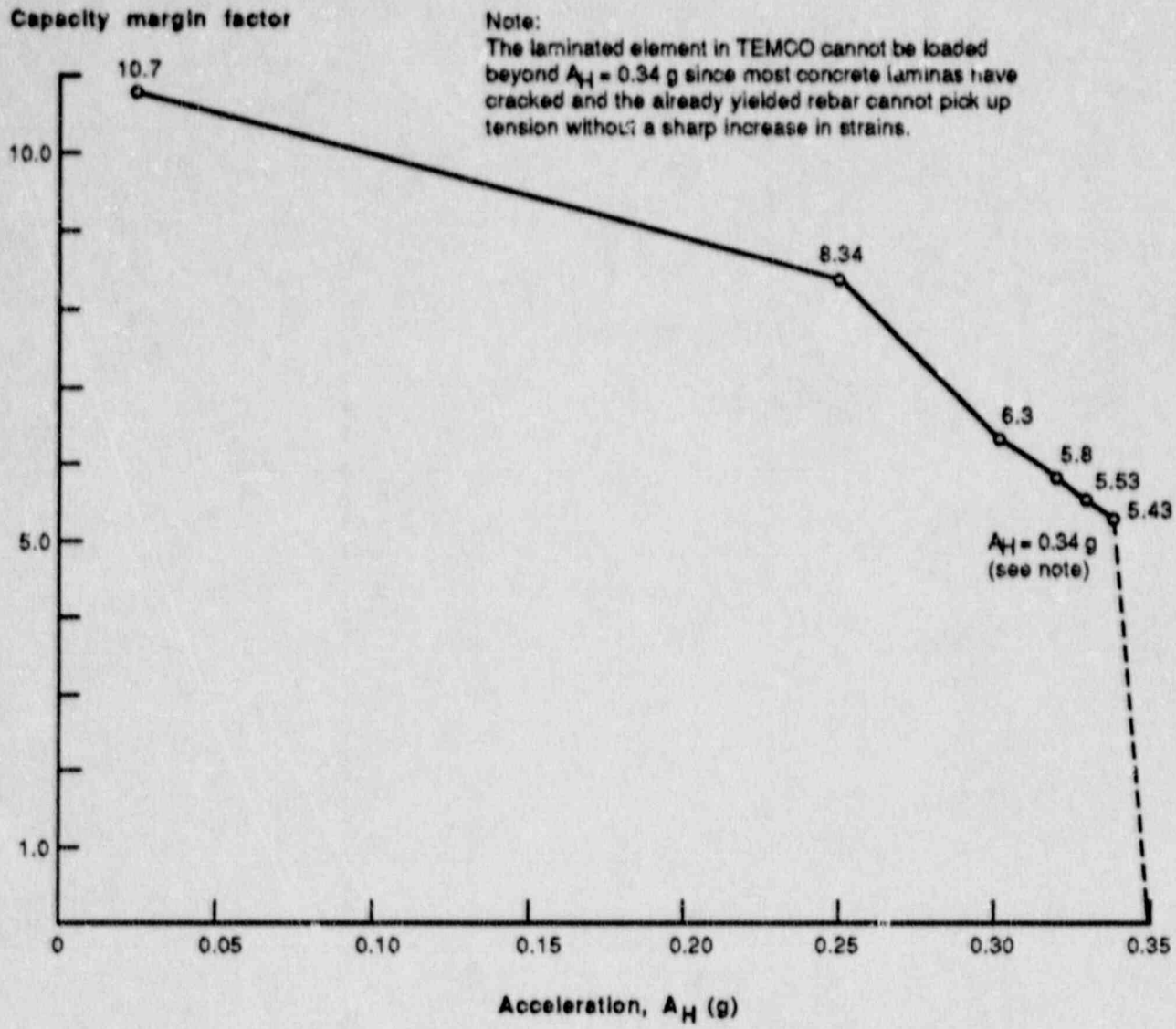

Figure 5.16 Variation of Margin with A_H for Reinforcing Bars in the Containment Wall Under Task 5 Loading

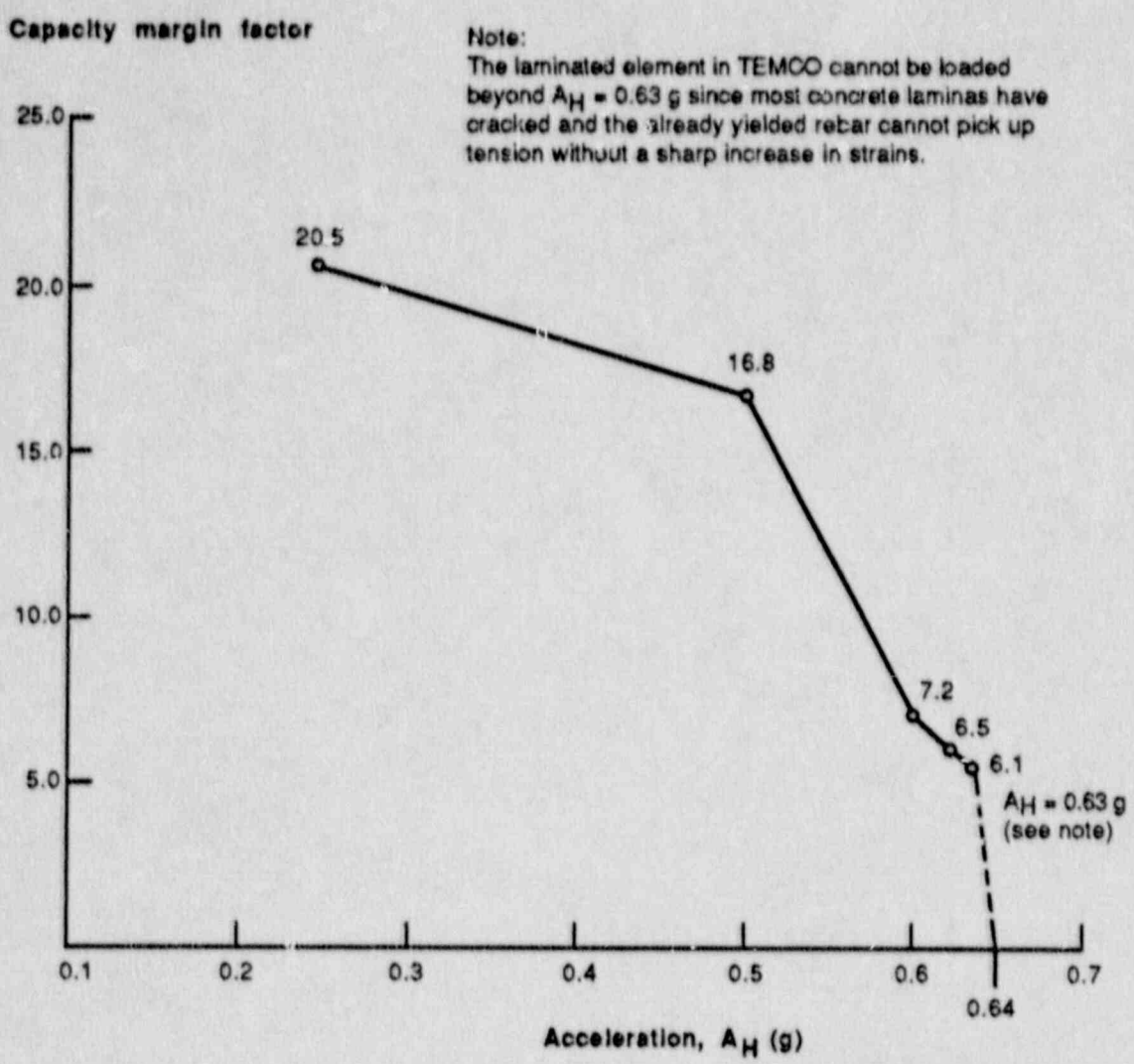

Figure 5.17 Variation of Margin with A_H for Reinforcing Bars in the Containment Wall Under Task 6 Loading

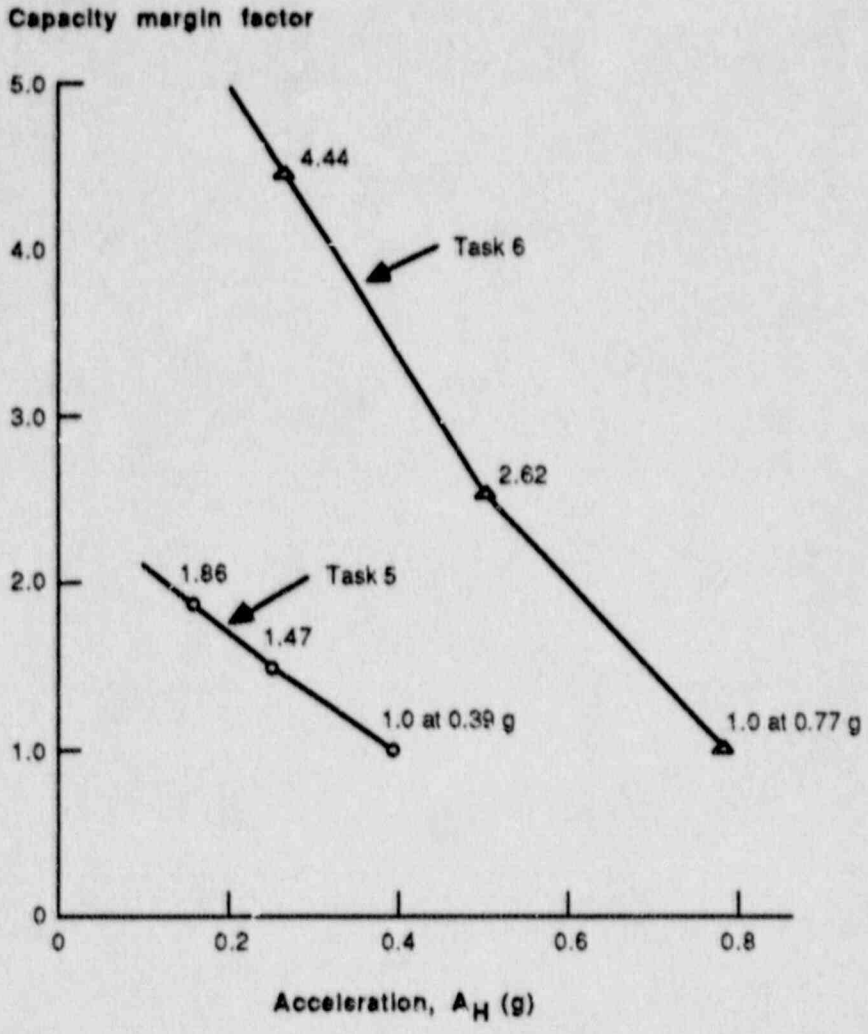

Figure 5.18 Variation of Margin with A_H for Transverse Shear In Containment Wall Under Task 5 and 6 Loading

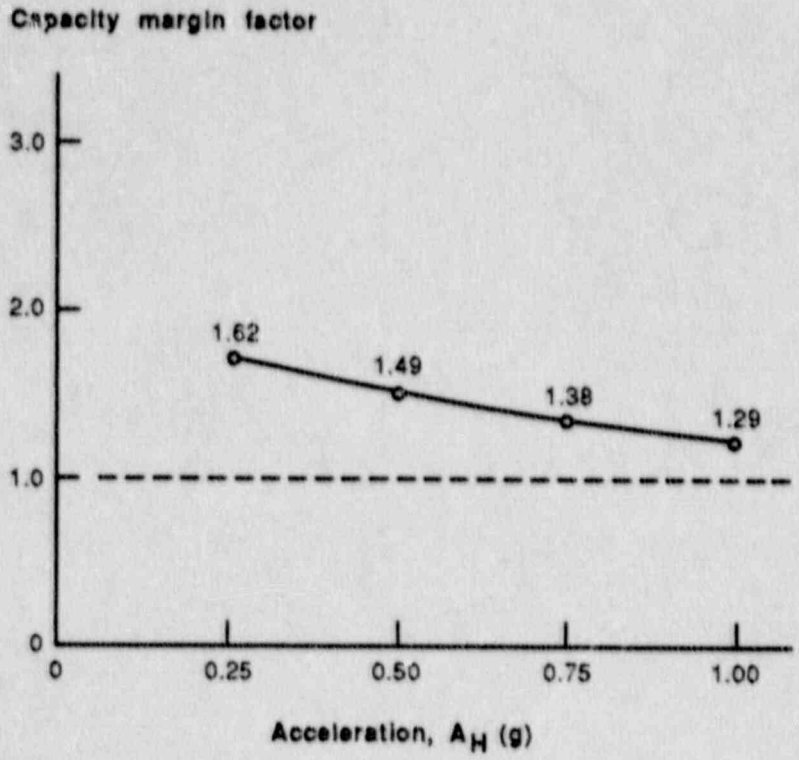

Figure 5.19 Variation of Margin with A_H for Transverse Shear in Basemat Under Task 5 Loading

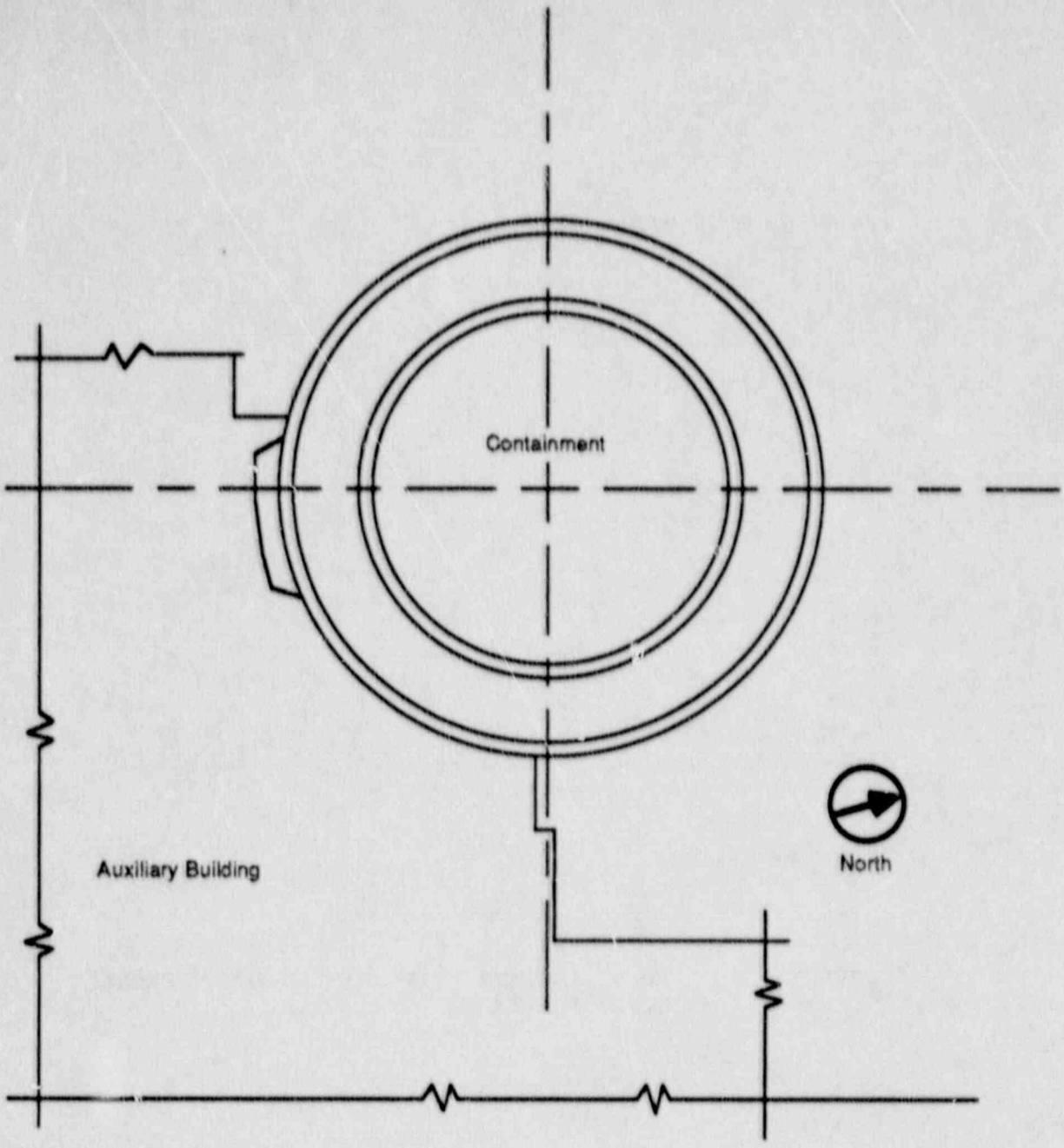

Figure 5.20 **Arrangement of Buildings at Zion Station Showing the Proximity of the Auxiliary Building to the Containment**

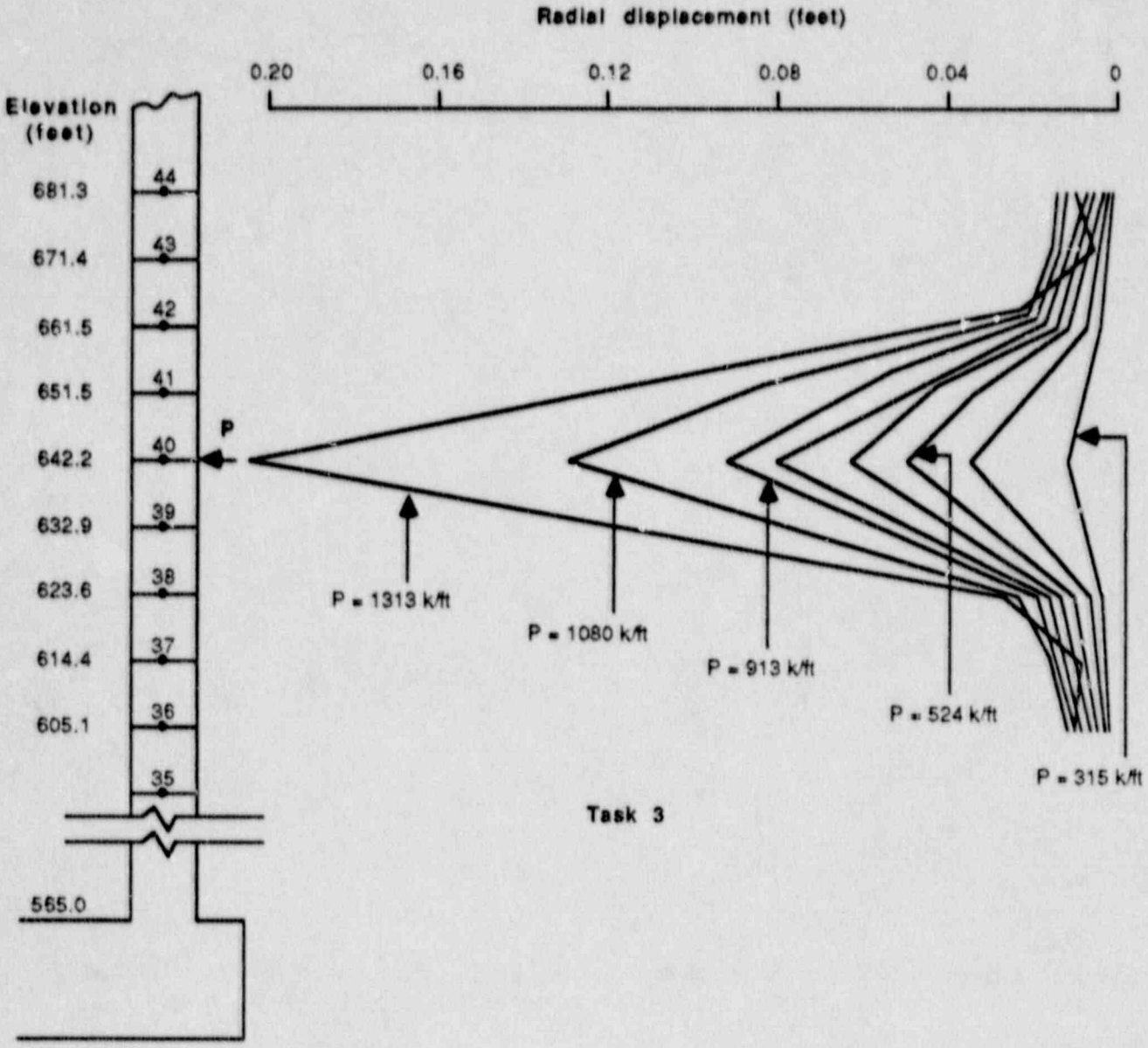

Figure 5.21 Deflection Pattern Under Ring Loading Due to Potential Impact Between Auxiliary Building and Containment

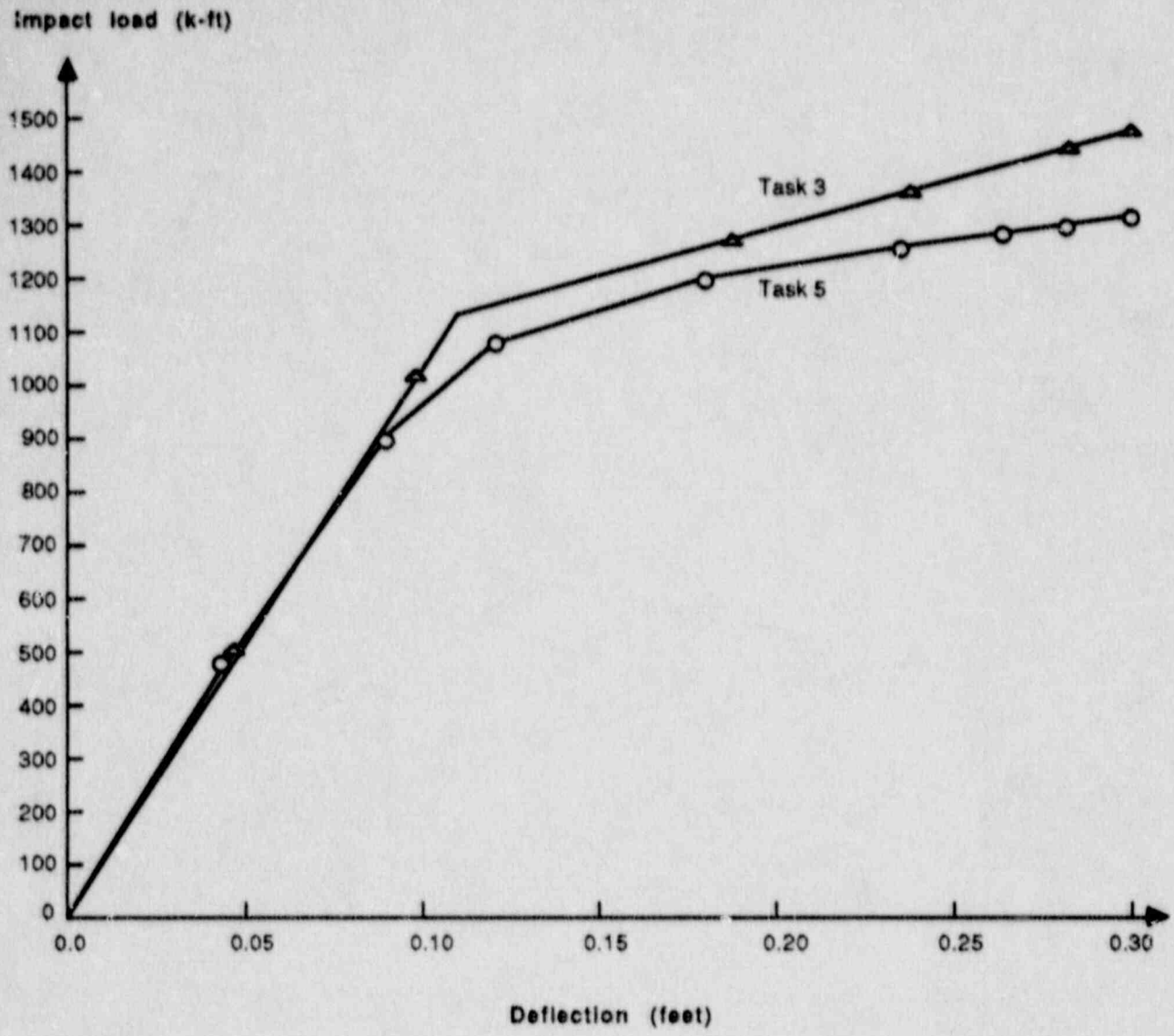

Figure 5.22 Load-Deflection Curves for Tasks 3 and 5 Due to Potential Impact Between Auxiliary Building and Containment

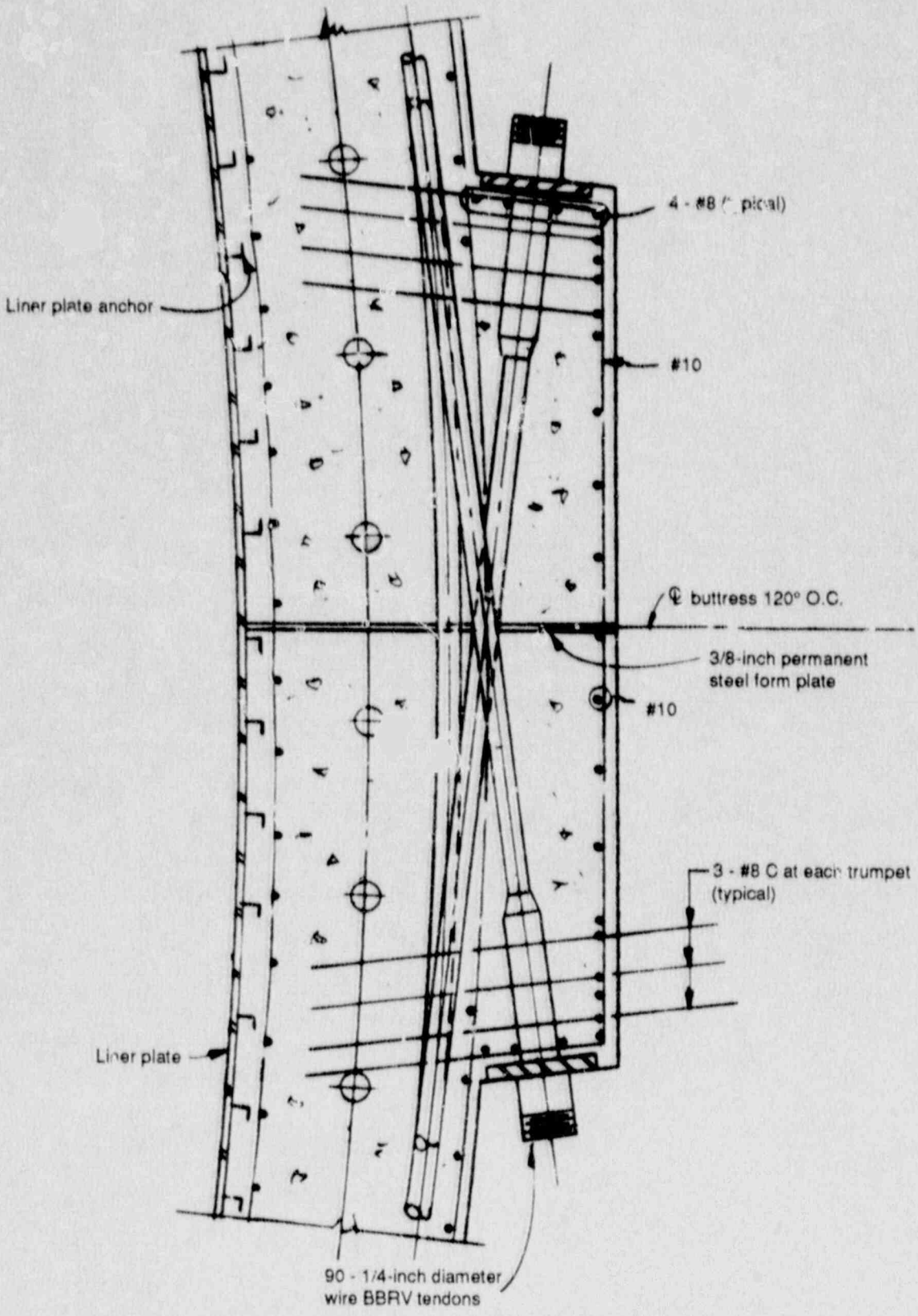

Figure 5.23 Details of the Vertical Buttress Plate and Reinforcing in the Vicinity of the Plate

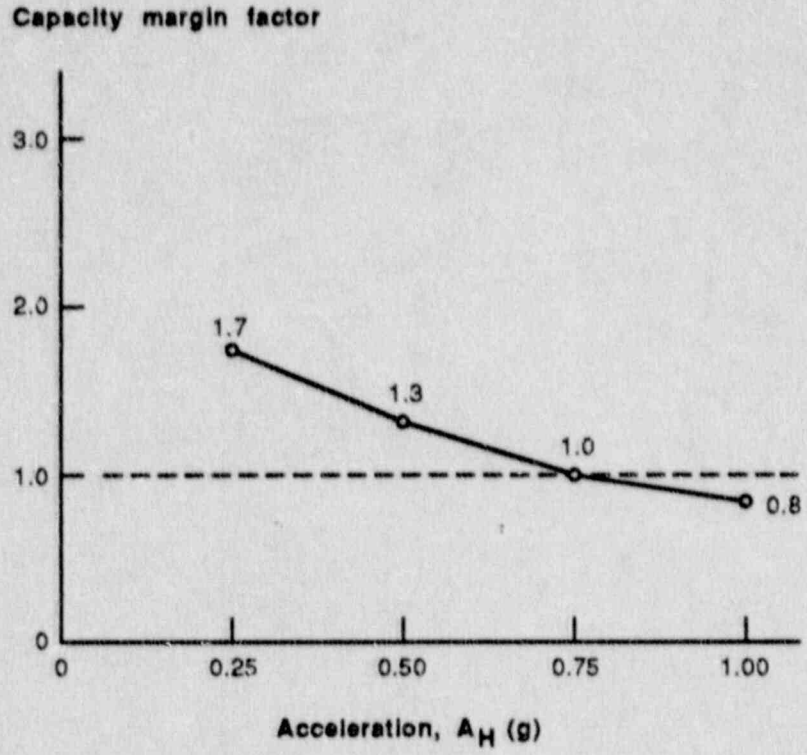

Figure 5.24 Variation of Margin with A_H for Shear Resistance at the Buttress Plate Under Task 5 Loading

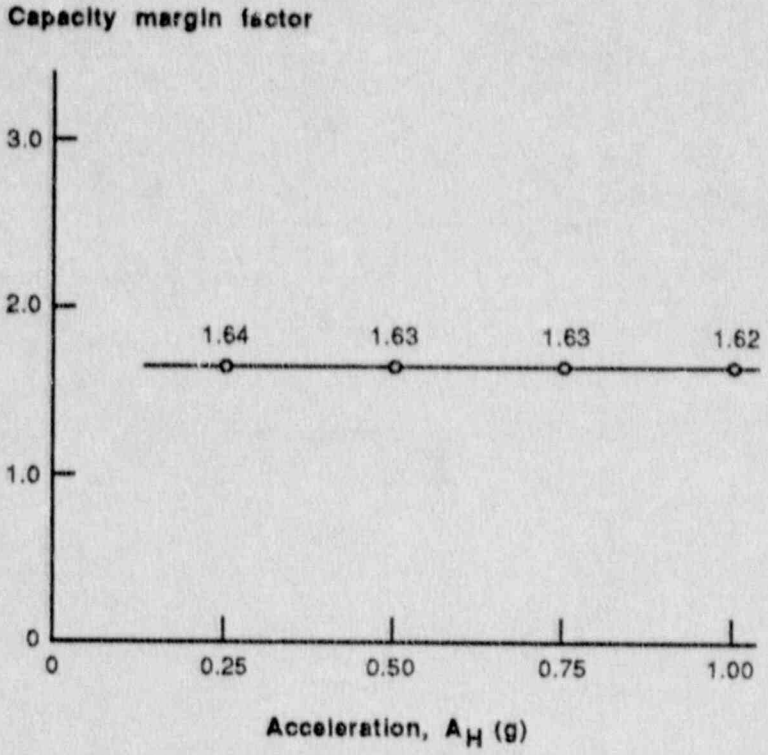

Figure 5.25 Variation of Margin with A_H for Strain at Meridional Tendons Under Task 5 Loading

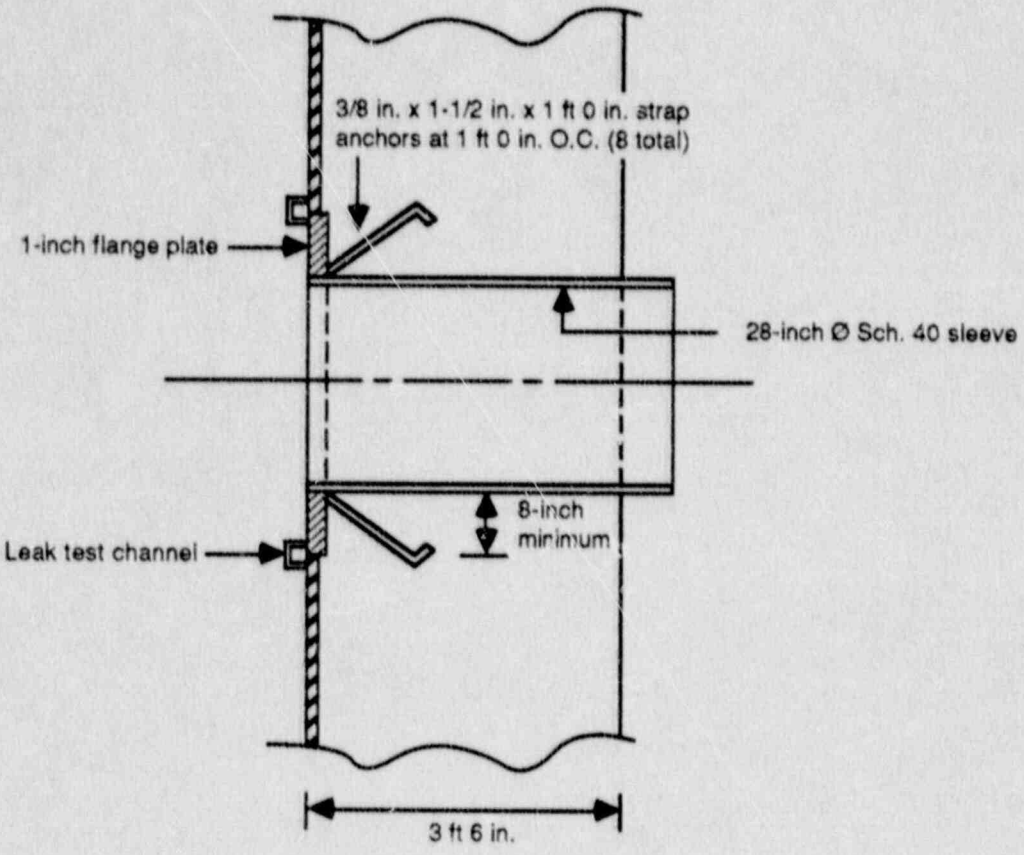

Figure 5.26 **Penetration Details for the 14-Inch Diameter Service Water Line at Elevation 604 Feet 5 Inches of the Containment Wall**

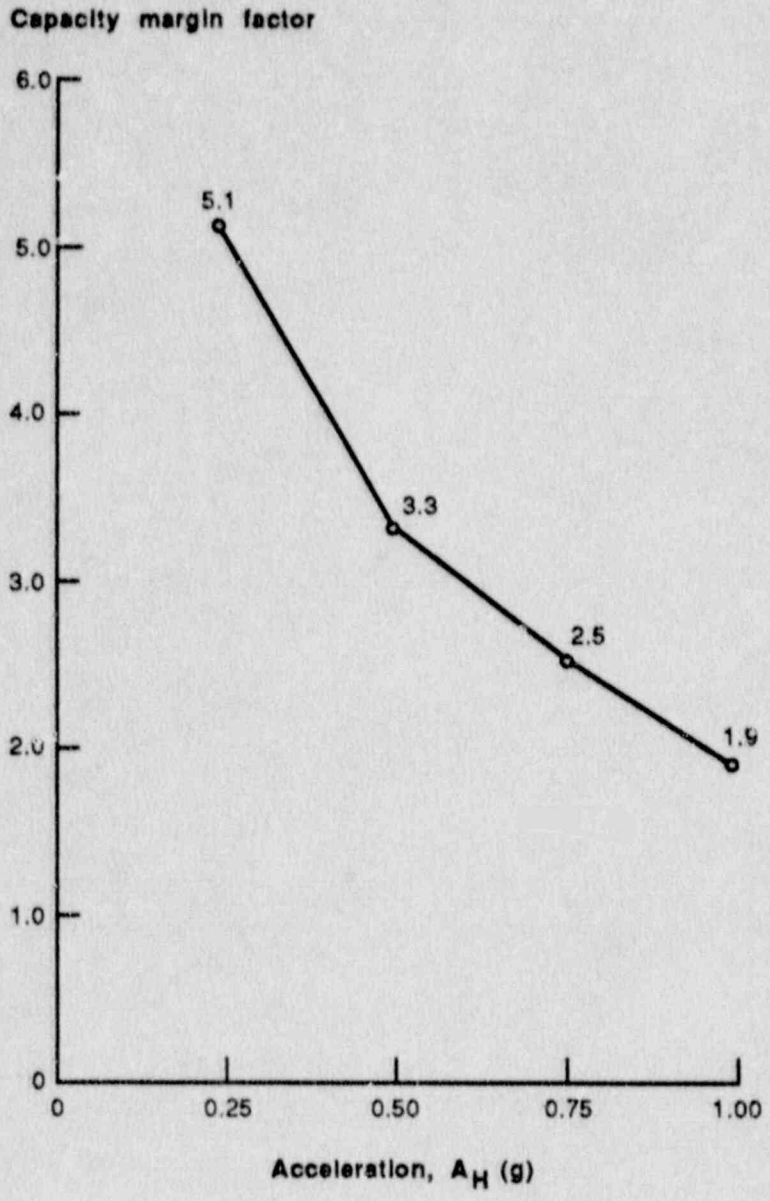

Figure 5.27 Variation of Margin with A_H for Pull-Out at the Penetration Under Task 5 Loading

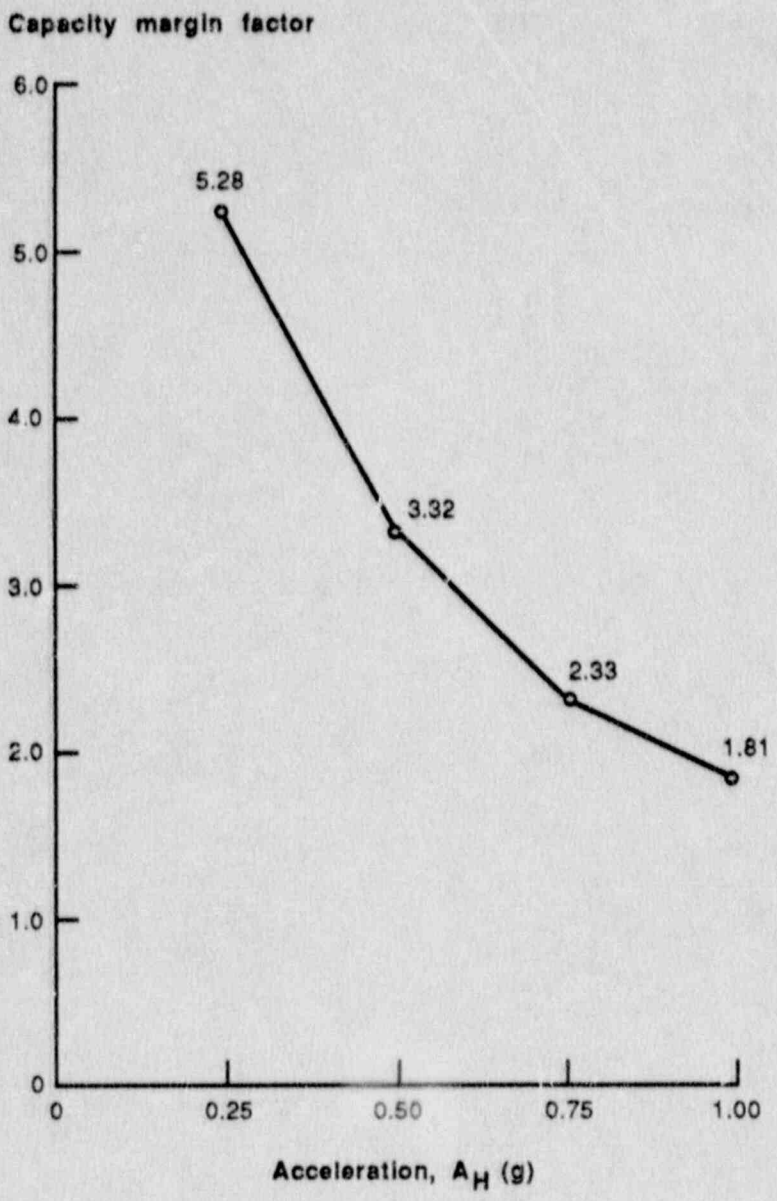

Figure 5.28 Variation of Margin with A_H for Bearing Pressure Failure of the Foundation, All Tasks

6. EVALUATION OF SEQUOYAH CONTAINMENT

6.1 Description of Sequoyah Containment and Shield Building

Figure 6.1 shows the Sequoyah reactor building elevation. The containment vessel is a free-standing steel structure consisting of a cylindrical wall, a hemispherical dome, and a bottom liner plate encased in concrete.

The containment structure consists of side walls measuring 113 feet 8-5/8 inches in height from the liner on the base to the spring line of the dome and has an inside diameter of 115 feet. The bottom liner plate is 1/4 inch thick, the cylinder varies from 1-3/8 inch thickness at the bottom to 1/2 inch thick at the spring line and the dome varies from 7/16 inch thickness at the spring line to 15/16 inch thickness at the apex.

The containment vessel is provided with both circumferential and vertical stiffeners on the exterior of the shell; see Figure 6.2. The circumferential stiffeners are spaced at approximately 10 foot centers, and vertical stiffeners are spaced at approximately 4°.

The bottom liner plate is encased in concrete. It is anchored to the concrete by welding it continuously to steel members embedded in and anchored into the concrete basemat.

An equipment hatch with an inside diameter of 20 feet has been provided to enable passage of large equipment and components into the containment during plant shutdown. Two personnel access locks are provided for the containment vessel.

The shield building is a reinforced concrete structure surrounding the steel containment. The cylindrical wall of the shield building is supported by a circular basemat, and is covered at the top by a spherical dome. The shield building is physically separated from the adjacent auxiliary building and other structures. The cylinder wall of the shield building is 149 ft. in height. It has an inside diameter of 125 ft. and a thickness of 3 ft. Conventional reinforcing bars were used throughout the structure and were placed in a horizontal and vertical pattern in each face of the wall. Reinforcing steel in the dome is arranged in a radial and circumferential pattern.

The basemat of the reactor building is a 9 ft. thick circular reinforced concrete structure, 131 ft 7 inches in diameter. To prevent hydrostatic uplift, the basemat is anchored to the rock by a concentric pattern of 155 #11 reinforcing bars grouted 15 ft. into rock near the outer periphery of the slab. The slab is further keyed and anchored into the rock in the central portion by the 8 ft. thick walls of the reactor cavity extending a total of 27 ft. into rock.

The basemat is founded on rock, which consists of alternating layers of hard limestone and softer shale. The rock was pressure grouted on 10 ft. centers to a depth of 45 ft. to assure a solid unyielding base for

support of the reactor. The shear wave velicity of the foundation rock is 7000 ft./sec.

6.2 Analysis for Gravity, Pressure, and Temperature Loads

The shell stresses were calculated using a combination of longhand calculations and CBI Computer Program E0781A, Kalnins Shells of Revolution Computer Code.

The meridional stresses due to gravity load were determined by dividing the accumulated gravity load at each elevation by the total cross sectional area of the shell plus vertical stiffeners.

The internal pressure stresses were determined in two ways. In areas subject to geometric discontinuities or to thermal gradients, the CBI Code E0781A was used to compute pressure and thermal stresses. This computer analysis was used for the embedment zone and the top of the internal insulation zone, i.e., from the top of the base slab (El. 678.3 ft.) to El. 720.5 ft. The effect of stiffeners was also included in the model for this analysis.

The hoop pressure stresses in the remainder of the cylinder were determined by use of longhand calculations. Stresses between stiffeners were determined by use of the equation, $\sigma_h = pR/t$, whereas, stresses at points at or near stiffener were found by $\sigma_h = 0.8\ pR/t$, where t is the shell thickness. The knockdown factor of 0.8 was an approximation to account for the localized effect of stiffener.

The meridional stresses due to pressure were determined by $\sigma_m = pR/2t$ where t is the equivalent shell thickness including the effect of stiffeners.

Tables 6.1 and 6.2 show the hoop and meridional stresses due to gravity, pressure, and temperature loads, for Tasks 4 and 5, respectively, at various elevations on the shell.

The minimum specified yield stress of the containment steel, which is SA516 Gr. 60, at Task 5 temperature of 360°F is 27.8 ksi. At a pressure of 24.8 psig, the hoop stress in the containment shell at elevations 764.8 ft and 781.0 ft is 27.4 ksi. Since the maximum stress intensity at these points is very close to the material yield stress, this pressure of 24.8 psig was adopted as the Task 5 pressure.

Because of the small difference between this pressure and the Task 4 pressure of 10.8 psig, no separate calculations for Task 6 were made.

6.3 Seismic Analysis

6.3.1 Overall Seismic Model

Figure 6.3 shows the overall seismic model used for the analysis of Sequoyah containment and shield building. The details of constructing

this model are described in Section 2.1.4. Additional information specific to this containment is provided in this section.

Since Sequoyah containment is founded on rock, foundation properties are considered independent of strain. A shear modulus value for rock equal to 259,000 ksf, Poisson's ratio of 0.33, unit weight of 170 pcf, and an equivalent basemat radius of 65.5 ft. were used to compute the foundation spring and dashpot constants based on equations given in Section 2.1.2. Table 6.3 lists the values of the total springs and dashpot constants. The note in the table also described the distribution of total constants among the individual foundation spring and dashpots that are shown in Figure 6.3.

The concrete compressive strength, f'_c, used in the Sequoyah analysis is 4680 psi, which includes an increase of 17% for aging. The yield stress of reinforcing bars is 60 ksi. The containment shell properties are given in Table 6.4. These properties are based on minimum specified material properties and therefore are considered conservative.

In order to construct the M-Ø diagram of containment beams, as discussed in Section 2.1.3, first the Sequoyah containment model was loaded with a uniform horizontal loading, and ratios of hoop to meridional stresses, α, were determined at various elevations. Then entire containment wall was divided in four zones along its height, and for each zone one M-Ø diagram was constructed for each Task based on the calculated values of α, the existing stresses due to gravity, pressure, and thermal loads shown in Tables 6.1 and 6.2, and the steel properties shown in Table 6.4.
The elevations of the four zones, and corresponding values of α and yield stresses for tension and compression loading, f_y^+ and f_y^- (See Figure 2.8 for explanation of f_y^+ and f_y^-) are shown in Table 6.5. It can be seen from this table that for Task 3 condition, the effective yield stress of 32 ksi is reduced to 27.8 ksi for Zone 1, and 18.3 ksi for Zone 3 due to biaxiality. Since the gravity load effect is small, and pressure loads are absent, the effective tension and compression yields are the same in Task 3.

For Task 5 condition, the material yield stress of 27.8 ksi is reduced to 22.0 ksi for Zone 1 and 16.3 ksi for Zone 4 for the tension effective yield. The corresponding compression yield values are 18.1 and 0.5 ksi, respectively. The significant reduction in Task 5, especially for Zone 4, is caused by the high tensile hoop stress condition due to the pressure loading, see Table 6.2, and the high value of α at this zone. Because of almost total depletion of the yield capacity in Zone 4, Von-Mises yield criterion was employed in this zone to improve the yield capacities to values shown within parentheses in Table 6.5. These higher yield capacities were used for this zone in the construction of M-Ø diagram. It is noted that the Von Mises yield criterion is more accurate; the Tresca criterion was used in other non-critical zones only because it is simpler and conservative.

The M-Ø diagrams for Zones 1-4 are shown in Figures 6.4 and 6.5 for Tasks 3 and 5, respectively. It should be noted that in Zone 1 the yield moment of the section is reduced by a factor of 1.5 in going from

Task 3 to 5 because of the effect of pre-existing pressure stresses and the reduction in yield stress due to elevated temperature. In Zone 4, this reduction is by a factor of 3.6, because of much higher pressure stresses.In the evaluation of the tensile limit force of the vertical rock springs, F_{t1} shown in Figure 2.11, 20 psi was used for adhesion when A_H is less than 0.25g. The basis for 20 psi is given in the discussion that follows Equation (2.12). For higher values of A_H, because of occurrence of uplift, a minimal value of 1 psi was used. In addition to this adhesion, the contributions from side friction and the yield force of the 155 #11 anchorage bars provided below the basemat were also included.

Fundamental frequencies of the structures included in the Sequoyah seismic model, for fixed base condition and assuming linear behavior, are summarized in Table 6.6.

6.3.2 Seismic Analysis Results

Sequoyah containment was analyzed for A_H = 0.25g, 0.50g, 0.75g and 1.0g. Because of the rock foundation at Sequoyah containment soil-structure interaction effect is negligible. However, basemat uplift starts to occur at A_H values between 0.25g and 0.50g. Figure 6.6 shows the vertical displacement time history at node point 81, the end node of the basemat in Figure 6.3, for A_H = 0.25g. As can be seen, the vertical displacement is always negative, indicating no uplift at this level of shaking. Figure 6.7 shows that the node point 81 has uplifted at A_H = 0.50g. Figure 6.8 shows that at A_H = 1.0g a significantly larger uplift occurs. Table 6.7 shows the maximum extent of the basemat uplift at various A_H values. As can be seen from this table, at A_H = 1.0g, approximately 90% of the basemat has uplifted.

Figures 6.9 and 6.10 show the horizontal and vertical response spectra, respectively, at node 6 on the containment shell, approximately 135 ft. above the basemat, for A_H = 1.0g, when significant uplift has occured. These spectra are compared with the spectra corresponding to A_H = 0.25g multiplied by four, which represents the same level of excitation but a condition of no uplift. It can be seen from these figures that due to hard impact significant amplification occurs at high frequencies (above 8Hz), especially in the vertical direction.

Table 6.8 shows the comparison of base shear and moment for the steel containment, shield building and interior structures at A_H = 1.0g, with and without uplift. This table shows that although the structural responses are somewhat affected, the effect is not significant. Because of the high fundamental frequency of the steel containment structure (See Table 6.6) the response of this structure is somewhat increased due to uplift, whereas the responses in the other two structures are somewhat reduced due to their lower fundamental frequencies. This result is consistent with the observations made in Reference 5.2.

The effect of uplift on the basemat response has also been investigated, as described for Zion containment in Section 5.3.2. Table 6.9 shows the results of this investigation. It can be seen from this table, that due

to hard impact condition at Sequoyah, the basemat responses are significantly increased due to uplift.

6.4 Capacity Margin Factors

The capacity margin factors, calculated using Equation (2.15) and the criteria given in Table 2.1, are listed in Tables 6.10 and 6.11. Table 6.10 contains margins for limit states that are directly related to the containment pressure boundary. Table 6.11 contains margins for those limit states whose realization may indirectly affect the containment performance; containment integrity beyond these limit states cannot be determined within the scope of this study.

The margin factors given in Tables 6.10 and 6.11 were computed using peak seismic responses at A_H = 1.0g, except where noted. If capacities less than A_H = 1.0g were found, peak responses were obtained from analyses performed at A_H = 0.25g, 0.50g, and 0.75g or appropriate interpolation.

Tables 6.10 and 6.11 list the limit state codes for correlation with Table 1.2, which describes the limit states to be evaluated. These tables also include a statement of the evaluation criteria used for each limit state.

Tables 6.10 and 6.11 list the direct and indirect limit states, respectively, in their decreasing order of criticality. Calculated margins, with engineering judgment, were used to arrive at this rank ordering. Additional comments on the relative criticality of various limit states are included in Section 6.5.

Specific comments about the capacity margin factors are given in the following subsections; concluding comments are given in Section 6.5.

6.4.1 Transverse Shear Failure in Basemat

The evaluation for the transverse shear failure in basemat was done using a similar approach as discussed for the Zion containment in Section 5.4.2. A companion ADINA analysis was performed using finite element model, since DYNAX analysis does not consider one-way springs. Results from this analysis provided factors which were used to modify the DYNAX results. These modified results were used for basemat evaluation.

The critical section for the basemat for transverse shear failure is at approximately mid-distance between the crane wall and the shield wall in Figure 6.1. The smallest capacity is calculated, for Task 3 condition, as A_H = 0.52g. For Tasks 4 and 5, the increase in temperature provides a beneficial compressive stress. The capacity in Task 4 is A_H = 0.89g and the margin in Task 5, at A_H = 1.0g, is 1.69. Variation of margin with increase in A_H is shown in Figure 6.11 for Tasks 3 and 4.

6.4.2 Failure of Reinforcing Bars in Basemat

The evaluation for reinforcing bar strains was done using computer program TEMCO, as discussed in Section 2.1.6. Modified DYNAX loads, as discussed in Section 6.4.1, were used in the evaluation. As shown in Table 6.10, the strains in the reinforcing bars are not critical for Task 4 or 5 condition due to the compression provided by higher temperatures. In Task 3, the critical section is near the containment shell, where margin falls below 1.0 at A_H = 1.0g, and a capacity of A_H = 0.84g is established by interpolation of forces obtained at A_H =0.75g and 1.0g.

6.4.3 Buckling of Steel Containment Shell

The buckling evaluation was performed using ASME Code Case N-284. Various shell panels between stiffeners as identified by various bay numbers in Figure 6.2, were evaluated using the combined stresses from earthquake, dead load, and pressure. Vertical and horizontal stiffeners were checked for their effectiveness using the Code Case provision. Local panel buckling was found to be the controlling failure mechanism.

For Task 3 condition, Bay number 7 in Figure 6.2 has the lowest margin. This results from the combined effects of shell thickness, spacing of vertical stiffeners and the compressive stress at that elevation. The capacity margin at A_H = 1.0g falls slightly below 1.0; a capacity of A_H = 0.96g is established by interpolation for this case. The variation of margin with increase in A_H is shown in Figure 6.12 for Task 3 loading in Bay 7.

For Task 4 condition, the margins improve due to the stiffening effect of internal pressure. The controlling bay under this task is Bay 3 in Figure 6.2. The change from Bay 7 in Task 3 to Bay 3 in this task is primarily because of the combined effect of higher seismic load and smaller beneficial effect from 10.8 psig internal pressure in this bay than in the upper, thinner plate bays. The calculated margin at A_H = 1.0g is 1.7 for Bay 3. Figure 6.13 shows the variation of margin for this bay with increase in A_H.

For Task 5 loading condition, compressive stresses are present only in Bays 1 and 2 at A_H = 1.0g. For all other bays the stresses are tensile due to higher pressure. The computed margin is 5.0 in Bay # 1 as shown in Table 6.10.

6.4.4 Failure of Pretensioned Bolted Connections at Equipment Hatch

The 20 ft. diameter equipment hatch at Sequoyah containment, which is pressure seated, is bolted with 20 1-1/4" diameter SA 320 L43 bolts. For evaluation of this limit state, the bolt preload was based on 75% of ASME bolt allowable stress. A 10% reduction for torque relaxation was then applied. The bolted connections at Sequoyah equipment hatch do not have a tongue and groove detail, therefore slippage after the overcoming of bolt preload was used as the criterion for failure. A friction coefficient of 0.4 between mating faces of flange was assumed. This is

based on steel to steel contact and grease-free in air condition (Reference 3.4). For seismic loading, the zero-period acceleration values of node point 29, Elevation 743'-0" in Figure 6.3 were used. The zero-period accelerations are used here because the effect of rigid body mode response of the component is being evaluated.

The margin factor for Task 3 loading drops below 1.0 at A_H = 1.0g, and the capacity is established as A_H = 0.96g by interpolation between A_H = 0.75g and A_H = 1.0g. The variation in the margin with increase in A_H values is shown in Figure 6.14 for this limit state.

For Tasks 4 and 5 loading conditions, the margins improve significantly due to existence of internal pressure and the pressure seated construction of the hatch. In Task 4, the margin is 2.2, and in Task 5 it is 4.2 at A_H = 1.0g, as shown in Table 6.10.

6.4.5 Tensile Failure of Steel Liner

As shown in Figure 6.1, the Sequoyah containment basemat has a sandwich liner. The liner strains were evaluated using computer program TEMCO, as discussed in Section 2.1.6. Modified DYNAX loads, as discussed in Section 6.4.1, were used in the evaluation. The critical section for the liner lies under the containment shell. the calculated margin under Task 3 is 7.7 at A_H = 0.84g, which is the capacity of reinforcing bars in the basemat, as discussed in Subsection 6.4.2. For Tasks 4 and 5 condition, the temperature induced compression makes the liner strain non-critical.

6.4.6 Failure of Containment Shell at Penetrations

A review of the original design report indicated that the most heavily loaded penetrations are those associated with the containment purge system. This suggests that all other penetrations either have expansion joints in the sleeved containment penetration or are part of a pipe system which is flexible enough to eliminate any significant load imposed on the containment vessel.

The maximum penetration load listed in the original design report is 29.59 kips at the upper compartment purge air penetration. The maximum seismic displacements of the containment shell and the internal structure at the purge line elevation are 0.24 in. and .84 in., respectively. Thus, conservatively a maximum total differential displacement of 1.08 inches can be postulated to occur at this penetration. To convert this differential displacement to a penetration load, a representative piping stiffness is needed. This stiffness was unavailable for the Sequoyah containtment. To proceed with evaluation, a piping stiffness of 14.3 k/in. was used. This is the stiffness determined from the analysis of a cold piping system for the Zion containment, which was also used in Section 5.4.6. The piping system evaluated for stiffness does not have bellows. Using this piping stiffness the total load imposed for a 1.08 inch differential displacement would be 15.44 kips. CBI's program E1027A was used to determine the stresses in the containment shell for this loading condition. The membrane stresses and surface stresses are

all well within the elastic range; specifically, the membrane stresses are about 8 ksi and the surface stresses about 19 ksi.

Based on the above discussion since yielding does not occur, a margin greater than 10 exists for this limit state using a limiting strain criterion of 0.02, and this is the value reported in Table 6.10.

6.4.7 Tensile Failure of Steel Containment Shell

Because of its large diameter, the tensile strains in the Sequoyah containment shell remain within elastic limits for all tasks. Therefore, a margin of greater than 10 exists, for all tasks, for this limit state, as reported in Table 6.10.

6.4.8 Failure of Containment Shell at Ice Chest Supports

A review of the ice chest support details shows that the ice chests are completely supported by the internal concrete structures. There are bearing bars at 24.9 inch centers between the ice chest and the steel containment shell, to ensure that the ice chest does not rest directly against shell, protecting it from the low temperatures of the ice chest. These bearing bars may transmit small horizontal inertia loads to the shell during a seismic event. The overall inertial effect of the ice chest support during a seismic event is appropriately included by incorporating the ice chest mass in the overall seismic model. Thus, seismic responses obtained from this model include the overall inertial effect of the ice chests.

A conservative evaluation of the local effects of the ice chest inertial forces, as transmitted to the shell through the bearing bars, showed that the seismic stresses will be a very small percentage of the pressure-induced stresses. Based on this general consideration, this limit state was not evaluated any further and therefore no margin factor is reported in Table 6.10.

6.4.9 Failure of Shield Building Wall

The shield building in Sequoyah is not part of the containment pressure boundary; therefore, its failure is not considered a direct limit state. However, failure of the shield building could introduce additional mass and seismic forces on the containment vessel, which may indirectly affect the vessel's structural integrity. A detailed evaluation of the effects of shield building failure on the integrity of the containment vessel is beyond the scope of this study, however, the failure of the shield building itself is identified as an indirect limit state.

The evaluation of the Sequoyah shield building was done using an approach similar to the one used for Fermi biological shield wall, as discussed in Section 3.4.7. The critical element for the shield building is, obviously, the section of the wall near the basemat junction. The capacity of the shield building wall calculated using ACI-318-83 Section A.7 is A_H = 0.30g. Using provisions of ACI Sections 11.10 (Special Provisions for Walls) and 11.7 (Shear Friction) the

calculated capacities were A_H = 0.35g and 0.24g, respectively. As discussed in Section 3.4.7 for Fermi biological shield wall, ACI Section A.7 is considered more applicable than these other two Sections of the Code, therefore the reported capacity in Table 6.10 is A_H = 0.30g, obtained using provision of Section A.7.

6.4.10 Bearing Failure of Foundation

The capacity margin factor for this limit state is based on the ultimate bearing capacity of 830 ksf, based on design information. The maximum vertical pressure during seismic event combined with the minimum contact area remaining after uplift was used in the evaluation. In spite of the significant basemat uplift, amounting to over 90% of the basemat area, at A_H = 1.0g, the margin calculated is 2.2 due to the very high bearing capacity of the competent rock foundation.

6.5 Conclusions

The following conclusions are drawm from the results discussed for Sequoyah containment in this chapter.

1. The governing limit state for seismic capacity of the Sequoyah containment is the indirect limit state associated with failure of shield building. The calculated capacity on this basis is A_H = 0.30g. But, as in the case of the Fermi biological shield wall, it is felt that a finite element analysis of the shield building, that considers material nonlinearity will yield a higher capacity.

   It should be noted that a capacity of A_H = 0.30g, is calculated using a time history consistent with Regulatory Guide 1.60 response spectra. This is over three times the design safe shutdown earthquake (SSE) of Sequoyah, which is A_H = 0.18g using Housner spectrum. This conclusion is based on a comparison of 0.30g capacity vs 0.18g SSE, and the fact that Regulatory Guide spectral accelerations at Sequoyah containment frequencies are about twice the value from the Housner spectrum, see Figure 2.2 and frequencies in Table 6.6.

2. Eight direct limit states were evaluated for the Sequoyah containment. Of these, the tensile failure of containment shell, the failure of shell due to local effects at penetrations and ice chest supports, and tensile failure of liner appear to be of no concern. Even at the high acceleration of A_H = 1.0g, the margins generally exceed 10 for all tasks.

   Of the remaining four direct limit states, the local panel buckling of the shell and pretensioned bolted connections at equipment hatch have a capacity very close to A_H = 1.0g in Task 3. With the existence of internal pressure in Tasks 4 and 5, the margins improve significantly in both these limit states.

The two remaining direct limit states are both associated with the basemat failure. The calculated capacity against reinforcing bars failure is A_H = 0.84g in Task 3, and A_H = 0.52g against transverse shear failure, again in Task 3. For both these limit states, the higher temperatures in Tasks 4 and 5 induce significant compression. Due to this temperature induced compression the reinforcing bars failure becomes non-critical in Tasks 4 and 5. The capacity against transverse shear failure improved to A_H = 0.89g in Task 4 and the margin in Task 5 is 1.69 at A_H = 1.0g. It may be noted that evaluation of both these limit states is considered conservative based on inherent conservatism in the evaluation criteria, as discussed in Subsections 2.2.2 and 2.2.6.

3. The basemat uplift starts to occur somewhere between A_H = 0.25g and 0.50g. At A_H = 1.0g, upto 90% of the basemat uplifts. The significant effect of the uplift is seen in the high frequency (beyond 8Hz) zone of the response spectra and on the basemat transverse shear and bending moment, where due to hard impact between the basemat and rock foundation, the responses are increased significantly. However, the effect of uplift on the steel containment base shear and moment is small.

   Even with an uplift of 90% of the basemat, because of the very high ultimate bearing capacity of the competent rock foundation, a margin of 2.2 was calculated against the bearing failure at A_H = 1.0g.

4. The main shock, up to a level of A_H = 1.0g. does not cause yielding in the steel containment, therefore it has no effect on the aftershock seismic capacity of the containment.

Table 6.1
Stresses Due To Gravity, Pressure and Temperature Loads (Task 4)
(Accident Condition: 10.? psig Pressure, 220°F Temp.)

Node No. (In Fig. 6.3)	Elevation (Ft)	Meridional Stress (psi)	Hoop Stress (psi)
68	682.0	2,209	5,788
62	690.9	2,200	6,206
56	700.5	2,554	5,021
47	714.3	2,940	5,274
44	720.5	3,157	5,779
38	729.5	3,801	7,949
32	739.5	4,240	8,671
26	749.5	4,710	9,539
24	758.5	4,707	9,539
22	764.8	4,778	11,923
20	771.2	4,826	8,825
18	777.5	4,868	9,539
16	781.0	4,901	11,923
14	787.0	5,958	10,336

Table 6.2
Stresses Due to Gravity, Pressure and temperature Loads (Task 5)

(Pressure 24.8 psig, Temp. 360°F)

Node No. (In Fig. 6.3)	Elevation (ft)	Meridional Stress (psi)	Hoop Stress (psi)
68	682.0	6,087	13,596
62	690.9	5,776	12,686
56	700.5	6,618	11,592
47	714.3	7,482	12,189
44	720.5	7,984	13,355
38	729.5	9,490	18,253
32	739.5	10,459	19,912
26	749.5	11,467	21,903
24	758.5	11,369	21,903
22	764.8	11.432	27,339
20	771.2	11,449	20,493
18	777.5	11,540	21,913
16	781.0	11,574	27,379
14	787.0	14,025	23,734

Table 6.3
Total Foundation Spring and Dashpot Constants

A_H (g)	K_H (K/Ft)	K_V (K/Ft)	K (K-ft/Rad)	C_H (K-Sec/ft)	C_V (K-Sec/Ft)	C (K-Ft-Sec/Rad)
All Values	8.34×10^7	1.02×10^8	2.89×10^{11}	4.50×10^5	8.09×10^5	5.06×10^8

Note: The two horizontal springs and dashpots in Figure 6.3 have values equal to one-half of the total values given in this table. The interior vertical springs and dashpots in Figure 6.3 have the same constants. The end elements have higher values. In the vertical direction this discrete system has total vertical and rocking constants equal to the values listed in this table.

Table 6.4

Values of Yield Stress and Modulus of

Elasticity for Containment Shell

Task	Temperature (^{o}F)	Yield Stress (ksi)	Modulus of Elasticity (ksi)
3	120	32.0	29,100
4	220	29.0	28,700
5	360	27.8	27,940

Table 6.5
Values of Effective Yield Stress Used in Constructing M-Ø Diagram

Zone & Elevation (ft)	α	f_y^+(ksi) Task 3	f_y^+(ksi) Task 4	f_y^+(ksi) Task 5	f_y^-(ksi) Task 3	f_y^-(ksi) Task 4	f_y^-(ksi) Task 5
1 678.8 (Basemat) to 700.5	-0.15	27.8	26.8	22.0	-27.8	-21.8	-18.1
2 700.5 to 724.0	-.020	26.7	26.1	20.3	-26.7	-21.2	-16.9
3 724.0 to 758.5	-0.40	22.9	24.7	17.3	-22.9	-16.0	-7.2
4 758.5 to 847.5	-0.75	18.3	19.3	16.3 (20.2)*	-18.3	-13.9 (-4.4)*	-0.5

α = ratio of hoop to meridional stress due to seismic load

f_y^+, f_y^- = yield stress values for tension and compression, respectively

* = value obtained using Von-Mises yield criterion in place of Tresca

Table 6.6
Fundamental Frequencies of Fixed Base Structures
in Sequoyah Seismic Model

Structure	Frequency (cps)
Shield Building	4.22
Interior Structure	5.86
Steel Containment	9.26

Table 6.7

Maximum Extent of Basemat Uplift

A_H	x (ft)
0.25g	0
0.50g	10.6
0.75g	74.3
1.0g	116.4

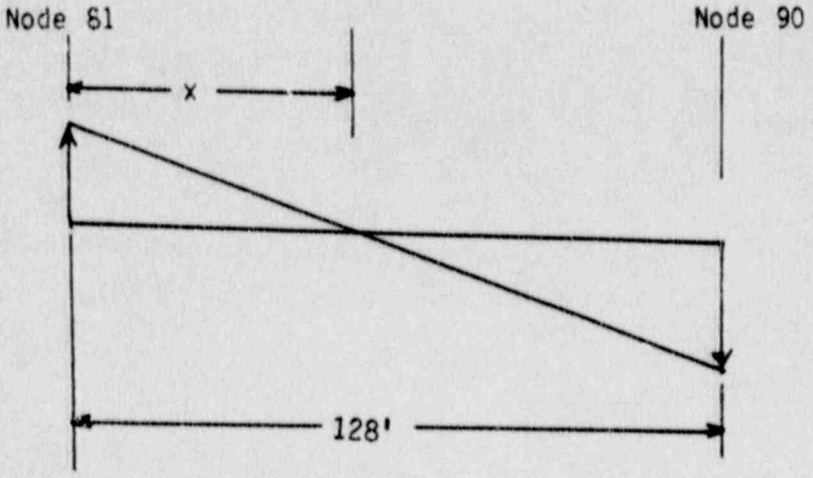

Table 6.8

Effect of Uplift on Base Shear and Moment (A_H = 1.0g)

Structure	Base Shear (kips)		Base Moment x 10^{-3} (ft. kips)	
	No uplift	With uplift	No uplift	With uplift
Steel Containment	8,280	9,560	680	837
Shield Building	94,800	85,700	10,200	9,280
Interior Structure	90,000	88,400	5,480	5,410

Table 6.9

Effect of Uplift on Transverse Shear and Bending Moment in Basemat (A_H = 1.0g)

$$\text{Ratio} = \frac{\text{Response With Uplift}}{\text{Response Without Uplift}}$$

	Shear	Positive Moment	Negative Moment
Compression Side	1.63	1.29	1.46
Tension Side	1.96	1.78	1.88

Table 6.10
Capacity Margin Factors for Sequoyah Containment at A_H = 1.0g (Except As Noted)
(Direct Limit States)
See Note 1

Code*	Description	Criterion	Tasks 3	Tasks 4	Tasks 5
6	Transverse Shear Failure in Basemat	Flexural shear capacity per ACI 11.3 / Ave. nominal shear	1.0 at A_H = 0.52g	1.0 at A_H = 0.89g	1.69
2	Failure of Reinforcing Bars in Basemat	$10\ \varepsilon_y/\varepsilon_s$	1.0 at A_H = 0.84g	>10	>10
5	Buckling of Steel Containment Shell	fcr/f	1.0 at A_H = 0.96g	1.7	5.0
9	Failure of Pretensioned Bolted Connections at Equipment Hatch	Shear capacity / Max shear	1.0 at A_H = 0.96g	2.2	4.2
1	Tensile Failure of Steel Liner	$0.02/\varepsilon_{principal}$	7.7 at A_H = 0.84g	>10	>10

Table 6.10 (Cont'd)
Capacity Margin Factors for Sequoyah Containment at A_H = 1.0g (Except As Noted)
(Direct Limit States)
See Note 1

Code*	Description	Criterion	Tasks		
			3	4	5
4	Failure of Containment Shell at Penetrations	$0.02/\epsilon_m$ Based on K = 14.3k/in. for purgeline	>10	>10	>10
4	Tensile Failure of Steel Containment Shell	$0.02/\epsilon$	>10	>10	>10

* Refers to limit state identification number in Table 1.2

Note 1: A comment similar to Note 1 of Table 3.9 applies to this table also.

Table 6.11
Capacity Margin Factors for Sequoyah Containment at A_H = 1.0g (Except as Noted)
(Indirect Limit States)
See Note 1

Code*	Description	Criterion	Tasks		
			3	4	5
16	Failure of Shield Building	Shear strength per ACI 318 Section A 7.3 / Lateral shear force	1.0 at A_H = 0.3g	1.0 at A_H = 0.3g	1.0 at A_H = 0.3g
13	Bearing Failure of Foundation	Ultimate bearing capacity / Peak average pressure	2.2	2.2	2.2

* Refers to limit state identification number in Table 1.2

Note 1: A comment similar to Note 1 of Table 3.9 applies to this table also.

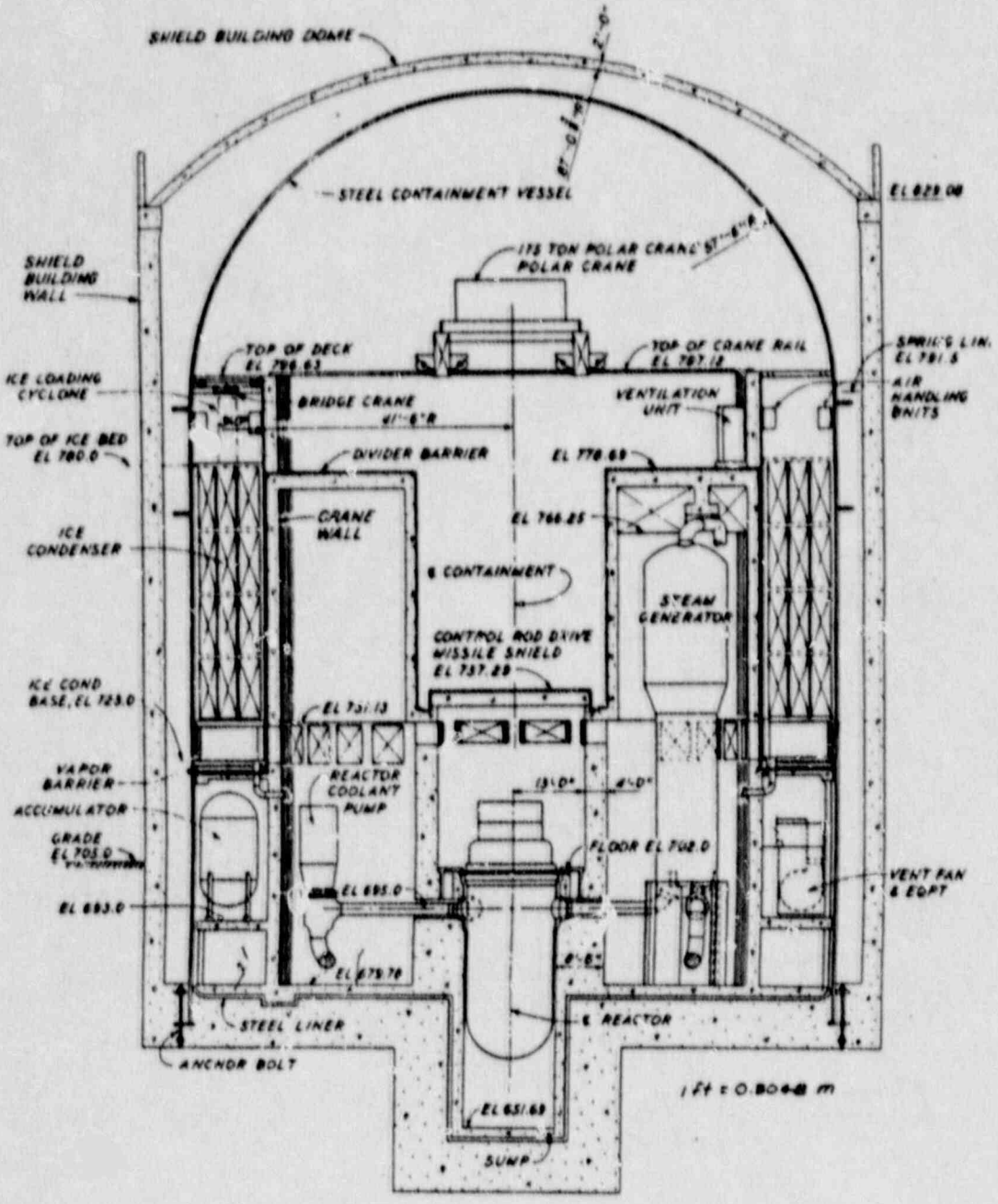

Figure 6.1 Sequoyah Reactor Building Elevation

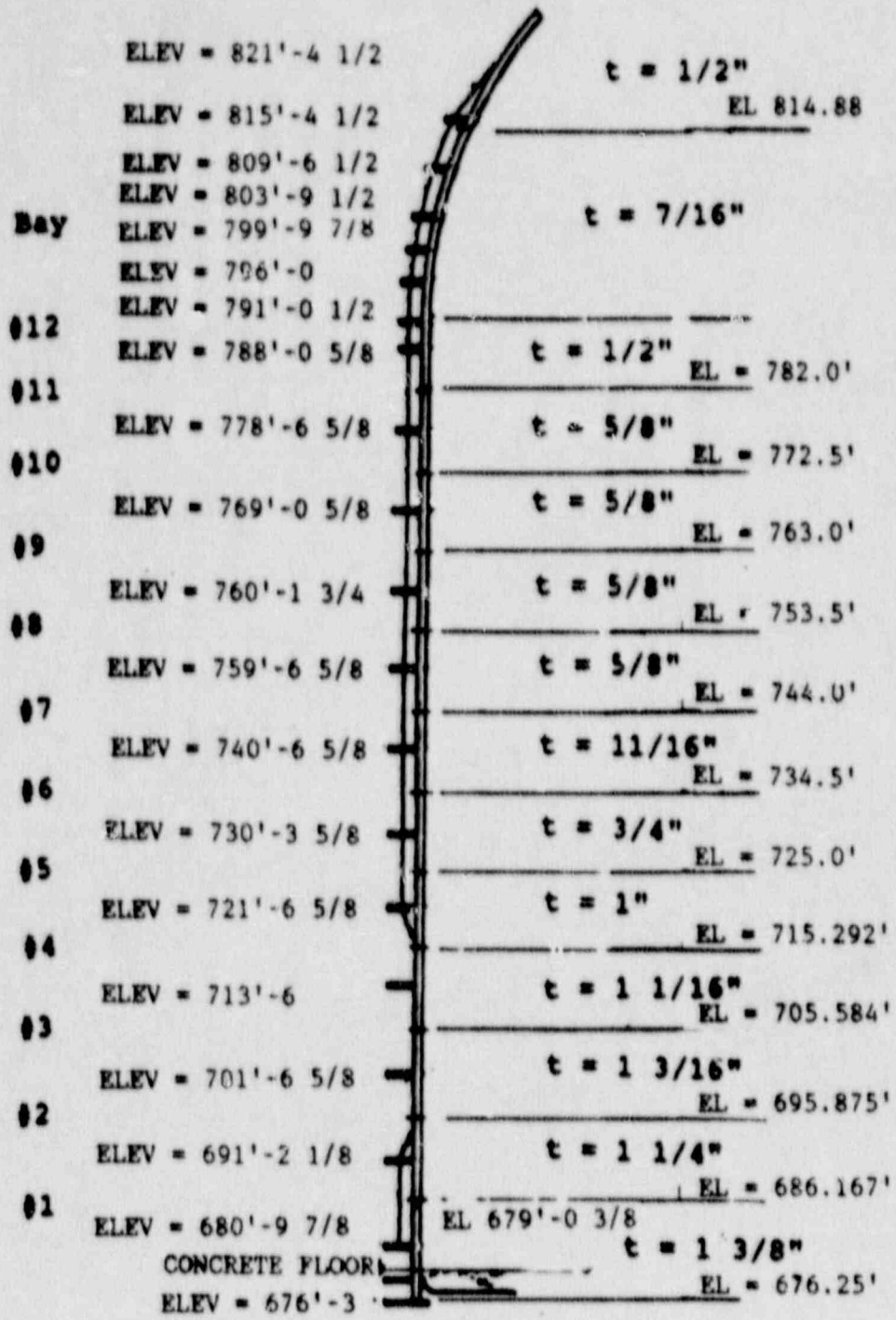

Figure 6.2 Analytical Model of Sequoyah Containment Vessel for Gravity, Pressure, and Temperature Loads

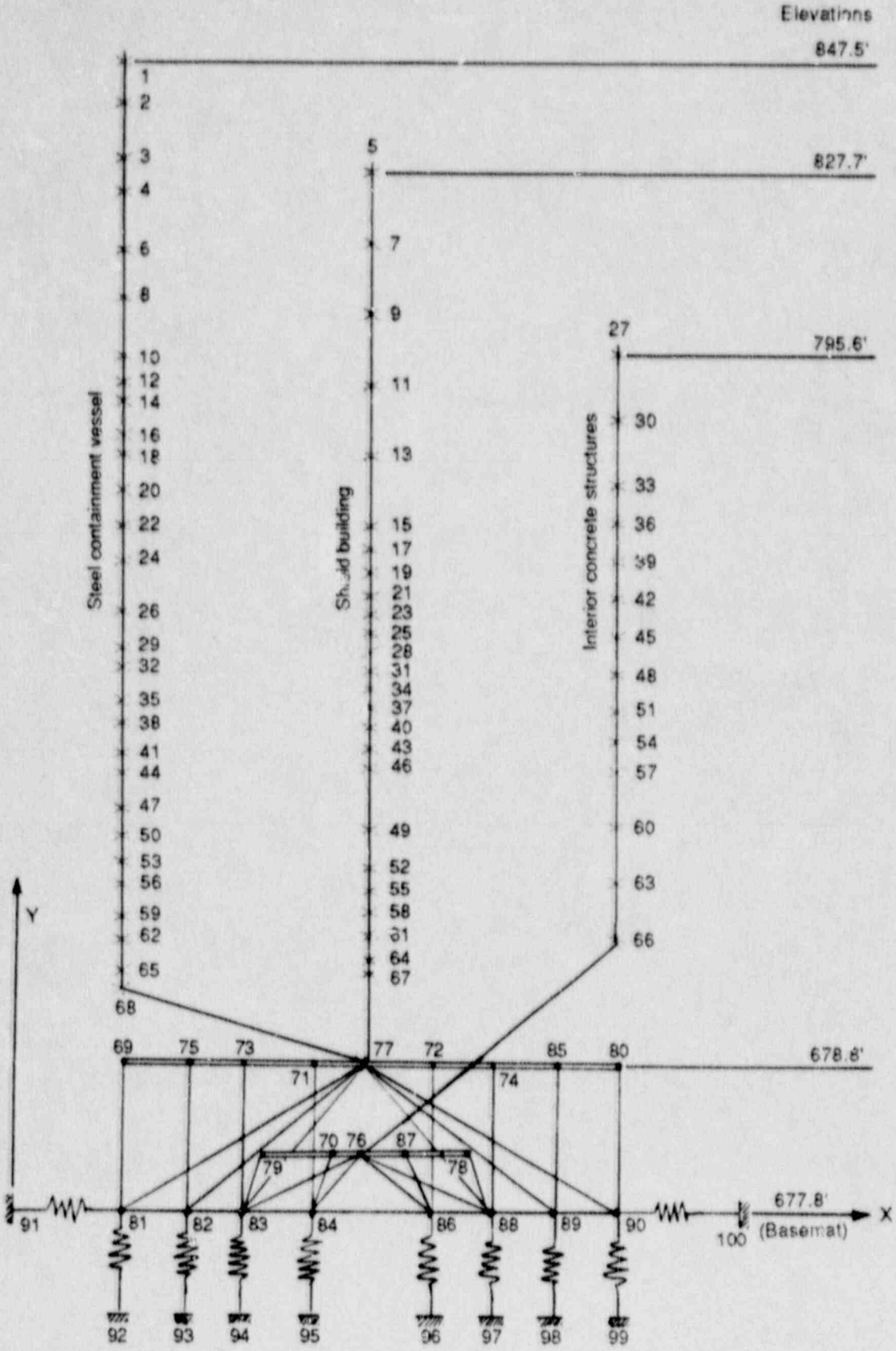

Figure 6.3 Sequoyah Seismic Analysis Model

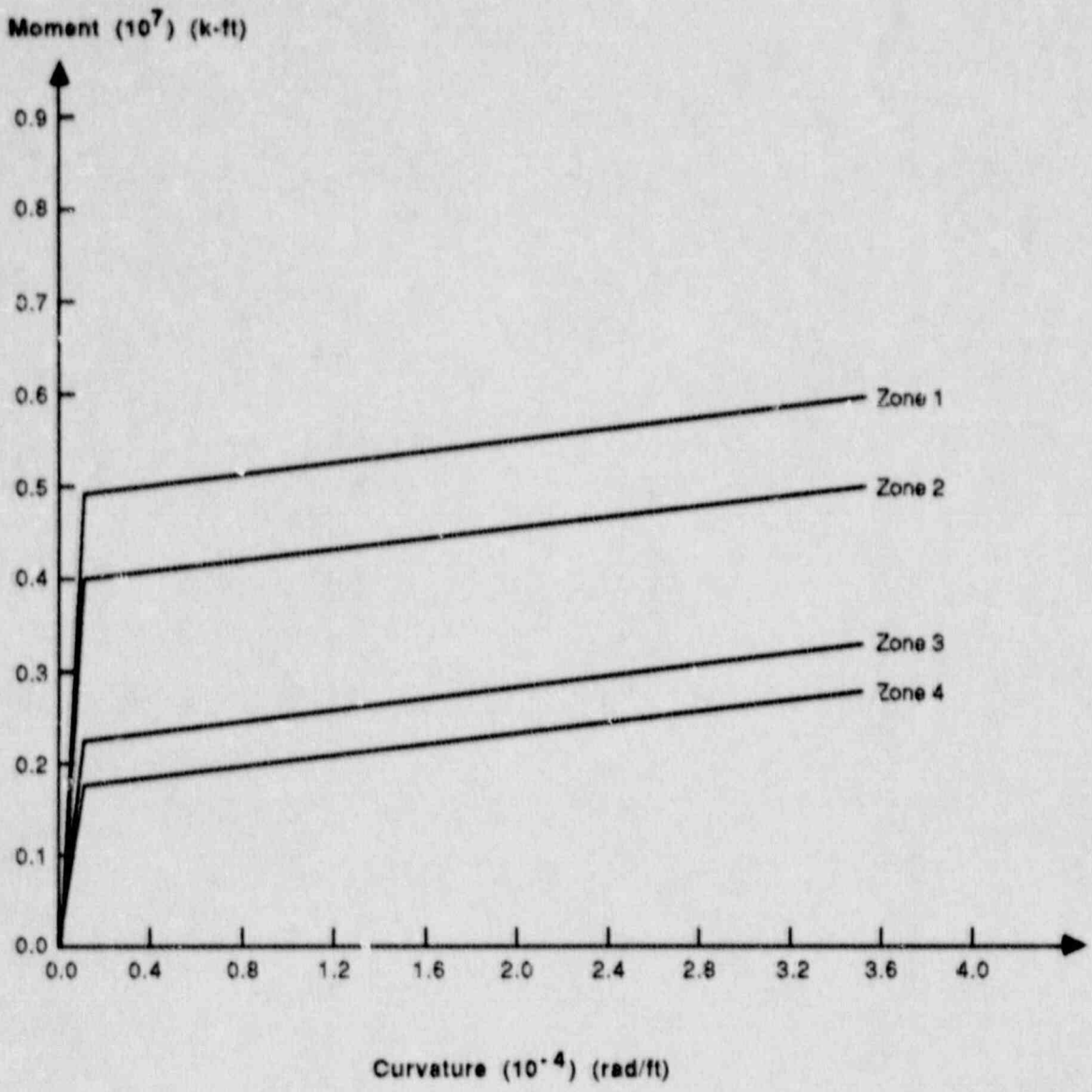

Figure 6.4 Moment-Curvature Diagrams Used for Task 3

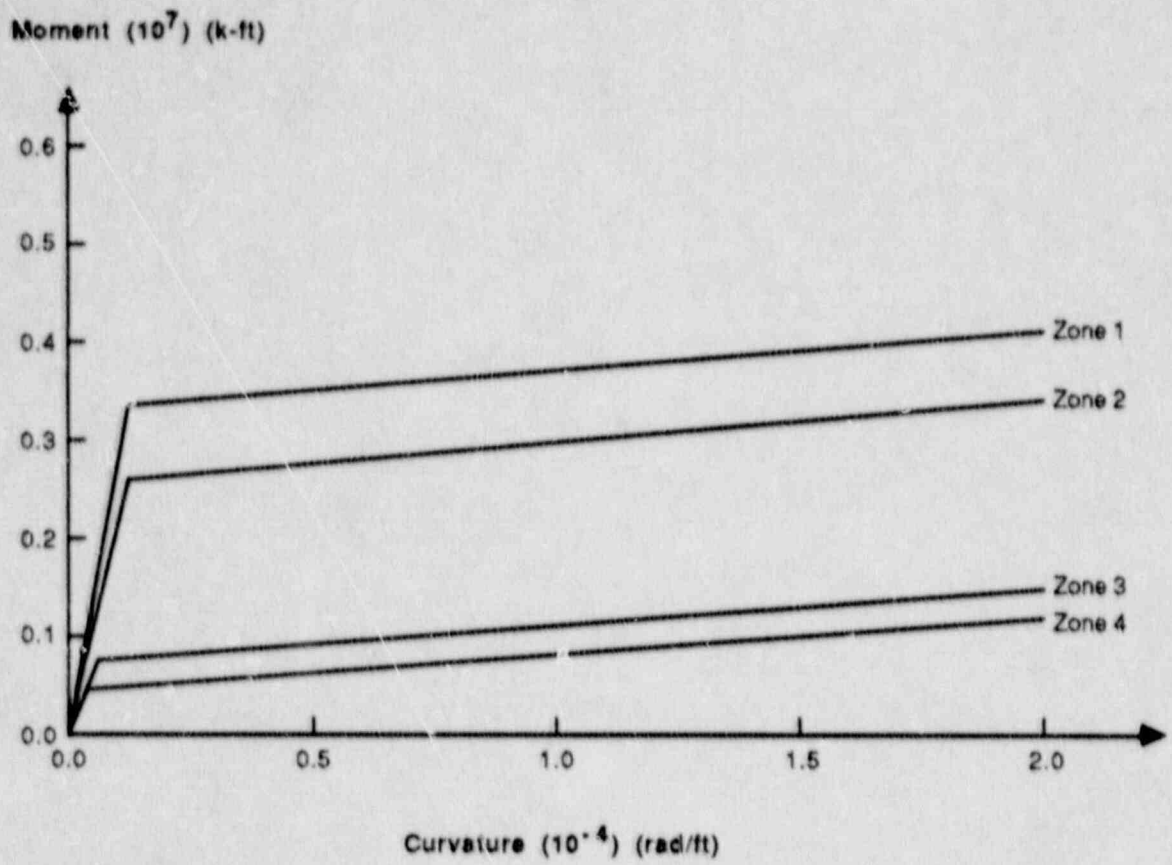

Figure 6.5 Moment-Curvature Diagrams Used for Task 5

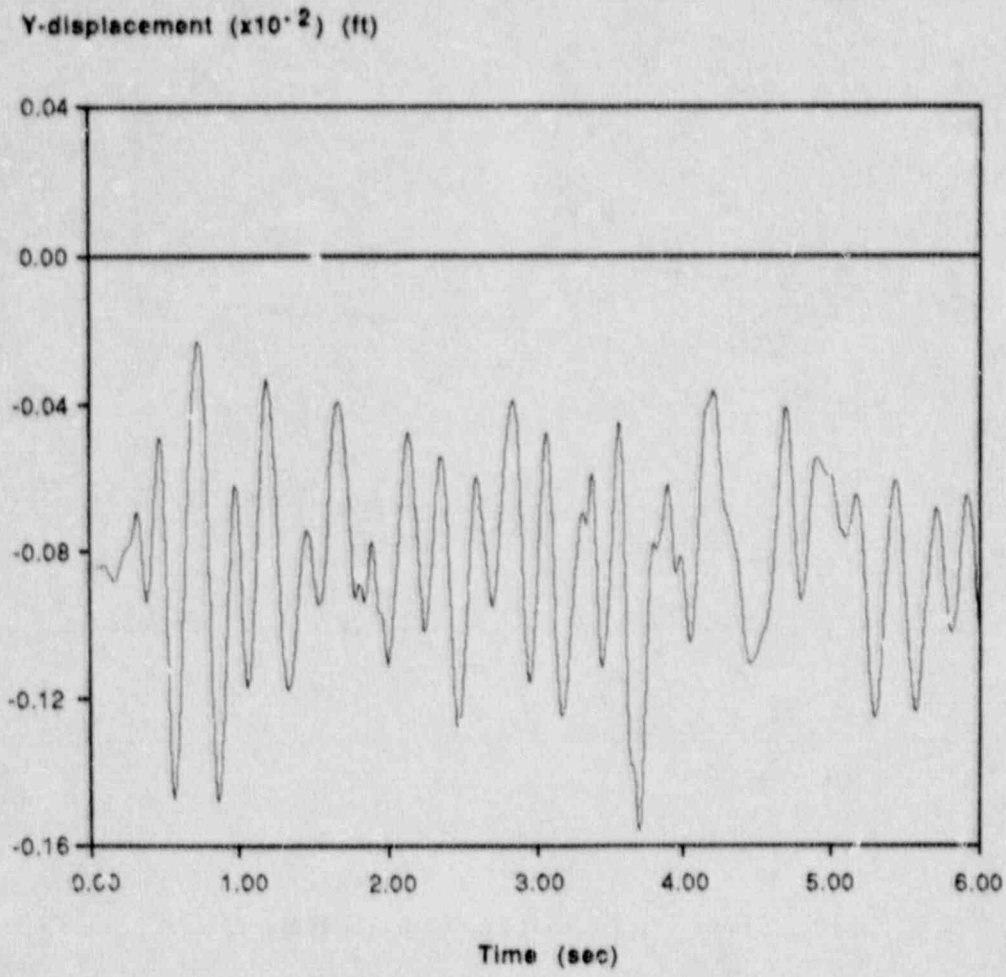

Figure 6.6 Vertical Displacement Time-History of Node 81 of the Seismic Model at A_H = 0.25 g, Showing No Uplift

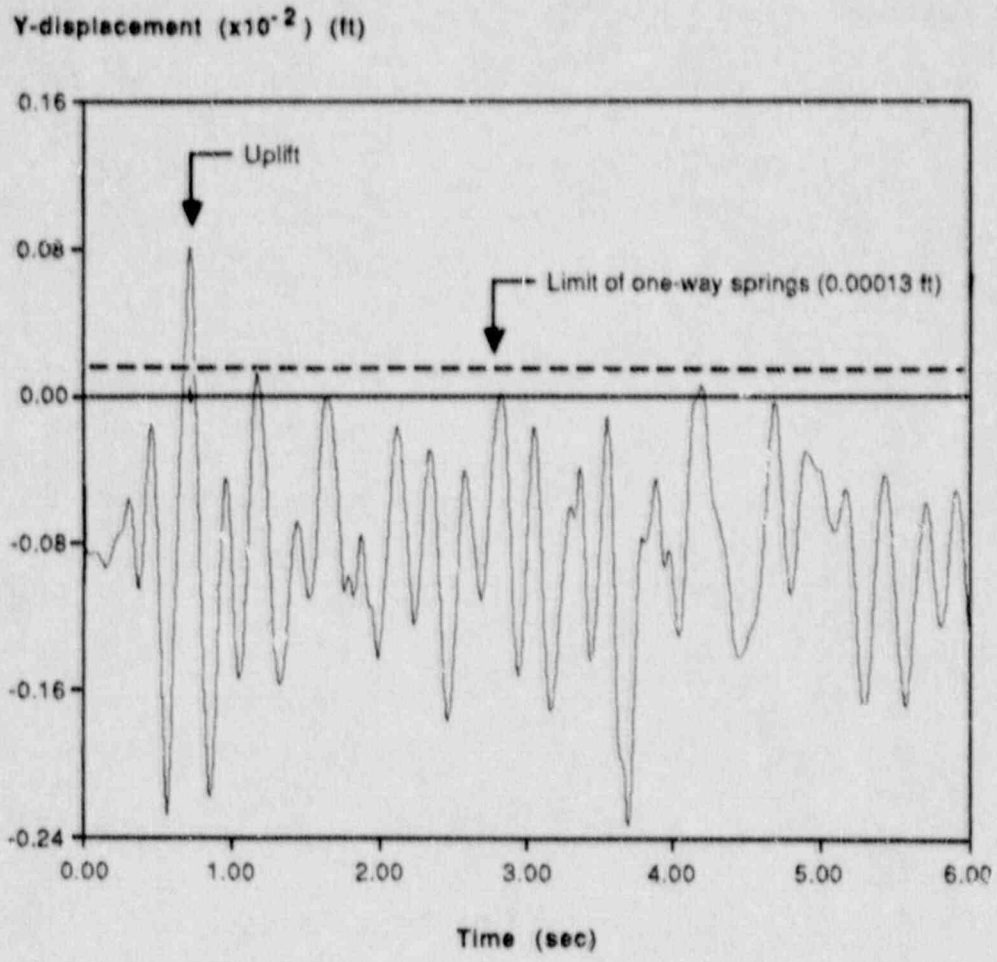

Figure 6.7 Vertical Displacement Time-History of Node 81 of the Seismic Model at A_H = 0.50 g, Showing Uplift

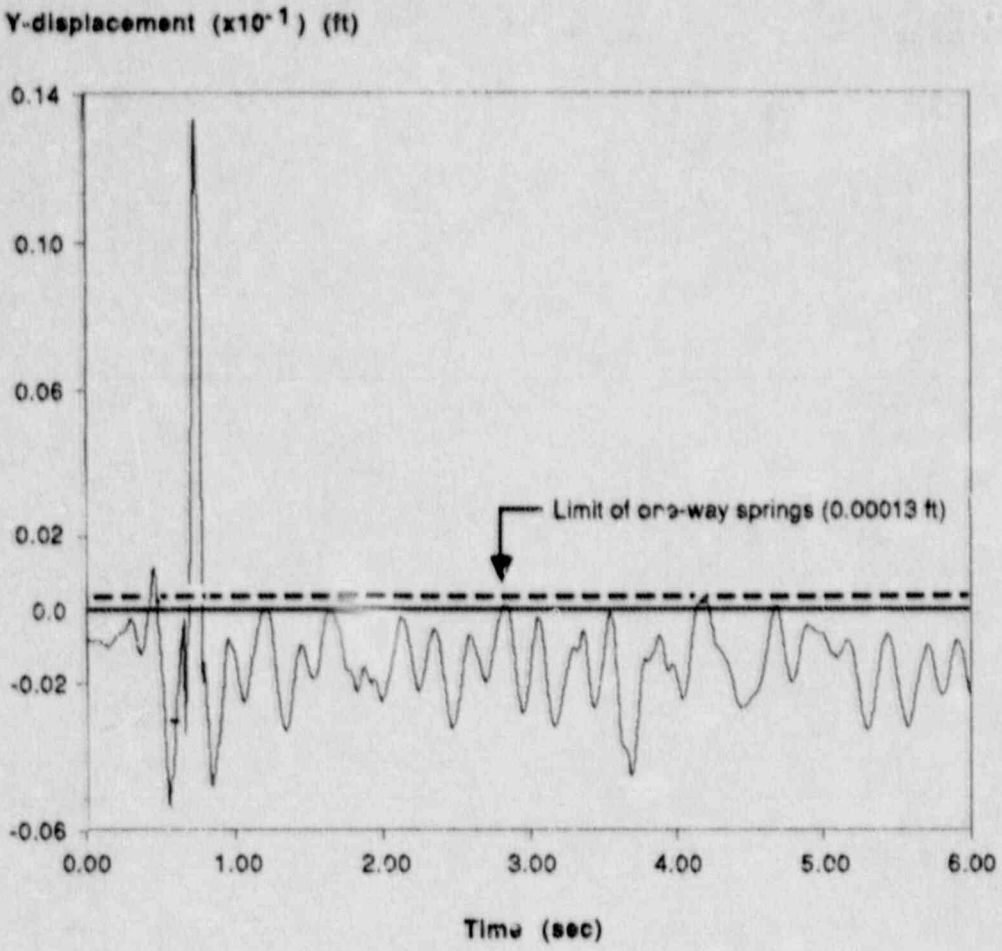

Figure 6.8 Vertical Displacement Time-History of Node 81 of the Seismic Model at A_H = 1.0 g, Showing Significant Uplift

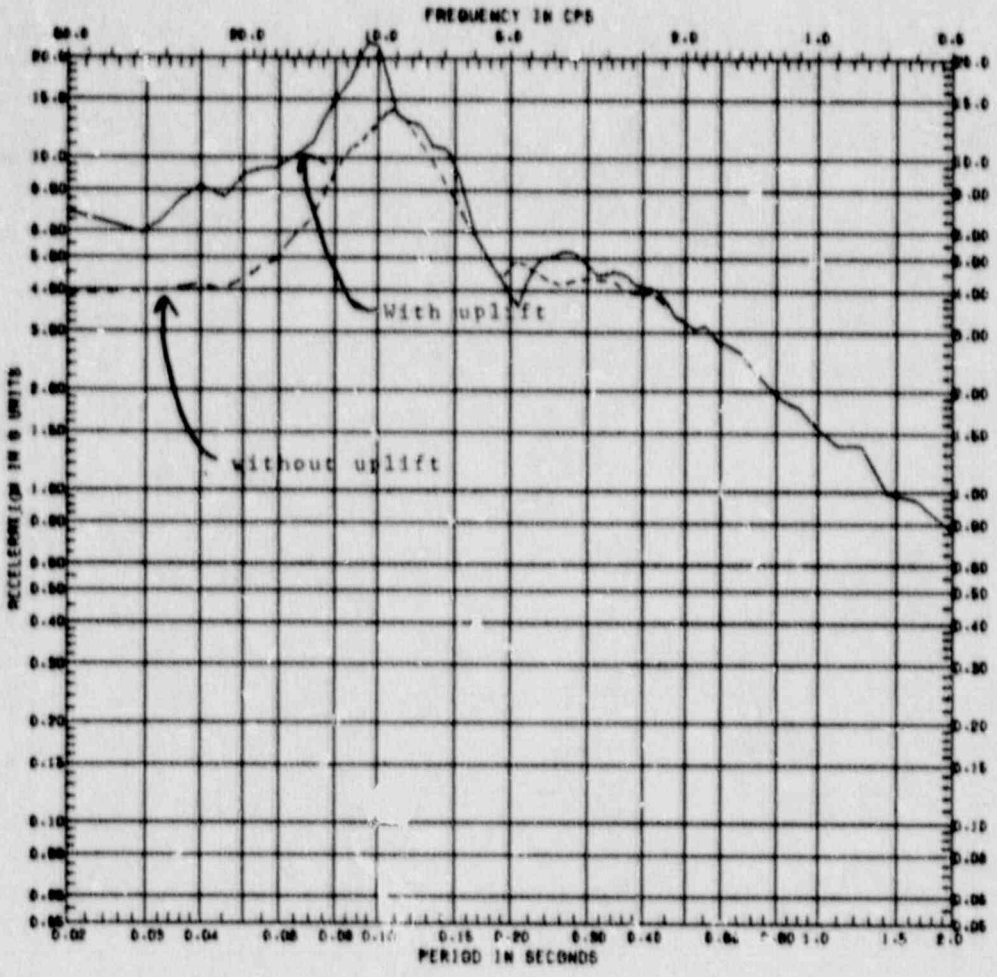

Figure 6.9 Comparison of Horizontal Response Spectra at Node 6 of the Seismic Model at A_H = 1.0g, Showing Effect of Uplift, Damping = 5%

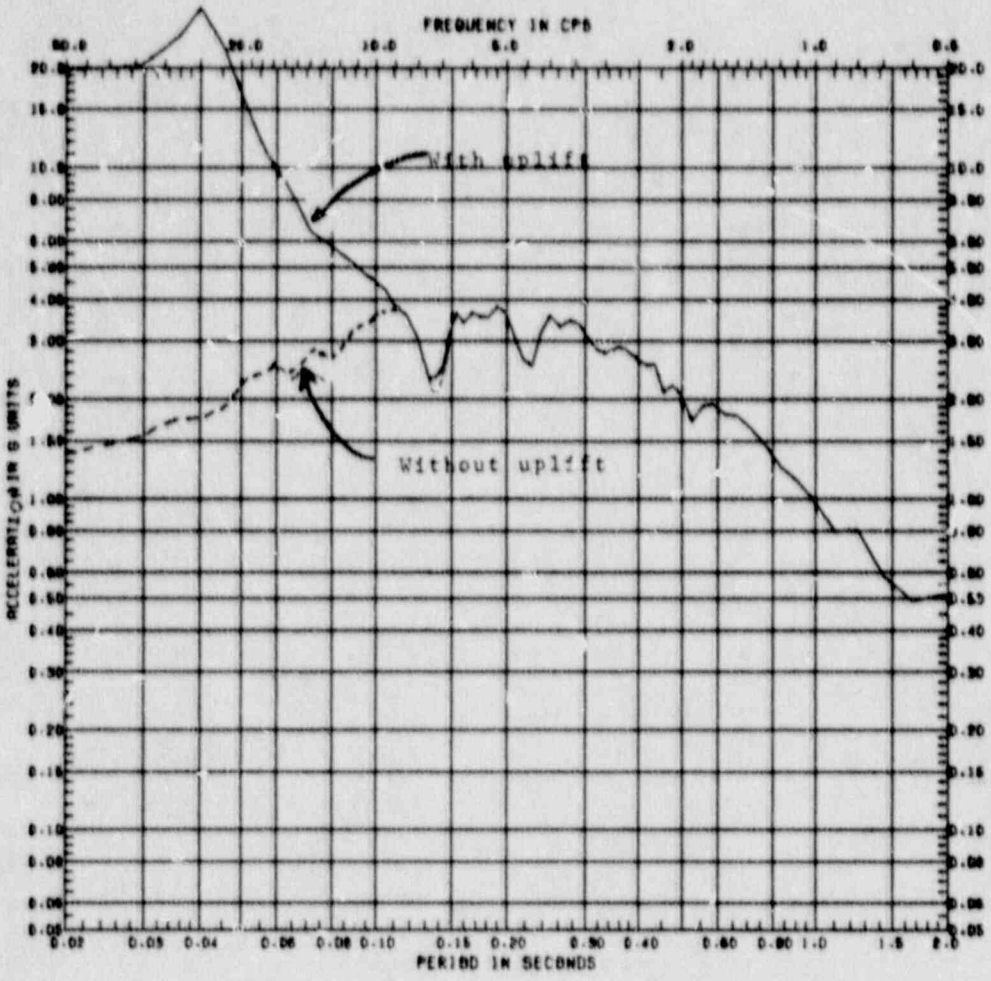

Figure 6.10 Comparison of Vertical Response Spectra at Node 6 of the Seismic Model at A_H = 1.0g, Showing Effect of Uplift, Damping = 5%

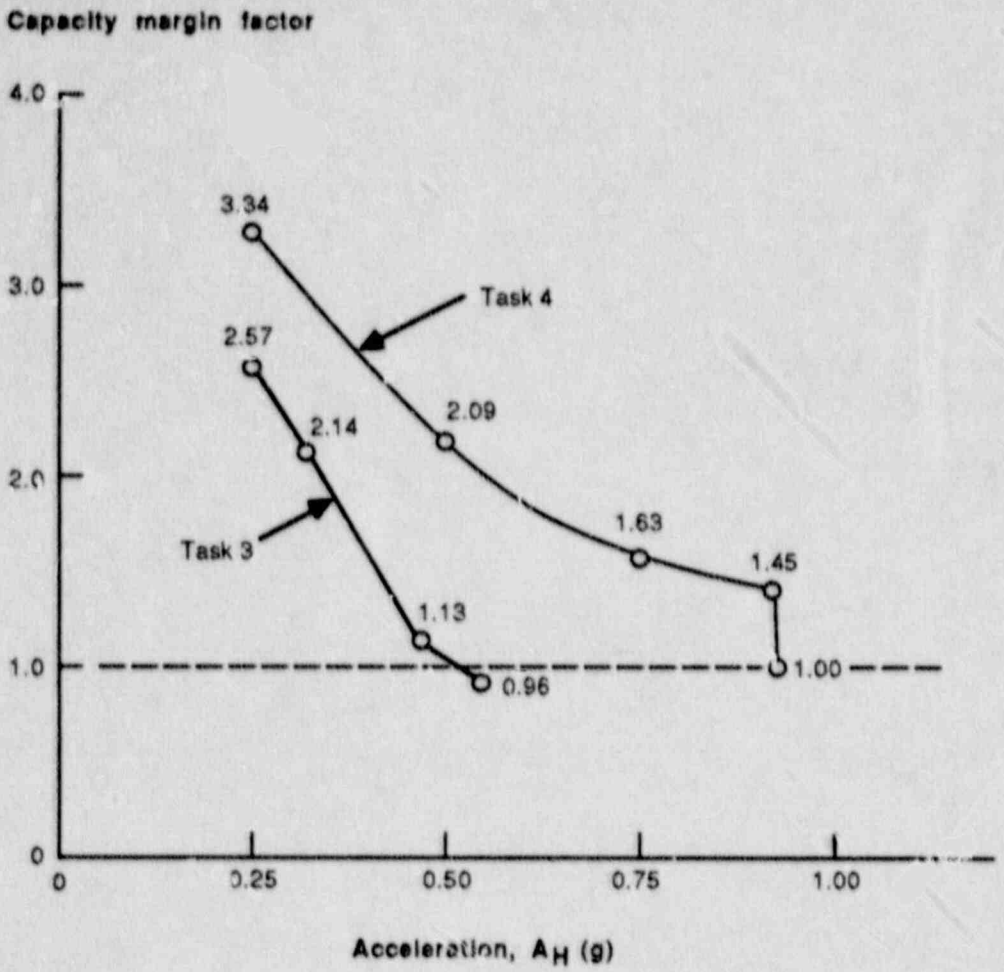

Figure 6.11 Variation of Margin with Increase in A_H for Transverse Shear Failure in Basemat Under Tasks 3 and 4 Loading

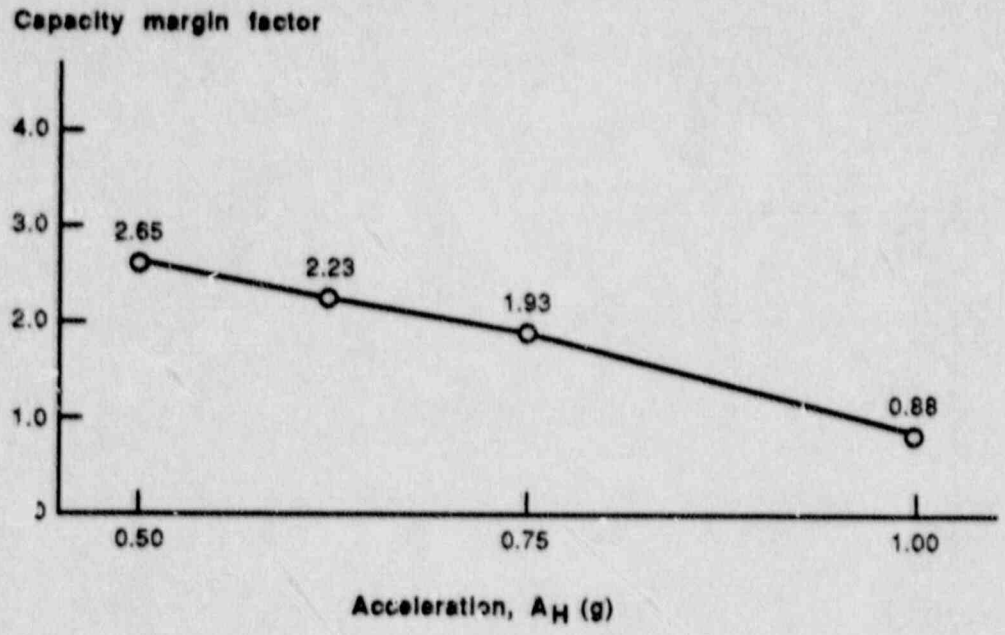

Figure 6.12 Variation of Margin with Increase in A_H for Panel Buckling in Containment Shell Under Task 3 Loading

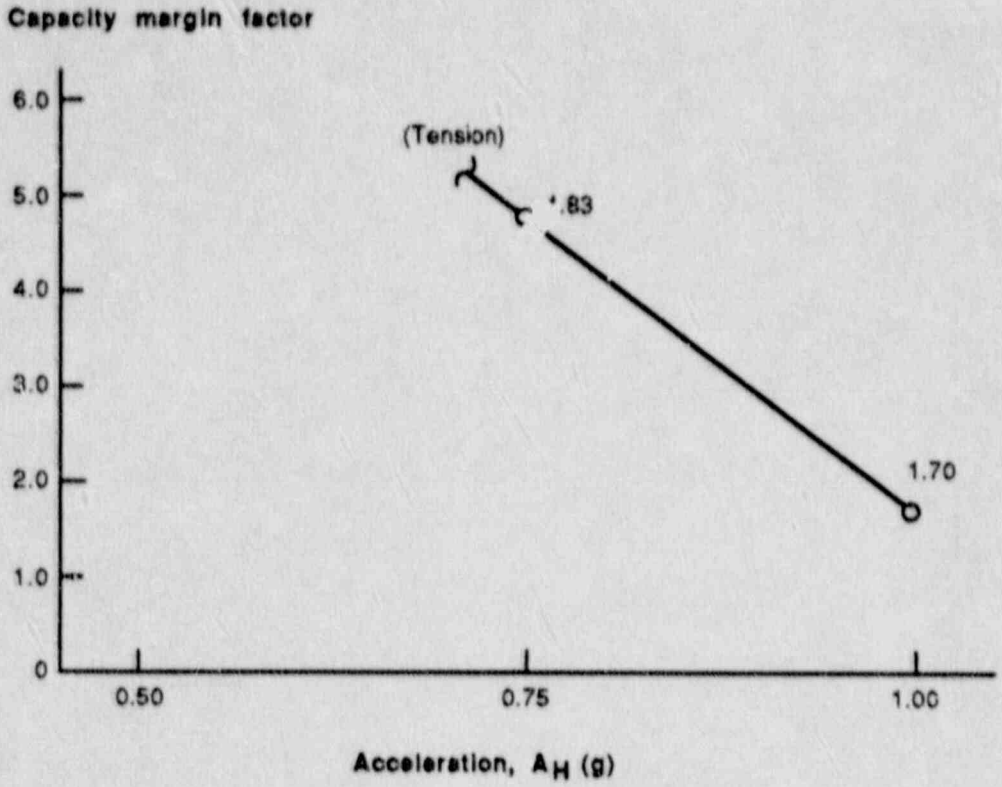

Figure 6.13 Variation of Margin with Increase in A_H for Panel Buckling in Containment Shell Under Task 4 Loading

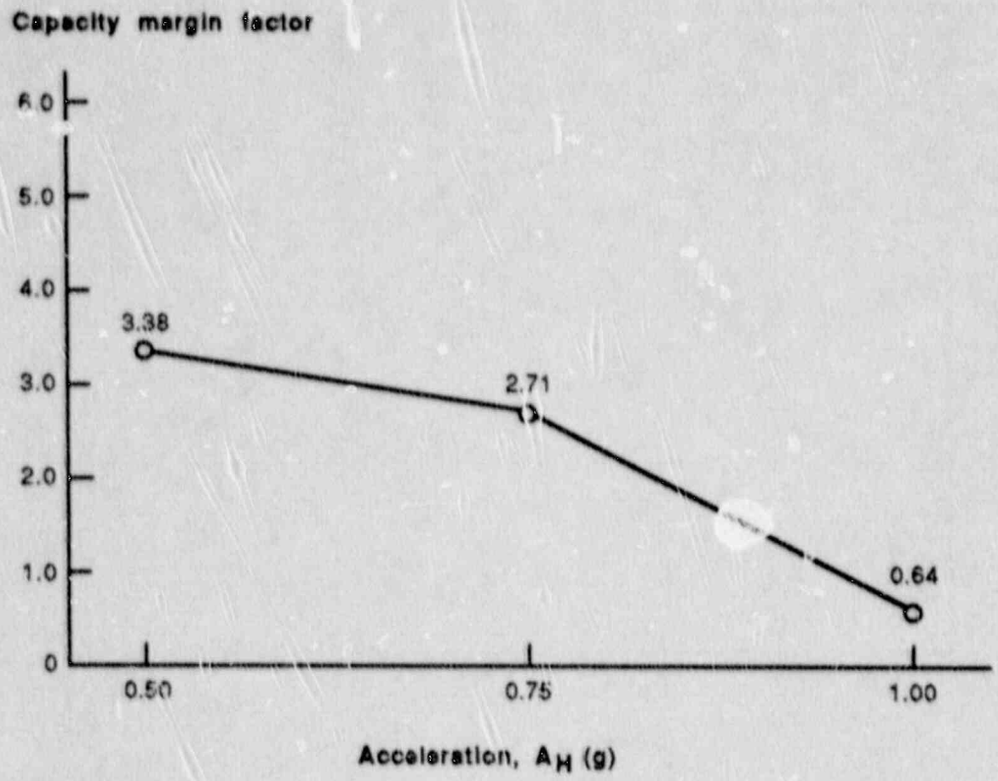

Figure 6.14 Variation of Margin with Increase in A_H for Slippage at Bolted Connection in Equipment Hatch Under Task 3 Loading

7. NONLINEAR FEM ANALYSIS OF CLINTON CONTAINMENT

7.0 General

This Chapter discusses a nonlinear quasi-static analysis of Clinton containment. Only material nonlinearity in the form of cracking in concrete and yielding in liner and reinforcing bars is considered. The analysis is performed using the ADINA program by subjecting the finite element model (FEM) of the containment to load combination of Task 3. The seismic part of the load is a combination of horizontal and vertical nodal loads. The spatial variation of this load is determined from the peak accelerations evaluated from the seismic analysis model of Figure 4.6. The amplitude of this load pattern is increased in the incremental static analysis from zero, corresponding to no seismic load, to a value which is consistent with $A_H = 1.0g$.

The purpose of the nonlinear analysis is to provide an assessment of the simplified analysis procedure used to determine shell element strains and transverse shear forces in concrete containments. This simplified analysis procedure is described in Section 2.1.6. In the simplified analysis, the quasi-static response of a shell was calculated using an elastic analysis in program DYNAX. The resulting shell element forces were then used either in program TEMCO to obtain strains in the liner and reinforcing bars, or directly for transverse shear evaluation of the containment wall and the basemat. The TEMCO evaluation considered cracking in the shell element being analyzed; it did not consider potential redistribution of forces which could take place due to cracking in concrete and yielding in steel in a concrete containment.

The focus of the work reported in this chapter is, therefore, to show how shell force distribution in the nonlinear model differs from that in a comparable elastic model and how peak steel and liner strains are affected by cracking and yielding. The comparisons described in this chapter also provide a means to assess the effect of two finite element idealizations in the evaluation of containment response. The FEM model for ADINA program uses three dimensional solid elements in the response zones where both membrane and bending response of the structure have to be considered. The corresponding DYNAX model for elastic analysis utilizes thin shell elements. Therefore comparison of the elastic response from ADINA and DYNAX evaluations also provides a basis for assessing the effect of the two types of idealizations.

Section 7.1 describes the FEM model for ADINA evaluation. Section 7.2 compares elastic responses determined from this model and the corresponding FEM model for the DYNAX program. Section 7.3 contains evaluation made for Task 3 loading. Conclusions of the Chapter are summarized in Section 7.4 and references are listed in Section 7.5.

7.1 FEM Model for ADINA Analysis

7.1.1 Geometry of Analytical Model

The containment model has an axisymmetric behavior for gravity and pressure loads. The seismic loading considers effects of one horizontal earthquake component in combination with the vertical component. Therefore, only one half of the containment cylinder, dome, and basemat under the containment is modeled. The assumed plane of symmetry is the diametral plane that contains the direction of horizontal seismic motion. The ignoring of the second horizontal component is not considered significant for the purposes of this chapter because nonlinear analysis results are compared to similarly loaded containment analyzed by the simplified procedure.

Figure 7.1 shows the elevation view of the analytical model. For ease in describing the types of elements used, the model in the figure is subdivided into six zones, R1 through R6. Figure 7.2 shows a developed view of the six zones. Table 7.1 summarizes the elements, material types, and integration order of elements within each zone. The choice of elements and material was governed by the consideration of being able to obtain a reasonable description of nonlinear containment response without being prohibitively costly.

Note that material nonlinearity is considered only in zones R2, i.e., basemat between drywell and containment walls plus the junction area of the containment wall and in R3, i.e., the membrane zone of the containment wall. Elements in the other zones, for purposes of analysis, are treated as elastic.

Figure 7.3a shows the arrangement of elements in the containment wall in zone R2. One three-dimensional 16 noded element is used to represent the containment wall. The size of this element is 14.25' x 14.25' x 3'. The plane stress element of the liner is connected to the solid element at the inside face nodes. Three-noded truss elements are used to represent the inside and the outside meridional and hoop reinforcements. Cross sectional areas of these bars were determined by lumping the reinforcement existing within elements at the nodal points.

Two-noded truss elements are used to represent the seismic reinforcement on the inside face of the solid element along the face diagonals. Again, existing reinforcement was lumped to obtain cross-sectional properties of these elements. Additional two-noded truss elements are used to represent the existing shear reinforcement.

The arrangement of elements in zone R2 for the basemat is shown in Figure 7.3b. This arrangement is similar to the arrangement used for the wall in zone R2 except that pie shaped solid elements are used with central polar angle of 12.9^{0}. The total thickness of the basemat is represented by one element. In Clinton basemat, the top reinforcement is in the hoop and radial pattern; the bottom reinforcement is arranged in an orthogonal grid. The truss elements used to represent this reinforcement in the model are in the radial and hoop directions. The steel

area per foot of the orthogonal grid at the radial boundaries of the element was used to determine tributary areas at the nodes and these were averaged to determine the area for the radial truss elements. No averaging was done for circumferential reinforcement.

Figure 7.4 shows the arrangement of the plane stress elements for concrete and liner, and the two-noded truss elements used to represent the main and seismic reinforcing bars in zone R3. The nodes of plane stress elements for liner and concrete are constrained to displace together. Because of plane-stress representation for concrete in zone R3, inside and outside reinforcing bars are lumped and considered to be at the mid-thickness of the wall.

Elastic, three-dimensional concrete elements are used in zones R1 and R6 for basemat, and in zone R4 for containment wall near the spring line. Plane-stress, elastic concrete elements are used for the dome, i.e., Zone R5. Elements in zones R1, R6, R4 and R5 are for purposes of applying required inertia loads and boundary conditions to the regions of interest in this study, which are the zones R2 and R3.

The model does not contain any elements for the drywell and RPV pedestal walls. A study of basemat displacement in the elastic range of response, showed that including or excluding these walls as elastic elements did not change the displacement patterr of the basemat. Effect of excluding the drywell and RPV walls on the containment and basemat internal forces is discussed in Section 7.2.

Table 7.2 shows the number of elements and nodes in the analytical model. It is recognized that, for reasons of economy, the mesh size used in the analytical model is coarse. There are two reasons for considering the information derived from this model to be still useful. One reason is that gross effects of material nonlinearity, rather than micro behavior, is of interest in this study. Another reason is that the predicted peak responses from the model in the elastic range are comparable with those from a DYNAX idealization which used finer mesh. This item is discussed in Section 7.2.

7.1.2 Parameters of Material Models

The solution of analytical model has been obtained using ADINA-84. A full description of the material models used is given in References 7.1 and 7.2. The input parameters for these models are briefly described below:

Concrete Model:

Eight sets of parameters are required for this model

a. Uniaxial stress strain curve. The parameters used for this curve are as follows:

   Compressive strength f_c' = 4680 psi
   Strain at maximum stress, ε_o = 0.002

Ultimate compressive strength = $0.85 f_c'$
Ultimate compressive strain = 0.003
Tensile strength cut-off, f_t = $6 f_c'$
Tangent modulus at zero strain, $E_o = 2f_c'/\varepsilon_o$

b. Poisson's ratio, ν = 0.17

c. Parameter of loading function, α = -0.01

d. Stiffness reduction factors:
Shear: 0.12
Normal to the crack: 0.05

e. Scaling parameter to modify value of ε_o in uniaxial stress-strain curve to consider the effect of multiaxial stress condition:

γ = 1.0 (the default value in Reference 7.1)

f. Failure envelopes: These envelopes are defined in terms of principal stresses and they are used to identify occurrence of cracking, crushing and modification of f_c' in uniaxial stress-strain curve to consider the effect of multiaxial stress condition. Table 7.3 shows the specific definition of failure envelopes used in terms of 24 principal stress ratios.

g. Parameter for isotropic or orthotropic conditions: When the minimum principal stress is smaller than $-K\sigma_c'$, where σ_c' is the modified f_c' for multiaxial conditions and K is a constant, the material is assumed orthotropic; otherwise, it is isotropic. The value of K = 0.7 has been used which is the default value in Reference 7.1.

To provide an indication of the performance of above concrete model, test results from two reinforced concrete test panels, loaded for in-plane normal and shear loads were evaluated. Test results were for 35" x 35" x 2.75" panels with reinforcement ratio ρ = 0.018. Test information was taken from Reference 7.3. The panel was modeled by nine plane-stress concrete elements with reinforcing lumped as truss members to conform with the selected mesh size.

Results for panel shear strain at several load levels as obtained from the ADINA analysis are compared to test information in Table 7.4 for two panel tests. The test shear strains in Table 7.4 refer to average panel shear strain obtained at each load level from linear strain measurements in a 3 x 3 grid on the test panel. These are taken directly from Reference 7.4. The ADINA strains are taken from the element at the center of the 3 X 3 grid of plane stress elements.

Strains computed by ADINA analysis are higher than the test strains in Table 7.4. Comparison improves at higher test load levels. This behavior is attributed, in part, to the fact that in ADINA analysis, tension stiffening is not considered. Considering that in this chapter

it is intended to assess the gross effects of concrete cracking and steel yielding, the comparison in Table 7.4 is considered to be close.

Steel Material Properties:

Table 7.5 summarizes the material properties used for the stainless steel and carbon steel liner, and the reinforcing bars. These parameters are the minimum specified values for each case. For ease of computation strain hardening modulus of the steel liner is assumed to be zero.

7.1.3 Boundary Conditions

The radius to Point A on the periphery of the analytical model in Figure 7.1 is 85 feet. This corresponds to the closest distance from center of containment in Figure 4.1 to the nearest wall of the reactor-control buildings. Because of continuous basemat, Point A is assumed to move with other buildings. Point B, directly above A, is constrained to follow A.

For dead load application to the model, it is assumed that all buildings move down together. Consequently, boundary at A is free to move vertically down. For seismic loading, Point A moves vertically from the dead load position at zero seismic load to the average position of nodes 38 and 49 of the seismic model in Figure 4.6 when peak seismic load is applied. Because one horizontal seismic movement is assumed, the model has symmetrical boundary condition on the vertical plane which contains the containment diameter along which horizontal seismic motion occurs.

The seismic effects include a horizontal component and a vertical upward component. These are quasi-static loads and they are applied as g-loading. The peak values of these g-loads and the manner by which they were determined from the peak accelerations determined in the seismic model of Figure 4.6 are shown in Figure 7.5. When peak horizontal accelerations shown on the model are applied, the total seismic moment at the base of the containment wall is 17% higher than the peak seismic moment calculated for A_H = 1.0g in NONLIN 2 program using model of Figure 4.6. Accordingly, all horizontal accelerations obtained from NONLIN 2 were scaled down by a factor 0.83 for seismic load corresponding to A_H = 1.0g applied in the FEM analysis.

7.1.4 Spatial Description of Loads

Figure 7.5 shows the description of loads applied to the model. The gravity load of the wall is applied as nodal loads which are uniform on circumference at each elevation. This information was obtained from the input masses to the seismic model of Figure 4.6. The correspondence between the nodes of the two models is summarized in Figure 7.5. The weight of the basemat is applied with a uniform density. Included in the dead load is the effect of water in the suppression pool, applied as nodal loads. Also applied to the model as ring loads is the weight per foot of the RPV and drywell walls as well as the effect of their overturning moments.

7.2 Comparison of Elastic Responses From ADINA and DYNAX Models

ADINA model here refers to the FEM model described in Section 7.1 and solutions obtained from that model assuming elastic behavior. The DYNAX model refers to the analytical model shown in Figure 4.18. The following differences exist between these two models:

a. The DYNAX model includes axisymmetric shell element idealizations for the pedestal and drywell wall. These structures are not included in the ADINA model; their reactions, however, are applied to the basemat.

b. Stiffnesses of all the shell elements in the DYNAX model are based on plain concrete properties. In the ADINA model steel element stiffeness are specifically included.

c. The DYNAX model has a more refined mesh.

d. In the DYNAX model vertical soil springs are distributed and horizontal soil spring are concentrated at external boundary node A'; see Figure 4.18. In ADINA model soil springs tributary to basemat under the containment are applied as concentrated nodal springs. The remaining part of the total horizontal stiffness is applied at boundary node A in Figure 7.1.

Peak forces determined assuming elastic behavior from the two models are listed in Table 7.6. Responses listed in this table are for dead load plus seismic loading which corresponds to A_H = 1.0g. Only major forces are listed at regions of interest. These include shell forces at the wall near the basemat junction and at 42 feet above the basemat, and basemat forces between the drywell and containment walls.

To show the effects of differences in mesh size, incorporation of steel stiffnesses, and inclusion of internal structures two values are given for each model and response; one without parantheses and the other within parantheses. Responses for ADINA model within parantheses were obtained by deleting the steel stiffness from the model in Section 7.1; ADINA results without parantheses include the steel stiffness effect. Responses for DYNAX model within parantheses refer to the model of Figure 4.18 from which internal walls are deleted; the values without parantheses refer to the model of 4.18 as shown.

The maximum percent difference between ADINA and DYNAX models, including all the listed differences in the two models, is 38% and it is in the meridional moment at the base of containment wall (responses of 1306 and 949 ft. kip/ft.). The maximum difference becomes 12% when effects of steel stiffness and internal structures are removed (responses of 1122 and 1000 ft. kip/ft.). The differences of the nature of 10% to 12% are caused by different types of finite elements used and the mesh size. It is, therefore, concluded that within consideration of economy for the size and extent of model, the ADINA model in Figure 7.1 is a reasonable

idealization of the containment to be considered in discussion of materially nonlinear response in the next section.

7.3 Discussion of Results

7.3.1 Application of Incremental Load

Table 7.7 lists the load increments applied to the model. Full dead load was applied in the first step and for this application boundaries at A in Figure 7.1 were free to move vertically down. During steps 2 through 21 seismic load was increased from 0% of that corresponding to A_H = 1.0g to 100%. No equilibrium iteration was performed in these steps to obtain incremental solutions; the stiffness, however, was reformulated at each step. During steps 22 and 23, loads were kept constant on the structure at their values for step 21 but stiffness was reformulated. The purpose of these two steps was to see if stable results are obtained at maximum seismic load.

7.3.2 Displacements

The deformed configuration of the containment after full application of dead and seismic loads is shown in Figure 7.6. Since the rotation of the base as calculated during time history was small, in the seismic load application the boundary at A was moved the same amount vertically for all values of azimuth (no tilting of basemat was considered). Figure 7.7 shows the horizontal displacement of a point about 8 feet below the spring line as seismic load is incrementally applied. Two items of information in this figure are important to note. During steps 22 and 23, when stiffness was reformulated but seismic load was kept at its A_H = 1.0g level, the horizontal displacement changed from 0.167 feet to 0.171 feet, which is only 2.3%. This shows that step sizes used for incremental loading have yielded a stable solution.

The second item refers to the comparison of calculated displacements relative to basemat from ADINA model and the time history evaluations using seismic model of Figure 4.6. These displacements are compared in Table 7.8. Displacement from time history analysis is 1.76 inches compared to 1.47 inches from the ADINA model. This comparison is considered favorable and it shows that the reduction for shear stiffness due to cracking used in dynamic analysis following Appendix A is reasonable.

7.3.3 Strains

The major principal tensile strains in the concrete for the containment wall is shown in Figures 7.8, 7.9, and 7.10 for A_H = 0.5g, 0.75g, and 1.0g, respectively. This information is given only for those elements at which through thickness cracking was calculated. For the part of wall modeled by solid elements, the strains refer to the outside face of the wall. Of the nine integration points near the outside surface of element, the strain at the center integration point is shown. For plane-stress elements, the tensile strains at all four integration points of the element are shown. Also shown in these figures is the

extent of elements at which through-thickness cracking occurs. This means all three integration points at each elevation of the wall have cracked. The cracking in the wall first occurred at the lower most integration point of the solid element next to the basemat at 0^{o} azimuth and at A_H = 0.3g to 0.4g. At A_H = 0.5g, the elements for which through-thickness cracking has occurred are limited to the first row of solid elements within a 80-degree arc length centered at 0 degree azimuth; see Figure 7.8. At A_H = 1.0g, the completely cracked elements in the zone where wall is modeled by solid elements extend over half of the circumference upto elevation 740'. Cracking extends into the first row of plane-stress elements (elevation 740' to 755'). Circumferentially completely cracked elements cover about half of the circumference.

Figure 7.11 shows the concrete principal strains in the top and bottom faces of basemat. About half of the basemat top and half of the basemat bottom is cracked at A_H = 1.0g. Figures 7.12 and 7.13 show the tensile principal strain in the wall and basemat liners. Correlation of liner strains with concrete strains is evident from the cross comparison of Figures 7.8 through 7.13. The information indicated in Figures 7.12 and 7.13 shows that liner yields only in the vicinity of the drywell wall at A_H = 1.0g.

The maximum principal tensile strain in wall liner is 0.00068 and in the basemat liner is 0.002.

Figures 7.14 through 7.17 show the variation of reinforcing bar strain with seismic load level for several reinforcing bars at highly strained parts of containment wall and basemat. This information shows that maximum strain in these bars is below rebar yield strain of 0.002. Upon occurrence of major cracking, rebars begin to be strained at higher rate. Moreover, during the last two steps of the solution when seismic load is kept corresponding to A_H = 1.0g, no appreciable change in the calculated strain of rebars occurs. This shows that numerically stable solutions have been obtained in the incremental loading process.

7.3.4 Major Shell Forces

A principal assumption in simplified analysis is to use shell forces determined from the elastic analysis in the computer program TEMCO to determine element strains. The elastic analysis of the cylindrical shell implies a sinusoidal variation of in-plane shear force and cosine variation of meridional forces along the circumference in the membrane zone of the shell. Figures 7.18 and 7.19 show the comparison of these shell forces from cracked and elastic analyses at containment wall elevation 751.7'. This elevation is within the zone R3 in Figure 7.1 where plane-stress elements are used to model the shell. Figure 7.10 shows that at A_H = 1.0g, these elements have cracked over about half of the circumference. The comparison in Figures 7.18 and 7.19 shows that although due to cracking local deviations from the distribution of elastic analysis occurs, the general trend of forces obtained using an analysis which permits cracking follows the elastic analysis distribution.

Table 7.9 compares the major shell forces in the lower portion of the containment wall and in the basemat from cracked and uncracked analyses. This comparison shows that in the cracked model, understandably, bending moments are significantly lower than those predicted from an uncracked analysis. The same is true for the transverse shear at the base of the containment wall. The transverse shear in the basemat, however, is not similarly affected by cracking. This difference in behavior is due to the fact that the transverse shear in the wall is caused by shell boundary effect. The shear on the basemat, however, is a shear induced directly by forces.

The meridional compression in the containment wall at 180^{o} azimuth, for analysis that considered cracking, is somewhat greater than that predicted from the uncracked analysis. This is due to the shift of the neutral axis of circular wall cross section as cracking occurs. The increase in compression is about 20% and it is considered small in comparison to other reductions which cracking causes.

The comparison in Table 7.9 shows that generally for total shell forces, conservative results are obtained by using forces from an uncracked analysis. In some cases this conservatism is quite significant.

7.3.5 Comparison of Strains to Those From Simplified Analysis

This comparison is shown in Table 7.10 for strains at several locations in the containment wall and in the basemat. The ADINA results are directly from the solution of model in Figure 7.1 for Task 3 loading at A_H = 1.0g. The simplified analysis results are the solution of elastic DYNAX model in Figure 4.18 followed by analysis in program TEMCO which considered cracking and yielding in an element level only.

The comparison in Table 7.10 shows that elements at locations which would be predicted to have maximum strains on the basis of an elastic analysis, are still highly strained in ADINA model and the prediction from ADINA for these strains is generally smaller or very close to the simplified analysis. This categorization involves strains in wall liner at elevation 719', outside meridional rebar at elevation 719', meridional rebar at elevation 742' and all the basemat strains. The average compressive strain is slightly underpredicted in the simplified analysis results, because of the shift in circular section neutral axis, which ADINA anlaysis considers and the simplified analysis ignores.

The strain in the inside meridional rebar at elevation 719' in the containment wall is underpredicted by the simplified analysis because cracking under seismic load reduces the moment at this location. Since moment causes compression in the inside rebar, its reduction increases the tensile strain of the rebar. This is an example where local redistribution due to cracking makes simplified analysis underpredict the fully cracked analysis results. This underprediction, however, is not important because the underpredicted strain is not controlling. A similar effect of local redistribution is responsible for the underprediction of strains in the liner at elevation 752'. Figure 7.12 shows that in the cracked membrane zone, direction of principal strain changes

from vertical to an inclined direction as azimuth increases from 0°. This inclination is due to the effect of shear stresses in the liner. Figure 7.18 shows that distribution of total shear forces on the circumference of containment wall follows the prediction of elastic analysis. However, since concrete cracks and carries less shear, and since no major redistribution occurs over the circumference, the reduced shear of concrete is transferred to stiffer liner and this phenomenon causes increased principal strains in the ADINA results. Figure 7.20 confirms that shear carried by liner from ADINA analysis is considerably more than that assumed in the simplified analysis.

7.4 Summary and Conclusions

Results from a materially nonlinear finite element model of the Clinton containment under dead plus quasi-static seismic load are presented in this chapter and compared to predictions from a linear shell analysis model followed by element level analysis that considerd concrete cracking. The simplified analysis has been used in Chapters 4 and 5 of this report for the Clinton and the Zion containments. The materially nonlinear model, herein called ADINA model used solid concrete elements in the zones of containment where bending occurs.

Principal findings of the study are as follows:

1. The ADINA model that used coarser mesh for limiting computational cost in the linear range of analysis, produced shell forces within 12% of the simplified analysis after the effects of internal structures and composite action of liner and steel were accounted for.

2. The ADINA model was loaded incrementally up to a level of seismic load corresponding to A_H = 1.0g. At this load level, considerable cracking occurred in the basemat and at the lower portion of the containment wall up to an elevation of 755' (42 feet above the basemat) and covering over half of the containment circumference.

3. At A_H = 1.0g, the calculated spring line horizontal deflection relative to basemat using ADINA model agreed with results from seismic beam model of containment with reduced shear stiffness factor of 0.12. This showed the shear reduction factor used in the seismic analysis model was reasonable.

4. At A_H = 1.0g, the only steel element which yielded was the basemat liner near the dyrwell wall. The corresponding simplified analysis showed strains at this location which were much higher than that predicted by ADINA model, showing conservative predications obtained through analysis.

5. The cracking of concrete in the cylinder produces through-thickness, circumferential, and possibly height-wise effects. Because only the lower 28 feet of containment wall was modeled by solid elements (for reasons of computational economy), the

height-wise effect of cracks is not discussed. The discussion considers only through-thickness and circumferential redistribution of the loads.

6. The major consequence of circumferential redistribution due to cracking is the shift in neutral axis of the circular containment section. This effect produced compressive strains in the wall which were about 20% higher than those which were obtained using the simplified anlaysis. Considering that in a time dependent seismic load this effect should be more limited than that seen in one cycle of a quasi-static load application, and since the membrane crushing of wall is not found to be a controlling limit state, this effect of redistribution due to cracking is considered to be unimportant.

7. The through-thickness redistribution caused by cracking produces results which are conservative relative to the simplified analysis results for peak rebar strain, transverse shear in the wall, and for liner principal strains when liner is strained in basically hoop or meridional directions. For liner locations in which the in-plane shear is also significant, through-thickness cracking yields strains which exceed values from simplified analysis. For the Clinton containment studied here, locations of high liner strain occurred where there was minor shear stress effect; therefore, results obtained from simplified analysis are considered to be conservative.

8. In the basemat, the liner yielded and concrete cracked near the drywell wall in the tension side (zero degree azimuth); as a result, a moment redistribution occurred in the ADINA model at this location. The liner and reinforcing bar strains determined from the simplified analysis for this location are more conservative than the ADINA model because the simplified analysis does not consider this redistribution. The transverse shears predicted by the two analyses were, however, close.

7.5 References

7.1 ADINA Engineering, "ADINA Users Manual," Report AE 84-1, December 1984.

7.2 ADINA Engineering, "ADINA Theory and Modeling Guide," Report AE 84-4, December 1984.

7.3 Vecchio, F., and Collins, M. P., "The Response of Reinforced Concrete to In-Plane Shear and Normal Stresses," University of Toronto, ISBN 0-7727-7029-8, Publication No. 82-03, 1982.

Table 7.1
Elements Used in ADINA Analysis

ZONE	TYPE OF ELEMENT	MATERIAL	INTEGRATION ORDER
R1	a. Three-dimensional solid for basemat	a. Elastic	2 x 2 x 2
	b. Horizontal and vertical spring elements for soil	b. Elastic	
R2	a. Three-dimensional solid for concrete	a. Nonlinear concrete	3 X 3 X 4 basemat 3 X 3 X 3 wall
	b. Three-dimensional plane-stress for liner	b. Elastoplastic with kinematic hardening	2 x 2 basemat 3 x 3 wall
	c. Truss for main reinforcement, seismic reinforcement and shear ties	c. Elastoplastic with kinematic hardening	2 for three noded 1 for two noded
	d. Horizontal and vertical spring elements for soil	d. Elastic	
R3	a. Three-dimensional plane-stress for concrete	a. Nonlinear concrete	2 x 2
	b. Three-dimensional plane-stress for liner	b. Same as b in R2	2 x 2
	c. Truss for main reinforcement and seismic reinforcement	c. Same as c in R2	
R4	Three-dimensional solid for wall	Elastic	2 x 2 x 2
R5	Three-dimensional plane stress	Elastic	2 x 2
R6	a. Three-dimensional solid for basemat	a. Elastic	2 x 2 x 2
	b. Horizontal and vertical spring elements for soil	b. Elastic	

Table 7.2
Number of Nodes and Elements Used in the ADINA Model

Number of nodes	890
Number of equations	1787
Maximum half band width	235
Number of soil springs	432
Number of 3D solids for concrete	126
Number of 3D plane stress for concrete	140
Number of 3D plane stress for liner	168
Number of trusses for rebars	978

Table 7.3
Parameters of Triaxial Compressive Failure Curves Used for Concrete

PRINCIPAL STRESS RATIOS	CURVE NUMBER, I					
	1	2	3	4	5	6
SP1 (I)	0.00	0.25	0.50	0.75	1.00	1.20
SP3 (I,1) (SP2 = SP1)	1.00	1.35	1.75	2.15	2.50	2.80
SP3 (I,2) (SP2 = βX SP3)	1.25	1.70	2.10	2.55	2.95	3.30
SP3 (I,3) (SP2 = SP3)	1.20	1.60	2.00	2.40	2.80	3.10

I = 1 to 6, stands for curve number

J = 1 to 3, stands for point on curve

SF1(I) = $\sigma_1(I)/ f'_C$

SP3(I,J) = $\sigma_3 (I,J)/F'_C$

f'_C = uniaxial compressive strength

β = principal stress ratio

Table 7.4
Comparison of Measured and Calculated Response of
Reinforced Concrete Test Panels Under In-plane Loads
(Panel Size: 35" x 35" x 2.75", ρ = 0.018)

In Plane N_v (kips)	Shear Strain ADINA	Shear Strain TEST	REMARKS
	a. Panel PV28 of Reference 7.3 under tension plus shear with $N = +0.32\ N_v$		
28.9	1.82×10^{-3}	0.141×10^{-3}	Test failure at N_v = 81 kips by sliding shear failure; ADINA did not converge beyond N_v = 91 kips
52.6	3.82×10^{-3}	2.12×10^{-3}	
71.5	5.27×10^{-3}	3.96×10^{-3}	
81.0	6.05×10^{-3}	5.8×10^{-3}	
	b. Panel PV25 of Reference 7.3 under compression plus shear with $N = -0.69\ N_v$		
38.0	0.33×10^{-3}	0.24×10^{-3}	Test Failure at N_v = 127 kips by concrete crushing; ADINA did not converge at N_v = 116 kips
76.0	2.81×10^{-3}	0.86×10^{-3}	
96.0	3.54×10^{-3}	1.61×10^{-3}	
115.0	4.48×10^{-3}	3.11×10^{-3}	

ρ = reinforcement ratio

Table 7.5
Steel Material Properties

Type of Steel	Yield Strength F_y (ksi)	Young's Modules E (ksi)	Strain Hardening Modules (ksi)
1. Stainless Steel Liner (SA-240, Type 304)	30	28300	0
2. Carbon Steel Liner (SA-516, Gr. 60)	32	29300	0
3. Reinforcing Steel (ASTM A615, Gr 60)	60	29000	1115

Table 7.6
Comparison of Elastic Responses from ADINA and DYNAX Models
(Dead Load Plus Seismic)

Elevation and Response	Azimuth = 0° ADINA	Azimuth = 0° DYNAX	Azimuth = 180° ADINA	Azimuth = 180° DYNAX
1. Base of containment wall				
Meridional moment (ft.kip/ft)	1306 (1122)*	949 (1000)*	957 (848)	757 (828)
Transverse shear (kip/ft)	129 (117)	108 (115)	97 (90)	95 (104)
Meridional force (kip/ft)	218 (223)	228 (226)	-322 (-325)	-340 (-338)
Hoop force (kip/ft)	473 (438)	366 (399)	-306 (-308)	-294 (-330)
2. Meridional force in containment wall 42 feet above basemat (kip/ft)	147 (146)	160 (160)	-229 (-228)	-248 (-248)
3. Basemat between drywell and containment walls, R = 49.5'				
Radial moment (ft. kip/ft) (2907)	3000 (2907)	3540 (2792)	2136 (2101)	2794 (2403)
Circumferential moment (ft kip/ft)	3287 (3194)	2987 (3160)	2607 (2375)	2206 (2450)
Transverse shear (kip/ft)	371 (369)	383 (375)	316 (318)	322 (336)

Elevation and Response	Aximuth = 90° ADINA	Aximuth = 90° DYNAX
4. Tangential shear in containment wall (kip/ft)		
42 feet above basemat	145 (145)	145 (145)

*Responses listed in paranthesis for ADINA column were obtained by ignoring steel element stiffnesses in calculation. Response listed in paranthesis for DYNAX column were obtained by deleting internal structures from Figure 4.18.

Table 7.7
Loading Increments

Step	Dead	Seismic (% Of Total For A_H = 1.0g)
1	100%	0
2	100%	20
3	100%	30
4	100%	40
5	100%	45
6	100%	50
7	100%	55
8	100%	60
9	100%	65
10	100%	70
11	100%	75
12	100%	77.5
13	100%	80
14	100%	82.5
15	100%	85
16	100%	87.5
17	100%	90
18	100%	92.5
19	100%	95
20	100%	97.5
21	100%	100
22	100%	100
23	100%	100

Table 7.8
Comparison Of Lateral Deflection Between ADINA
and NONLIN2 Models at A_H = 1.0 g

Location	ADINA Deflection (in)	NONLIN2 Deflection (in)
Elev. 854'-6"	1.47	1.76

Table 7.9
Effect of Cracking On Major* Shell Forces at
Base of Containment Wall and In Basemat (Task 3, A_H = 1.0g)

Elevation and Response	Aximuth = 0°		Aximuth = 180°	
	With Cracking	Without Cracking	With Cracking	Without Cracking
1. Base of containment wall Elev. 712'-0"				
1.1 Meridional moment (ft.kip/ft)	527	1306	1019	957
1.2 Transverse shear (kip/ft)	-48	-129	-100	-98
1.3 Meridional force (kip/ft)	171	218	-383	-322
2. Basemat (R = 49'6")				
2.1 Radial moment (ft.kip/ft)	2592	3000	1514	2136
2.2 Transverse shear (kip/ft)	375	371	-316	-316

*In-plane shear force is also major force, but values are not conveniently available to provide comparison.

Table 7.10
Comparison of Strains from ADINA Model
and Simplified Analysis (SA) (Task 3, A_H = 1.0g)

	Location of Strain	Strains x 10^{-3} ADINA	SA
1.	Containment wall at Elev. 719'-0"		
1.1	Principal tensile strain in liner		
	- Azimuth = 0°	0.500	0.766
	- Azimuth = 30°	0.676	0.669
	- Azimuth = 60°	0.470	0.440
1.2	Outside meridional rebar strain		
	- Azimuth = 0°	1.260	1.731
	- Azimuth = 30°	1.100	1.500
	- Azimuth = 60°	0.680	1.072
1.3	Inside meridional rebars strain		
	- Azimuth = 0°	0.129	0.061
	- Azimuth = 30°	0.120	0.053
	- Azimuth = 60°	0.096	0.059
1.4	Average concrete meridional strain		
	- Azimuth = 180°	-0.150	-0.131
2.	Containment wall at Elev. 752'-0"		
2.1	Principal tensile strain		
	- Azimuth = 0°	0.350	0.290
	- Azimuth = 30°	0.560	0.250
	- Azimuth = 60°	0.490	0.200
2.2	Meridional rebar strain		
	- Azimuth = 0°	0.330	0.492
	- Azimuth = 30°	0.390	0.489
	- Azimuth = 60°	0.267	0.393
2.3	Average concrete meridional strain		
	- Azimuth = 180°	-0.129	-0.110
3.	Basemat at radius of 49'-6" (between drywell and containment walls)		
3.1	Principal tensile strain in liner		
	- Azimuth = 0°	0.602	0.923
3.2	Top radial rebar		
	- Azimuth = 0°	0.524	0.925
3.3	Bottom radial rebar		
	- Azimuth = 180°	0.610	1.240

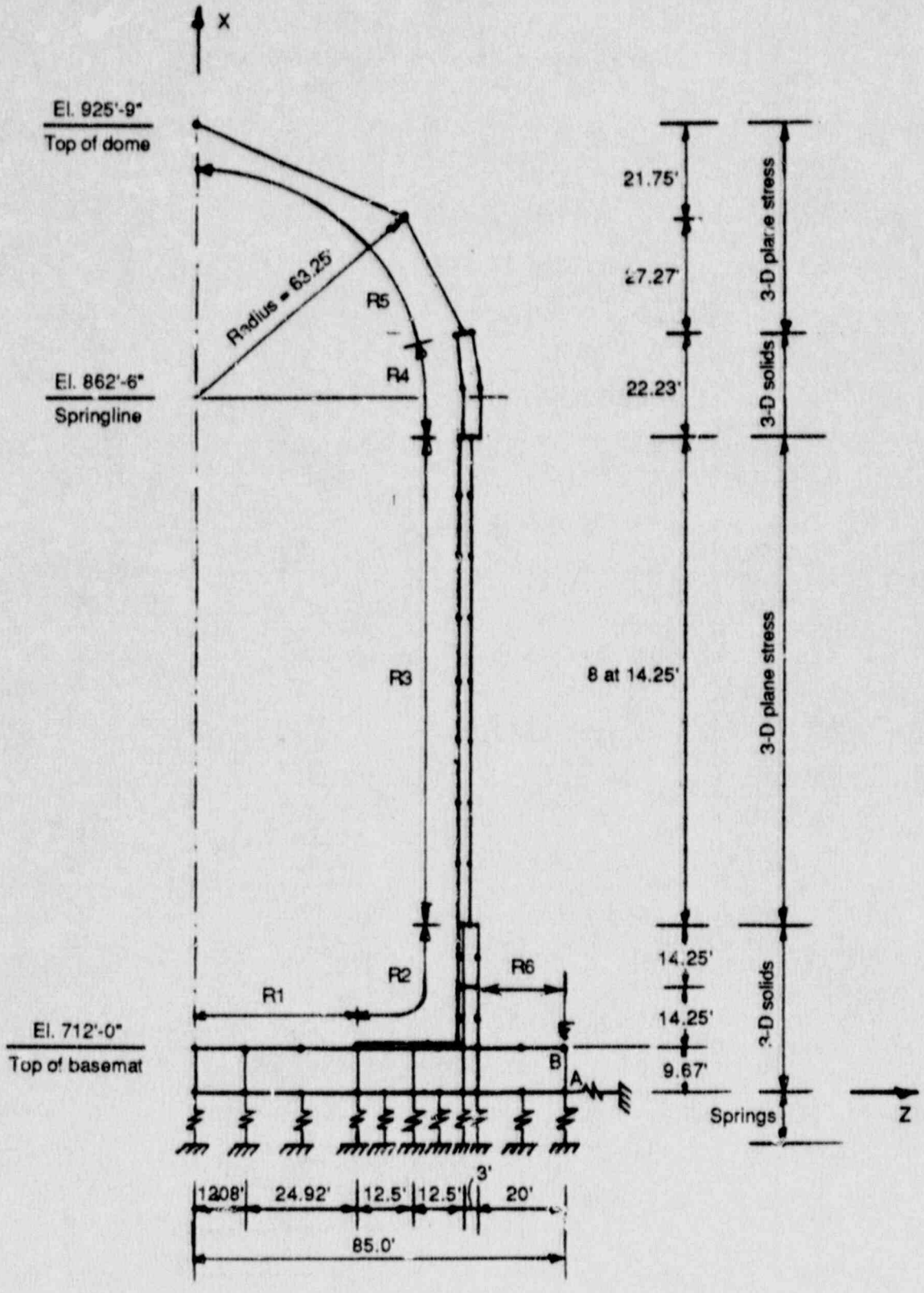

Figure 7.1 Elevation View of the Analytical Model

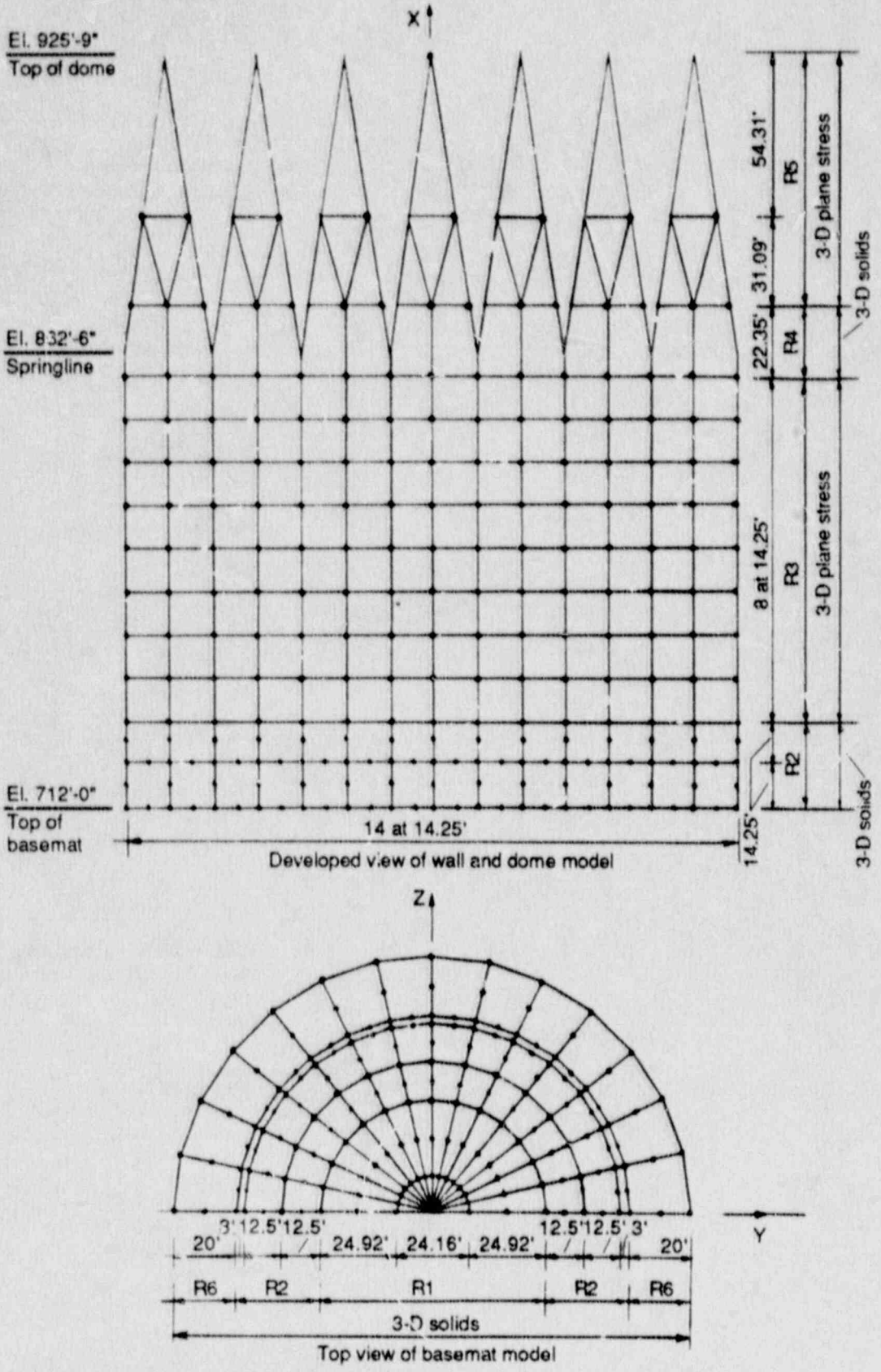

Figure 7.2 Developed View of the Analytical Model

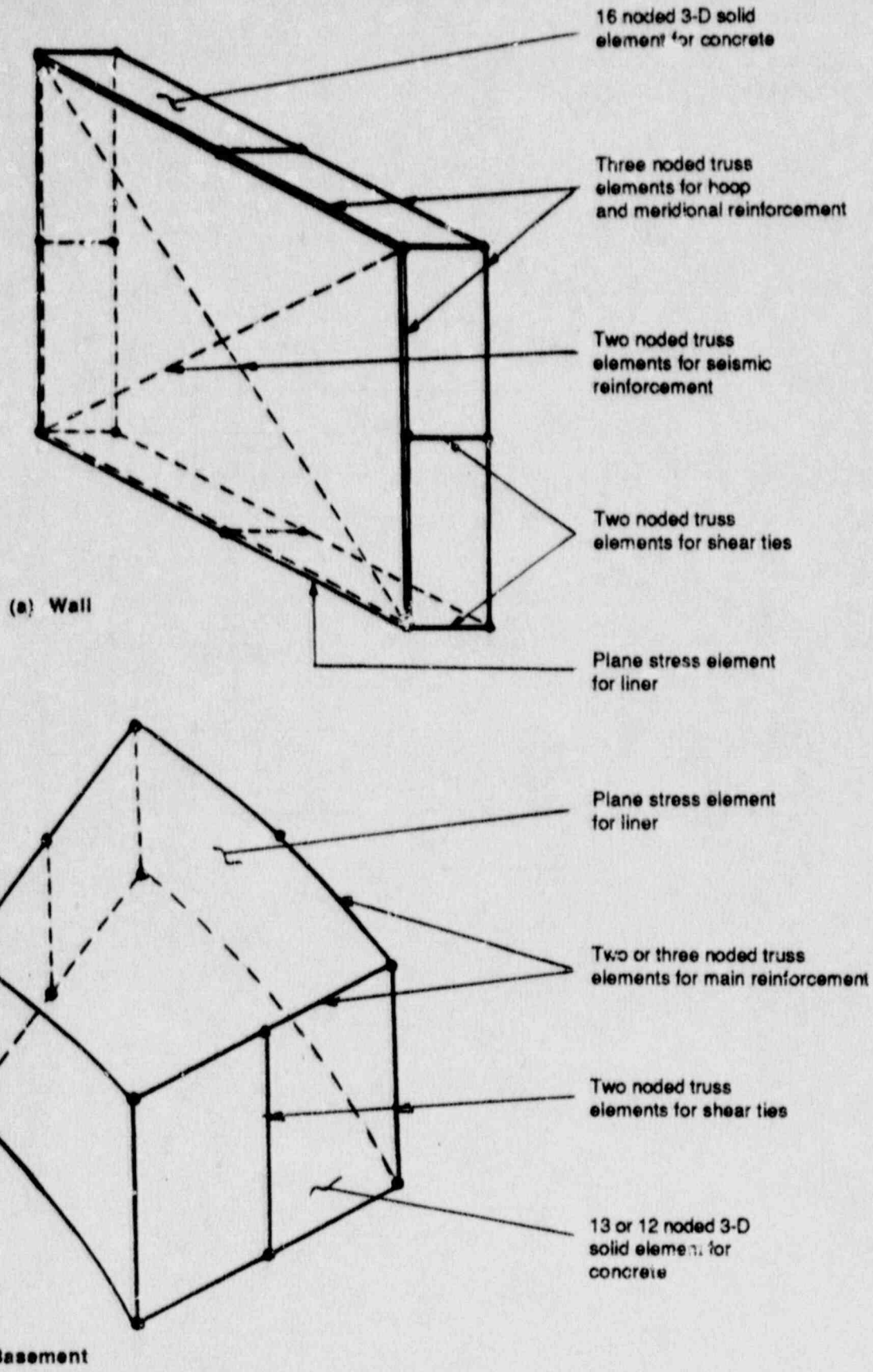

Figure 7.3 Arrangement of Elements in Zone R2

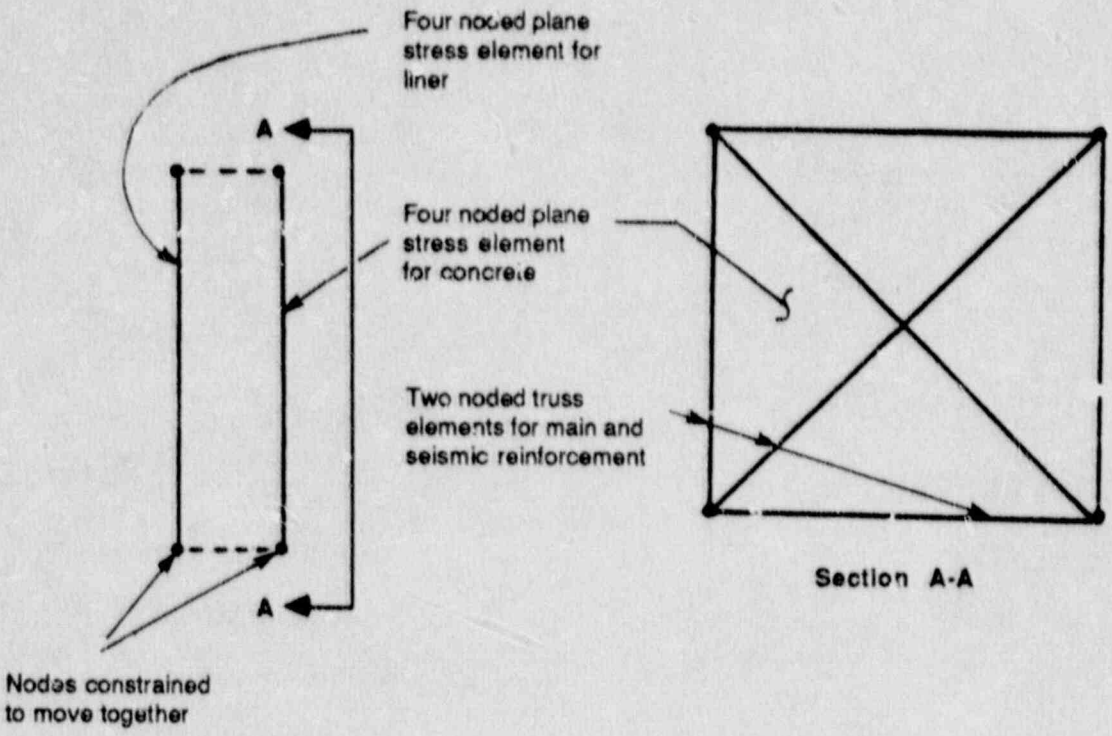

Figure 7.4 Arrangement of Elements in Zone R3

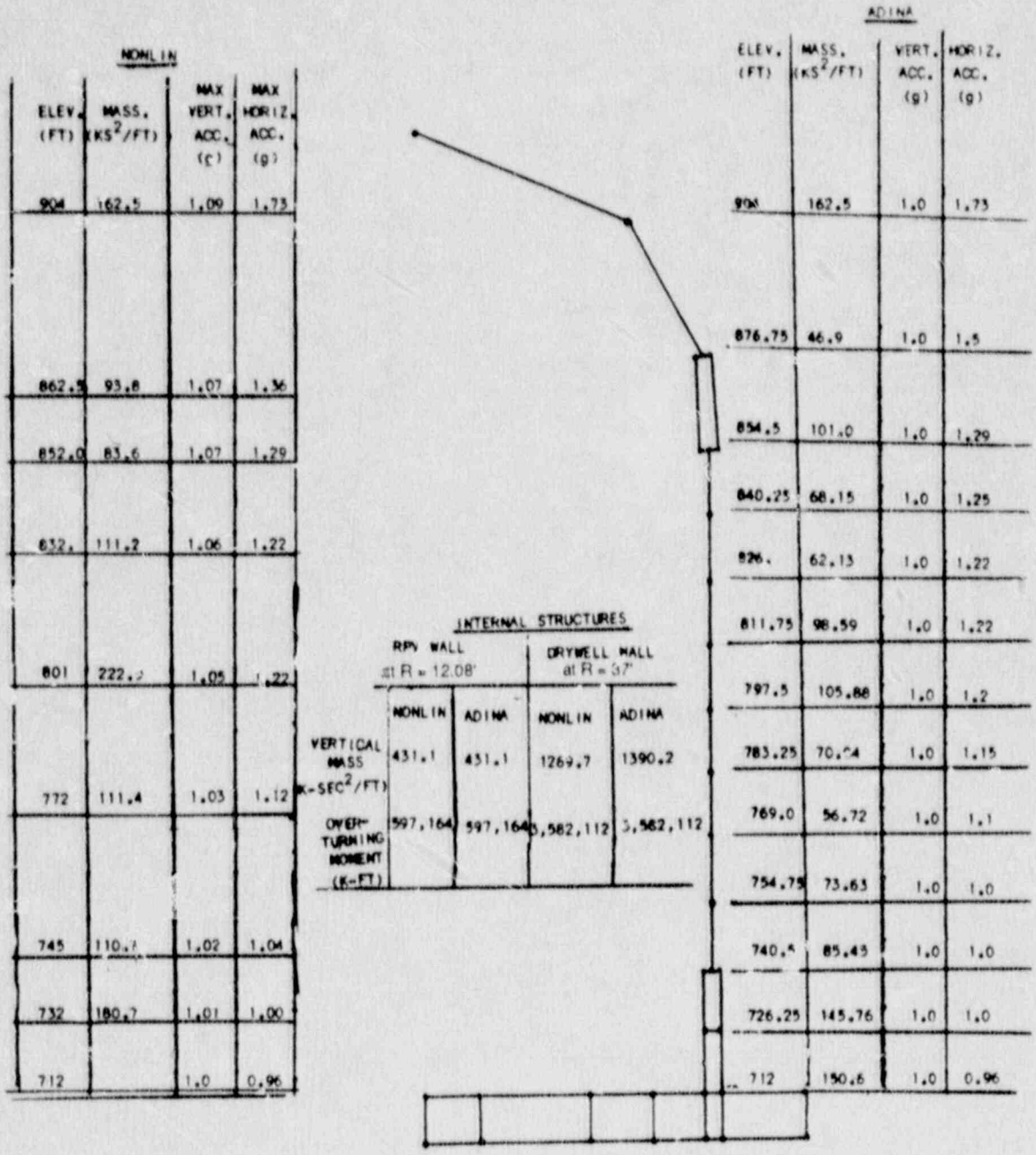

Figure 7.5 Description of Peak Loads Statically Applied in ADINA

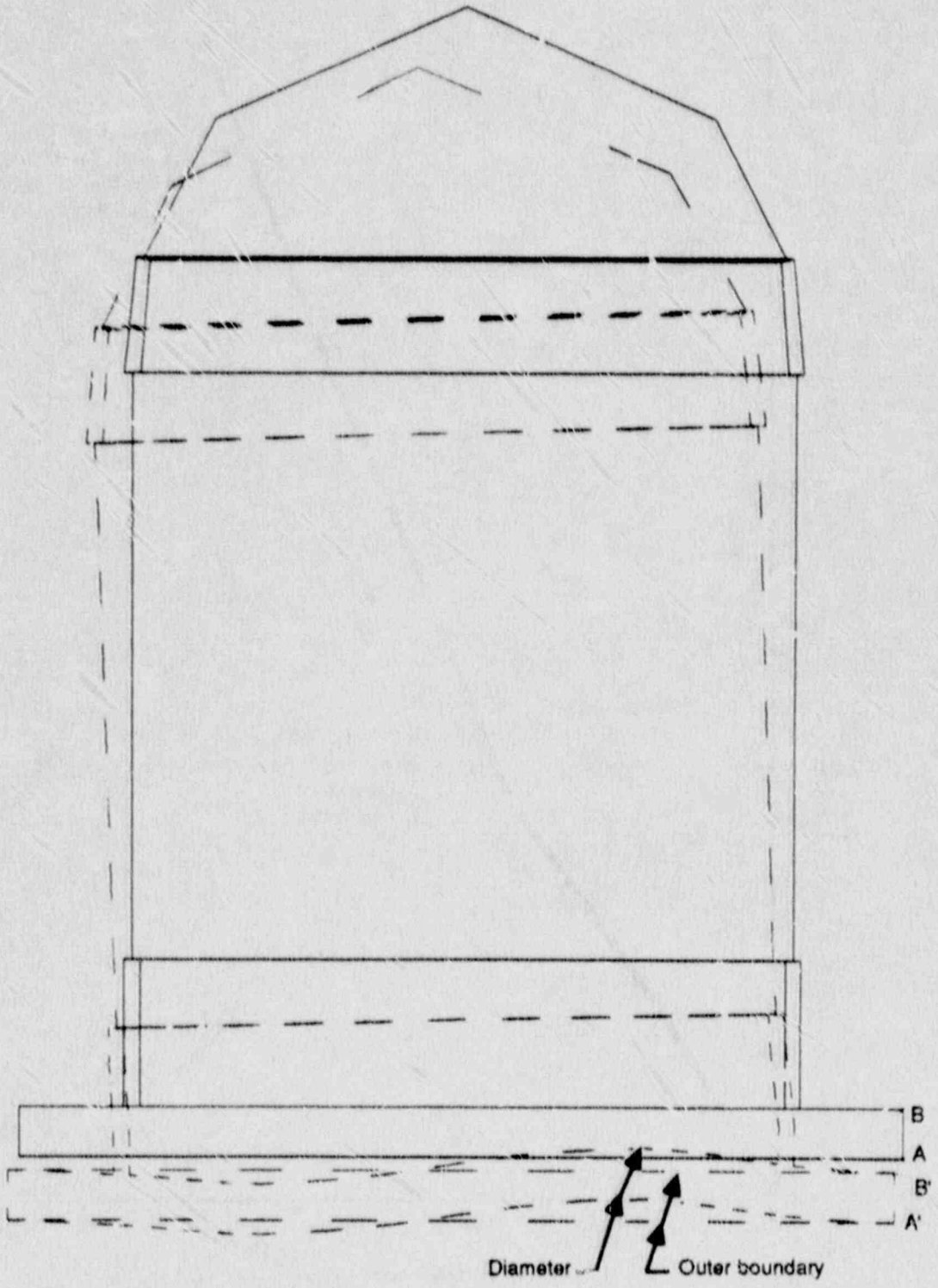

Figure 7.6 Deformed Shape of Structure for Task 3 (Dead Load plus Seismic at A_H = 1.0 g)

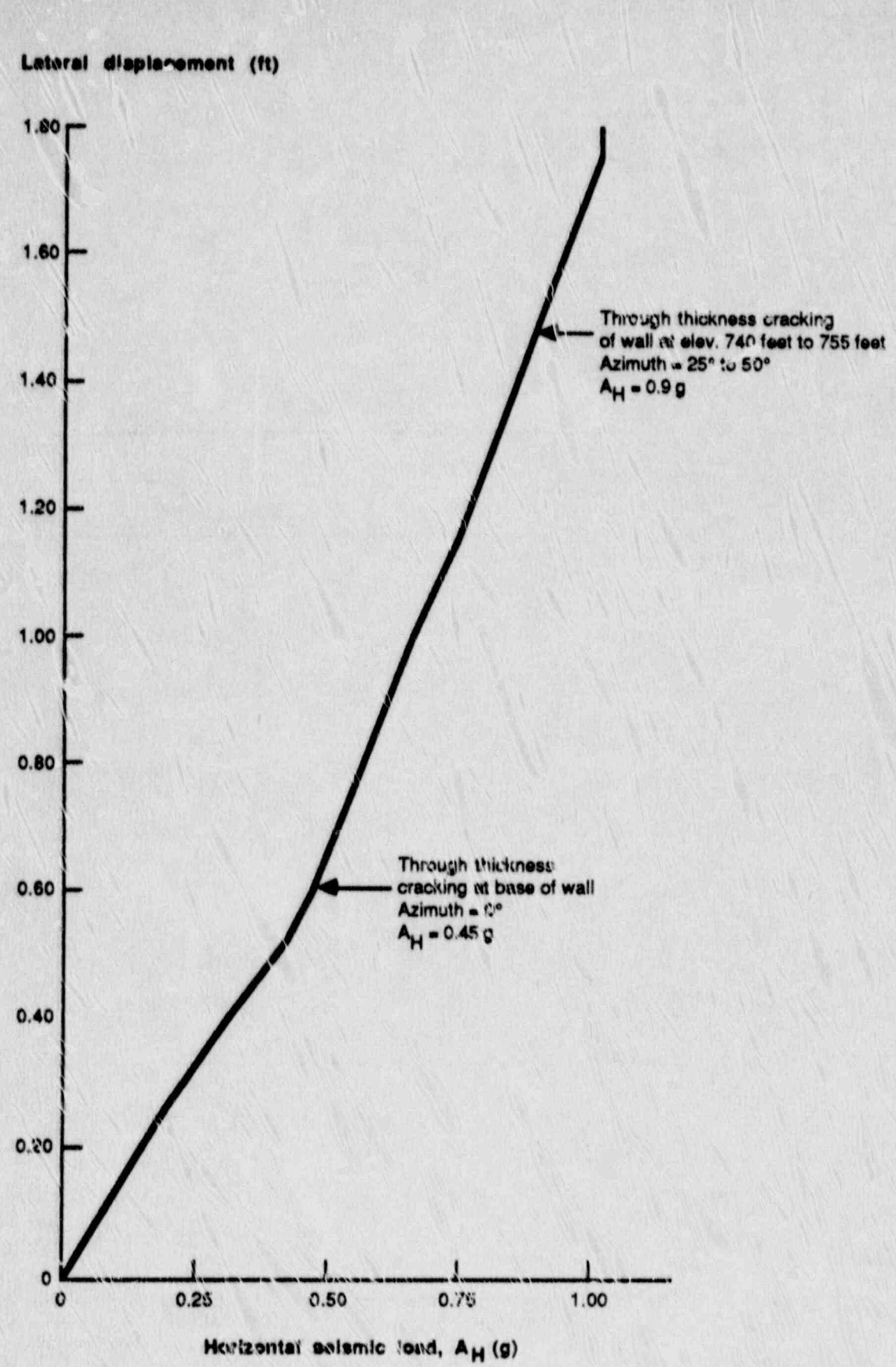

Figure 7.7 Horizontal Displacement Near Spring Line as Function of Seismic Load (Elevation 854.5 Feet, Azimuth = 90°)

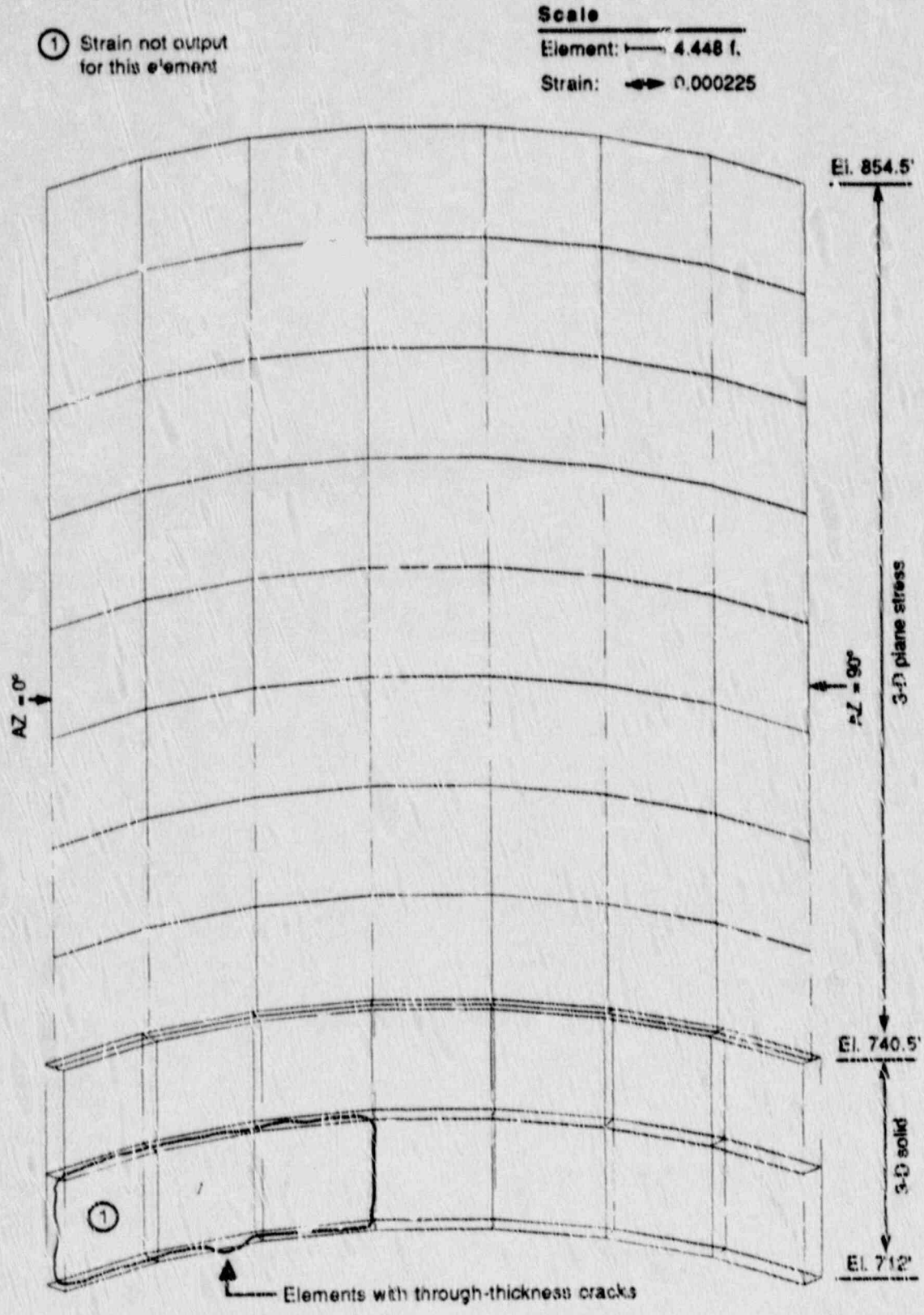

Figure 7.8 Major Principal Tensile Strain in Concrete Elements Having Through-Thickness Cracks (Containment Wall, $0° \leq AZ \leq 90°$, Task 3, $A_H = 0.5$ g)

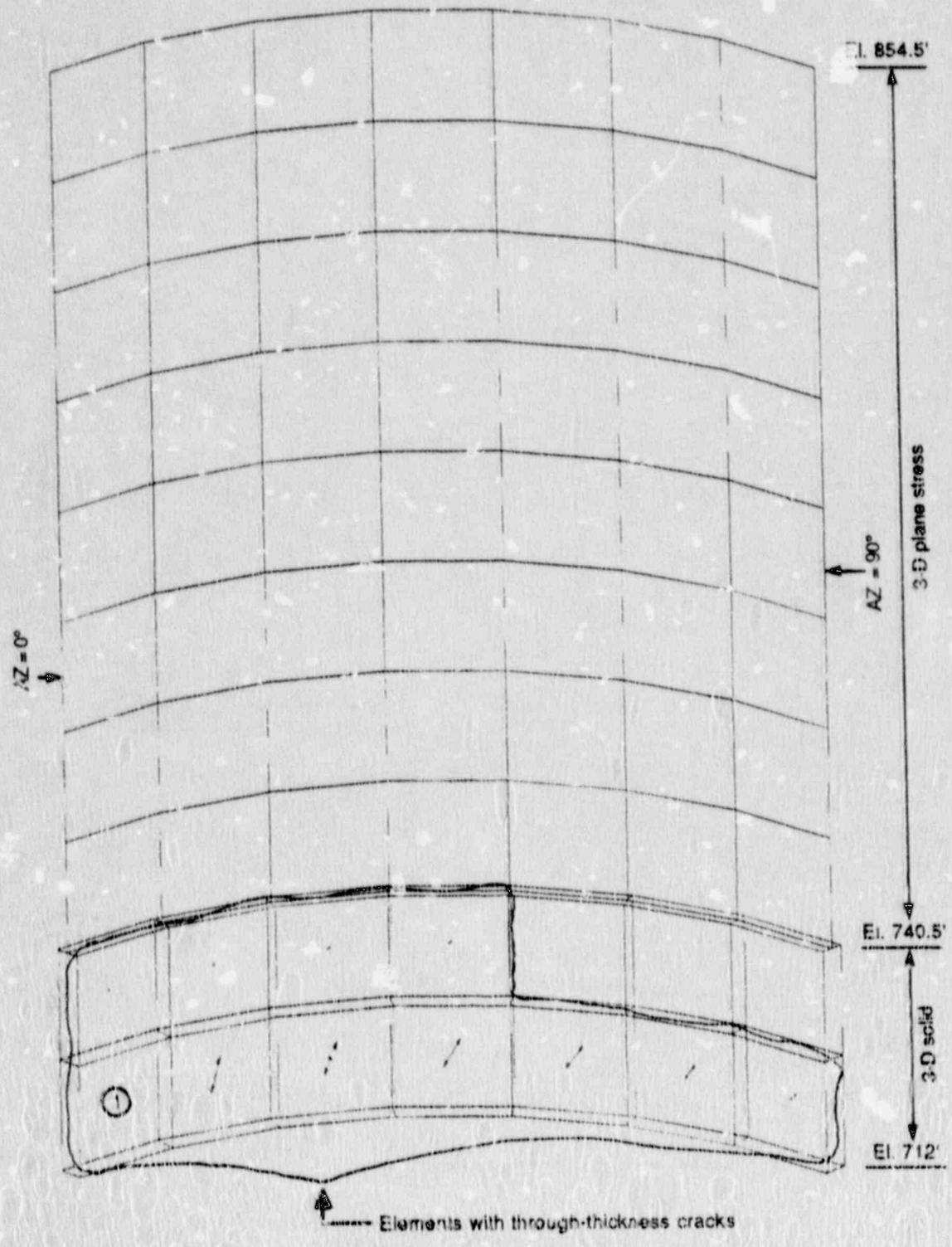

Figure 7.9 Major Principal Tensile Strain in Concrete Elements Having Through-Thickness Cracks (Containment Wall, $0° \leq AZ \leq 90°$, Task 3, $A_H = 0.75$ g)

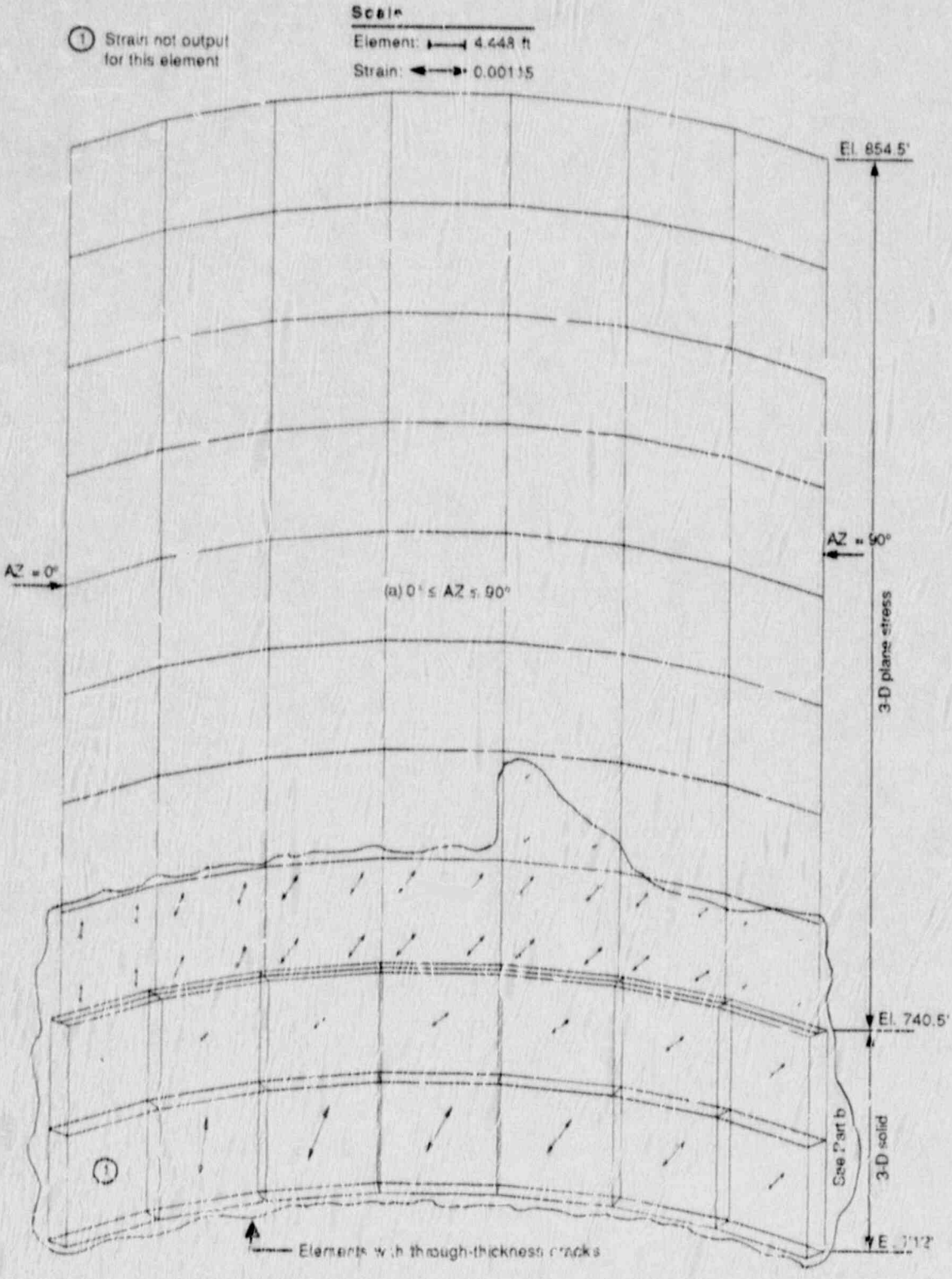

Figure 7.10a Major Principal Tensile Strain in Concrete Elements Having Through-Thickness Cracks (Containment Wall, a - 0° ≤ AZ ≤ 90°, b - 90° ≤ AZ ≤ 180°, Task 3, A_H = 1.0 g)

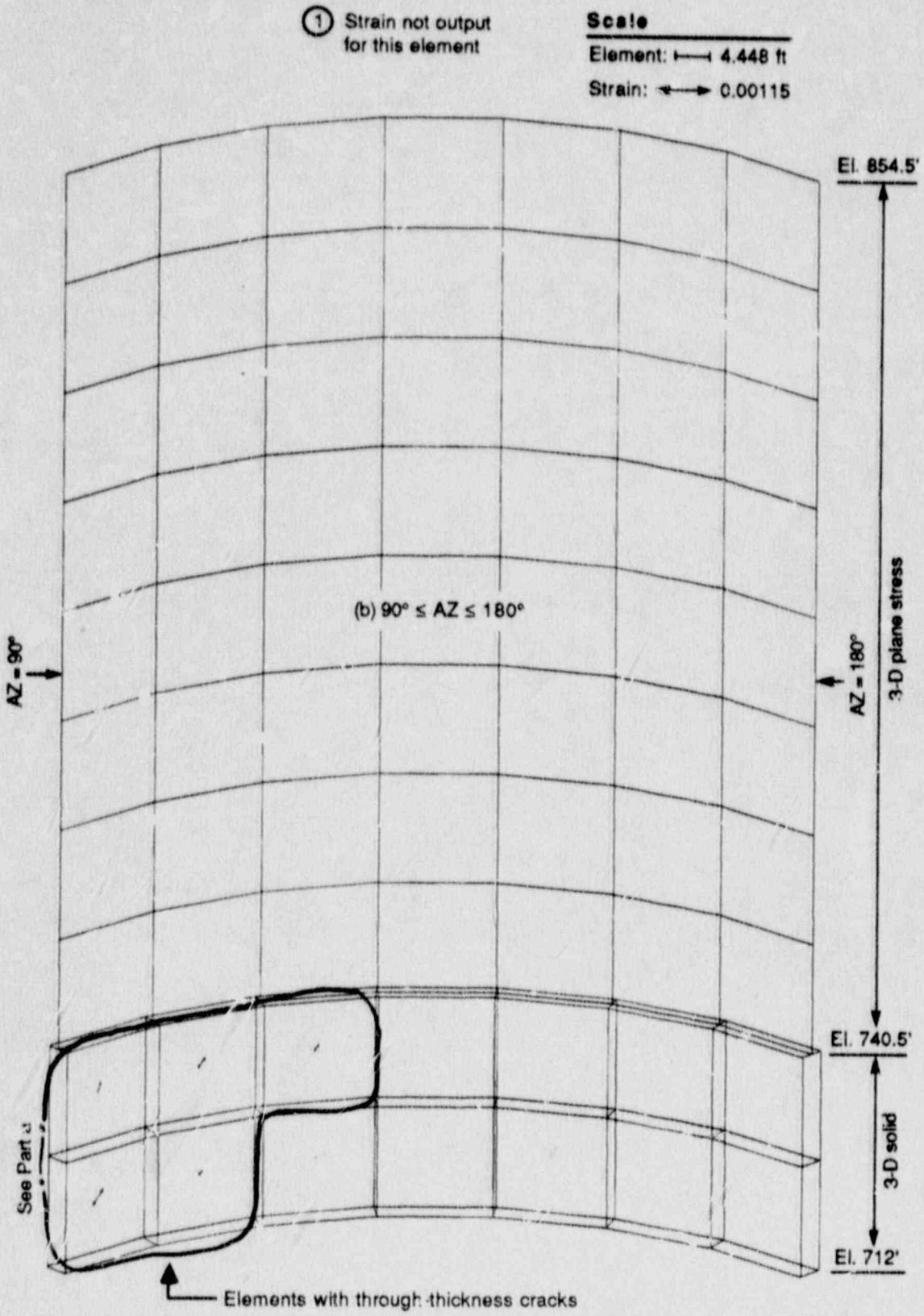

Figure 7.10b Major Principal Tensile Strain in Concrete Elements Having Through-Thickness Cracks (Containment Wall, a - 0° ≤ AZ ≤ 90°, b - 90° ≤ AZ ≤ 180°, Task 3, A_H = 1.0 g)

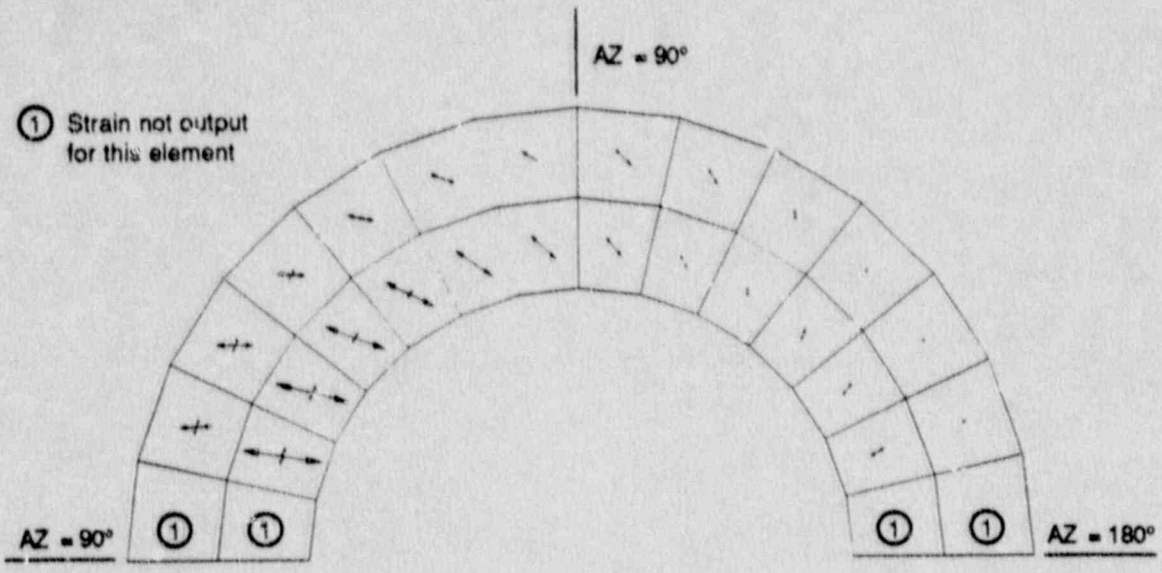

(a) Top face

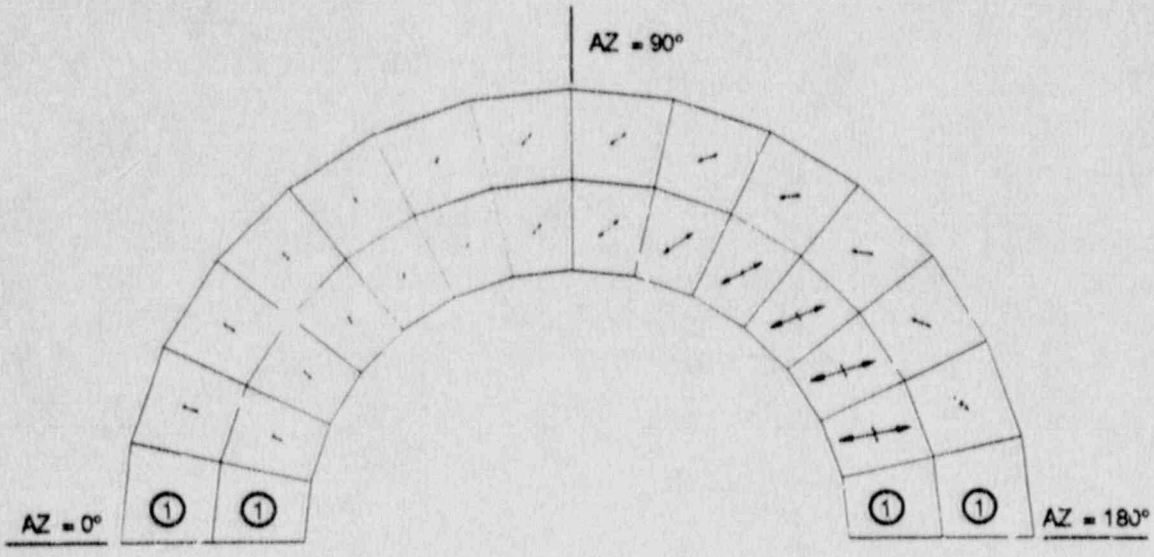

(b) Bottom face

Figure 7.11 Principal Tensile Strains at Top and Bottom Faces of Concrete Elements in Basemat Zone R2 (Task 3, A_H = 1.0 g)

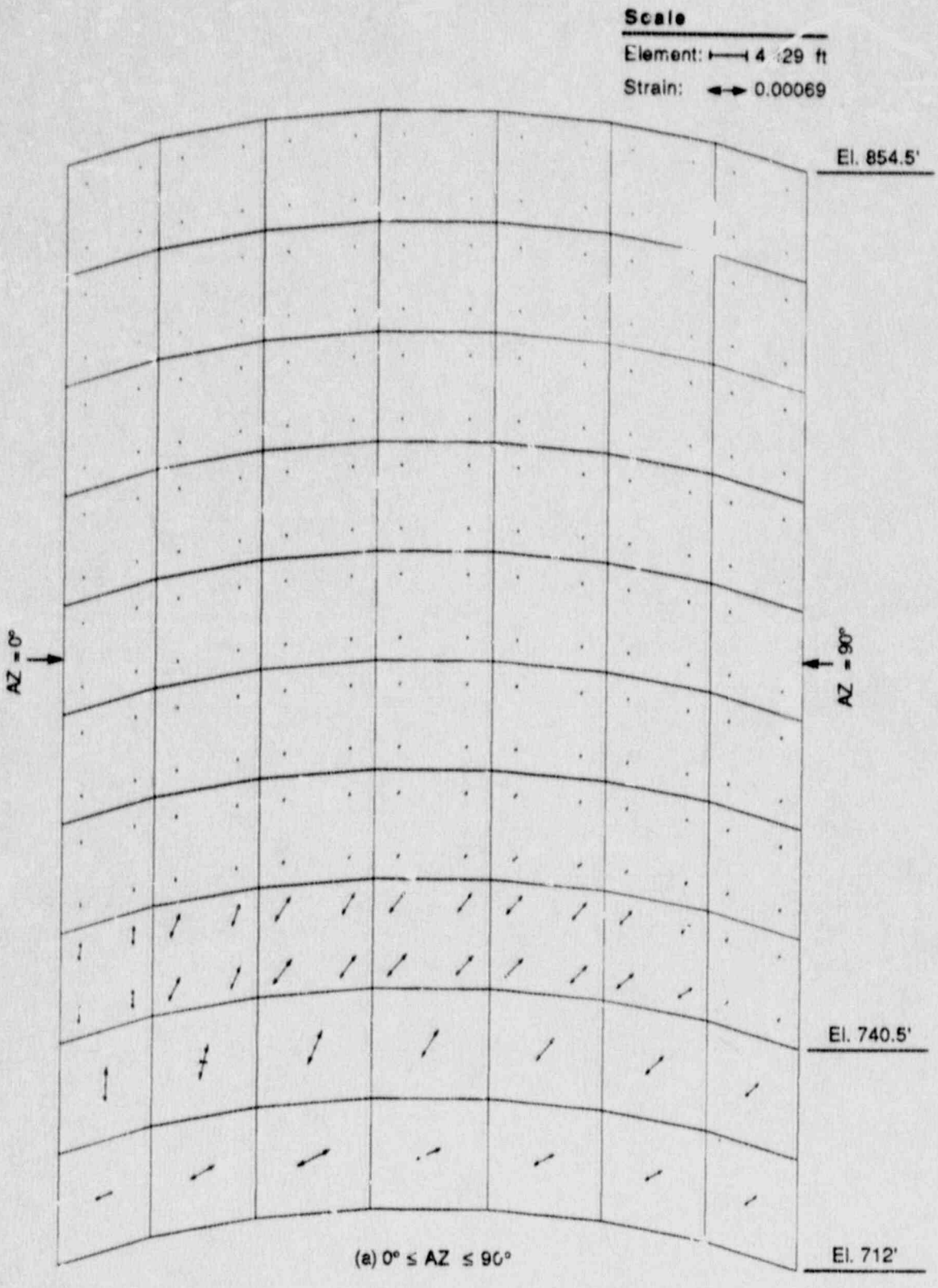

Figure 7.12a Principal Tensile Strains in Containment Wall Liner (a - 0° ≤ AZ ≤ 90°, b - 90° ≤ AZ ≤ 180°, Task 3, A_H = 1.0 g)

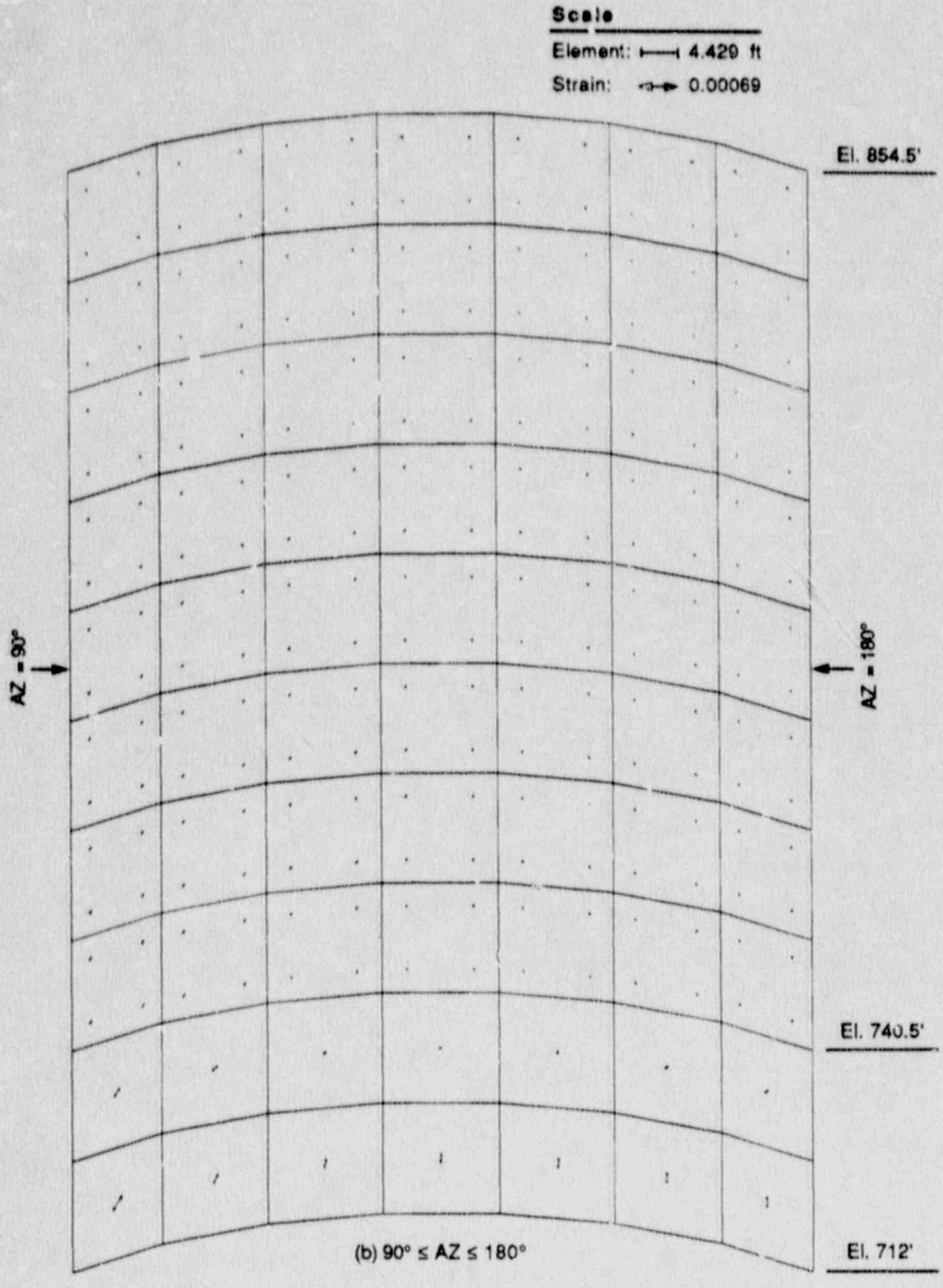

Figure 7.12b Principal Tensile Strains in Containment Wall Liner (a - 0° ≤ AZ ≤ 90°, b - 90° ≤ AZ ≤ 180°, Task 3, A_H = 1.0 g)

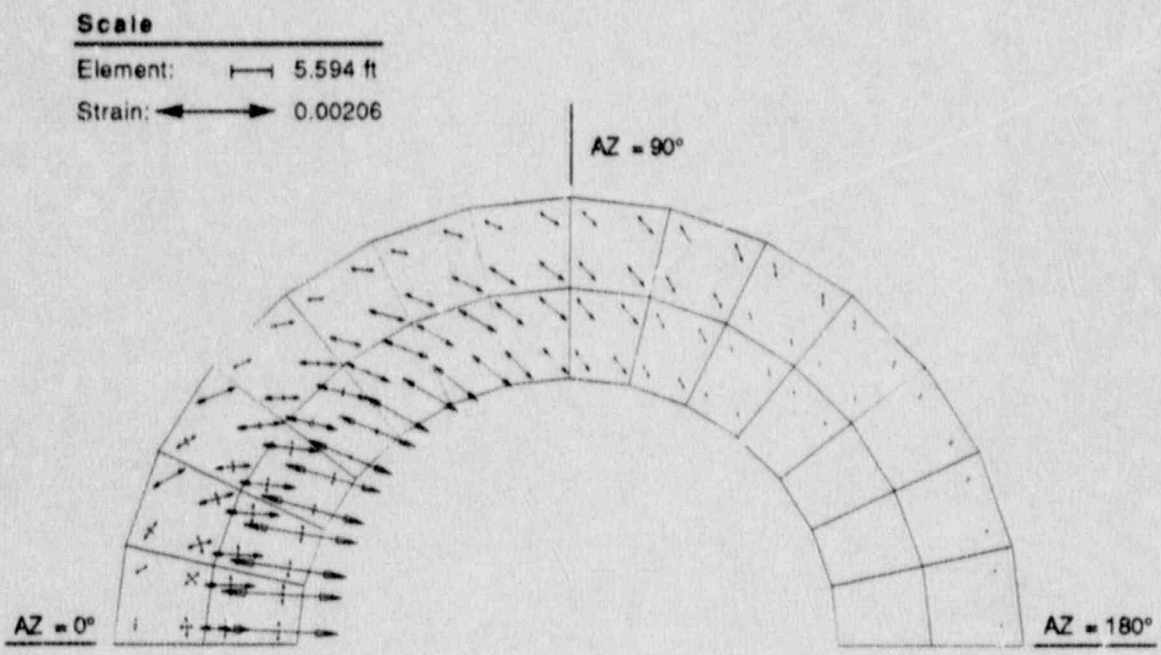

Figure 7.13 Principal Tensile Strains in Basemat Liner (Zone R2, Task 3, A_H = 1.0 g)

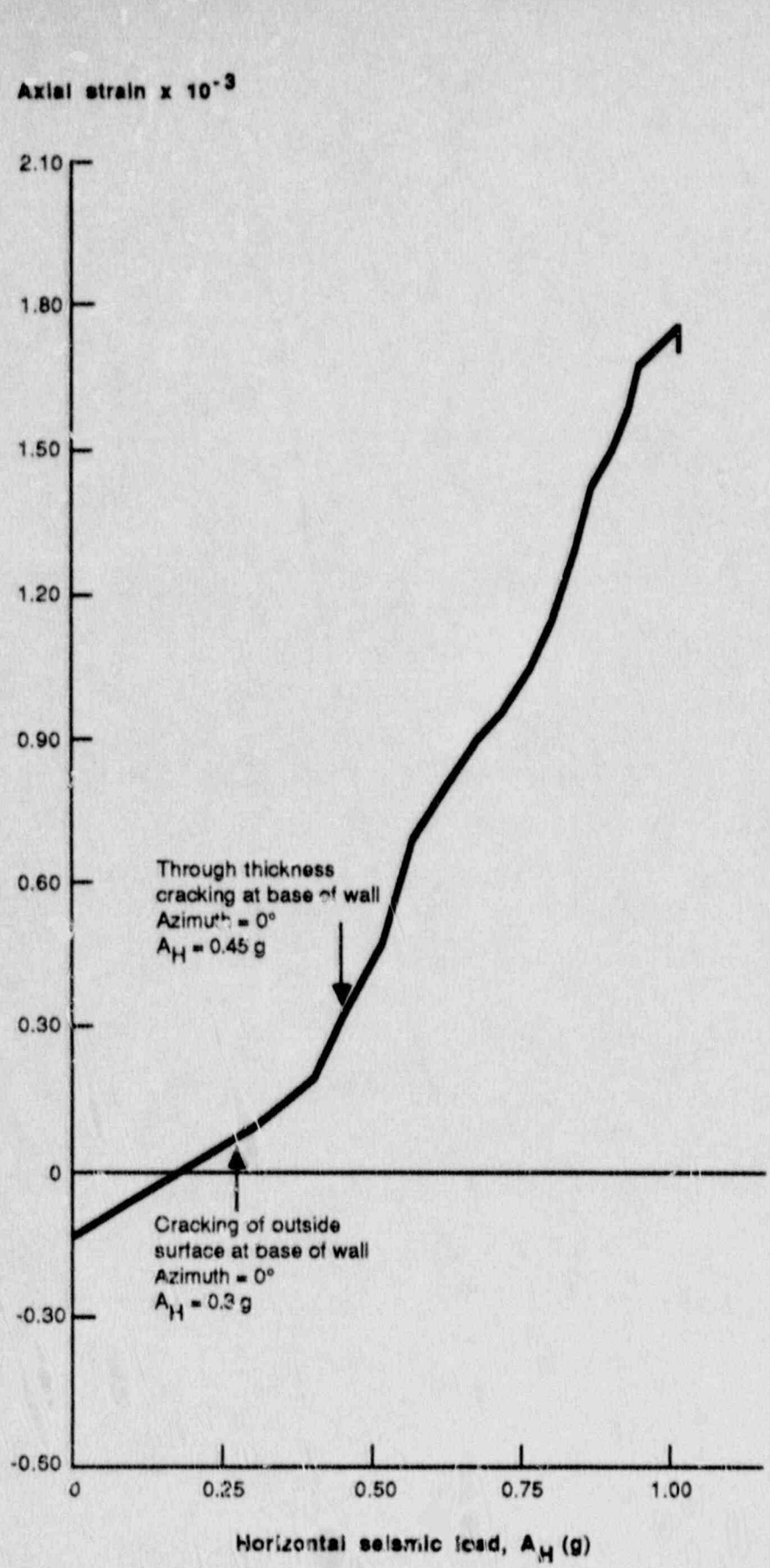

Figure 7.14 Variation of Meridional Wall Rebar Strain with Seismic Load Level (Task 3, Outside Rebar, Elevation = 715 Feet, Azimuth = 0°)

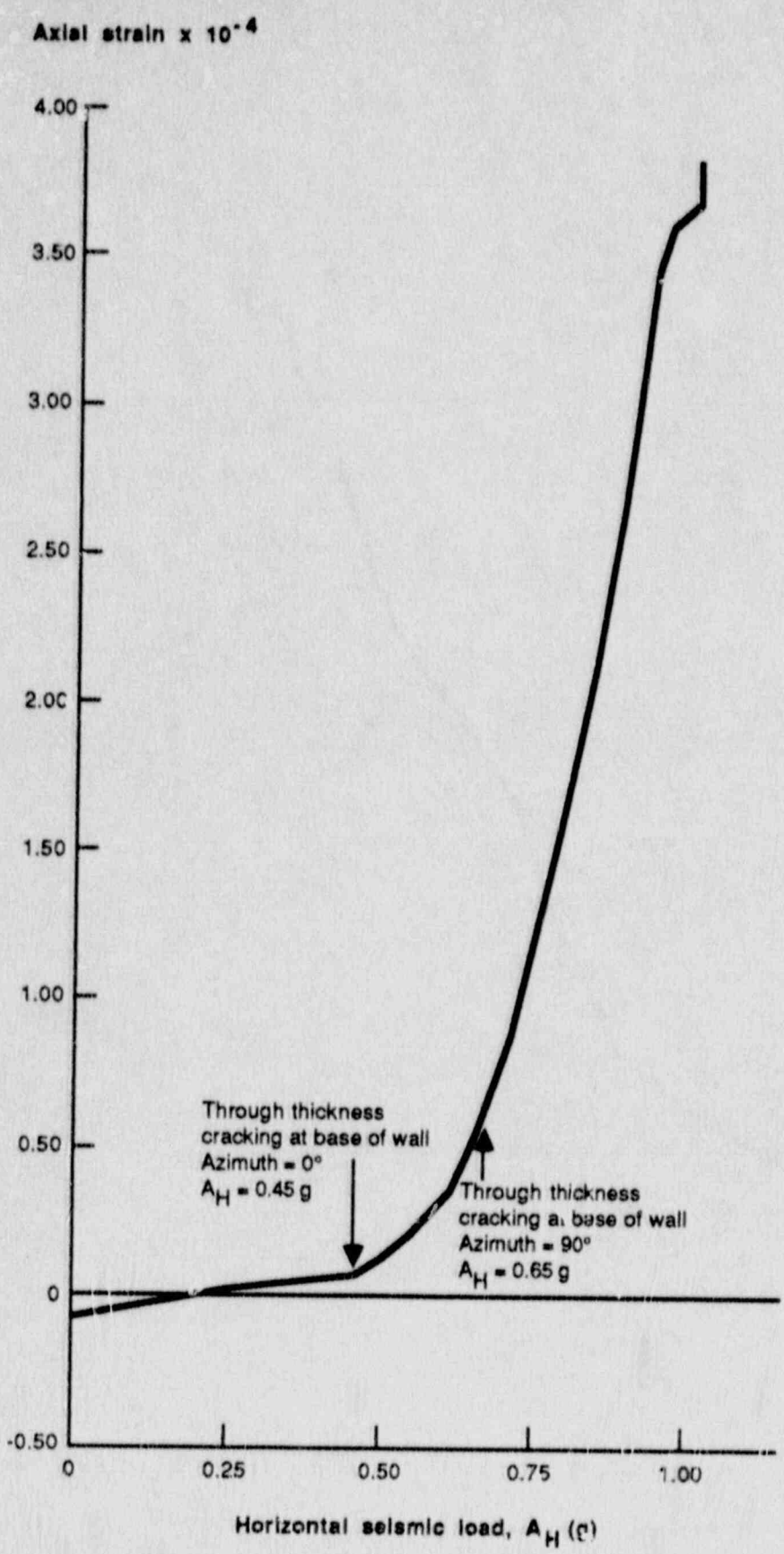

Figure 7.15 Variation of Seismic Rebar Strain with Seismic Load Level (Task 3, Containment Wall, Elevation = 719 Feet, Azimuth = 84°)

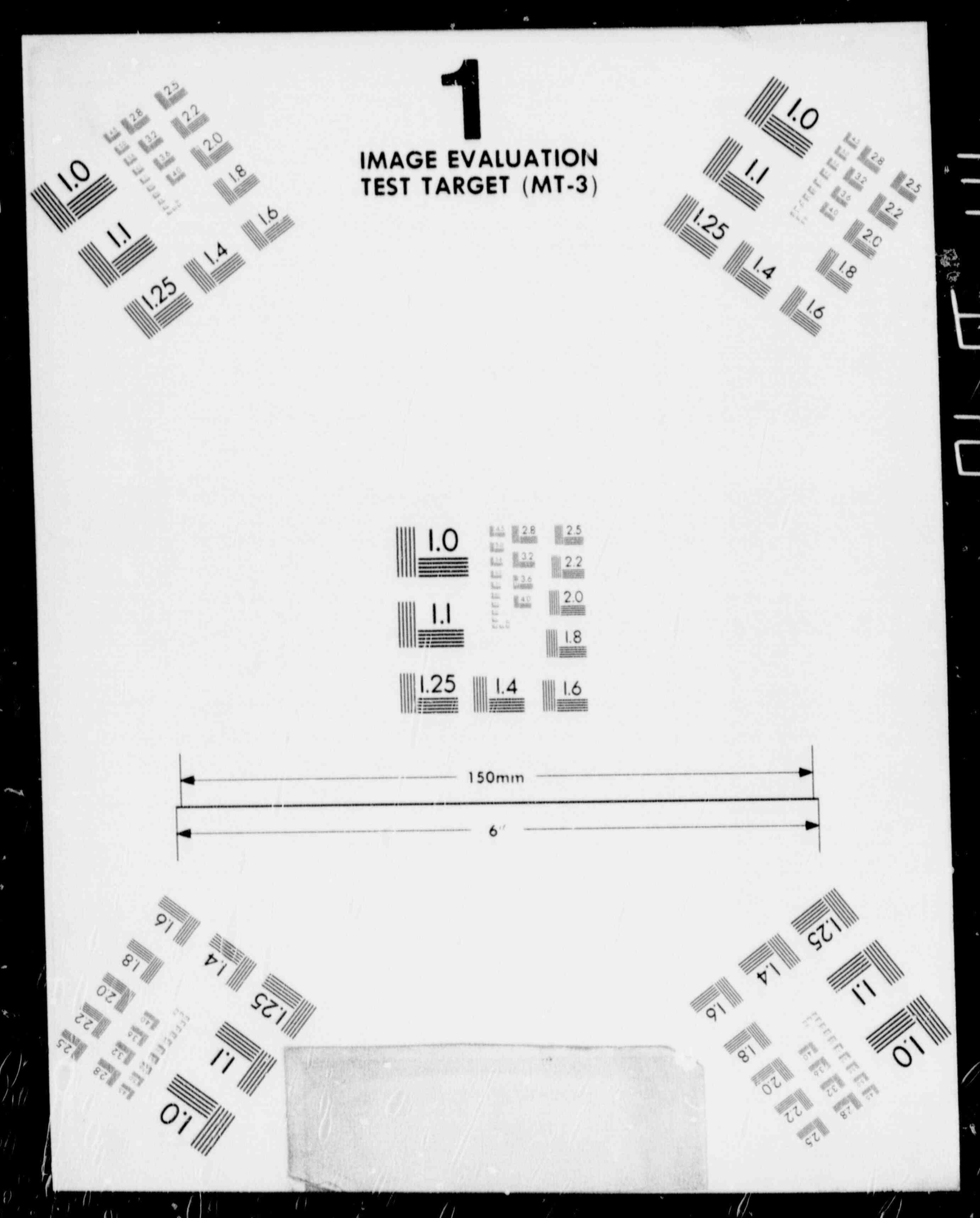
1
IMAGE EVALUATION
TEST TARGET (MT-3)
1.0
1.1
1.25
1.4
1.6
1.8
2.0
2.2
2.5
2.8
3.2
3.6
4.0
150mm
6"

1

IMAGE EVALUATION TEST TARGET (MT-3)

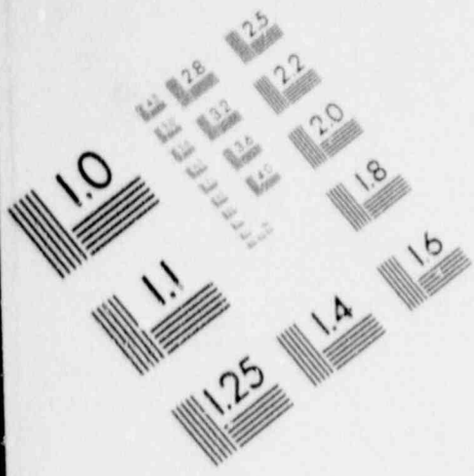

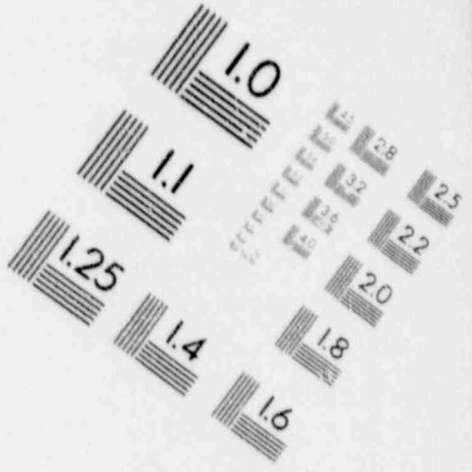

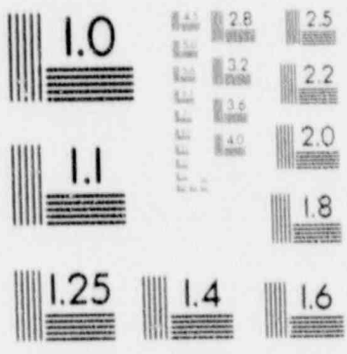

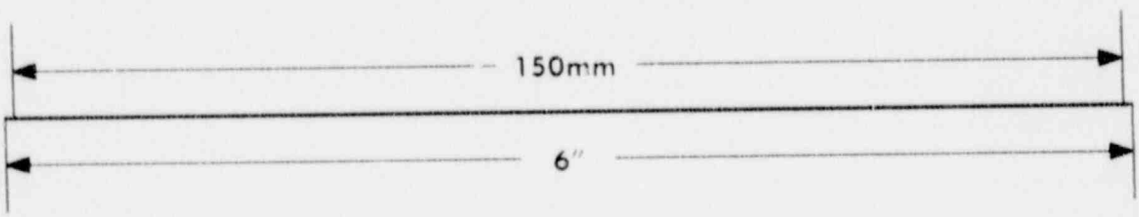

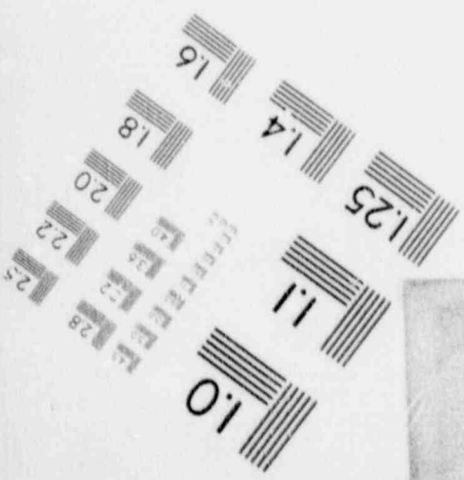

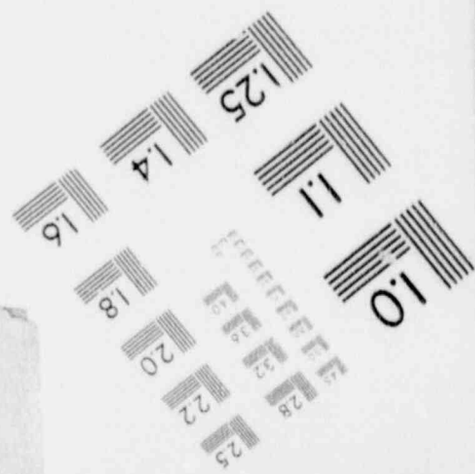

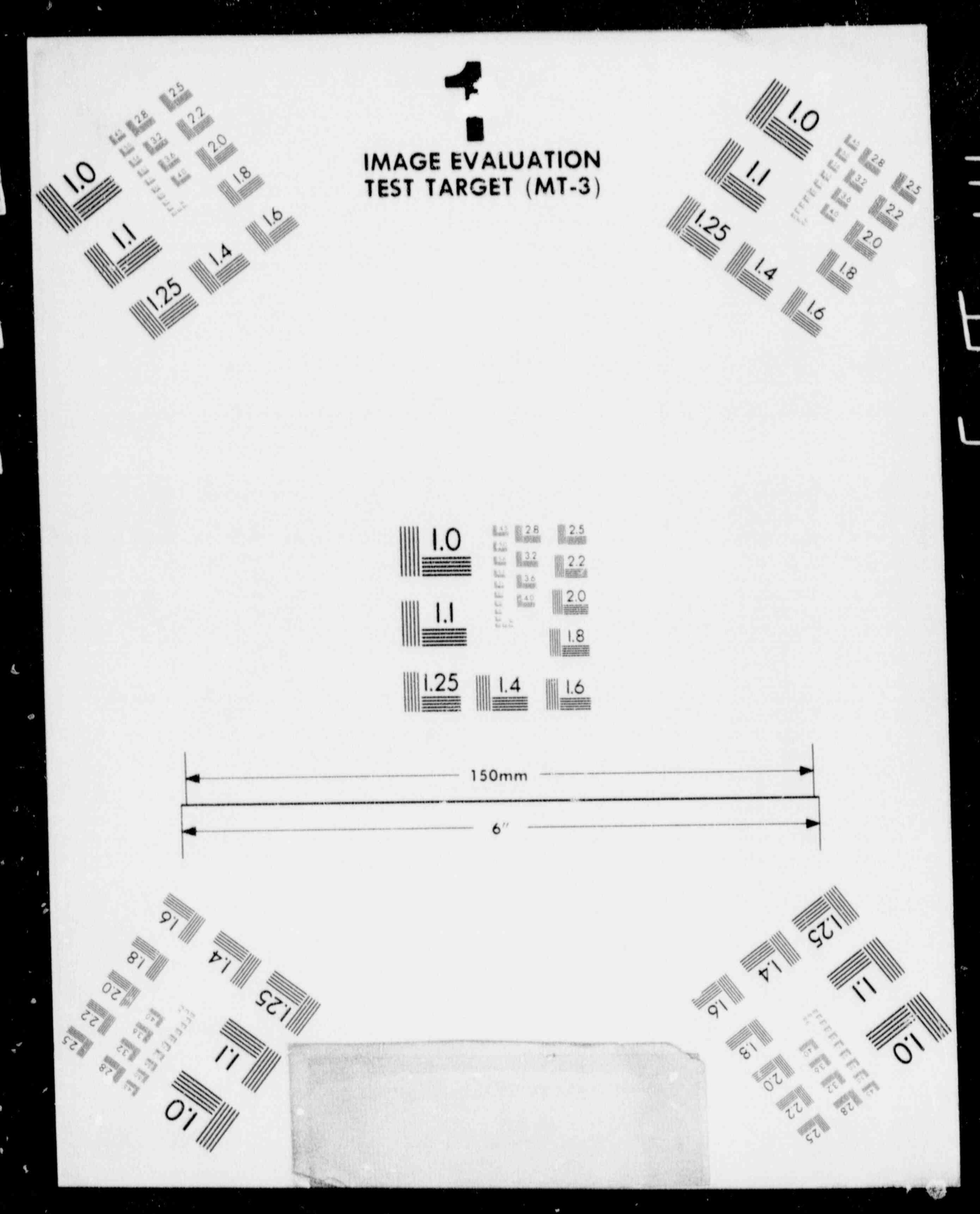
IMAGE EVALUATION
TEST TARGET (MT-3)
1.0
1.1
1.25
1.4
1.6
1.8
2.0
2.2
2.5
2.8
3.2
3.6
4.0
150mm
6"

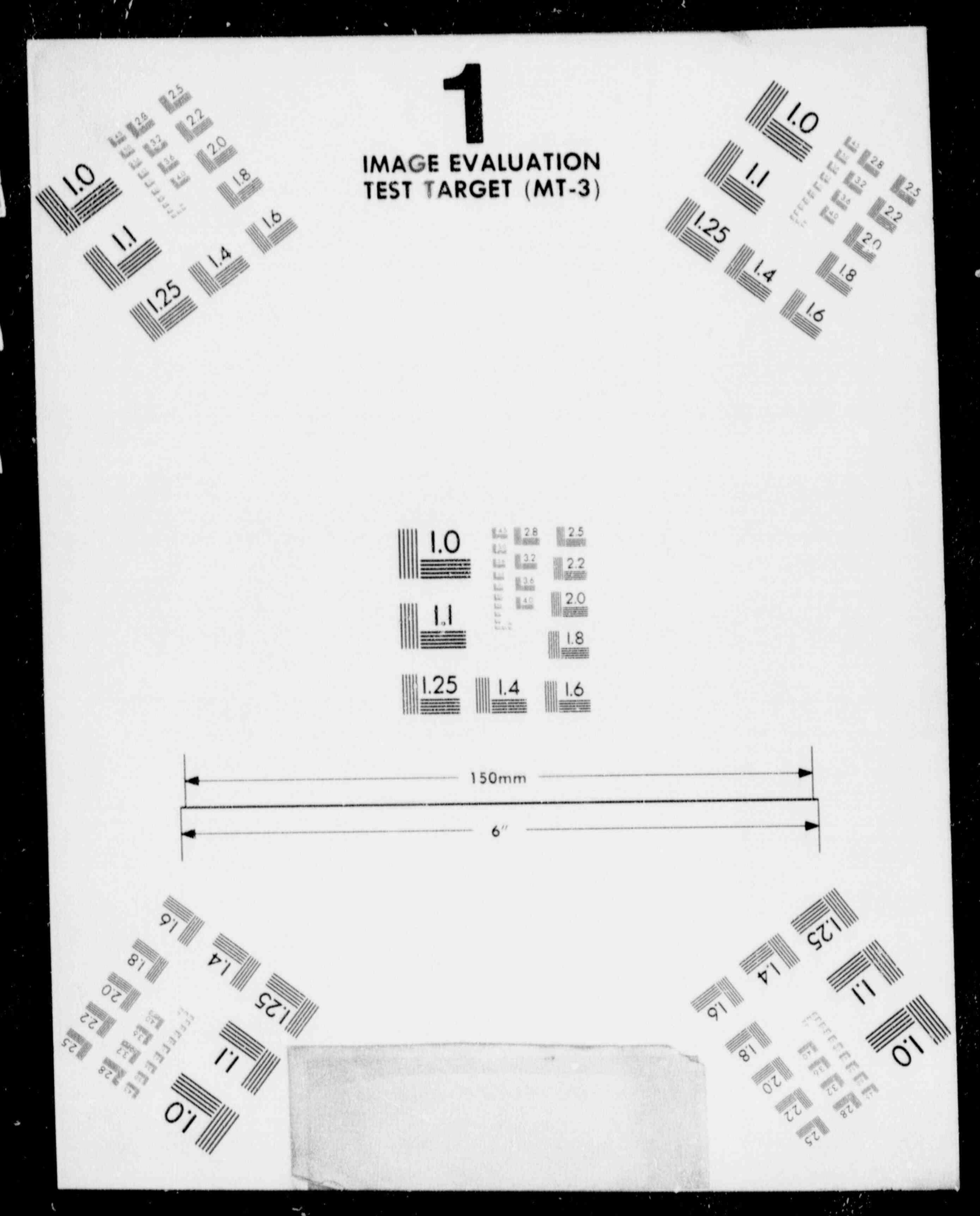
1
IMAGE EVALUATION
TEST TARGET (MT-3)
1.0
1.1
1.25
1.4
1.6
1.8
2.0
2.2
2.5
2.8
3.2
3.6
4.0
150mm
6"

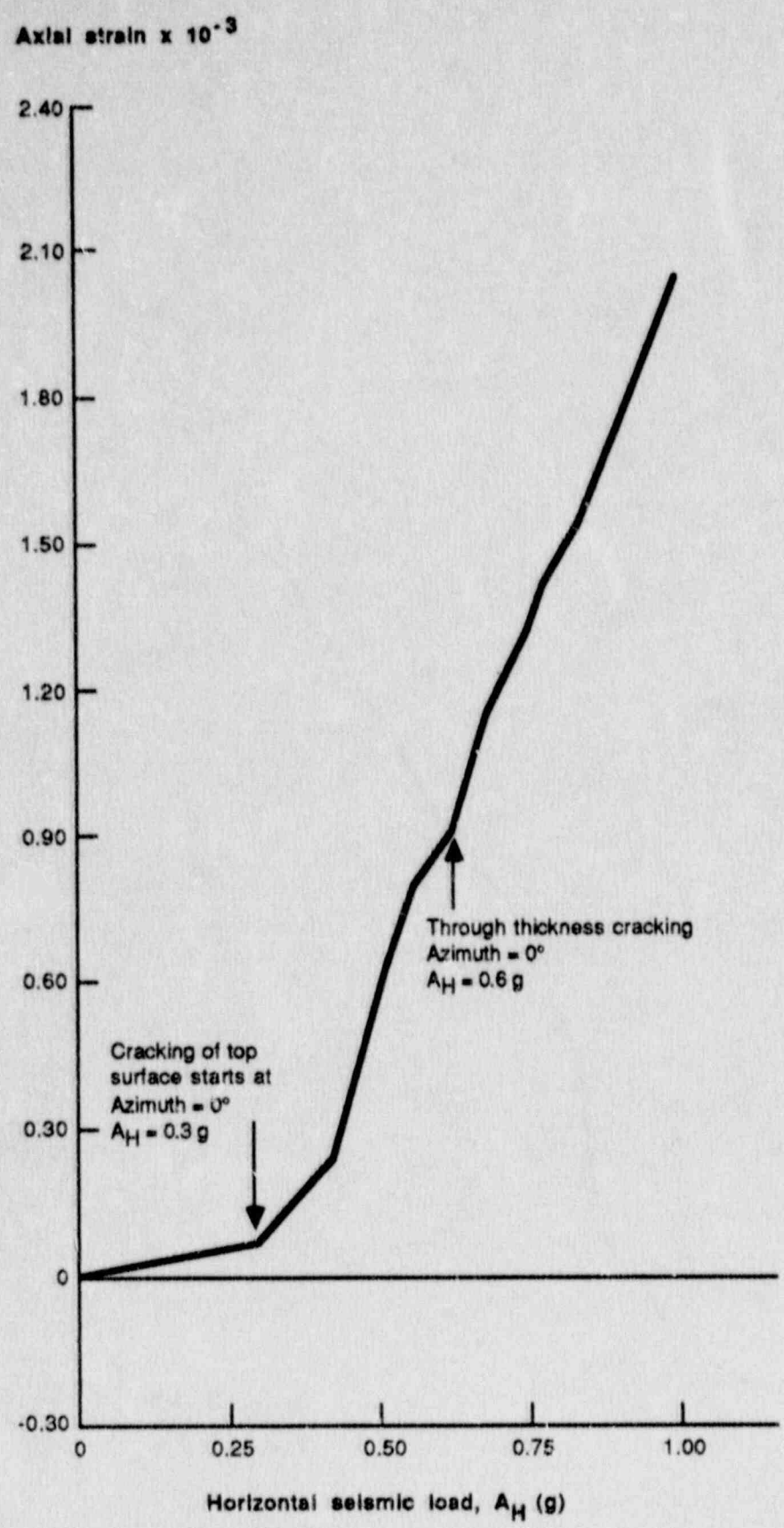

Figure 7.16 Variation of Top Basemat Rebar Strain with Seismic Load Level (Task 3, Radial Rebar Near Drywell, R = 39.6 Feet, Azimuth = 0°)

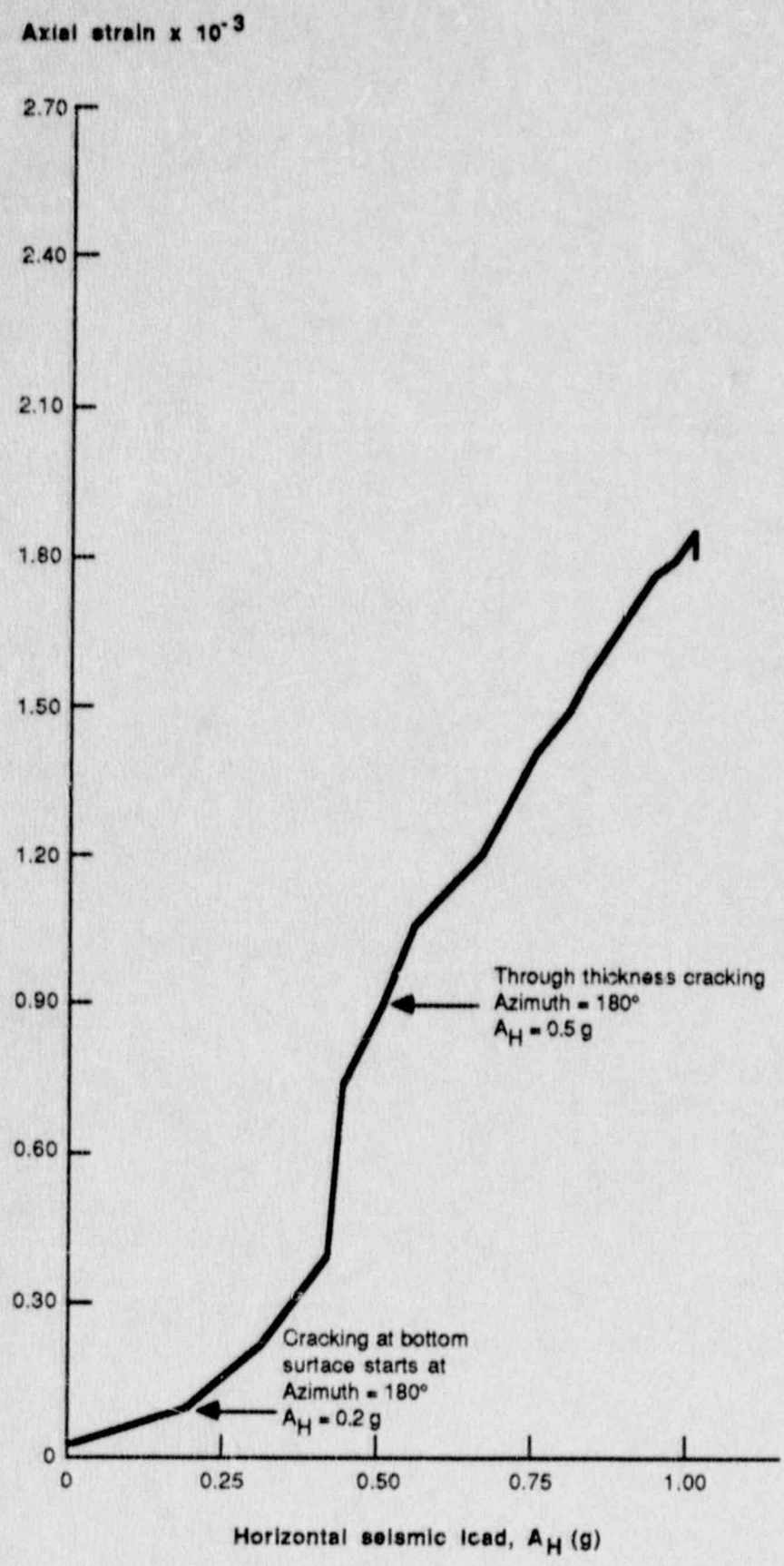

Figure 7.17 Variation of Bottom Basemat Rebar Strain with Seismic Load Level (Task 3, Radial Rebar Near Drywell Wall, R = 39.6 Feet, Azimuth = 180°)

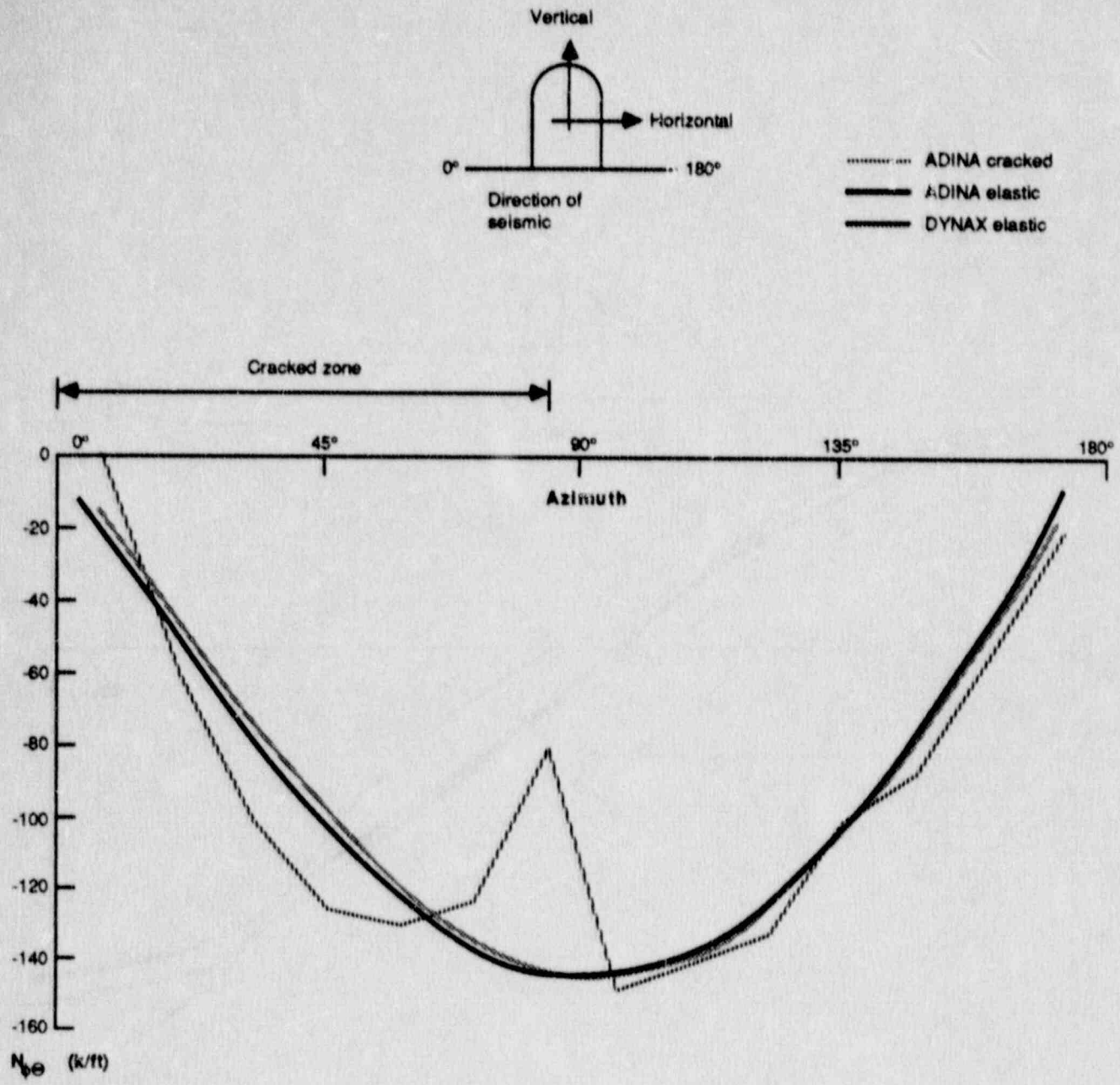

Figure 7.18 Circumferential Variation of Total In-Plane Shear Force in Containment Wall (Task 3, Elevation = 751.7 Feet, A_H = 1.0 g)

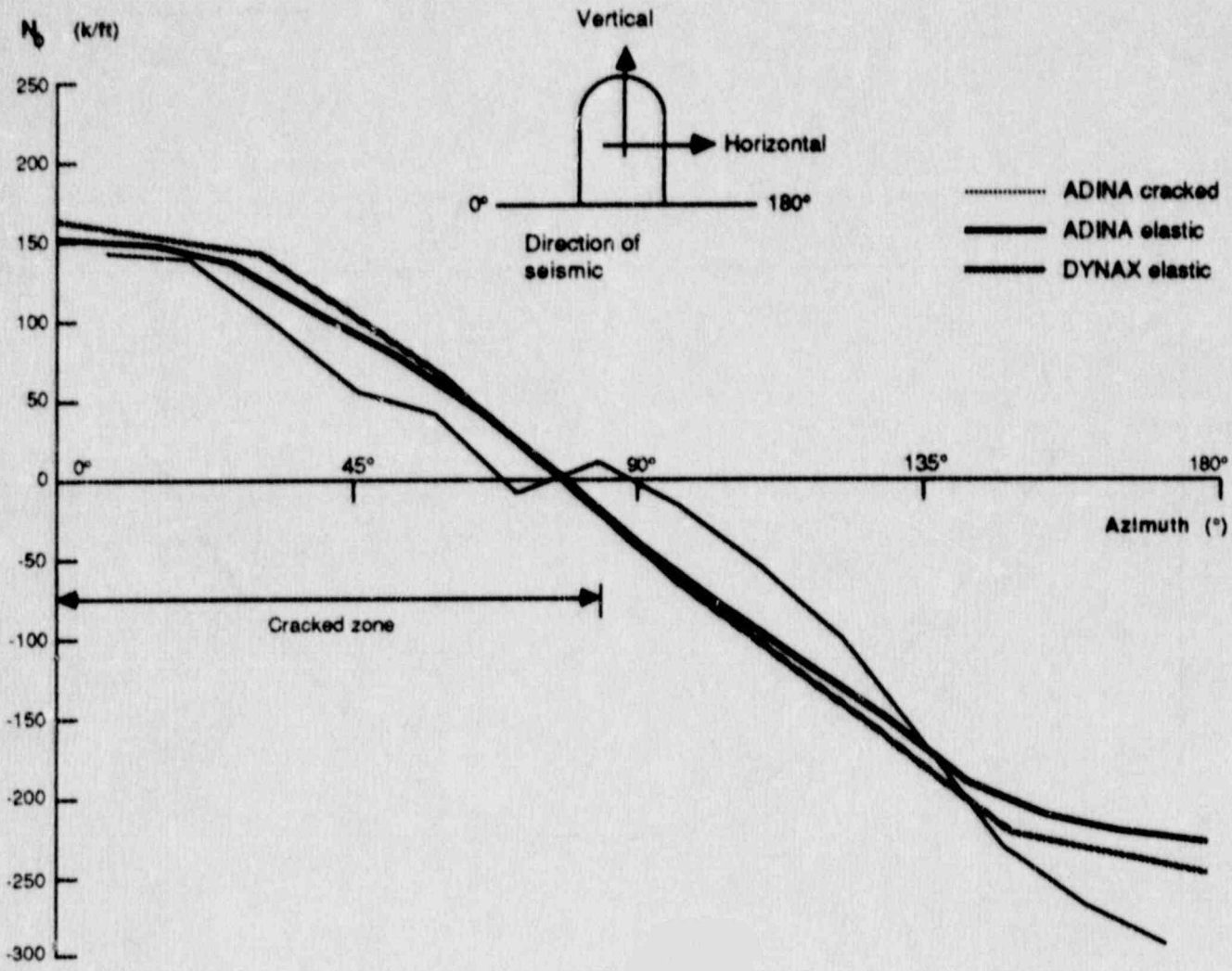

Figure 7.19 Circumferential Variation of Total Meridional Force in Containment Wall (Task 3, Elevation = 751.7 Feet, A_H = 1.0 g)

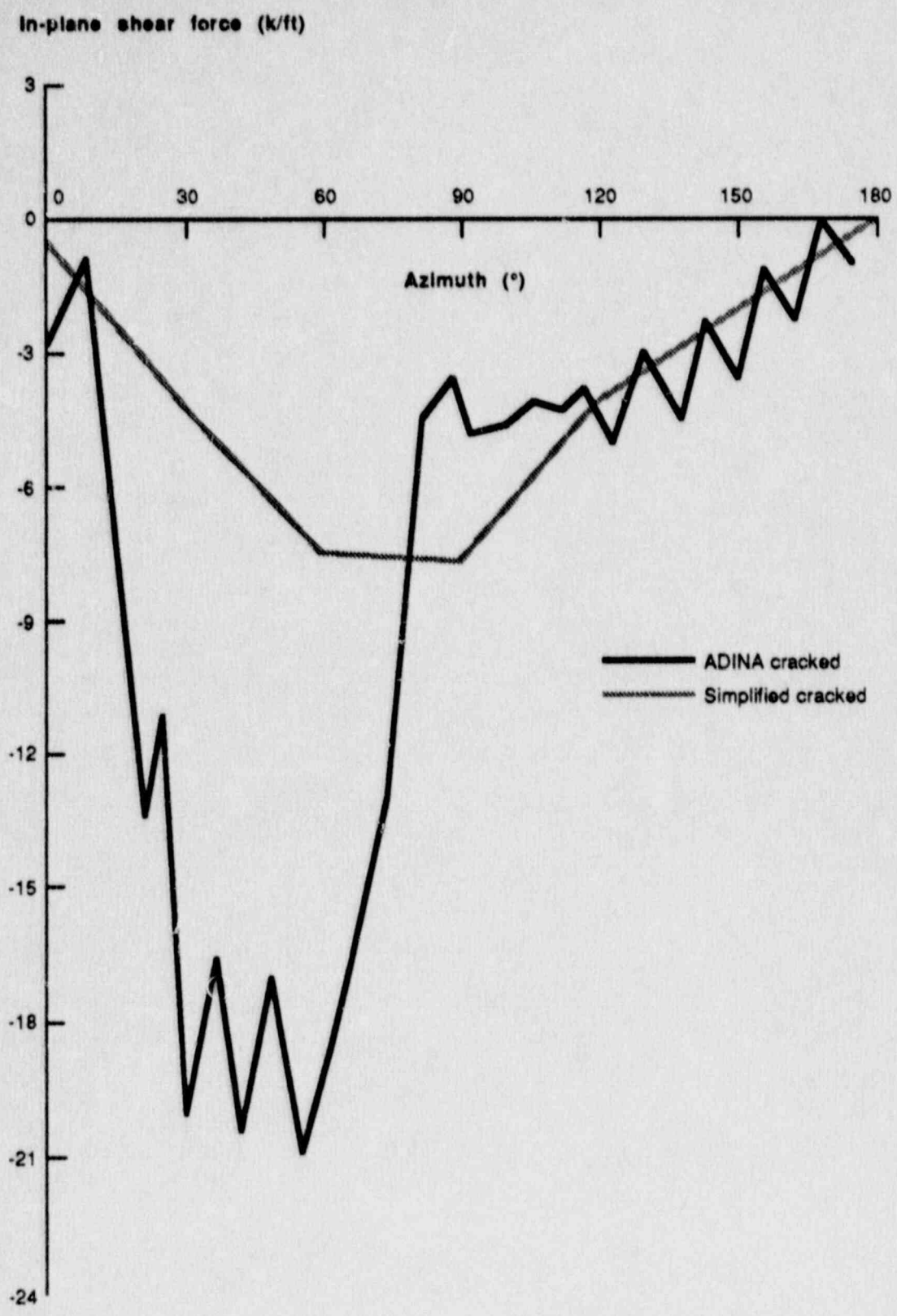

Figure 7.20 Circumferential Variation of In-Plane Shear Force in Wall Liner (Task 3, Elevation = 751.7 Feet, A_H = 1.0 g)

8. ASSUMPTIONS, UNCERTAINTIES, AND THEIR IMPACT ON THE RESULTS

8.0 General

In general, in the process of performing seismic analysis and evaluation one has to make a number of idealizations and parameter selections to arrive at the final results. A general and detailed discussion of uncertainties is included in Reference 8.1. The evaluation of containment seismic capacity, in this study, required additional idealizations and parameter selections, involving additional uncertainties. This chapter is devoted to a discussion of the important assumptions and parameter selections specific to this study, which have been variously discussed throughout the report. Where possible, the impact of choices made to arrive at the final results is also assessed.

The assumptions and uncertainties discussed are classified under four groups. These groups are: definition of seismic input, seismic analysis chain, basic material strength parameters, and evaluation criteria. Sections 8.1 through 8.4 discuss items in these four categories. The conclusions of the discussion are given in Section 8.5.

8.1 Definition of Seismic Input

The calculated capacity margin factors are stated with reference to a peak horizontal ground acceleration value A_H. In our evaluations we have assumed that there will be three time histories simultaneously acting on the structure, i.e., two horizontal components with peak amplitude A_H and a vertical component, the peak value of which is also equal to A_H. This basis is consistent with Regulatory Guide 1.60 and Standard Review Plan 3.7.1. Given this fact, the additional parameters for defining seismic input are a description of frequency content and duration of seismic excitation. In this study these items are defined by requiring that synthetic time histories used have response spectra consistent with the NRC Regulatory Guide 1.60 spectra. The duration of motion used in most cases of time history analysis is 6.0 Seconds.

With the exception of soil liquefaction limit state, all other limit states considered in this study depend on the maximum responses. For the time histories used maximum responses generally occur within the first six seconds of time history. The effect of cycles of oscillation to cause initiation of liquefaction has been properly considered within the criteria used for the liquefaction limit state. Consequently, it is our judgment that the seismic motion duration used in our study does not introduce any uncertainty into the reported results.

The frequency content of the synthetic time histories used introduces certain conservatism into the results given in this report. This is quantified as follows. consider horizontal motion first. Figure 2.5 compares the 5% damped spectrum of motion used to the corresponding Regulatory Guide 1.60 spectrum. The frequency range of interest for containment structural responses is from 1 cps to 20 cps. In this range of frequency, the spectrum of motion used is about 14% conservative relative to the Regulatory Guide 1.60 spectrum. There is an additional

conservatism arising from the Regulatory Guide spectrum itself. Figure 8.1 shows comparison of the Regulatory Guide spectrum to the median spectrum of spectral data set which generated the Regulatory Guide spectrum. Based on this figure a conservatism of 25% is obtained in the frequency range from 1 cps to 20 cps. Combining this information, the conservatism factor for the horizontal motion used is 1.14 x 1.25 = 1.43 relative to the median spectra of actual seismic records.

For the vertical motion comments similar to above discussion for horizontal motion can be made. Additional consideration is related to the proper definition of the vertical motion spectra. According to Reference 2.2, a more proper definition of the vertical spectra is to consider them to be two-thirds of the horizontal spectra. The comparison given in Figure 8.2 shows that between 3 and 33 cps, where most vertical frequencies of containments lie, the Regulatory Guide vertical spectrum is 1.5 times higher than the 2/3 of the Regulatory Guide horizontal spectrum.

Although certain component responses may be more sensitive to vertical earthquake input, the majority of the containment limit states in this report are more significantly influenced by the horizontal seismic component. Accordingly, the conservatism of horizontal input is considered to better represent the conservatism of the input motion.

8.2 Seismic Analysis Chain

8.2.1 Foundation Soil Spring and Dashpot Constants

The soil shear modulus and the method used for calculating the soil spring and dashpot constants are principal sources of uncertainty in the determination of these constants.

The high levels of seismic input considered in this study will introduce high strain levels in the foundation material. Data in Reference 8.2 shows that at shear strain levels near 0.1%, the soil shear modulus will have a variability of approximately 25% about the mean values used in this study.

In the present study, soil spring and dashpot constants were evaluated using equivalent half-space equations. An alternative approach would have been to use the impedance function approach which yields spring and dashpot constants as a function of frequency. One would then determine frequency independent constants required for the studies in this report by selecting the value at zero frequency. Figure 8.3 shows the horizontal spring constant for Clinton obtained as a function of frequency for A_H = 0.50g. The result obtained from the half-space calculation is also shown in this figure. Using the value at zero frequency, it is concluded that the alternative calculation of spring constant could have introduced a variability of approximately 10%.

Combining the effects of variability in horizontal spring constant from soil shear modulus, and from the method of calculation, we arrive at a combined variability of approximately 38%.

Table 8.1 lists horizontal spring constants used in Clinton seismic model and seismic responses obtained at the base of the containment. This information is listed for values of A_H = 0.45g and 1.0g. Note that for these two values of A_H, the horizontal spring constant changes by a factor of 2.3, i.e., from 3.3×10^6 kip/ft to 1.43×10^6 kip/ft. If we multiply the responses for A_H = 0.45g by 1/0.45 and compare them to the responses at A_H = 1.0g in Table 8.1, we conclude that seismic responses change by a factor of 1.4 due to a change in spring constant by a factor of 2.3.

Based on above comparisons, we can conclude that variability in seismic forces, used in containment evaluations in this report, due to a 38% variability in horizontal foundation spring constant could be estimated as (0.38/2.3) x 1.4 = 1.23, i.e., 23%.

The above attempt at quantification of the effects of variability in foundation spring and dashpot constants is obviously quite approximate. It is based on a comparison of only Clinton containment responses, and a comparison of only horizontal spring constant in the Clinton seismic model. There are vertical and rocking spring constants and three dashpots also in the seismic model, which have different amounts of variability in different containments. Rock foundation properties may have different variability than soil foundation properties. Therefore, the variability in foundation spring and dashpot constants may be quite different under different circumstances.

In addition to the variability in seismic responses due to foundation constant variability, the basemat shear and moment due to non-seismic loads are also significantly affected by the choice of foundation spring constants.

As seen from the comparison and discussion provided above, the containment and basemat responses are rather significantly affected by foundation constants. It is concluded from this discussion that any specific evaluation of containment seismic capacity should recognize the variability in foundation constants and appropriately consider its effect on the results.

8.2.2 Parameters Affecting Initiation of Uplift

Factors preventing the occurrence of uplift are dead load, adhesion at the basemat foundation interface, and side friction on the basement walls. Clearly, adhesion and friction values have considerably more variability than dead load. After uplift occurs, stiffness characteristics of the structure are affected somewhat. More significant influences of uplift are an increase in bearing pressure due to reduced area of contact between the basemat and foundation and increases in the high frequency range of the response spectra (8 cps and above) and basemat shear and moment because of hard impact between basemat and the stiff rock foundation material.

Only minimal changes in containment wall structural response were calculated for the three containments (Zion, Fermi, and Sequoyah) for

which uplift occurred. Consequently, variability in parameters initiating uplift is not considered important for containment wall response.

The nature of response spectra is quite sensitive to uplifting on rock foundations, and this may have consequence for qualification of some components. Two types of components evaluated in this report used in-structure response spectra. These are bolted connections in Fermi and Sequoyah and beam seats in Fermi. The margin factors computed for these components are high; as a result, these components do not govern the seismic capacity. Consequently, the effect of variability in uplift parameters is not considered important for the results of this report.

The increase in basemat response because of uplift is, however, important. As indicated in Section 3.4.8, the basemat capacity of Fermi could become controlling soon after uplift occurs, rather than the reported value of A_H = 0.45g in Table 3.8. Preliminary studies show that based on a variability of 50% in frictional and adhesion effects, the basemat capacity could be reduced to A_H = 0.32g.

The increases in basemat response due to uplift have been factored into basemat evaluation of Zion and Sequoyah containments. However, if due to variability in the adhesion and side friction, the initiation of uplift is delayed beyond the calculated basemat capacity, then the actual capacities will be higher.

It is noted that treatment of uplift in the seismic model in this study is rather simplified. Before the basemat uplifts, it has to push the side soil up. This behavior has been modeled in our analysis by considering static side friction. It is believed that a more detailed modeling of this phenomenon will show initiation of uplift at higher acceleration levels than predicted in this study.

It should also be noted that, within the scope of this study, component failures unrelated to containment integrity were not investigated. In view of significantly high spectral accelerations (over 20g's in the case of Sequoyah) obtained at high frequencies after uplift, components which are susceptible to such high frequency accelerations may be affected, and their failure may influence the progression of a severe accident. Therefore, uncertainties in the parameters affecting uplift may play a significant role when such components are evaluated.

8.2.3 Stiffness Parameters of Reinforced Concrete Elements

Generally values of concrete shear modulus, G, moment of inertia, I, and normal area, A_n, were reduced from those applicable to a solid concrete section to allow for the effect of cracking. Appendix A discusses the logic used to obtain reduced shear modulus values for concrete containments at Clinton and Zion. The discussion in Section 7.3 showed that for the Clinton containment, the selected value of reduced shear stiffness was reasonable because of the favorable comparison for deflections computed from the seismic analysis model using NONLIN2 program and the detailed finite element analysis of that containment.

Section 2.1.4 discussed the approach used in this report for obtaining reduced values of moment of inertia and normal area. Although we have used a procedure which is often used in practice, it is pertinent to note that calculated containment responses are not sensitive to the selection of moment of inertia and normal area values. This is so, because nuclear plant structures are basically deforming in shear as they respond to seismic ground motion. Therefore, it is the shear stiffness which is of primary significance. To illustrate this point, Table 8.2 shows the effect of variability in shear stiffness for Clinton containment. In this comparison results of two analyses are given. All parameters in these analyses are the same except for shear modulus values which differ by a factor of two. It is seen that the shear and moment increases by almost 30% due to an increase in shear modulus by a factor of two.

Figure 8.4 compares the response spectra, obtained at the Clinton containment node 15 of Figure 4.6, from the two analyses. The sensitivity of the response to shear stiffness variation is evident from the shift in the frequency response of the structure.

To illustrate the relative insensitivity of the containment response to the changes in moment of inertia, Table 8.3 shows a comparison of the total seismic base shear and moment obtained from two analyses of the Zion seismic model of Figure 5.2. In these two analyses the only difference was in the value of moment of inertia used for containment beam. In one case the value used corresponds to a fully cracked section. In the other analysis, the moment of inertia corresponds to the gross concrete section. Table 8.3 shows that a variation of nearly four times in moment of inertia produced very little difference in seismic response.

It is our conclusion, therefore, that effect of variabilities in moment of inertia and normal area for concrete containments is not significant.

Since shear stiffness of concrete containment beams have used reasonable values, it is our conclusion that the results presented for containment structure in this report are realistic relative to the choice of stiffness parameters.

8.2.4 Structural Damping

In the seismic models, structural damping has been considered using viscous damping as given by Equation (2.14). The constants of proportionality for mass and stiffness matrices in Equation (2.14) were selected to provide modal damping from 4% to 10% in the frequency range of interest. These values compare favorably with the NRC Regulatory Guide 1.61 damping values, which are 4% to 7%, for concrete and steel structures and for SSE level of excitation. There has been a considerable amount of discussion in the nuclear industry on the conservative nature of the NRC Regulatory Guide 1.61 damping values. For example Table 8.4, taken from Reference 8.1, compares the Regulatory Guide damping values with other recommendations and with the measured test results. It can be seen from this table that for concrete structures

and SSE level of excitation, up to 18.7% damping was measured in testing. Even based on the Newmark & Hall recommended value of 10%, it can be concluded that damping values used in this study are on the conservative side for concrete structures. For steel containments, it would appear from the data of Table 8.4 that the damping values used are reasonable.

The seismic analysis done in this study have provisions to consider effect of material yielding. Therefore, any effect of hysteretic damping beyond yielding is considered in the analysis.

8.2.5 Calculation of Maximum Shell Forces and Element Strains In Containment

For concrete containments the evaluation of containment shell and basemat has been performed by an elastic shell analysis using program DYNAX, followed by strain calculation using program TEMCO. This simplified chain of analysis was evaluated using a nonlinear shell analysis model for Clinton containment in Chapter 7. This evaluation showed that for maximum strains in the liner and rebar, the results from simplified analysis were on the conservative side by a factor which varies from 10% to 75%. Results for transverse shear force in the containment wall were found to be conservative by a factor of nearly two. The transverse shear force on the basemat was closely predicted in the simplified analysis. Thus, in general, the results presented in this report on concrete containments should be considered conservative. A more detailed finite element evaluation is expected to improve the margins as shown for Clinton containment in Chapter 7.

For steel containments, effect of seismic force on the containment shell was derived through an approximate procedure based on reduced yield stress and a beam analysis. Although this analysis showed sufficient margin against failure criteria in Fermi containment, and no yielding in Sequoyah containment, the confirmation of the simplified analysis results through a nonlinear shell analysis may be desirable.

In both steel and concrete containments, the evaluation of basemat forces when foundation uplift occurs, such as in Zion and Sequoyah, is complicated by the fact that time history results are available from a plane frame seismic model, and the forces for the three dimensional basemat model have to be postulated from this information. For the results presented in this report, this information was obtained by applying the pattern of inertial loads generated from the seismic beam model on the three-dimensional basemat model. In this analysis the displacements of the foundation beam at its ends were enforced. This approach for a partially lifted structure is considered quite approximate. Although a time history analysis using an uplifting, materially nonlinear model is not considered feasible because of prohibitive computational cost, analysis of an elastic, three-dimensional model with potential for uplift is feasible. Such an analysis with a refined basemat mesh is recommended to better define forces acting on various portions of a basemat subject to uplift.

8.3 Basic Material Strength Parameters

Yield stress, f_y, for steel elements and concrete compressive strength, f'_c, are the basic material strength parameters used in this study. The minimum specified values of yield stress for various steels and concrete design compressive strength, increased by 17% for aging, were used in all evaluations.

It is well known that the mean actual material strength properties are higher than the minimum specified values. The variability of concrete and reinforcing bar strength values has been discussed in Reference 8.1. Considering mean values, the increase in concrete compressive strength, f_c', over the minimum specified value is approximately 30%, which includes effect of aging. Since effect of aging has been explicitly considered in this study, the f_c' values used are approximately 15% lower than the mean actual values. Similarly, the yield stress of reinforcing bars is usually 10% to 20% higher depending on the bar size, see Reference 8.1. The mean actual yield stress of liner material is usually higher by 30%, and that of steel plates used in a steel containment shell is by 10% to 20% higher than the minimum specified values.

Based on the above, it can be concluded that the material strength properties used in this study are conservative with respect to their actual mean values. However, the estimated effect of this conservatism on the calculated containment capacities is not substantial; it could be of the order of 5% to 20%.

The capacities for limit states associated with foundation failure depend upon the shear strength of the foundation material. The variability in this parameter could be much higher than those for concrete and steel, thus having a greater impact on the final results. However, except for liquefaction potential in Clinton containment, the foundation failures were not found to be governing. The uncertainty in the liquefaction potential at Clinton is recognized, and could be explored further.

8.4 Evaluation Criteria

As shown in Table 2.1, and discussed in Section 2.2, the evaluation criteria for eleven out of sixteen limit states is considered conservative, and the remaining five are considered as close, meaning that there is no inherent conservatism in their use. The quantification of conservatism inherent in the evaluation criteria is beyond the scope of this study. It is pertinent to note, however, that the first few controlling limit states, for each of the four containments, involve evaluation criteria which are considered conservative. The only exception to this is the limit state associated with the interference between the containment and auxiliary building at Zion, where the containment capacity is determined by an inability to further load the analytical model, which in the context of present discussion is considered as close, rather than conservative.

It should also be noted that the shear capacity of the basemat, which was found to be one of the controlling limit states in Fermi, Clinton and Sequoyah containments, is based on conservative ACI Code provisions. A similar consideration applies to the failure of biological shield wall at Fermi and shield building at Sequoyah. It is believed that use of a three-dimensional analysis which employs failure criteria in terms of reinforcing bar strain, or the inability to further load the analytical model, can substantially improve the seismic capacity of the containments in these limit states.

8.5 Conclusions

Based on a discussion of uncertainties and assumptions in this chapter, the following conclusions can be drawn:

1. The input ground motion, for a given maximum horizontal ground acceleration, used in the analysis is conservative with respect to a median ground motion associated with the same horizontal ground acceleration. This conservatism is approximately 43%.

2. The foundation soil spring and dashpot constants involve a significant amount of uncertainty. The effect of uncertainty in this area on the seismic responses, while difficult to quantify could be also significant. Therefore, it is important to address this area of uncertainty, either probabilistically or deterministically, in any further study of containment seismic capacity.

3. The modeling and treatment of basemat uplift phenomenon in this study are considered approximate. Since uplift has a significant effect on the basemat response, which has been found to be one of the common controlling limit states, refinement of uplift consideration is considered appropriate.

4. Out of the three stiffness parameters for the concrete containment beams, i.e., normal cross sectional area, moment of inertia, and effective shear area, the effect of normal cross-sectional area and moment of inertia is minor. The effect of effective shear area on containment response is important, and this effect has been reasonably considered in the analysis.

5. Structural damping values used in the analysis are on the conservative side for concrete, and reasonable for steel elements.

6. Based on a comparison of the results obtained from the simplified analysis and a three-dimensional, quasi-static, nonlinear finite element evaluation of Clinton containment, it is concluded that the simplified evaluation procedure yields conservative estimates of containment wall reinforcing bar and liner strains.

7. The evaluations performed for the shield wall in Fermi and Sequoyah, are considered conservative, based on the evaluation criteria employed. A three-dimensional, materially nonlinear analysis could significantly improve the capacities reported here.

8. The basemat transverse shear evaluations performed in this study are considered conservative in view of the ACI Code shear capacities used. A three-dimensional quasi-static, materially nonlinear analysis could improve the predicted capacities significantly. Also, where basemat uplift occurs, it is believed that prediction of forces in this study is somewhat approximate. A time-history analysis using an elastic, three-dimensional model of containment and basemat, with consideration of uplifting foundation, is considered an appropriate improvement for determination of basemat forces.

9. Analyses of steel containment, at Fermi and Sequoyah, consider the effect of biaxial state of stress in an approximate manner. Confirmatory studies using three-dimensional shell models that consider plasticity and quasi-static loading, are considered feasible and appropriate for this purpose.

10. The basic material strength parameters, i.e., concrete compressive strength and steel yield stress, used in this study are based on the minimum specified values, rather than on actual strength values. The effect of this conservatism on the calculated containment capacity is, however, not significant; it may range from 5% to 20%. The variability in soil shear strength may be more significant. However, except for liquefaction potential at Clinton, the limit states associated with the foundation were not found to be controlling.

11. The evaluation criteria used in this study for all the governing limit states, with the exception of interference of Zion containment with the adjacent auxiliary building, are considered conservative.

8.6 References

8.1 Working Group on Quantification of Uncertainties, "Uncertainties and Conservatism in the Seismic Analysis and Design of Nuclear Facilities," American Society of Civil Engineers, 1986.

8.2 Seed, H. B., and Idriss, I. M., "Soil Moduli and Damping Factors for Dynamic Response Analyses," EERC Report No. 70-10, December 1970.

8.3 Stevenson, J. D., "Structural Damping Values As A Function of Dynamic Response Stress and Deformation Levels," Nuclear Engineering and Design, Vol. 60, 1980, pp. 211-237.

Table 8.1

Effect of Variation in the Horizontal Spring Constant on Base Shear and Moment for Clinton Containment

Item	A_H = 0.45g	A_H = 1.0g
Horizontal Spring Constant (kip/ft.)	3.30×10^6	1.43×10^6
Base shear (kips)	20,296	32,383
Base Moment (ft-kip)	2.31×10^6	3.66×10^6

Table 8.2

Effect of Variation in Concrete Shear Stiffness on Containment Seismic Response (Clinton, A_H = 0.25g)

Shear Stiffness Reduction Factor (Gcr./Go)	Response at Base of Cylinder Wall Shear (kips)	Moment (ft. kip)
0.12 per Appendix A	14,200	1.82×10^6
0.24	18,300	2.33×10^6

Table 8.3

Effect of Variation of Containment Moment of Inertia
On Containment Seismic Response
(Zion, A_H = 1.0g)

Values of I Used for Containment Beam (ft^4)	Response at Base of Cylinder Wall Shear (kips)	Moment (ft-k)
0.89×10^6 (Fully cracked)	42,000	5.76×10^6
4.06×10^6 (Gross section)	43,000	5.82×10^6

Table 8.4

Comparison of Available Nuclear Station Experimentally Measured Damping and Regulatory Requirements and Recommendations

	Best Estimate or Mean Value Damping Values								
	(1)	(2)	(3)	(4)	(5)	(6)	(7)	(8)	(9)
Reactor system piping	3.4	2.0	8.1	2.0	10.0	3.0	3.0	12.7	16.2
Mechanical components	3.8	3.0	5.7	2.0	6.5	4.0	7.0	7.7	9.1
Concrete Structures	5.2	5.0	7.5	4.0	13.9	7.0	10.0	18.7	25.0

Column Headings:

(1) Average of measured data for stress levels at or less than 0.1 yield for components and piping, and 0.25 yield for concrete, from Table B.1 of Reference 8.3.

(2) Suggested Newmark and Hall values at approximately 0.5 yield (Newmark and Hall, "Development of Criteria for Seismic Review of Selected Nuclear Power Plants," NUREG/CR-0098, May 1978.)

(3) Measured damping values normalized to 0.5 yield stress, using procedures shown in Appendix B of Reference 8.3.

(4) Regulatory Guide 1.61 values for stress levels of approximately 0.67 yield (OBE).

(5) Measured damping values normalized to 0.67 yield stress, using procedures shown in Appendix B of Reference 8.3.

(6) Regulatory Guide 1.61 values for stress levels of approximately 0.90 yield (SSE).

(7) Suggested Newmark and Hall values at approximately 0.9 yield (Newmark and Hall, "Development of Criteria for Seismic Review of Selected Nuclear Power Plants," NUREG/CR-0098, May 1978.)

(8) Measured damping values normalized to 0.9 yield stress (faulted: buildings; emergency: component supports).

(9) Measured damping values normalized to 1.2 yield stress (faulted: component supports).

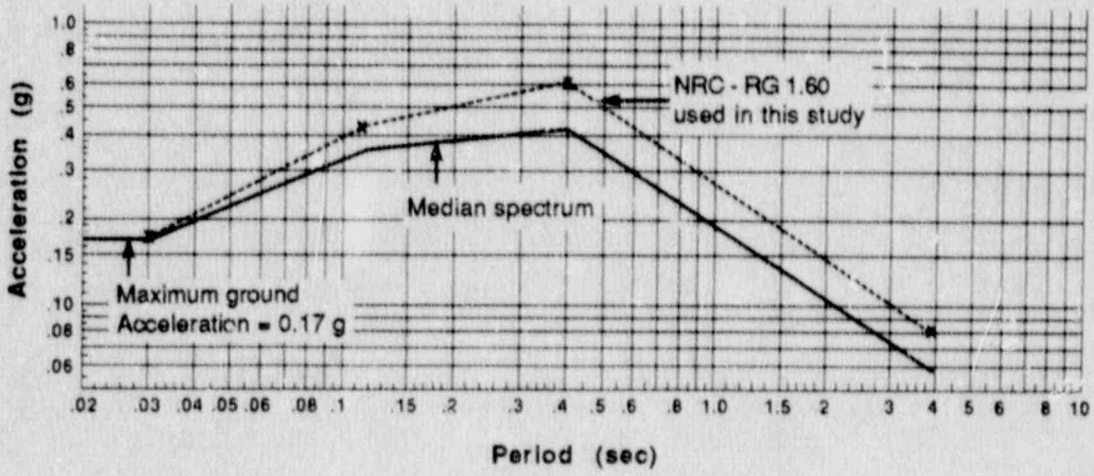

Figure 8.1 Comparison of Regulatory Guide 1.60 and Median Horizontal Response Spectra, 5% Damping

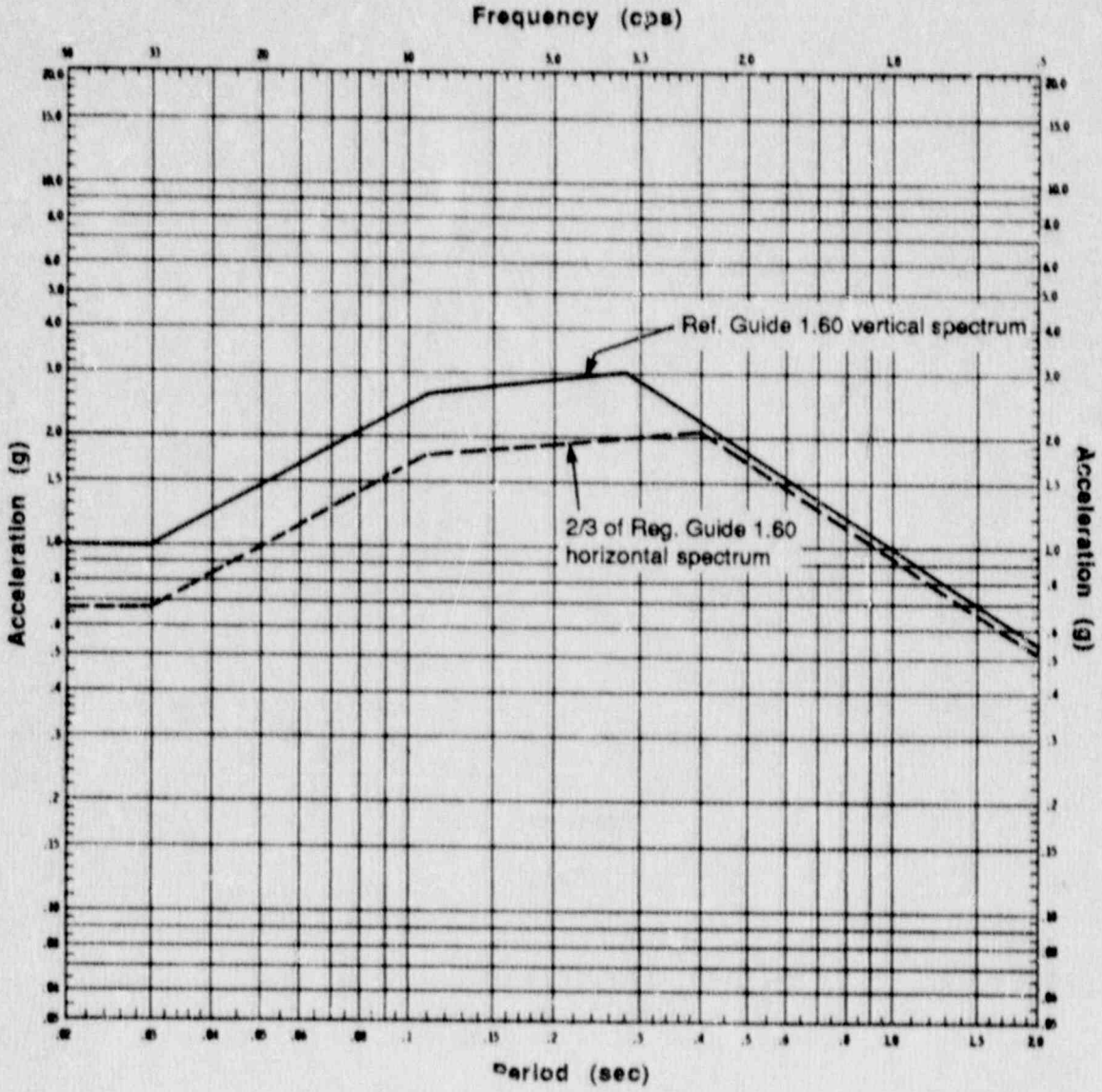

Figure 8.2 Comparison of Regulatory Guide 1.60 Vertical Spectrum with Two-Thirds Reg. Guide Horizontal Spectrum, 5% Damping

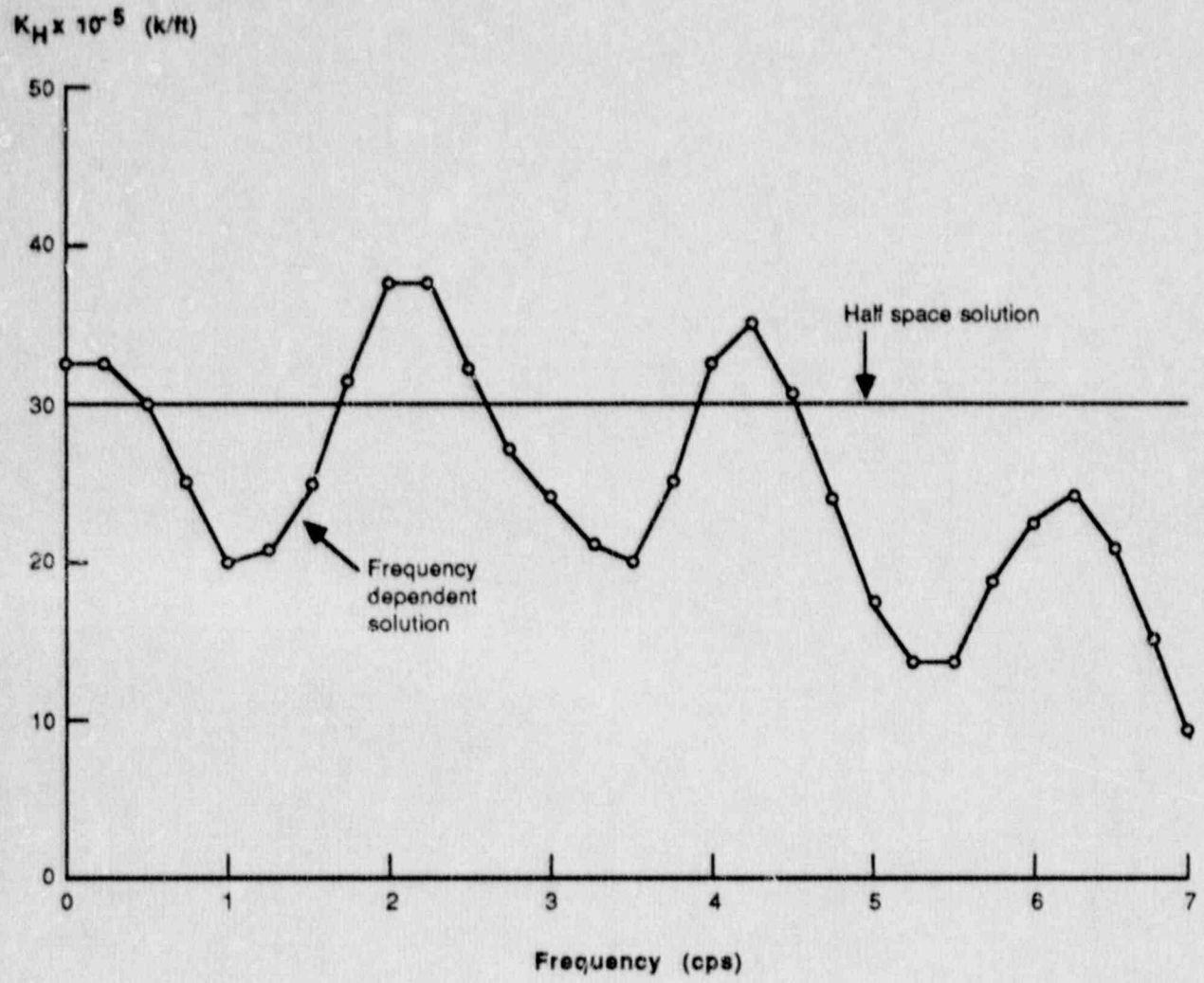

Figure 8.3 Comparison of Horizontal Foundation Spring Constant, Half Space Solution vs. Frequency—Dependent Solution (Clinton, A_H = 0.50 g)

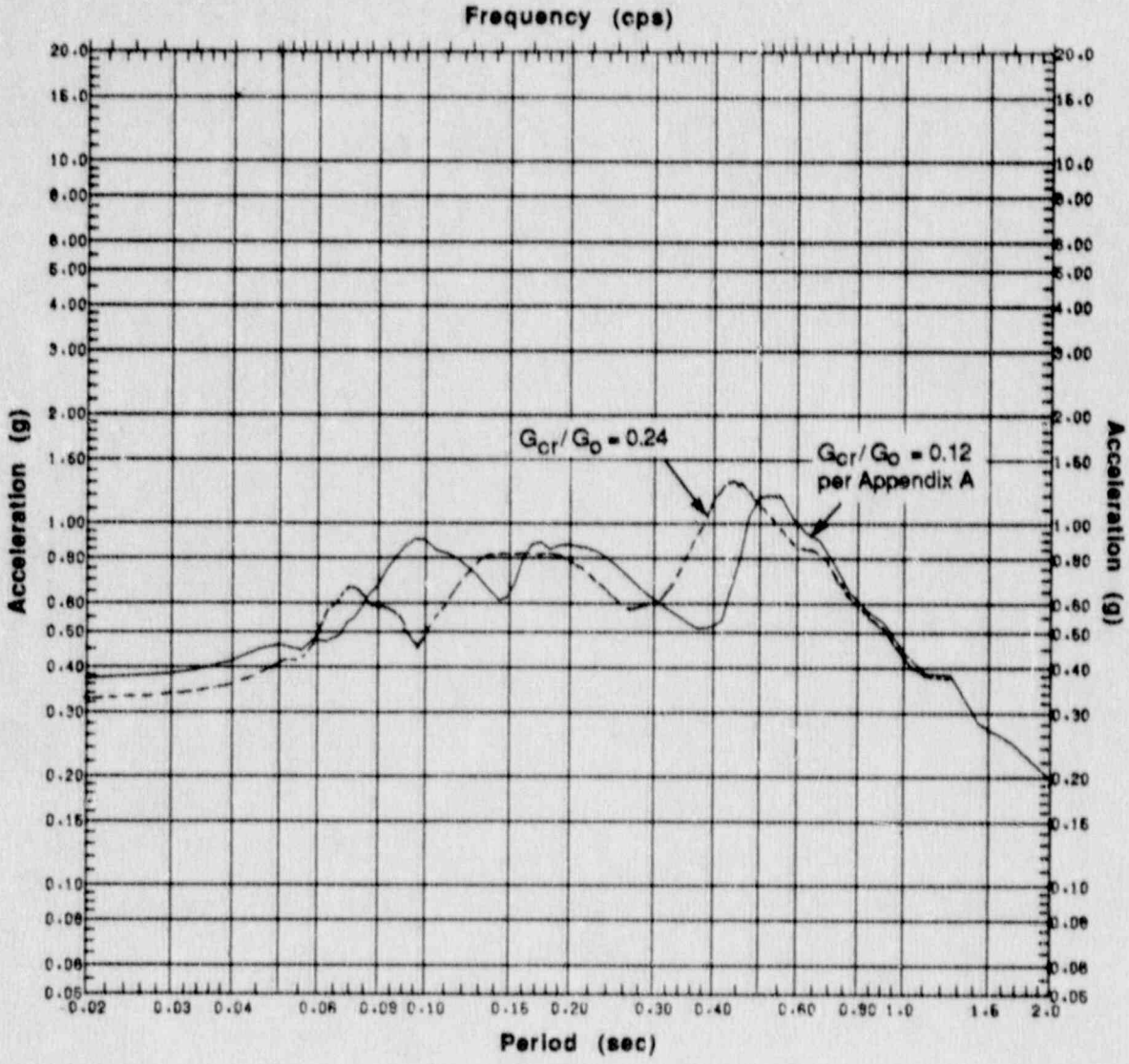

Figure 8.4 Effect of Shear Stiffness Reduction Factor, G_{cr}/G_o, on Response Spectra at Clinton Containment Node 15 of Figure 4.6, 5% Damping

9.0 OVERALL CONCLUSIONS AND RECOMMENDATIONS FOR FUTURE STUDIES

Specific conclusions from this study of the four containments are given in Chapters 3 through 8. Overall conclusions and recommendations for future studies are given in this chapter.

Overall Conclusions

The overall conclusions of this study are as follows:

1. All four containments evaluated have seismic capacities at least three times higher than their respective design-basis SSE. Table 9.1 lists the first few governing limit states for each containment and their associated capacities for Tasks 3 and 5. For earlier vintage containments, i.e., Fermi, Zion and Sequoyah, the design SSE spectral shape is the Housner spectra, which is less intense than the Regulatory Guide 1.60 spectra by a factor of about 2 for the frequency range of interest to containments. Consequently, this effect should be taken into account for these containments when capacities in Table 9.1 are used to calculate the margin relative to the design-basis. For the Fermi biological shield wall, for example, the design-basis margin should be interpreted as

$$\frac{0.39}{0.15} \times 2 = 5.2$$

2. Many of the governing limit states listed in Table 9.1 for the Fermi, Clinton, and Sequoyah containments are indirect limit states, i.e., they are not directly related to the containment pressure boundary, and for this reason may not have been considered in other containment seismic capacity evaluations. The calculated seismic capacities in these instances are not affected by the presence of accident pressure and temperature in the containment.

3. None of the governing limit states for Task 3 in Table 9.1 are associated with a significant straining of containment concrete elements in compression to cause partial crushing, or with significant tensile straining of containment steel elements that could cause depletion of ductility. Consequently, effects of such initial shock weakening of containments are not considered important. For Fermi and Sequoyah, the failure of the shield wall or building due to an initial shock could cause additional loading on steel containments. The capacities given in this report do not consider effects of such interactions for aftershock capacity evaluation. From the study of the four containments, it does not appear that an initial main shock has a significant effect on the subsequent seismic capacity of the containment.

4. It can be seen from Table 9.1 that basemat failure in the transverse shear is an important direct limit state in the Fermi and Sequoyah containments. Although shear failure of the basemat should be considered a structural failure, determination of its

significance for providing a potentially severe leak path requires further considerations.

5. The interaction of accident-imposed thermal and pressure loads with seismic loads on the aftershock seismic capacity is important. In some cases, the capacity is increased, as is illustrated by the effect of thermal compression to increase Sequoyah basemat shear capacity (see Table 9.1). In other cases, membrane tension due to pressure reduces the seismic capacity. Table 9.1 illustrates this effect on the Zion and the Clinton containments.

6. From a comparison of the results of the simplified methodology and the three-dimensional Clinton containment analysis, the simplified methodology used here for concrete containments appears to provide conservative estimates of reinforcing bar and liner strains. The estimates for transverse shear in the wall from this simplified procedure are also conservative. Basemat shear and moment predictions are reasonably close.

7. From a review of inherent uncertainties and the assumptions made in the analysis performed, as discussed in Chapter 8, the results of this study are generally conservative. The approach taken in this study can be viewed as the Conservative Deterministic Failure Margin (CDFM) method for determining the High Confidence of Low Probability of Failure (HCLPF) seismic capacity of containments.

8. Based on the discussion of Chapter 8 on uncertainties for a seismic capacity evaluation, the significant parameters subject to uncertainty include seismic input, soil spring and dashpot constants, parameters defining the initiation of uplift phenomenon, reduction in concrete shear stiffness due to cracking, and definition of evaluation criteria for shear failure of concrete plate and shell structures. It is important to properly define the variability of these parameters in any further study of containment seismic capacity.

9. Basemat uplift initiates somewhere after A_H = 0.25g for the Fermi, Zion, and Sequoyah containments. Due to its large extent, the Clinton basemat does not uplift even at A_H = 1.0g. The effect of basemat uplift is significant for the Fermi and the Sequoyah containments because of the hard impact condition between the basemat and rock foundation. The in-structure response spectra in high frequency range (above 8 Hz) increase significantly, and the basemat shear and moment are also significantly increased. The base shear and moment in the containment wall, however, are not significantly affected by uplift; they generally decrease slightly. For the Zion containment, the effects of uplift are relatively small because hard impact conditions at the basemat-soil interface are not present.

10. For the two containments founded on soil, i.e., Clinton and Zion, the soil-structure interaction effect reduces the structural response and the in-structure response spectra amplitudes in the high frequency region. With intensification of motion and associated soil softening, this attenuation increases further.

Recommendations for Future Studies

To perform this scoping study, several simplifying assumptions and approximations were made. The study concentrated on considering structural and foundation limit states. To confirm some of the assumptions made, or to investigate critical equipment failures, the following studies are recommended:

1. The failure of the biological shield wall in Fermi and shield building in Sequoyah yielded the lowest seismic capacities for these containments. The evaluations made are considered conservative based on the ACI Code capacities used. A three-dimensional, quasi-static, materially nonlinear analysis is recommended to better predict the capacity of these shield walls, which may significantly improve the capacities reported herein. If such an evaluation does not improve the seismic capacity or if additional capacity needs to be investigated, the effect of potential interactions of these failed buildings with containments in determining seismic aftershock capacity should be considered.

2. The occurrence of uplift for containments founded on rock significantly affects the in-structure response spectra for frequencies higher than 8 Hz. An investigation is necessary to show whether high frequency excitations of the type calculated can affect the functionality of critical components. In case these conditions exist, it is important to establish, through analytical studies and/or testing, whether basemat uplift would occur in containments embedded into a rock foundation as is assumed in this report.The study should include a proper representation of actual construction practices used and their effect on the foundation uplift.

3. Since for steel containments the effect of biaxial stress states on the containment shell was derived through an approximate procedure based on reduced yield stress and a beam analysis, the confirmation of this simplified analysis procedure through a quasi-static, nonlinear, three-dimensional shell analysis is recommended.

4. The basemat evaluations performed in this study are considered approximate; where uplift of basemat occurs, the prediction of basemat forces is complex. The source of this complexity is in providing appropriate definitions of simultaneous wall reactions, mat inertia, and soil reactions including damping, that act on the basemat. A time history analysis using an elastic, three-dimensional model of containment and basemat with consideration of uplifting foundation is recommended to improve the prediction of forces. This improved basemat force distribution should be used to investigate basemat seismic capacity.

Table 9.1 Governing Limit States and Conservative Estimates of Capacities[1]

Containment	Design SSE and Spectra	Task 3[2]		Task 5[2]	
		Limit State	Capacity	Limit State	Capacity
Fermi	0.15g Housner[3]	Failure of biological shield wall	0.39g	Failure of biological shield wall	0.39g
		Failure of basemat in shear and bending	0.45g	Failure of basemat in shear and bending	0.45g
Clinton	0.25g RG 1.60	Liquefaction of soil under basemat	0.83g	Liquefaction of soil under basemat	0.83g
				Failure of wall reinforcing bars and liner	1.0g
Zion	0.17g Housner[3]	Failure by interference between containment and auxiliary buildings	0.75g	Failure of wall reinforcing bars	0.34g
				Failure of wall in transverse shear	0.39g
				Failure by interference between containment and auxiliary buildings	0.75g
				Shear failure at buttress plates	0.75g
Sequoyah	0.18g Housner[3]	Failure of shield building	0.30g	Failure of shield building	0.30g
		Failure of basemat in transverse shear	0.52g	Failure of basemat in transverse shear	> 1.0g[4]

1. Capacities are given in terms of peak horizontal ground acceleration, A_H, and time histories consistent with Regulatory Guide 1.60 spectra.
2. The loads considered in Task 3 include dead load, prestress (if applicable), and seismic load. The loads considered in Task 5 include the same loads in Task 3 plus high pressure and temperature corresponding to a severe accident (see Table 1.4).
3. In the frequency range of interest to containment structural response, the Regulatory Guide 1.60 spectra are about a factor of two higher than the Housner spectra (see Figure 2.2). This difference must be accounted for when calculating margins to failure relative to the original design basis.
4. The basemat shear capacity is higher in Task 5 than in Task 3 due to the beneficial effect of compression resulting from thermal loads in Task 5.

APPENDIX A

SHEAR MODULUS REDUCTION FACTOR FOR BEAM MODELS OF CONCRETE CONTAINMENTS

A.1 Proposed Criterion

When concrete cracking is expected at a level of peak ground acceleration being considered the shear modulus of beam elements should be reduced. The following values of G_{cr}/G_o are used in this report.

G_{cr} = Shear modulus of equivalent beam when, within the beam length, concrete is expected to crack.

G_o = Shear modulus of equivalent beam when concrete is not expected to crack.

Containment	G_{cr}/G_o
Clinton	0.12
Zion	0.42

A.2 Discussion

Values of G_{cr}/G_o determined in tests of reinforced concrete panels loaded in biaxial tension with membrane shear, pure membrane shear, and biaxial compression with membrane shear were examined. These test results are reported in References A.1, A.2 and A.3. Through this examination and using a secant shear modulus corresponding to failure shear, it was concluded that the modulus ratio is about 0.05 for specimens loaded in tension plus shear, 0.10 for specimens in pure shear and a function of compressive stress when compression is less than about 1400 psi. No reduction in modulus occurs when compression exceeds 1400 psi.

The above postulated element behavior was translated into an average shear modulus reduction factor for a tubular section which is used to represent the cross-section of concrete containment. Figure A.1 shows the assigned values of ratio G_{cr}/G_o on 12 elements covering one half of a containment circumference. In assigning these values to elements, stresses from 2.5 (SSE) + DL + Prestress (where applicable) were considered.

The average value of ratio G_{cr}/G_o for the center six elements in the figure was used to determine the listed ratio G_{cr}/G_o above. The center portion was considered because this is the area where most shear is resisted.

The shear area to be used for shear stiffness calculation of tubular section will be 0.5 x the area of the tubular section.

A.3 References

A.1 Perdikaris, P. C., White, R. N. and Gergly, P., "Strength and Stiffness of Tension Reinforced Concrete Panels Subjected to Membrane Shear, Two-Way Reinforcing," NUREG/CR-1602, July 1980.

A.2 Oesterle, R. G. and Russel, H. G., "Shear Transfer in Large Scale Reinforced Concrete Containments," NUREG/CR-1374, April 1980.

A.3 Vecchio, F. and Collins, M. P., "The Response of Reinforced Concrete to In-Plane Shear and Normal Stresses," Report No. 82-03, Department of Civil Engineering, University of Toranto, March 1982.

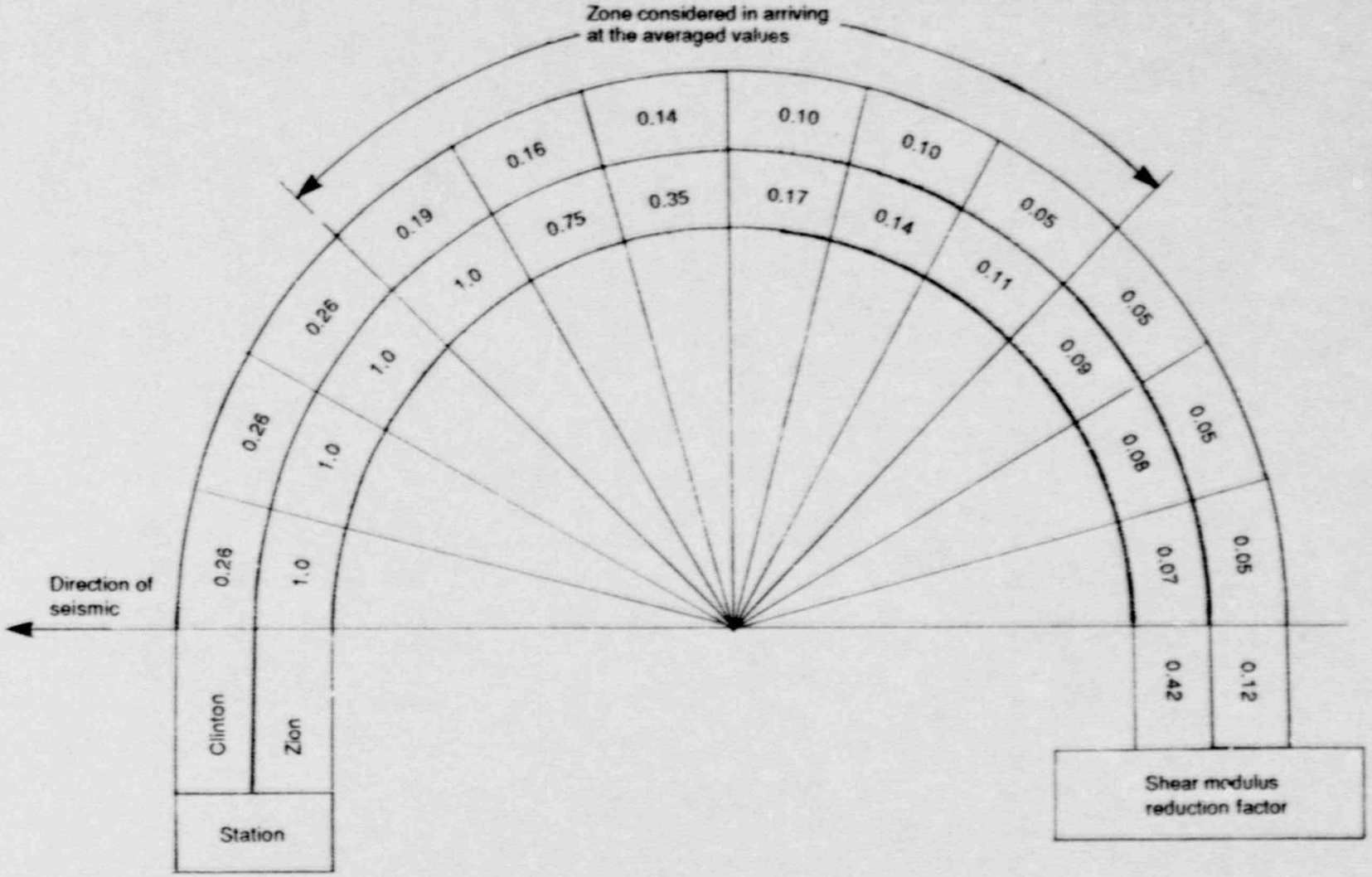

Figure A.1 Assigned Values of G_{CF}/G_O on the Circumference of Containment Section

APPENDIX B

BUCKLING CRITERIA USED FOR FERMI CONTAINMENT: MODIFIED CODE CASE N-284 AND BOSOR ANALYSIS

B.1 Modification of the Theoretical Buckling Value

The buckling criteria described in ASME Section III, Code Case N-284 is based upon determining the theoretical critical buckling stress

$$\sigma_{ct} = 0.605\ Et/R \qquad (B.1)$$

where E is the modulus of elasticity, t is the shell thickness, and R is the constant radius of the spherical shell.

This theoretical buckling value as presented in the reference Code Case is based on a spherical shell of uniform thickness in which the unidirectional compressive stress is of a constant magnitude at all points, both along the meridian and around the circumference. The orthogonal stress is understood for this formula to be equal to zero.

The loading combinations shown in Table 1.3 of this report cause a meridional compressive stress which increases in magnitude at descending elevations along the shell meridian. Corresponding respective circumferential tensile stresses also vary in a similar fashion. Recognizing that this loading condition cannot be realistically represented by use of the Code Case formula, Equation (B.1), the computer code BOSOR is utilized, which is an equivalent formulation used to calculate the critical buckling value for the varying magnitude loading. The input for use in this solution consists of the calculated meridional and circumferential stresses at some selected points along the shell meridian. BOSOR output consists of eigenvalues, which, when multiplied by the actual stress, provide the theoretical values for critical buckling of a shell not subject to any imperfections.

B.2 Modification of the Capacity Reduction Factor

The theoretical buckling value is multiplied by a "capacity reduction factor," see Figure B.1, herein referred to as a "knockdown factor," which accounts for the effects of construction imperfections. Using the curve of uniaxial compression from Figure B.1, a knockdown factor of 0.207 can be obtained for an unstiffened shell. Although the analysis presented in this report could conservatively utilize this knockdown factor, further modification has been made to account for the case wherein first direction compression is accompanied by orthogonal tension. This orthogonal tensile stress has the effect of rounding the shell and reducing the effect of imperfections experienced during the fabrication and construction phase. To quantify the critical buckling stress, S_{cr}, including this effect, the following technique is used.

$$S_{cr} = 0.125\ E(t/R) + \Delta\sigma_{cr} \qquad (B.2)$$

where $\Delta\sigma_{cr}$ is the term which accounts for the stiffening effect of the equivalent internal pressure and is found in accordance with "The Stability of Thin-Walled Unstiffened Circular Cylinders Under Axial Compression Including the Effects of Internal Pressure" by Harris, Suer, Skene and Benjamin which appeared in Journal of the Aeronautical Sciences - August 1957.

Using this reference, the parameter x may be determined to be

$$x = \left(\frac{P}{E}\right)\left(\frac{R^2}{t}\right) \qquad (B.3)$$

Where P is the equivalent pressure; and E, t and R are the same as in Equation (B.1). The equivalent internal pressure, P, is the pressure which would result in a tensile stress equal to the calculated orthogonal stress, S, and may be found as follows

$$P = \frac{2t}{R} \times S \text{ (tensile)} \qquad (B.4)$$

Using the calculated value of x from Equation (B.3), determine the $\Delta\sigma_{cr}$ as follows:

$$Y = .01983 + .7886\,x - 1.5272\,x^2 + 1.5208\,x^3 - .73323\,x^4 + .13399\,x^5 \qquad (B.5)$$

$$\Delta\sigma_{cr} = \frac{Et}{R} Y \qquad (B.6)$$

Equation (B.5) is a curve fit for charts included in the paper listed above. Use of $\Delta\sigma_{cr}$, from Equation (B.6), in Equation (B.2) gives S_{cr}.

The ratio of the critical buckling stress S_{cr} to the theoretical buckling stress σ_{ct}, is used to determine a modified "capacity reduction factor." This accounts for the enhanced ability of the shell to resist buckling. Thus, the modified knockdown factor

$$KD_{mod} = \frac{S_{cr}}{\text{(theoretical compressive allowable, } (\sigma_{ct})} \qquad (B.7)$$

B.3 Evaluation of Margin for Buckling

The capacity margin factor of the containment shell is determined as follows:

1. Determine the theoretical buckling stress using computer code BOSOR, CBI Code No. 1443.

2. Determine the modified knockdown factor from Equation (B.7).

3. Multiply the theoretical buckling stress by the modified knockdown factor. Calculate the capacity margin factor by dividing the critical buckling stress thus obtained by the actual calculated compressive stress at the section.

CASE
N-284

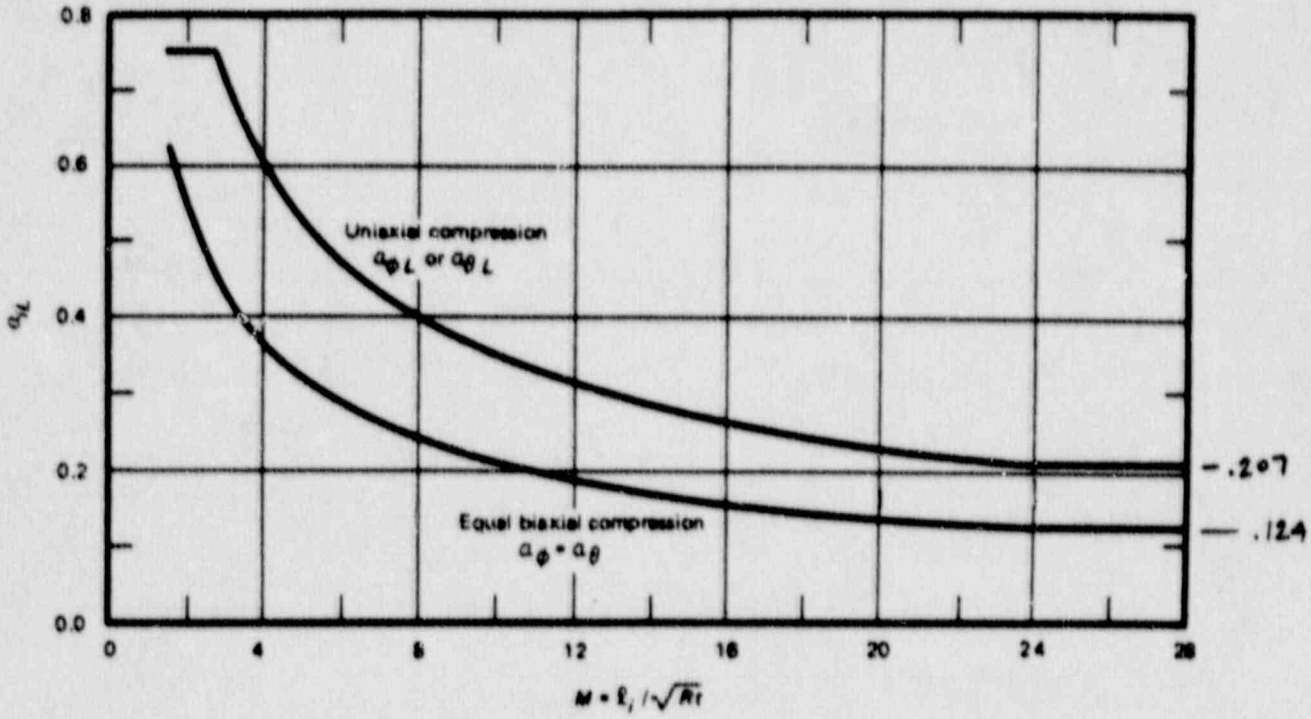

i = ϕ, θ corresponding to meridional and circumferential directions, respectively

ℓ_i = Distance in i direction between lines of support or stiffeners, in.

t = Shell thickness, in.

R = Shell radius, in.

Figure B.1 Capacity Reduction Factors For Local Buckling of Stiffened and Unstiffened Spherical Shells

APPENDIX C

SELECTED RESPONSES FROM SEISMIC ANALYSIS MODELS

This Appendix contains the following responses at selected locations of the Fermi, Clinton, Zion and Sequoyah Seismic analysis models.

* Maximum values of seismic shears and moments
* Maximum horizontal displacements relative to basemat
* Maximum of horizontal and vertical absolute acceleration
* Nodal response spectra

Responses are presented for values of peak horizontal ground acceleration, A_H, for which time history analyses were performed for purposes of this report. For reasons discussed in the next paragraph, these responses are identical for Tasks 3, 4, 5, and 6.

The seismic analysis models were intended to capture four types of nonlinearity

a. cracking of concrete,
b. change in soil properties at high acceleration levels,
c. uplift of basemat and
d. membrane yielding

Nonlinearities a and b were treated by changing the stiffness parameters in the model at various A_H values; selected stiffness did not change during the integration of equations of motion. Nonlinearity c occurred for Fermi, Zion and Sequoyah containments and its instantaneous effect was considered in the solution of equations of motion. Membrane yielding occurred at different locations of only the Fermi containment in different tasks. Results presented here for Fermi do not consider this membrane yielding effects, because the solution process of yielding models did not cover the full duration time history for reasons of computational economy. Consequently, in the seismic results presented, task identification is not given and the results are considered to apply for all tasks.

For convenience of reference the following table lists tables and figures of this Appendix and their relation to the seismic analysis models presented elsewhere in this report.

Key to Information Summarized

CONTAINMENT	RESPONSE	TABLE	FIGURE
Fermi	Moments and shears	C.1-1	
See Figure 3.7	Accelerations	C.1-2	
for Seismic Model	Displacements	C.1-3	
Nodal response	spectra	C.1-24 *	C.1-1 through
Clinton	Moments and shears	C.2-1	
See Figure 4.6	Accelerations	C.2-2	
for Seismic Model	Displacements	C.2-3	
Nodal response	spectra	C.2-48 *	C.2-1 through
Zion	Moments and shears	C.3-1	
See Figure 5.2	Accelerations	C.3-2	
for Seismic Model	Displacements	C.3-3	
Nodal response	spectra	C.3-40 *	C.3-1 through
Sequoyah	Moments and shears	C.4-1	
See Figure 6.3	Accelerations	C.4-2	
for Seismic Model	Displacements	C.4-3	
Nodal response	spectra	C.4-36 *	C.4-1 through

*These figures appear in microfiche form on the back cover of this report.

Table C.1-1
Maximum Values of Moments and Shears for Fermi Seismic Model (1)

ELEMENT(4) LOCATION	ELEMENT IN MODEL	MOMENT(3) (x10⁴ k-ft) 0.30g(2)	0.45g	0.60g	SHEAR (x10⁴ k) 0.30g	0.45g	0.60g
Drywell Pedestal at basemat	11 - 18	356.76	534.86	634.30	3.562	5.320	6.181
Steel Containment at Embedment	18 - 23	27.88	41.81	50.62	.384	.576	.696
Steel Containment at Elev. 597'	26 - 27	18.52	27.77	34.02	.350	.525	.637
Steel Containment at Elev. 636'	41 - 39	5.48	8.22	10.21	.307	.460	.568
Concrete Shield at Elev. 584'	22 - 30	165.05	247.52	302.16	2.332	3.496	4.126
Reactor-auxiliary Building at Basemat	16 - 21	798.41	1197.00	1461.00	6.914	10.288	11.808

NOTES: (1) See Figure 3.7
(2) Values in this row refer to the peak horizontal ground accelerstion, A_H
(3) Moment refers to the lower end of the element
(4) End nodes of element are listed

Table C.1-2
Maximum Values of Horizontal Displacement Relative To Basemat For Fermi Seismic Model (1)

NODE IN LOCATION	MODEL	DISPLACEMENT - ft 0.30g(2)	0.45g	0.60g
Steel Containment at Drywell Head	46	.099	.148	.198
Steel Containment at Equator	26	.037	.055	.080
Top of Drywell Pedestal	18	.017	.036	.039
Reactor-aux. bldg. Elev. 685'	43	.132	.198	.259
Reactor-aux. bldg. Elev. 642'	37	.107	.161	.211
Reactor-aux. bldg. Elev. 614'	28	.057	.085	.115
Reactor-aux. bldg. Elev. 584'	21	.033	.051	.060

NOTES: (1) See Figure 3.7
(2) Values in this row refer to peak horizontal ground acceleration, A_H

Table C.1-3
Maximum Values of Absolute Horizontal and Vertical Acceleration for Fermi Seismic Model (1)

NODE IN LOCATION	MODEL	HORIZONTAL ACCELERATION - g			VERTICAL ACCELERATION - g		
		0.30g(2)	0.45g	0.60g	0.30g	0.45g	0.60g
Steel Containment at Drywell Head	46	.841	1.276	1.719	.421	.631	1.086
Steel Containment at Equator	26	.464	.698	1.392	.398	.596	.796
Top of Drywell Pedestal	18	.398	.598	.966	.384	.575	.767
Pedestal at Basemat	11	.342	.513	.684	.374	.561	.748
Top of Concrete Shield	50	1.045	1.588	2.391	.447	.671	1.076
Reactor-aux. bldg. at Elev. 685'	43	1.124	1.686	2.220	.608	.911	4.231
Reactor-aux. bldg. at Elev. 642'	31	.796	1.200	1.393	.567	.851	2.852
Reactor-aux. bldg. at Elev. 584'	21	.521	.781	1.042	.452	.679	3.804

Notes: (1) See Figure 3.7
(2) Values in this row refer to the peak horizontal ground acceleration, A_H

Table C.2-1
Maximum Values of Moments and Shears for Clinton Seismic Model (1)

ELEMENT(4) LOCATION	MOMENT (3) (x10⁴ k-ft)					SHEAR (x10⁴ kip)			
	IN MODEL	.25g(2)	.45g	.75g	1.00g	.25g	.45g	.75g	1.00g
Containment at Basemat	33 - 24	152.8	231.3	302.7	365.6	1.313	2.030	2.744	3.238
Containment at Elev. 745'	15 - 6	117.5	177.7	232.8	283.9	1.165	1.767	2.345	2.724
Drywell Wall at Basemat	37 - 28	126.3	196.6	270.3	314.3	1.810	2.834	3.880	4.515
RPV Pedestal at Basemat	37 - 29	19.4	31.6	45.8	55.4	.350	.575	.842	1.022
Reactor-Control Bldg. at Basemat	46 - 44	458.4	721.8	1020.0	1212.0	6.731	10.560	14.630	17.160

Notes: (1) See Figure 4.6
(2) Values in this row refer to the peak horizontal ground acceleration, A_H
(3) Moment refers to the lower end of the element
(4) End node of element are listed

Table C.2-2
Maximum Values of Horizontal Displacement
Relative To Basemat for Clinton Seismic Model (1)

NODE IN LOCATION	MODEL	DISPLACEMENT - ft .25g(2)	.45g	.75g	1.00g
Top of Containment	1	.098	.163	.282	.395
Containment at Elev. 832'	4	.075	.127	.221	.315
Containment at Elev. 801'	10	.061	.105	.187	.273
Containment at Elevation 745'	15	.031	.059	.122	.190
Top of Drywell Wall	8	.102	.169	.260	.362
Top of RPV	11	.090	.153	.239	.319
Top of Reactor Control Bldg.	5	.085	.139	.239	.339
Reactor-Control Bldg. At Elev. 801'	17	.063	.105	.194	.279

Note: (1) See Figure 4.6
(2) Values in this row refer to peak horizontal ground acceleration, A_H

Table C.2-3
Maximum Values of Absolute Horizontal and Vertical Acceleration For Clinton Seismic Model (1)

NODE IN LOCATION	MODEL	HORIZONTAL ACCLERATION - g				VERTICAL ACCELERATION - g			
		.25g(2)	.45g	.75g	1.00g	.25g	.45g	.75g	1.00g
Top of Containment	1	.635	.959	1.383	1.725	.339	.568	.866	1.086
Containment at Elev 832'	4	.474	.734	1.001	1.224	.324	.547	.840	1.058
Containment at Elev. 801'	10	.400	.642	.981	1.217	.314	.533	.827	1.047
Containment at Elev. 745'	15	.303	.527	.823	1.040	.291	.504	.793	1.016
Top of Drywell Wall	8	.657	1.037	1.442	1.693	.305	.521	.813	1.038
Top of RPV	11	.726	1.192	1.748	2.127	.300	.520	.824	1.058
Top of Reactor Control Bldg.	5	.931	1.527	2.219	2.681	.438	.737	1.130	1.423
Reactor Control Bldg. at Elev. 801'	17	.561	.897	1.275	1.523	.355	.609	.955	1.223

Notes: (1) See Figure 4.6
(2) Values in this row refer to peak horizontal ground acceleration, A_H

Table C.3-1
Maximum Values of Moments and Shears for Zion Seismic Model [1]

ELEMENT IN[4] LOCATION	MODEL	MOMENT [3] (x10⁴ k-ft) .25g[2]	.50g	.75g	1.00g	SHEAR (x10⁴ kip) .25g	50g	.75g	1.00g
Containment at Basemat	15 - 10	270.0	387.6	474.4	572.8	1.854	2.737	3.516	4.289
Containment at Elev. 592'	9 - 8	226.3	326.8	391.8	483.6	1.795	2.564	3.255	3.965
Containment at Elev. 628'	7 - 6	163.5	238.3	278.0	365.9	1.647	2.331	2.880	3.488
Primary Shield at Basemat	31 - 45	14.5	24.9	34.5	44.1	.506	.879	1.224	1.570
Crane Wall at Basemat	31 - 46	27.7	47.5	65.7	84.0	.742	1.276	1.771	2.265

Note: (1) See Figure 5.2
(2) Value in row refer to peak horizontal ground acceleration, A_H
(3) Moment refers to the lower end of the element
(4) End nodes of element are listed

Table C.3-2
Maximum Values of Displacement Relative
To Basemat for Zion Seismic Model (1)

LOCATION	NODE	DISPLACEMENT - ft .25g(2)	.50g	.75g	1.00g
Containment at Elev. 755'	1	.143	.374	.602	.898
Containment (3) at Elev. 646'	6	.070	.190	.302	.438
Containment at Elev. 582'	9	.034	.097	.158	.216
Top of Primary Shield	50	.054	.135	.222	.324
Top of Crane Wall	53	.053	.135	.221	.322

Notes: (1) See Figure 5.2
(2) Values in row refer to peak horizontal ground acceleration, A_H
(3) This elevation approximatly represents the location of potential impact with the auxiliary building

Table C.3-3
Maximum Values of Absolute Horizontal and Vertical Accleration for Zion Seismic MODEL (1)

NODE IN LOCATION	MODEL	HORIZONTAL ACCELERATION - g				VERTICAL ACCELERATION - g			
		.25g(2)	.50g	.75g	1.00g	.25g	.50g	.75g	1.00g
Containment at Elev. 755'	1	.454	.705	.771	1.035	.434	.810	1.176	1.543
Containment at Elev. 646'	6	.256	.446	.582	.713	.346	.663	.972	1.281
Containment at Elev. 592'	9	.253	.443	.676	.908	.284	.557	.825	1.094
Top of Primary Shield	50	.611	1.055	1.463	1.877	.277	.539	.797	1.054
Top of Crane Wall	53	.598	1.018	1.408	1.802	.268	.525	.774	1.026

Notes: (1) See Figure 5.2
(2) Values in this row refer to peak horizontal ground acceleration, A_H

Table C.4-1
Maximum Values of Moments and Shears for Sequoyah Seismic Model [1]

LOCATION	ELEMENT IN[4] MODEL	MOMENT [3] (x10⁴ k-ft) 0.25g[2]	0.50g	0.75g	1.00g	SHEAR (x10⁴ kip) 0.25g	0.50g	0.75g	1.0g
Steel Containment at Basemat	77 - 68	17.00	33.90	50.90	83.70	0.207	0.414	0.620	0.956
Steel Containment at Elev. 692'	62 - 59	14.51	29.01	43.52	72.22	0.198	0.396	0.595	0.926
Steel Containment at Elev. 722'	44 - 41	9.04	18.07	27.11	46.30	0.165	0.331	0.496	0.794
Steel Containment at Elev. 760'	24 - 22	3.79	7.59	11.49	21.00	0.100	0.200	0.300	0.505
Shield Building at Basemat	77 - 67	256.00	513.00	770.00	927.60	2.370	4.730	7.120	8.570
Crane Wall at Basemat	76 - 77	137.00	275.00	410.00	541.00	2.250	4.500	6.710	8.840

Notes: (1) See Figure 6.3
(2) Values in this row refer to the peak horizontal ground acceleration, A_H
(3) Moment refers to the lower end of the element
(4) End nodes of element are listed

Table C.4-2
Maximum Value of Horizontal Displacement Relative
To Basemat for Sequoyah Seismic Model (1)

LOCATION	NODE	DISPLACEMENT - ft .025g(2)	0.50g	0.75g	1.00g
Top of Steel Containment	1	.012	.024	.036	.068
Steel Containment at Elev. 791'	12	.009	.018	.026	.048
Steel Containment at Elev. 750'	26	.006	.011	.017	.030
Steel Contaiment at Elev. 700'	56	.002	.003	.006	.009
Shield Building at Elev. 829'	5	.053	.107	.164	.209
Shield Building at Elev. 791'	11	.041	.082	.126	.161
Top of Crane Wall	27	.031	.063	.094	.126

Notes: (1) See Figure 6.3
(2) Values in this row refer to peak horizontal ground acceleration, A_H

Table C.4-3
Maximum Values of Absolute Horizontal and Vertical Acceleration for Sequoyah Seismic Model (1)

NODE IN LOCATION	MODEL	HORIZONTAL ACCELERATION - g				VERTICAL ACCELERATION - g			
		0.25g(2)	0.50g	0.75g	1.00g	0.25g	0.50g	0.75g	1.00g
Top of Steel Containment	2	1.072	2.144	3.217	7.271	.341	.682	1.023	10.607
Steel Containment at Elev. 791'	12	.857	1.714	2.572	4.200	.332	.665	.997	7.989
Steel Containment at Elev. 750'	26	.631	1.262	1.893	2.852	.316	.633	.949	6.378
Steel Containment at Elev. 700'	56	.363	.726	1.089	1.553	.299	.598	.897	7.333
Shield Building at Elev. 829'	5	1.113	2.227	3.334	4.022	.600	1.200	1.799	5.860
Shield Building at Elev. 791'	11	.903	1.807	2.717	3.387	.557	1.115	1.672	3.905
Top of Crane Wall	27	1.201	2.402	3.605	4.793	.462	.923	1.385	8.491

Notes: (1) See Figure 6.3
(2) Values in this row refer to peak horizontal ground acceleration, A_H

Distribution:

J. F. Costello (20 Copies)
USNRC/RES
Mail Stop NL/S-217A
5650 Nicholson Lane
Rockville, MD 20852

H. L. Graves, III
USNRC/RES
Mail Stop NL/S-217A
5650 Nicholson Lane
Rockville, MD 20852

US Department of Energy
Office of Nuclear Energy
Attn: A. Millunzi
Bernard J. Rock
D. Giessing (3 copies)
Mail Stop B-107
NE-540
Washington, DC 20545

CBI NaCon, Inc.
Attn: Thomas J. Ahl
800 Jorie Boulevard
Oak Brook, IL 60521

Wilfred Baker Engineering
Attn: Wilfred E. Baker
P. O. Box 6477
San Antonio, TX 78209

Battelle Columbus Laboratories
Attn: Richard Denning
505 King Avenue
Columbus, Ohio 43201

Bechtel Power Corporation
Attn: Asadour H. Hadjian
12400 E. Imperial Highway
Norwalk, CA 90650

Bechtel Power Corp.
Attn: T. E. Johnson, Subir Sen
K. Y. Lee (3 copies)
15740 Shady Grove Rd.
Gaithersburg, MD 20877

Babcock & Wilcox Co.
Attn: James R. Farr
20 S. van Buren Ave.
Barberton, OH 44203

City College of New York
Dept. of Civil Engineering
Attn: C. Costantino
140 Street and Convent Ave.
New York, NY 10031

1245 Newmark CE Lab
University of Illinois
Attn: Prof. Mete A. Sozen
208 N. Romine
MC-250
Urbana, IL 61801

Stevenson & Associates
Attn: John D. Stevenson
9217 Midwest Ave.
Cleveland, Ohio 44125

United Engineers & Constructors, Inc.
Attn: Joseph J. Uicciferro
30 S. 17th St.
Philadelphia, PA 19101

Electrical Power Research Institute
Attn: H. T. Tang, Y. K. Tang
Raf Sehgal, J. J. Taylor,
W. Loewenstein (5 copies)
3412 Hillview Avenue
PO Box 10412
Palo Alto, CA 94304

School of Civil & Environ. Engr.
Attn: Professor Richard N. White
Hollister Hall Cornell University
Ithaca, NY 14853

NUTECH Engineers, Inc.
Attn: John Clauss
1111 Pasquinelli Drive, Suite 100
Westmont, Illinois 60559

Iowa State University
Department of Civil Engineering
Attn: L. Greimann
420 Town Engineering Bldg.
Ames, IA 50011

TVA
Attn: D. Denton, W9A18
400 Commerce Ave.
Knoxville, TN 37902

Los Alamos National Laboratories
Attn: C. Anderson
PO Box 1663
Mail Stop N576
Los Alamos, NM 87545

EQE Inc.
Attn: M. K. Ravindra
3300 Irvine Aveune
Suite 345
Newport Beach, CA 92660

University of Illinois
Attn: C. Siers
Dept. of Civil Engineering
Urbana, IL 61801

EBASCO Services, Inc.
Attn: Robert C. Iotti
Two World Trade Center
New York, NY 10048

EG&G Idaho
Attn: B. Barnes, T. L. Bridges
(2 copies)
Willow Creek Bldg. W-3
PO Box 1625
Idaho Falls, ID 83415

Sargent & Lundy Engineers
Attn: A. Walser
P. K. Agrawal (15 copies)
55 E Monroe St.
Chicago, IL 60603

General Electric Company
Attn: E. O. Swain, D. K. Henrie,
R. Gou (3 copies)
175 Curtner Ave.
San Jose, CA 95125

Westinghouse Electric Corp.
Attn: Vijay K. Sazawal
Waltz Mill Site
Box 158
Madison, PA 15663

Quadrex Corporation
Attn: Quazi A. hossain
1700 Dell Ave.
Campbell, CA 95008

ANATECH International Corp.
Attn: Y. R. Rashid
3344 N. Torrey Pines Court
Suite 320
LaJolla, CA 92037

Oak Ridge National Laboratory
Attn: Steve Hodge
PO Box Y
Oak Ridge, TN 37830

Brookhaven National Laboratory
Attn: C. Hofmayer, T. Pratt
M. Reich (3 copies)
Building 130
Upton, NY 11973

Argonne National Laboratory
Attn: J. M. Kennedy,
R. F. Kulak,
R. W. Seidensticker (3 copies)
9700 South Cass Avenue
Argonne, IL 60439

Tennessee Valley Authority
Attn: Nathaniel Foster
400 Summit Hill Rd.
W9D24C-K
Knoxville, Tennessee 37902

University of Wisconsin
Nuclear Engineering Dept.
Attn: Prof. Michael Corradini
Madison, WI 53706

Brookhaven National Laboratory
Attn: Ted Ginsberg
Building 820M
Upon, NY 11973

Dept. of Chemical & Nuclear Engineering
University of California Santa Barbara
Attn: T. G. Theofanous
Santa Barbara, CA 93106

Northern Illinois University
Mechanical Engineering Dept.
Attn: A. Marchertas
DeKalb, IL 60115

Department of Civil Engineering
University of California Irvine
Attn: A. H.-S. Ang
Irvine, CA 92717

Department of Civil Engineering
& Operation Research
Princeton University
Attn: M. Shinozuka
Princeton, NJ 08544

Department of Civil Engineering
The Johns Hopkins University
Attn: B. R. Ellingwood
Baltimore, MD 21218

Institut fur Mechanik
Universitaet Innsbruck
Attn: Prof. G. I. Schueller
Technikerstr. 13
A-6020 Innsbruck
AUSTRIA

Nuclear Studies & Safety Dept.
Ontario Hydro
Attn: W. J. Penn
700 University Avenue
Toronto, Ontario
M5G 1X6
CANADA

University of Alberta
Dept. of Civil Engineering
Attn: Prof. D. W. Murray
Edmonton, Alberta
CANADA T6G 2G7

Commissariat a L'Energie Atomique
Centre d'Etudes Nucleaires de Saclay
Attn: M. Livolant, P. Jamet (2 copies)
F-91191 Gif-Sur-Yyette Cedex
FRANCE

Institut de Protection et de
Surete Nucleaire
Commissariat a l'Energie Atomigue
Attn: M. Barbe
F-92660 Fontenay-aux-Roses
FRANCE

Kernforschungszentrum Karlsruhe GmbH
Attn: R. Krieg, P. Gast (2 copies)
Postfach 3640
D-7500 Karlsruhe
FEDERAL REPUBLIC OF GERMANY

Lehrstuhl fuer Reakordynamik
und Reaktorsicherheit
Technische Universitaet Muenchen
Attn: Prof. H. Karwat
D-8046 Garching
FEDERAL REPUBLIC OF GERMANY

Staatliche Materialpruefungsanstalt (MP
University of Stuttgart
Attn: Prof. K. F. Kussmaul
Pfaffenwaldring 32
D-7000 Stuttgart 80 (Vaihingen)
FEDERAL REPUBLIC OF GERMANY

Gesellschaft fuer Reaktorsicherheit
Attn: H. Schulz, A. Hoefler,
F. Schleifer (3 copies)
Schwertnergasse 1
D-5000 Koeln 1
FEDERAL REPUBLIC OF GERMANY

Kraftwerk Union AG
Attn: M. Hintergraber
Hammerbacherstr. 12-14
D-8520 Erlangen
FEDERAL REPUBLIC OF GERMANY

Ente Nazionale per l'Energia Elettrica
Attn: Francesco L. Scotto
v. le Regina Margherita, 137
Rome, ITALY

ISMES
Attn: A. Peano
Viale Giulio Cesare 29
I-24100 Bergamo
ITALY

ENEA-DISP
ACO-CIVME
Attn: Giuseppe Pino
Via Vitaliano Brancati, 48
I-00144 Roma
ITALY

Nuclear Equipment Design Dept.
Hitachi Works, Hitachi, Ltd.
Attn: O. Oyamada
3-1-1 Saiwai-Cho
Hitachi-Shi
Ibaraki-ken
JAPAN

Division of Technical Information
Japan Atomic Energy Research Institute
Attn: Jun-ichi Shimokawa
2-2, Uchisaiwai-cho 2-chome
Chiyoda, Tokyo 100
JAPAN

University of Tokyo
Institute of Industrial Science
Attn: Prof. H. Shibata
22-1, Roppongi 7
Minatu-ku, Tokyo
JAPAN

Civil Engineering Laboratory
Central Research Institute of
Electric Power Industry
Attn: Yukio Aoyagi
1646 Abiko Abiko-Shi Chiba
JAPAN

Kajima Corporation
Attn: K. Umeda
No. 1-1, 2-Chome Nishishinjuku
Shinjuku-ku
Tokyo 160
JAPAN

Muto Institute of Structural Mechanics
Attn: Tadashi Sugano
Room 3005 Shinjuku Mitsui Building
Shinjuku-ku
Tokyo, 163
JAPAN

Nuclear Power Engineering Test Center
Attn: Yoshio Tokumaru
6-2, 3-Chome, Toranomor
Minatoku
Tokyo 105
JAPAN

Japan Atomic Energy Research Inst.
Attn: Kunihisa Soda
Toshikuni Isozaki (2 copies)
Tokai-Mura, Ibaraki-Ken 319-11
JAPAN

Shimizu Construction Co., Ltd.
Attn: Toshihiko Ota
No. 4-17, Etchujima 3-Chome
Koto-Ku
Tokyo 135
JAPAN

Shimizu Construction Co., Ltd.
Attn: Toshiaki Fujimori
No. 18-1, Kyobashi 1-Chome
Chuo-ku
Tokyo 104
JAPAN

Universidad Politecnica
Escuela Tecnica Superior
de Ingenieros Industriales
Attn: Agustin Alonso
Madrid
SPAIN

Unidad Electrica S.A.
Attn: Jose Puga
UNESA
ES-28020 Madrid
SPAIN

Principia Espana, SA
Attn: Joaquin Marti
Orense, 36-2
28020 Madrid
SPAIN

Studsvik Energiteknik AB
Attn: Kjell O. Johansson
S-611 82 Nykoping
SWEDEN

Swedish State Power Board
Nuclear Reactor Safety
Attn: Hans Cederberg
Per-Eric Ahlstrom
Ralf Espefaelt (3 copies)
S-162 87 Vallingby
SWEDEN

Swiss Federal Institute of Technology
Institute of Structural Engineering
Attn: W. Ammann
ETH-Hoenggerberg, HIL
CH-8093 Zurich
SWITZERLAND

Motor-Columbus Consulting Engineers, Inc.
Attn: K. Gahler, A. Huber
A. Schopfer (3 copies)
Parkstrasse 27
CH-5401 Baden
SWITZERLAND

EIR (Swiss Federal Institute for
Reactor Research)
Attn: O. Mercier
P. Housemann (2 copies)
CH-5303 Wuerlingen
SWITZERLAND

Swiss Federal Nuclear Safety Inspectorate
Federal Office of Energy
Attn: S. Chakraborty
CH-5303 Wuerenlingen
SWITZERLAND

Swiss Federal Institute of Technology
Attn: Prof. F. H. Wittmann
Chemin de Bellerive 32
CH-1007 Lausanne
SWITZERLAND

Elektrowatt Ingenieurunternehmung AG
Attn: John P. Wolf
Bellerivestr. 36
CH-8022 Zurich
SWITZERLAND

Atomic Energy Establishment
Attn: Peter Barr
Winfrith
Dorchester Dorset
DT2 8DH
UNITED KINGDOM

Atomic Energy Authority
Safety and Reliability Directorate
Attn: D. W. Phillips
Wigshaw Lane
Culcheth
Warrington WA3 4NE
UNITED KINGDOM

HM Nuclear Installation Inspectorate
Attn: R. J. Stubbs
St. Peter's House
Stanley Precinct
Bootle L20 3LZ
UNITED KINGDOM

Taylor Woodrow Construction Limited
Attn: Carl C. Fleischer
Richard Crowder (2 copies)
345 Ruislip Road
Southall, Middlesex
UB1 2QX
UNITED KINGDOM

Central Electricity Generating Board
Attn: J. Irving
Barnett Way
Barnwood, Gloucester
GL4 7RS
UNITED KINGDOM

Central Electricity Generating Board
Attn: Carl Lomas
Booths Hall
Chelford Road
Knutsford, Cheshire
WA16 8QG
UNITED KINGDOM

HM Nuclear Installations Inspectorate B
Attn: Iain Todd
St. Peter's House
Bootle, Mereyside L20 3LZ
UNITED KINGDOM

3141	S. A. Landenberger (5)
3151	W. I. Klein
3153	R. Gardner
6410	D. A. Dahlgren
6419	M. P. Bohn
6422	T. Fuketa
6500	A. W. Snyder
6510	J. V. Walker
6520	A. W. Snyder, Actg.
6523	W. A. von Riesemann (30)
6523	D. B. Clauss
6523	R. N. Eyers
6523	D. S. Horschel
6523	L. D. Lambert
6523	M. B. Parks
6523	J. J. Westmoreland
8524	J. A. Wackerly

NRC FORM 335 (2-89) NRCM 1102, 3201, 3202

U.S. NUCLEAR REGULATORY COMMISSION

BIBLIOGRAPHIC DATA SHEET

(See instructions on the reverse)

1. REPORT NUMBER (Assigned by NRC, Add Vol., Supp., Rev., and Addendum Numbers, if any.)

NUREG/CR-5098
SAND88-7018

2. TITLE AND SUBTITLE

An Analytical Study of Seismic Threat to Containment Integrity

3. DATE REPORT PUBLISHED

MONTH: August YEAR: 1989

4. FIN OR GRANT NUMBER

A1401

5. AUTHOR(S)

M. Amin, P. K. Agrawal, S&L
T. J. Ahl, CBI

6. TYPE OF REPORT

Topical

7. PERIOD COVERED (Inclusive Dates)

8. PERFORMING ORGANIZATION – NAME AND ADDRESS (If NRC, provide Division, Office or Region, U.S. Nuclear Regulatory Commission, and mailing address; if contractor, provide name and mailing address.)

Sargent & Lundy
55 East Monroe
Chicago, IL 60603

CBI Na-Con
800 Jorie Boulevard
Oak Brook, IL 60522

Under contract to:
Sandia National Laboratories
Albuquerque, NM 87185

9. SPONSORING ORGANIZATION – NAME AND ADDRESS (If NRC, type "Same as above"; if contractor, provide NRC Division, Office or Region, U.S. Nuclear Regulatory Commission, and mailing address.)

Division of Engineering
Office of Nuclear Regulatory Research
U.S. Nuclear Regulatory Commission
Washington, DC 20555

10. SUPPLEMENTARY NOTES

11. ABSTRACT (200 words or less)

The methodology used and the results of an analytical scoping study of the seismic capacity of four containment buildings located in the Eastern United States are described in this report. The study was undertaken to provide quantitative information of containment seismic capacity considering a rather complete list of limit states. This type of information was not available previously.

The four containments represent a cross-section of containment, reactor, and foundation types. Evaluations included time history analyses, four combinations of seismic with pressure and temperature loading to consider different severe accident conditions and seismic aftershocks. Containments are evaluated for applicable limit states from a list of sixteen limit states that include structural, penetration, and foundation failures.

The results are presented in terms of capacity margin factors at a prescribed value of peak horizontal ground acceleration or by stating the seismic capacity in the governing limit states when the capacity is smaller than the acceleration value at which margin factors are listed. For certain critical limit states, curves showing variation of capacity margin factor with peak horizontal ground acceleration are presented. The report also includes a discussion of factors that are significant for determining seismic capacity and provides recommendations for future work.

12. KEY WORDS/DESCRIPTORS (List words or phrases that will assist researchers in locating the report.)

Seismic Threat
Containment Integrity
Analytical Scoping Study

13. AVAILABILITY STATEMENT

Unlimited

14. SECURITY CLASSIFICATION

(This Page) Unclassified

(This Report) Unclassified

15. NUMBER OF PAGES

16. PRICE

NRC FORM 335 (2-89)

*U.S. GOVERNMENT PRINTING OFFICE: 1989-244-592

UNITED STATES
NUCLEAR REGULATORY COMMISSION
WASHINGTON, D.C. 20555

OFFICIAL BUSINESS
PENALTY FOR PRIVATE USE, $300

SPECIAL FOURTH-CLASS RATE
POSTAGE & FEES PAID
USNRC
PERMIT No. G-67

120555139531 1 1AN
US NRC-OADM
DIV FOIA & PUBLICATIONS SVCS
TPS PDR-NUREG
P-209
WASHINGTON DC 20555

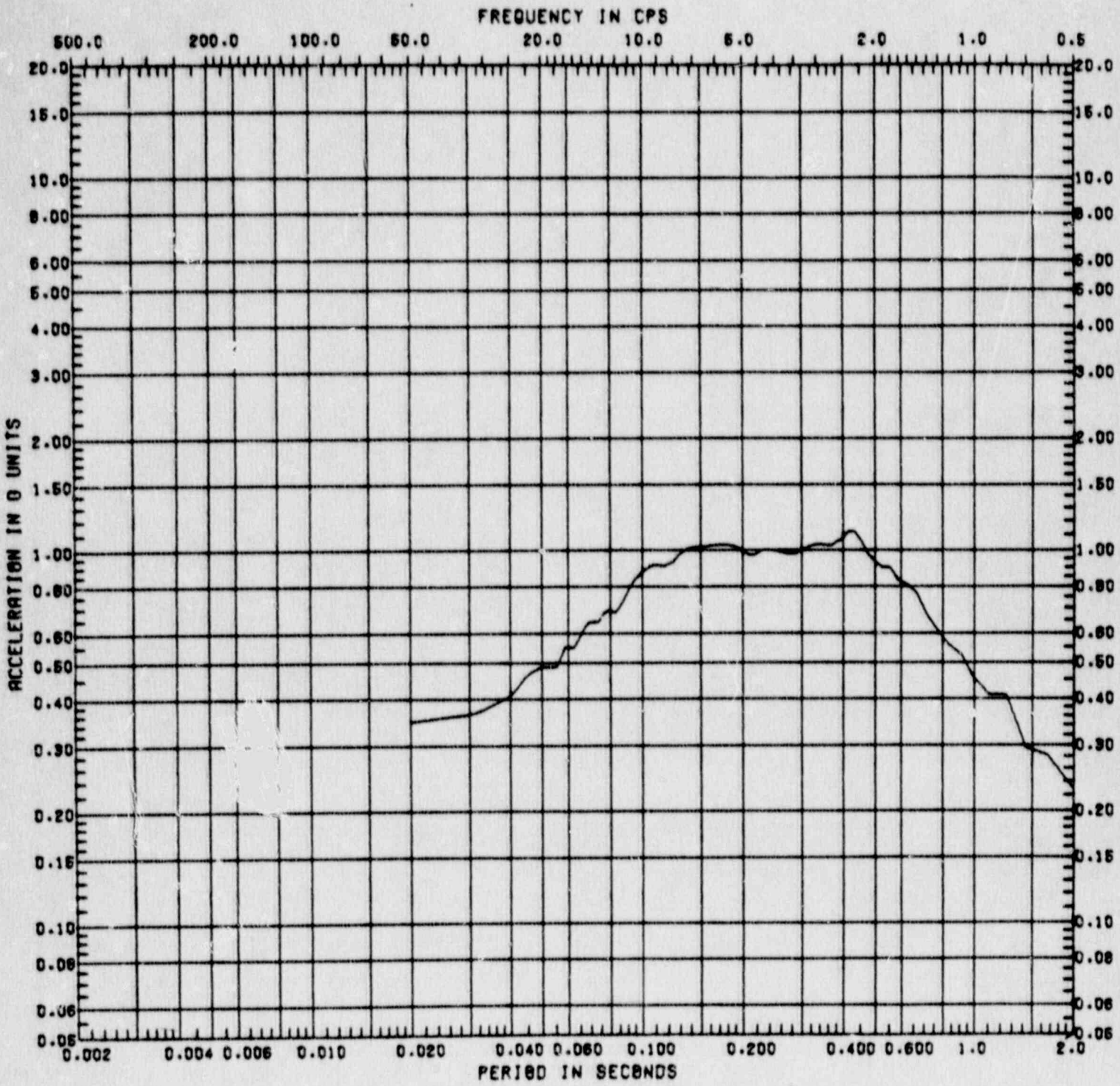

Figure C.1-1 Horizontal Response Spectrum at Fermi Model Node 11 (A_H = 0.30g, Damping = 5%, Location = Containment Pedestal at Basemat Elevation 540')

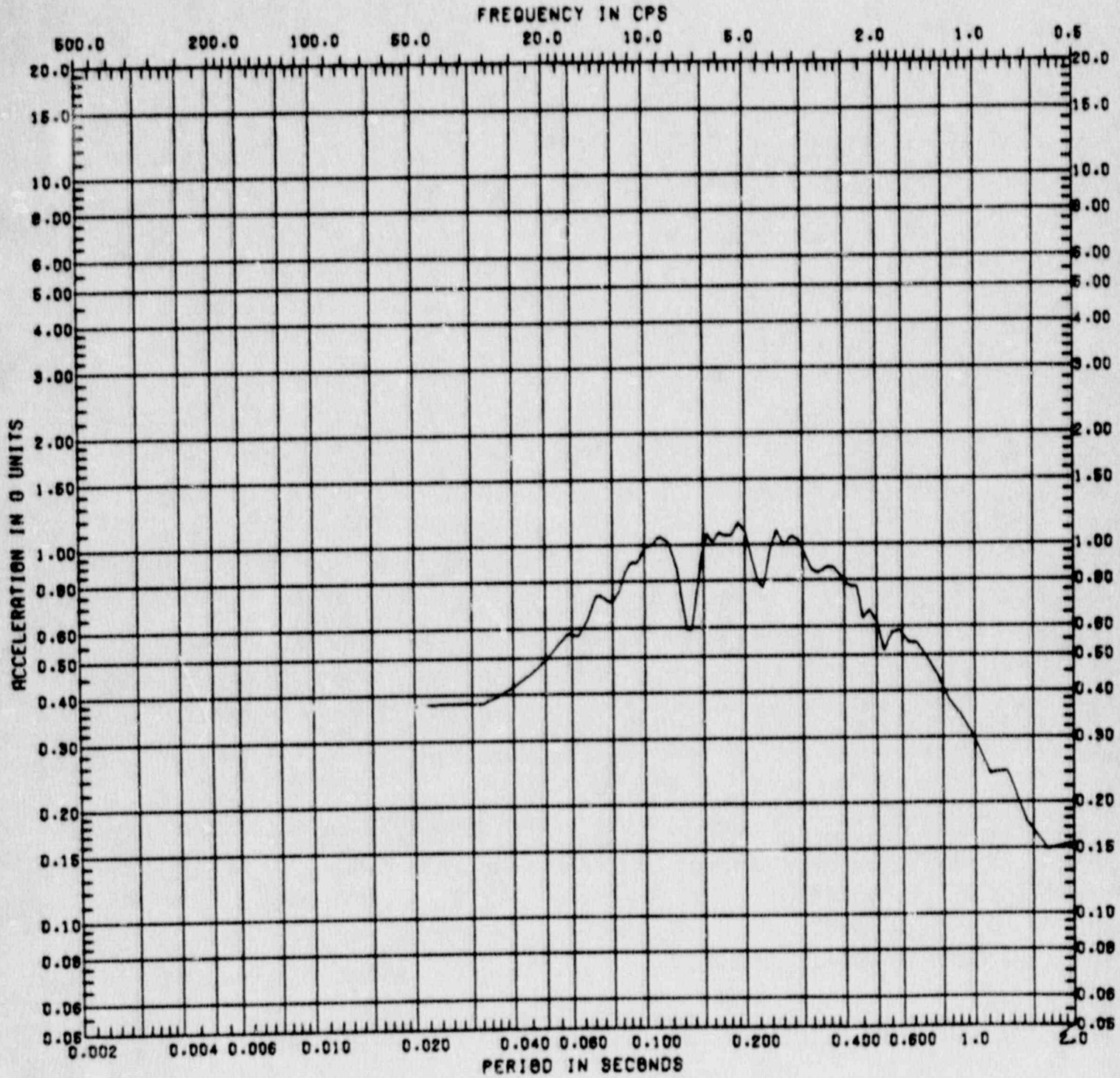

Figure C.1-2 Vertical Response Spectrum at Fermi Model Node 11 (A_H = 0.30g, Damping = 5%, Location = Containment Pedestal at Basemat Elevation 540')

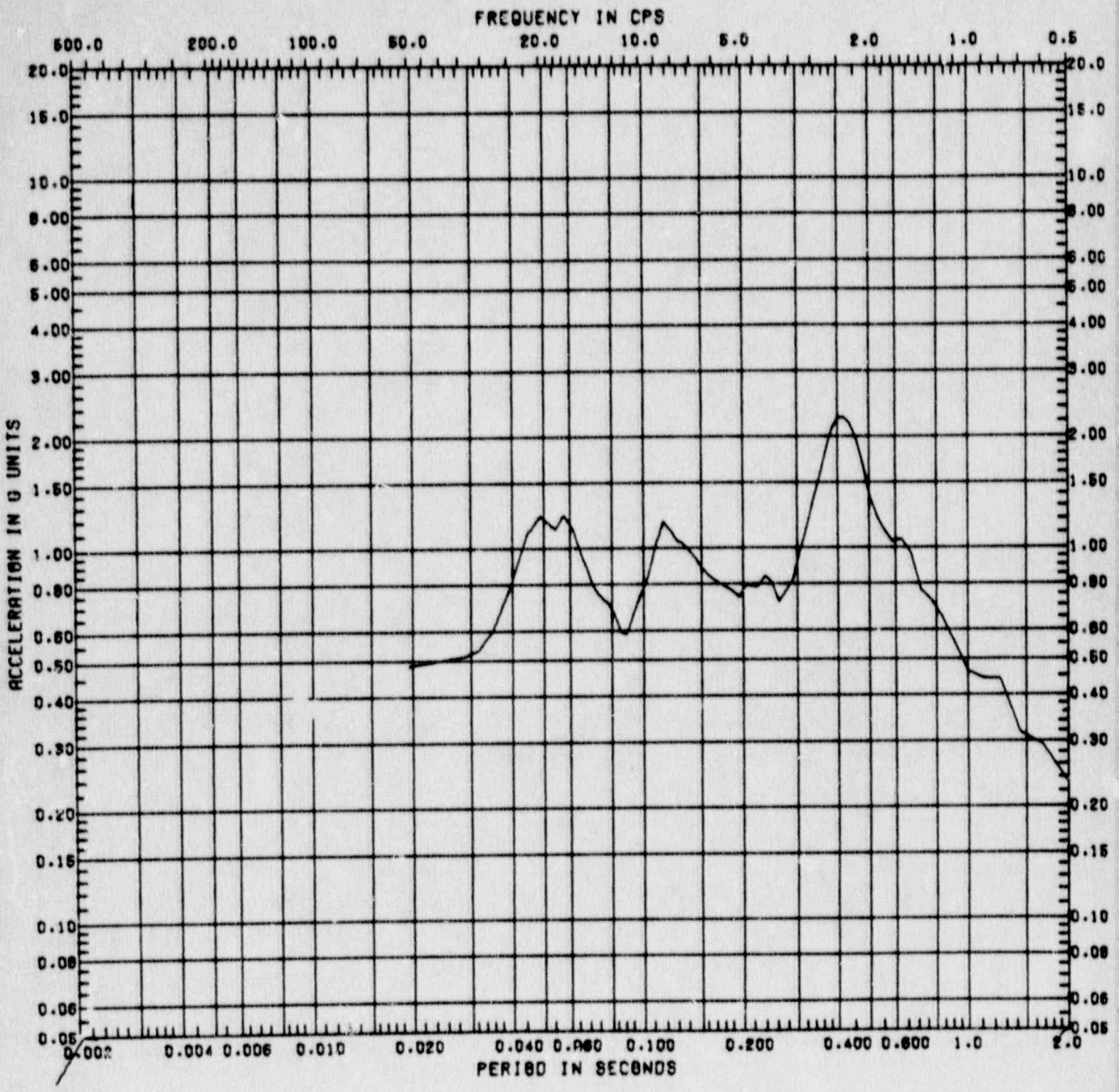

Figure C.1-3 Horizontal Response Spectrum at Fermi Model Node 26 (A_H = 0.30g, Damping = 5%, Location = Steel Containment at Equator Elevation 597')

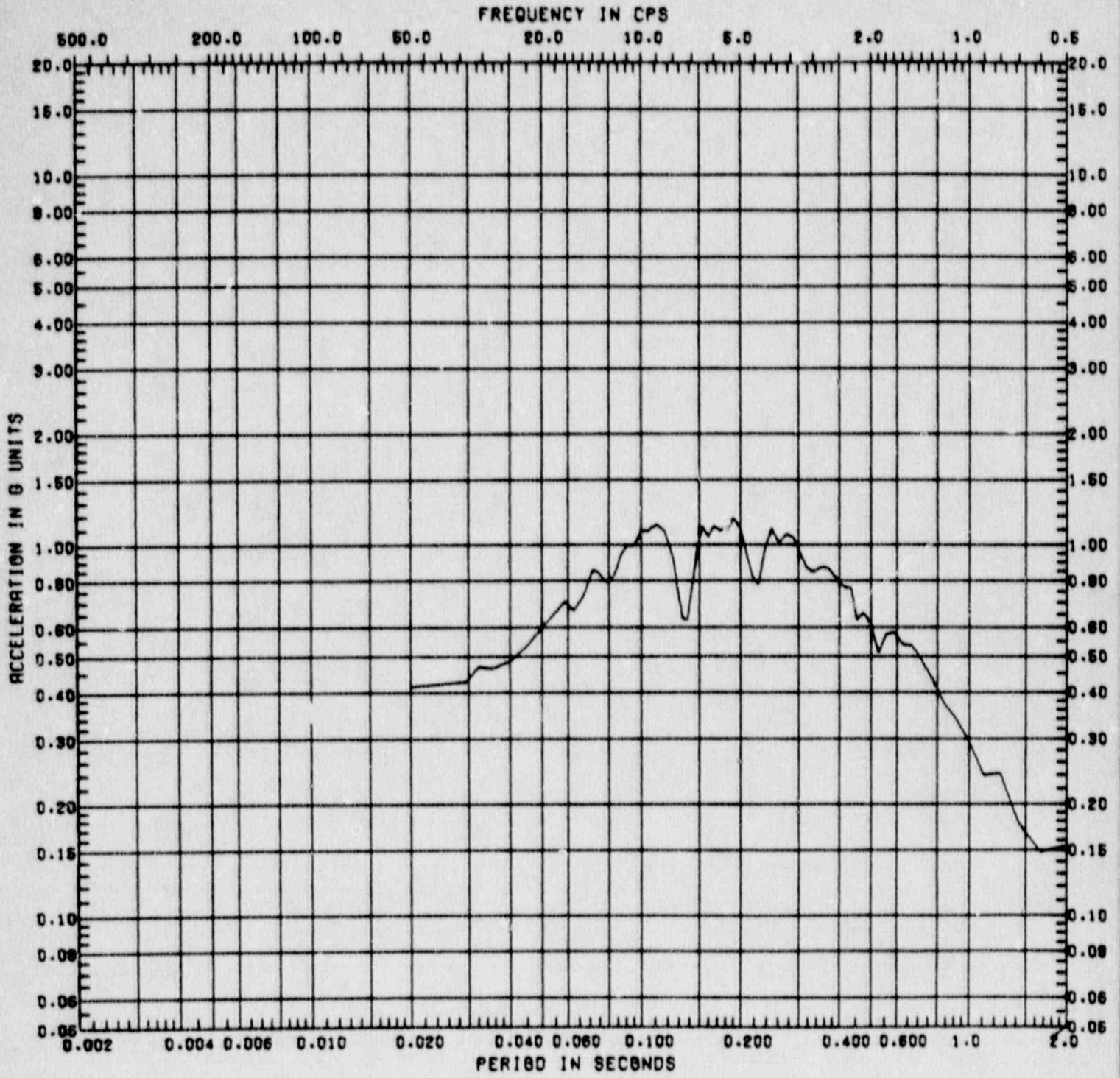

Figure C.1-4 Vertical Response Spectrum at Fermi Model Node 26 (A_H = 0.30g, Damping = 5%, Location = Steel Containment at Equator, Elevation 597')

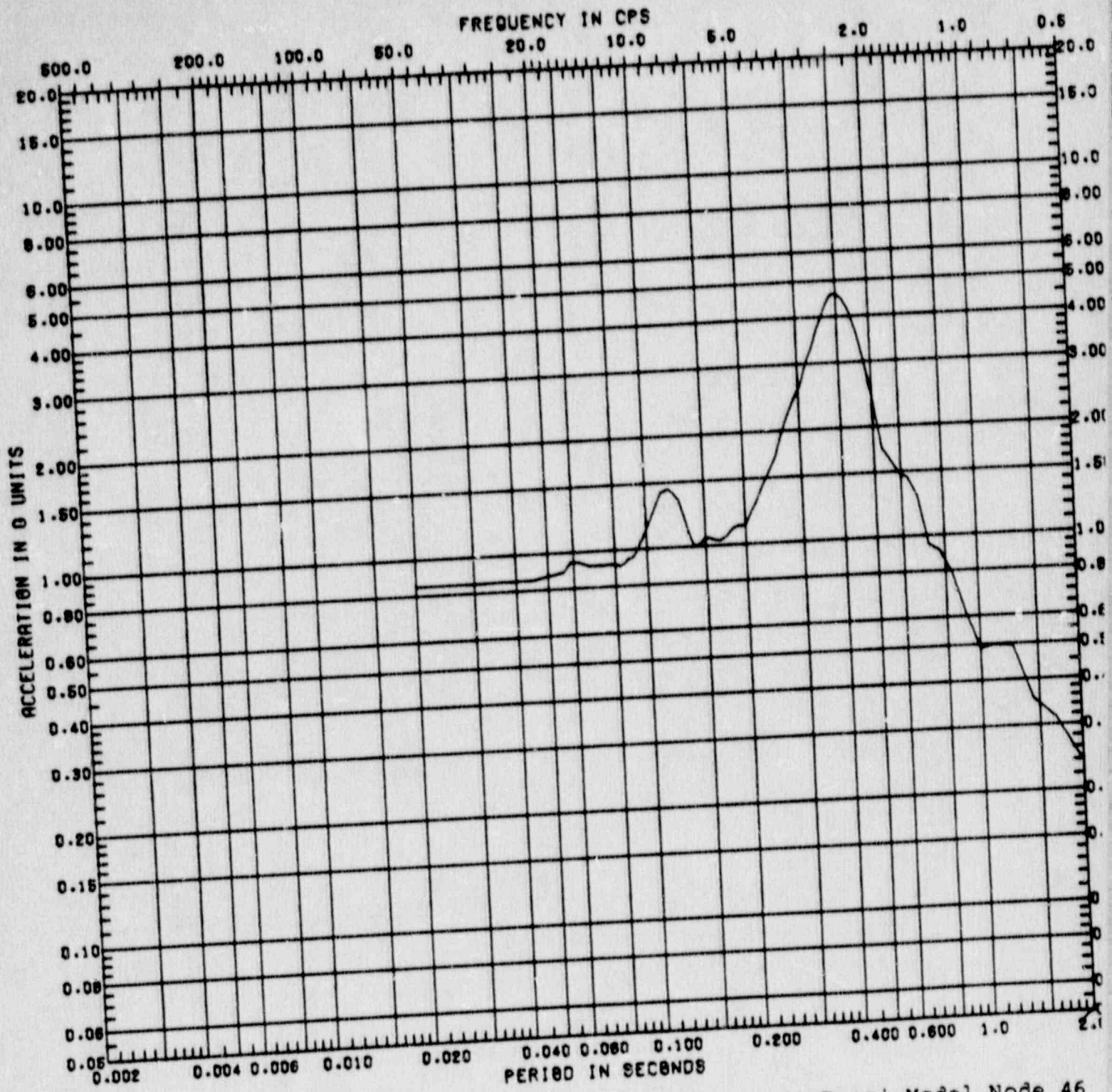

Figure C.1-5 Horizontal Response Spectrum at Fermi Model Node 46 (A_H = 0.30g, Damping = 5%, Location = Steel Containment at Elevation 659')

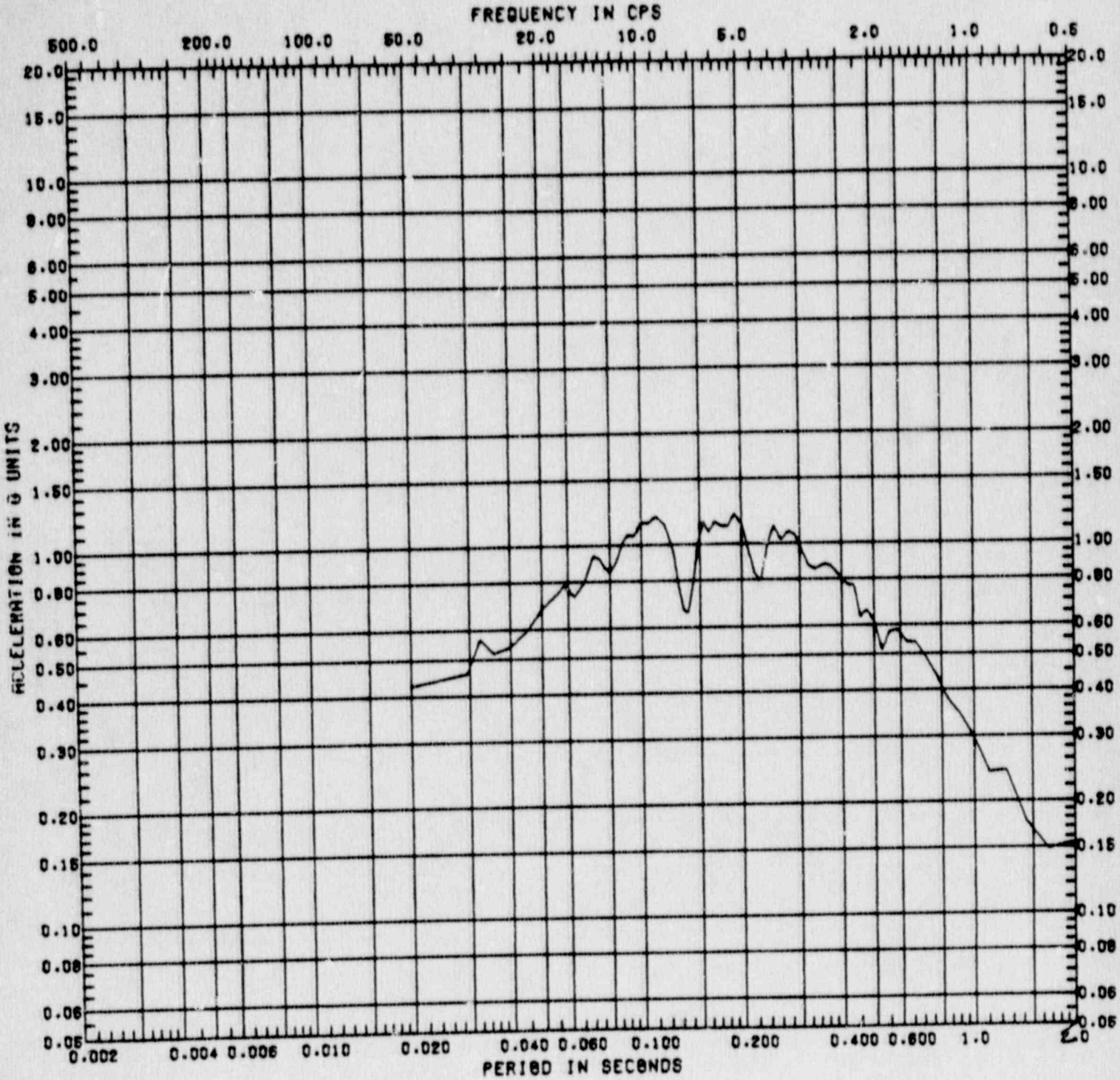

Figure C.1-6 Vertical Response Spectrum at Fermi Model Node 46 (A_H = 0.30g, Damping = 5%, Location = Steel Containment at Elevation 659')

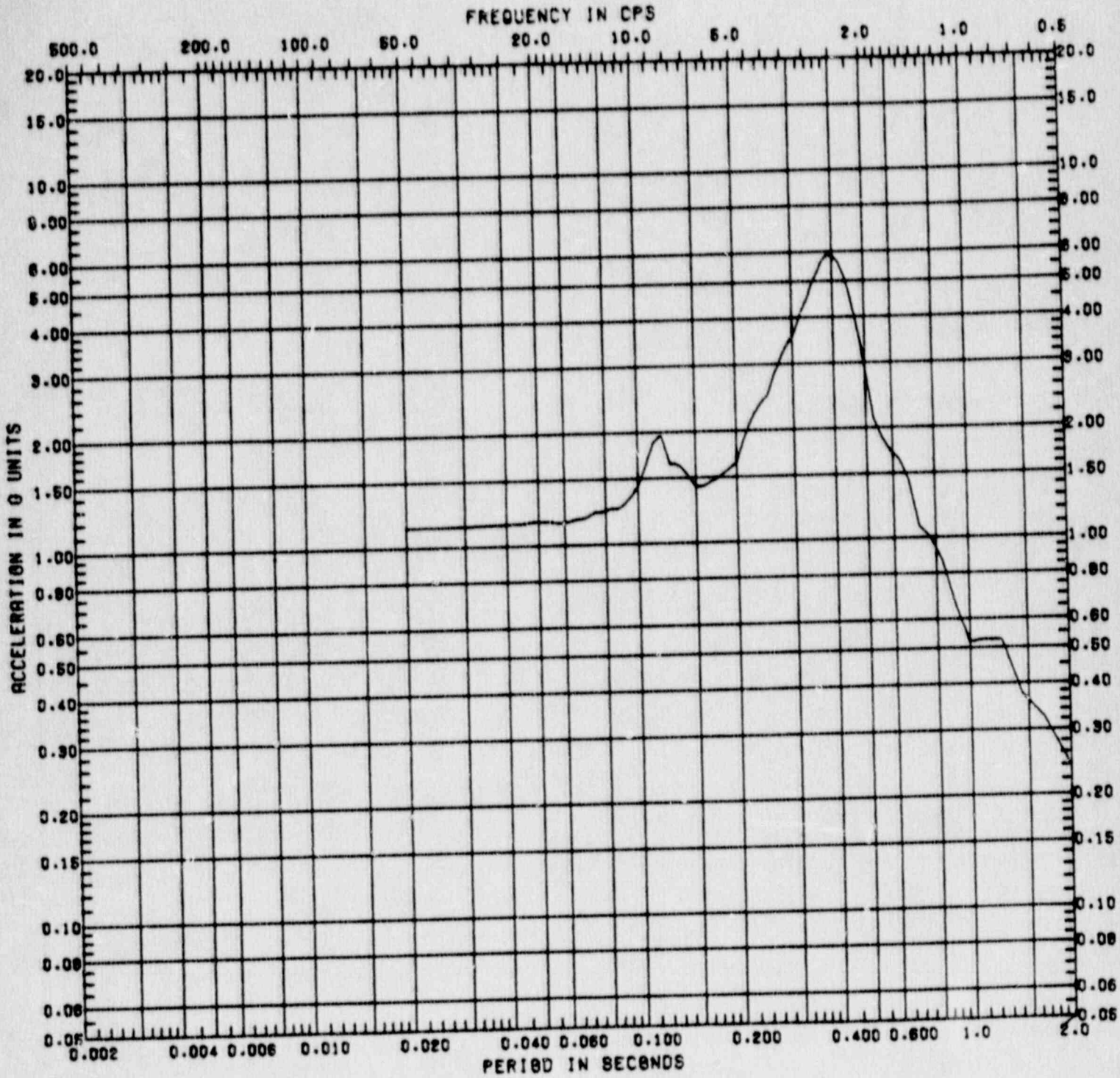

Figure C.1-7 Horizontal Response Spectrum at Fermi Model Node 43 (A_H = 0.30g, Damping = 5%, Location = Reactor Building Wall at Elevation 684')

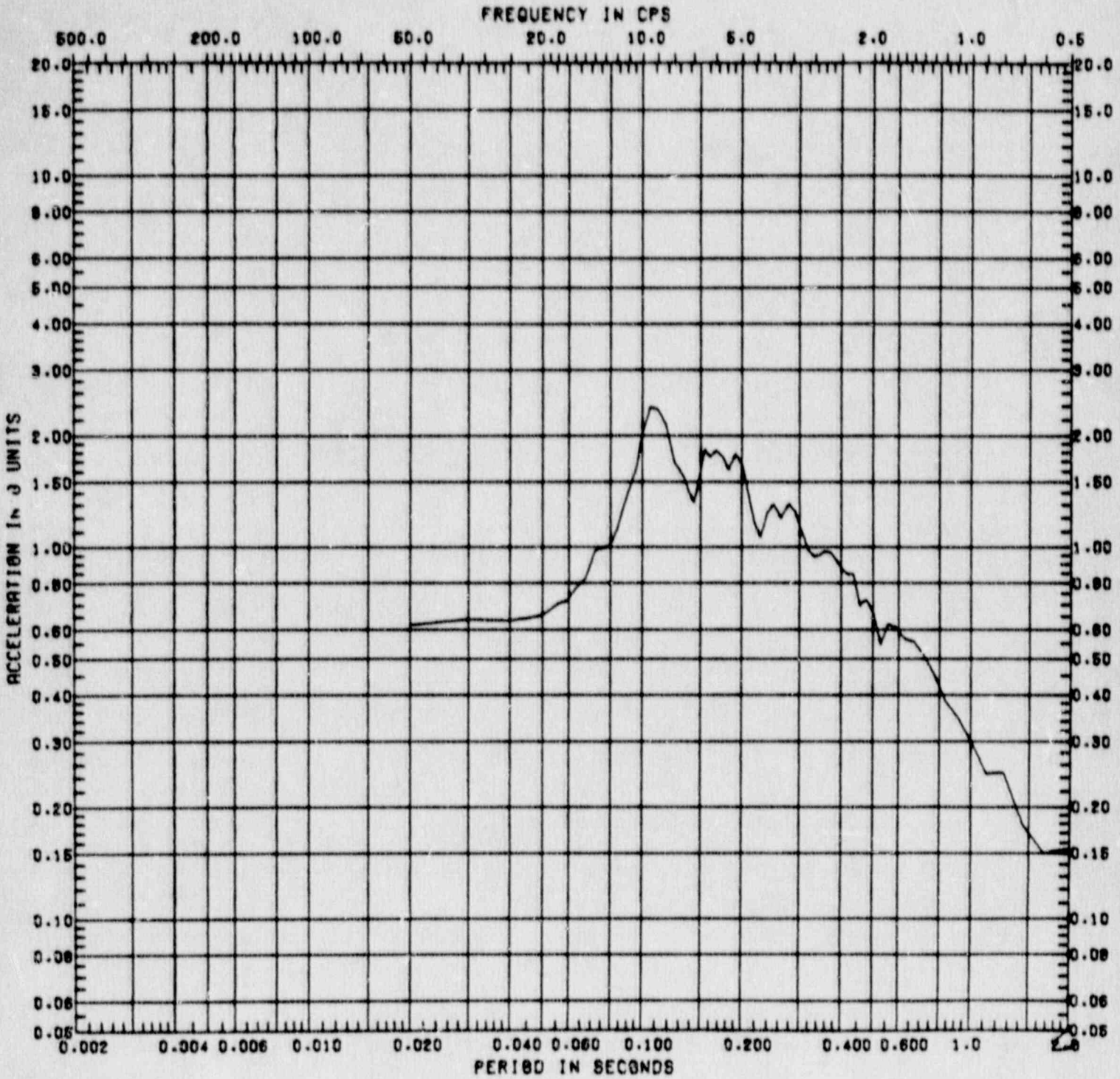

Figure C.1-8 Vertical Response Spectrum at Fermi Model Node 43 (A_H = 0.30g, Damping = 5%, Location = Rector Building Wall at Elevation 684')

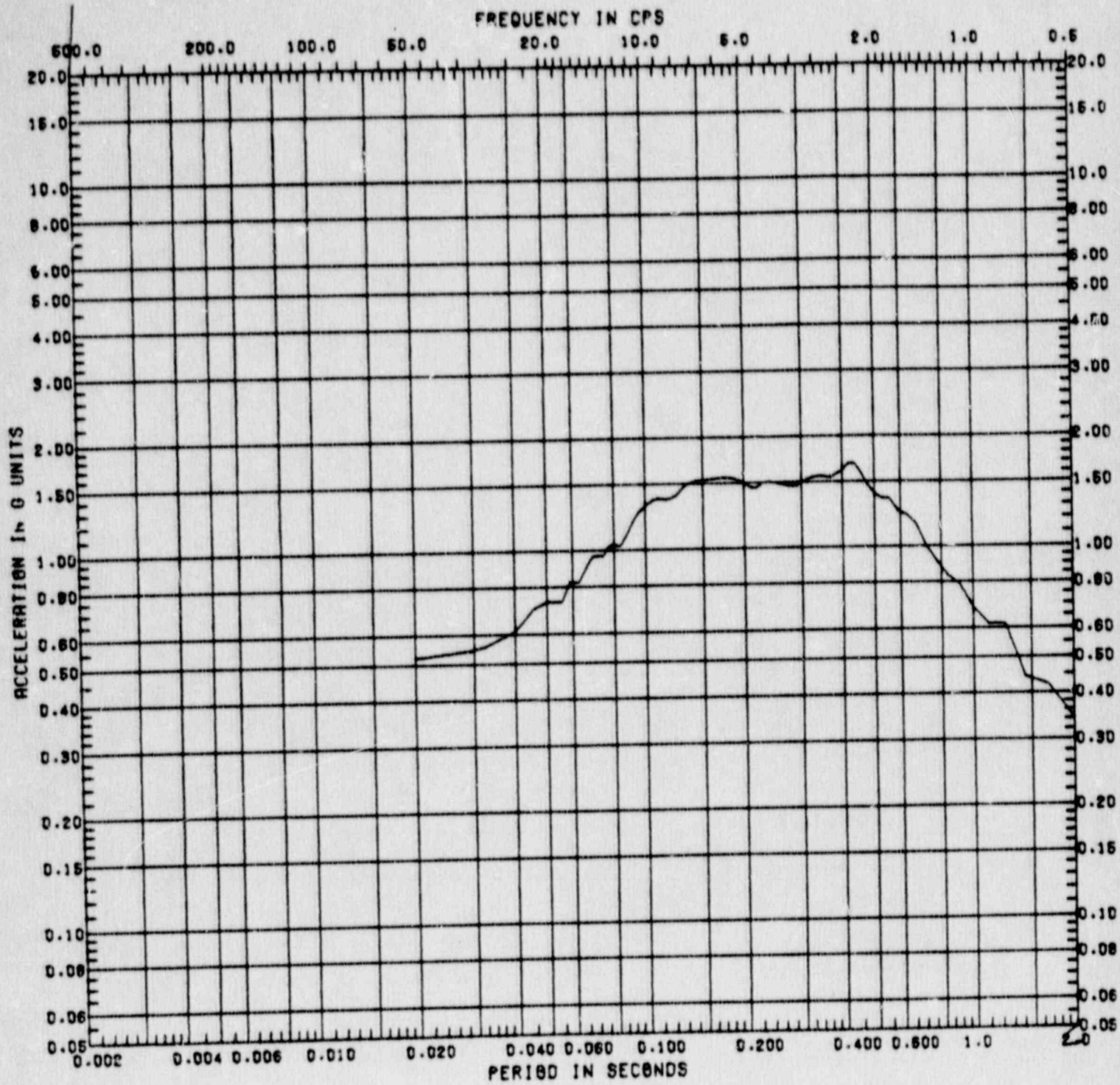

Figure C.1-9 Horizontal Response Spectrum at Fermi Model Node 11 (A_H = 0.45g, Damping = 5%, Location = Containment Pedestal at Basemat Elevation 540')

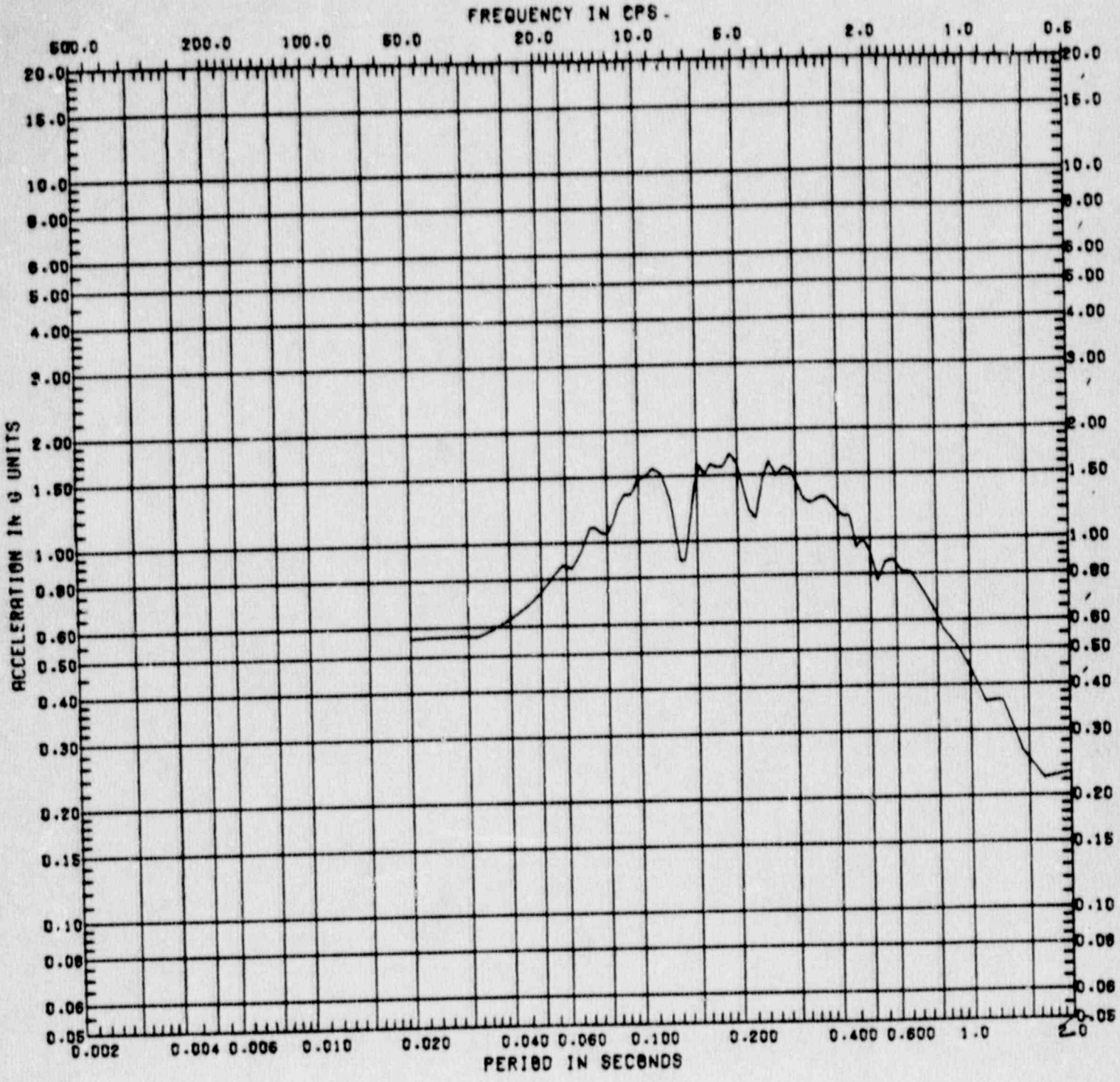

Figure C.1-10 Vertical Response Spectrum at Fermi Model Node 11 (A_H = 0.45g, Damping = 5%, Location = Containment Pedestal at Basemat Elevation 540')

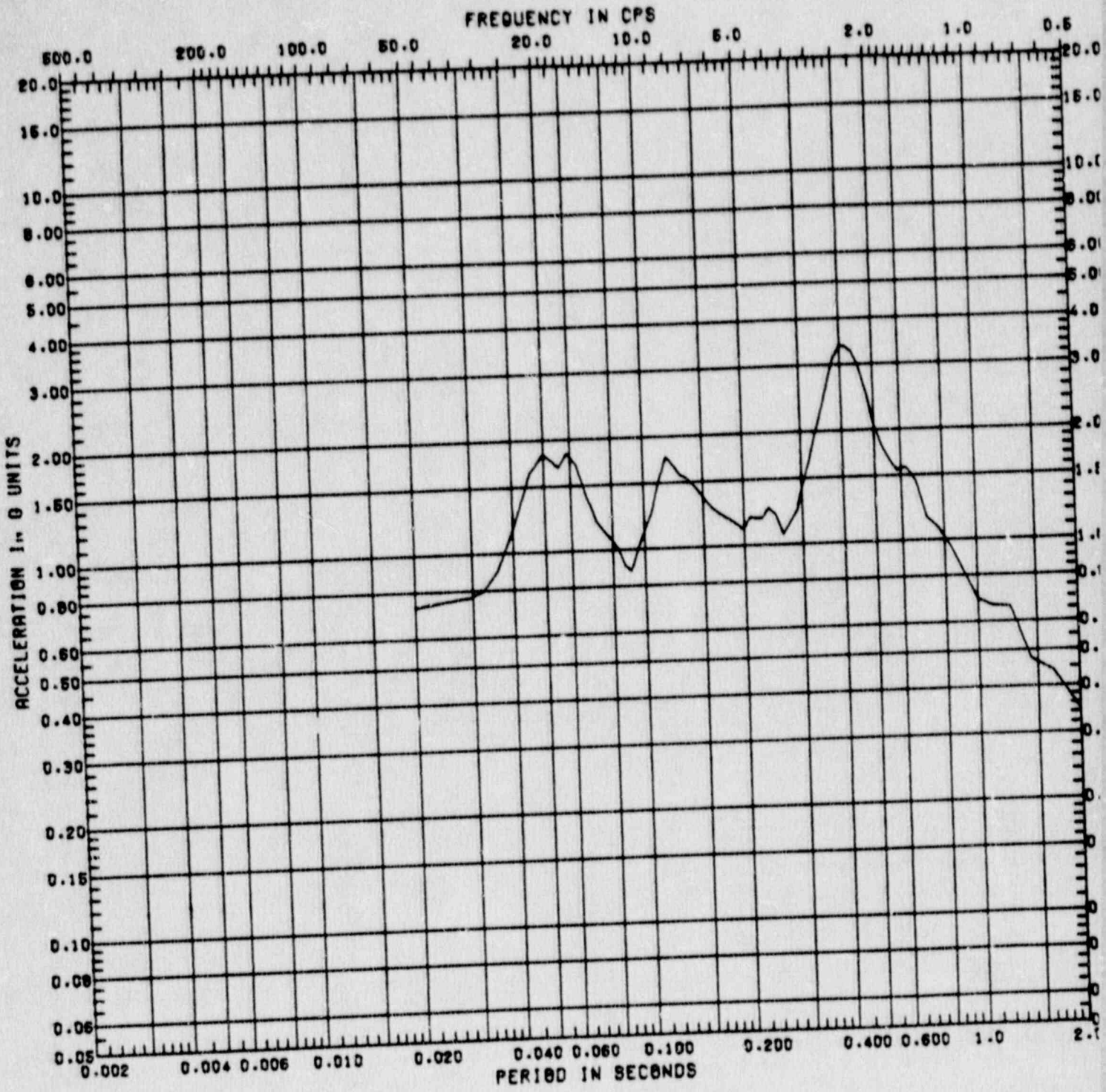

Figure C.1-11 Horizontal Response Spectrum at Fermi Model Node 26 (A_H = 0.45g, Damping = 5%, Location = Steel Containment at Equator Elevation 597')

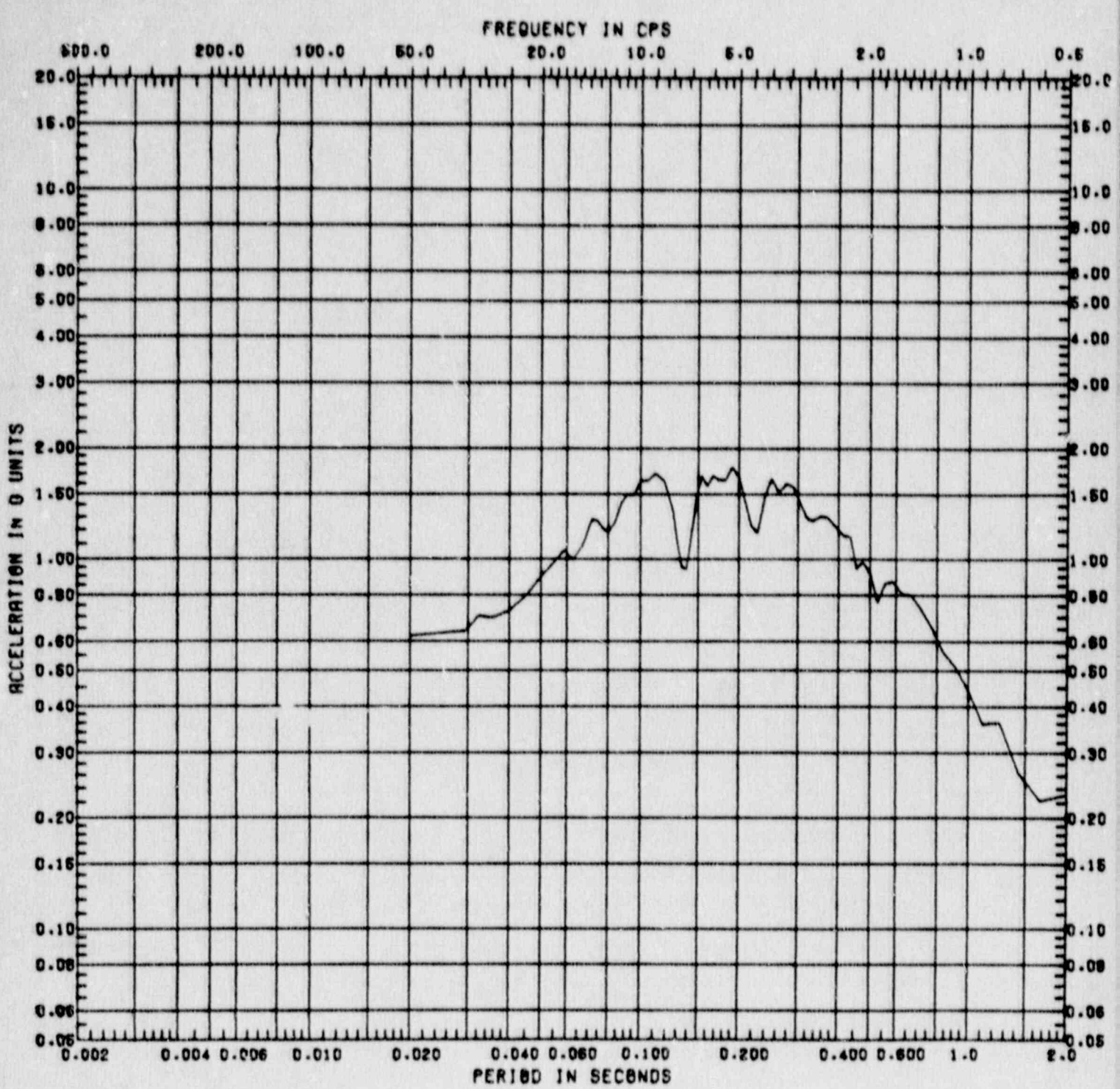

Figure C.1-12 Vertical Response Spectrum at Fermi Model Node 26 (A_H = 0.45g, Damping = 5%, Location = Steel Containment at Equator Elevation 597')

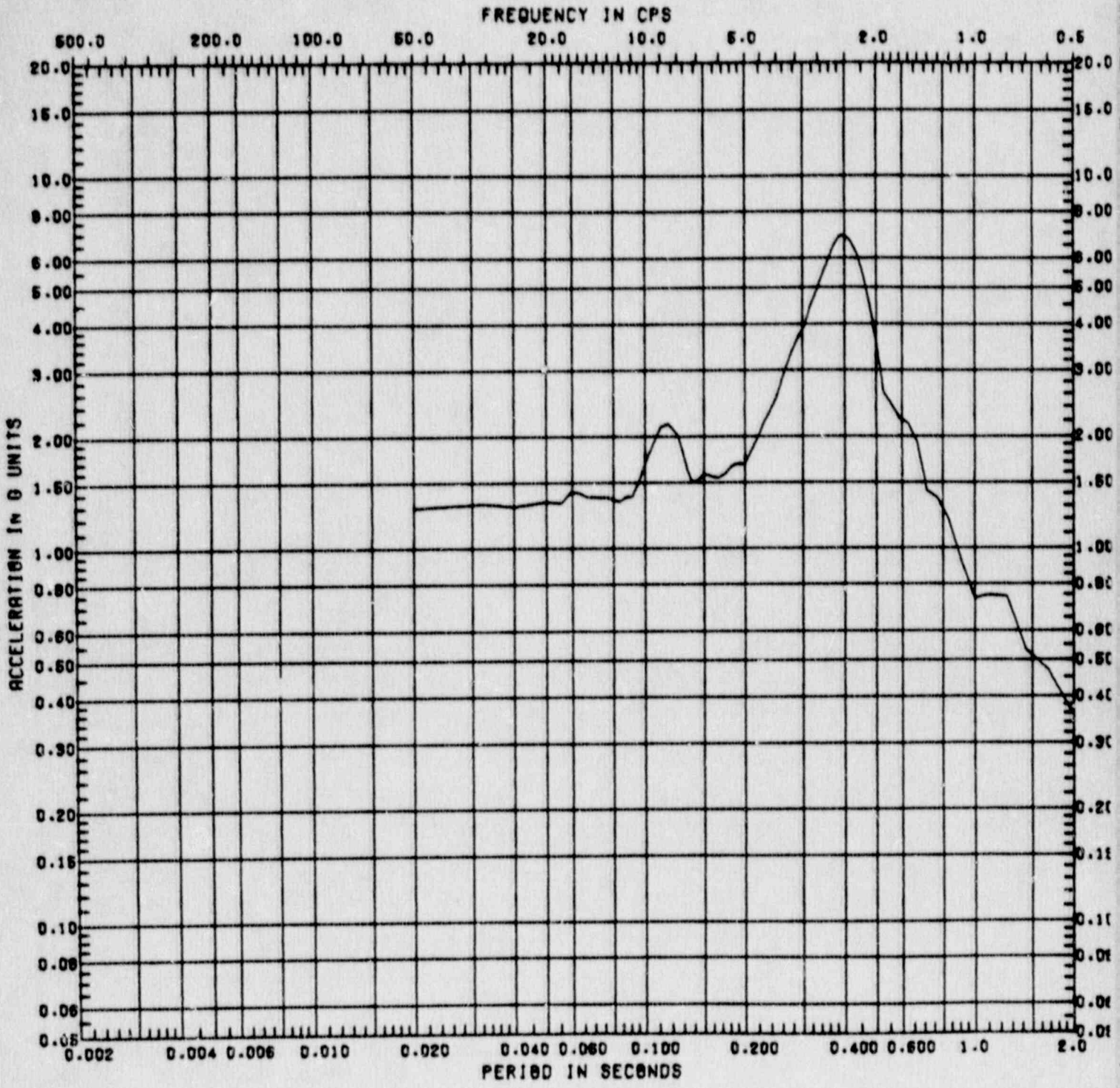

Figure C.1-13 Horizontal Response Spectrum at Fermi Model Node 46 (A_H = 0.45g, Damping = 5%, Location = Steel Containment at Elevation 659')

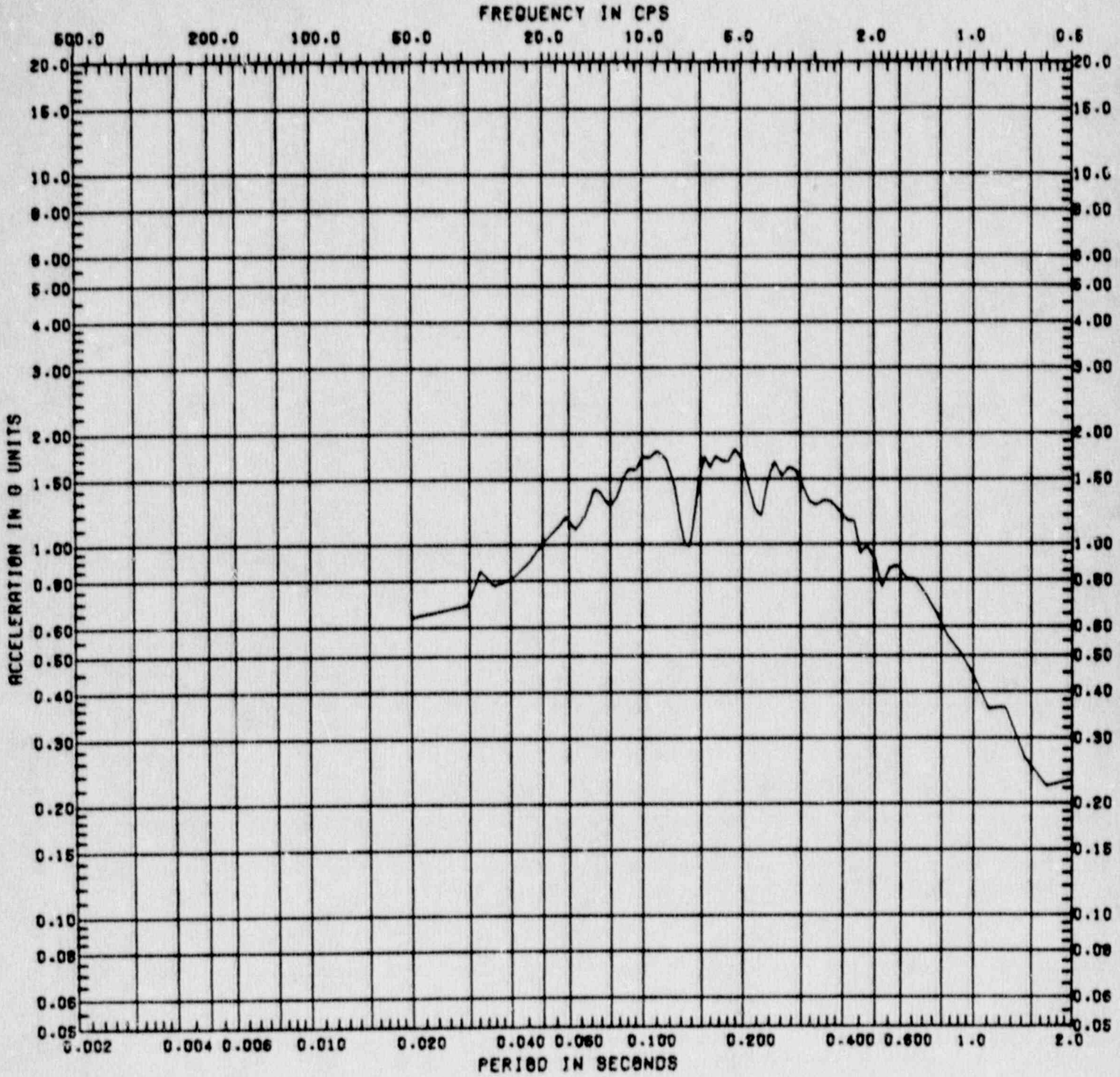

Figure C.1-14 Vertical Response Spectrum at Fermi Model Node 46 (A_H = 0.45g, Damping = 5%, Location = Steel Containment at Elevation 659')

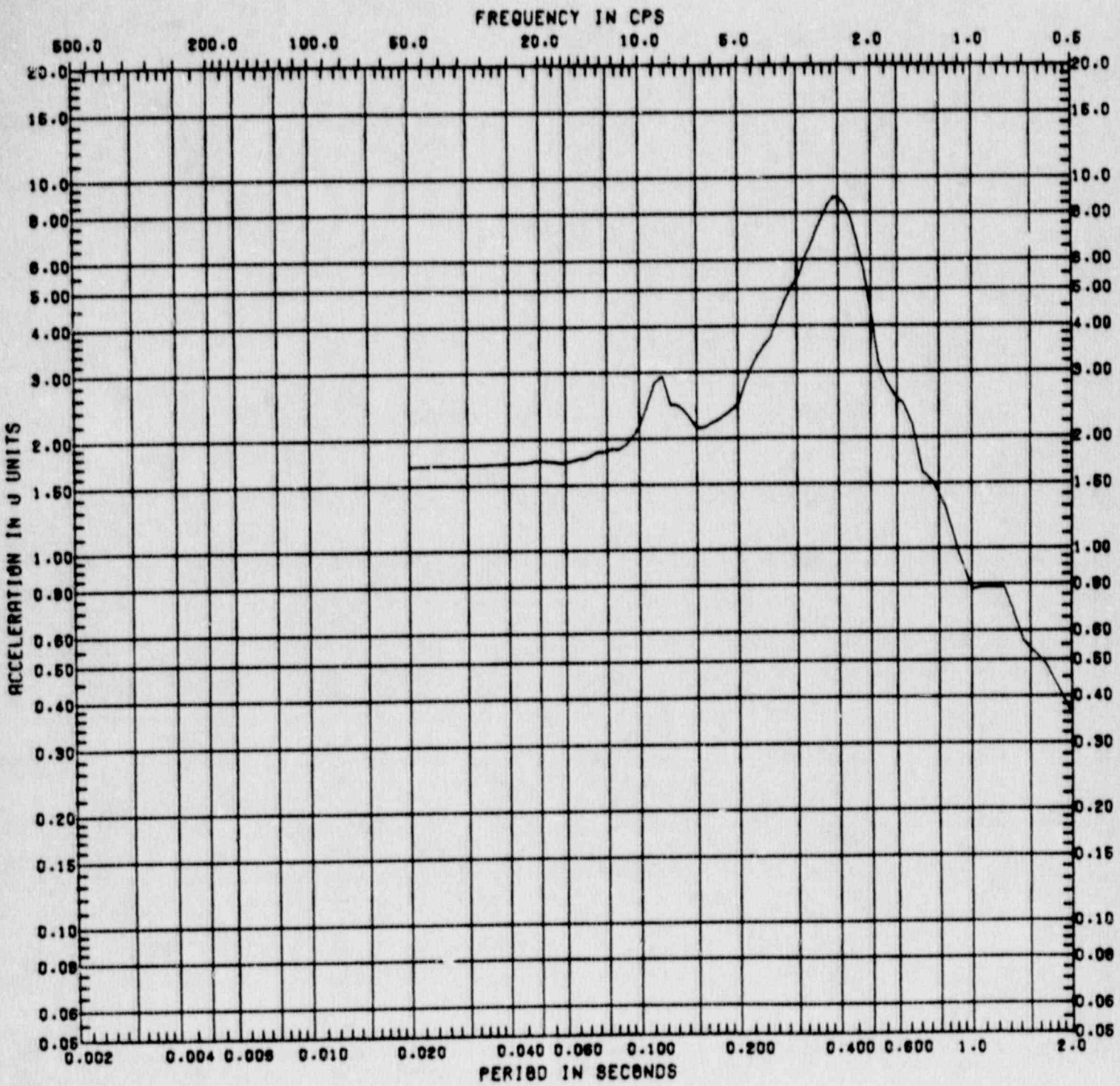

Figure C.1-15 Horizontal Response Spectrum at Fermi Model Node 43 (A_H = 0.45g, Damping = 5%, Location = Reactor Building Wall at Elevation 684')

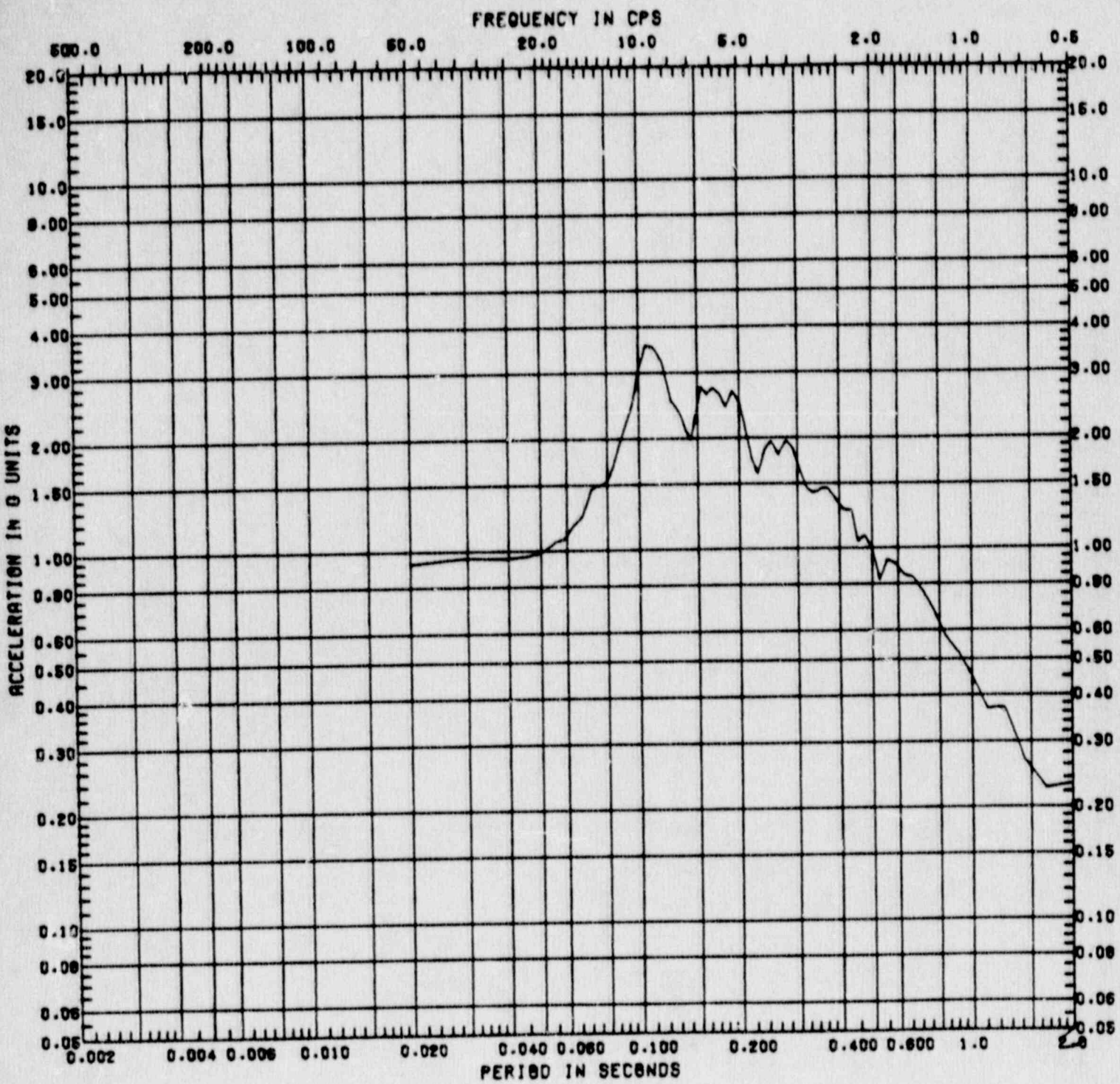

Figure C.1-16 Vertical Response Spectrum at Fermi Model Node 43 (A_H = 0.45g, Damping = 5%, Location = Reactor Building Wall at Elevation 684')

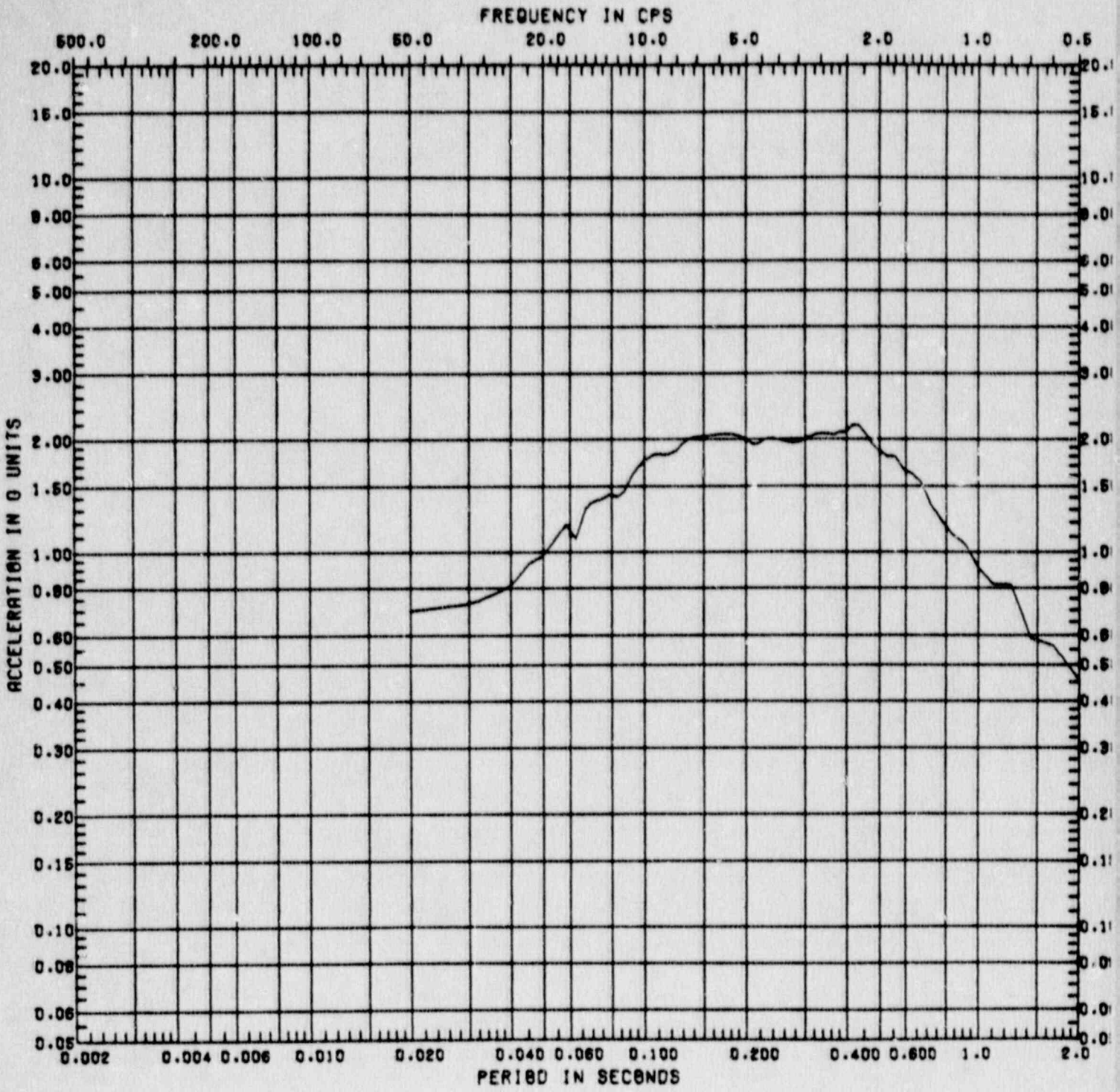

Figure C.1-17 Horizontal Response Spectrum at Fermi Model Node 11 (A_H = 0.60g, Damping = 5%, Location = Containment Pedestal at Basemat Elevation 540')

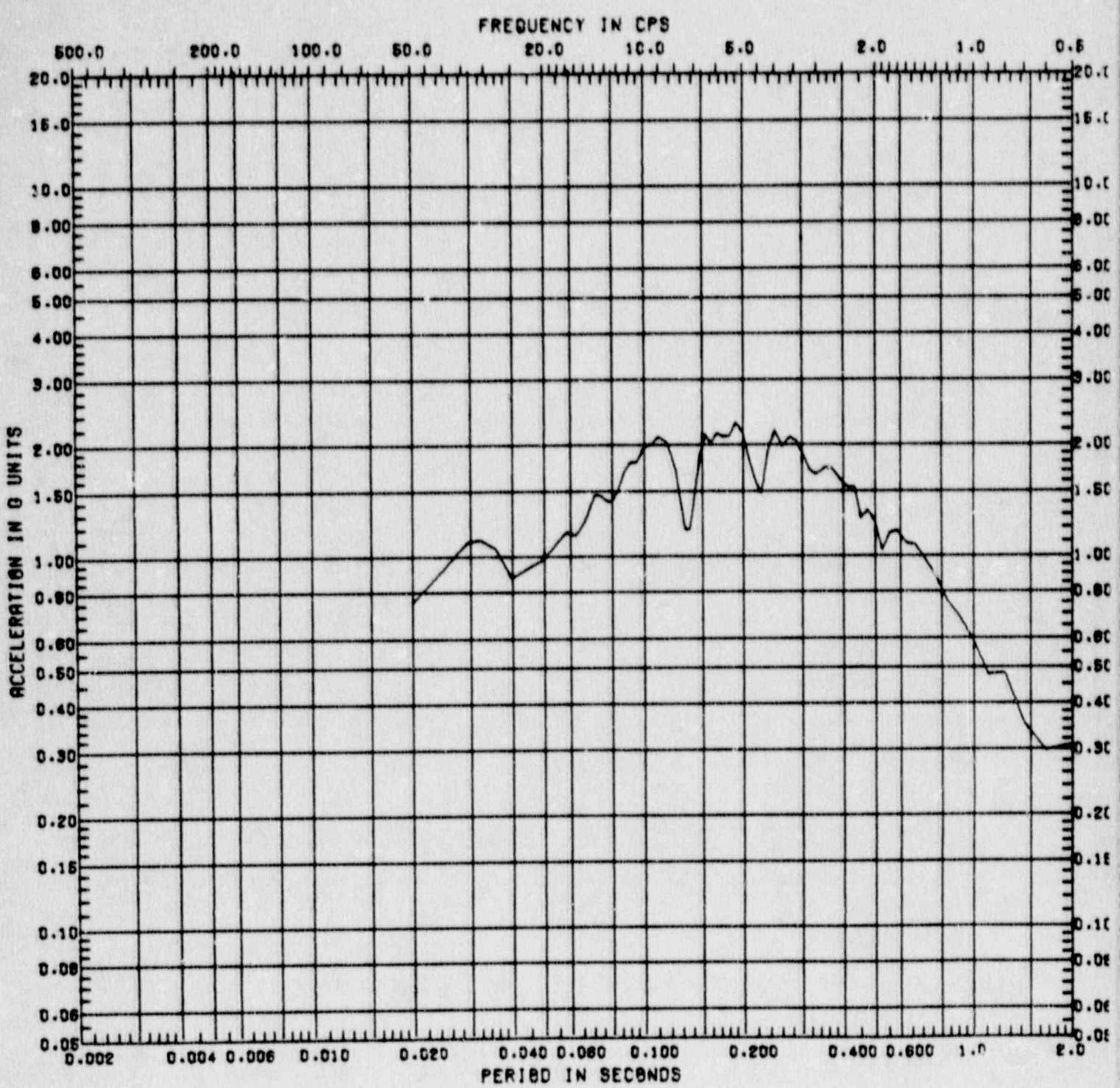

Figure C.1-18 Vertical Response Spectrum at Fermi Model Node 11 (A_H = 0.60g, Damping = 5%, Location = Containment Pedestal at Basemat Elevation 540')

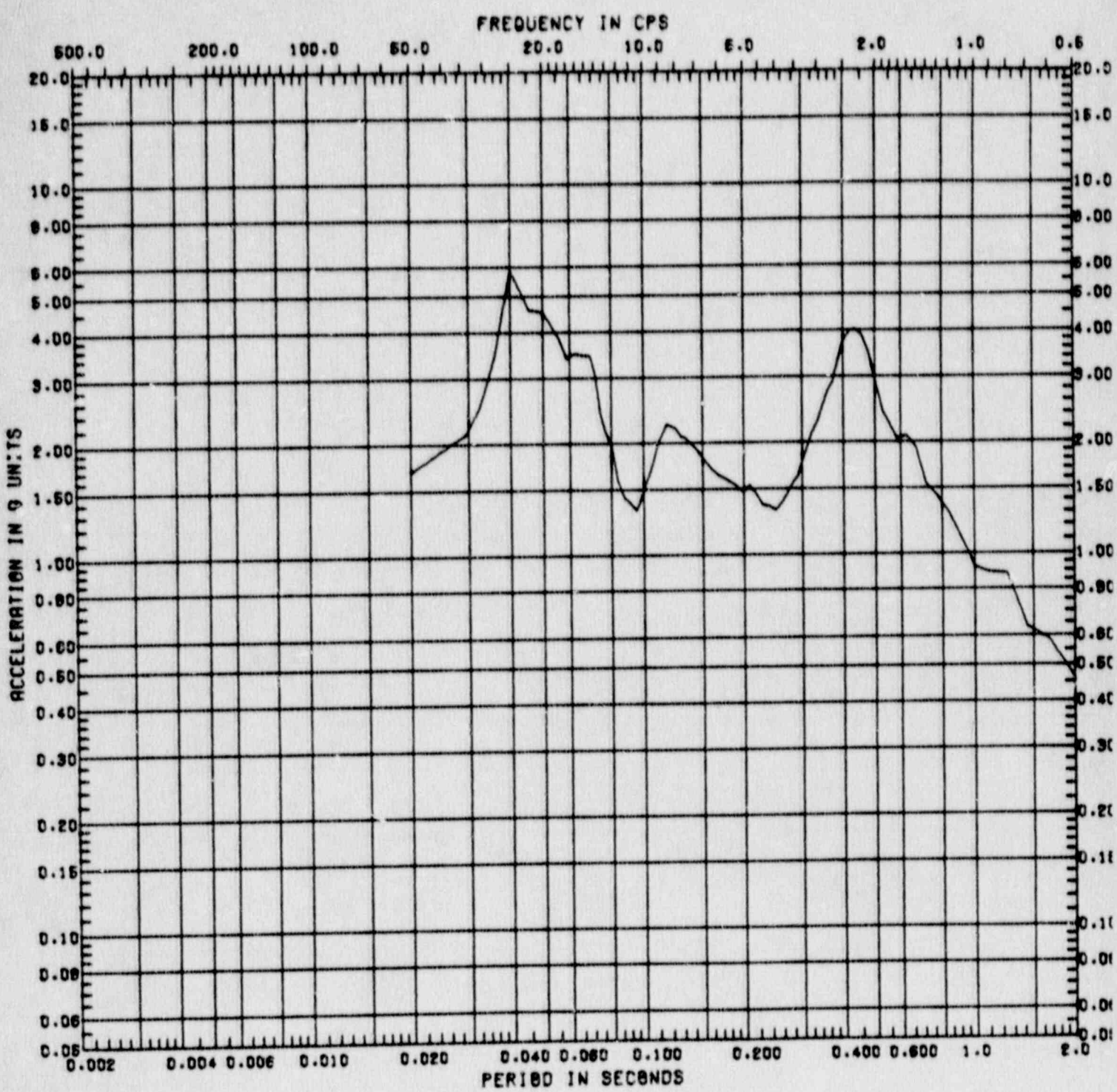

Figure C.1-19 Horizontal Response Spectrum at Fermi Model Node 26 (A_H = 0.60g, Damping = 5%, Location = Steel Containment at Equator Elevation 597')

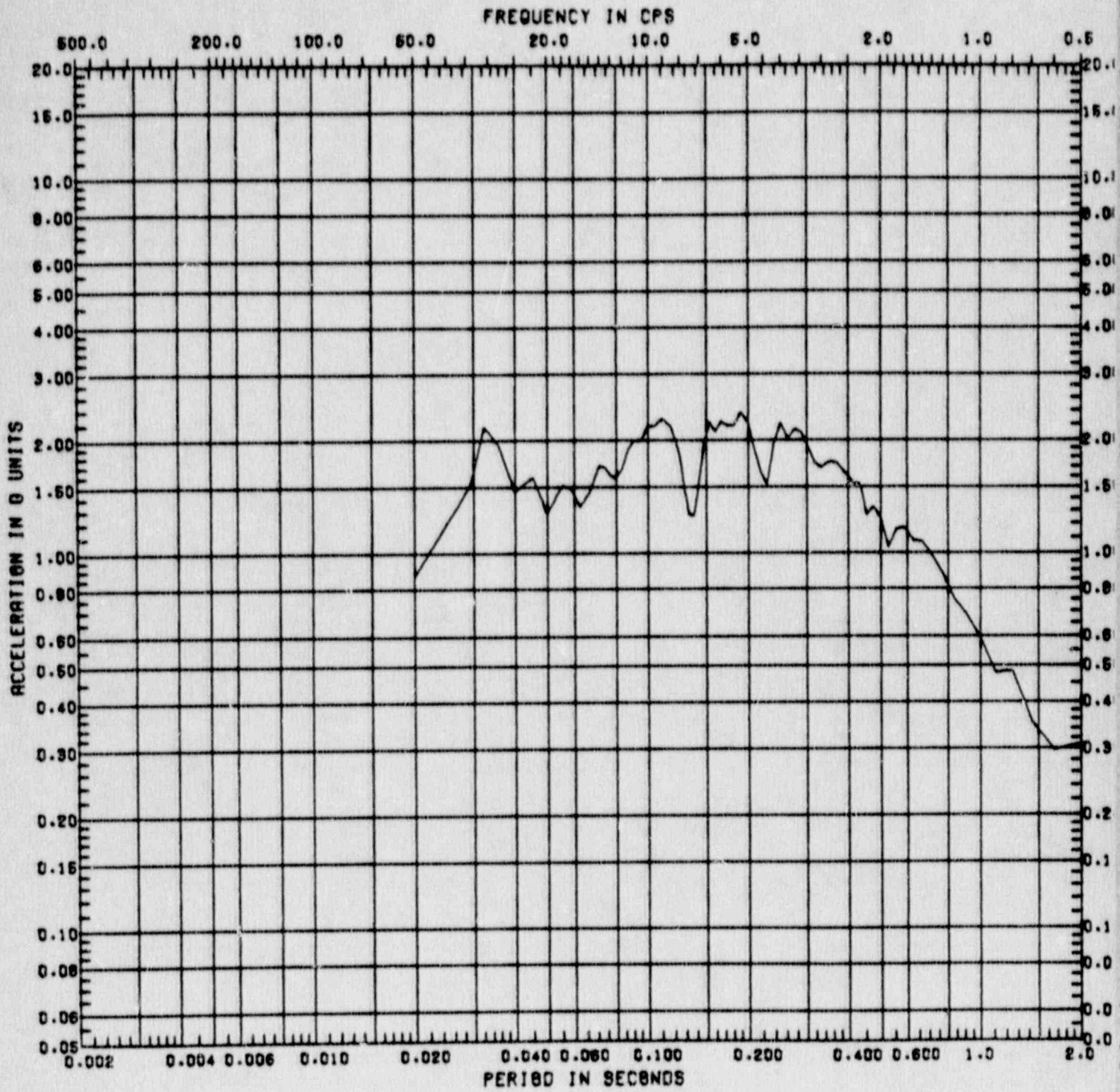

Figure C.1-20 Vertical Response Spectrum at Fermi Model Node 26 (A_g = 0.60g, Damping = 5%, Location = Steel Containment at Equator Elevation 597')

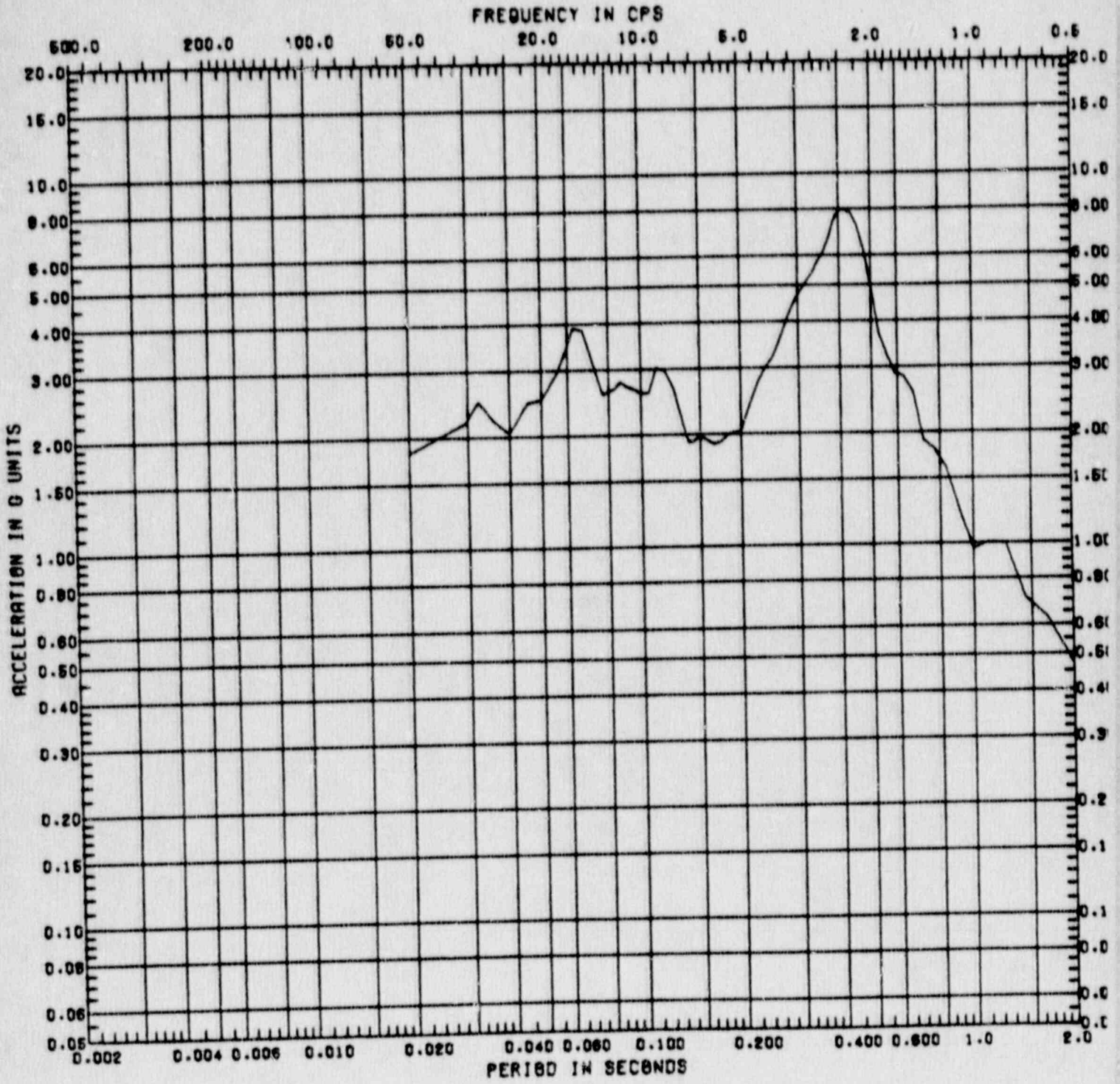

Figure C.1-21 Horizontal Response Spectrum at Fermi Model Node 46 (A_H = 0.60g, Damping = 5%, Location = Steel Containment at Elevation 659')

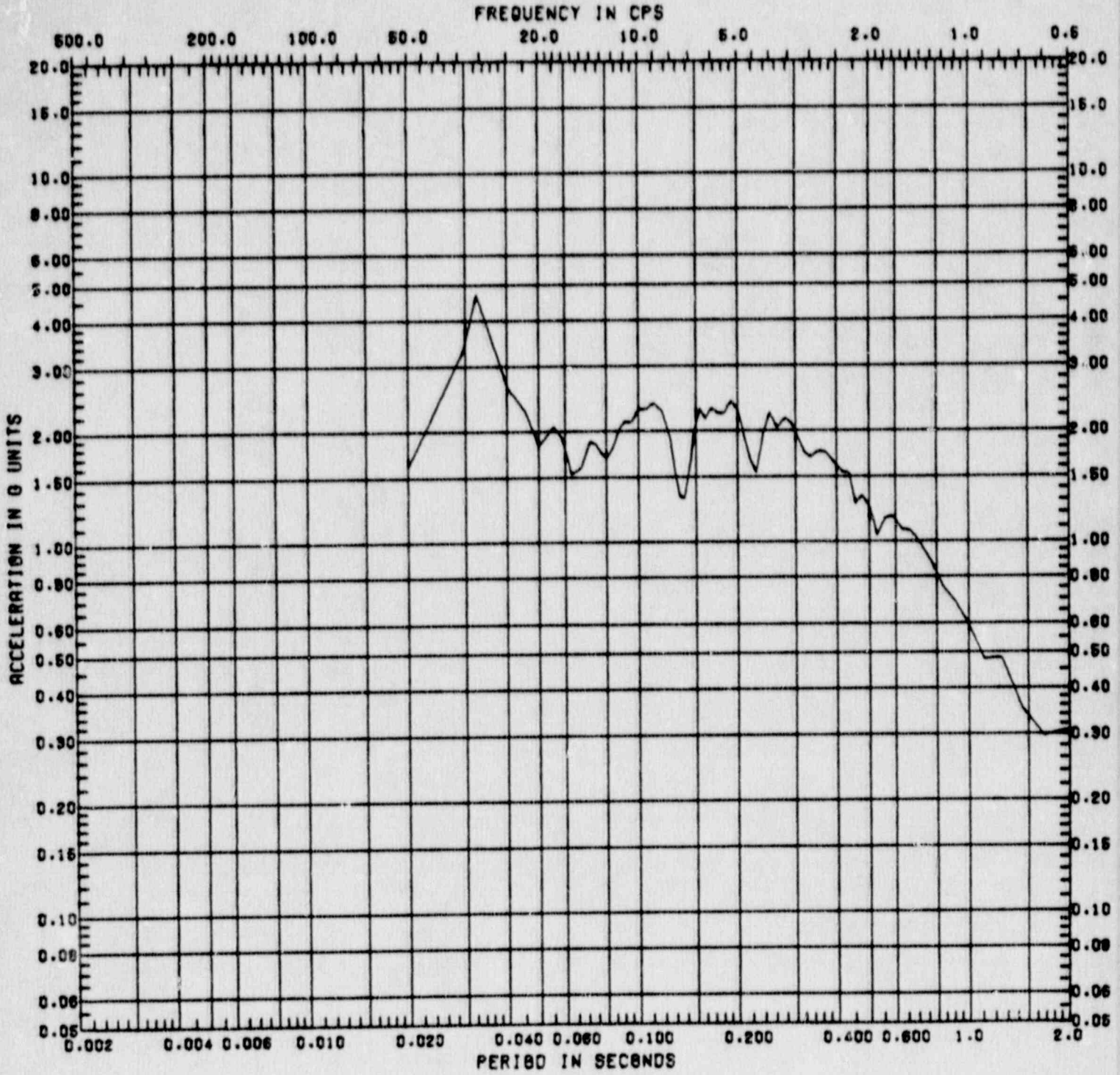

Figure C.1-22 Vertical Response Spectrum at Fermi Model Node 46 (A_H = 0.60g, Damping = 5%, Location = Steel Containment at Elevation 659')

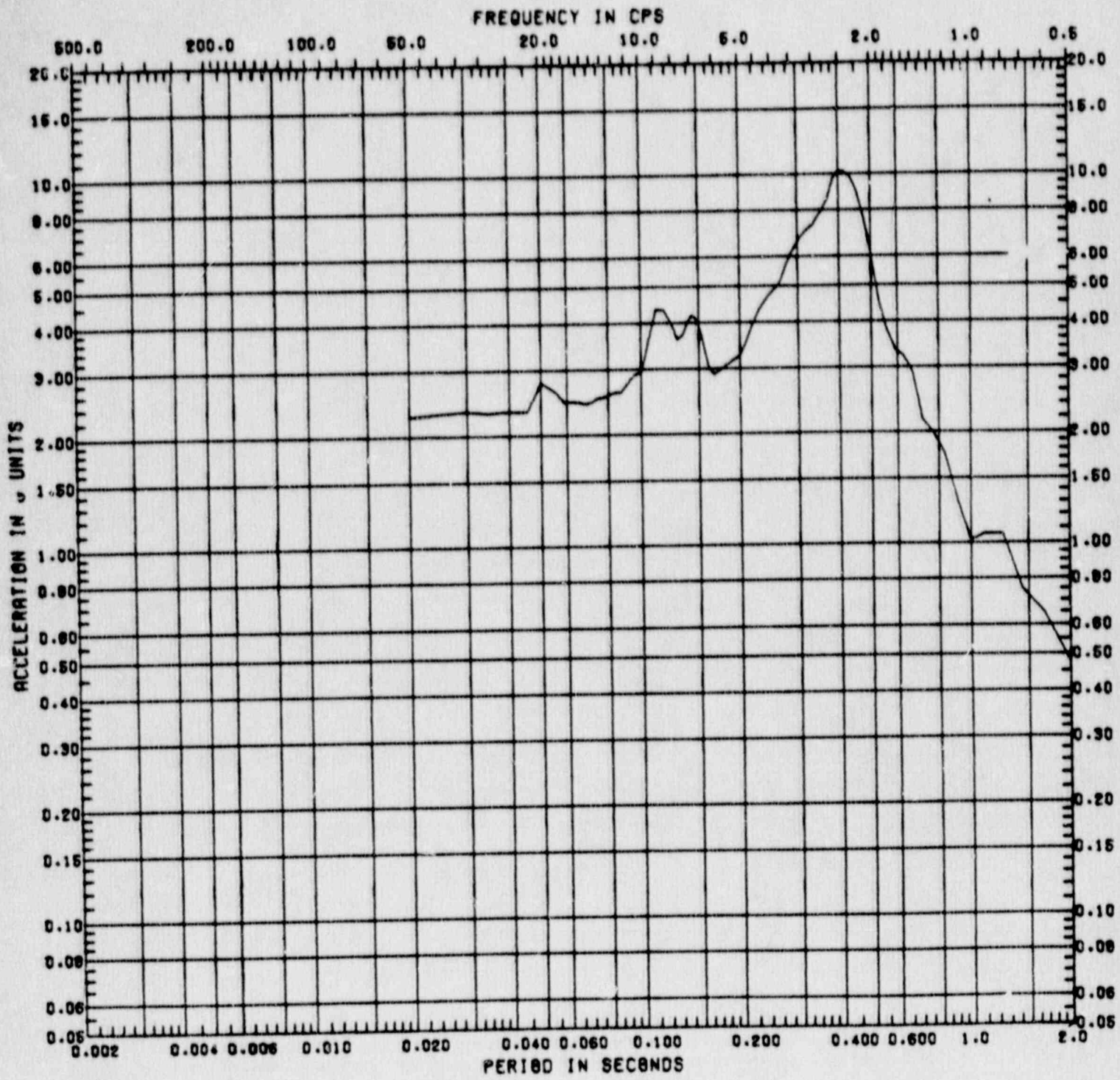

Figure C.1-23 Horizontal Response Spectrum at Fermi Model Node 43 (A_H = 0.60g, Damping = 5%, Location = Reactor Building Wall at Elevation 684')

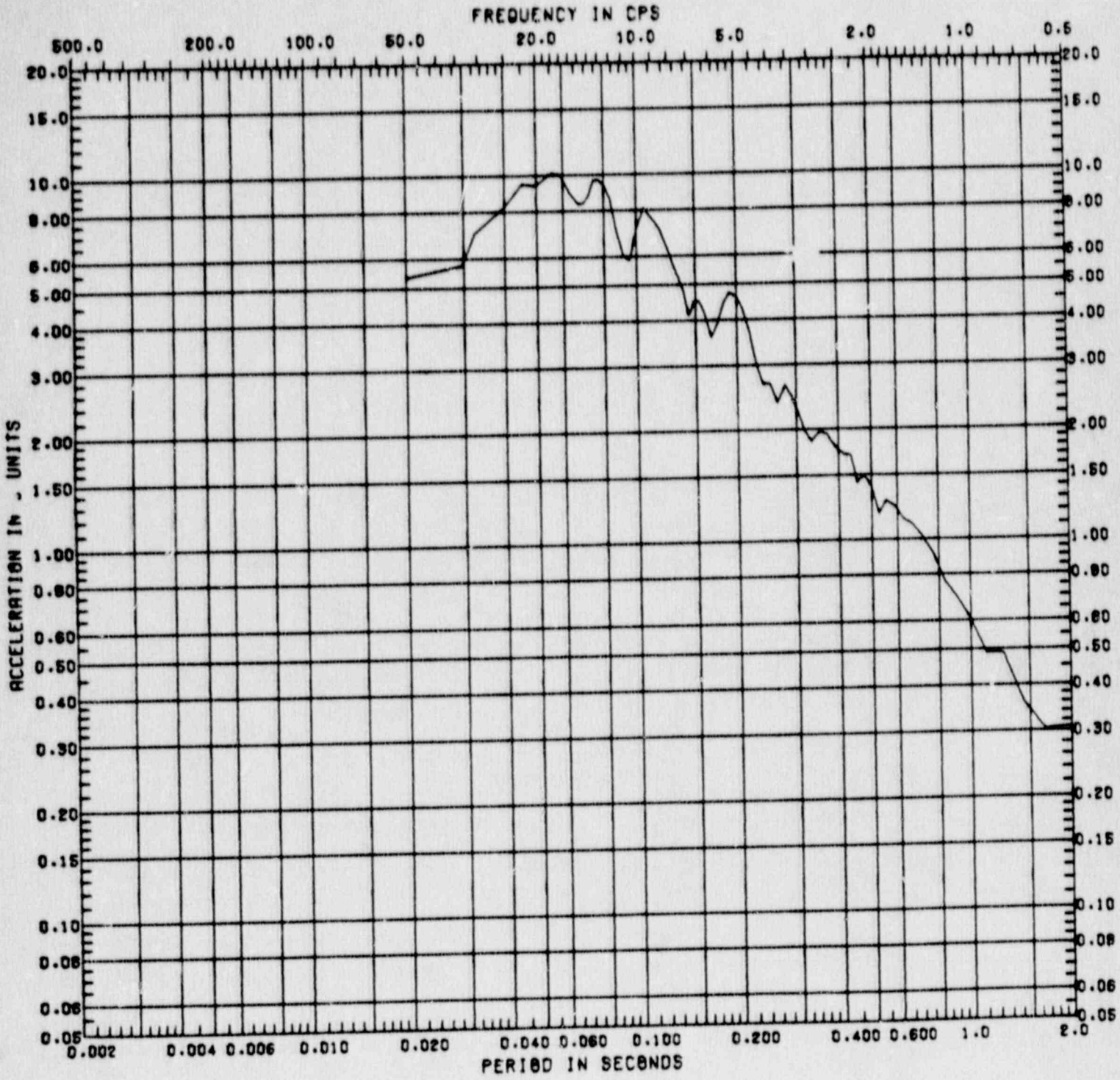

Figure C.1-24 Vertical Response Spectrum at Fermi Model Node 43 (A_H = 0.60g, Damping = 5%, Location = Reactor Building Wall at Elevation 684')

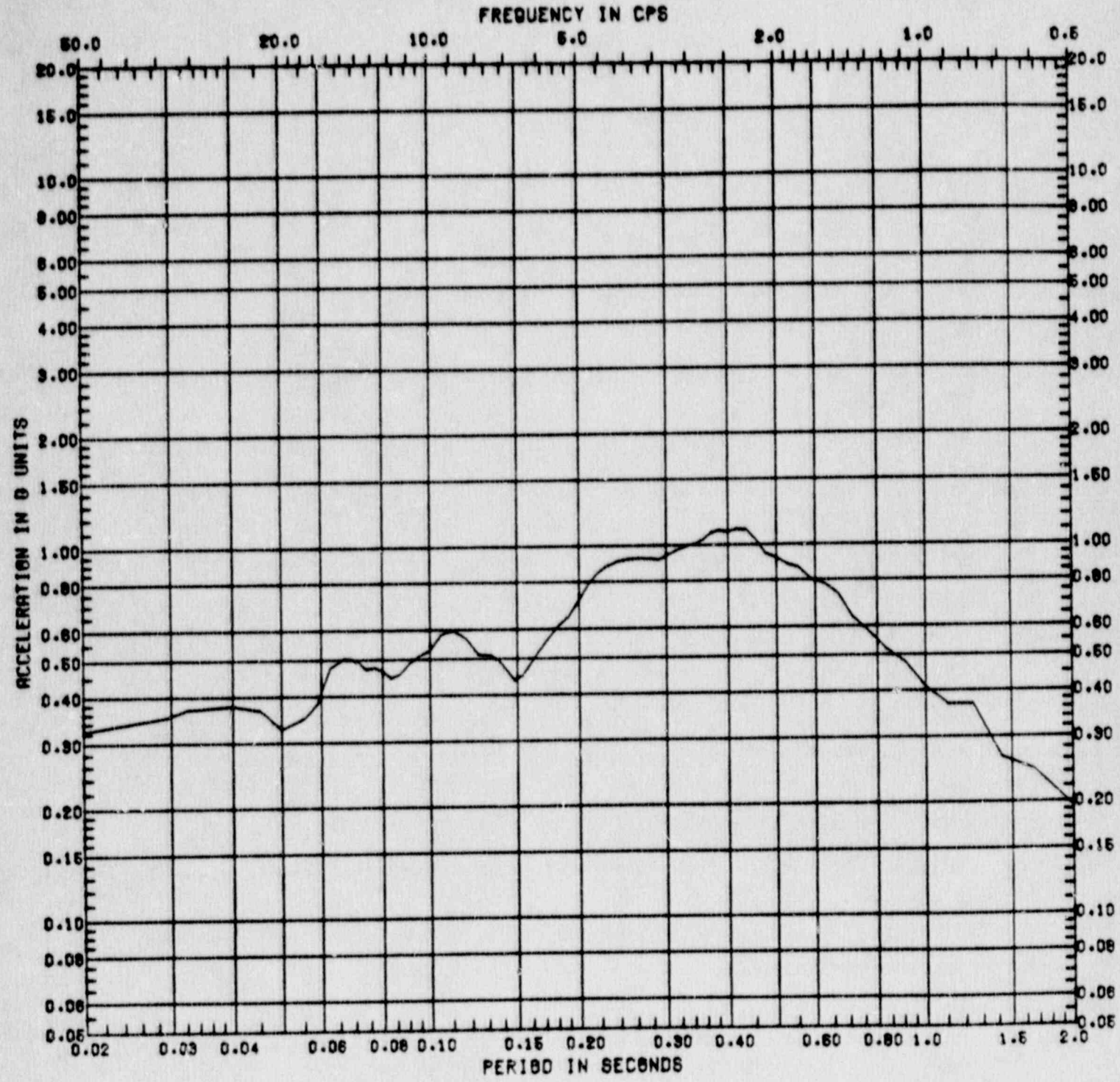

Figure C.2-1 Horizontal Response Spectrum at Clinton Model Node 15 (A_H = 0.25g, Damping = 5%, Location = Containment Wall at Elevation 745')

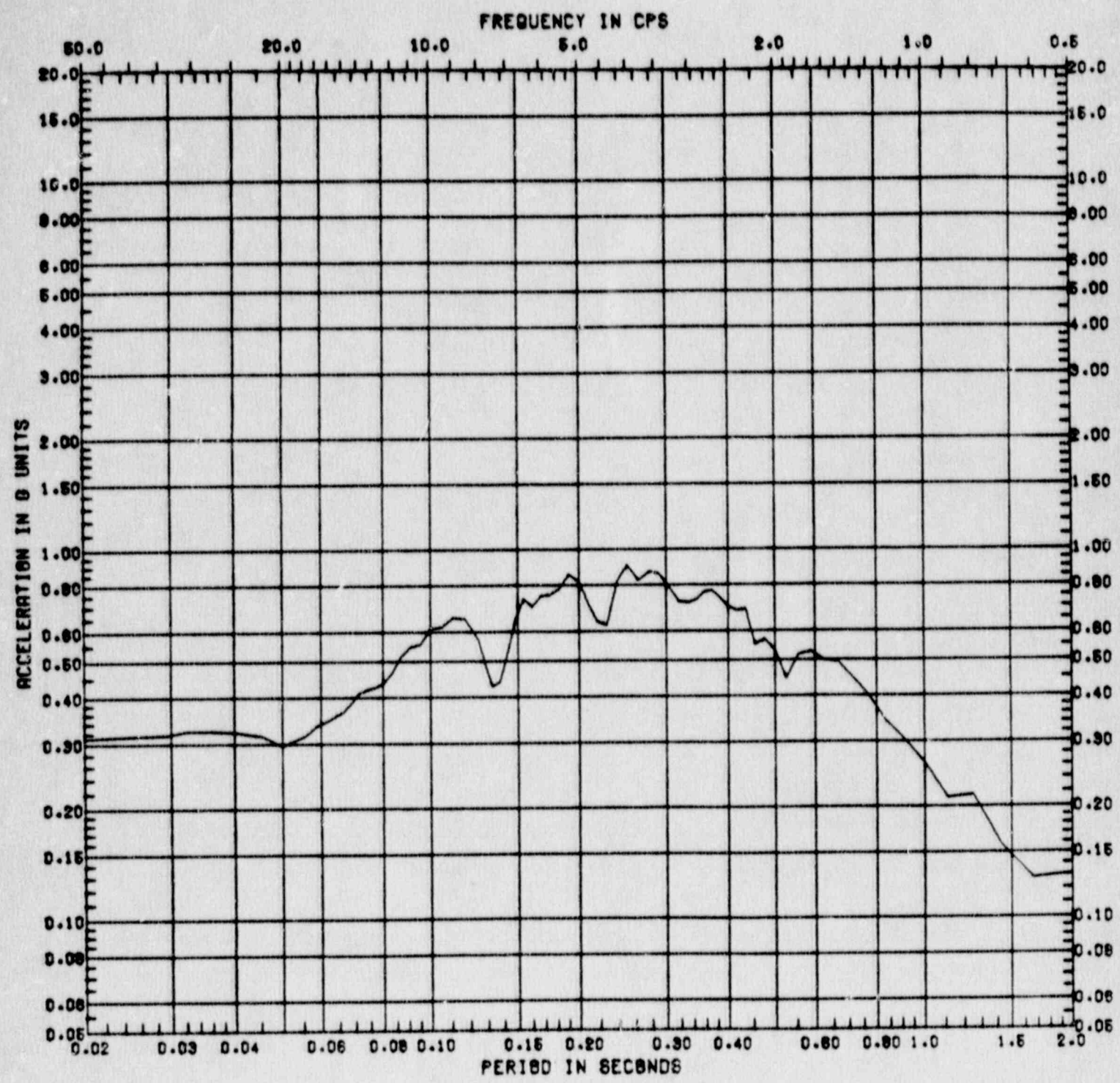

Figure C.2-2 Vertical Response Spectrum at Clinton Model Node 15 (A_H = 0.25g, Damping = 5%, Location = Containment Wall at Elevation 745')

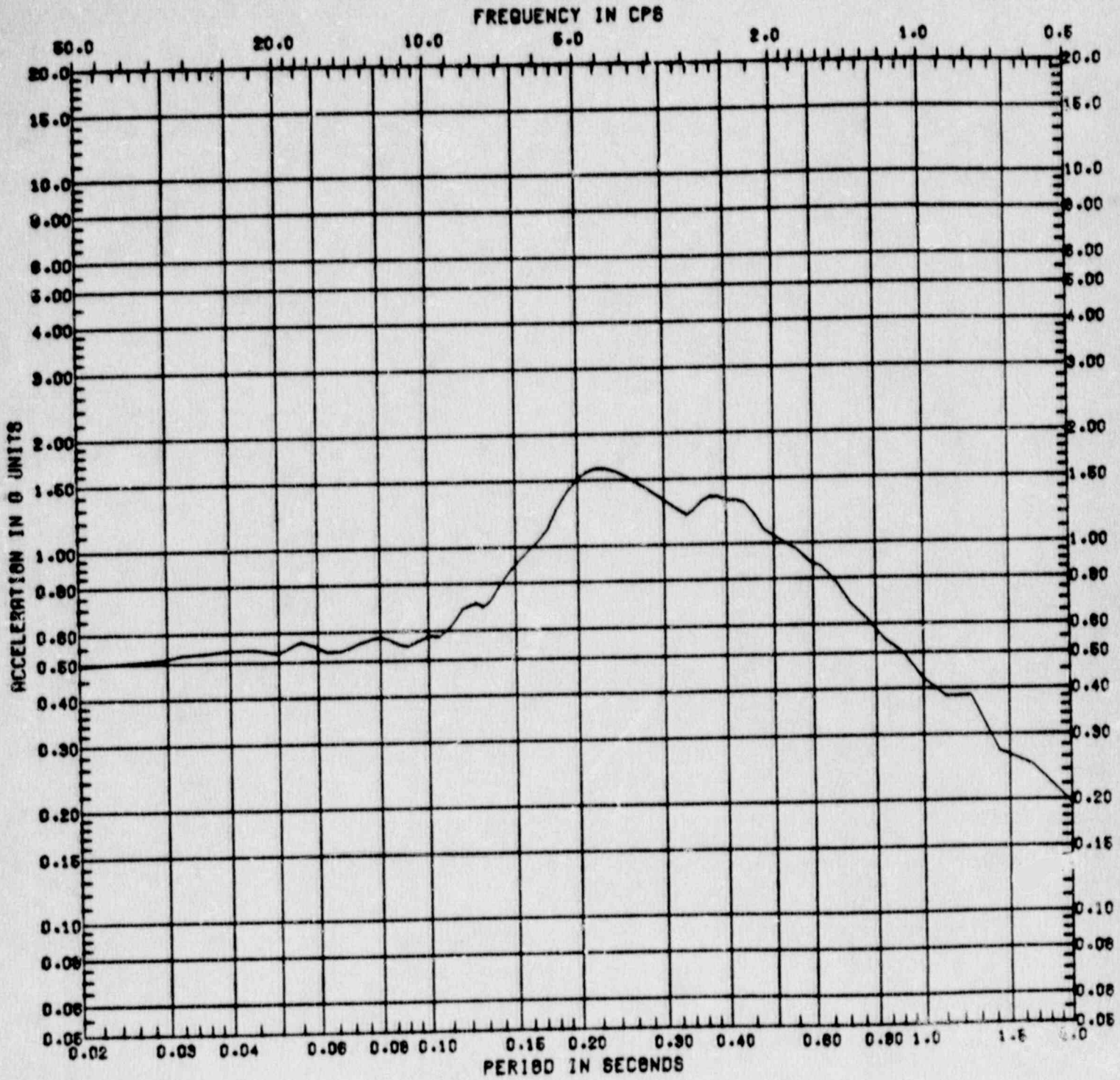

Figure C.2-3 Horizontal Response Spectrum at Clinton Model Node 4 (A_H = 0.25g, Damping = 5%, Location = Containment Wall at Elevation 832')

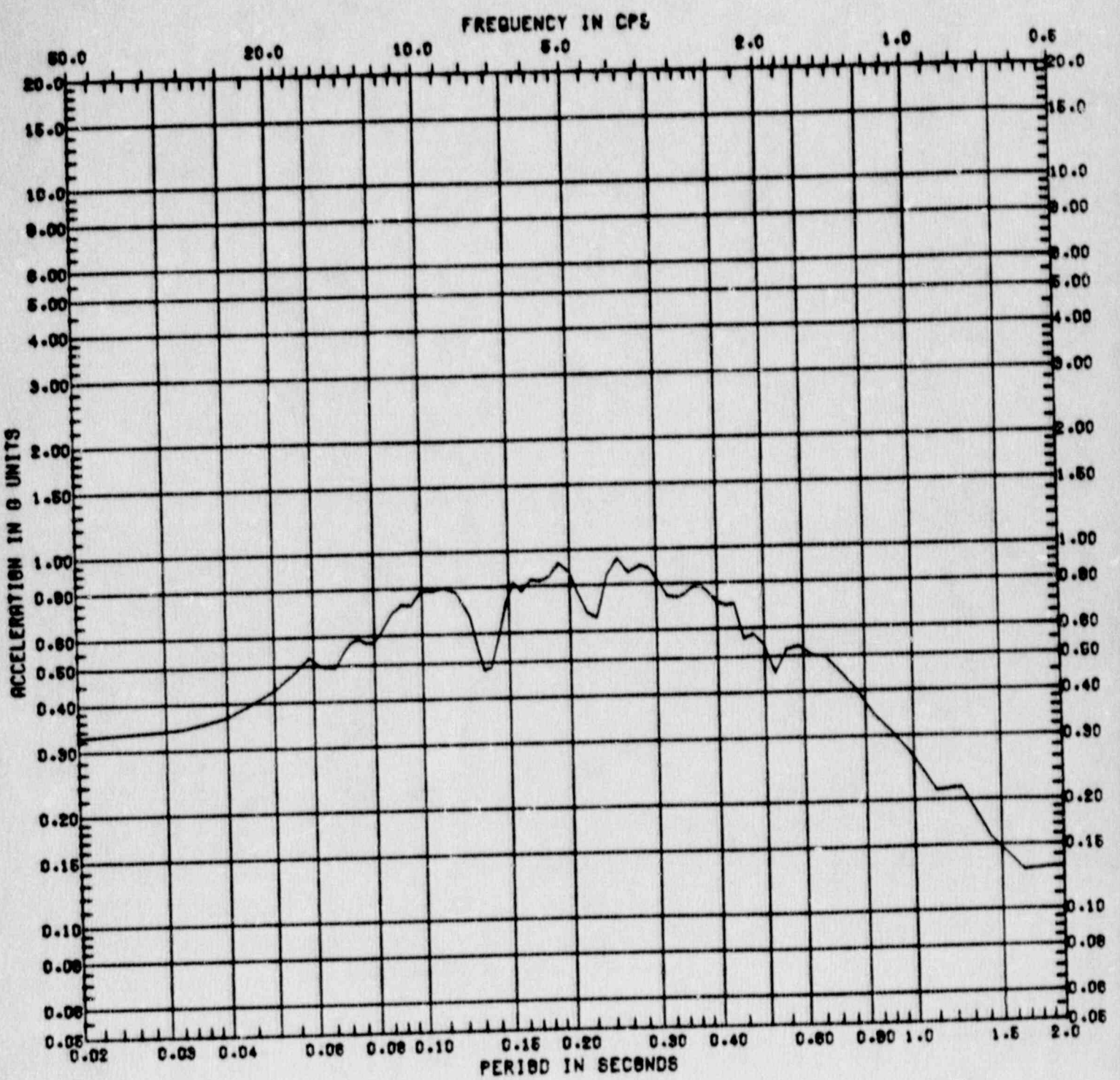

Figure C.2-4 Vertical Response Spectrum at Clinton Model Node 4 (A_H = 0.25g, Damping = 5%, Location = Containment Wall at Elevation 832')

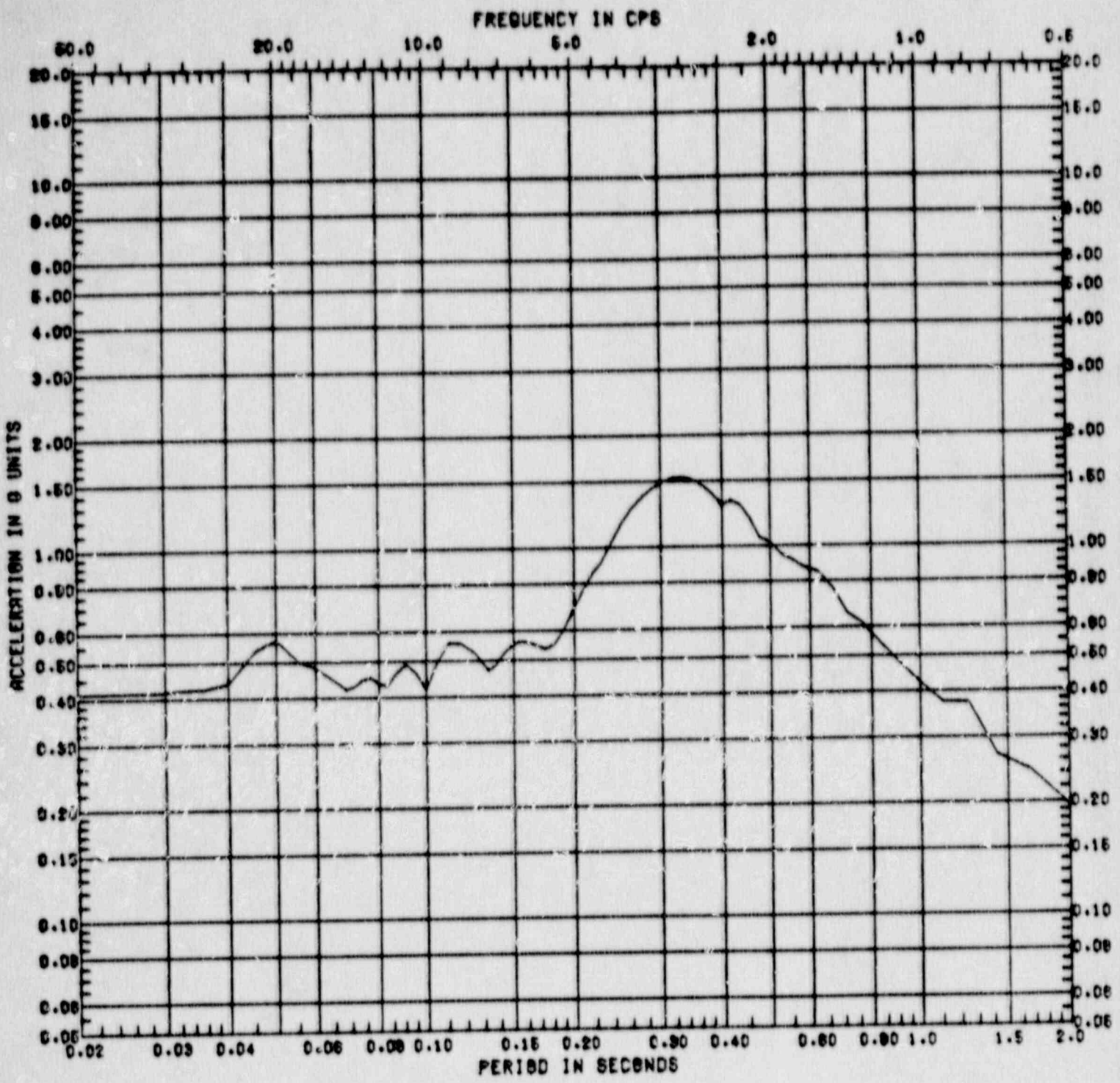

Figure C.2-5 Horizontal Response Spectrum at Clinton Model Node 13 (A_H = 0.25g, Damping = 5%, Location = Drywell Wall at Elevation 745')

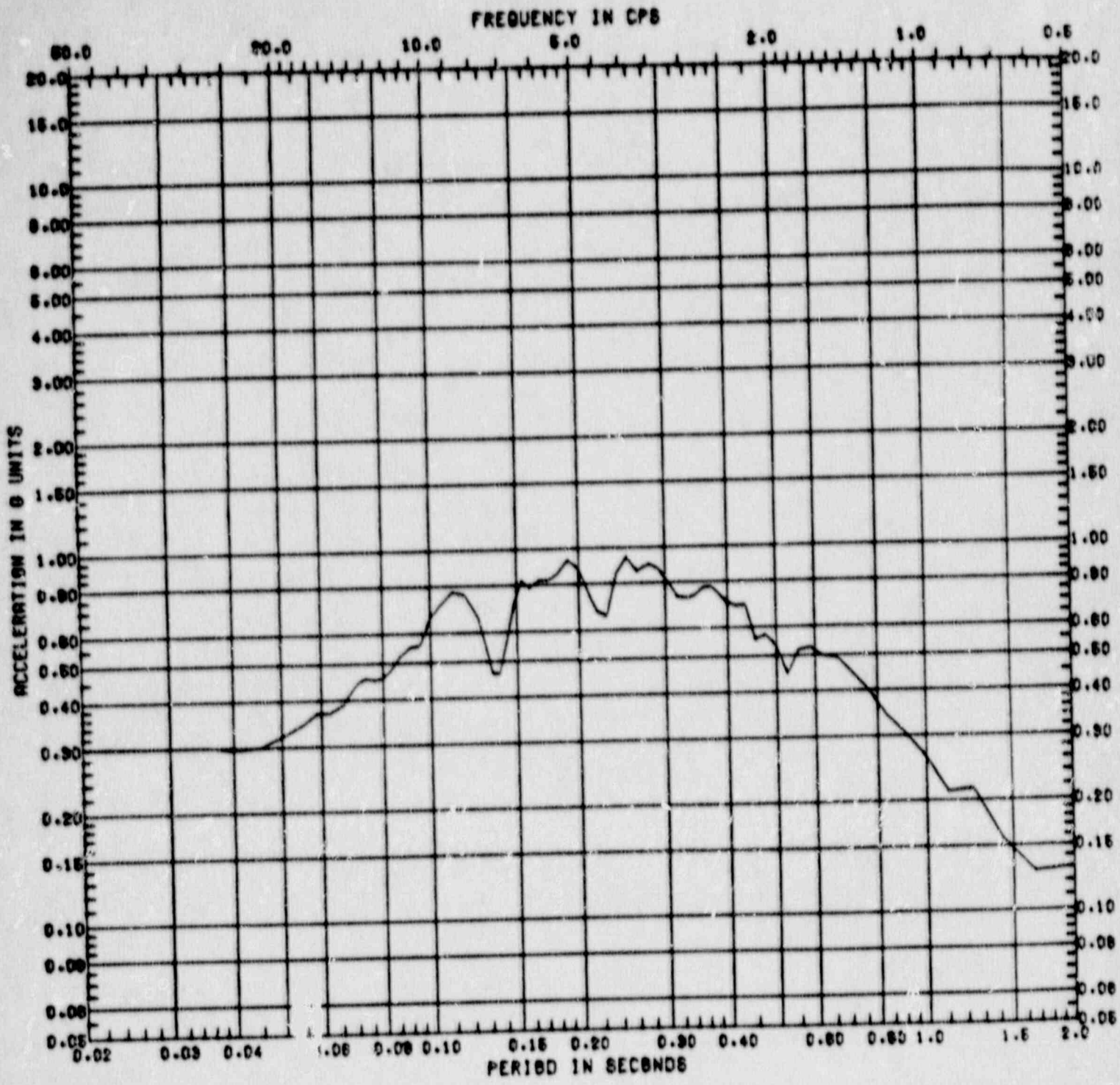

Figure C.2-6 Vertical Response Spectrum at Clinton Model Node 13 (A_R = 0.25g, Damping = 5%, Location = Drywell Wall at Elevation 745')

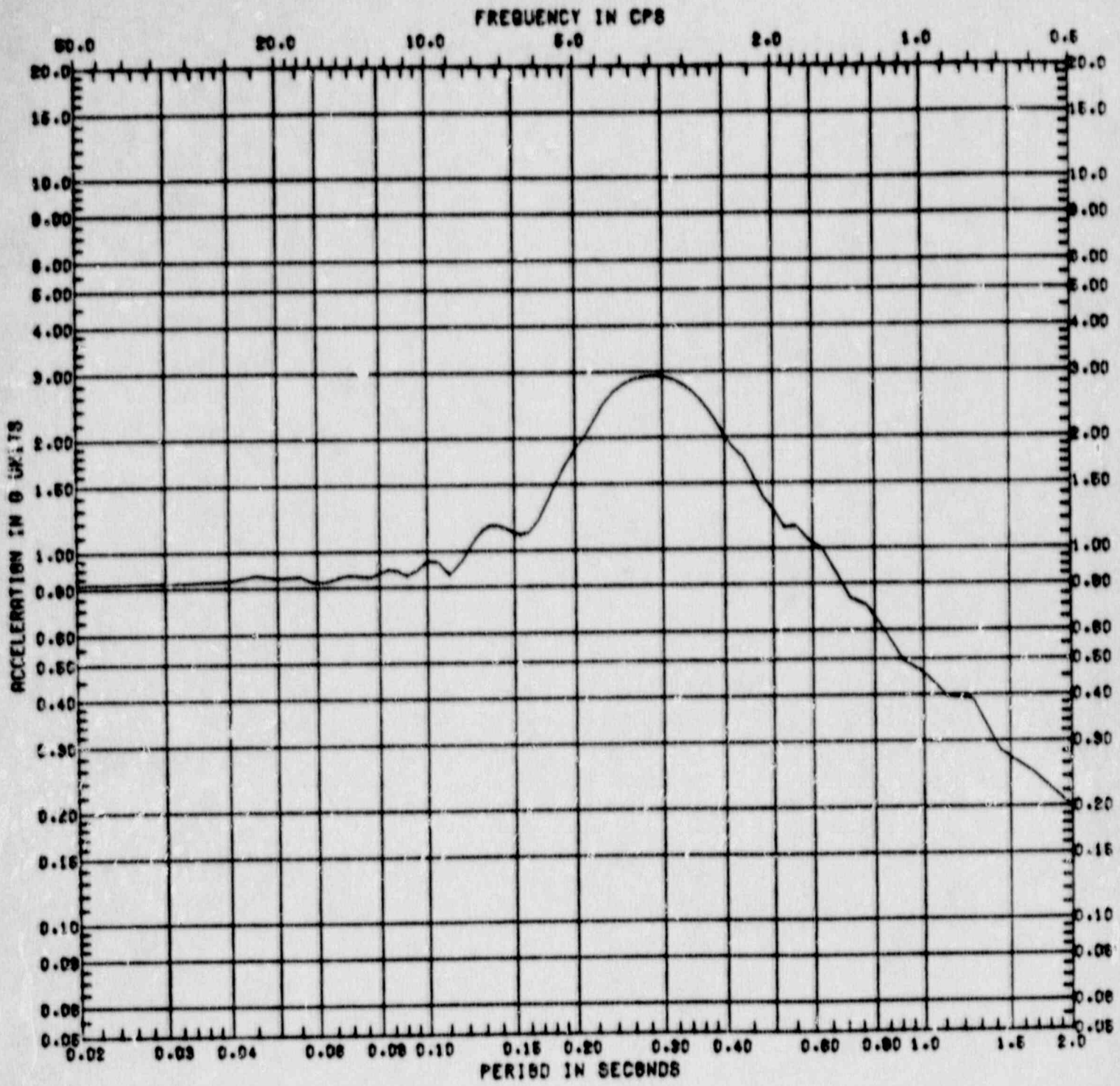

Figure C.2-7 Horizontal Response Spectrum at Clinton Model Node 8 (A_H = 0.25g, Damping = 5%, Location = Drywell Wall at Elevation 801')

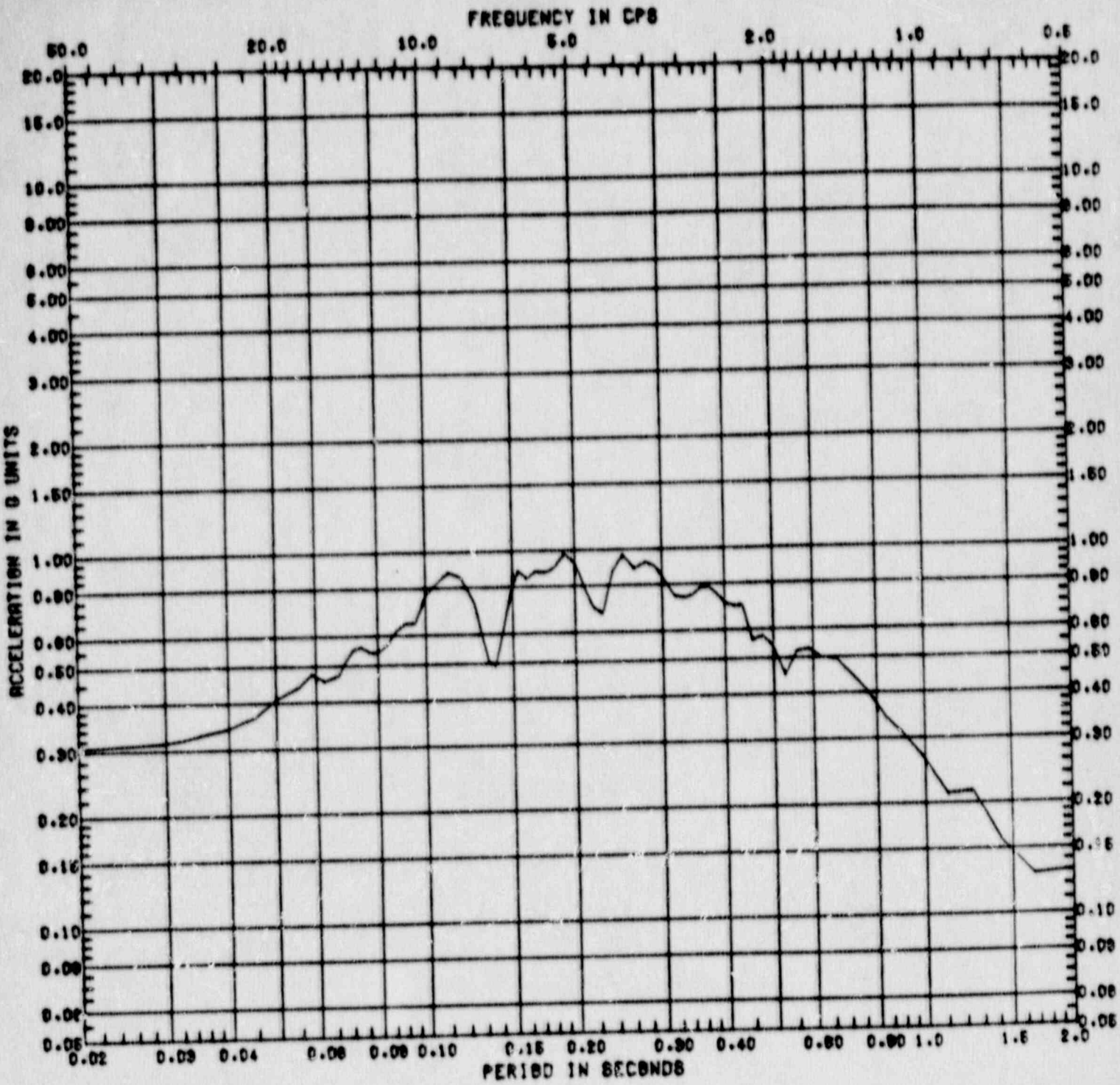

Figure C.2-8 Vertical Response Spectrum at Clinton Model Node 8 (A_H = 0.25g, Damping = 5%, Location = Drywell Wall at Elevation 801')

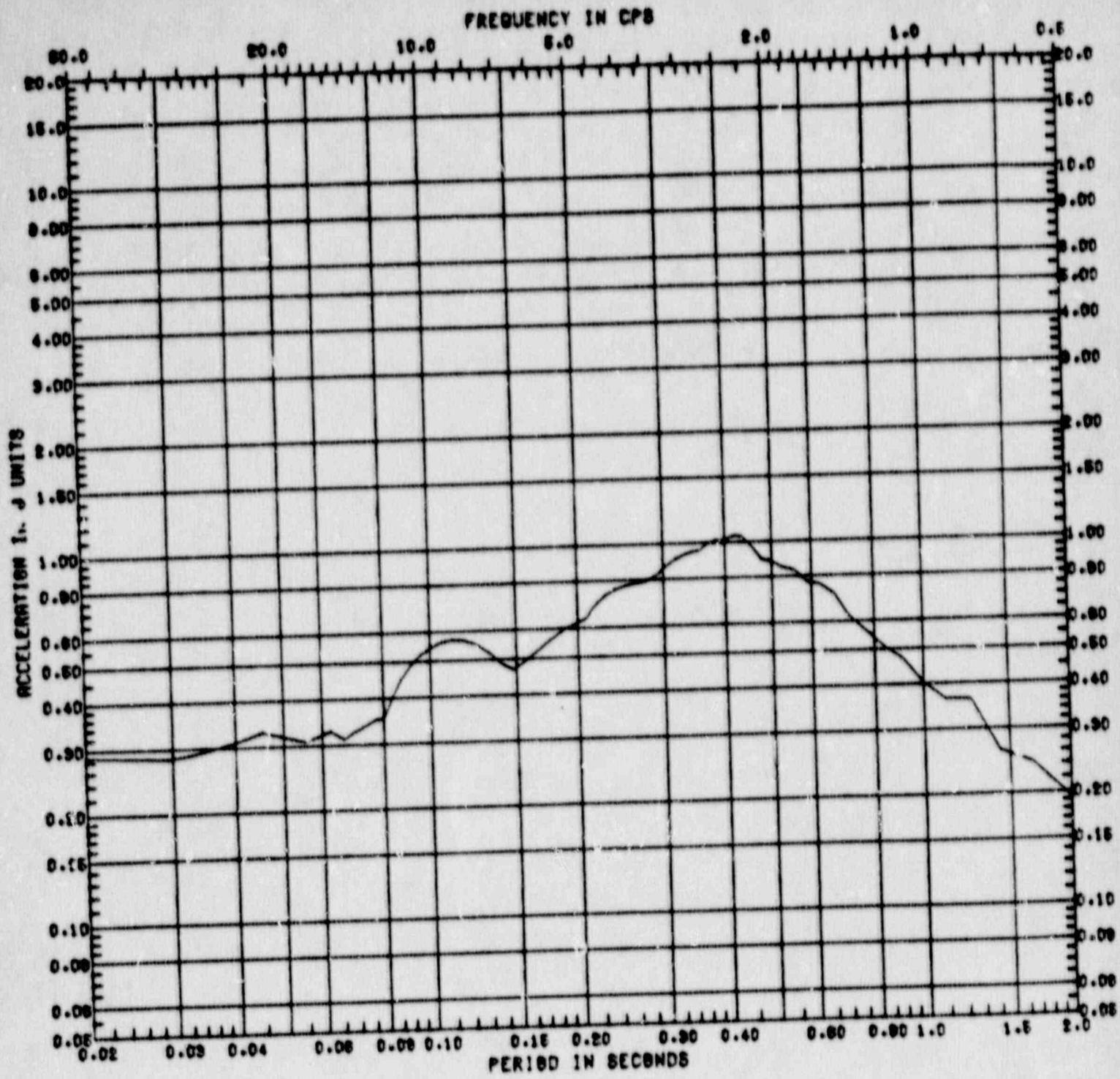

Figure C.2-9 Horizontal Response Spectrum at Clinton Model Node 46 (A_H = 0.25g, Damping = 5%, Location = Reactor-Control Building at Basemat, Elevation 712')

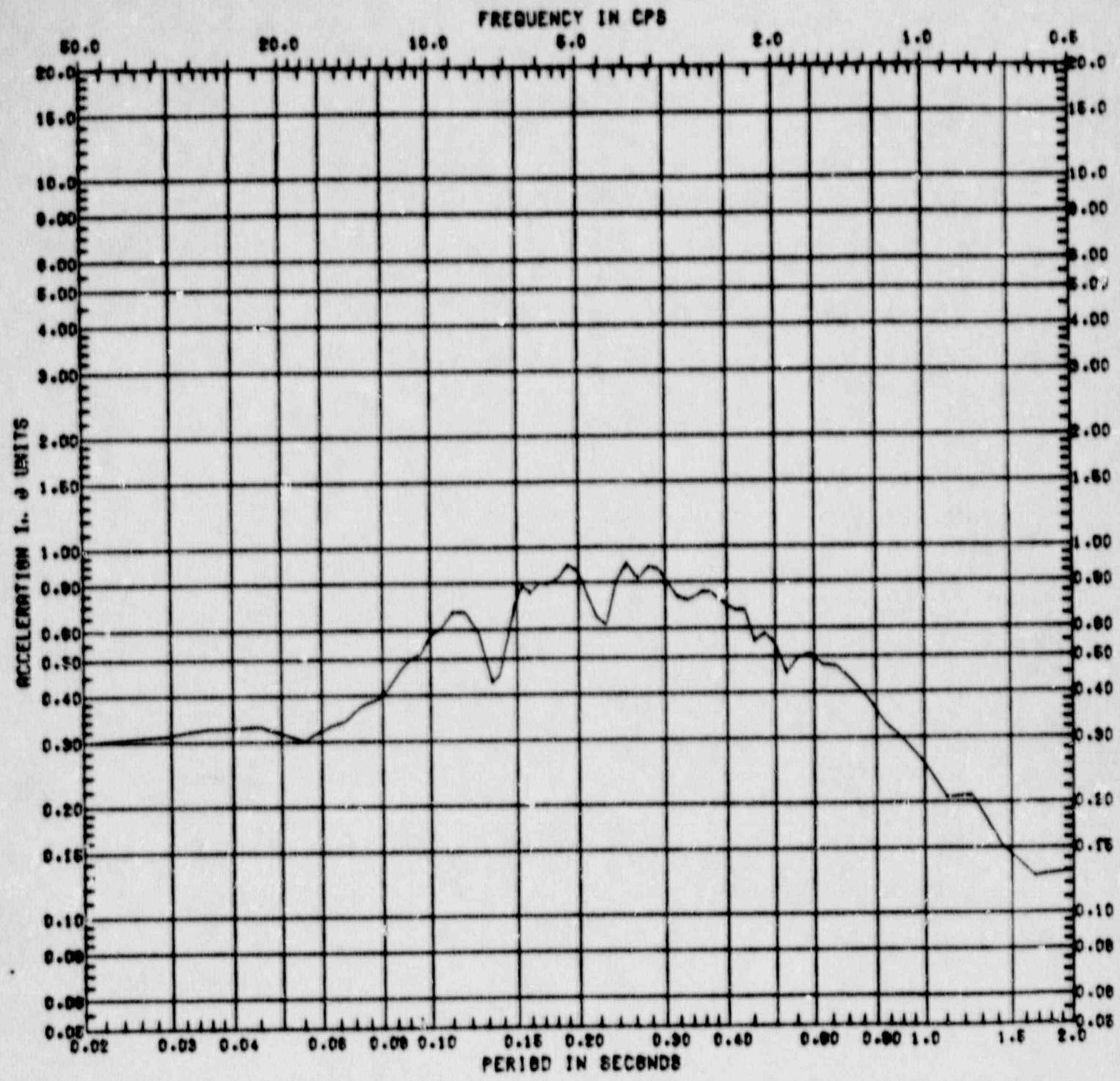

Figure C.2-10 Vertical Response Spectrum at Clinton Model Node 46 (A_H = 0.25g, Damping = 5%, Location = Reactor-Control Building at Basemat, Elevation 712')

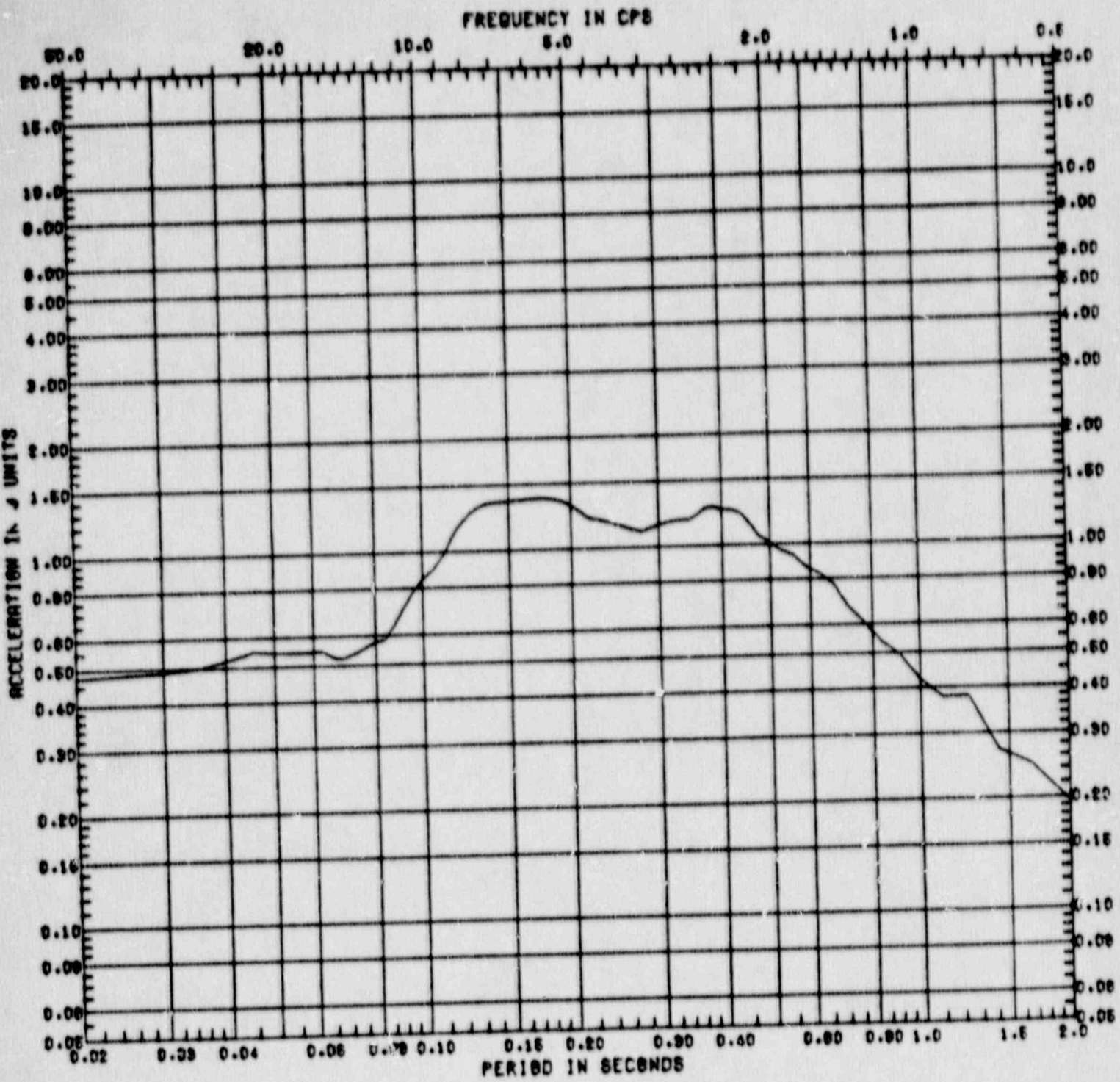

Figure C.2-11 Horizontal Response Spectrum at Clinton Model Node 17 (A_H = 0.25g, Damping = 5%, Location = Reactor-Control building at Elevation 801')

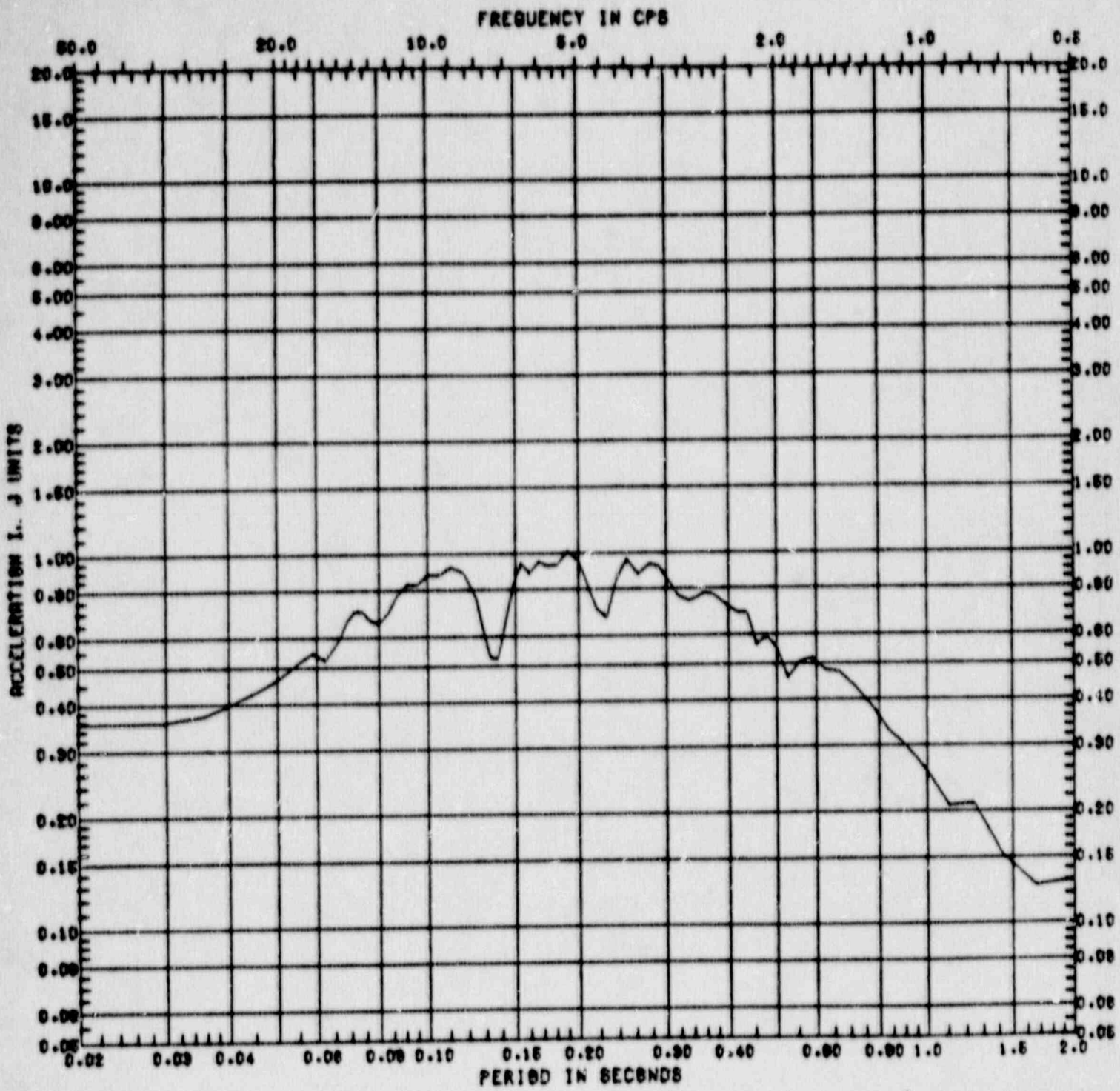

Figure C.2-12 Vertical Response Spectrum at Clinton Model Node 17 (A_H = 0.25g, Damping = 5%, Location = Reactor-Control Building at Elevation 801')

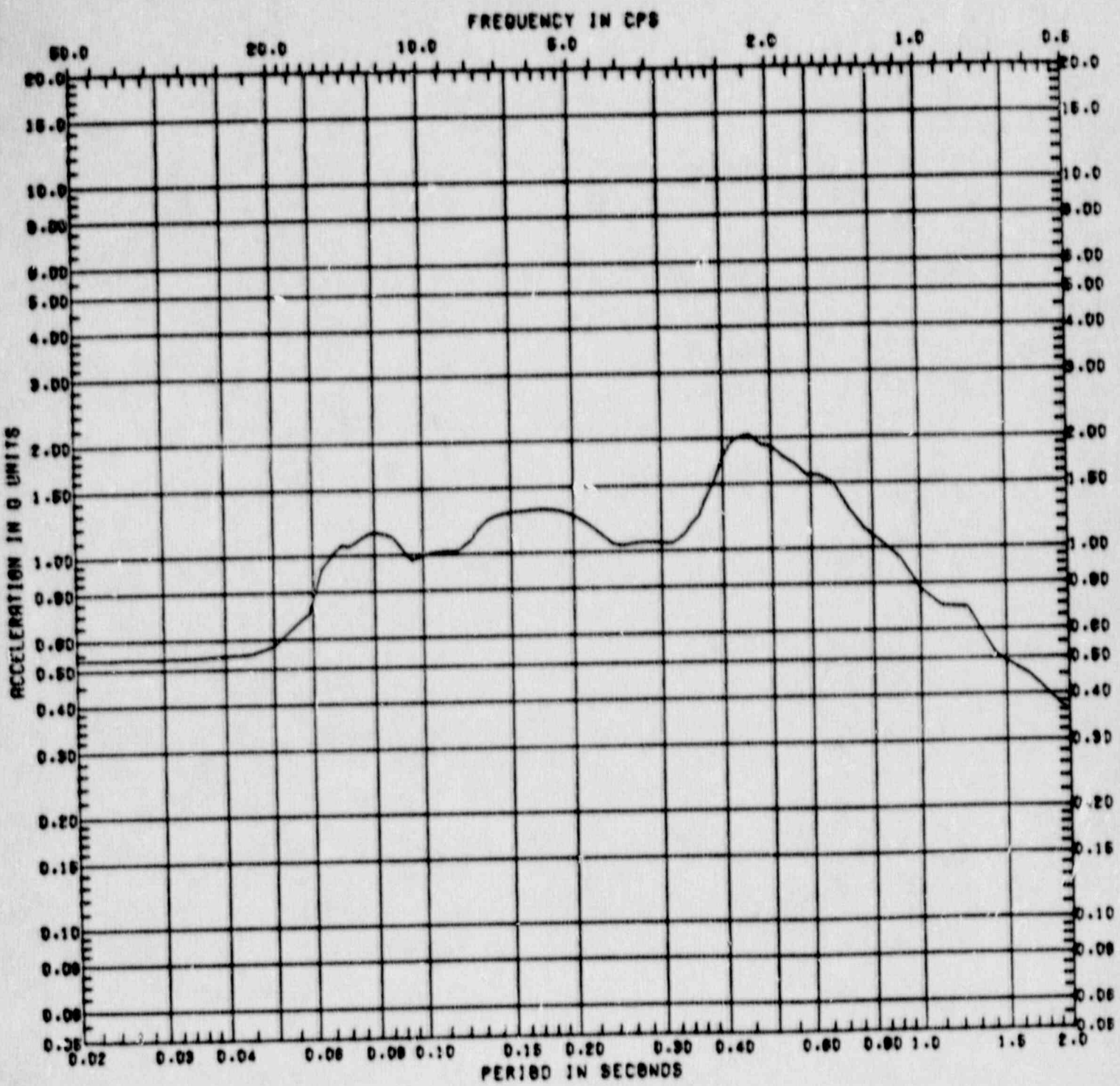

Figure C.2-13 Horizontal Response Spectrum at Clinton Model Node 15 (A_H = 0.45g, Damping = 5%, Location = Containment Wall at Elevation 745')

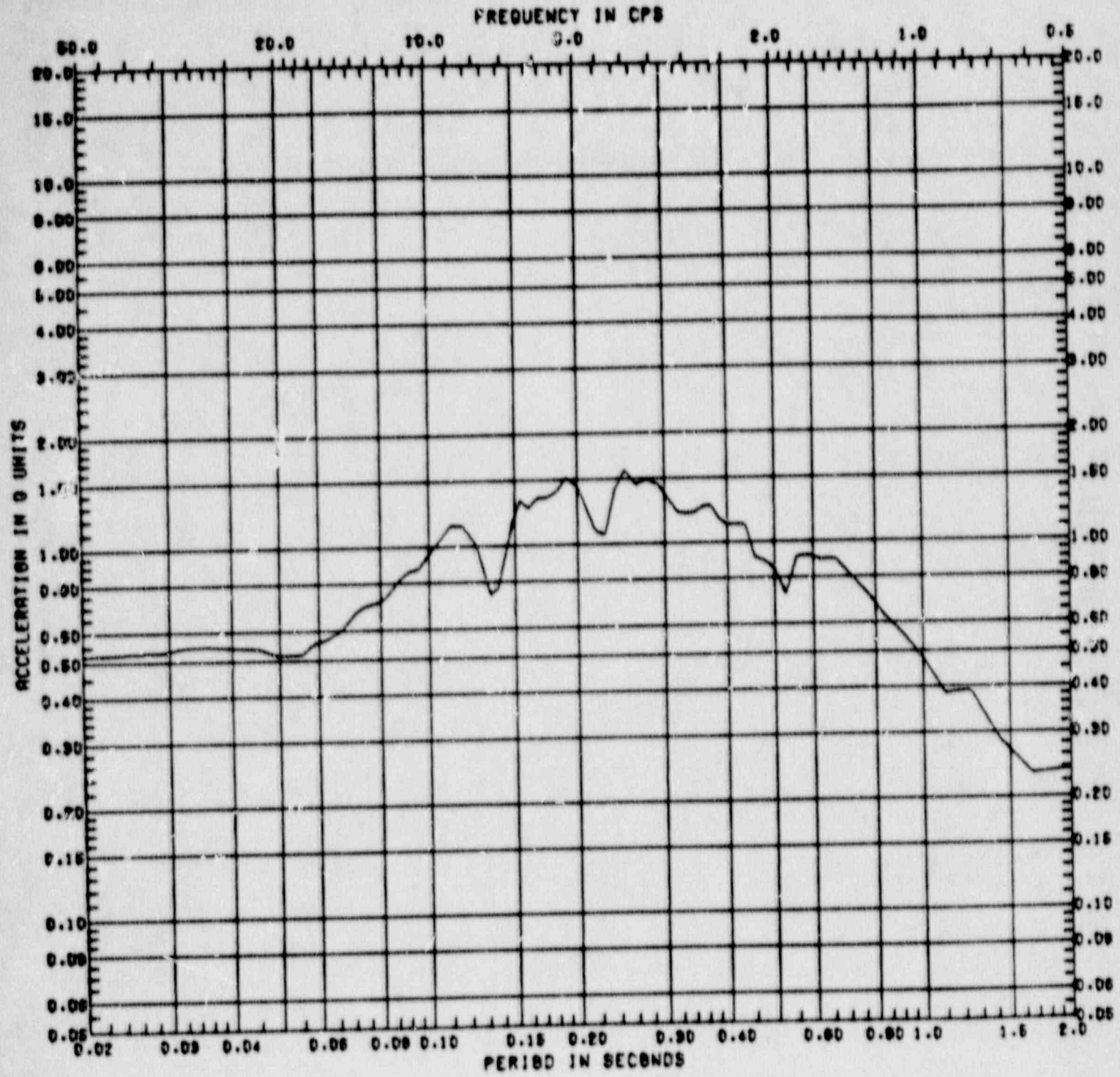

Figure C.2-14 Vertical Response Spectrum at Clinton Model Node 15 (A_H = 0.45g, Damping = 5%, Location = Drywell Wall at Elevation 745')

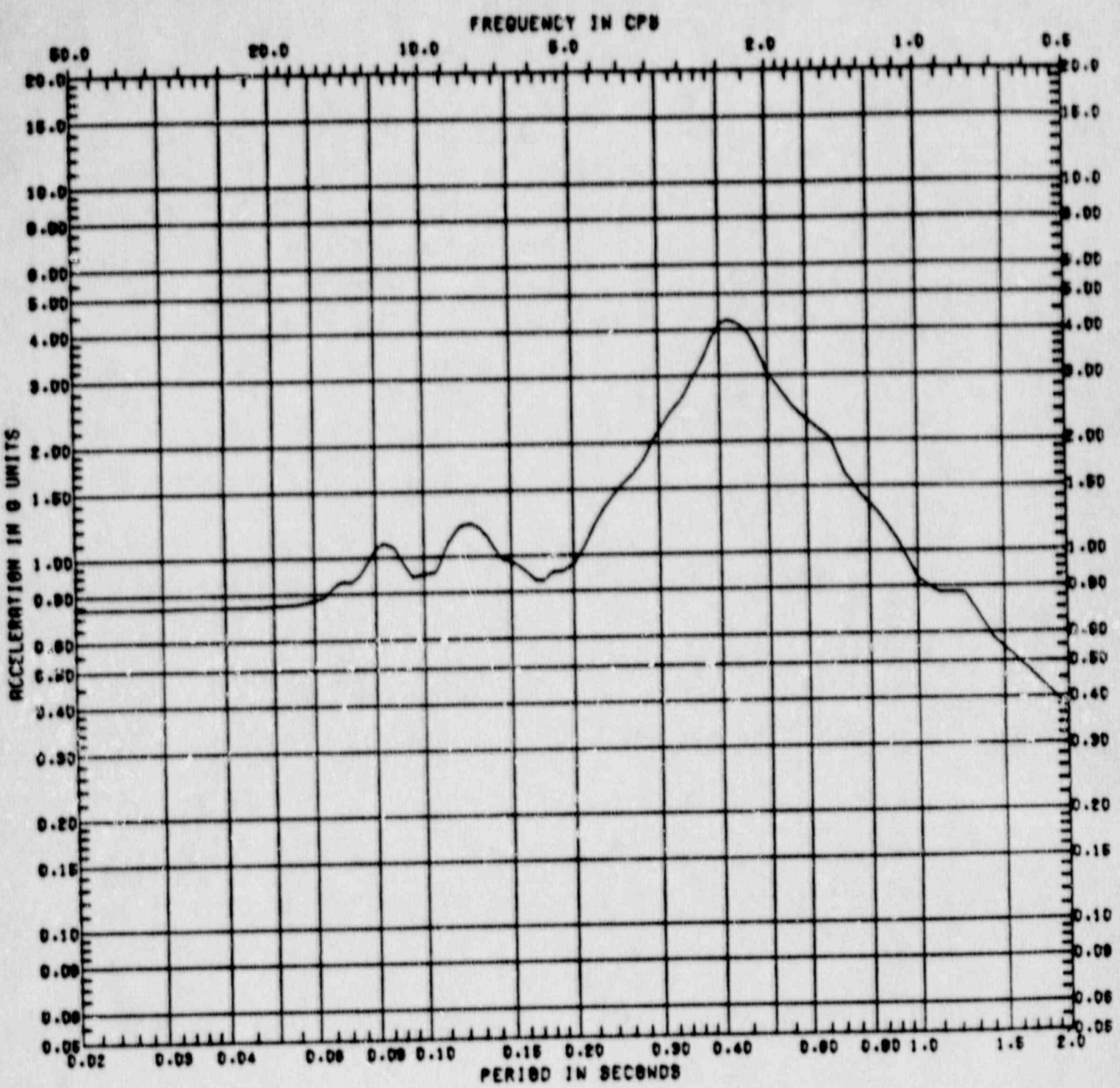

Figure C.2-15 Horizontal Response Spectrum at Clinton Model Node 4 (A_H = 0.45g, Damping = 5%, Location = Containment Wall at Elevation 832')

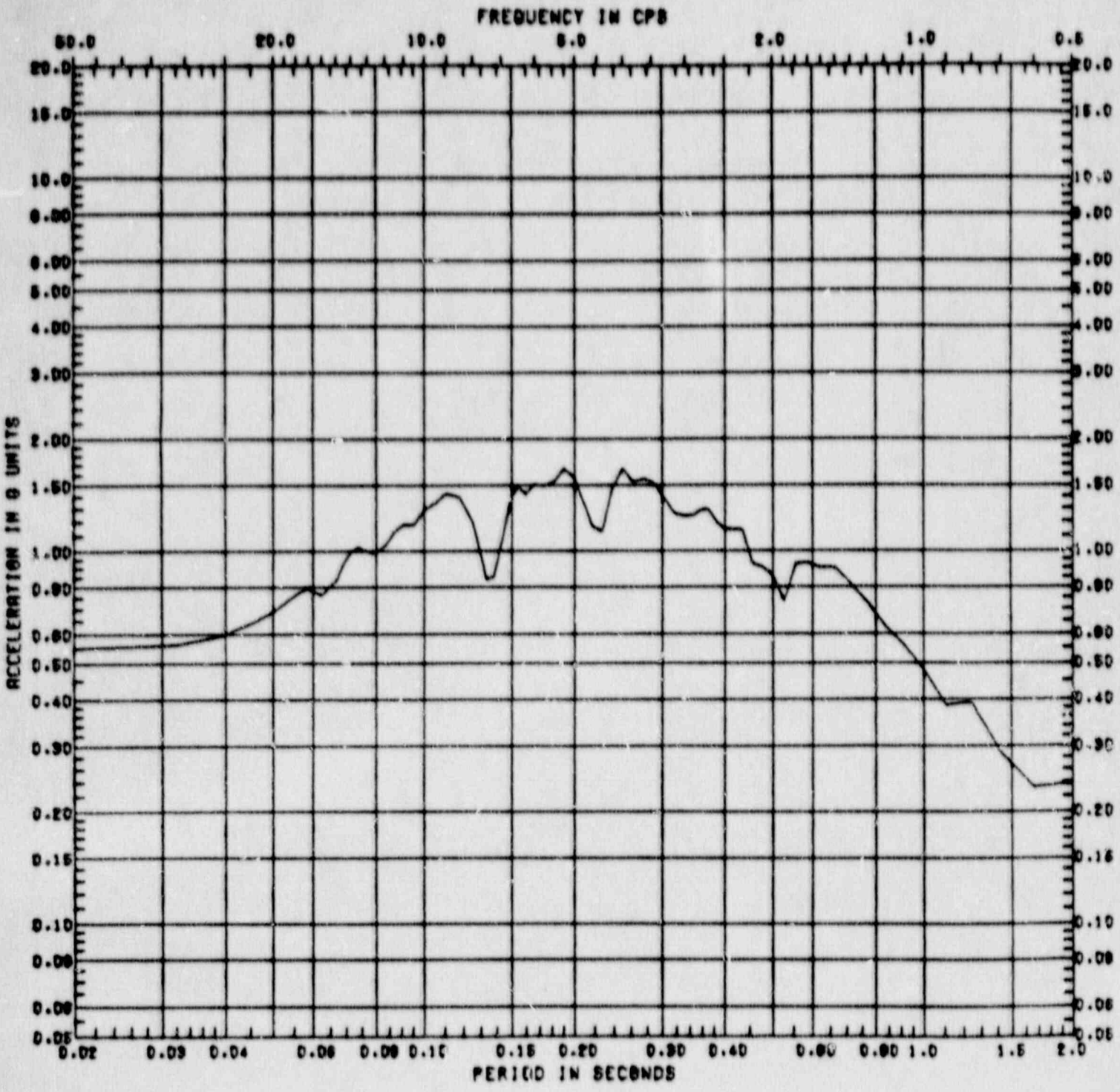

Figure C.2-16 Vertical Response Spectrum at Clinton Model Node 4 (A_H = 0.45g, Damping = 5%, Location = Containment Wall at Elevation 832')

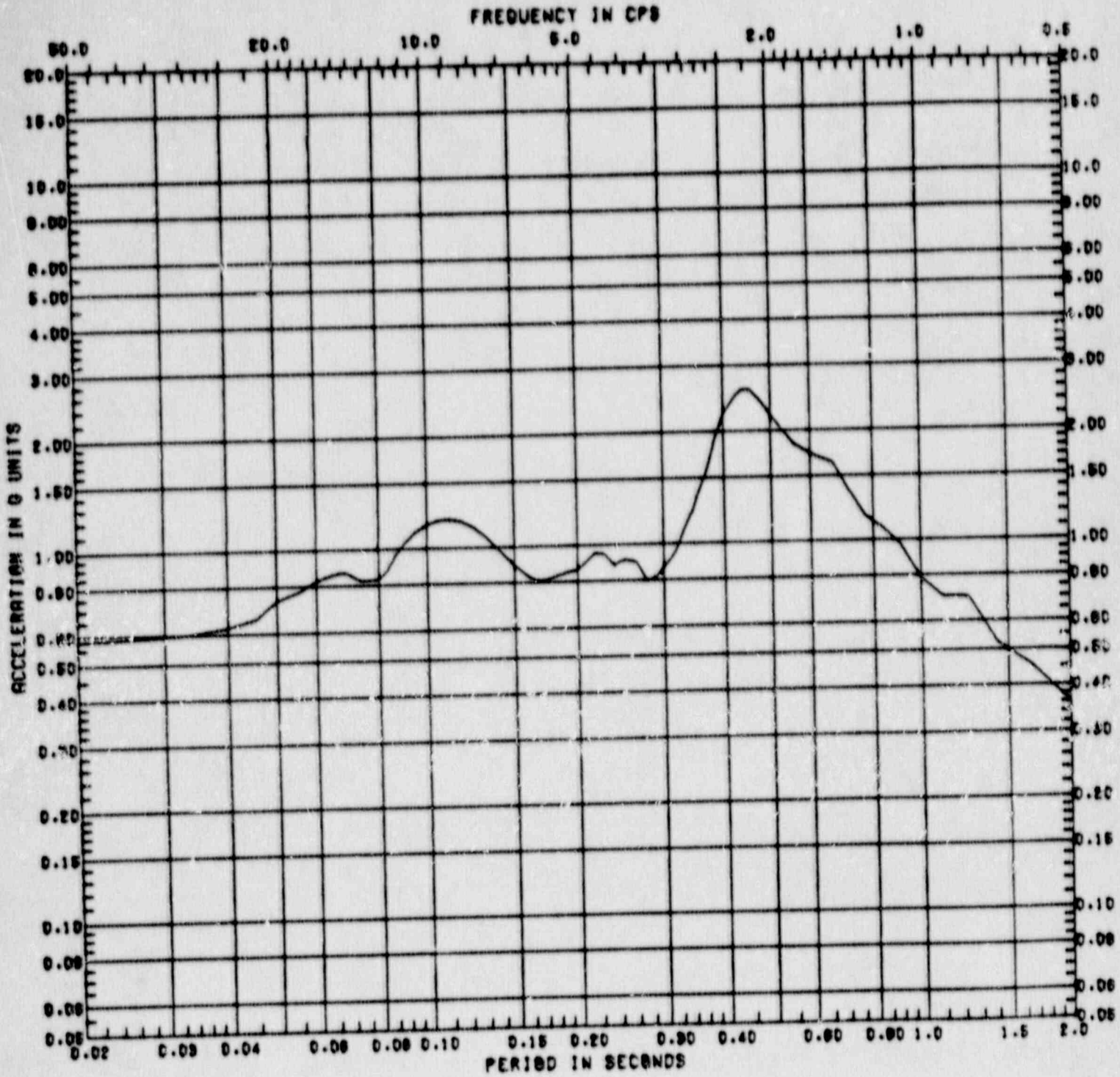

Figure C.2-17 Horizontal Response Spectrum at Clinton Model Node 13 (A_H = 0.45g, Damping = 5%, Location = Drywell Wall at Elevation 745')

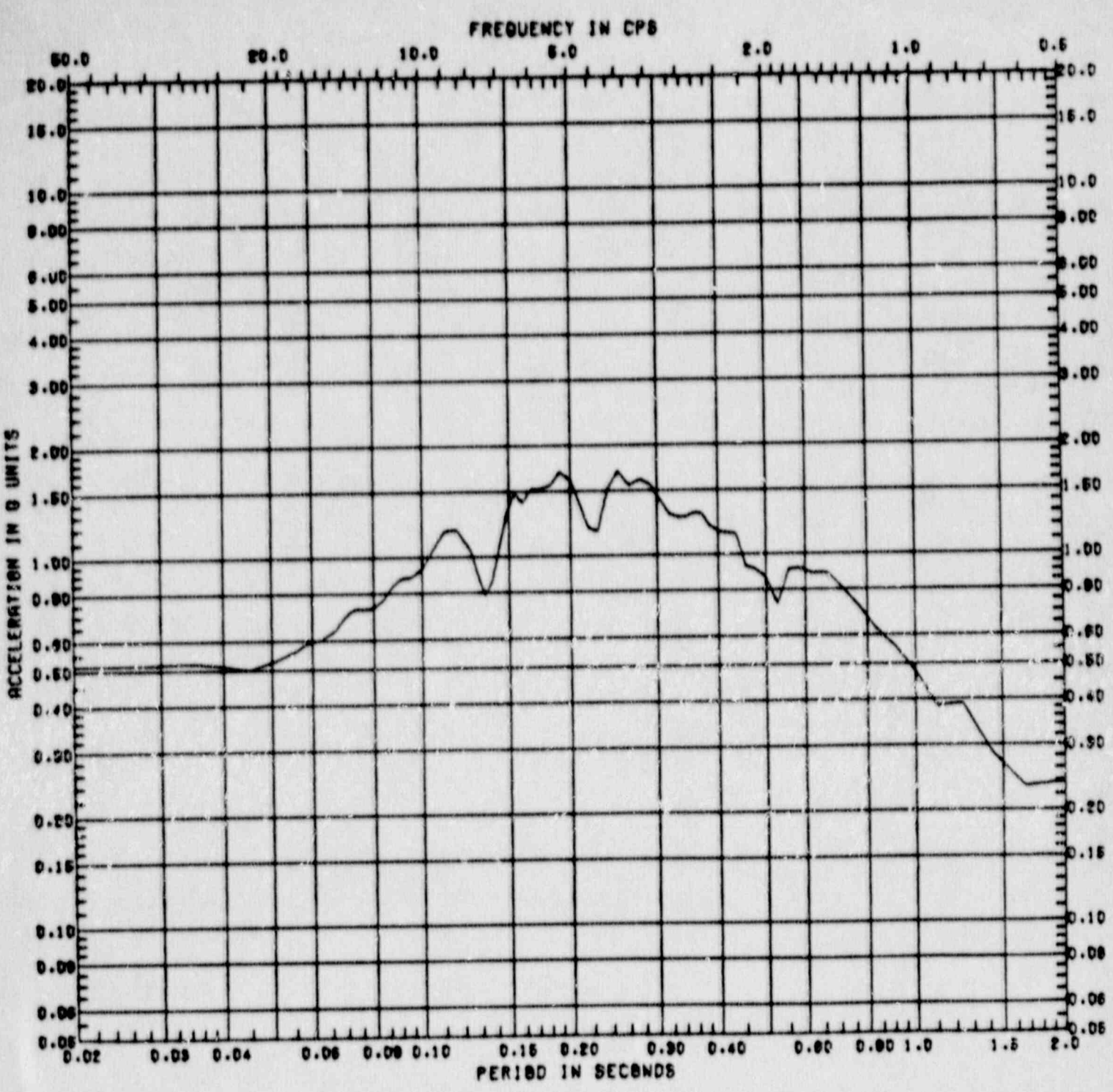

Figure C.2-18 Vertical Response Spectrum at Clinton Model Node 13 (A_H = 0.45g, Damping = 5%, Location = Drywell Wall at Elevation 745')

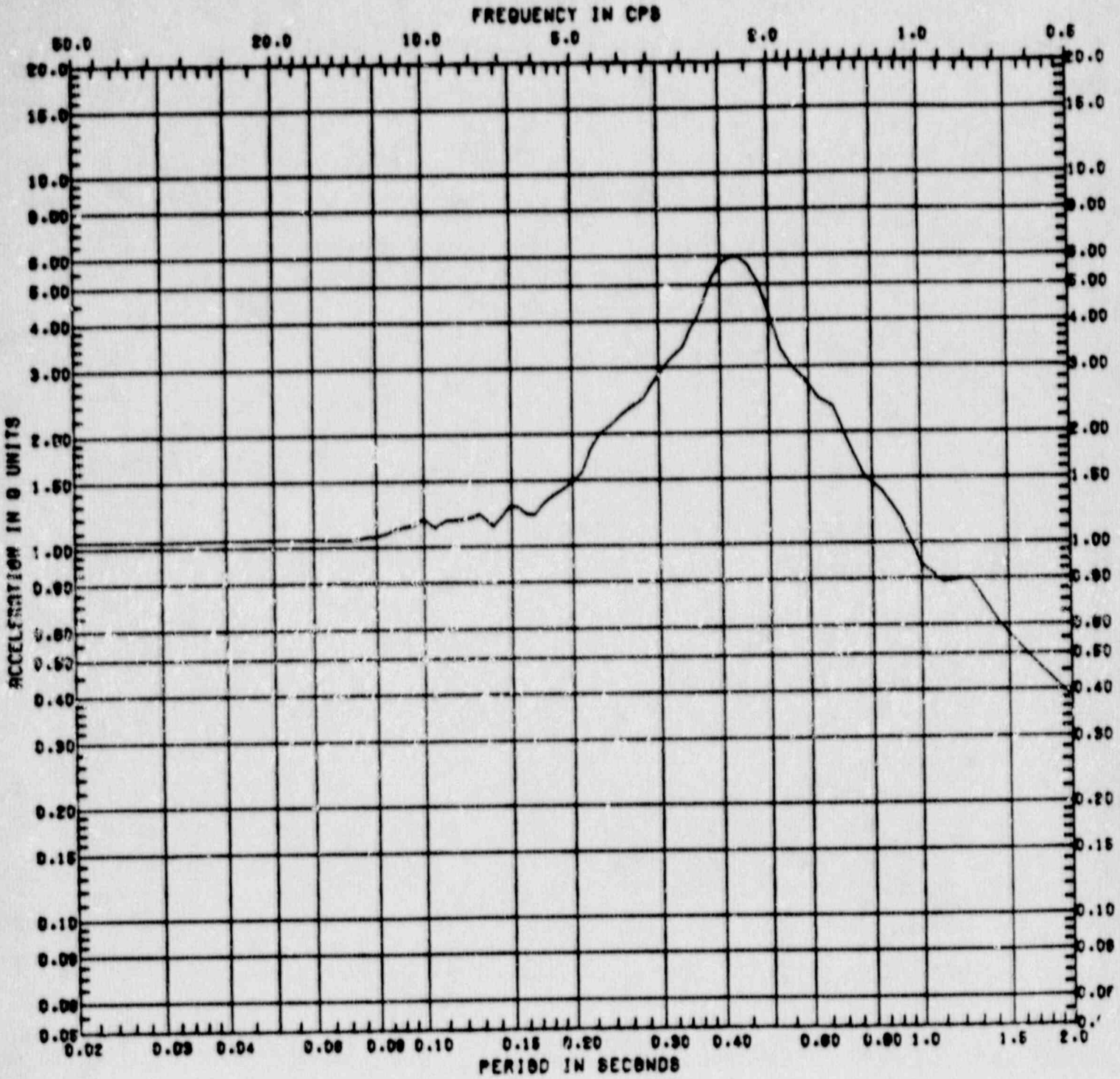

Figure C.2-19 Horizontal Response Spectrum at Clinton Model Node 8 (A_H = 0.45g, Damping = 5%, Location = Drywell Wall at Elevation 801')

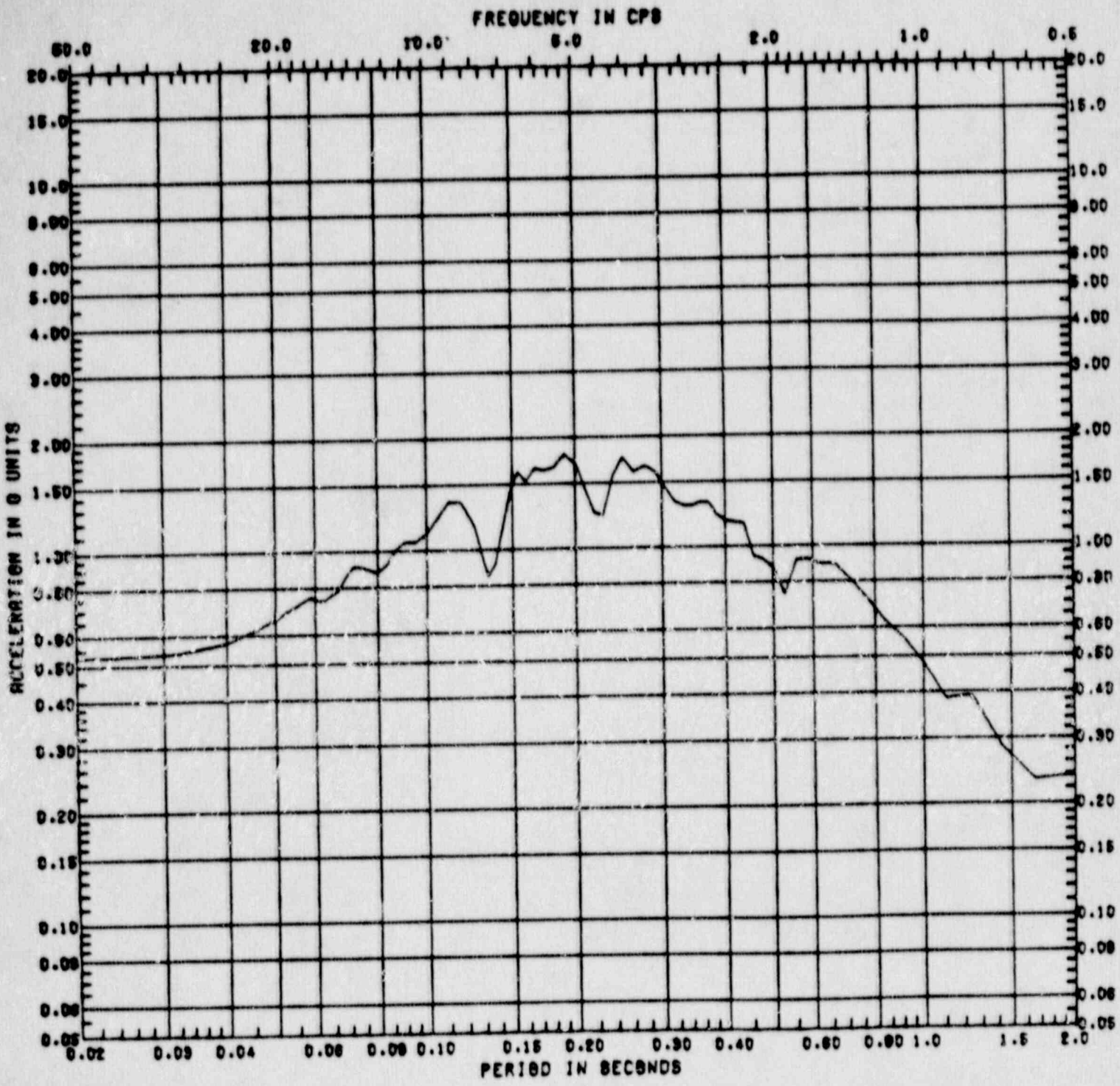

Figure C.2-20 Vertical Response Spectrum at Clinton Model Node 8 (A_H = 0.45g, Damping = 5%, Location = Drywell Wall at Elevation 801')

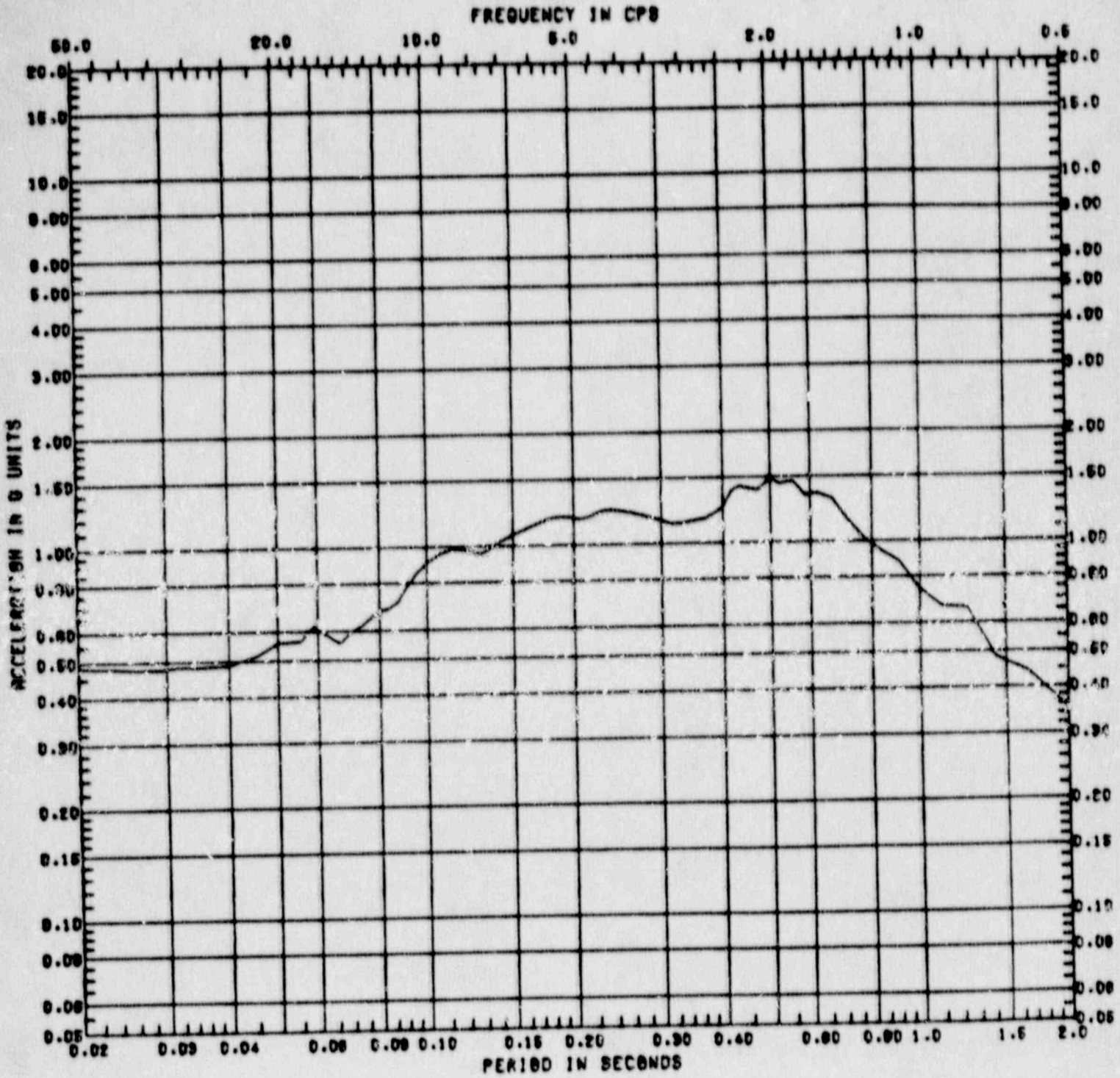

Figure C.2-21 Horizontal Response Spectrum at Clinton Model Node 46 (A_H = 0.45g, Damping = 5%, Location = Reactor-Control Building at Basemat, Elevation 712')

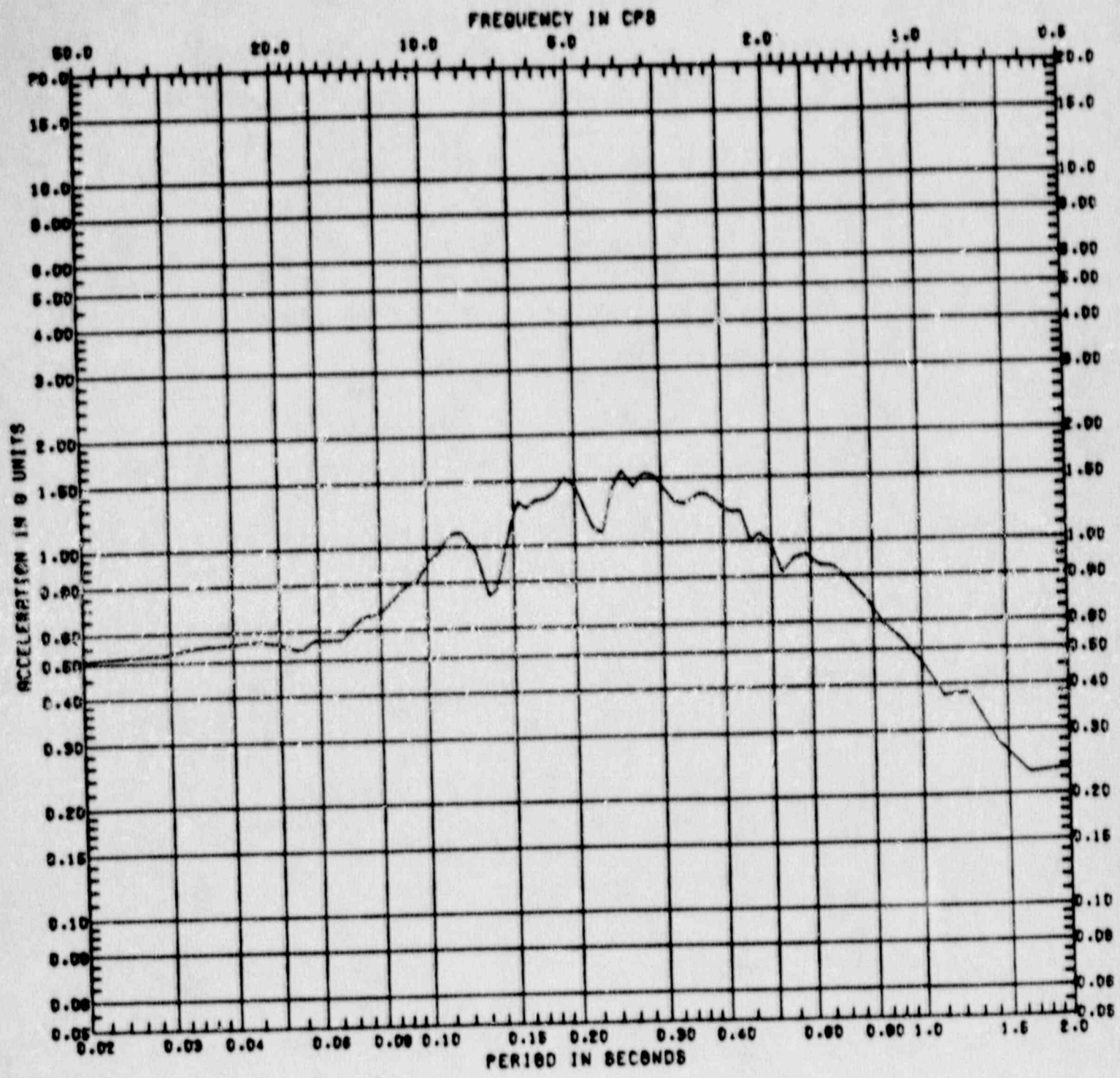

Figure C.2-22 Vertical Response Spectrum at Clinton Model Node 46 (A_H = 0.45g, Damping = 5%, Location = Reactor-Control Building at Basemat, Elevation 712')

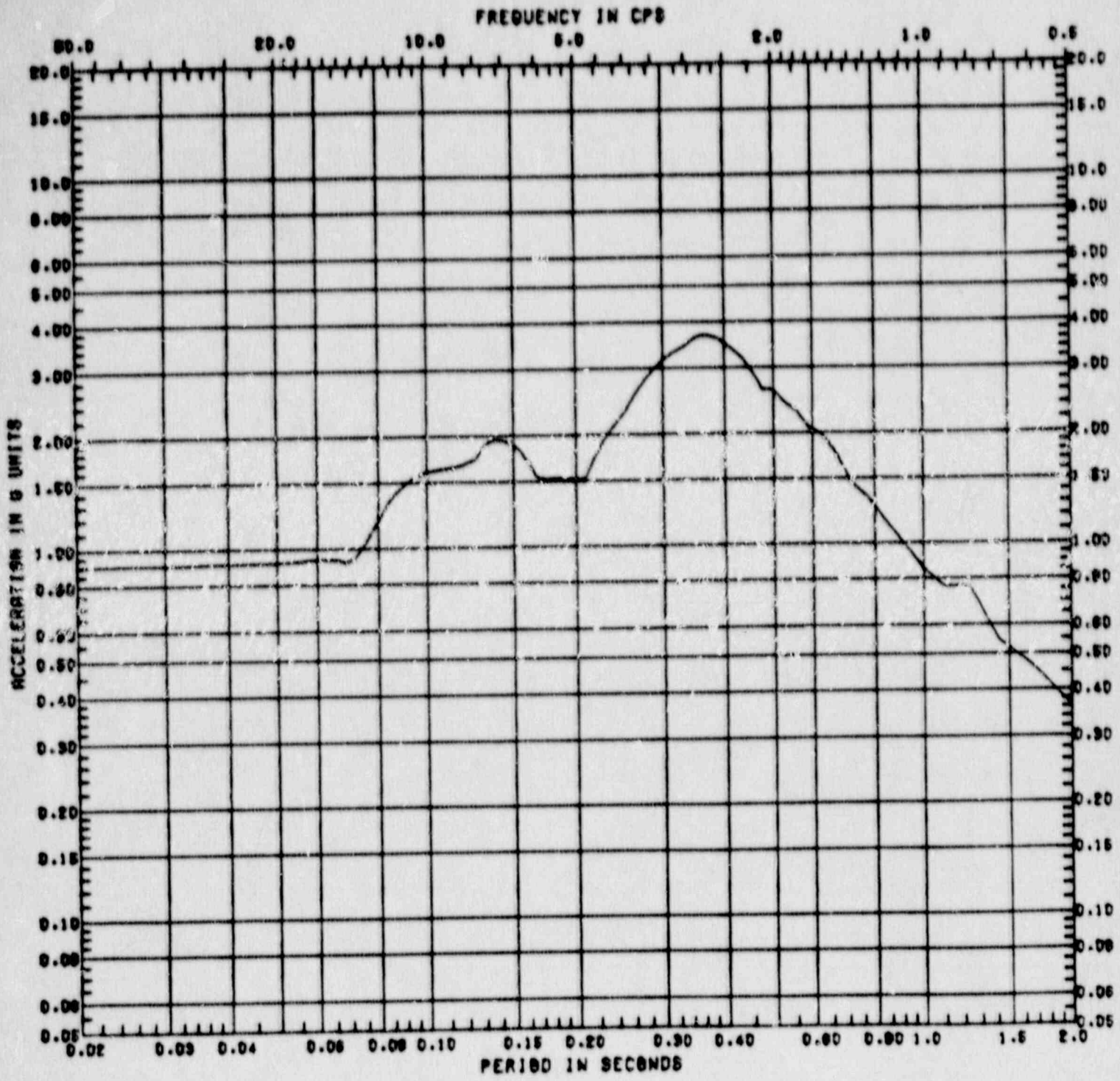

Figure C.2-23 Horizontal Response Spectrum at Clinton Model Node 17 (A_H = 0.45g, Damping = 5%, Location = Reactor-Control Building at Elevation 801')

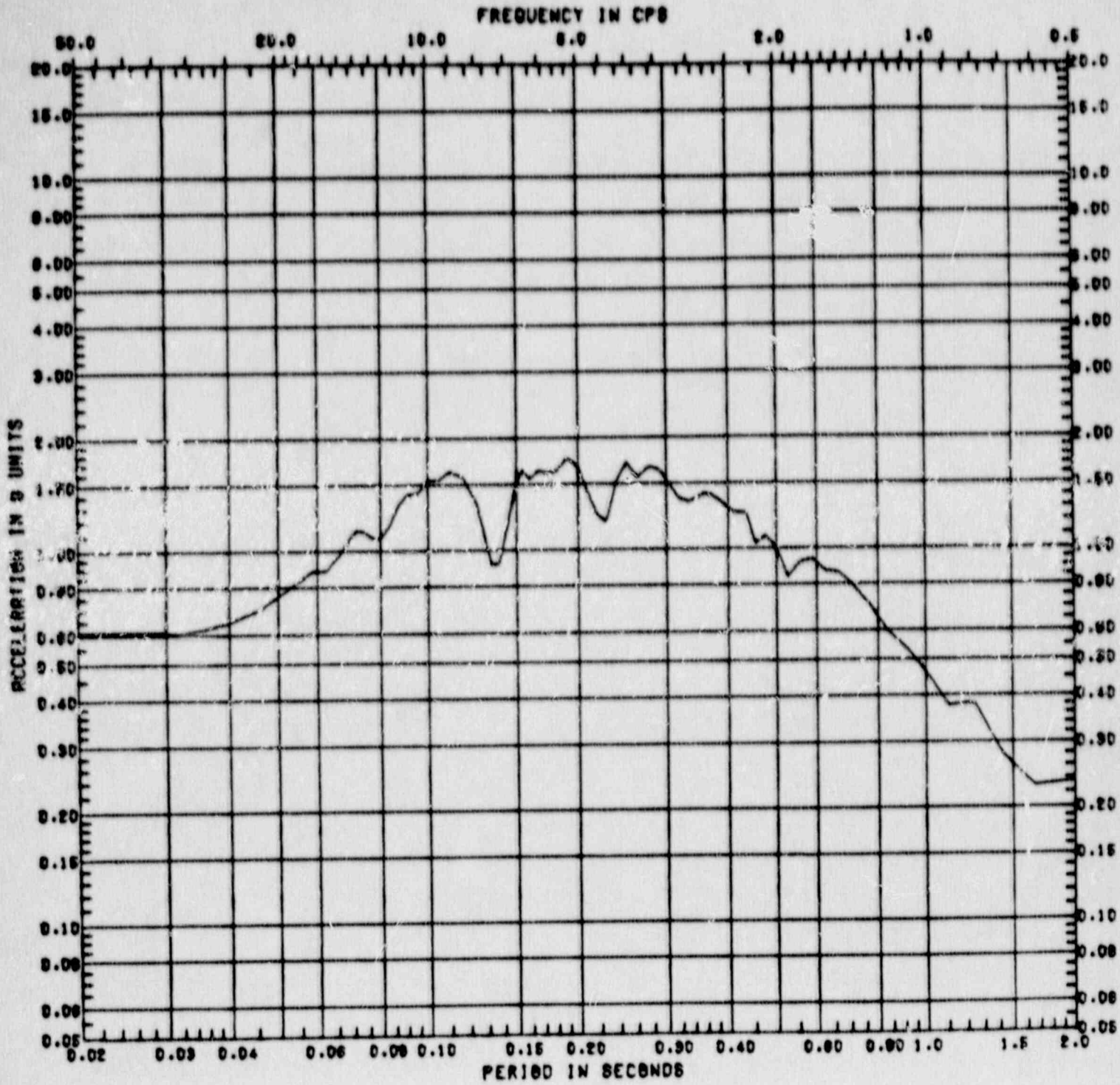

Figure C.2-24 Vertical Response Spectrum at Clinton Model Node 17 (A_H = 0.45g, Damping = 5%, Location = Reactor-Control Building at Elevation 801')

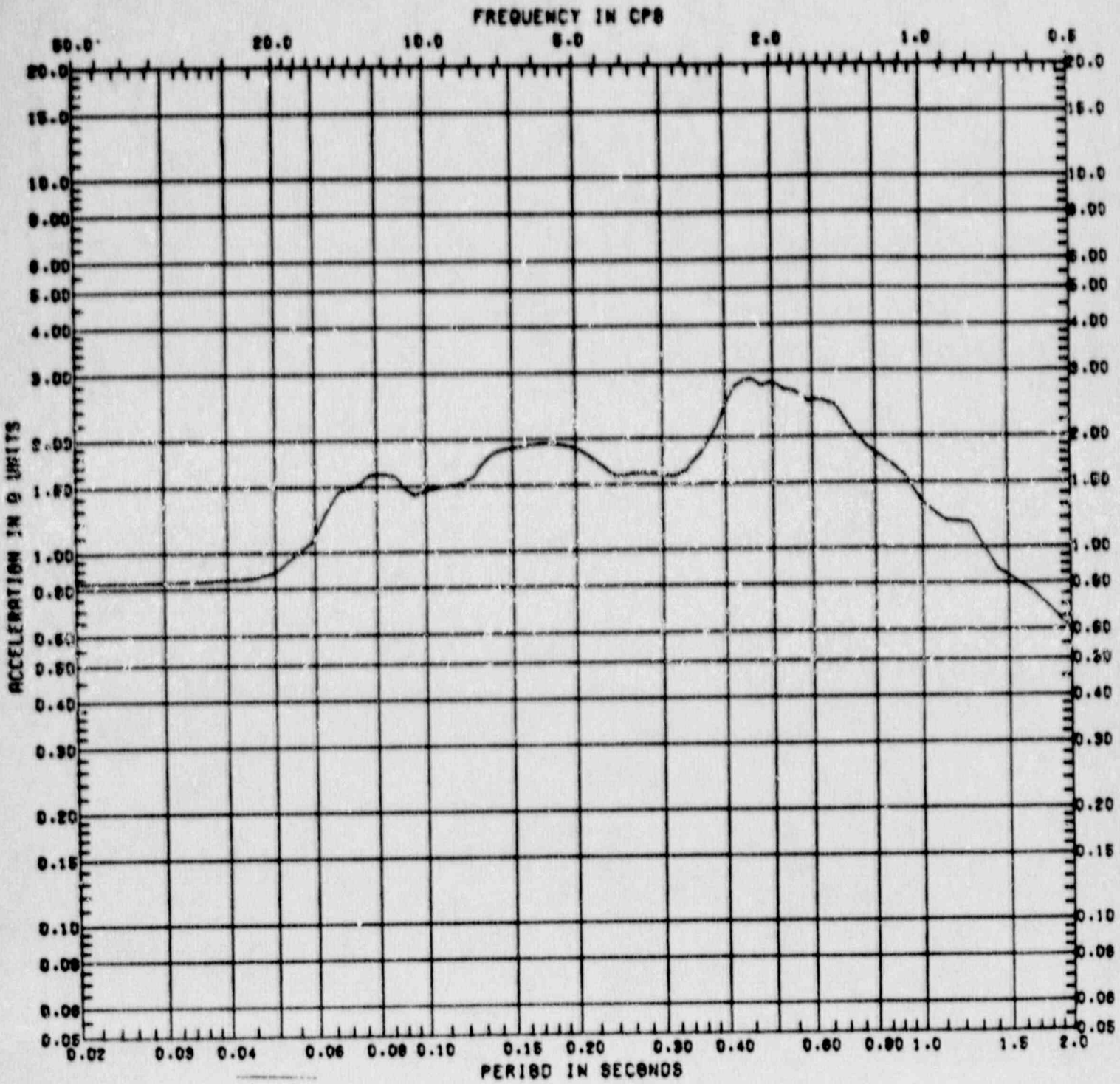

Figure C.2-25 Horizontal Response Spectrum at Clinton Model Node 15 (A_H = 0.75g, Damping = 5%, Location = Containment Wall at Elevation 745')

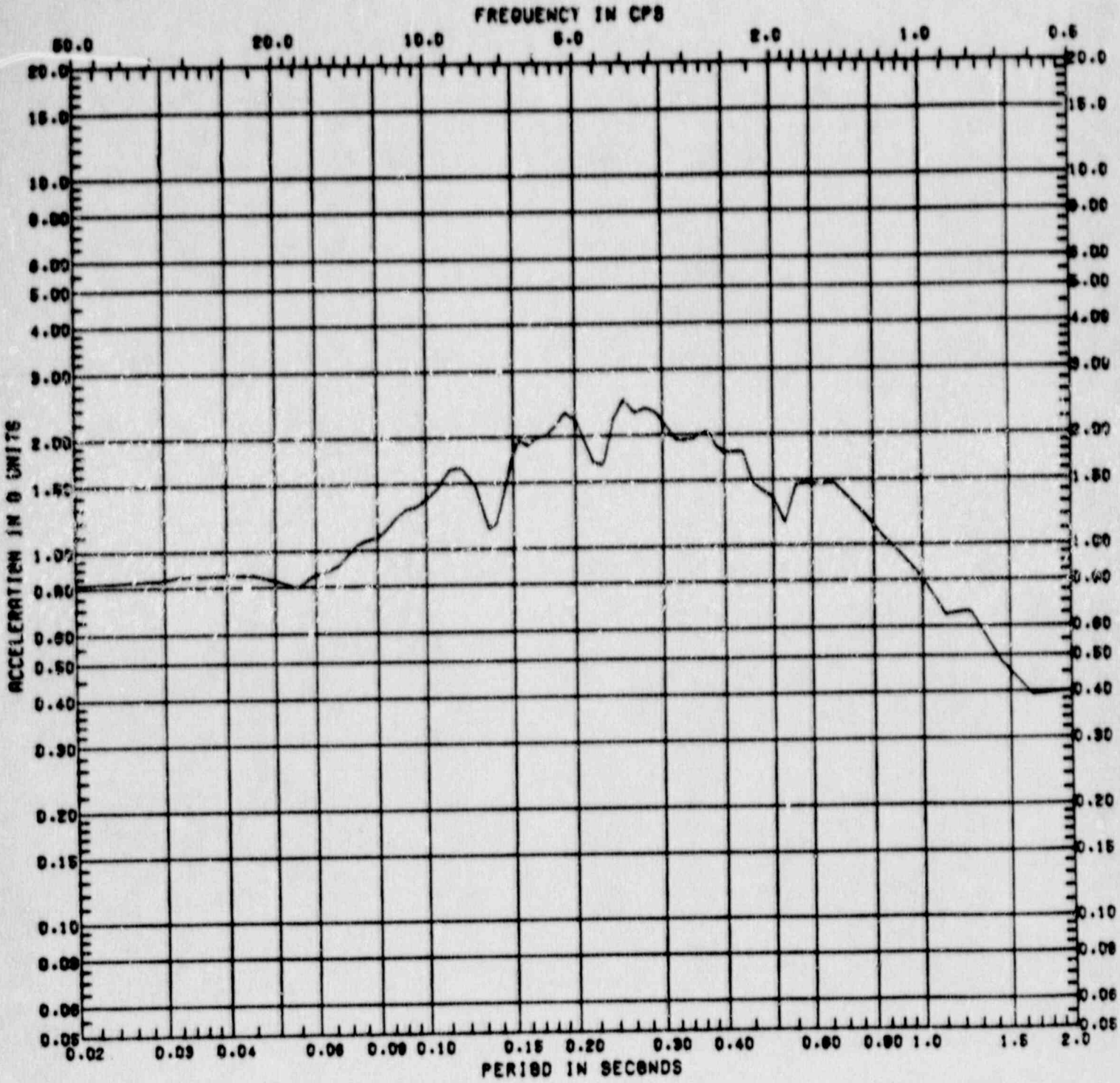

Figure C.2-26 Vertical Response Spectrum at Clinton Model Node 15 (A_H = 0.75g, Damping = 5%, Location = Containment Wall at Elevation 715')

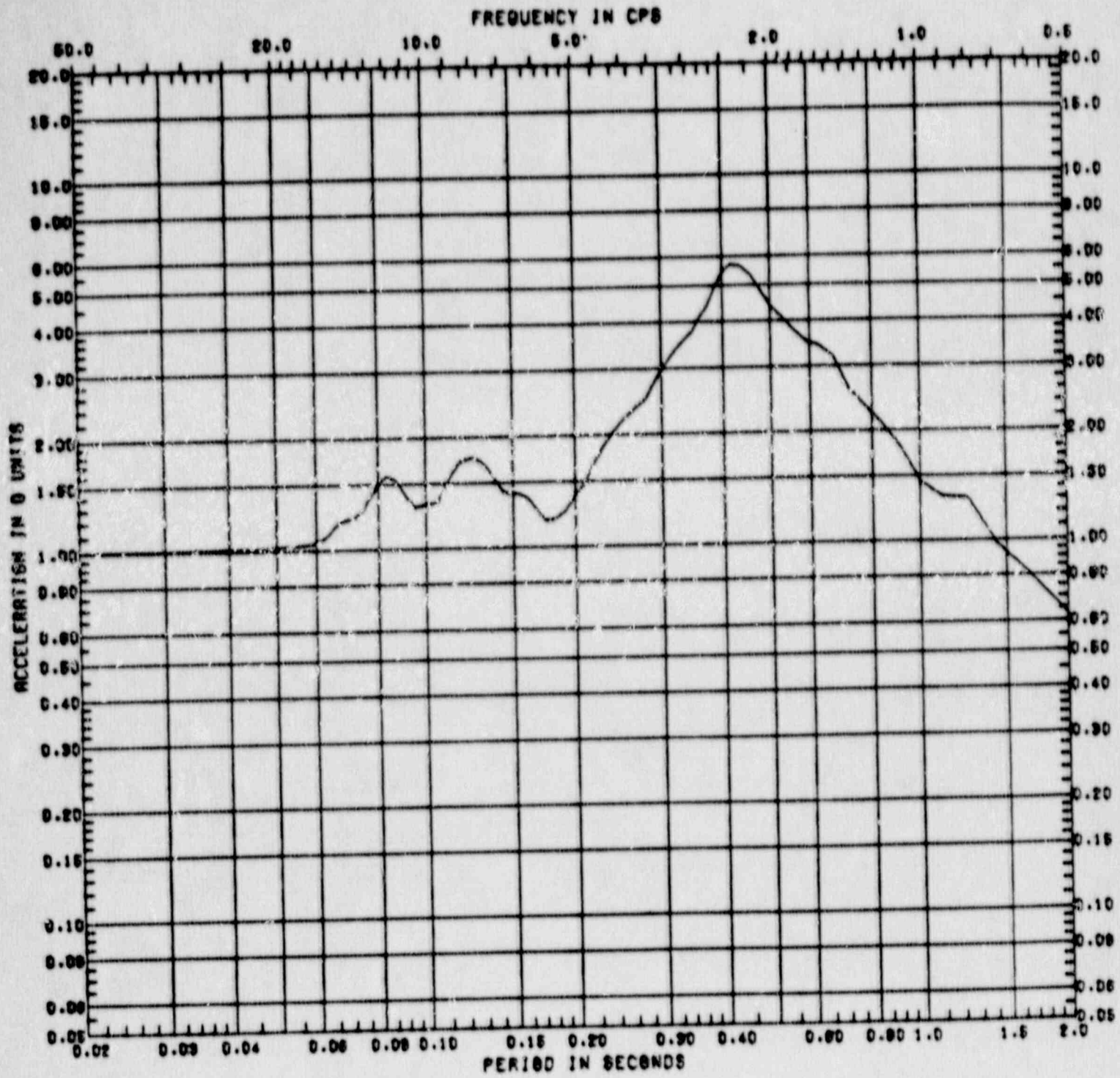

Figure C.2-27 Horizontal Response Spectrum at Clinton Model Node 4 (A_H = 0.75g, Damping = 5%, Location = Containment Wall at Elevation 832')

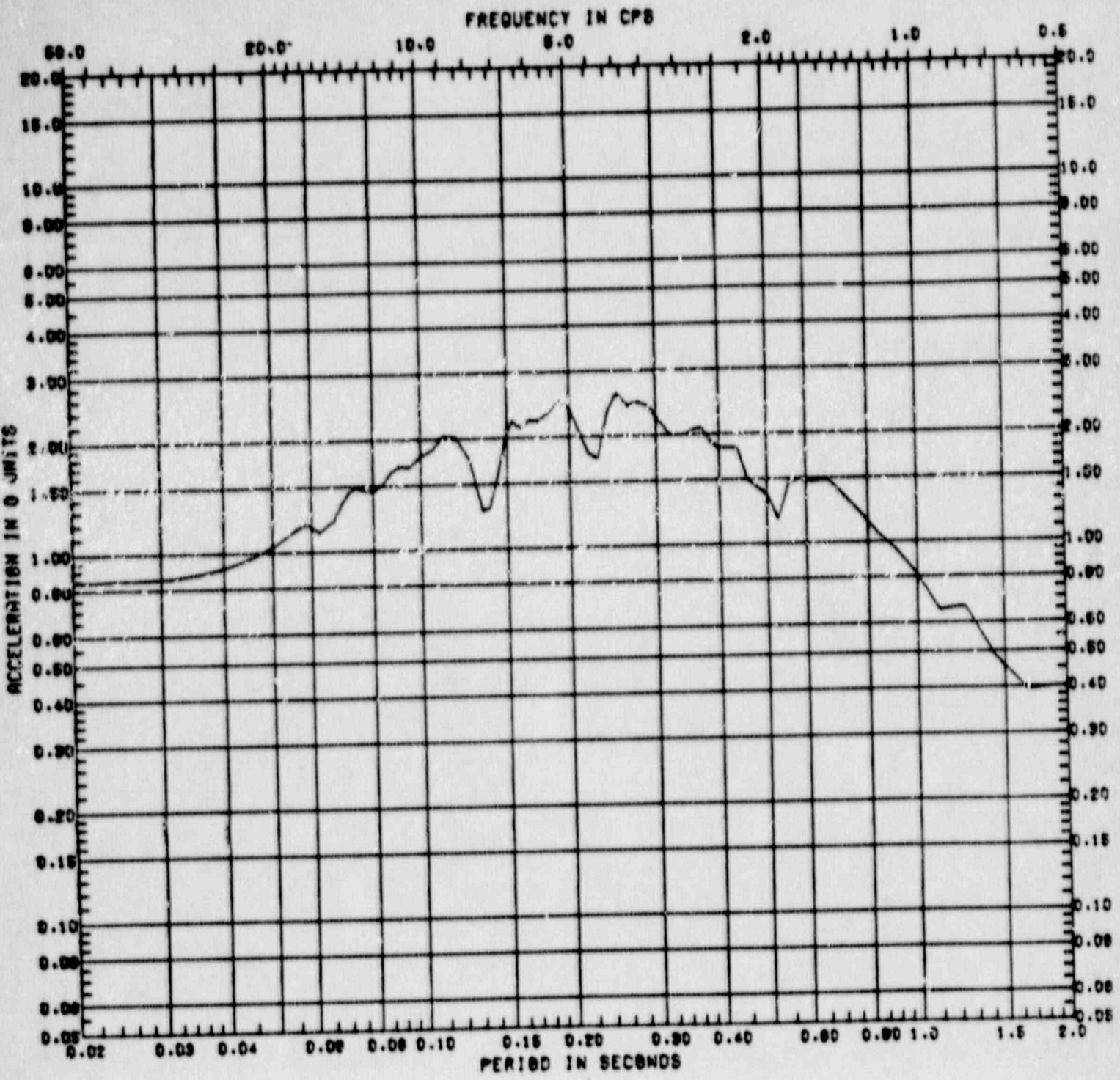

Figure C.2-28 Vertical Response Spectrum at Clinton Model Node 4 (A_H = 0.75g, Damping = 5%, Location = Containment Wall at Elevation 832')

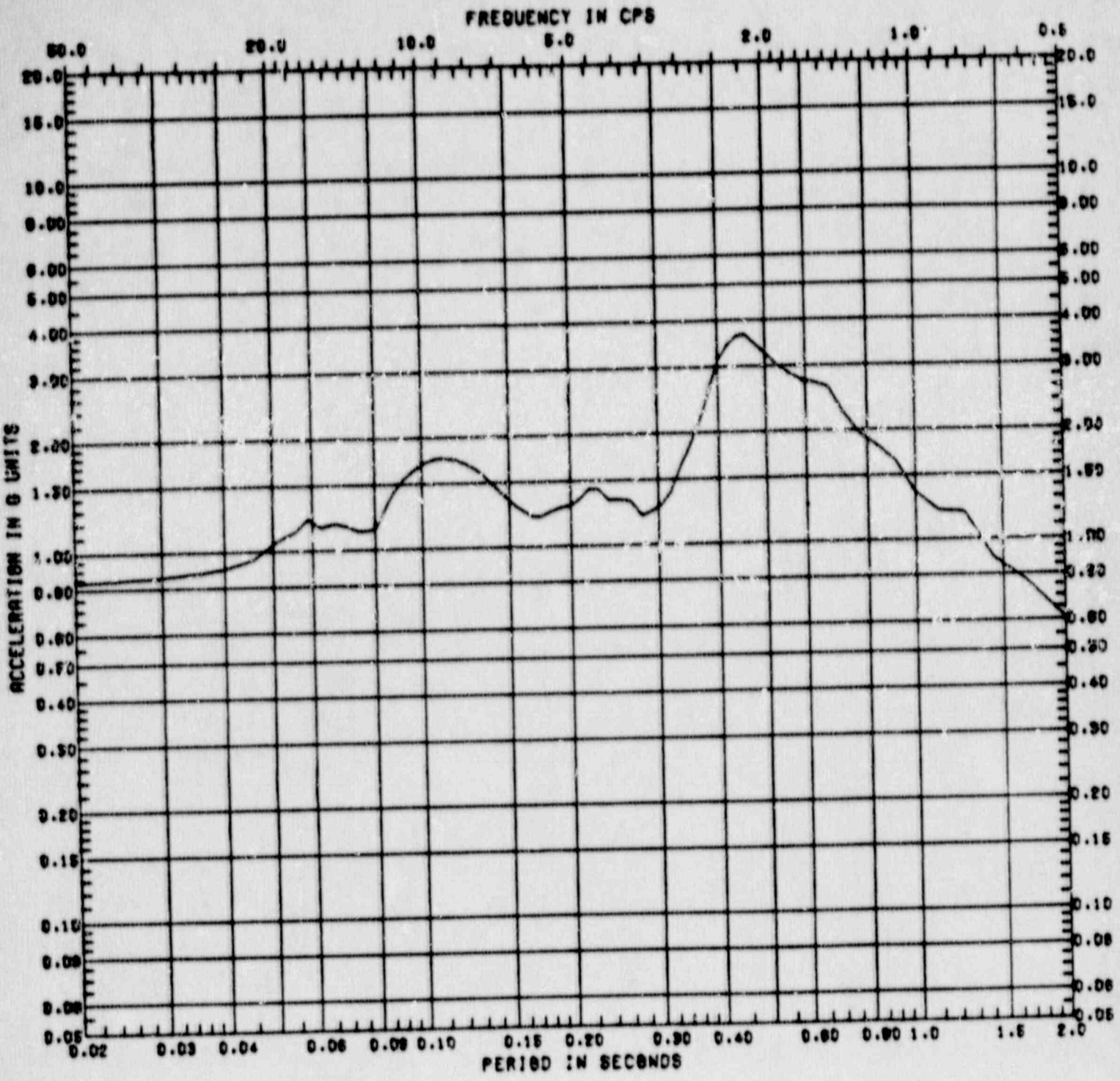

Figure C.2-29 Horizontal Response Spectrum at Clinton Model Node 13 (A_H = 0.75g, Damping = 5%, Location = Drywell Wall at Elevation 745')

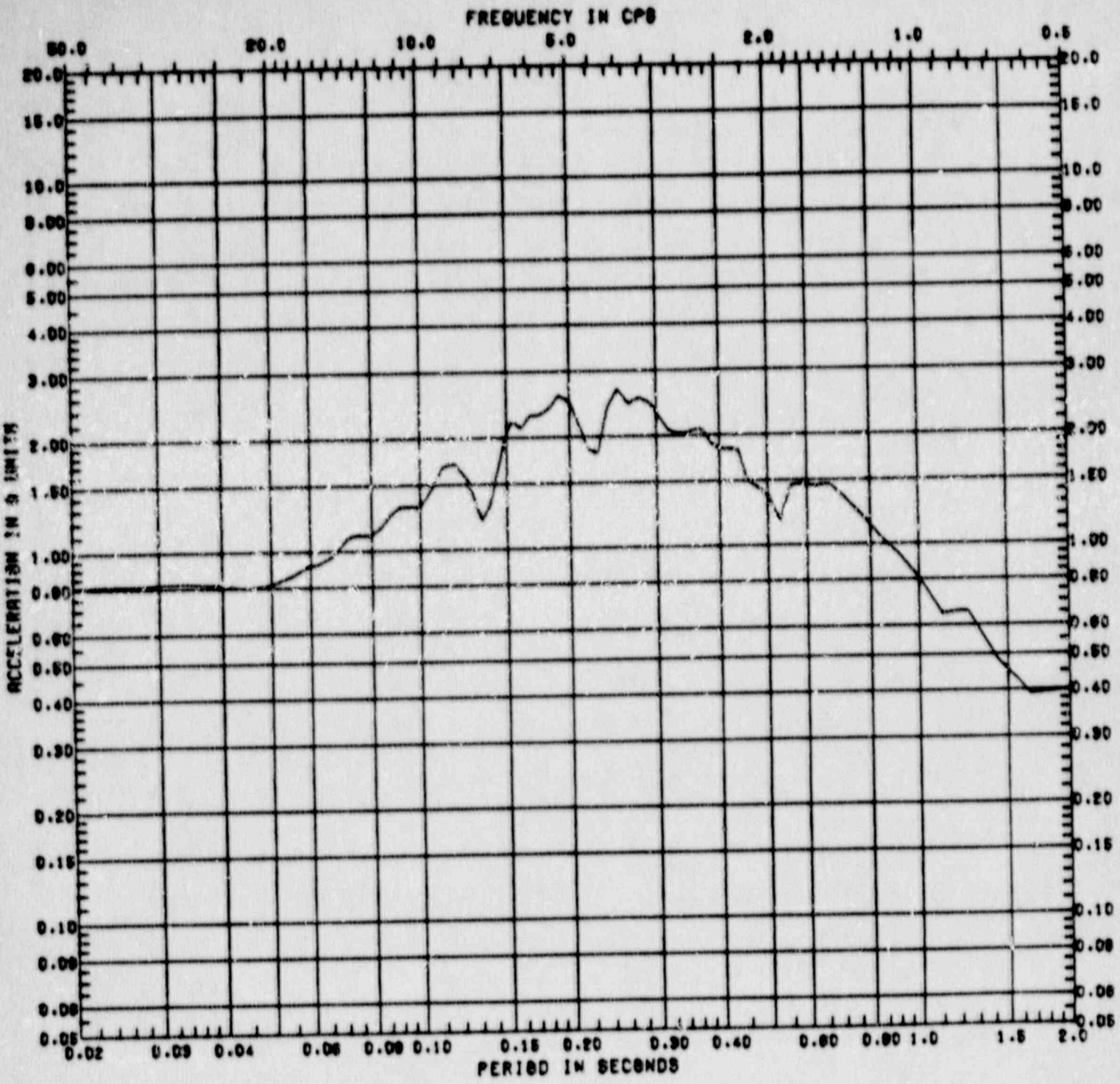

Figure C.2-30 Vertical Response Spectrum at Clinton Model Node 13 (A_H = 0.75g, Damping = 5%, Location = Drywell Wall at Elevation 745')

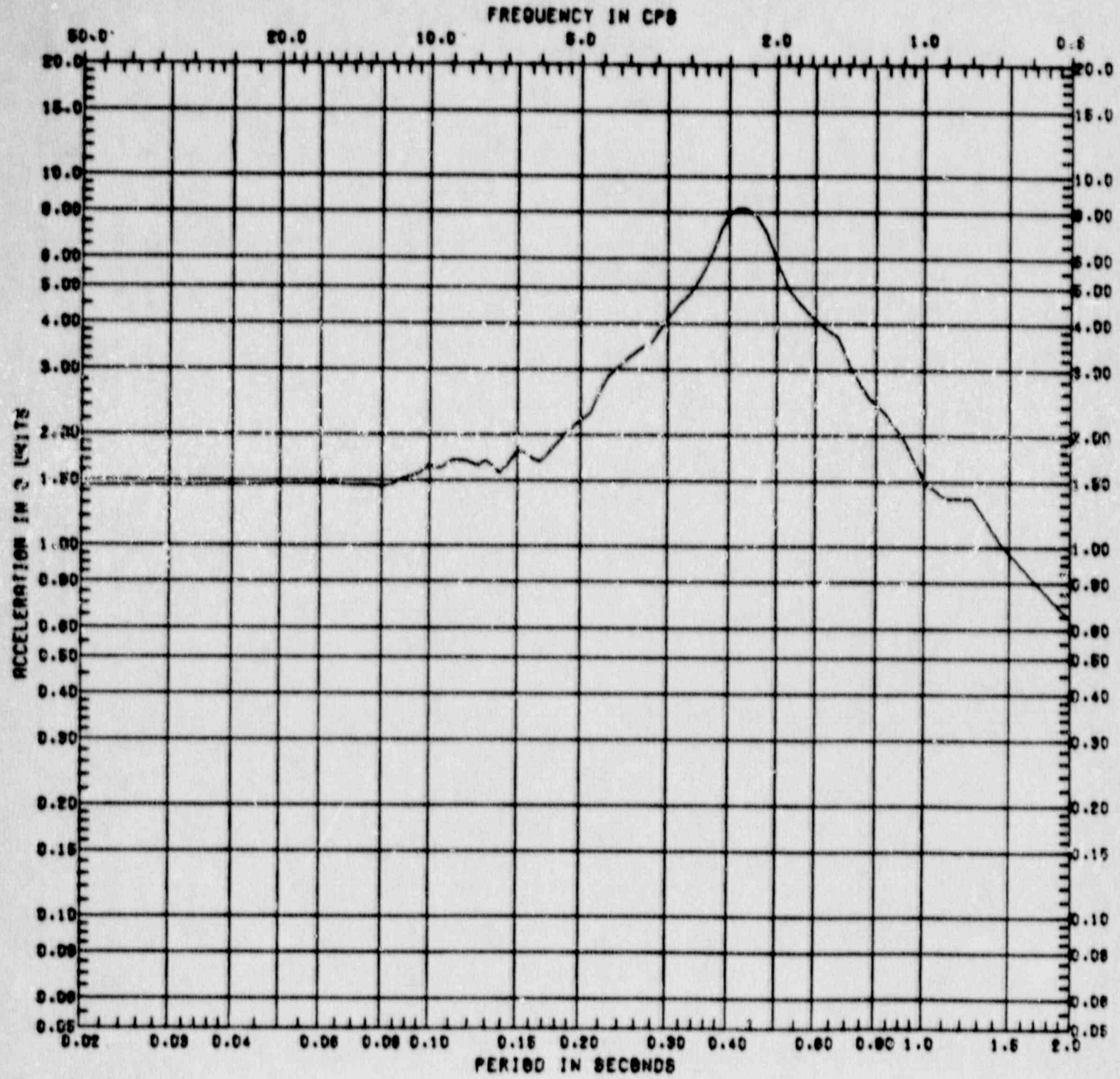

Figure C.2-31 Horizontal Response Spectrum at Clinton Model Node 8 (A_H = 0.75g, Damping = 5%, Location = Drywell Wall at Elevation 801')

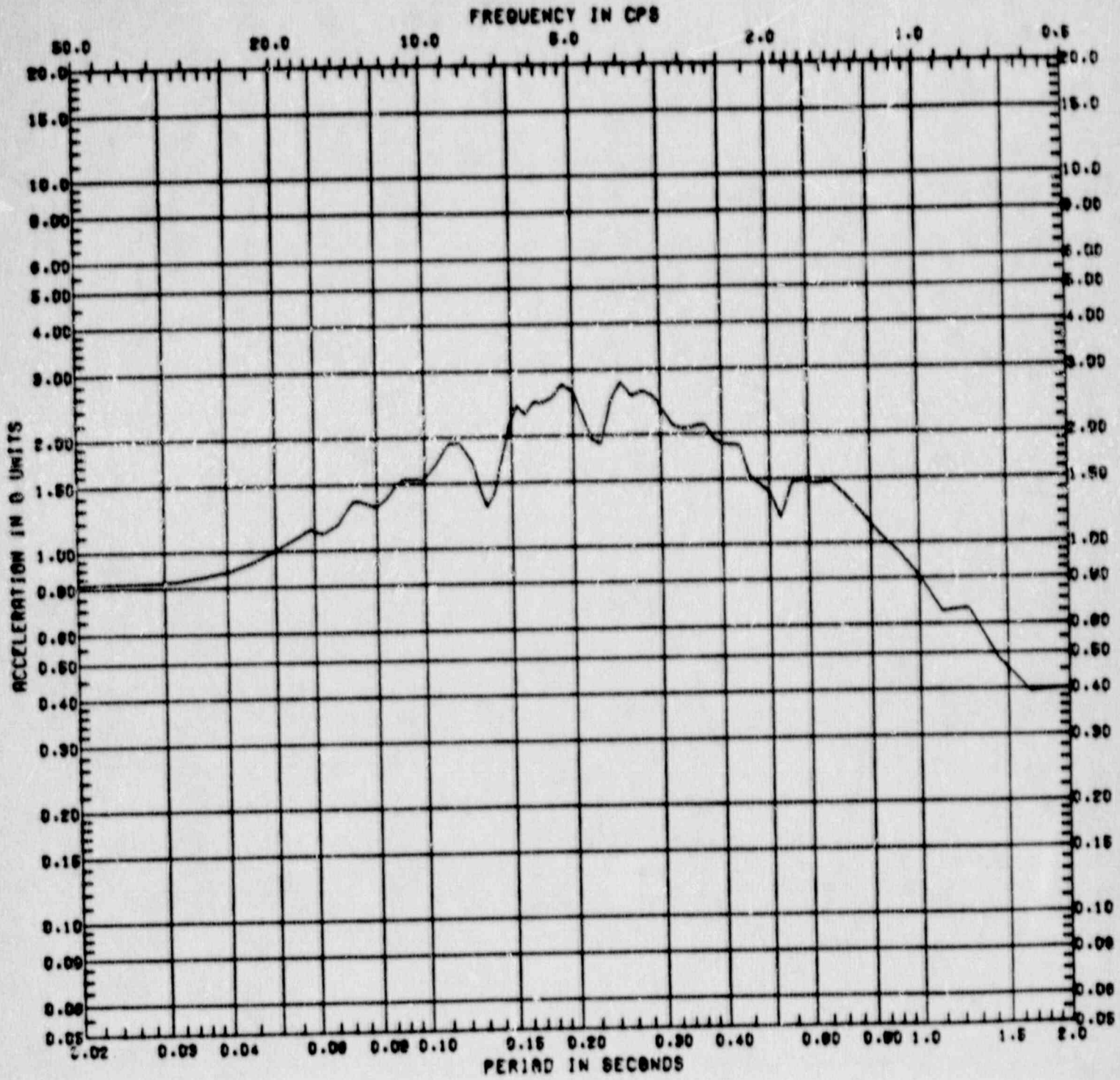

Figure C.2-32 Vertical Response Spectrum at Clinton Model Node 8 (A_H = 0.75g, Damping = 5%, Location = Drywell Wall at Elevation 801')

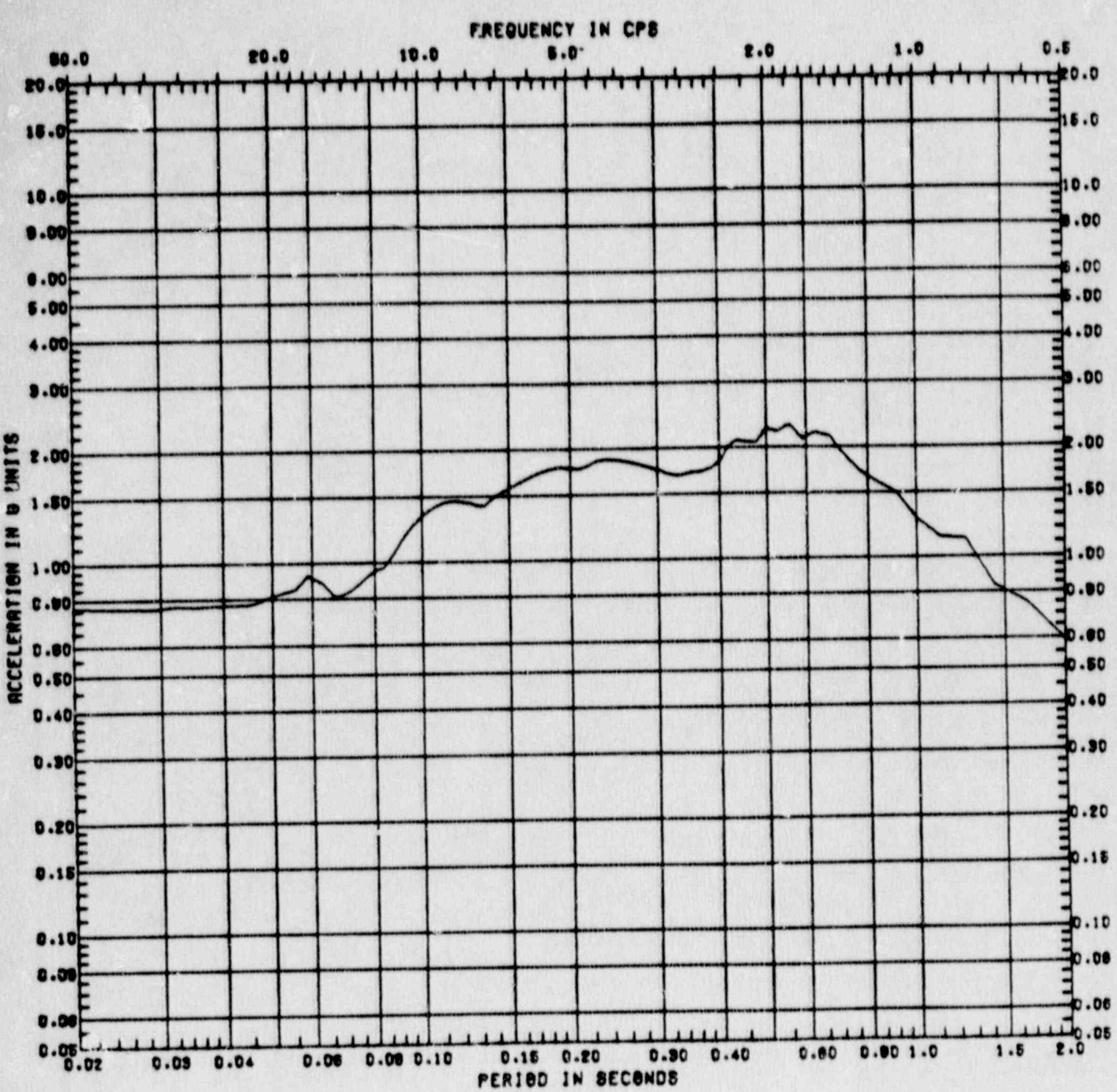

Figure C.2-33 Horizontal Response Spectrum at Clinton Model Node 46 (A_H = 0.75g, Damping = 5%, Location = Reactor-Control Building at Basemat, Elevation 712')

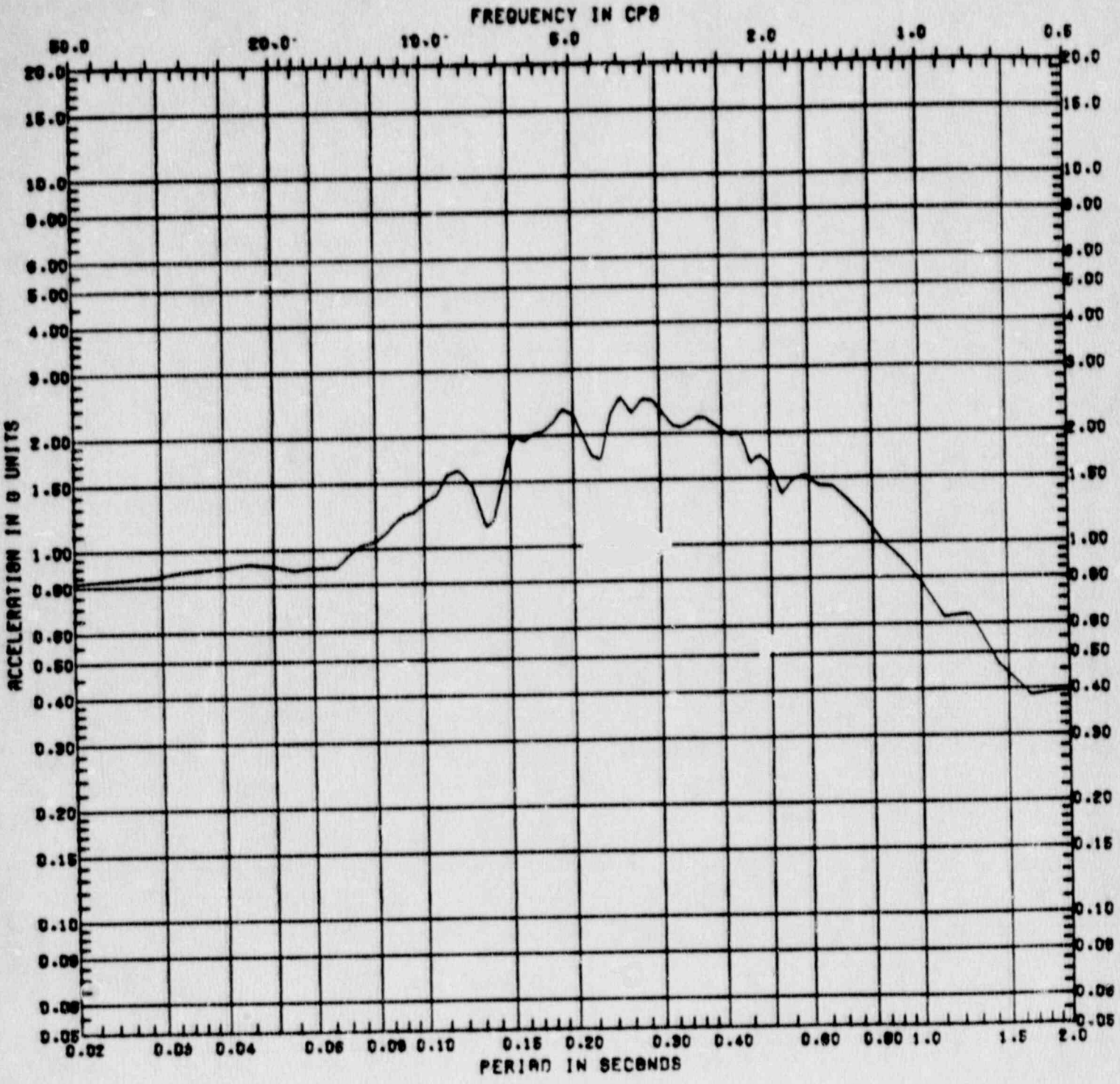

Figure C.2-34 Vertical Response Spectrum at Clinton Model Node 46 (A_H = 0.75g, Damping = 5%, Location = Reactor-Control Building at Basemat, Elevation 712')

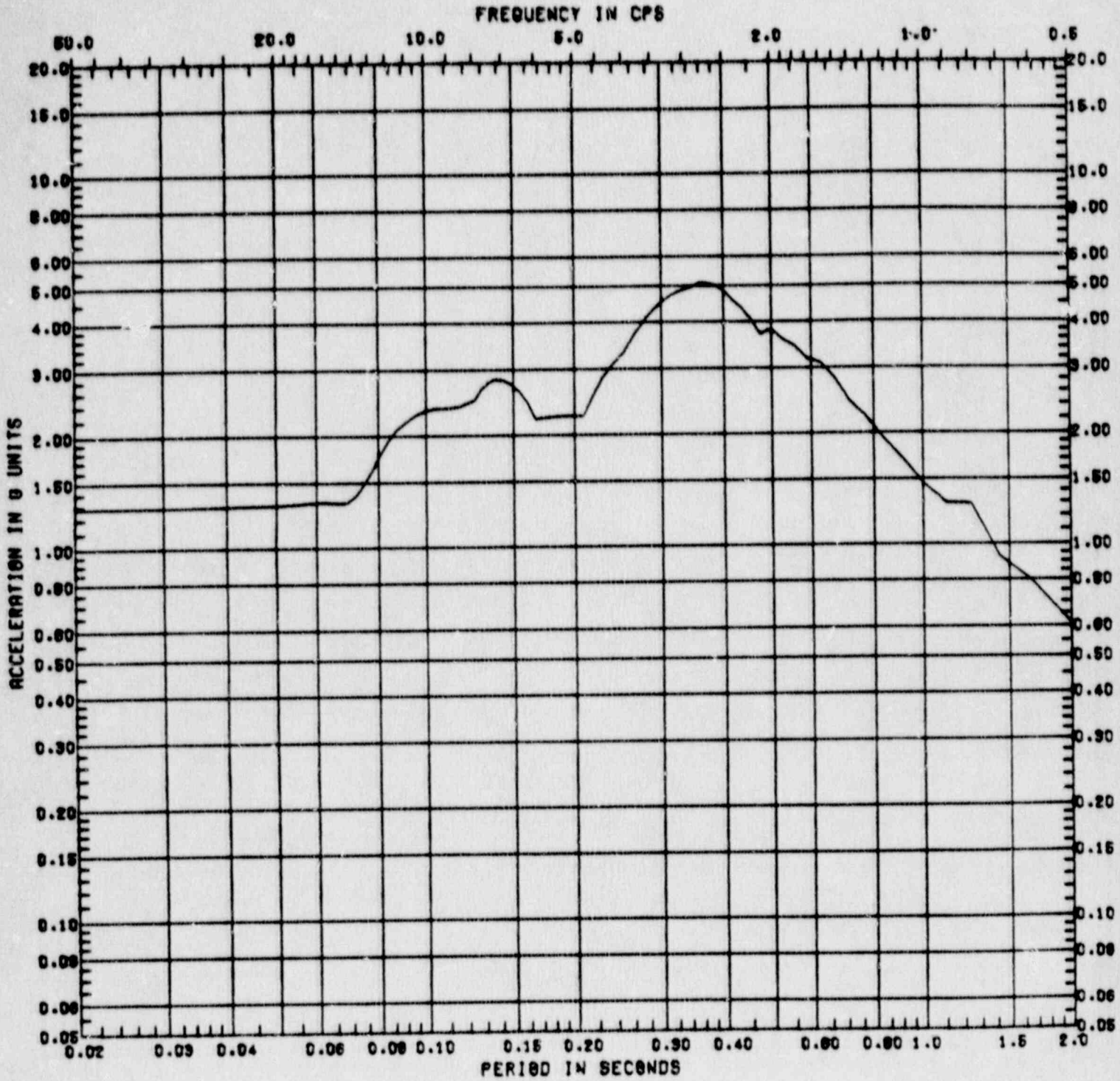

Figure C.2-35 Horizontal Response Spectrum at Clinton Model Node 17 (A_H = 0.75g, Damping = 5%, Location = Reactor-Control building at Elevation 801')

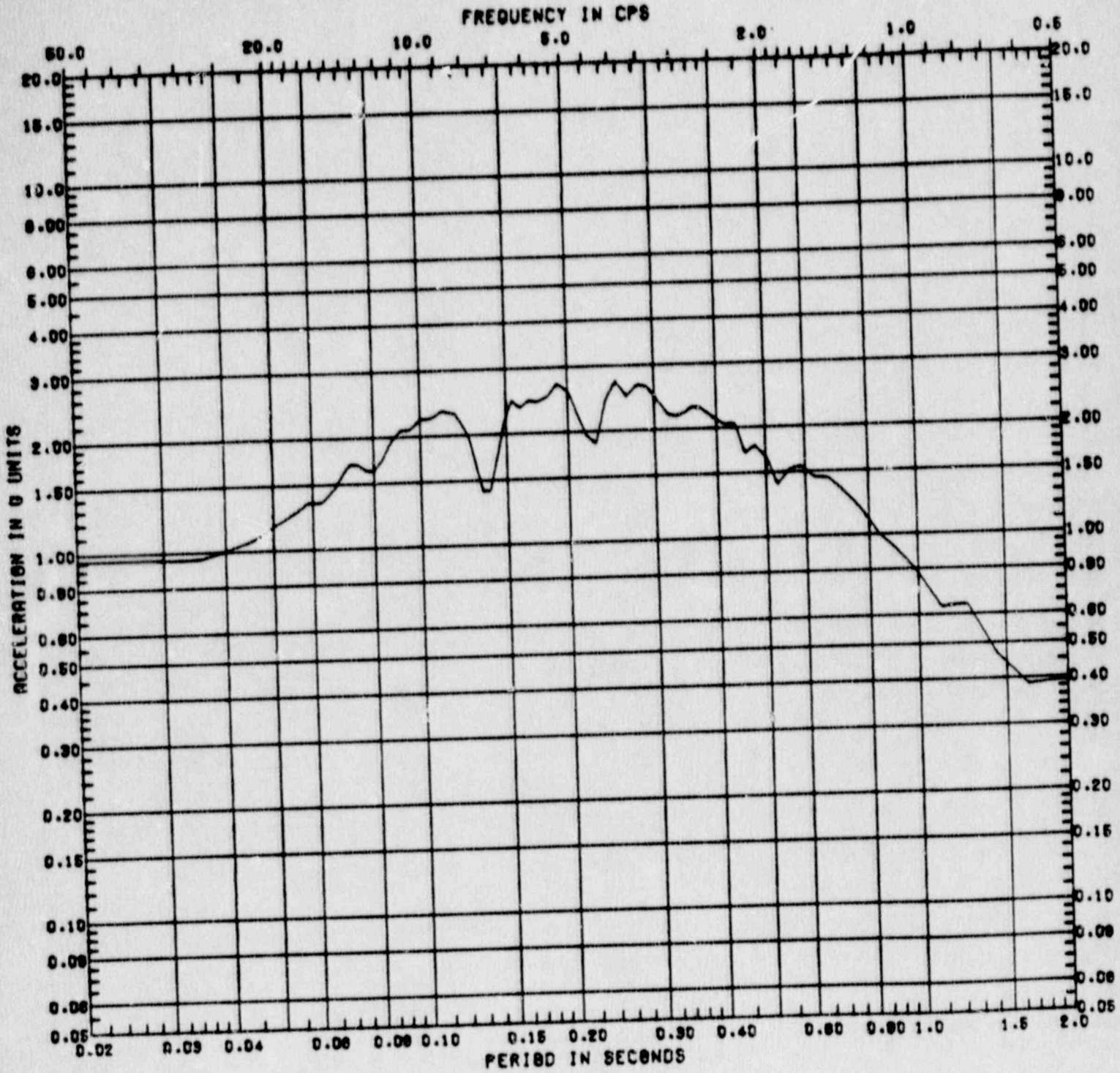

Figure C.2-36 Vertical Response Spectrum at Clinton Model Node 17 (A_H = 0.75g, Damping = 5%, Location = Reactor-Control Building at Elevation 801')

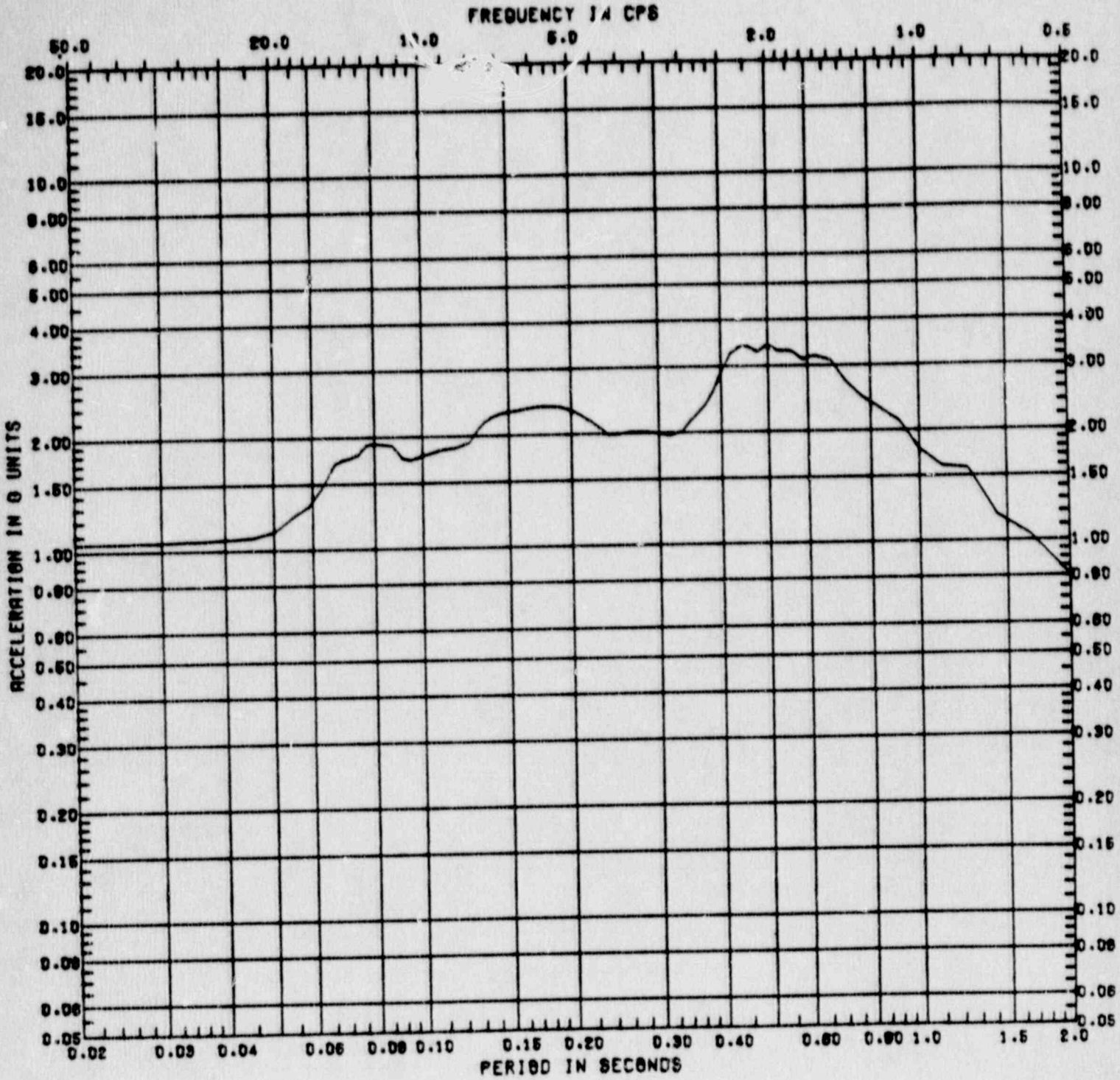

Figure C.2-37 Horizontal Response Spectrum at Clinton Model Node 15 (A_H = 1.0g, Damping = 5%, Location = Containment Wall at Elevation 745')

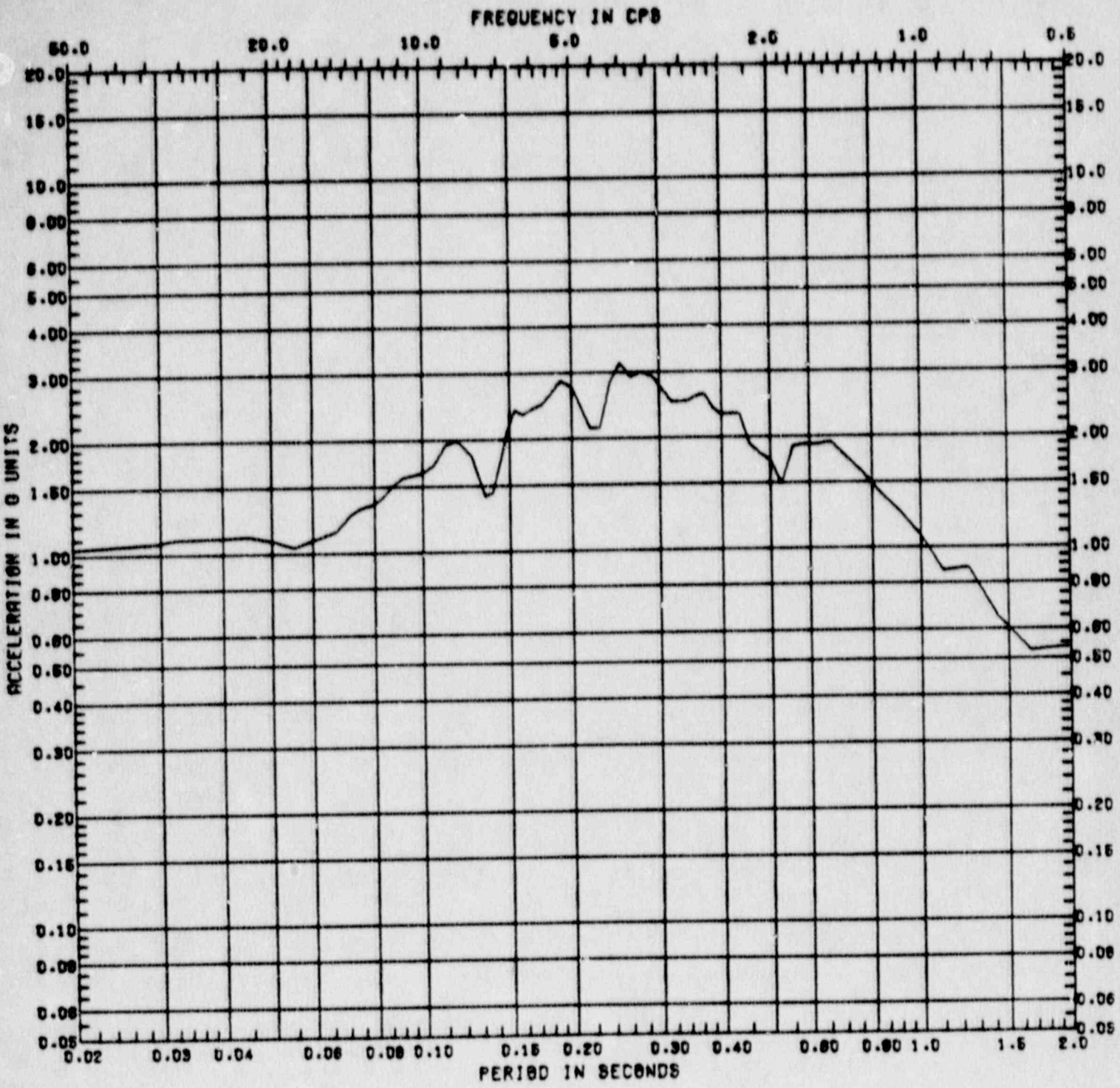

Figure C.2-38 Vertical Response Spectrum at Clinton Model Node 15 (A_H = 1.0g, Damping = 5%, Location = Containment Wall at Elevation 745')

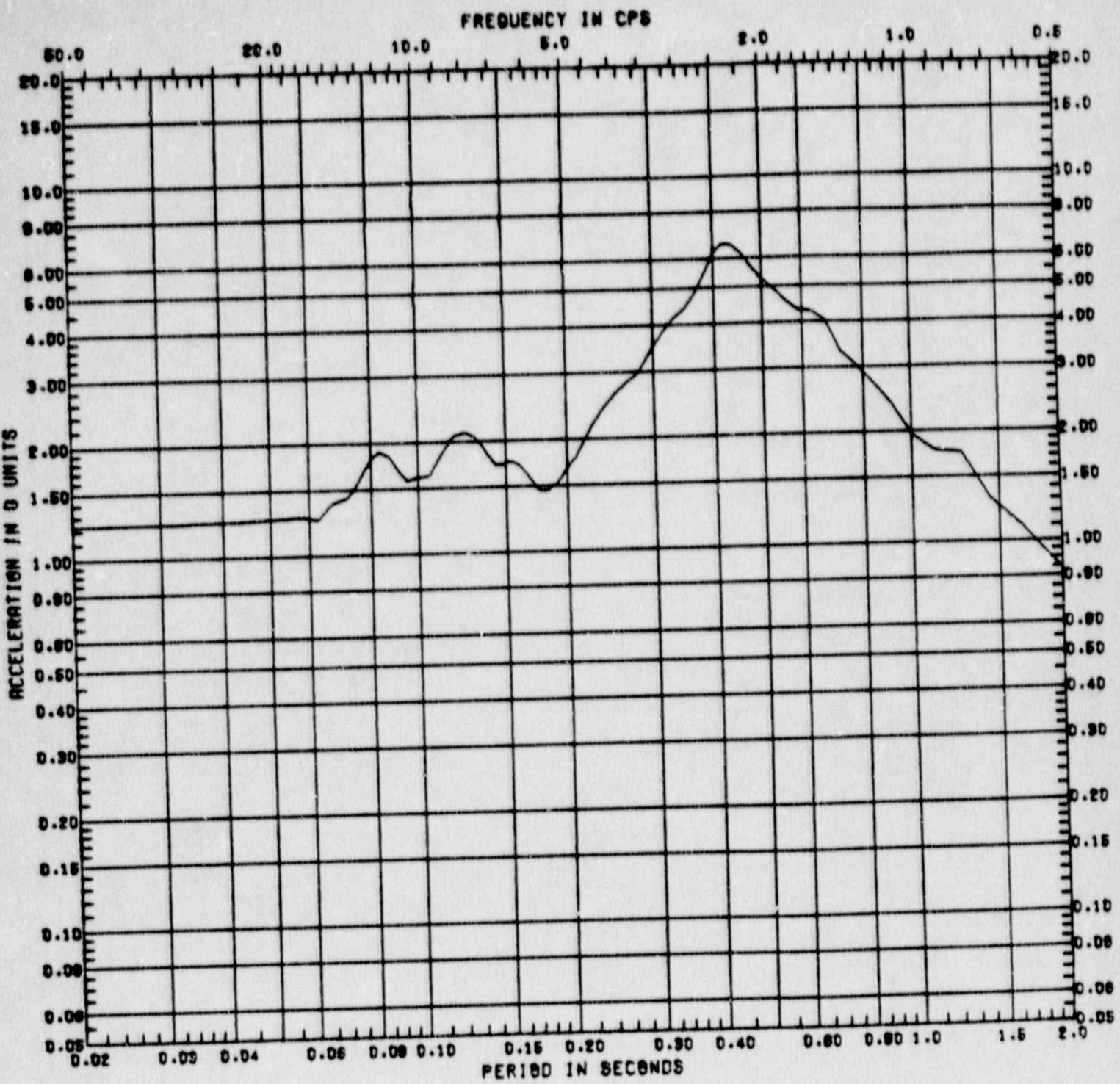

Figure C.2-39 Horizontal Response Spectrum at Clinton Model Node 4 (A_H = 1.0g, Damping = 5%, Location = Containment Wall at Elevation 832')

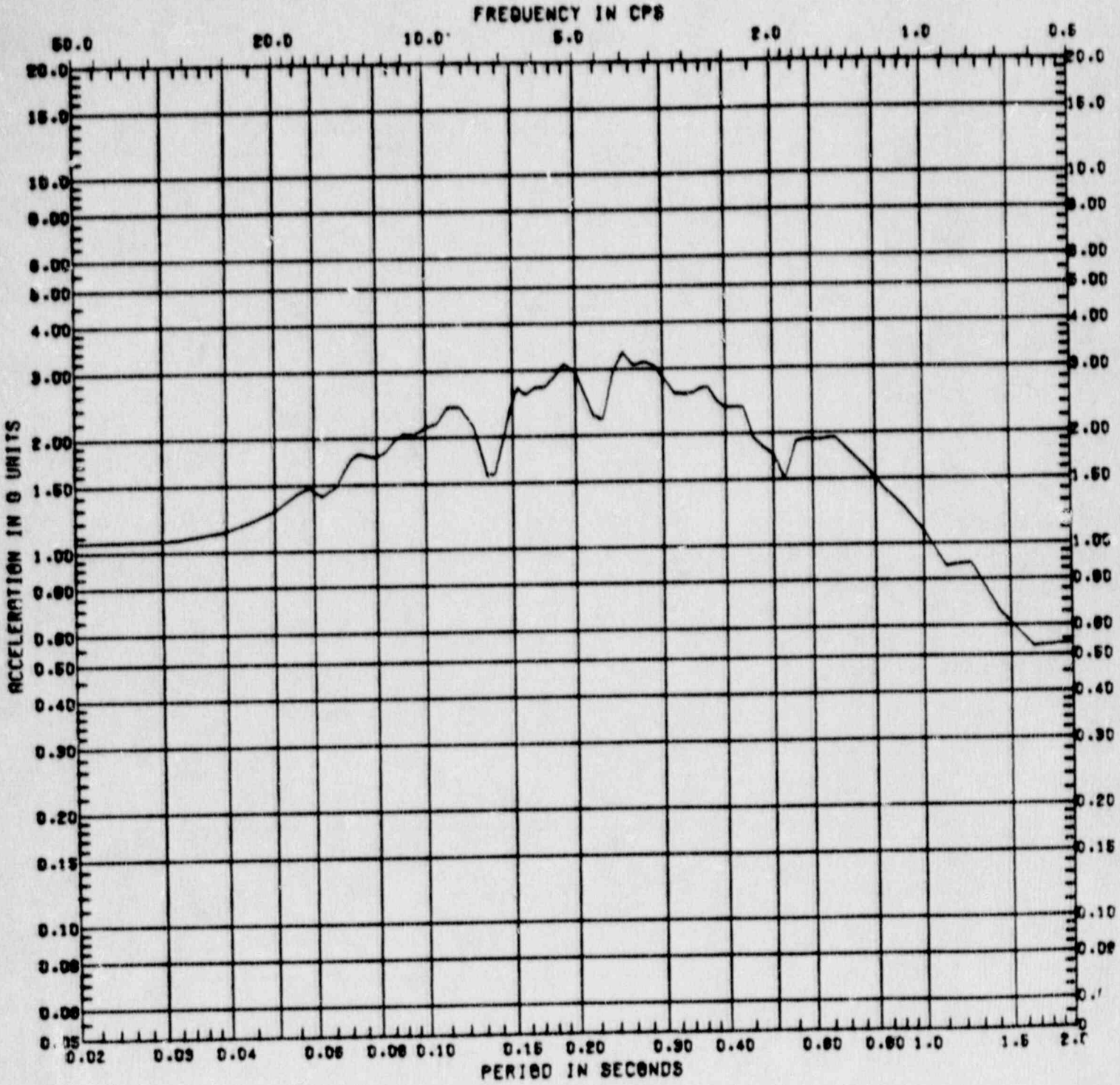

Figure C.2-40 Vertical Response Spectrum at Clinton Model Node 4 (A_H = 1.0g, Damping = 5%, Location = Containment Wall at Elevation 832')

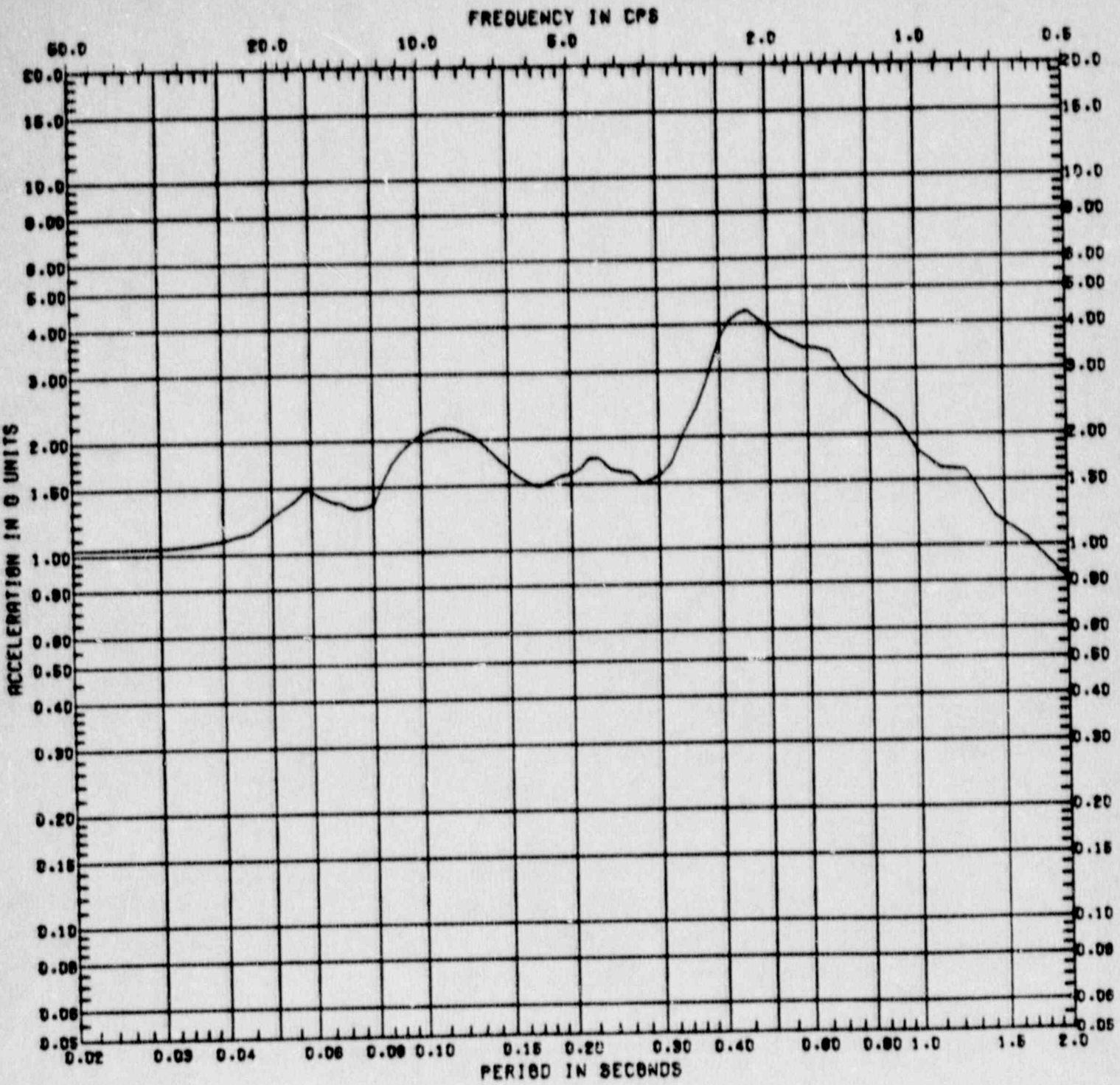

Figure C.2-41 Horizontal Response Spectrum at Clinton Model Node 13 (A_H = 1.0g, Damping = 5%, Location = Drywell Wall at Elevation 745')

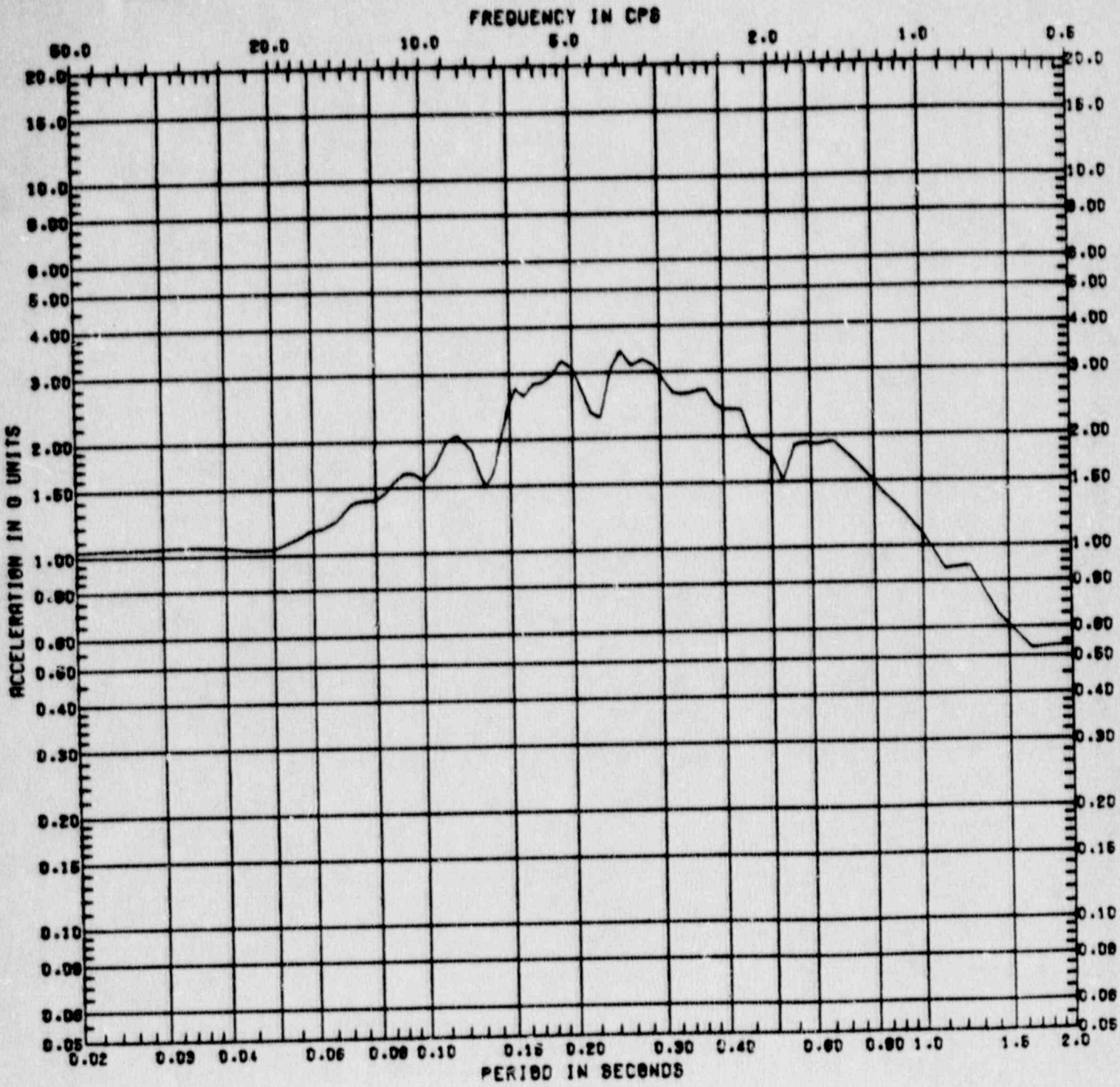

Figure C.2-42 Vertical Response Spectrum at Clinton Model Node 13 (A_H = 1.0g, Damping = 5%, Location = Drywell Wall at Elevation 745')

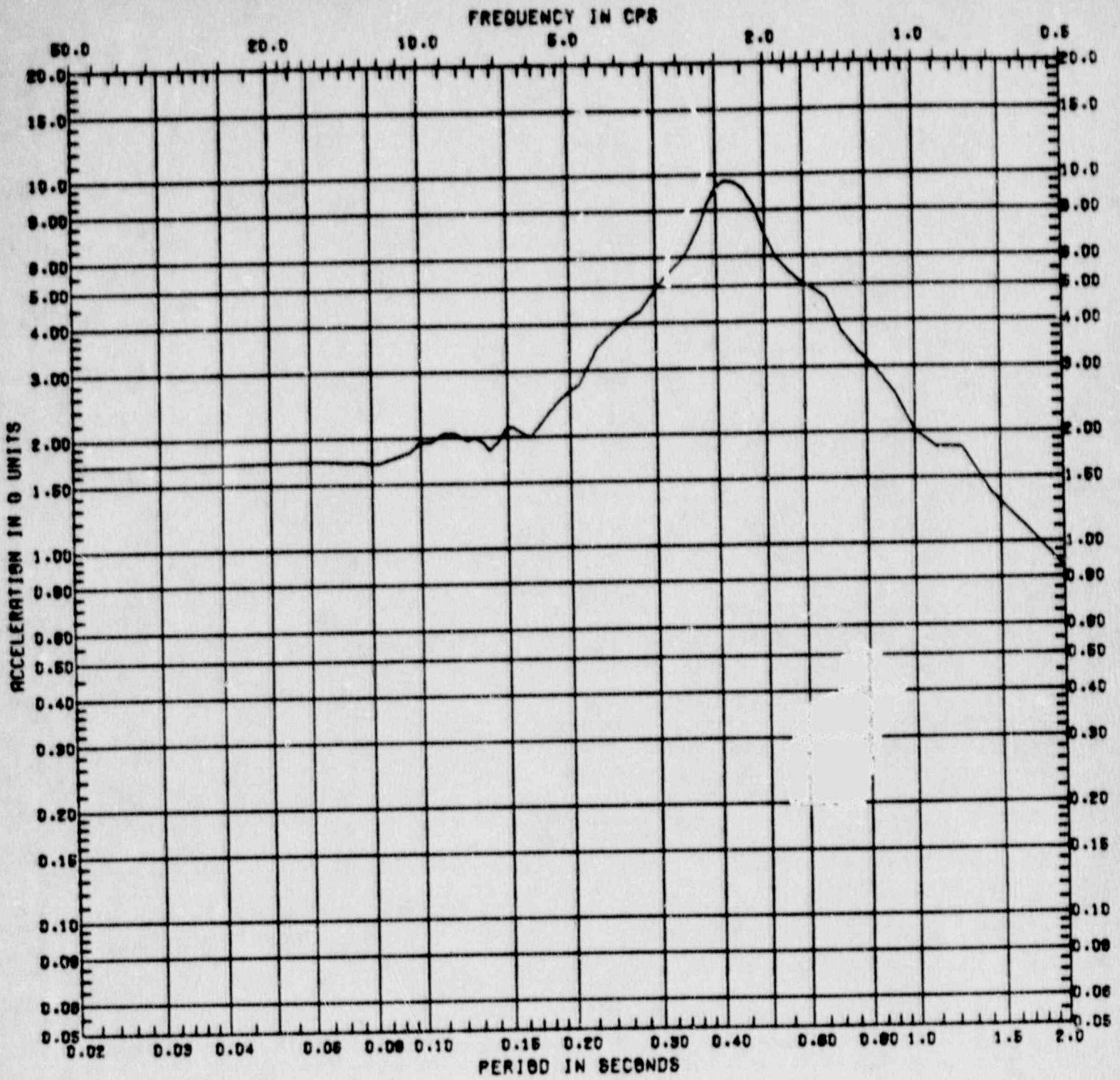

Figure C.2-43 Horizontal Response Spectrum at Clinton Model Node 8 (A_H = 1.0g, Damping = 5%, Location = Drywell Wall at Elevation 801')

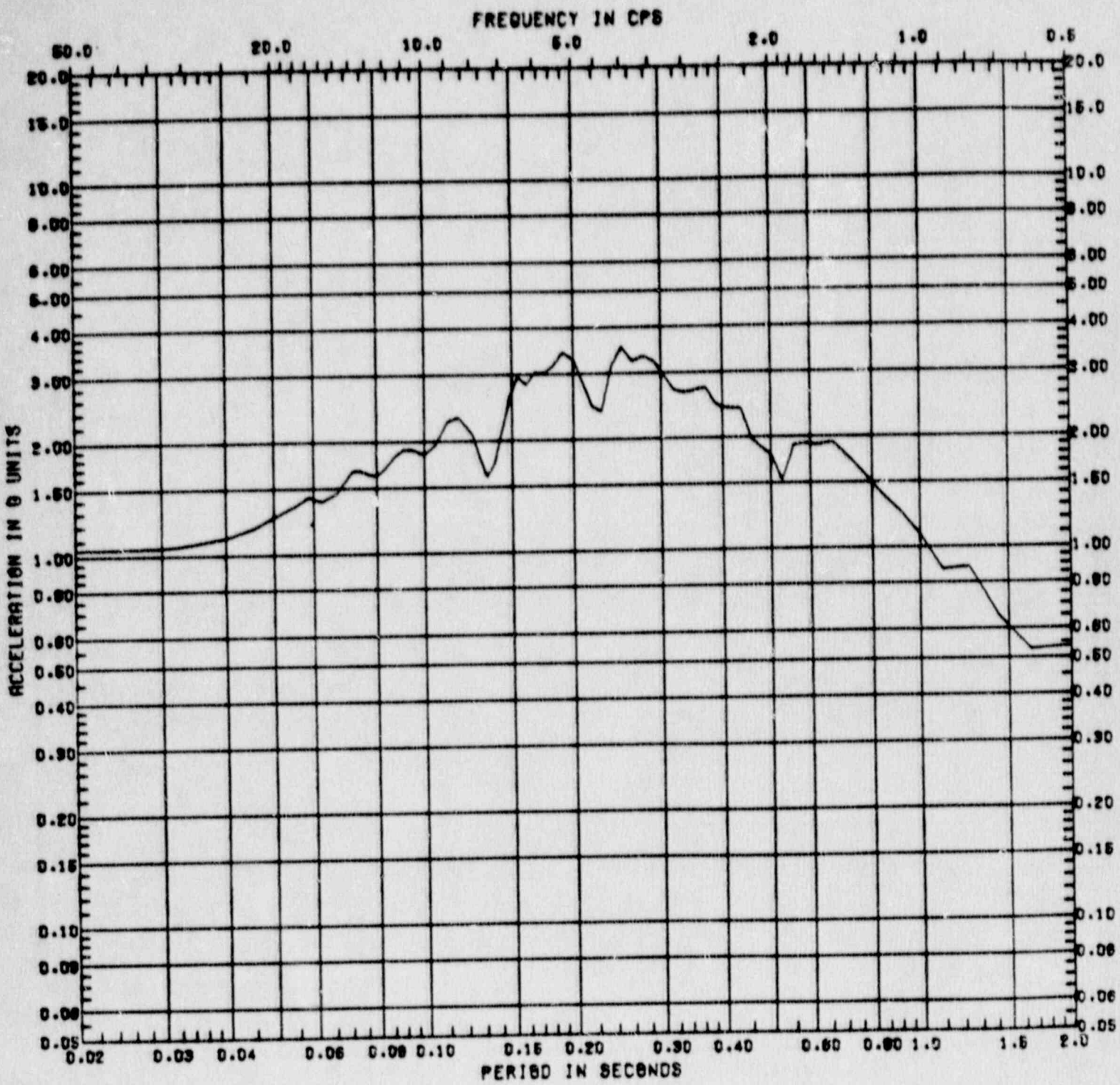

Figure C.2-44 Vertical Response Spectrum at Clinton Model Node 8 (A_H = 1.0g, Damping = 5%, Location = Drywell Wall at Elevation 801')

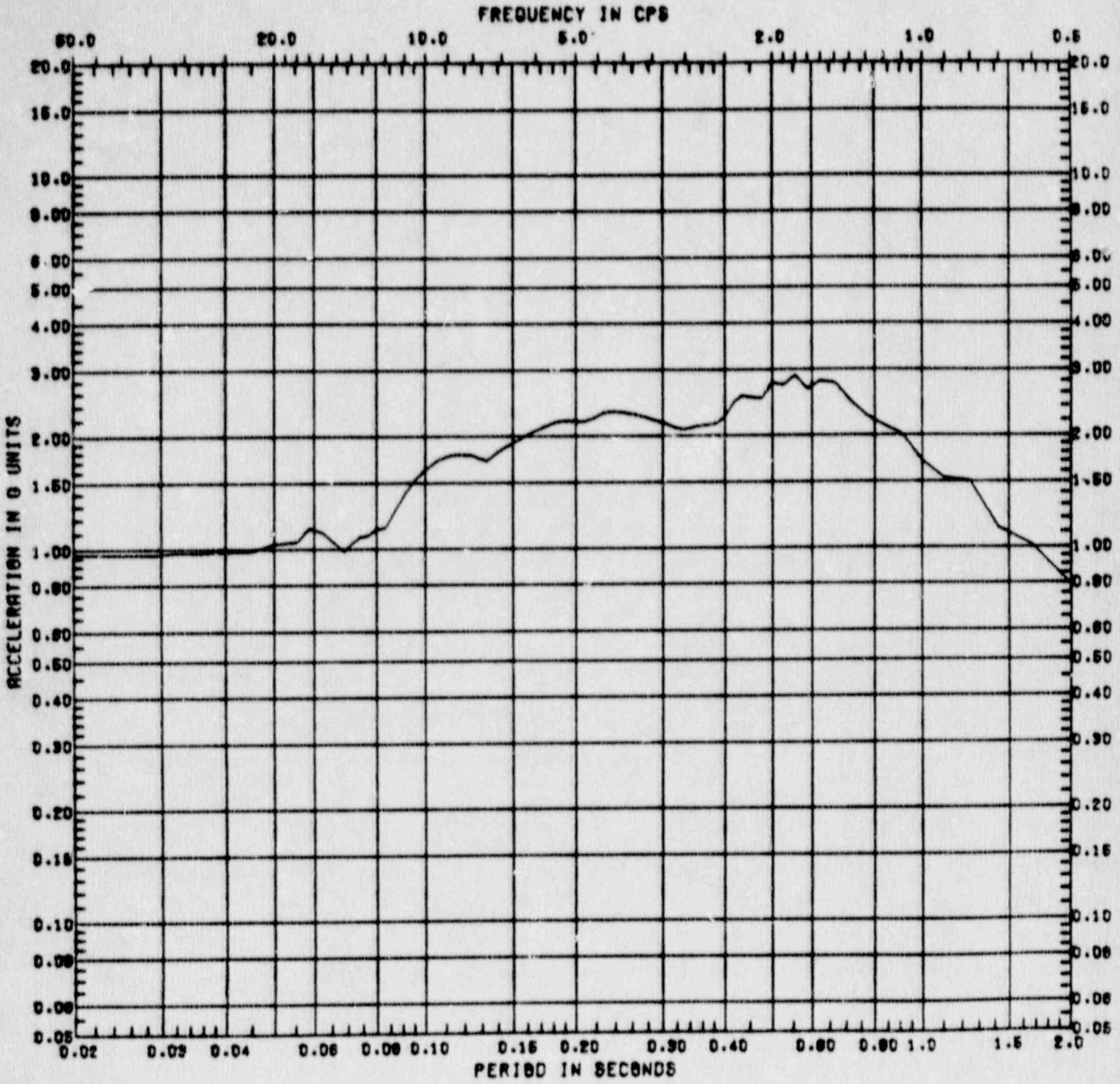

Figure C.2-45 Horizontal Response Spectrum at Clinton Model Node 46 (A_H = 1.0g, Damping = 5%, Location = Reactor-Control Building at Basemat, Elevation 712')

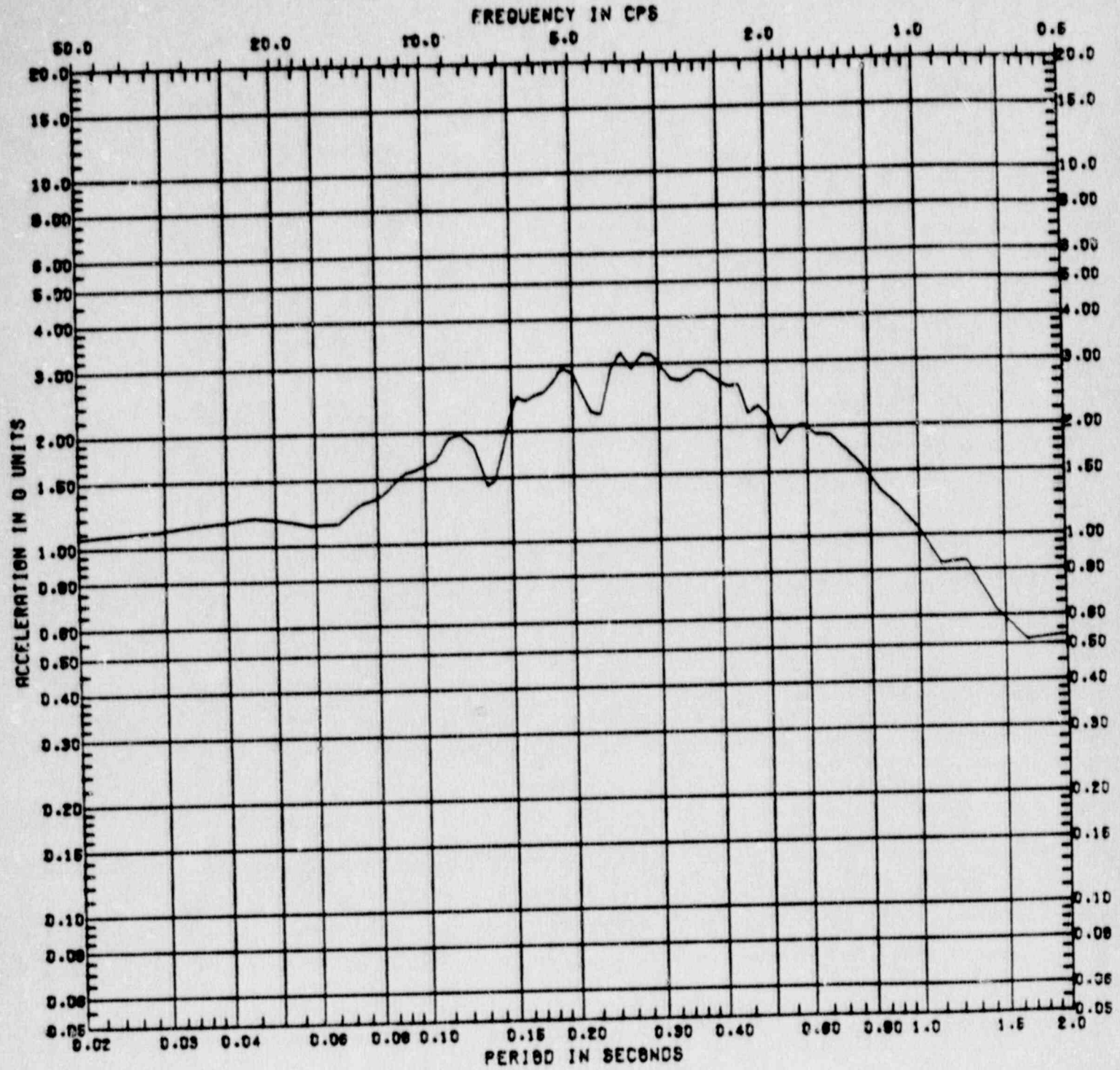

Figure C.2-46 Vertical Response Spectrum at Clinton Model Node 46 (A_H = 1.0g, Damping = 5%, Location = Reactor-Control Building at Basemat, Elevation 712')

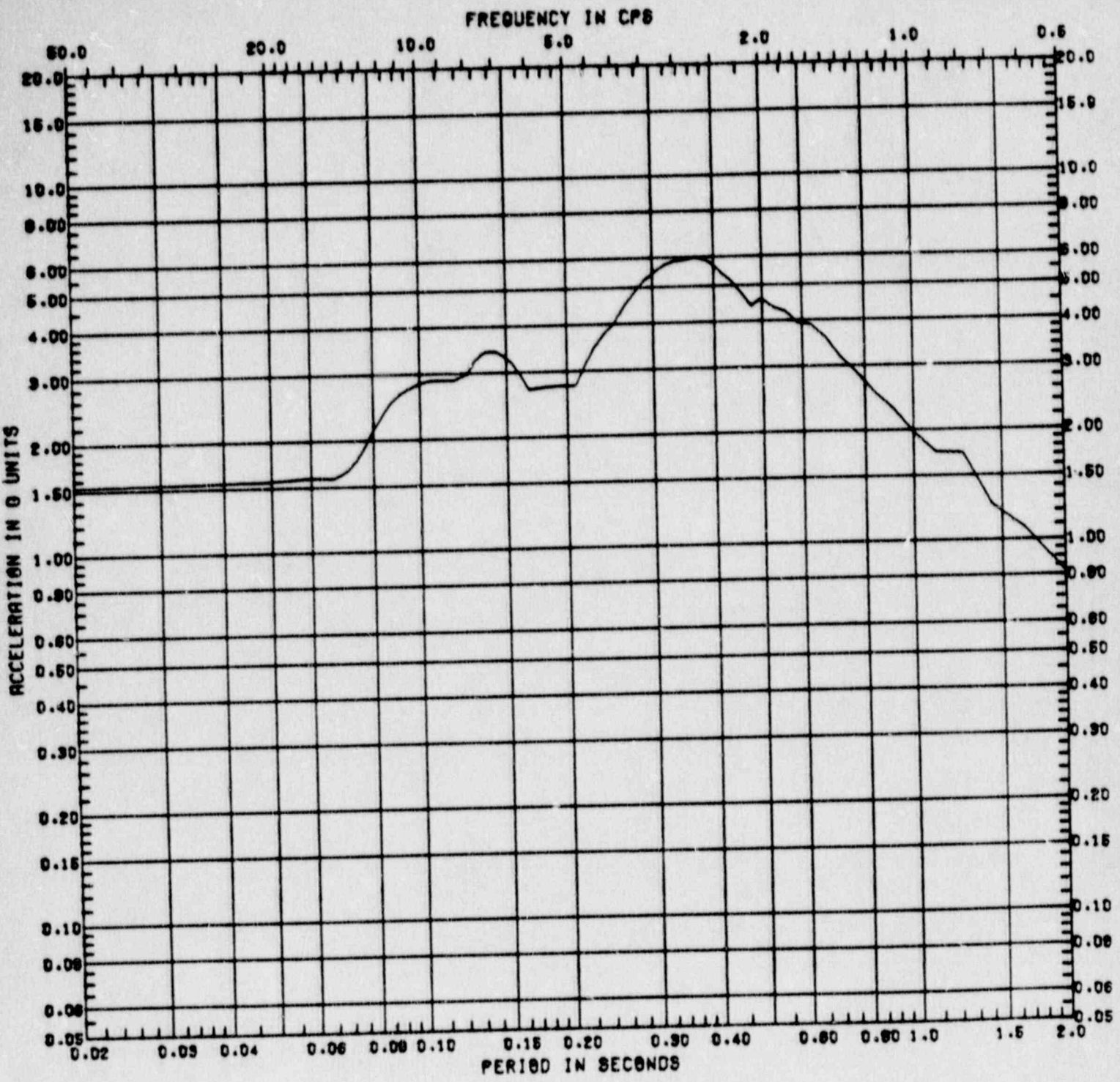

Figure C.2-47 Horizontal Response Spectrum at Clinton Model Node 17 (A_H = 1.0g, Damping = 5%, Location = Reactor-Control building at Elevation 801')

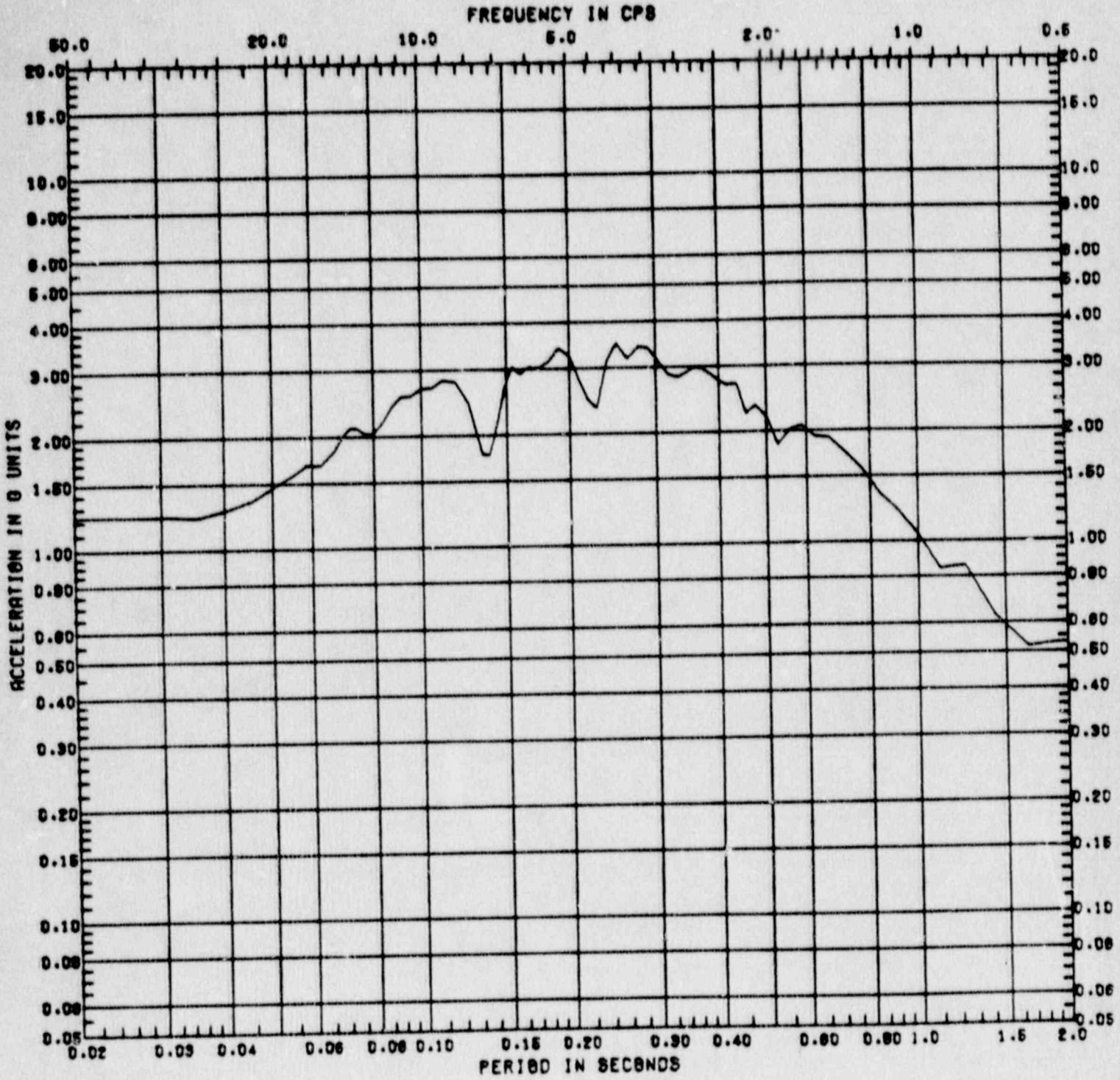

Figure C.2-48 Vertical Response Spectrum at Clinton Model Node 17 (A_H = 1.0g, Damping = 5%, Location = Reactor-Control Building at Elevation 801')

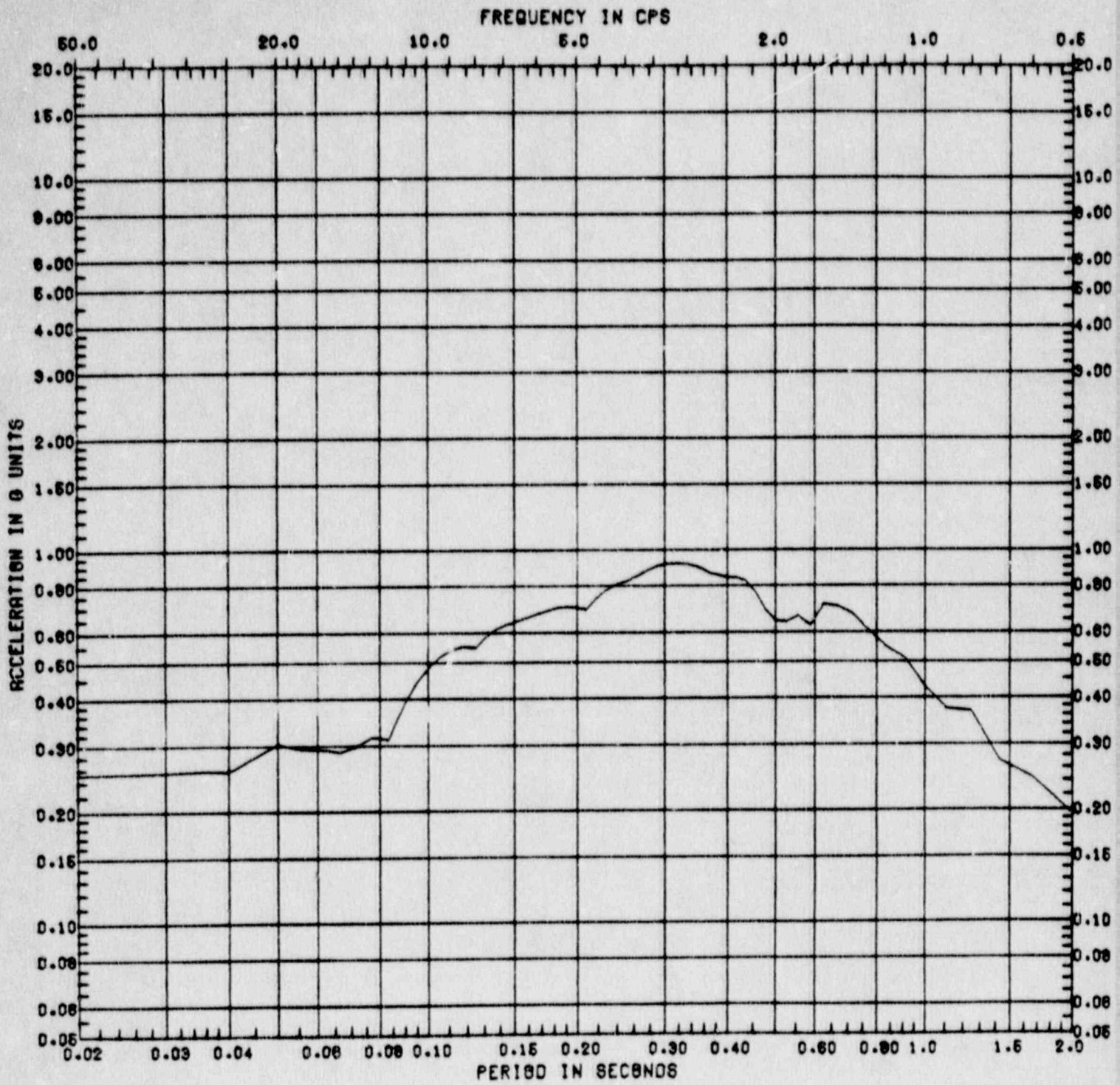

Figure C.3-1 Horizontal Response Spectrum at Zion Model Node 15 (A_H = 0.25g, Damping = 5%, Location = Containment Basemat, Elevation 568')

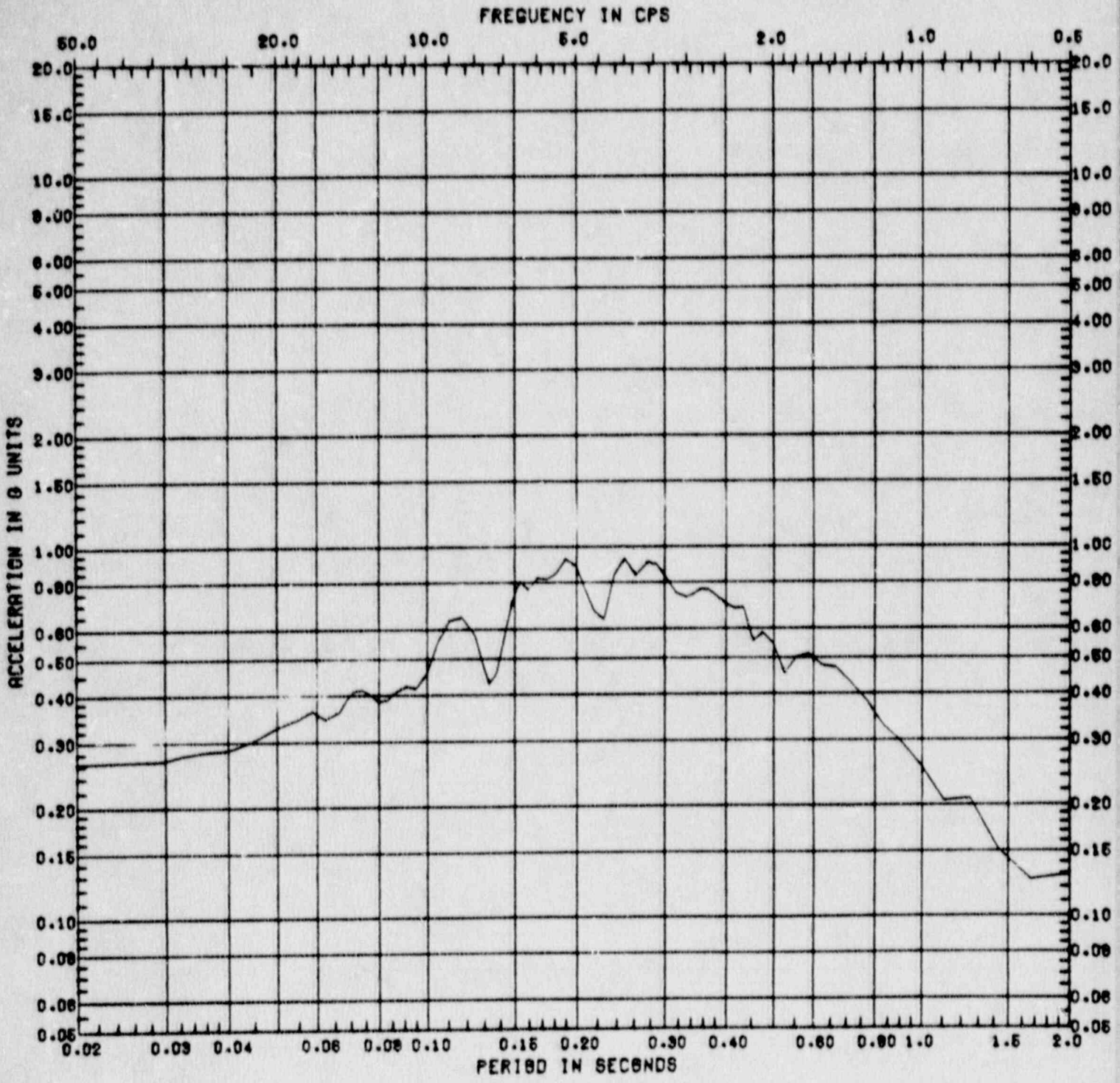

Figure C.3-2 Vertical Response Spectrum at Zion Model Node 15 (A_H = 0.25g, Damping = 5%, Location = Containment Basemat, Elevation 568')

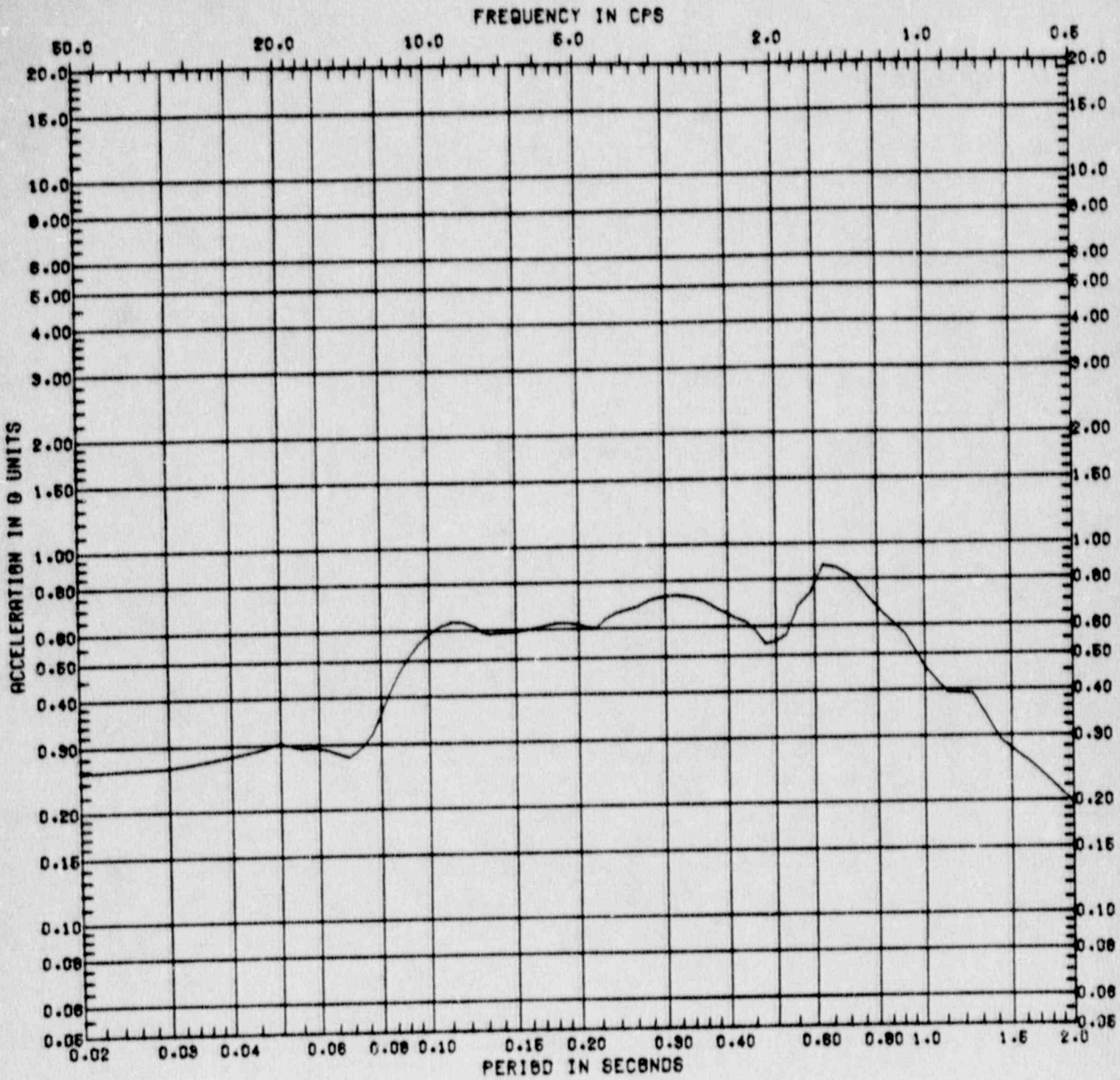

Figure C.3-3 Horizontal Response Spectrum at Zion Model Node 9 (A_H = 0.25g, Damping = 5%, Location = Containment Wall at Elevation 592')

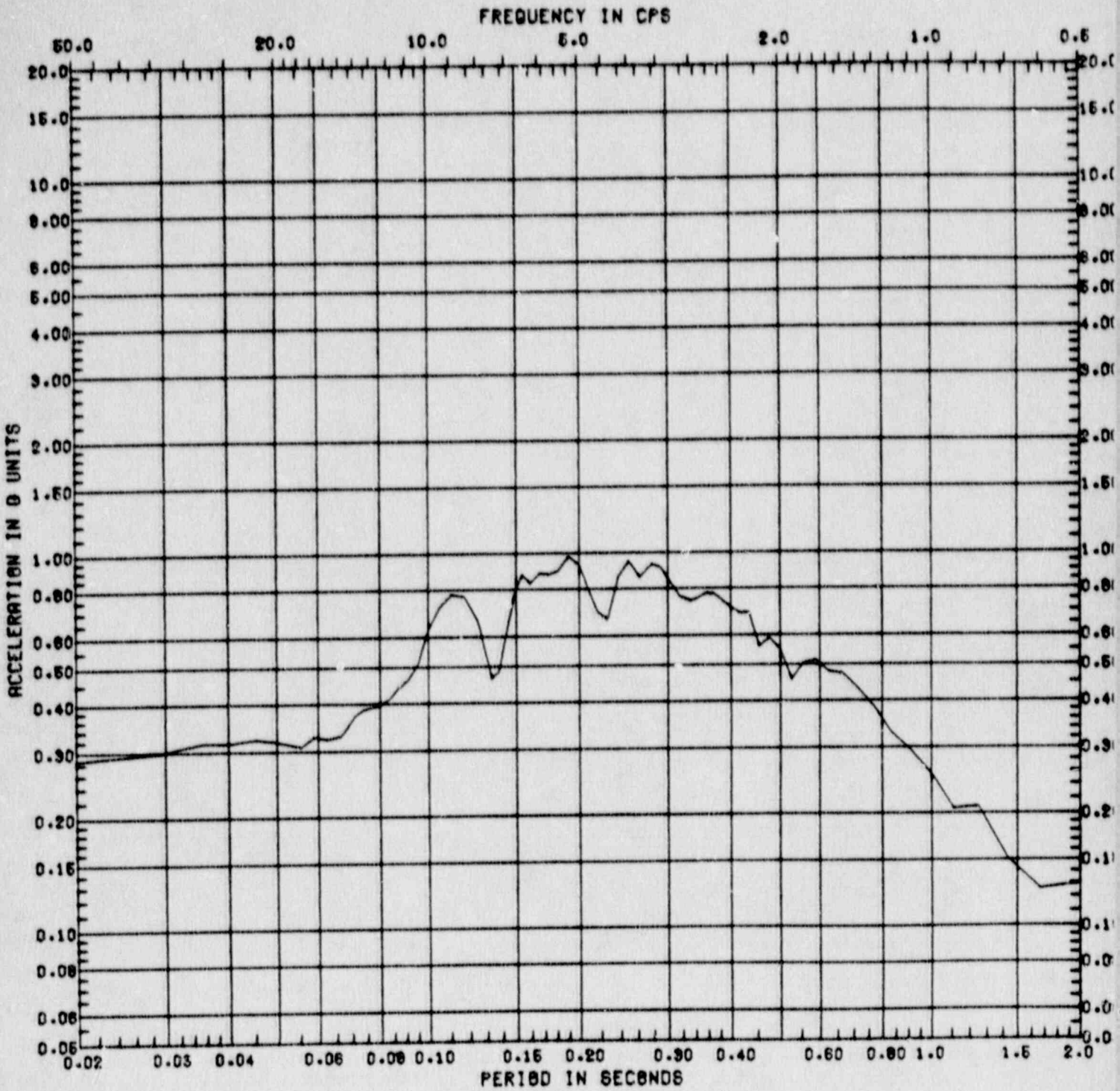

Figure C.3-4 Vertical Response Spectrum at Zion Model Node 9 (A_H = 0.25g, Damping = 5%, Location = Containment Wall at Elevation 592')

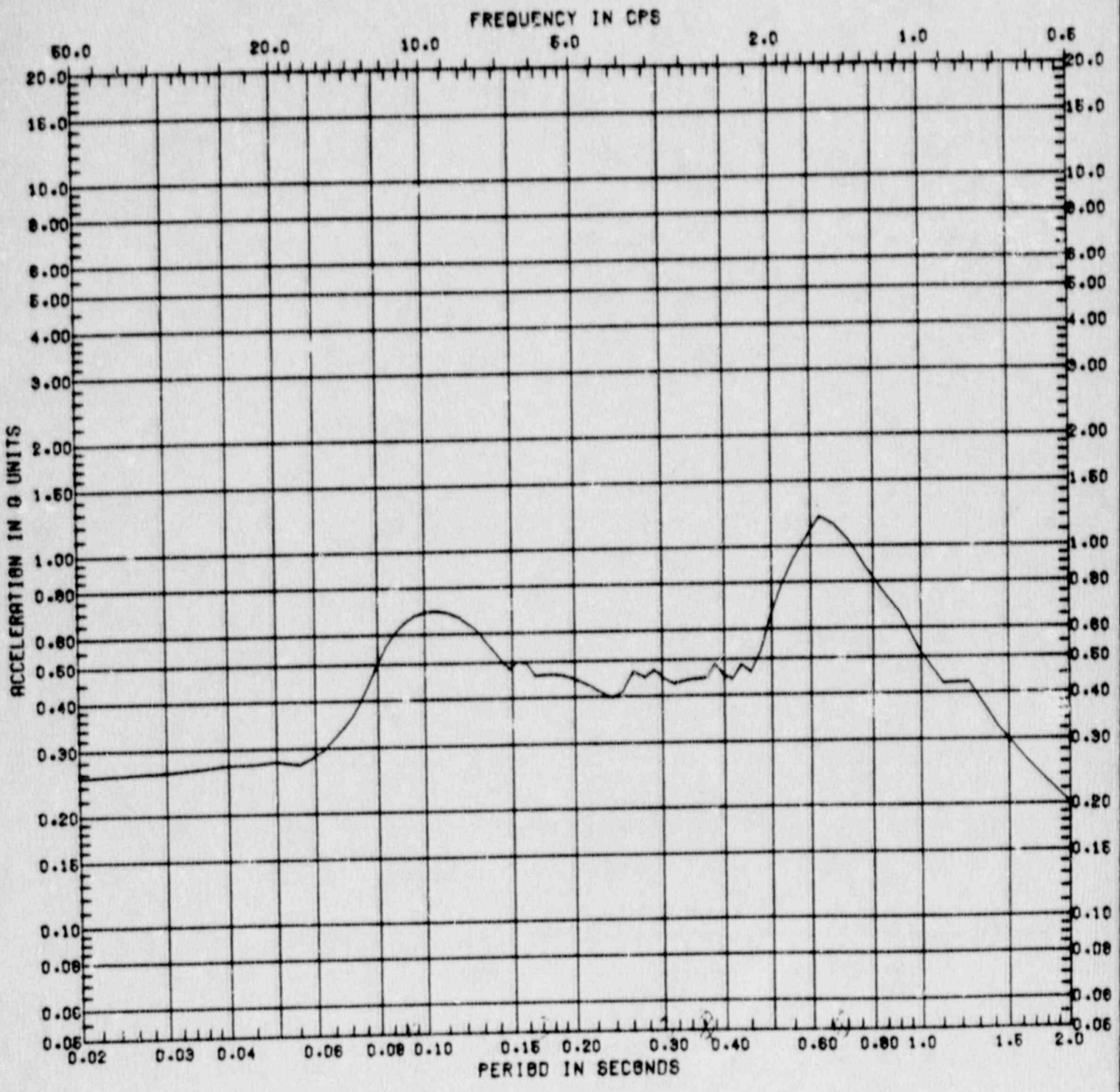

Figure C.3-5 Horizontal Response Spectrum at Zion Model Node 7 (A_H = 0.25g, Damping = 5%, Location = Containment Wall at Elevation 628')

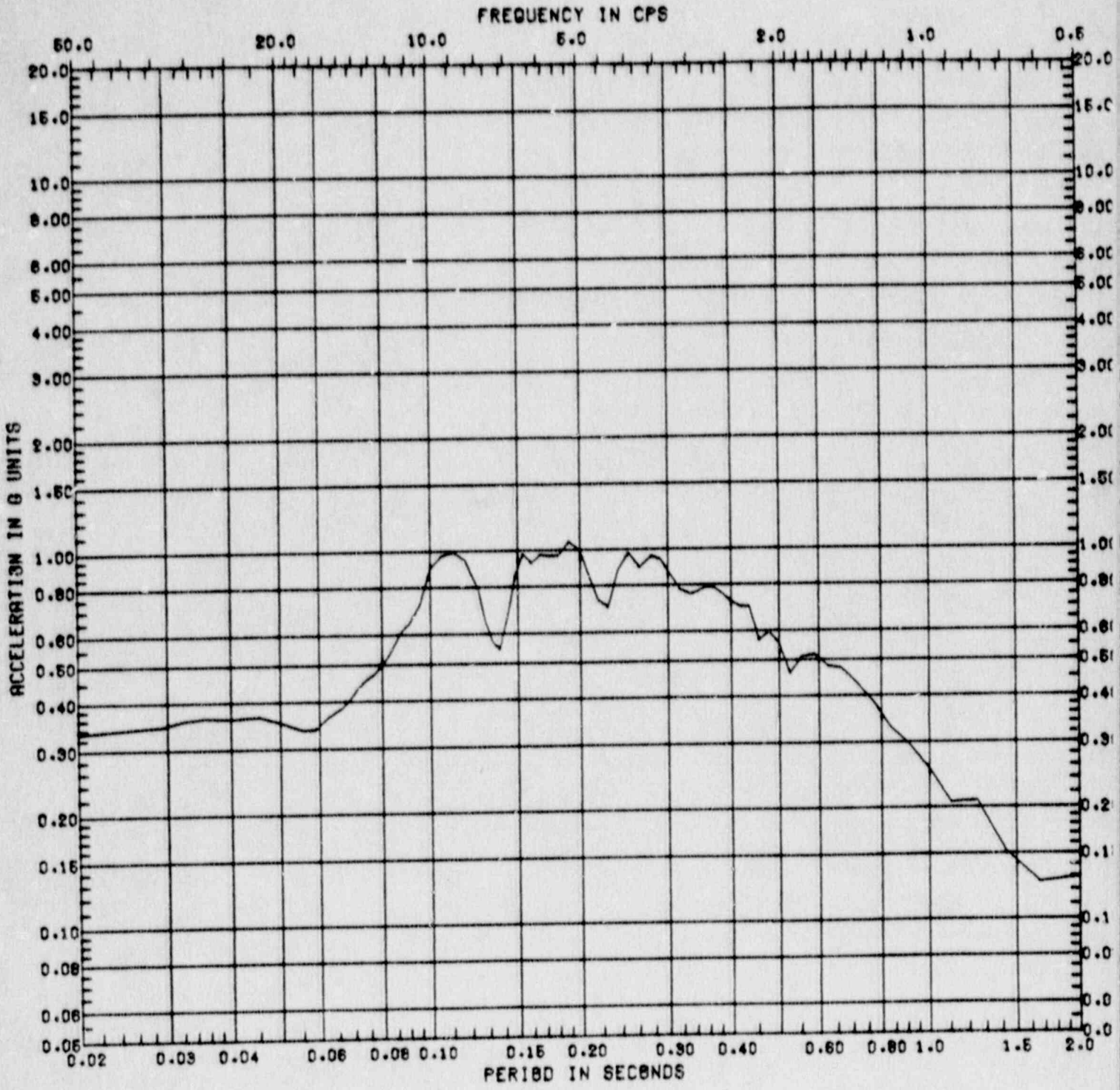

Figure C.3-6 Vertical Response Spectrum at Zion Model Node 7 (A_H = 0.25g, Damping = 5%, Location = Containment Wall at Elevation 628')

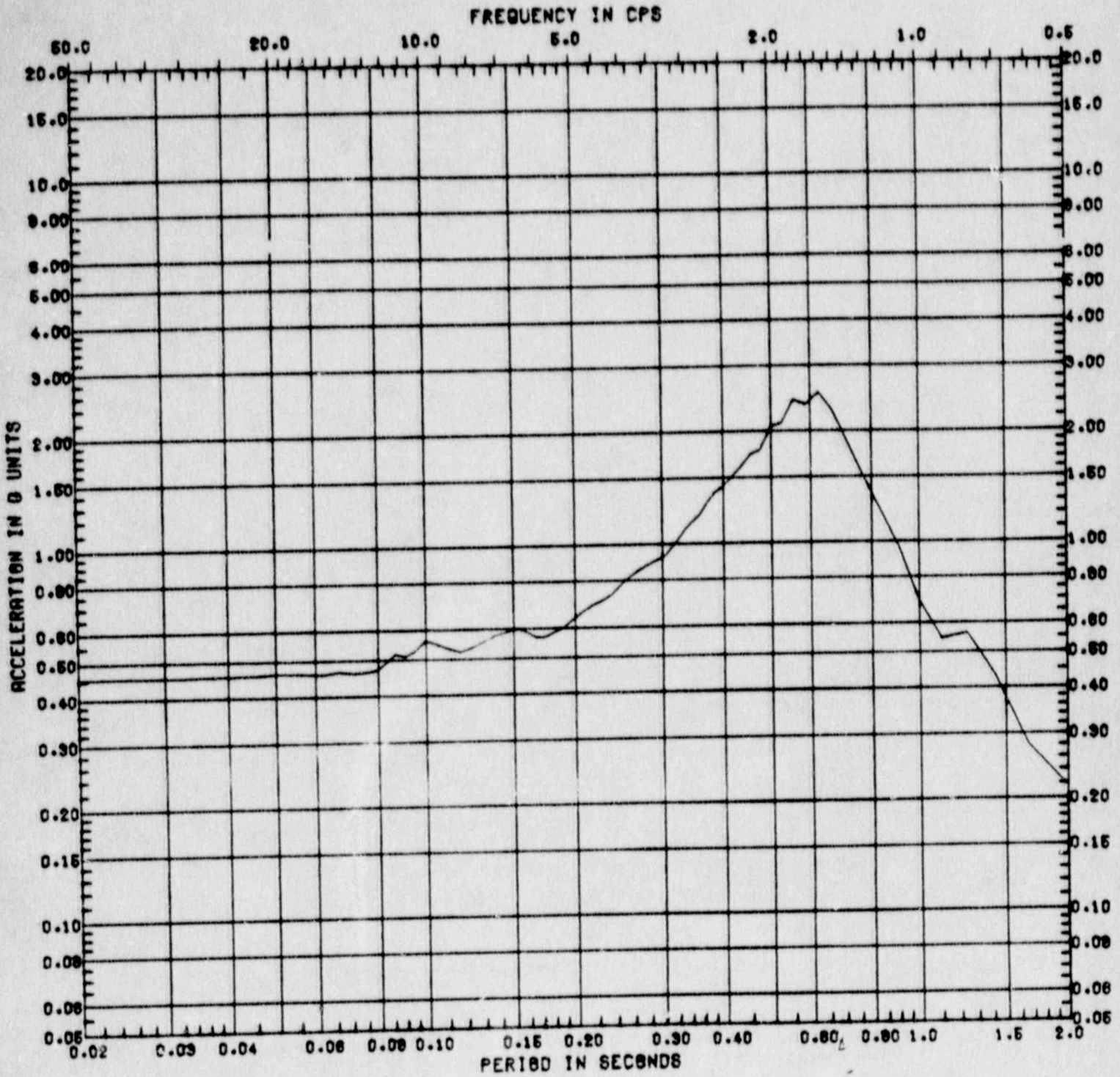

Figure C.3-7 Horizontal Response Spectrum at Zion Model Node 1 (A_H = 0.25g, Damping = 5%, Location = Containment Wall at Elevation 755')

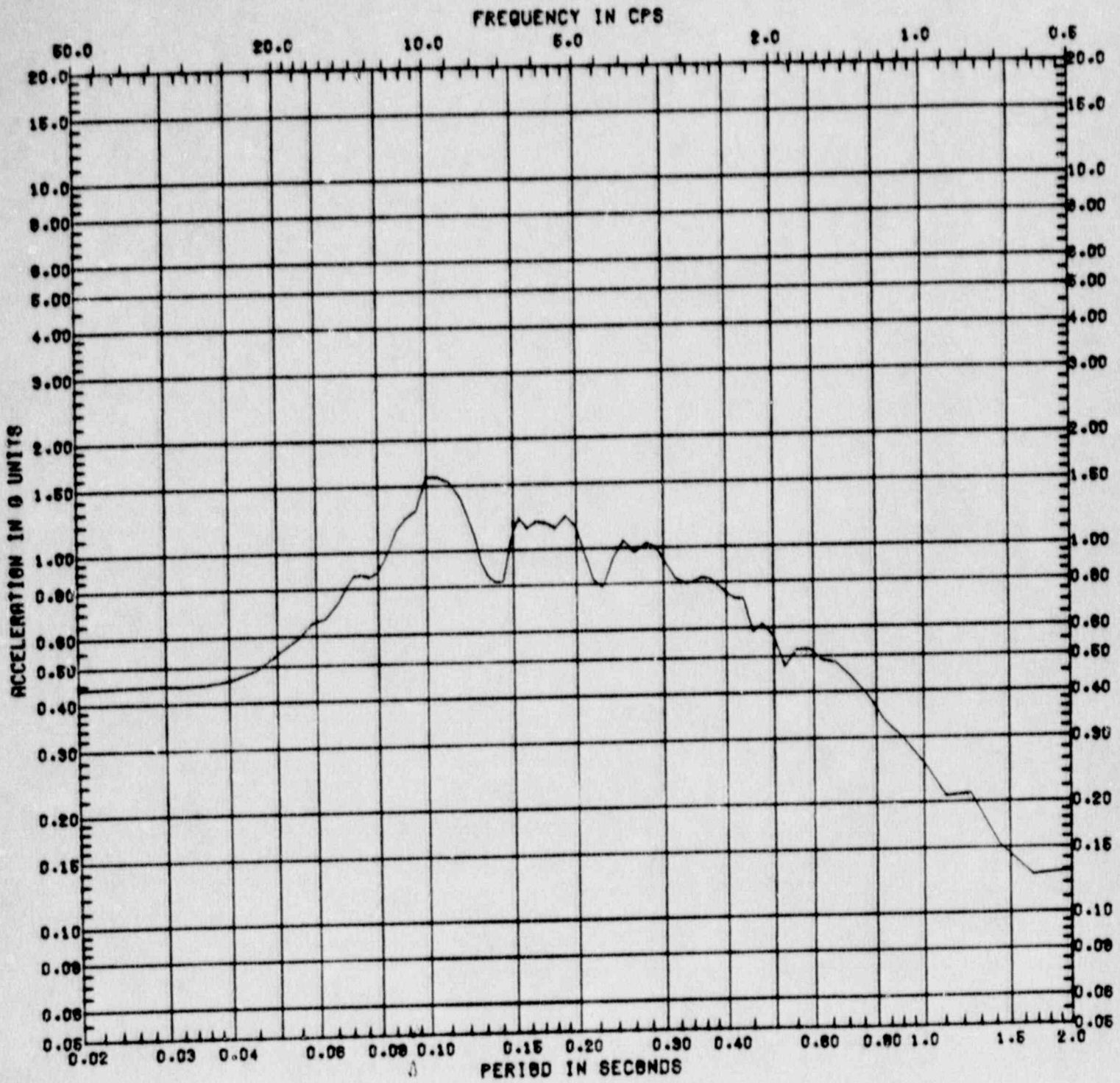

Figure C.3-8 Vertical Response Spectrum at Zion Model Node 1 (A_H = 0.25g, Damping = 5%, Location = Containment Wall at Elevation 755')

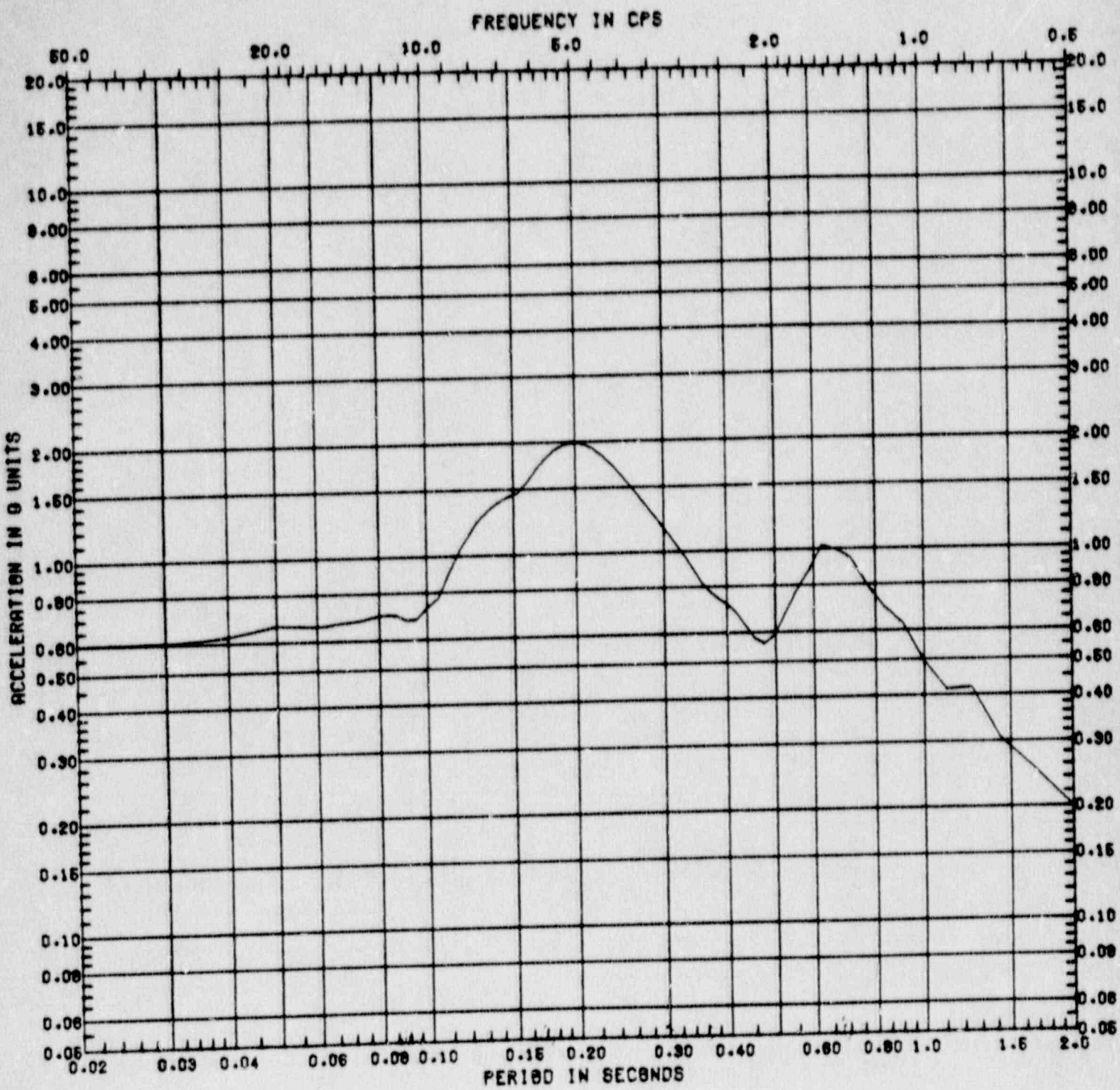

Figure C.3-9 Horizontal Response Spectrum at Zion Model Node 53 (A_H = 0.25g, Damping = 5%, Location = Crane Wall at Elevation 617')

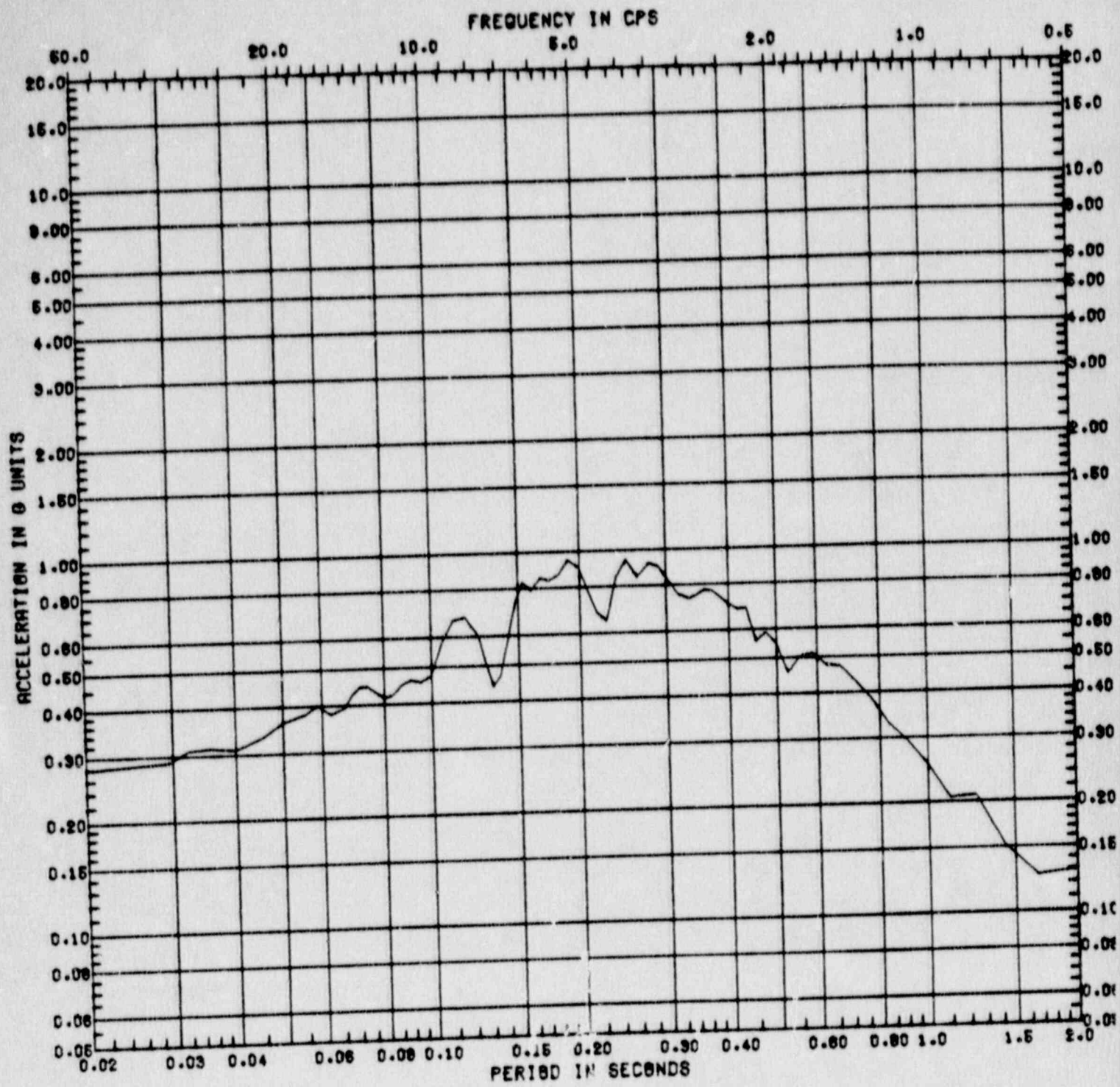

Figure C.3-10 Vertical Response Spectrum at Zion Model Node 53 (A_H = 0.25g, Damping = 5%, Location = Crane Wall at Elevation 617')

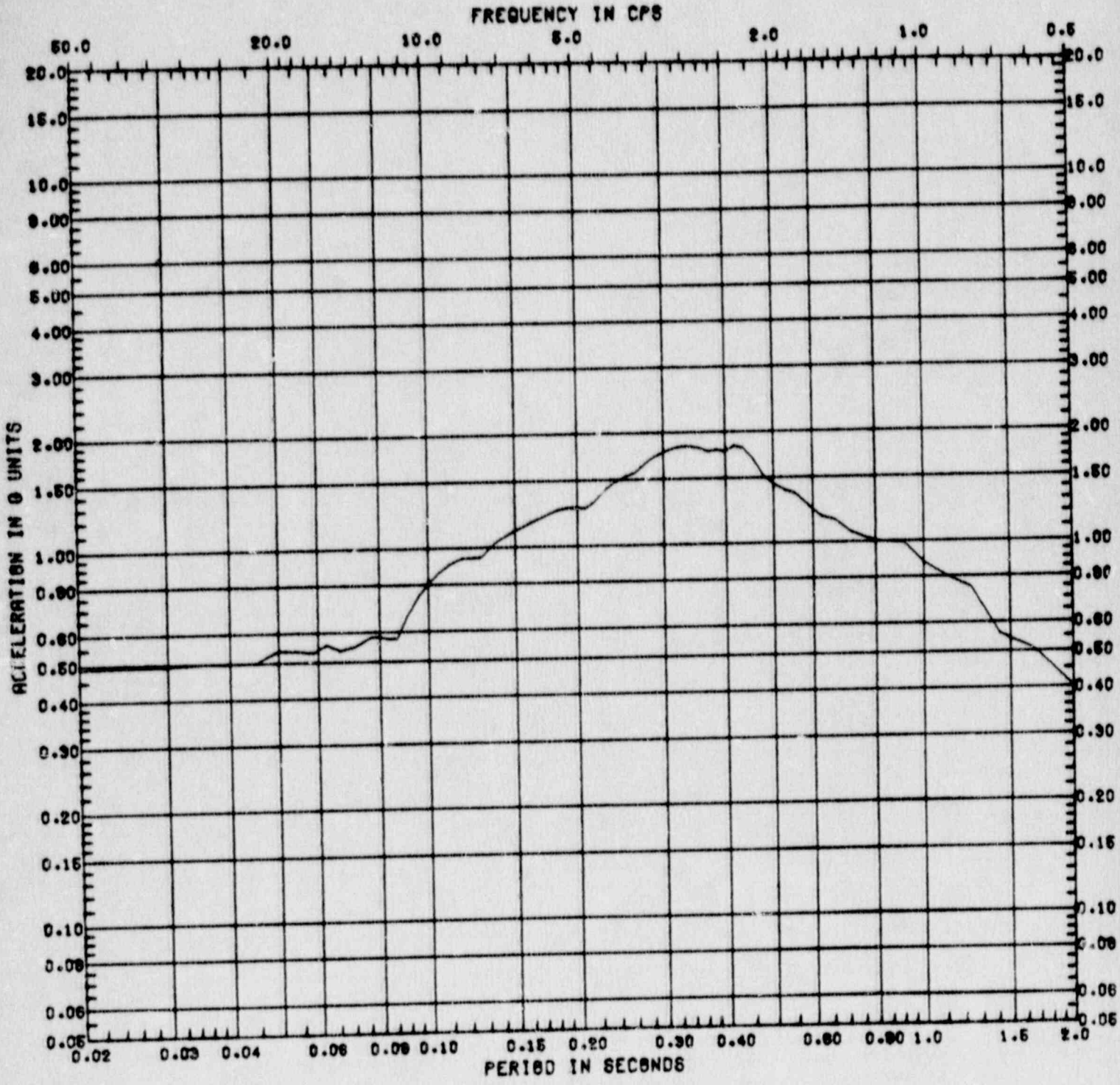

Figure C.3-11 Horizontal Response Spectrum at Zion Model Node 15 (A_H = 0.50g, Damping = 5%, Location = Containment Basemat, Elevation 568')

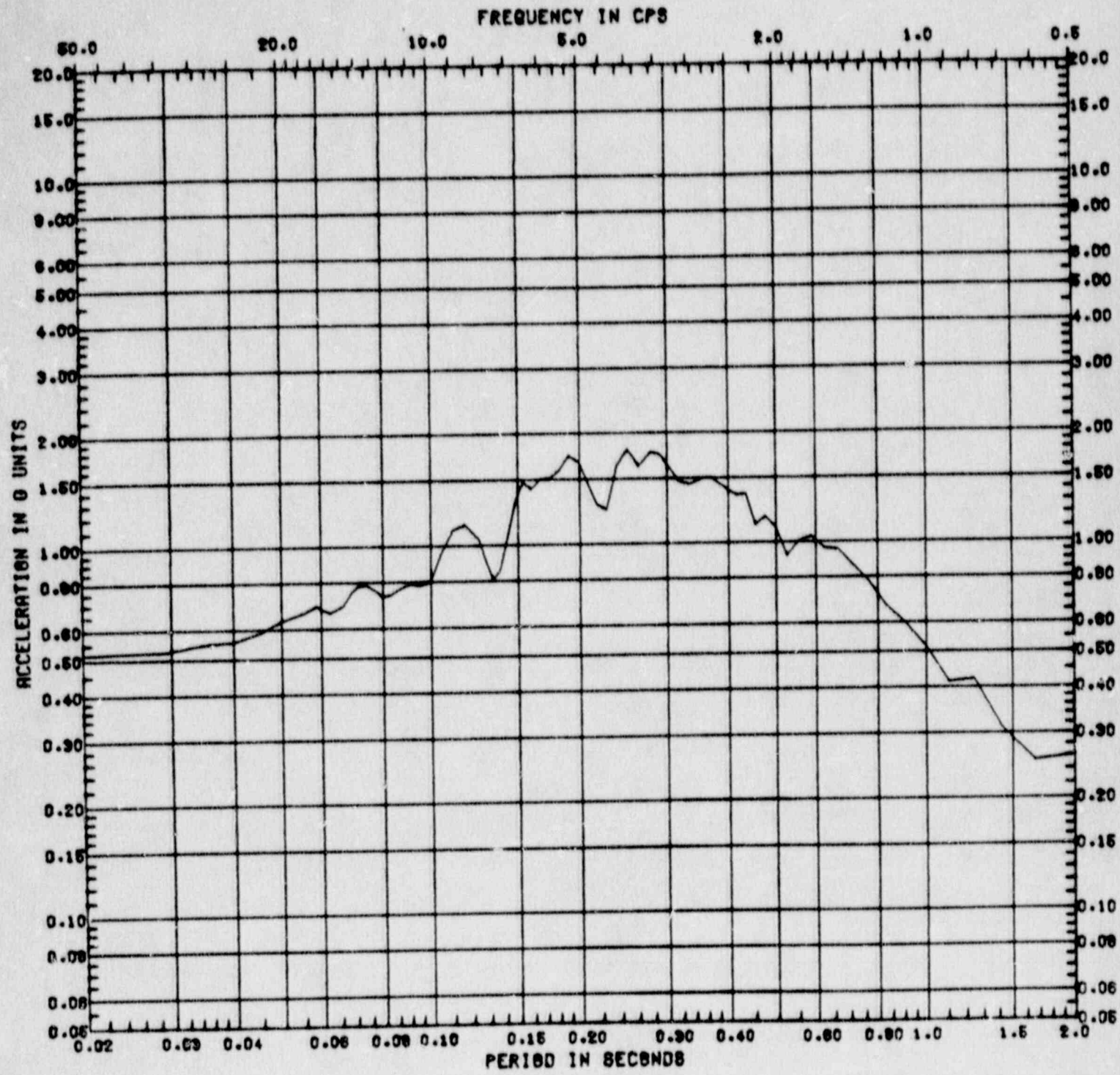

Figure C.3-12 Vertical Response Spectrum at Zion Model Node 15 (A_H = 0.50g, Damping = 5%, Location = Containment Basemat, Elevation 568')

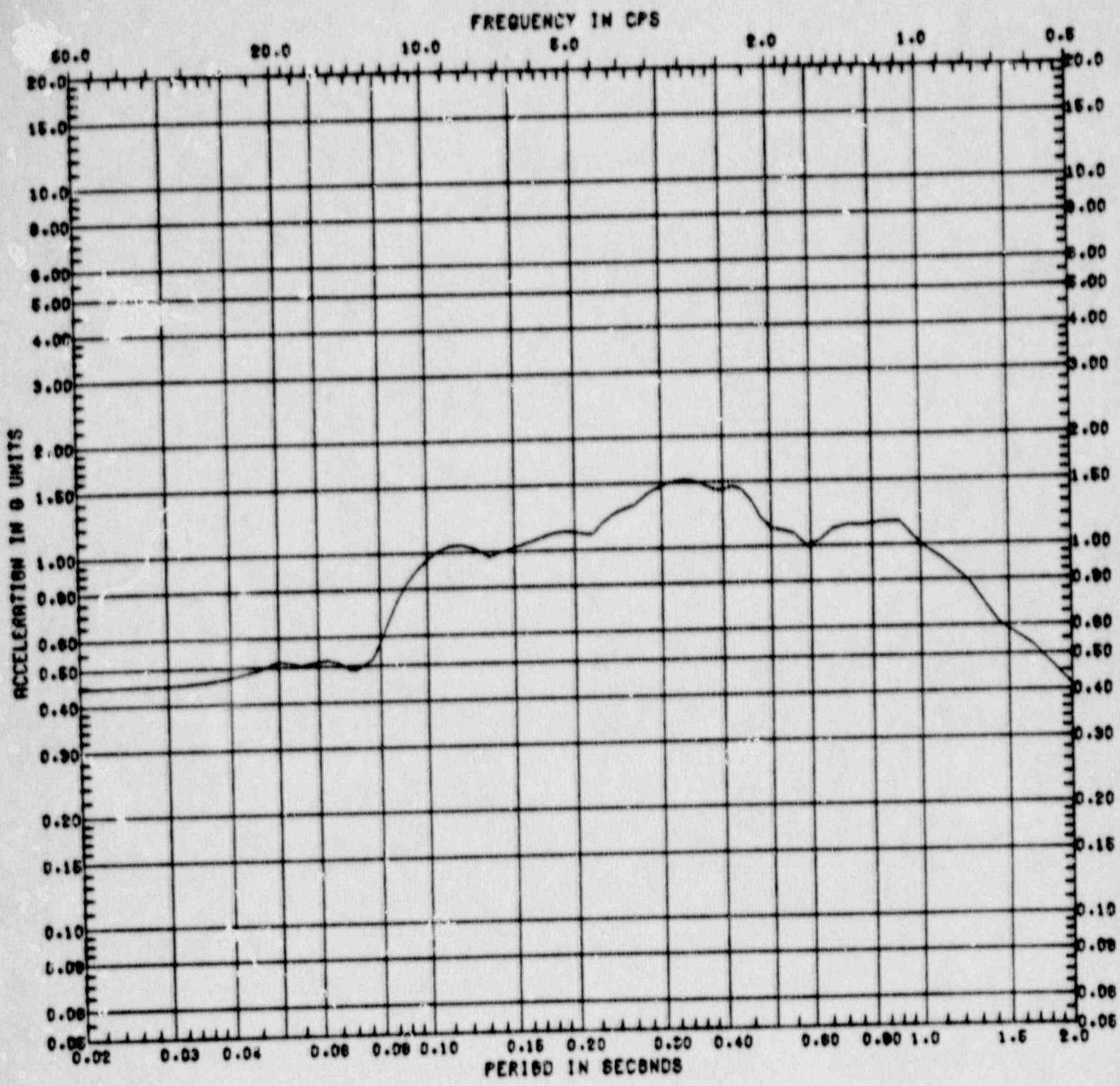

Figure C.3-13 Horizontal Response Spectrum at Zion Model Node 9 (A_H = 0.50g, Damping = 5%, Location = Containment Wall at Elevation 592')

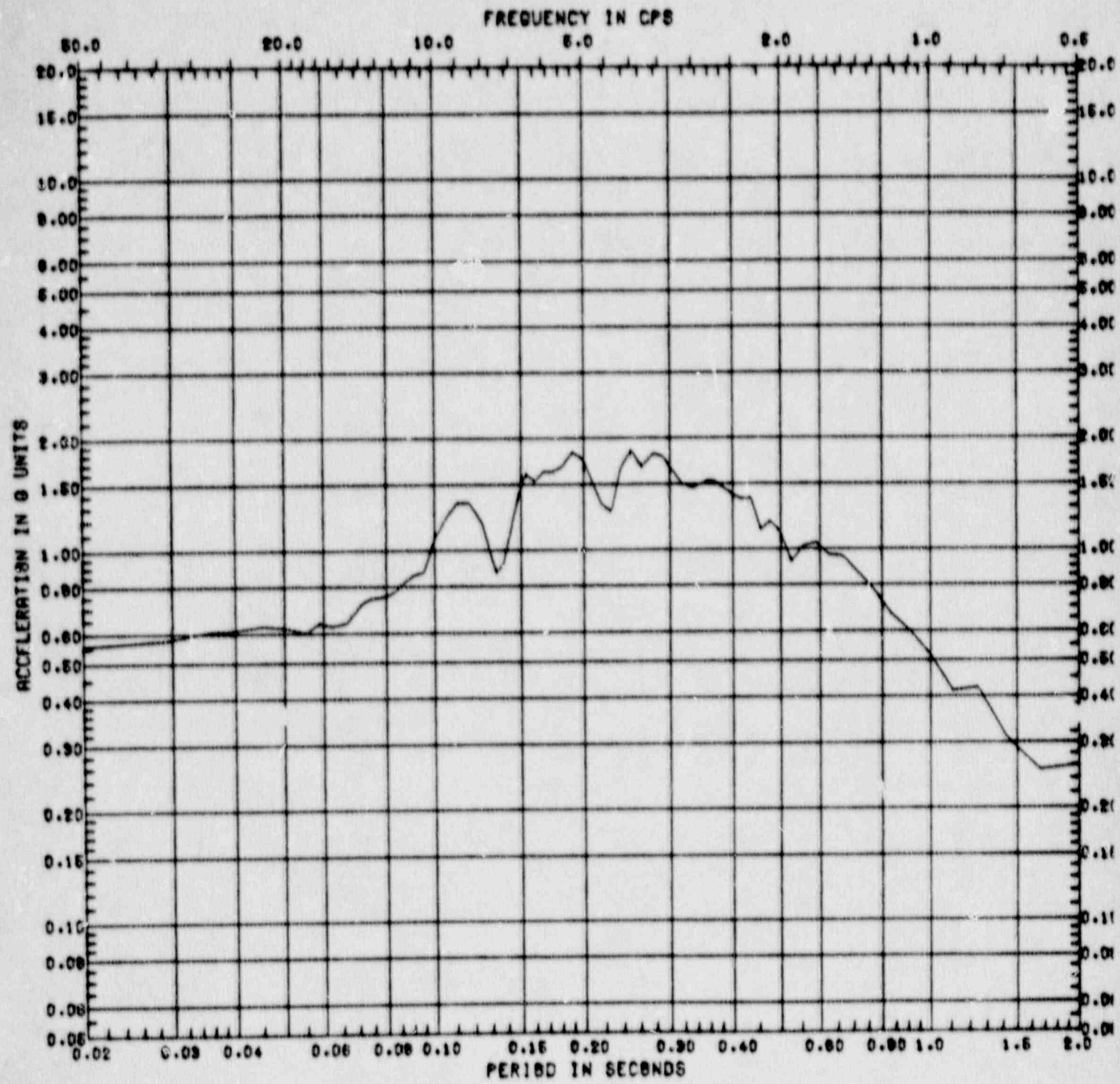

Figure C.3-14 Vertical Response Spectrum at Zion Model Node 9 (A_H = 0.50g, Damping = 5%, Location = Containment Wall at Elevation 592')

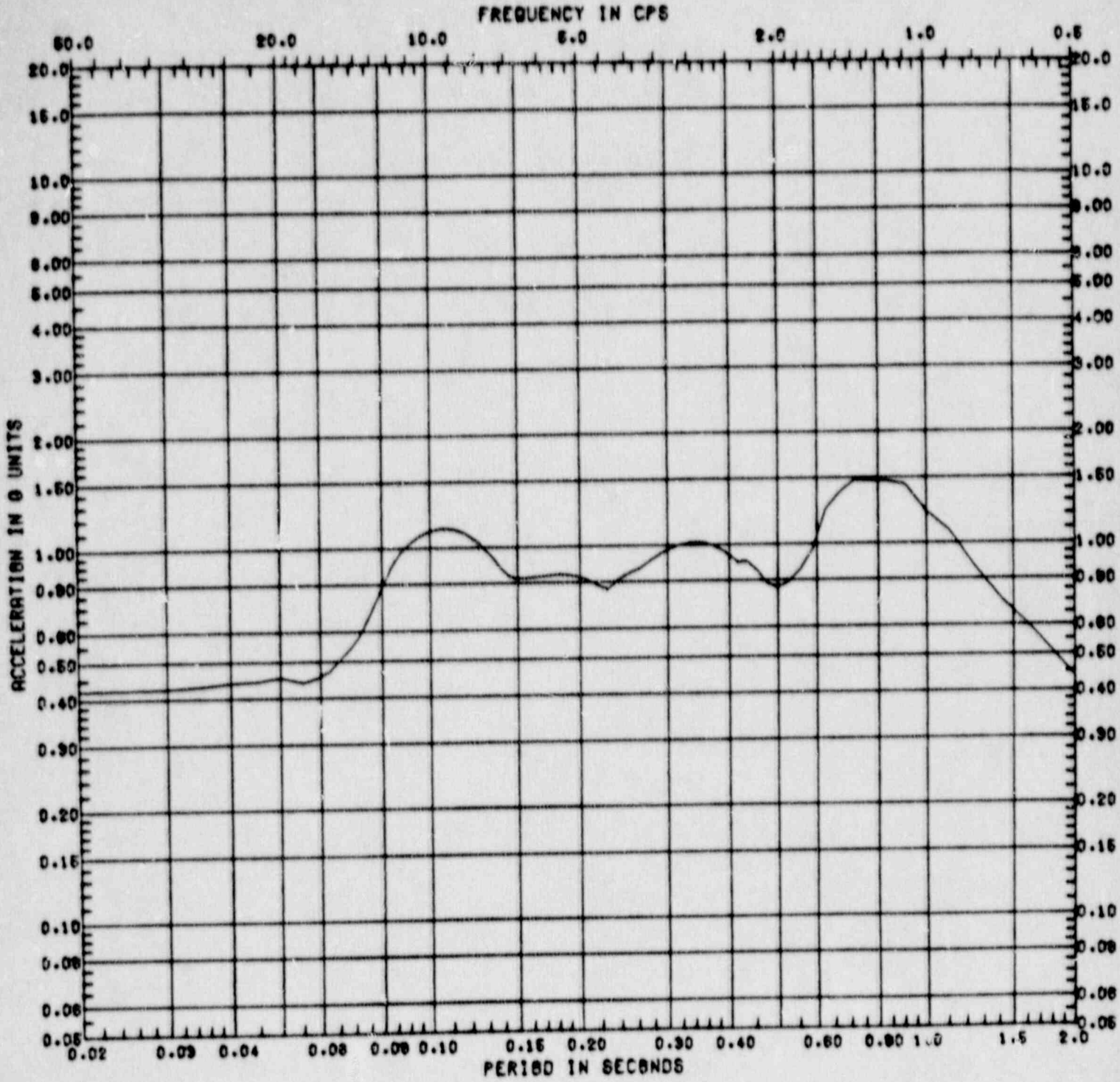

Figure C.3-15 Horizontal Response Spectrum at Zion Model Node 7 (A_H = 0.50g, Damping = 5%, Location = Containment Wall at Elevation 628')

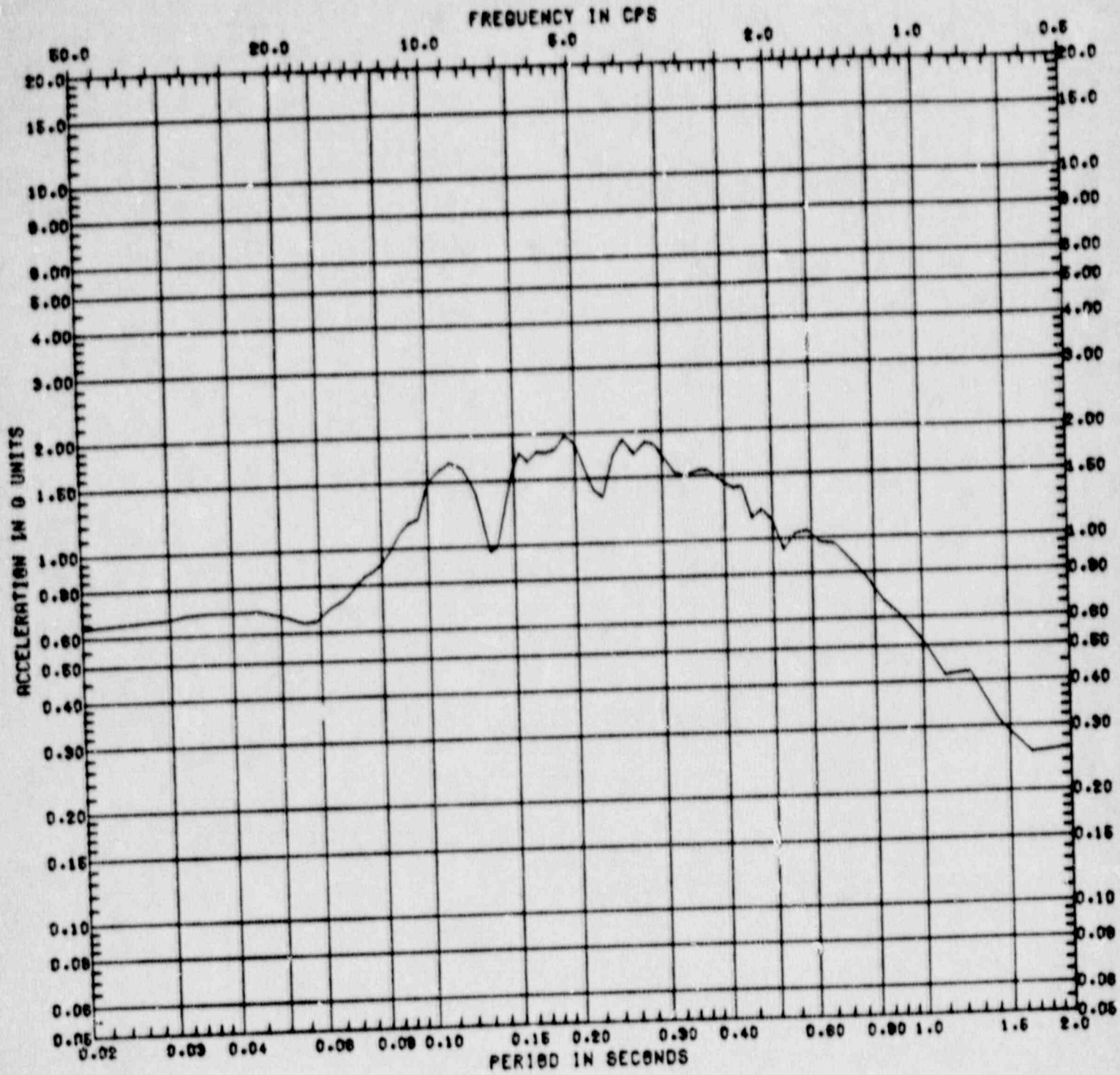

Figure C.3-16 Vertical Response Spectrum at Pion Model Node 7 (A_H = 0.50g, Damping = 5%, Location = Containment Wall at Elevation 628')

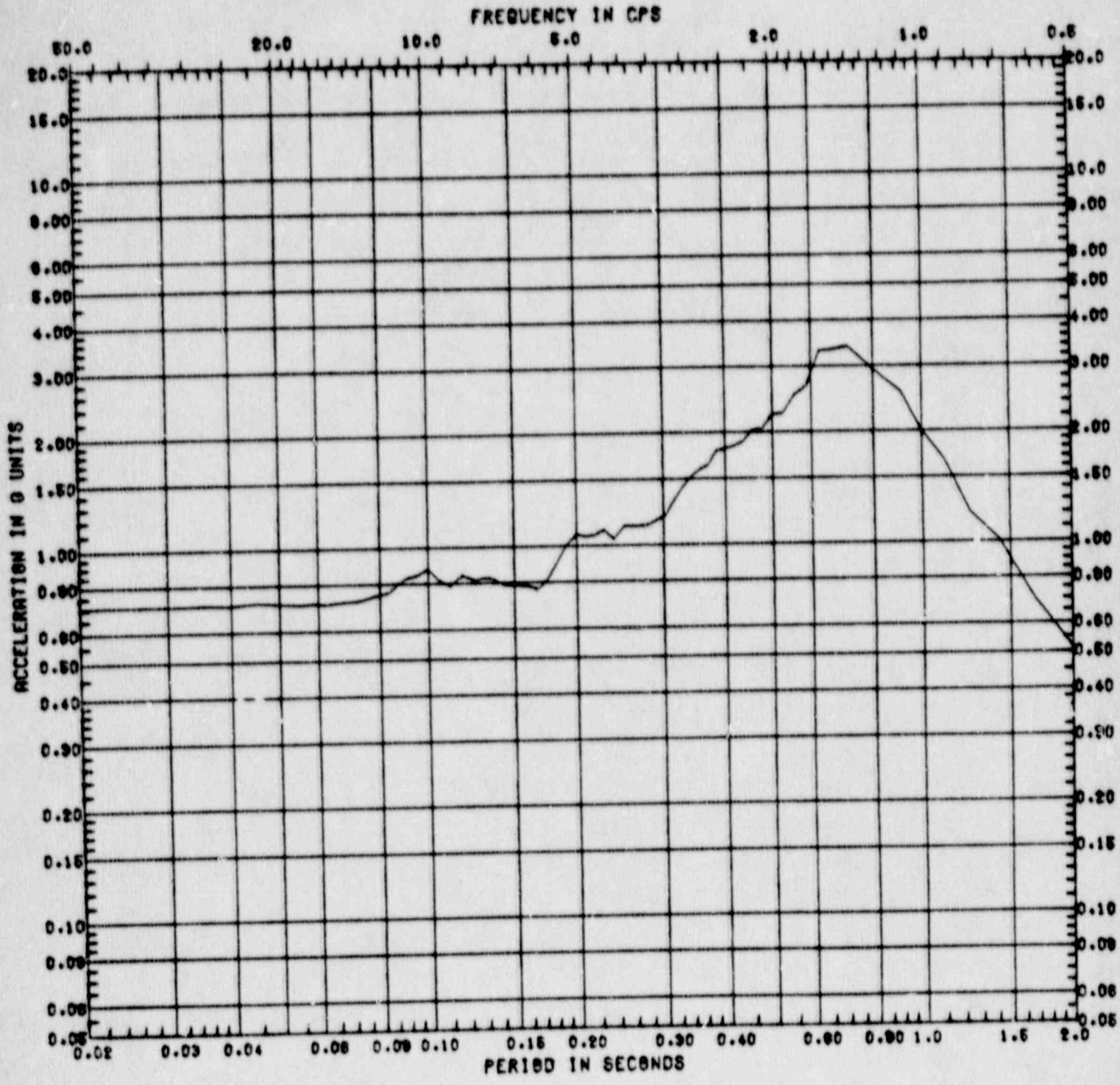

Figure C.3-17 Horizontal Response Spectrum at Zion Model Node 1 (A_H = 0.50g, Damping = 5%, Location = Containment Wall at Elevation 755')

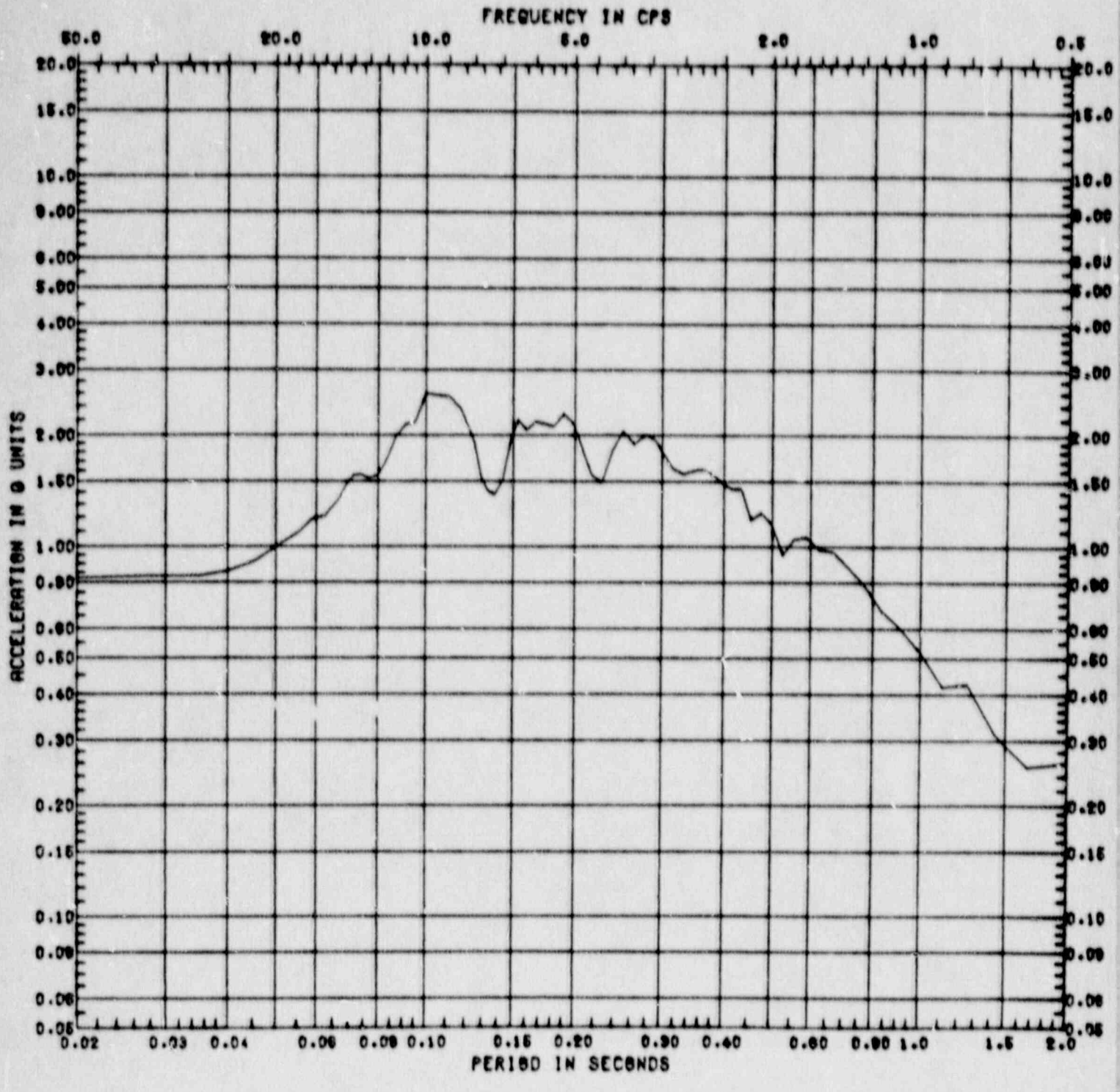

Figure C.3-13 Vertical Response Spectrum at Zion Model Node 1 (A_H = 0.50g, Damping = 5%, Location = Containment Wall at Elevation 755')

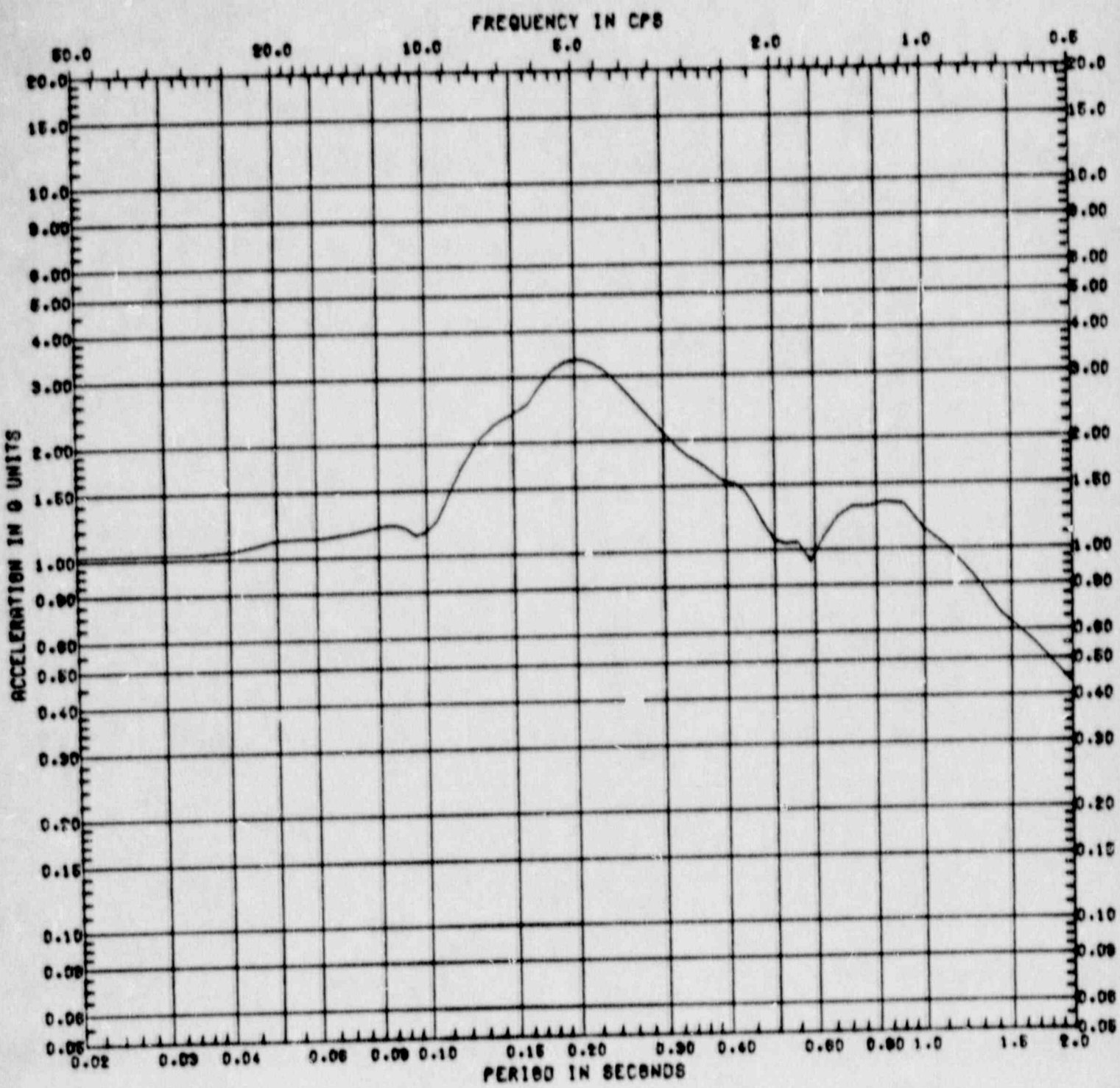

Figure C.3-19 Horizontal Response Spectrum at Zion Model Node 53 (A_H = 0.50g, Damping = 5%, Location = Crane Wall at Elevation 617')

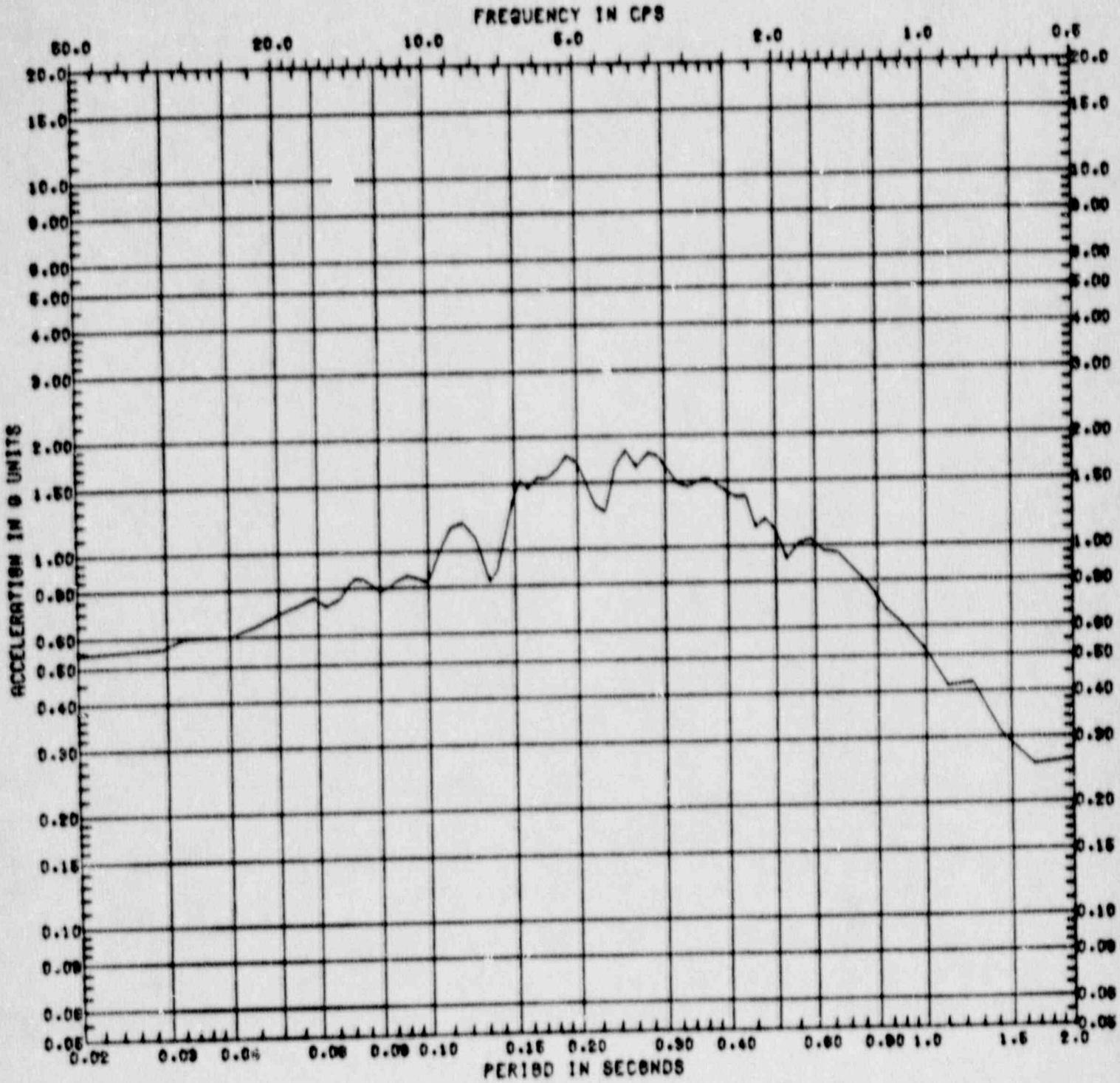

Figure C.3-20 Vertical Response Spectrum at Zion Model Node 53 (A_H = 0.50g, Damping = 5%, Location = Crane Wall at Elevation 617')

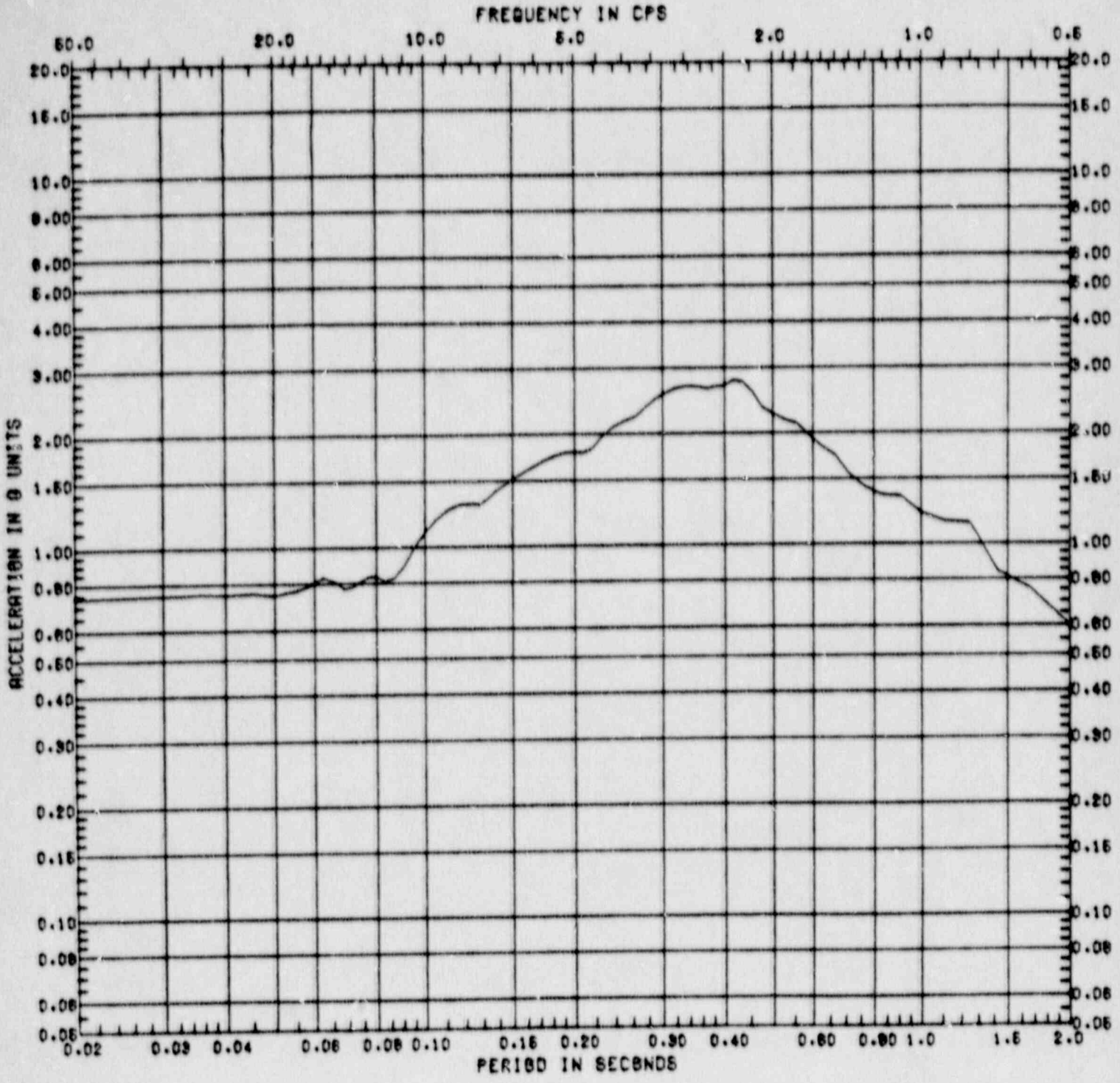

Figure C.3-21 Horizontal Response Spectrum at Zion Model Node 15 (A_H = 0.75g, Damping = 5%, Location = Containment Basemat, Elevation 568')

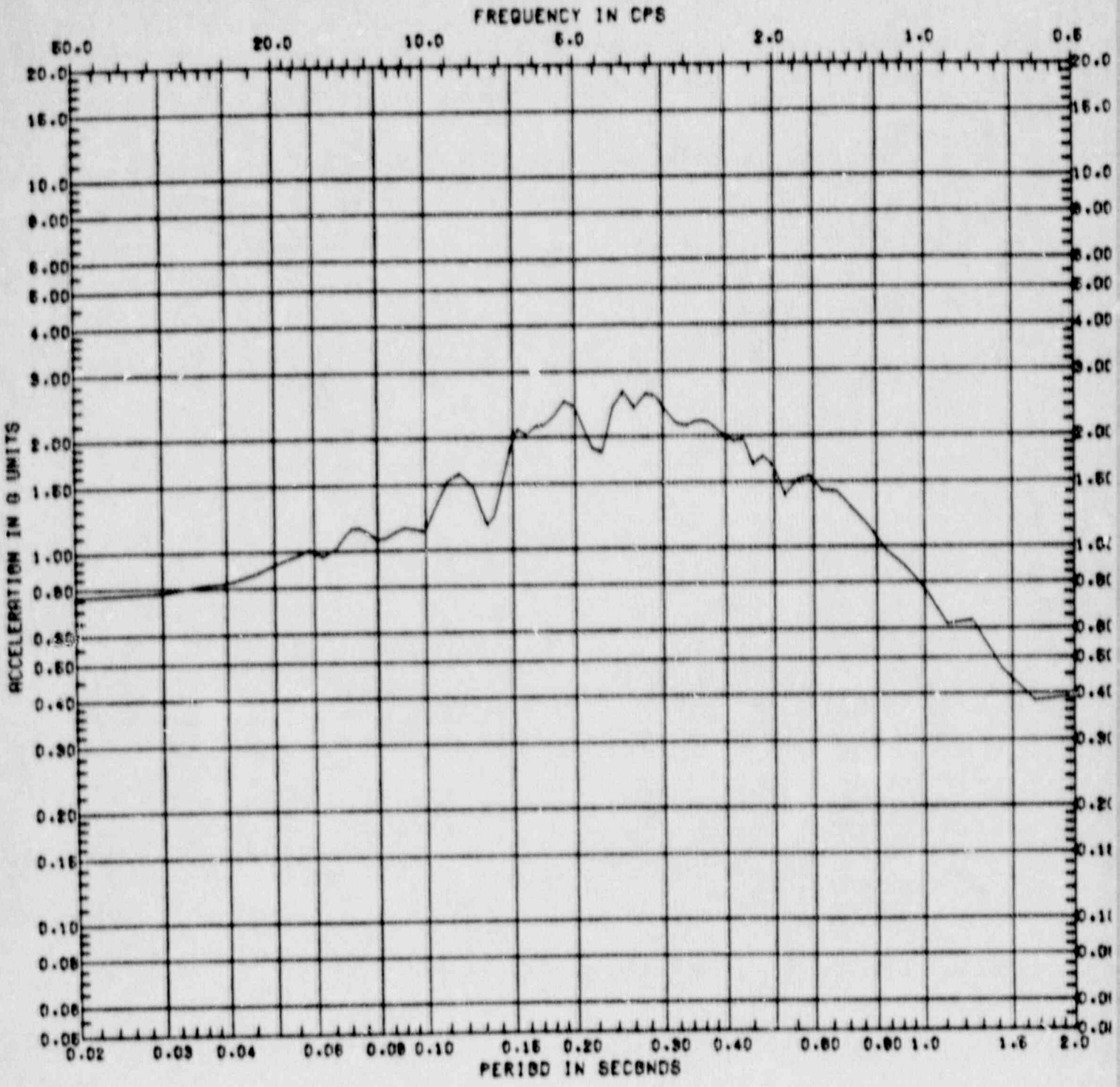

Figure C.3-22 Vertical Response Spectrum at Zion Model Node 15 (A_H = 0.75g, Damping = 5%, Location = Containment Basemat, Elevation 568')

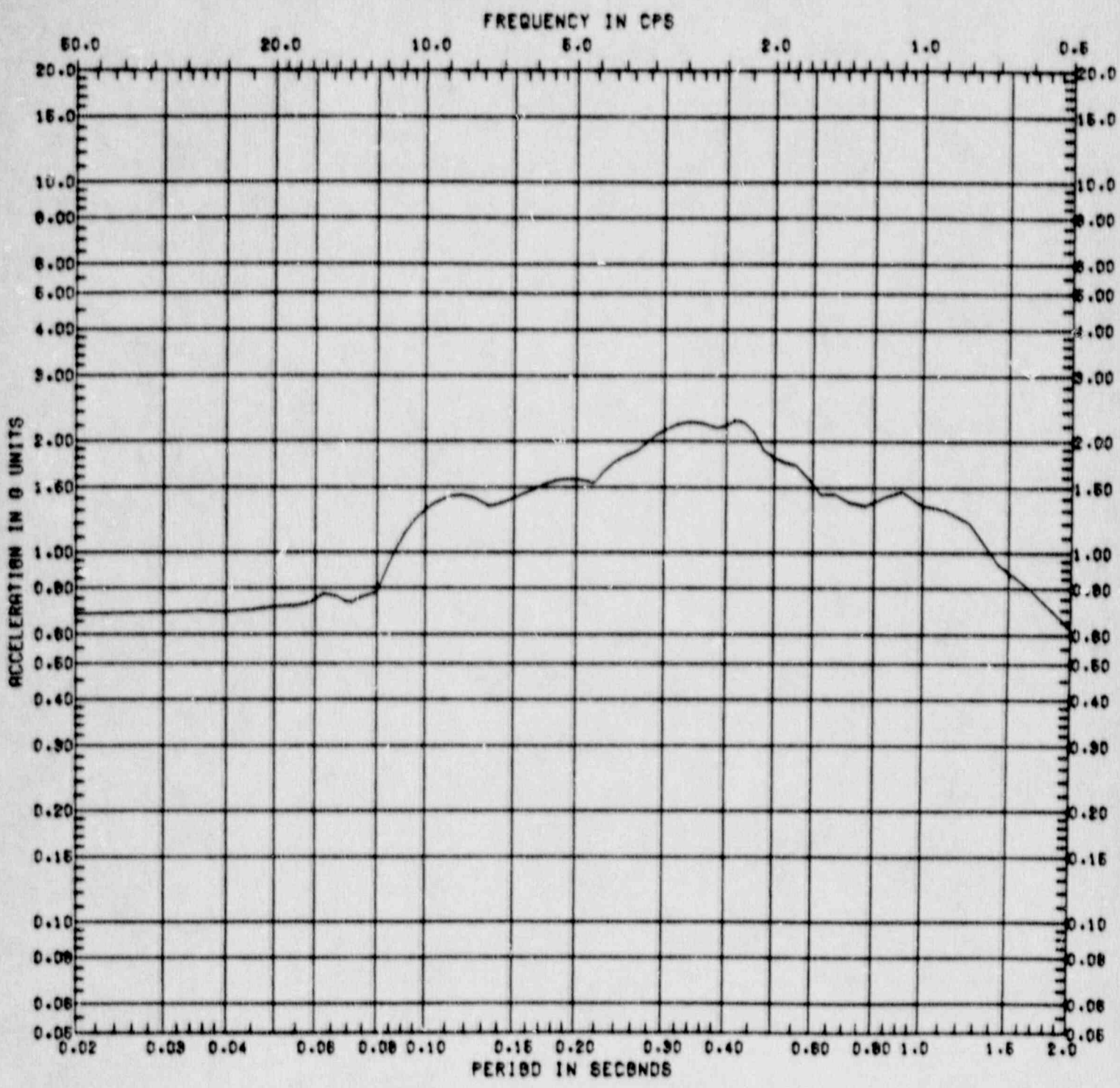

Figure C.3-23 Horizontal Response Spectrum at Zion Model Node 9 (A_g = 0.75g, Damping = 5%, Location = Containment Wall at Elevation 592')

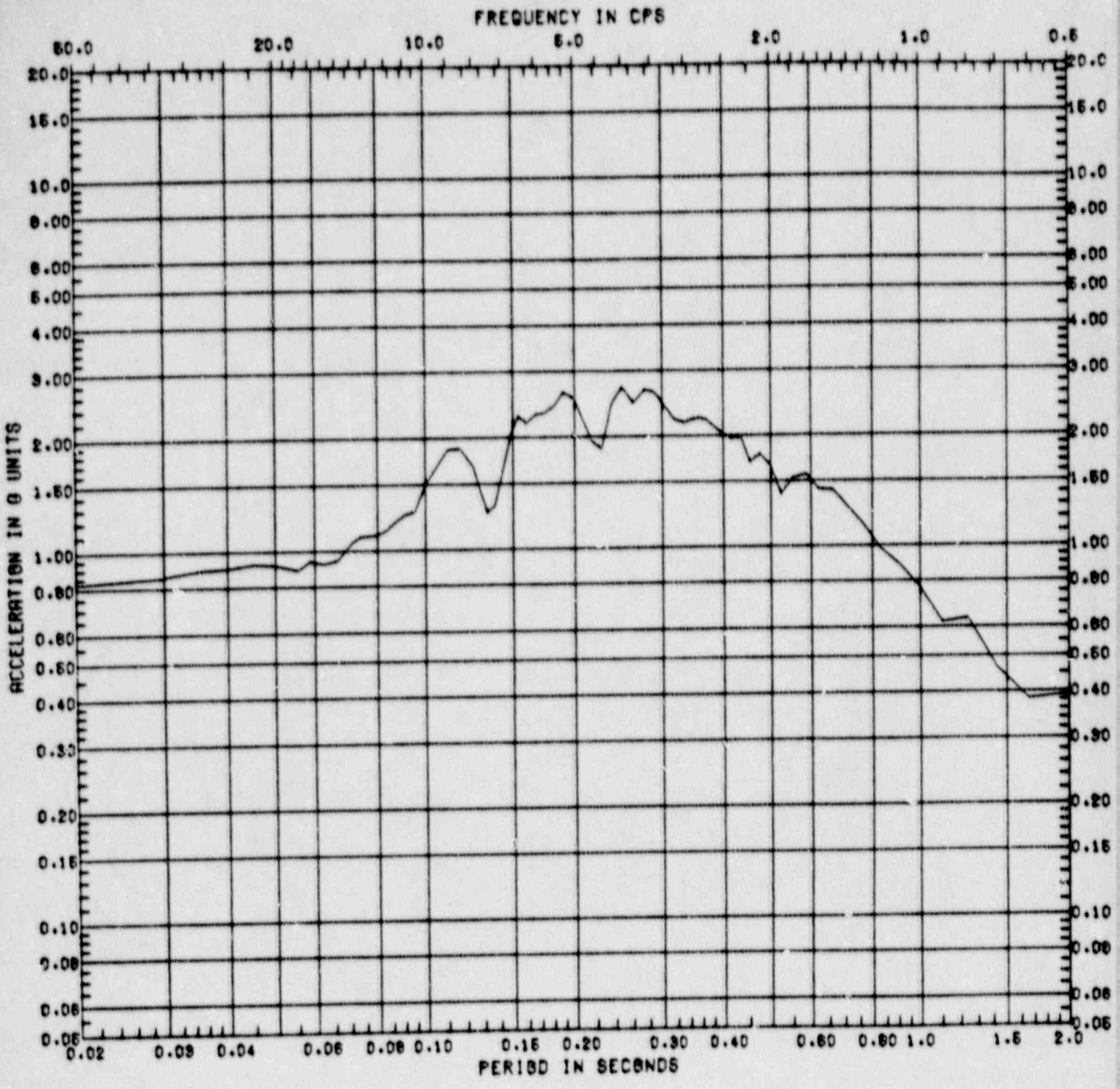

Figure C.3-24 Vertical Response Spectrum at Zion Model Node 9 (A_H = 0.75g, Damping = 5%, Location = Containment Wall at Elevation 592')

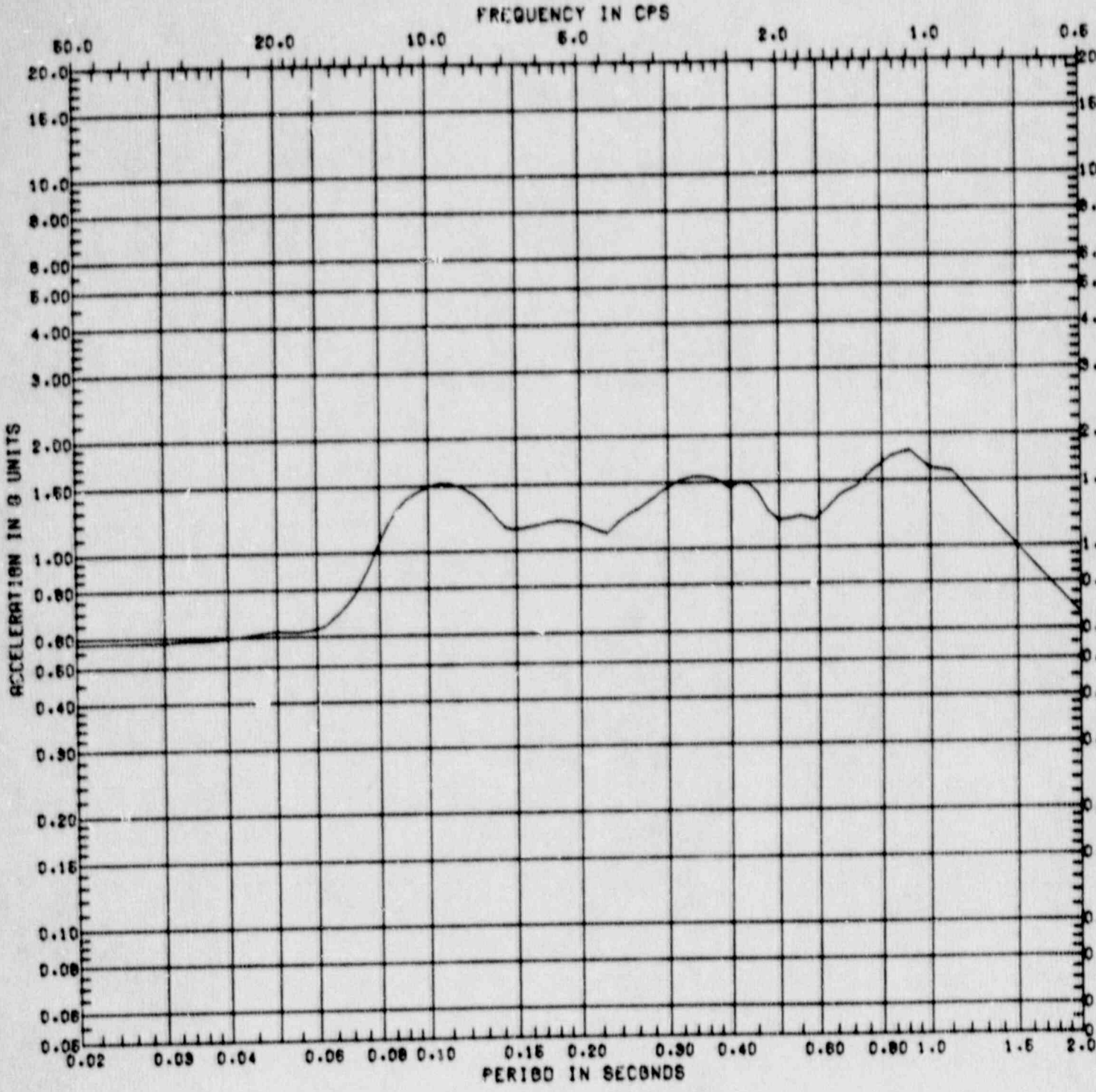

Figure C.3-25 Horizontal Response Spectrum at Zion Model Node 7 (A_H = 0.75g, Damping = 5%, Location = Containment Wall at Elevation 628')

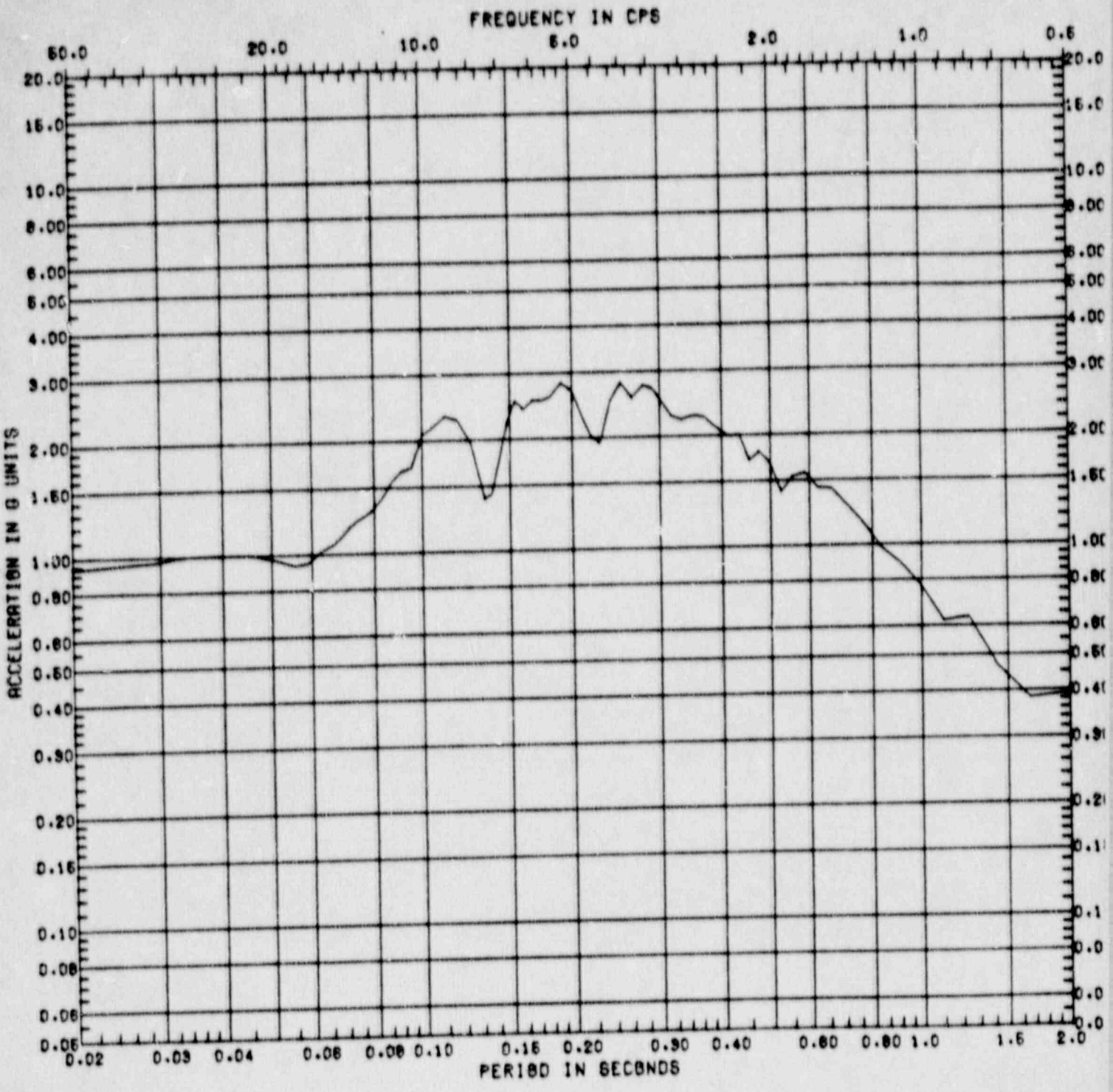

Figure C.3-26 Vertical Response Spectrum at Zion Model Node 7 (A_H = 0.75g, Damping = 5%, Location = Containment Wall at Elevation 628')

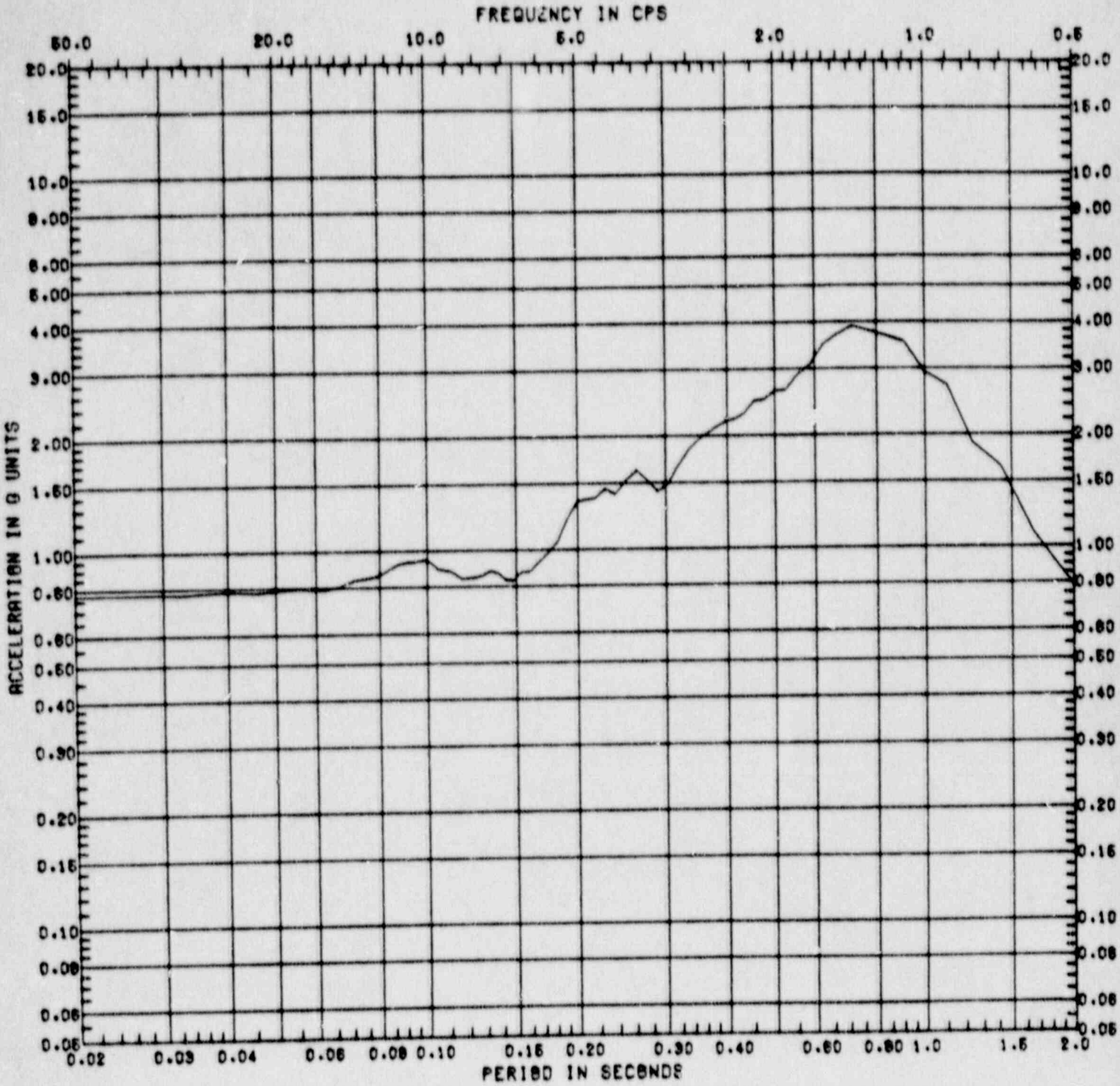

Figure C.3-27 Horizontal Response Spectrum at Zion Model Node 1 (A_H = 0.75g, Damping = 5%, Location = Containment Wall at Elevation 755')

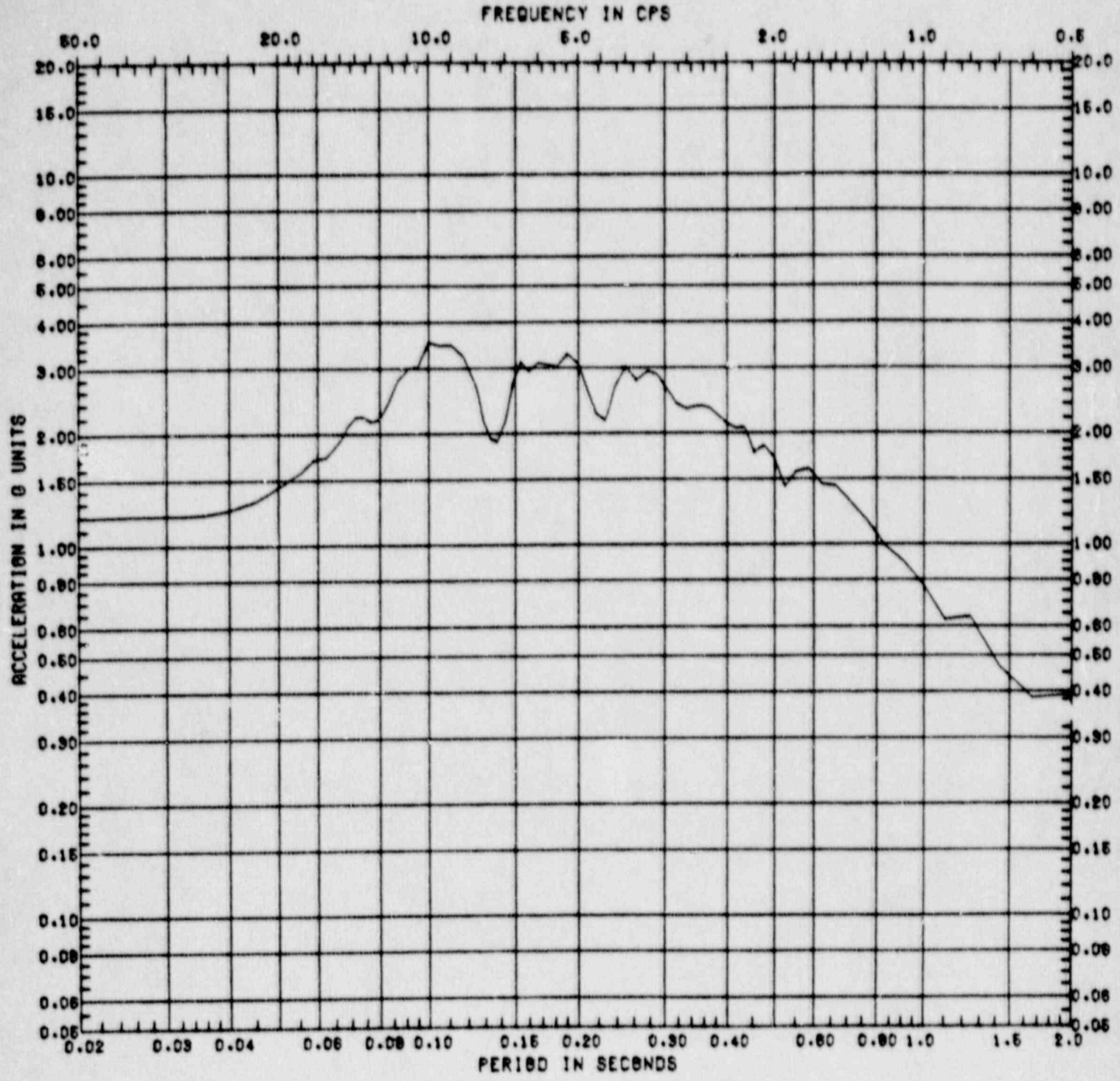

Figure C.3-28 Vertical Response Spectrum at Zion Model Node 1 (A_H = 0.75g, Damping = 5%, Location = Containment Wall at Elevation 755')

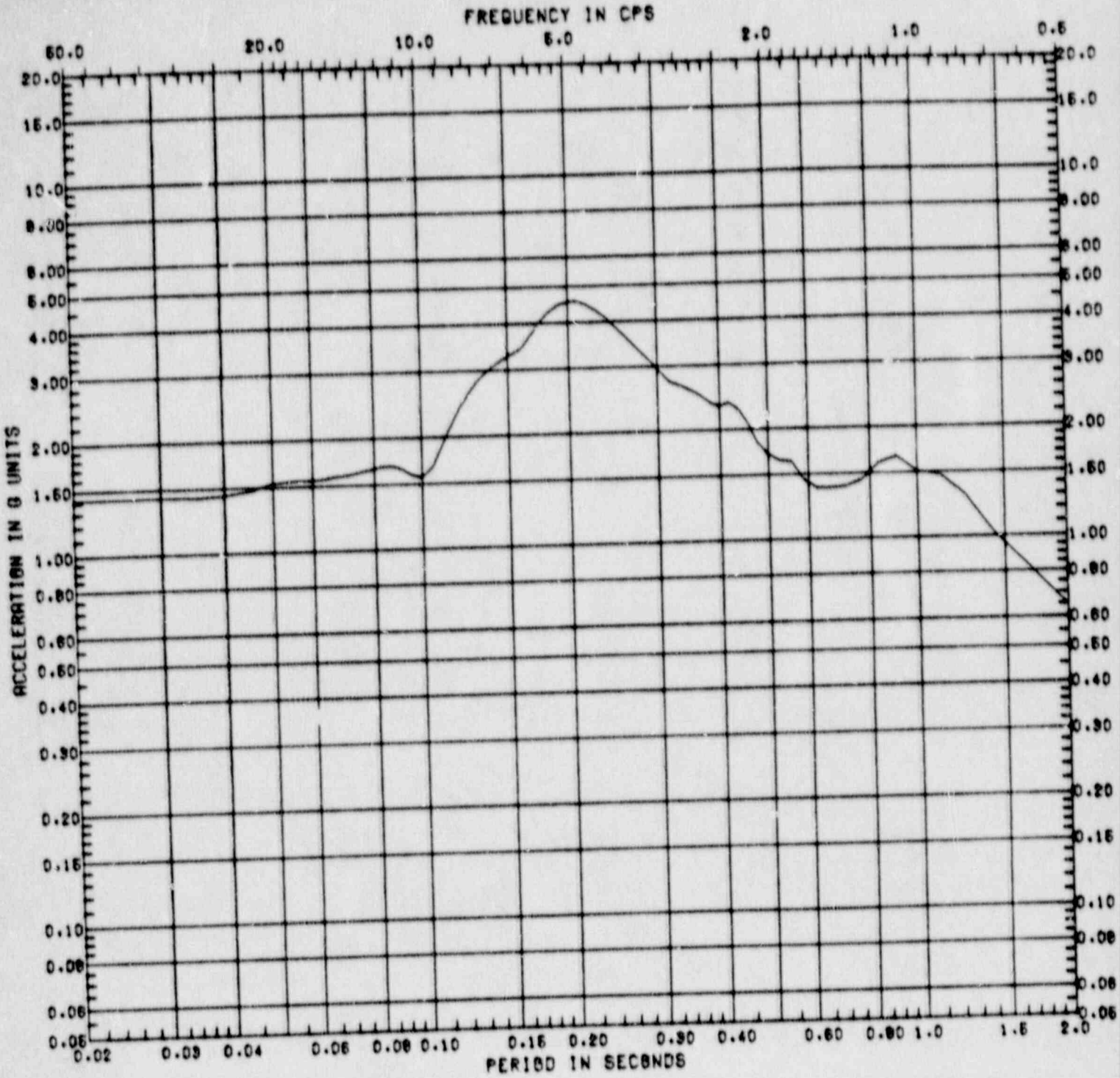

Figure C.3-29 Horizontal Response Spectrum at Zion Model Node 53 (A_H = 0.75g, Damping = 5%, Location = Crane Wall at Elevation 617')

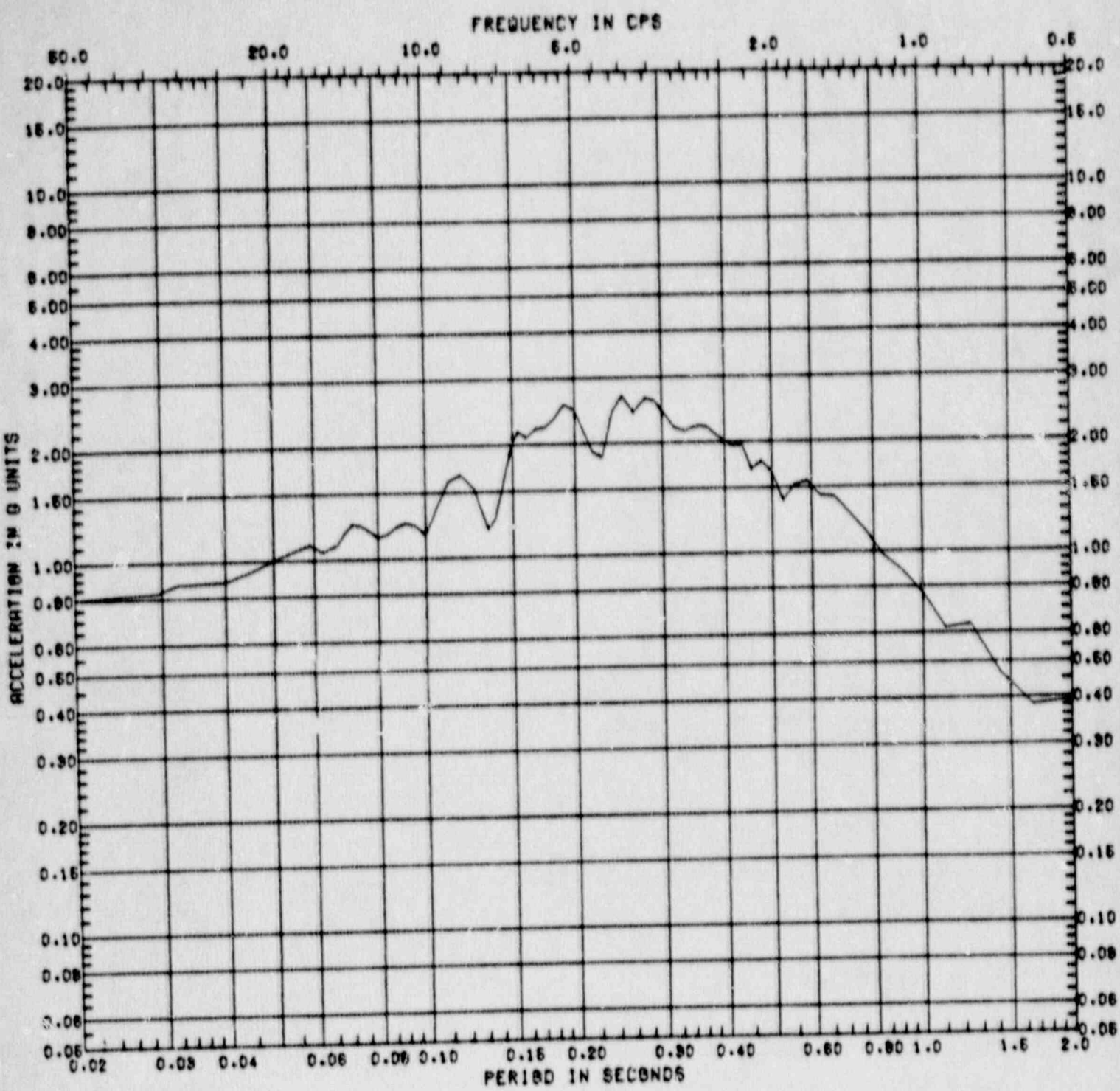

Figure C.3-30 Vertical Response Spectrum at Zion Model Node 53 (A_H = 0.75g, Damping = 5%, Location = Crane Wall at Elevation 617')

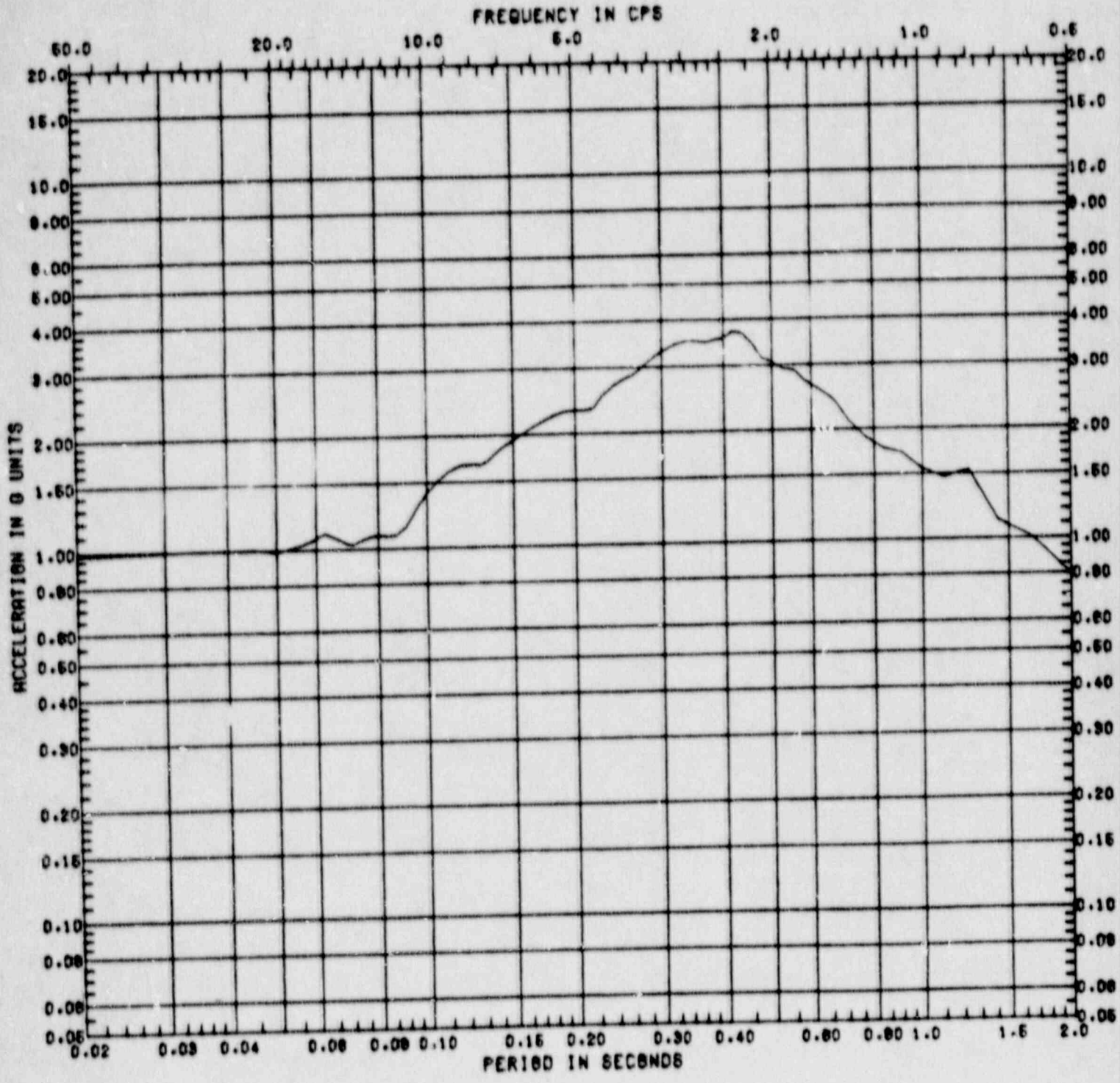

Figure C.3-31 Horizontal Response Spectrum at Zion Model Node 15 (A_H = 1.0g, Damping = 5%, Location = Containment Basemat, Elevation 568')

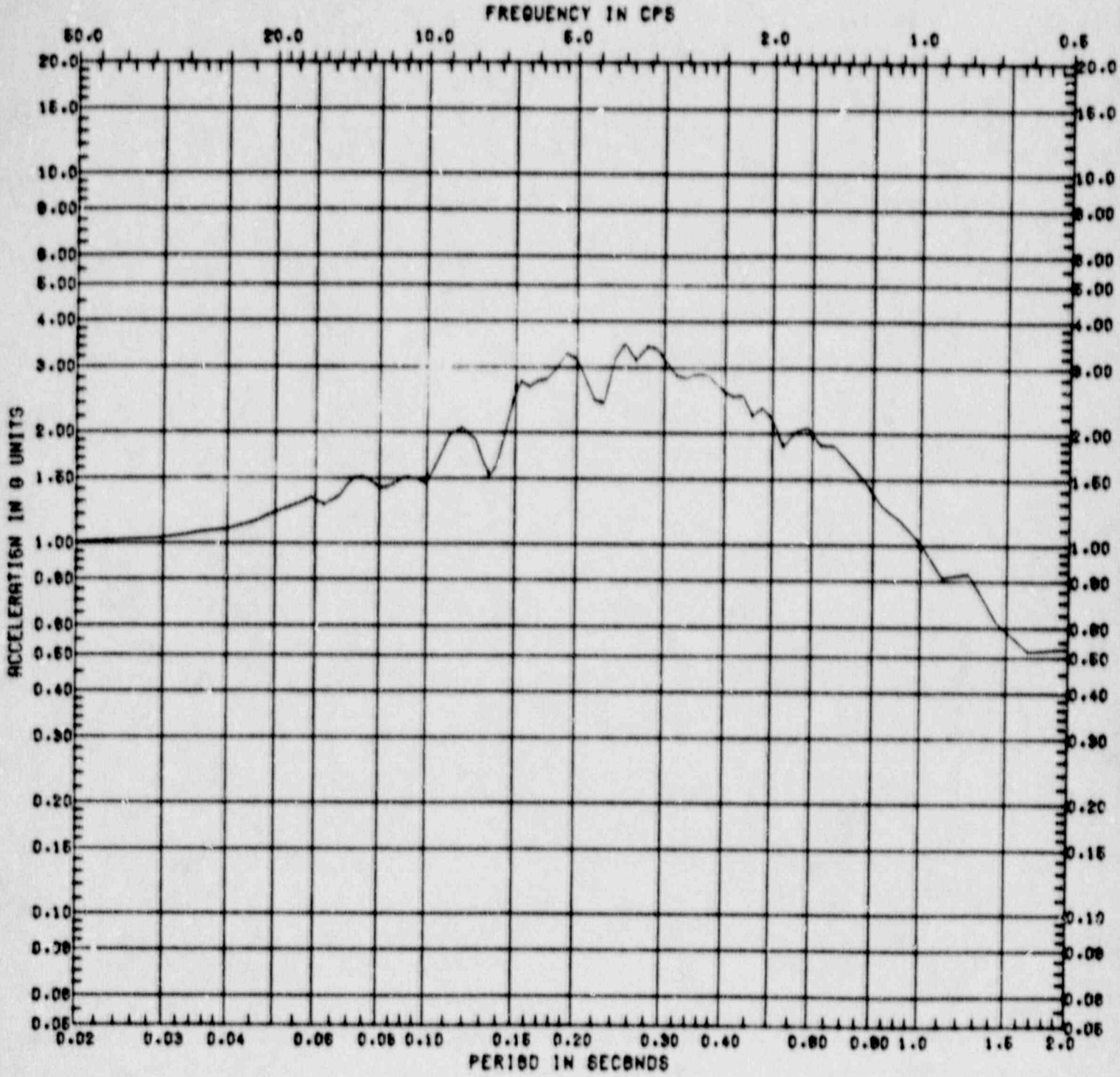

Figure C.3-32 Vertical Response Spectrum at Zion Model Node 15 (A_H = 1.0g, Damping = 5%, Location = Containment Basemat, Elevation 568')

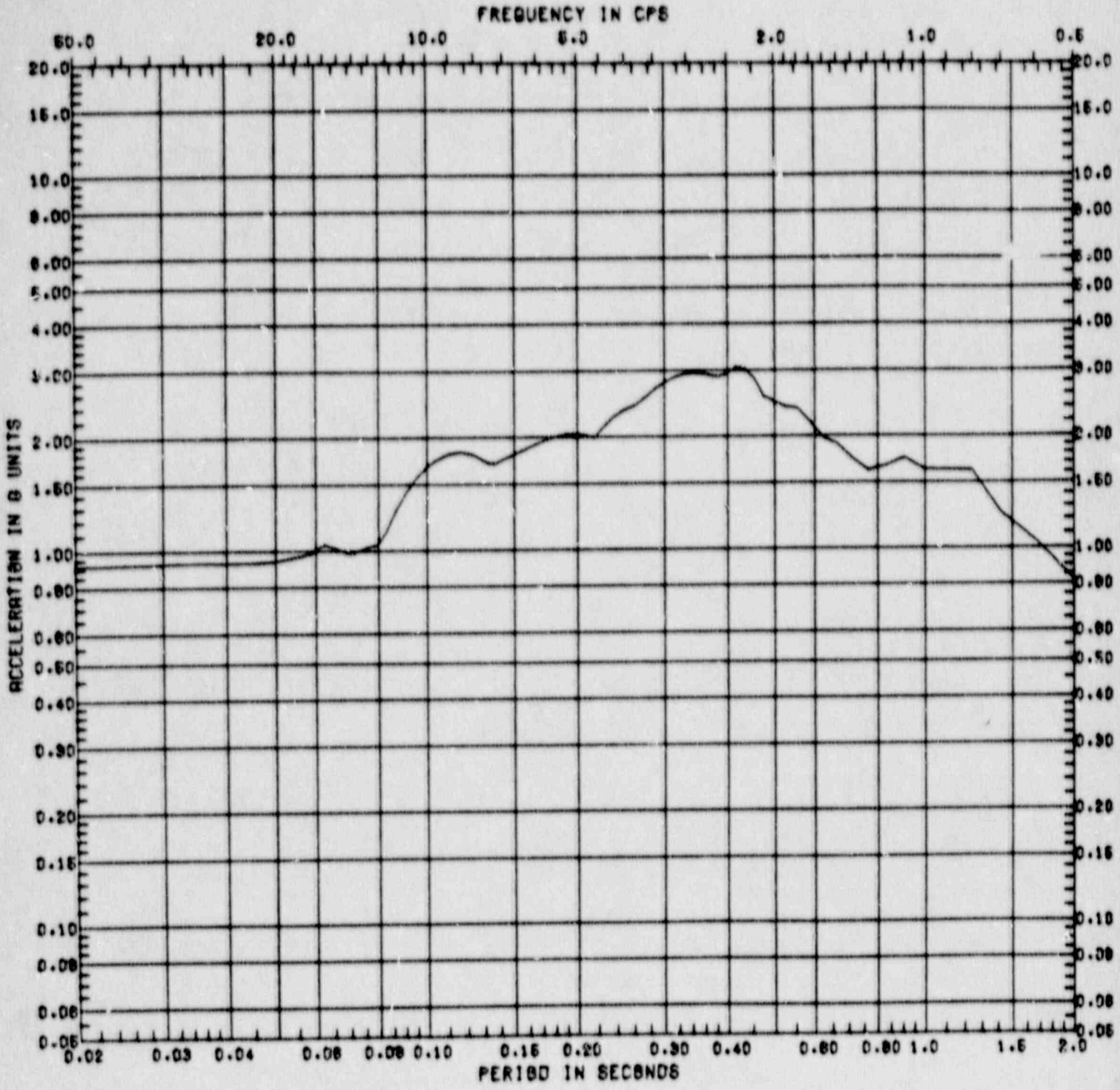

Figure C.3-33 Horizontal Response Spectrum at Zion Model Node 9 (A_H = 1.0g, Damping = 5%, Location = Containment Wall at Elevation 592')

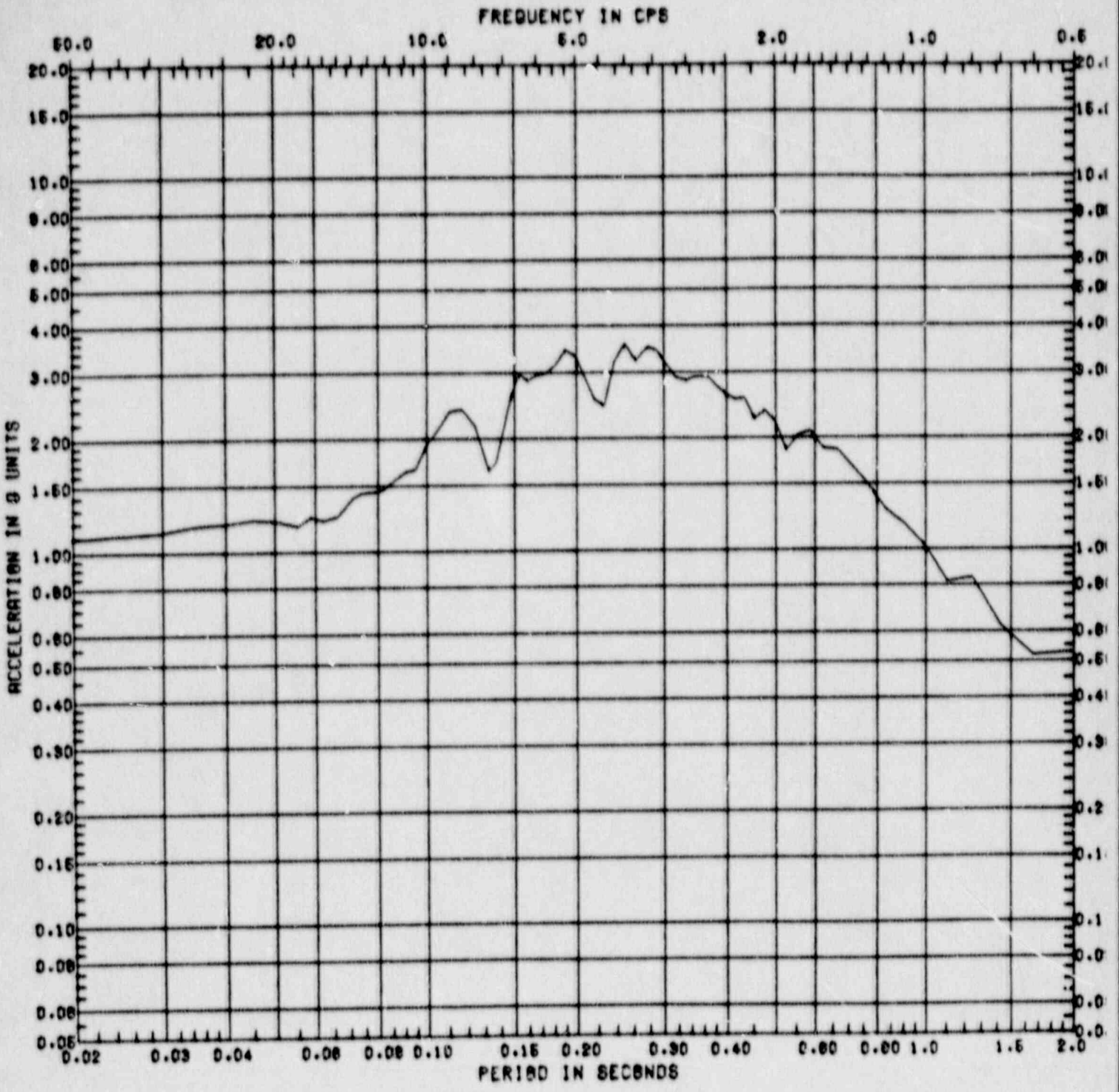

Figure C.3-34 Vertical Response Spectrum at Zion Model Node 9 (A_g = 1.0g, Damping = 5%, Location = Containment Wall at Elevation 592')

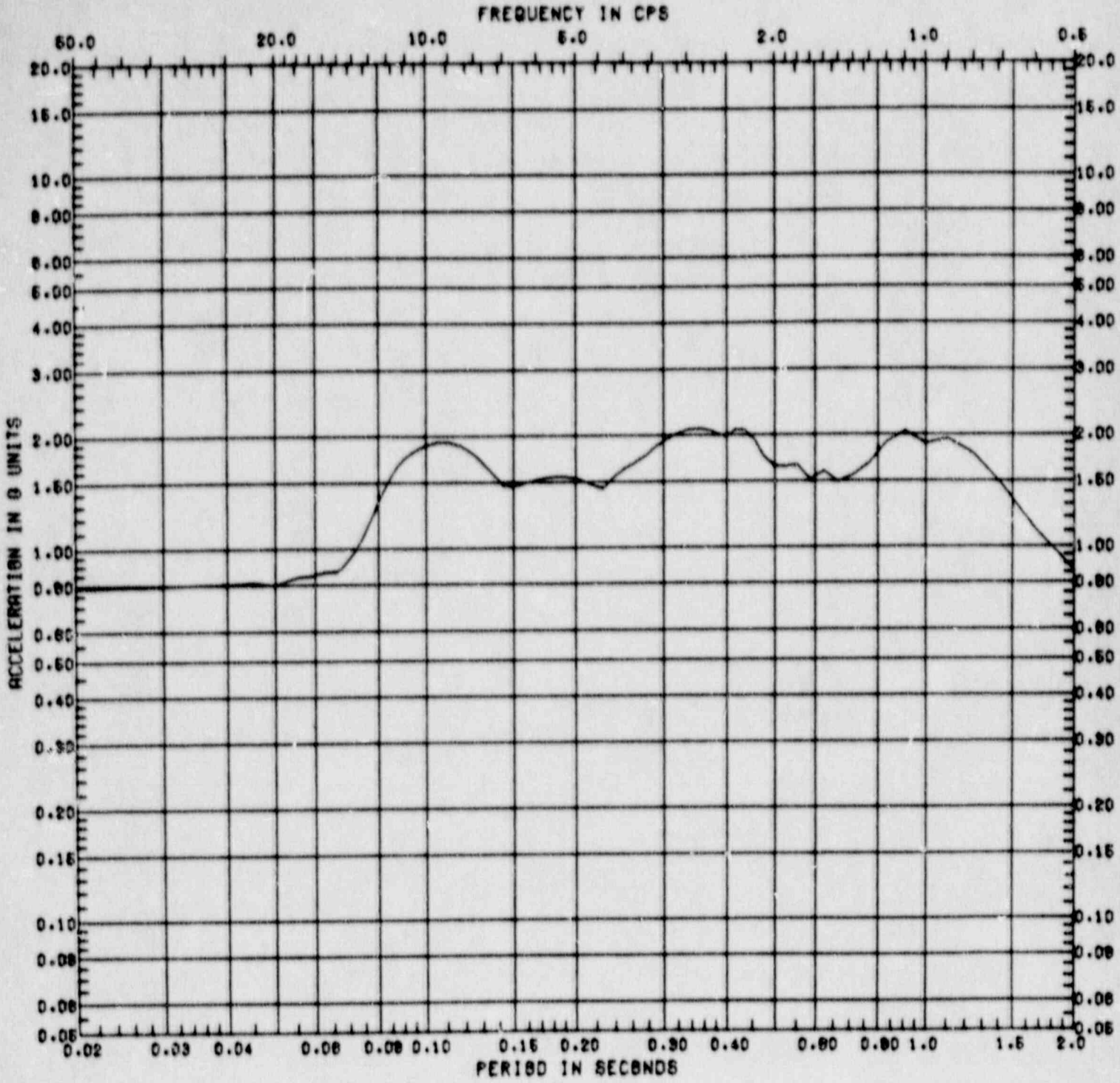

Figure C.3-35 Horizontal Response Spectrum at Zion Model Node 7 (A_H = 1.0g, Damping = 5%, Location = Containment Wall at Elevation 628')

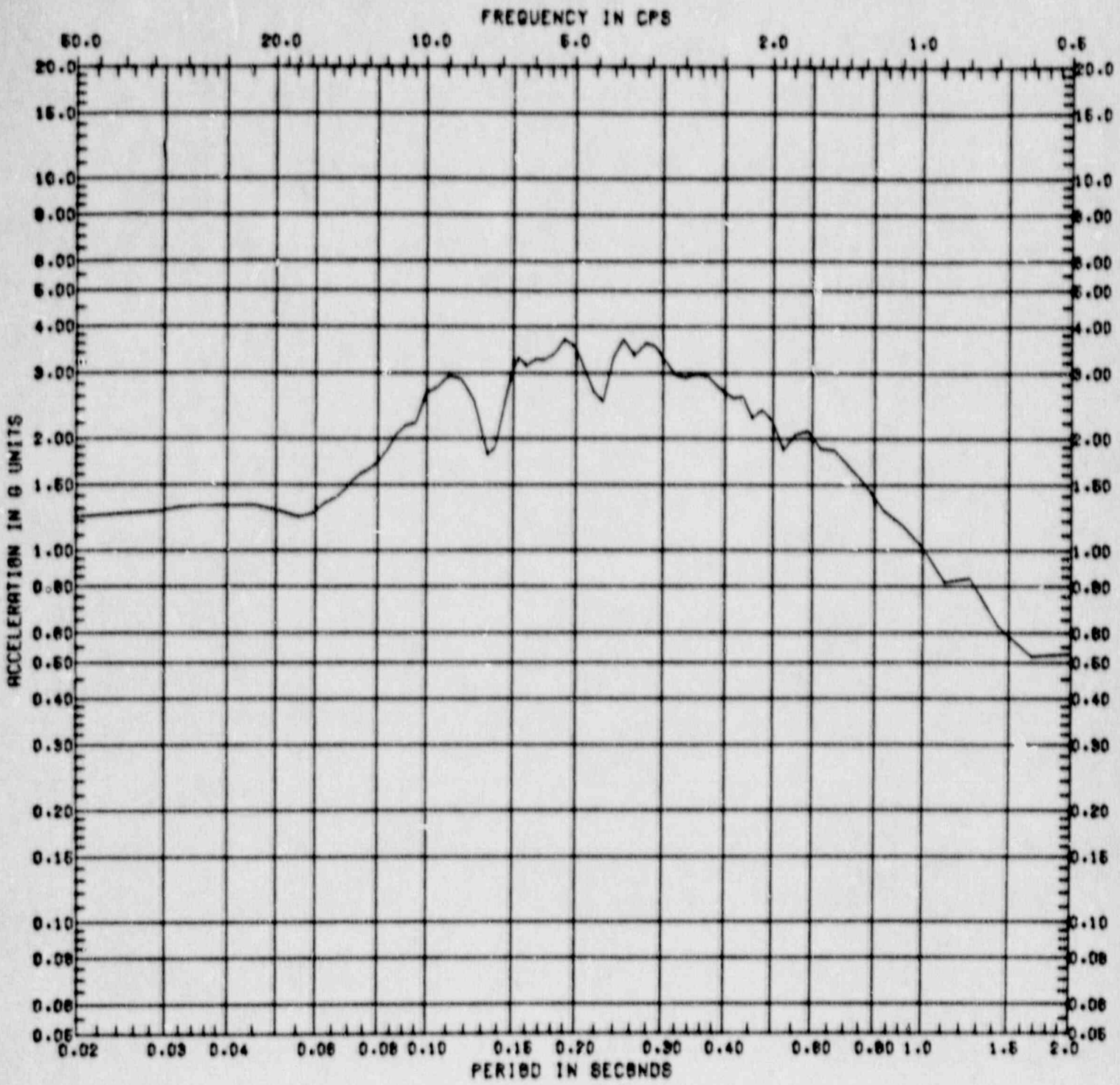

Figure C.3-36 Vertical Response Spectrum at Zion Model Node 7 (A_H = 1.0g, Damping = 5%, Location = Containment Wall at Elevation 628')

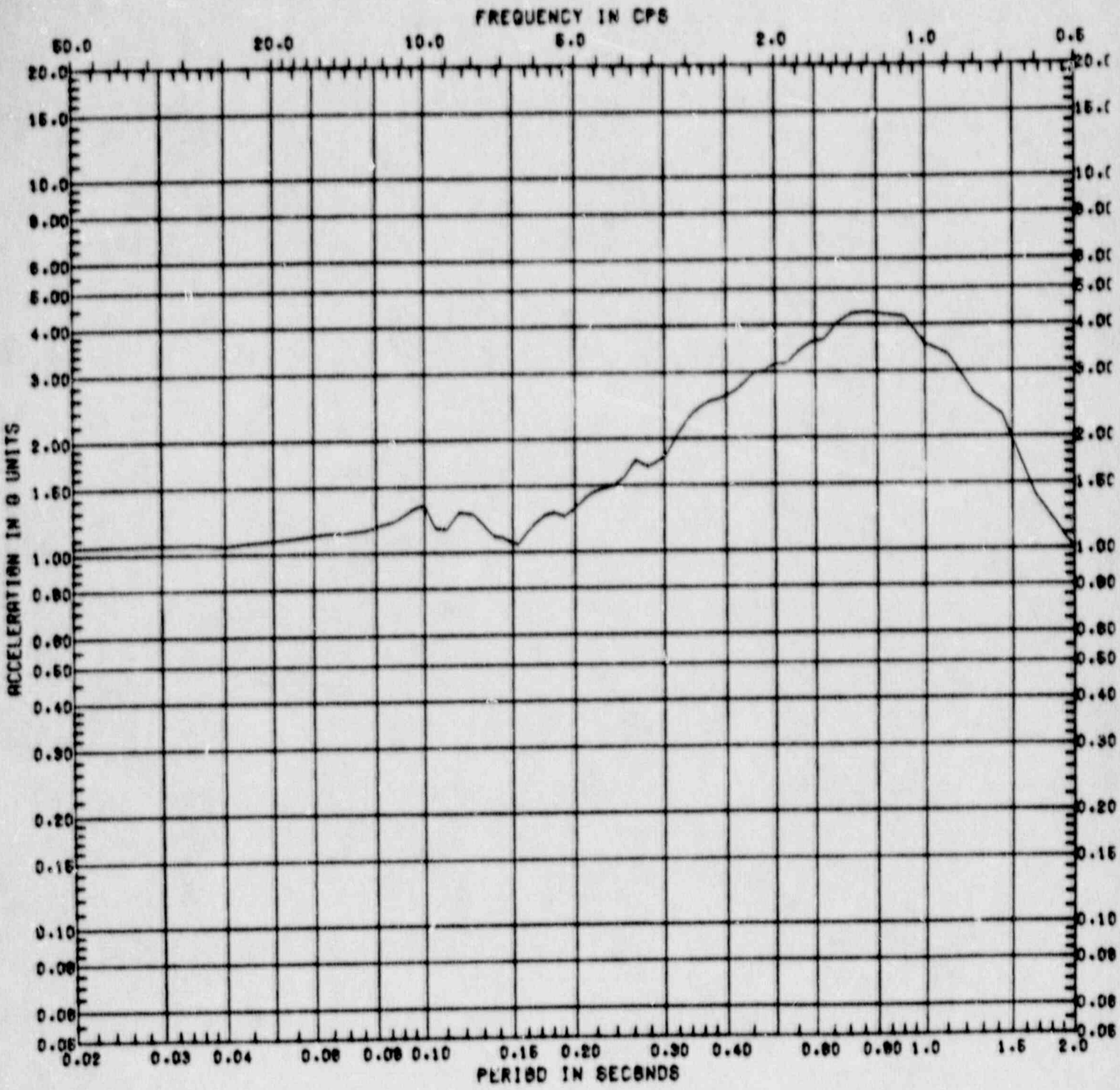

Figure C.3-37 Horizontal Response Spectrum at Zion Model Node 1 (A_H = 1.0g, Damping = 5%, Location = Containment Wall at Elevation 755')

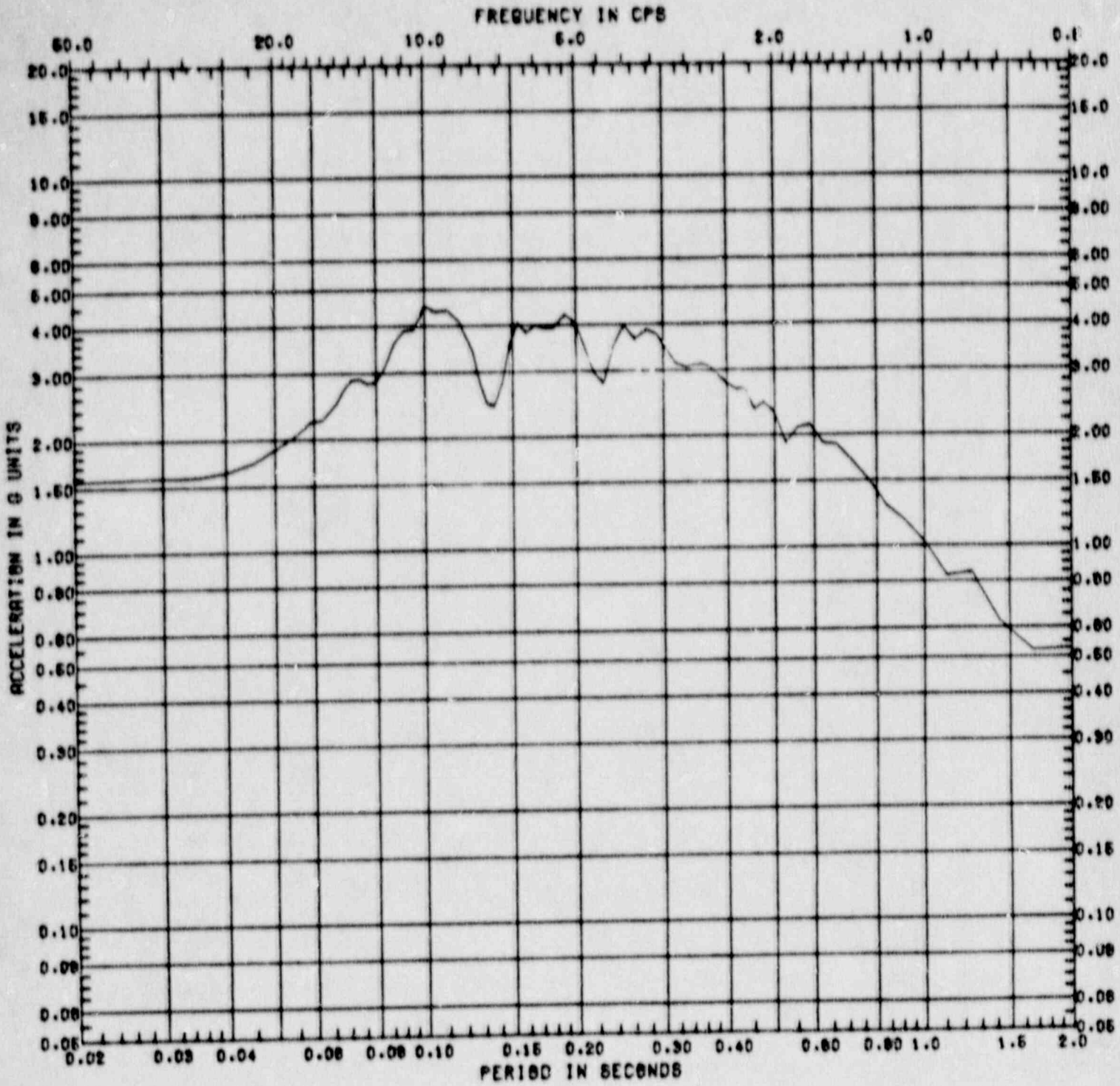

Figure C.3-38 Vertical Response Spectrum at Zion Model Node 1 (A_H = 1.0g, Damping = 5%, Location = Containment Wall at Elevation 755')

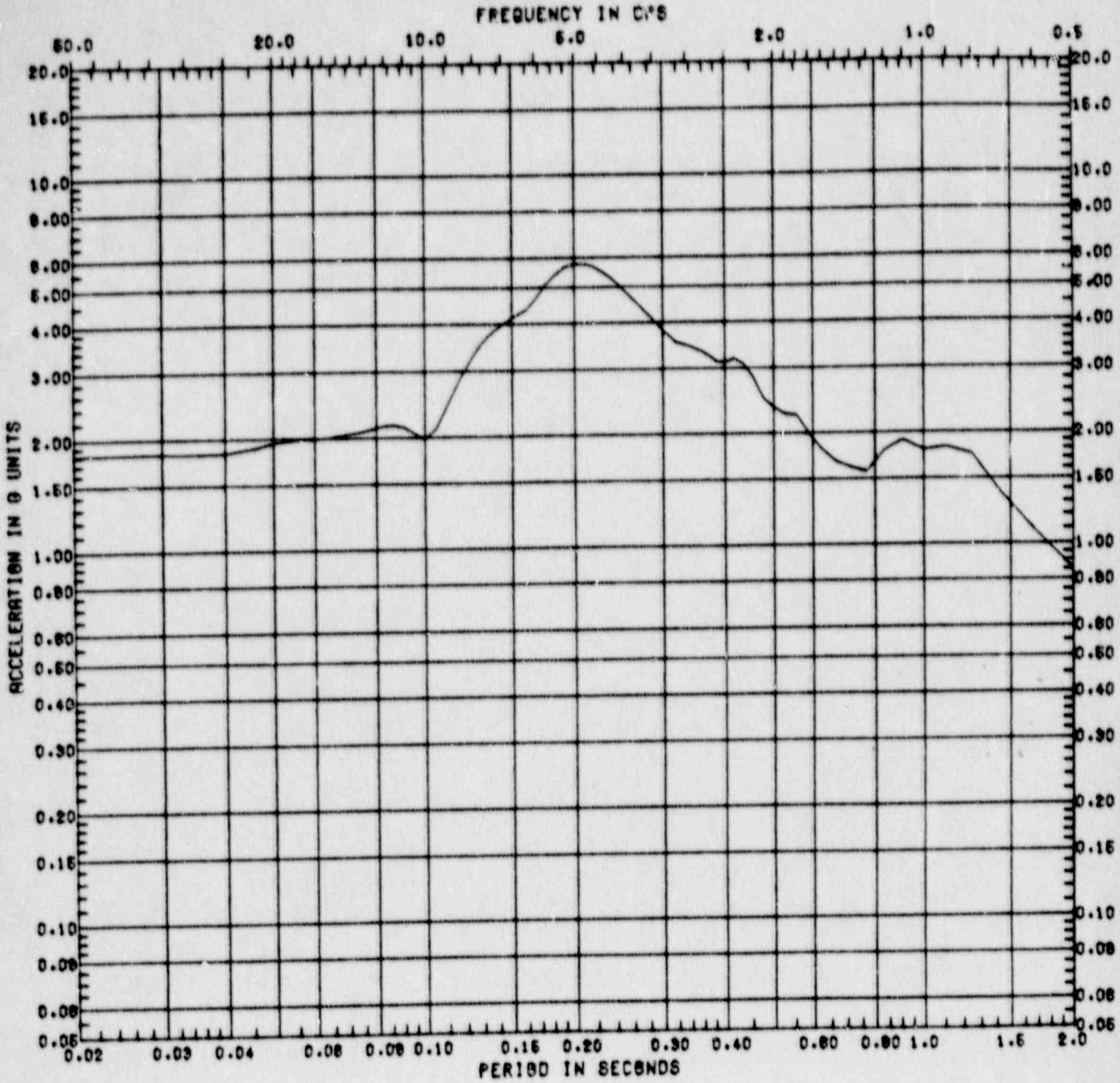

Figure C.3-39 Horizontal Response Spectrum at Zion Model Node 53 (A_H = 1.0g, Damping = 5%, Location = Crane Wall at Elevation 617')

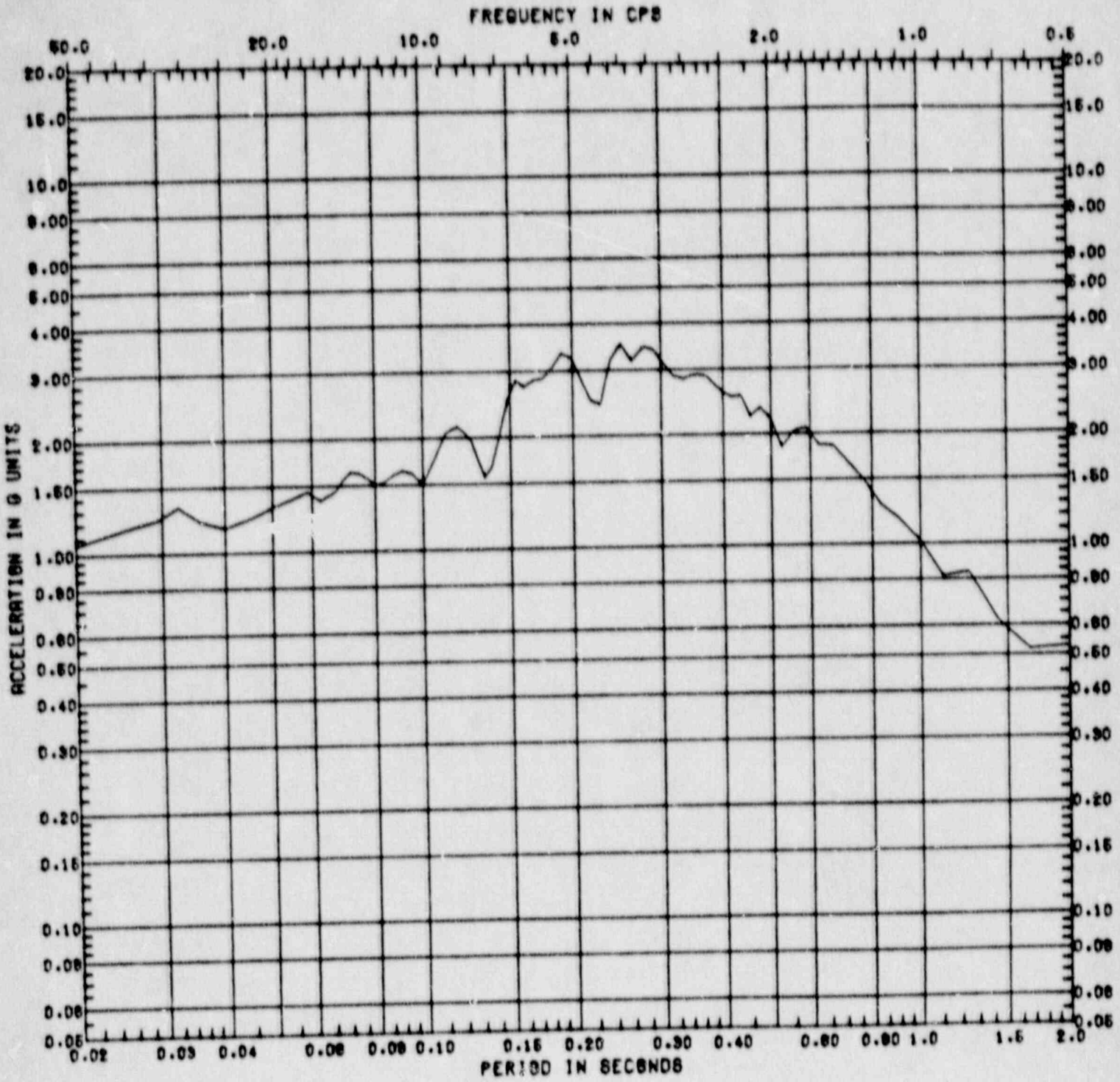

Figure C.3-40 Vertical Response Spectrum at Zion Model Node 53 (A_H = 1.0g, Damping = 5%, Location = Crane Wall at Elevation 617')

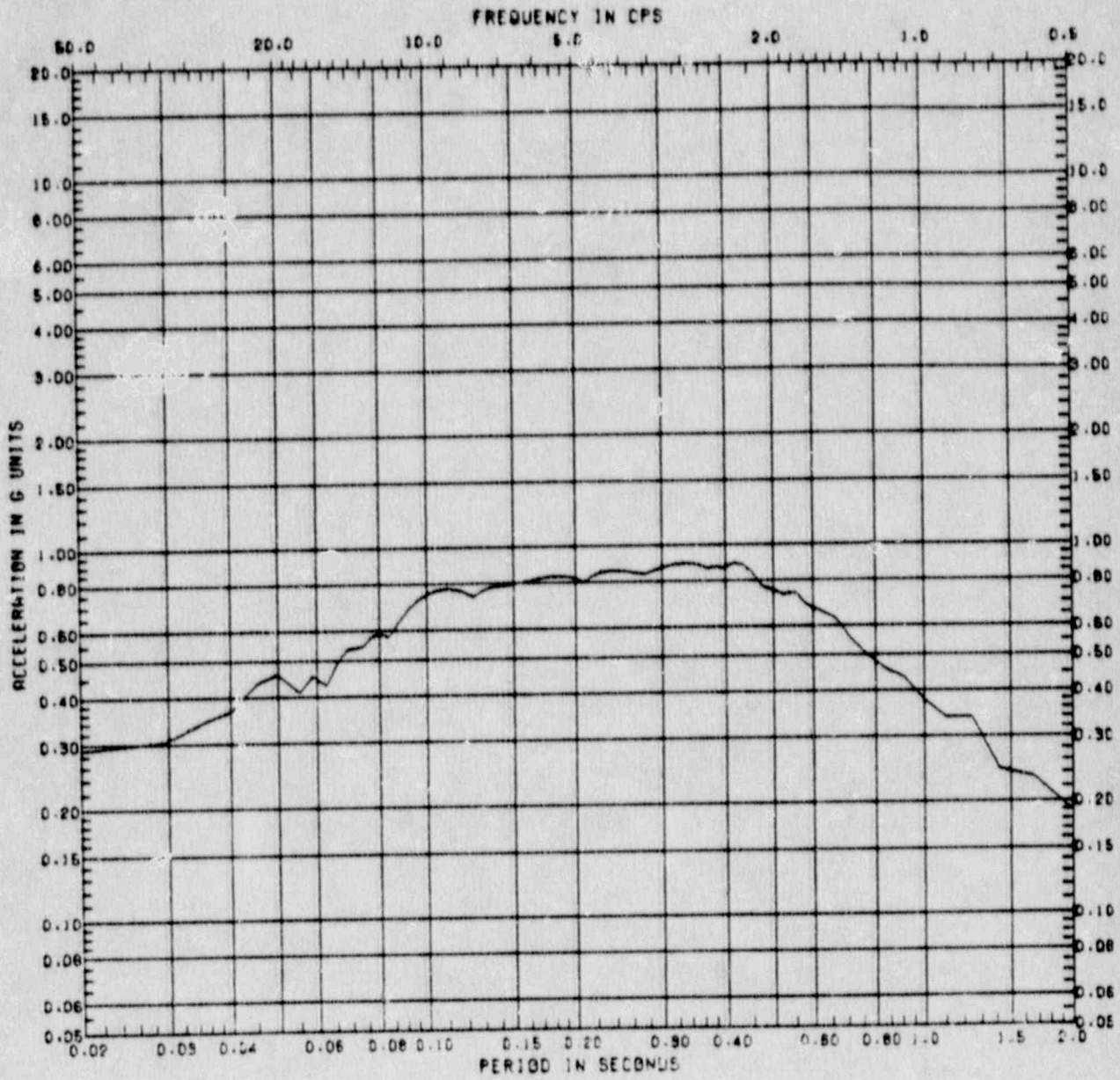

Figure C.4-1 Horizontal Response Spectrum at Sequoyah Model Node 84 (A_H = 0.25g, Damping = 5%, Location = Containment Basemat, Elevation 677')

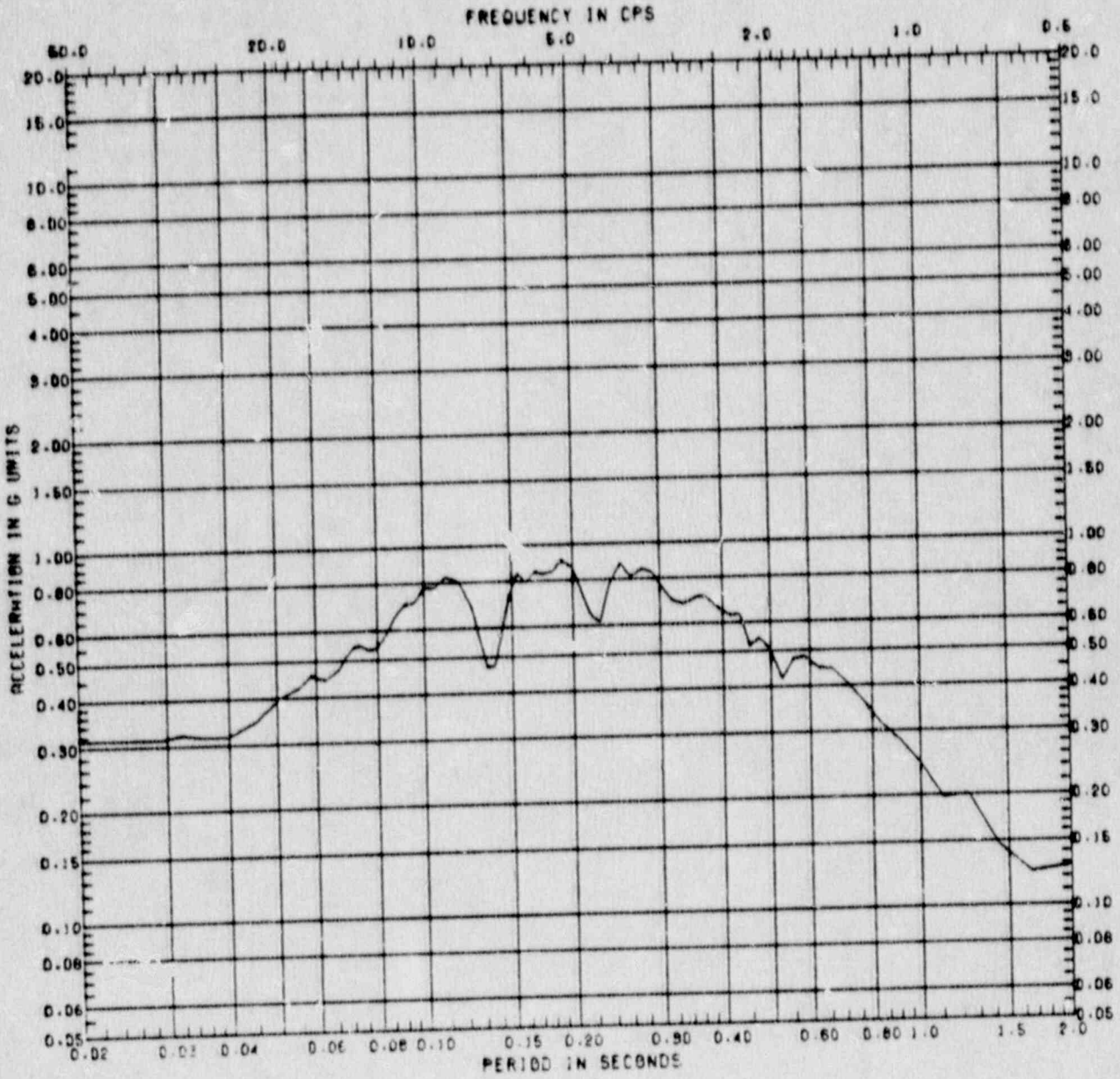

Figure C.4-2 Vertical Response Spectrum at Sequoyah Model Node 84 (A_H = 0.25g, Damping = 5%, Location = Containment Basemat, Elevation 677')

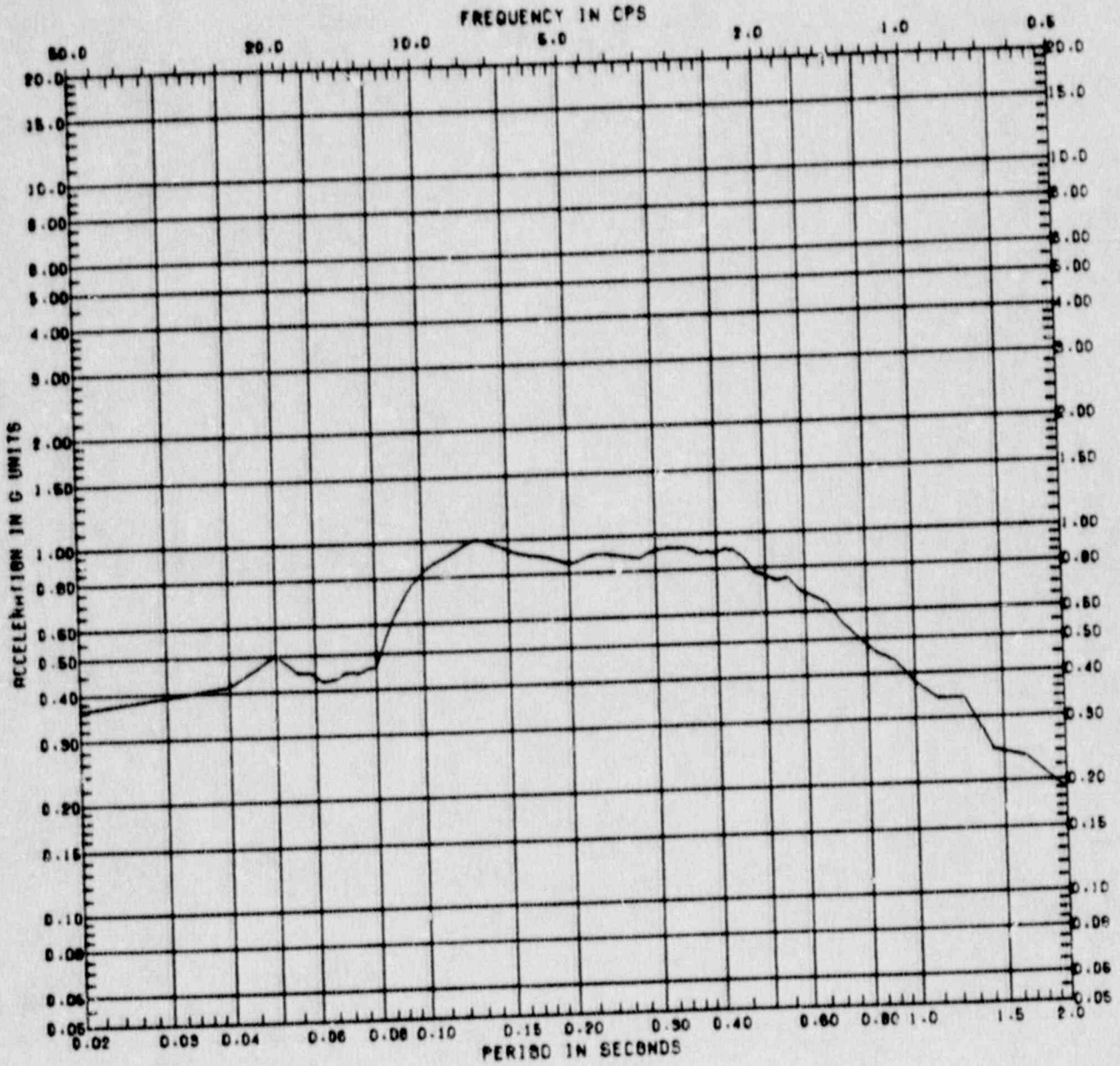

Figure C.4-3 Horizontal Response Spectrum at Sequoyah Model Node 56 (A_H = 0.25g, Damping = 5%, Location = Steel Containment at Elevation 700')

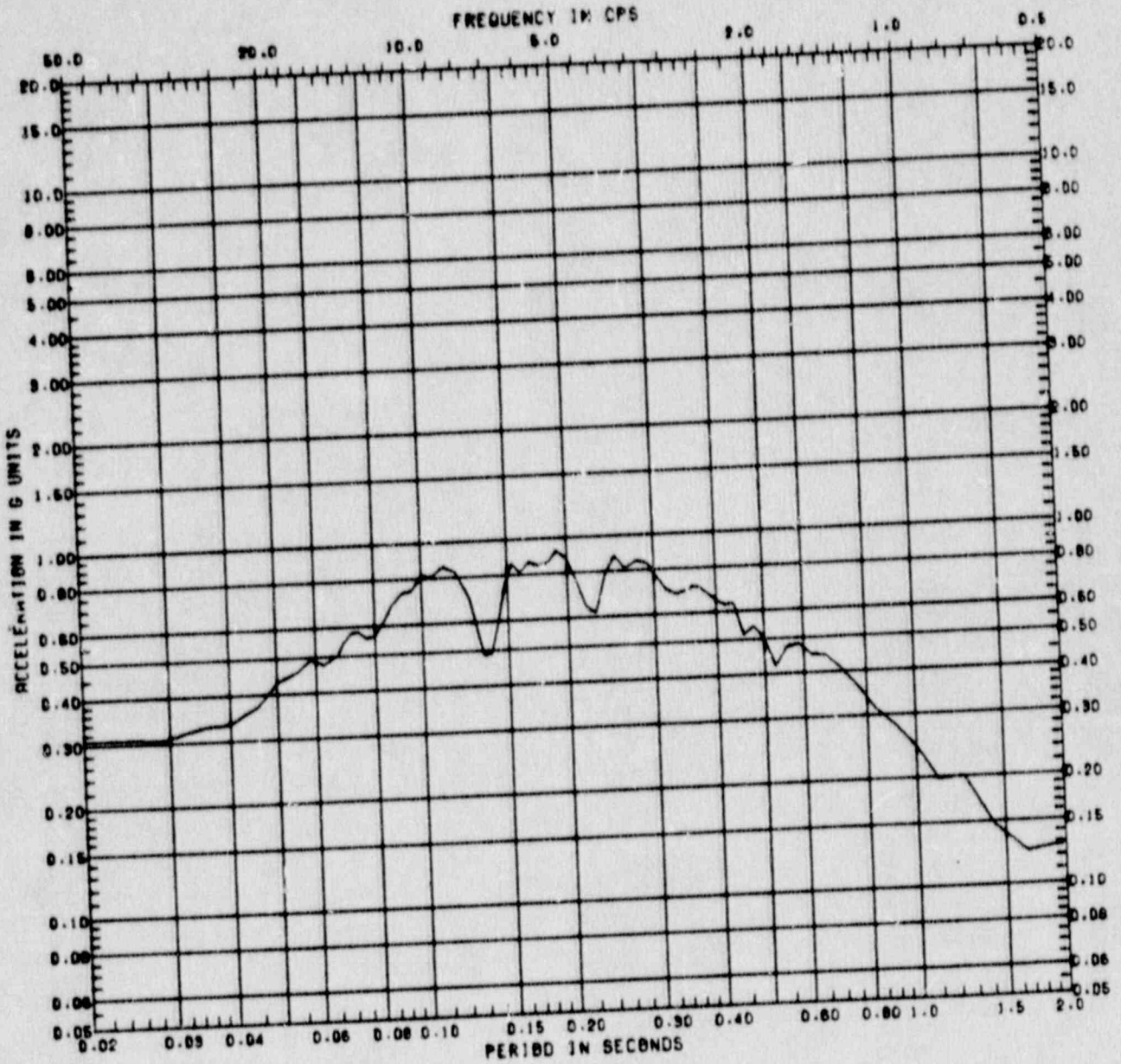

Figure C.4-4 Vertical Response Spectrum at Sequoyah Model Node 56 (A_H = 0.25g, Damping = 5%, Location = Steel Containment at Elevation 700')

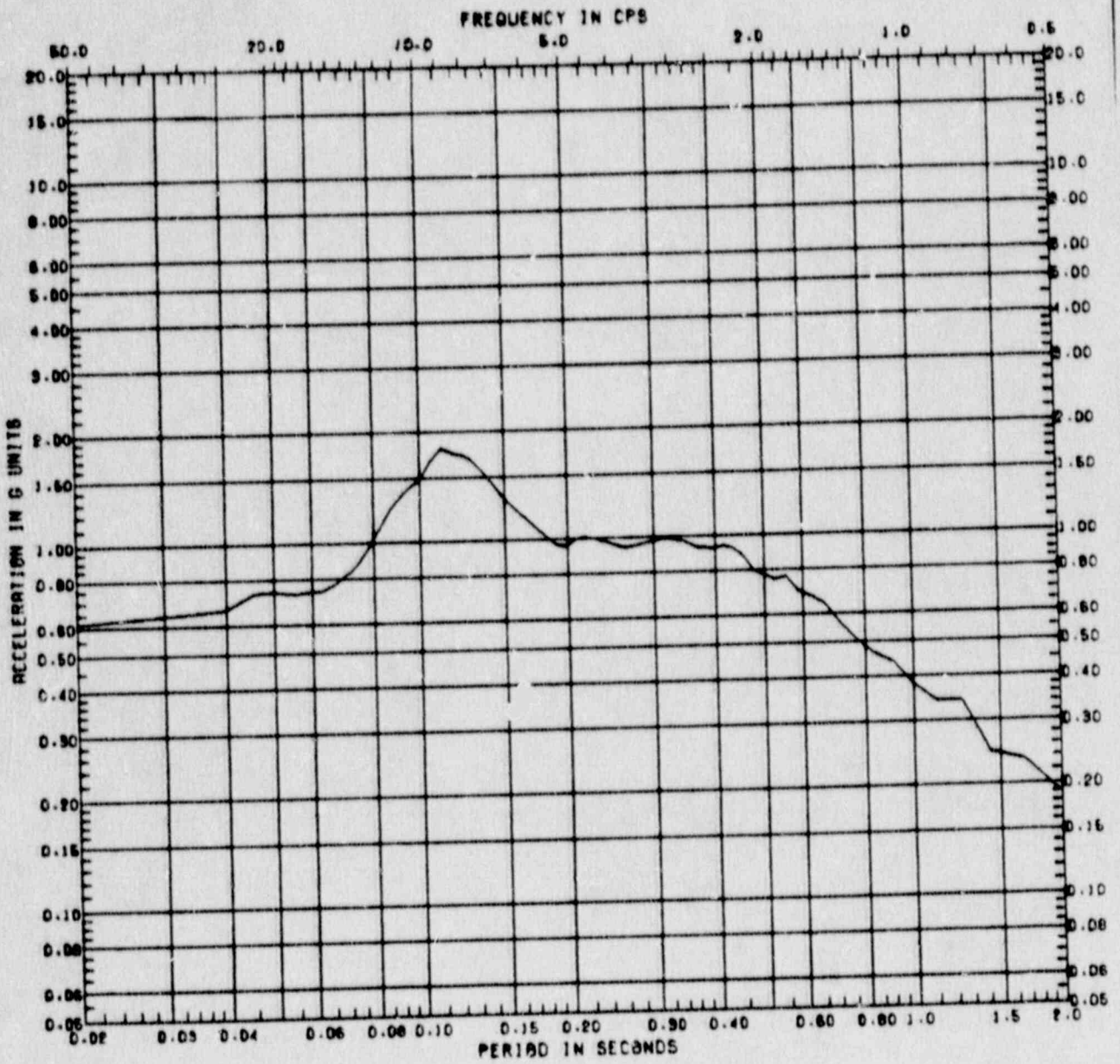

Figure C.4-5 Horizontal Response Spectrum at Sequoyah Model Node 29 (A_H = 0.25g, Damping = 5%, Location = Steel Containment at Elevation 743')

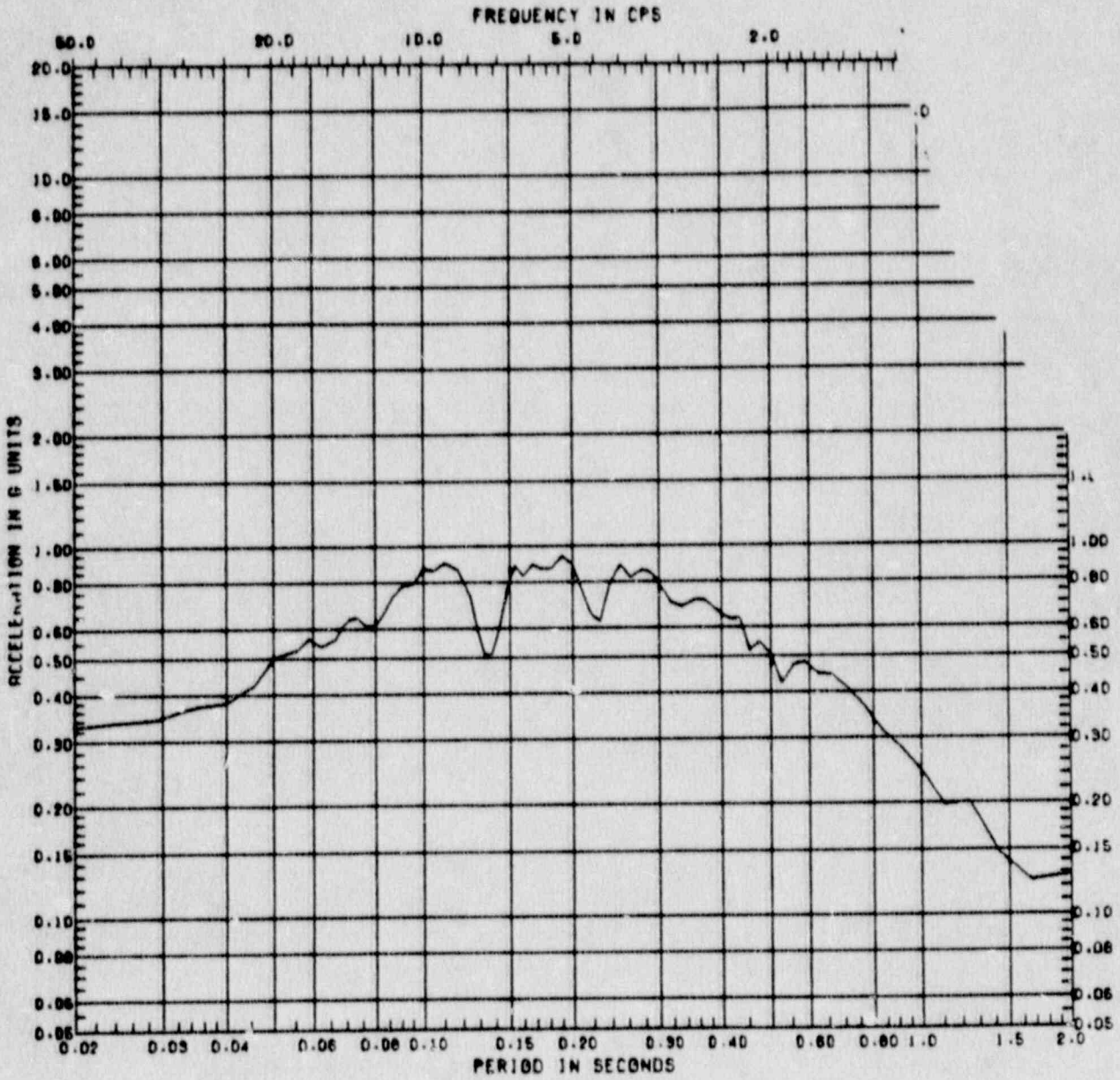

Figure C.4-6 Vertical Response Spectrum at Sequoyah Model Node 29 (A_H = 0.25g, Damping = 5%, Location = Steel Containment Wall at Elevation 743')

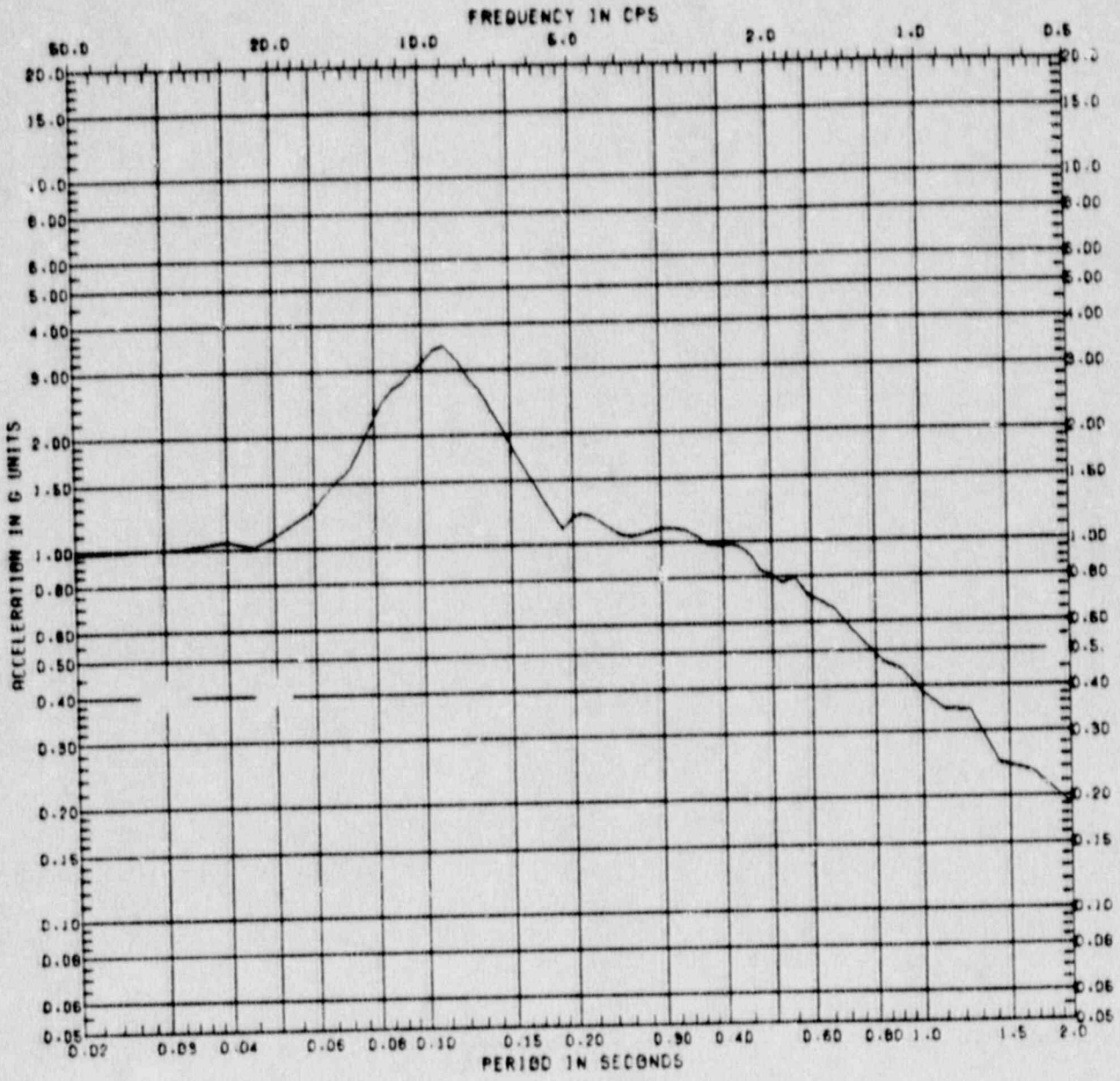

Figure C.4-7 Horizontal Response Spectrum at Sequoyah Model Node 6 (A_H = 0.25g, Damping = 5%, Location = Steel Containment at Elevation 813')

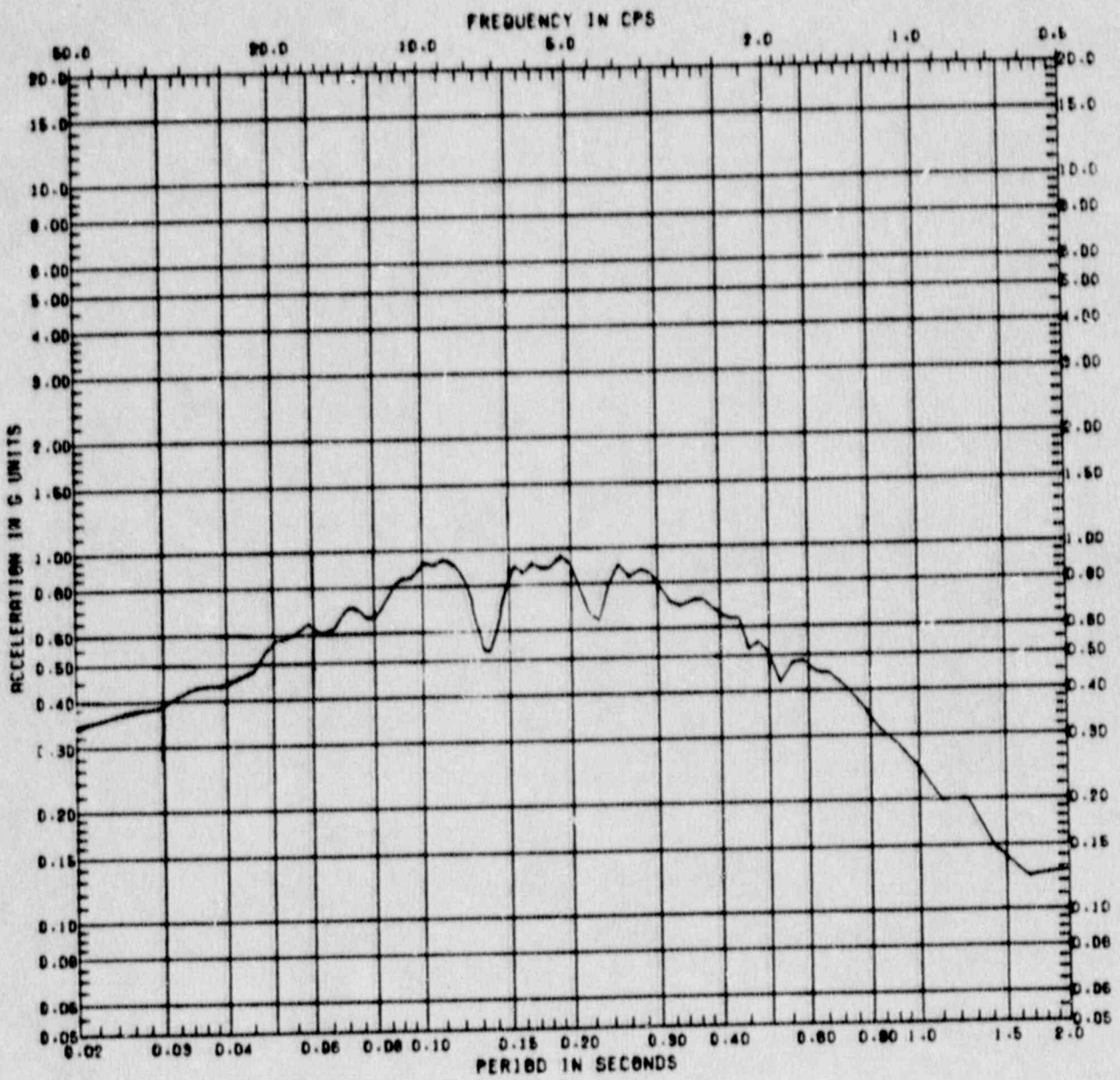

Figure C.4-8 Vertical Response Spectrum at Sequoyah Model Node 6 (A_H = 0.25g, Damping = 5%, Location = Steel Containment at Elevation 813')

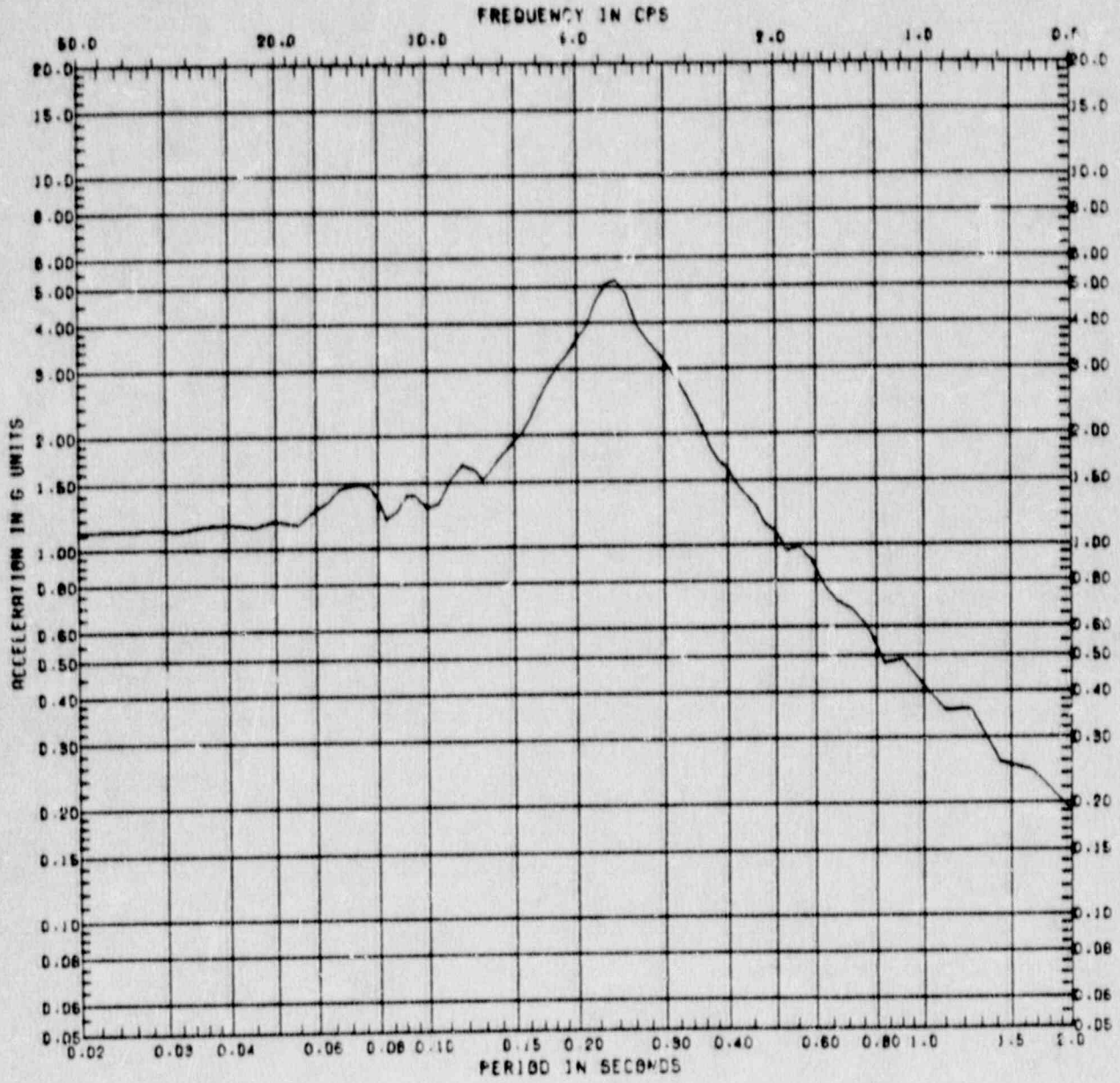

Figure C.4-9 Horizontal Response Spectrum at Sequoyah Model Node 5 (A_H = 0.25g, Damping = 5%, Location = Top of Shield Building, at Elevation 828')

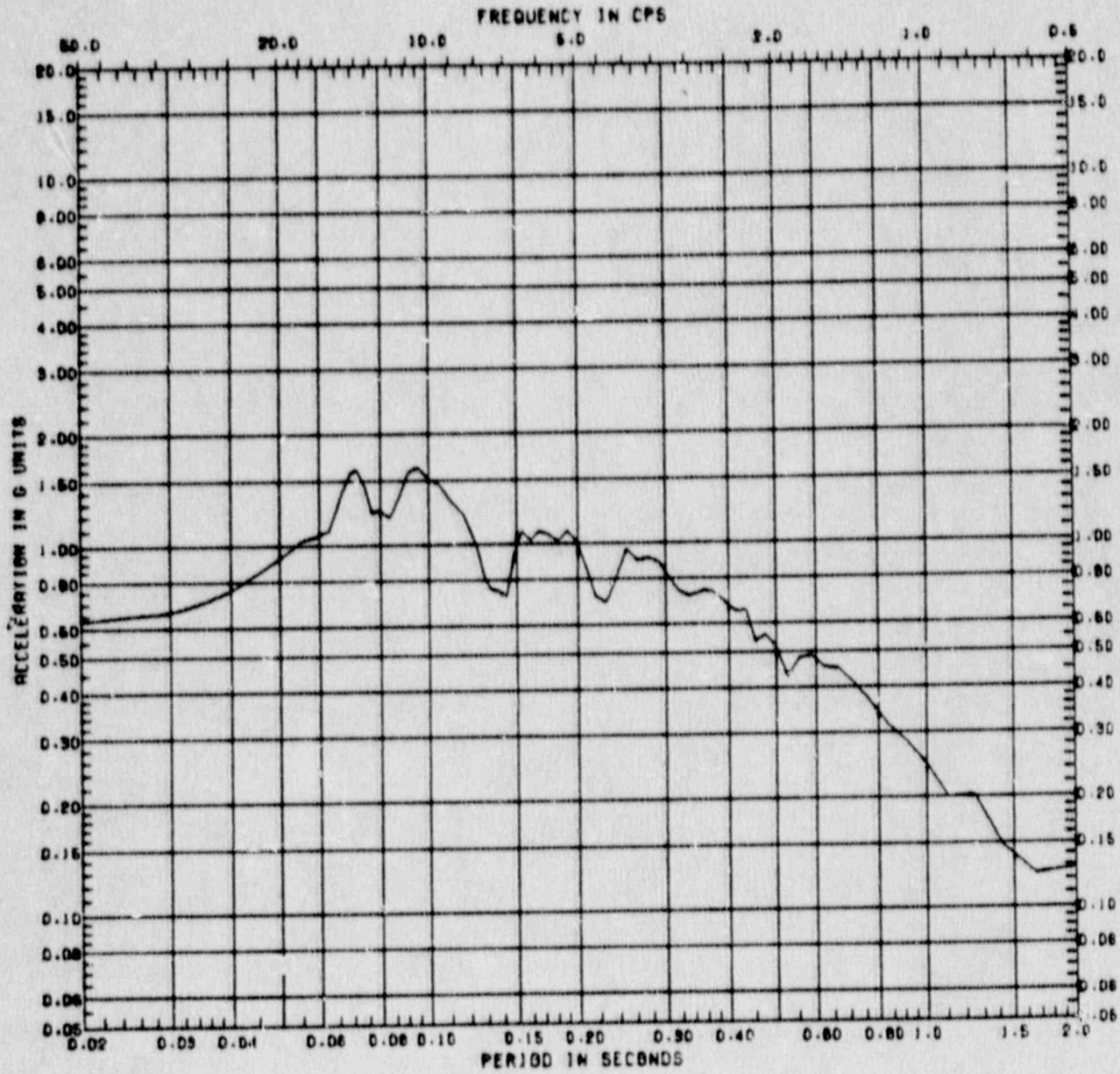

Figure C.4-10 Vertical Response Spectrum at Sequoyah Model Node 5 (A_H = 0.25g, Damping = 5%, Location = Top of Shield Building at Elevation 828')

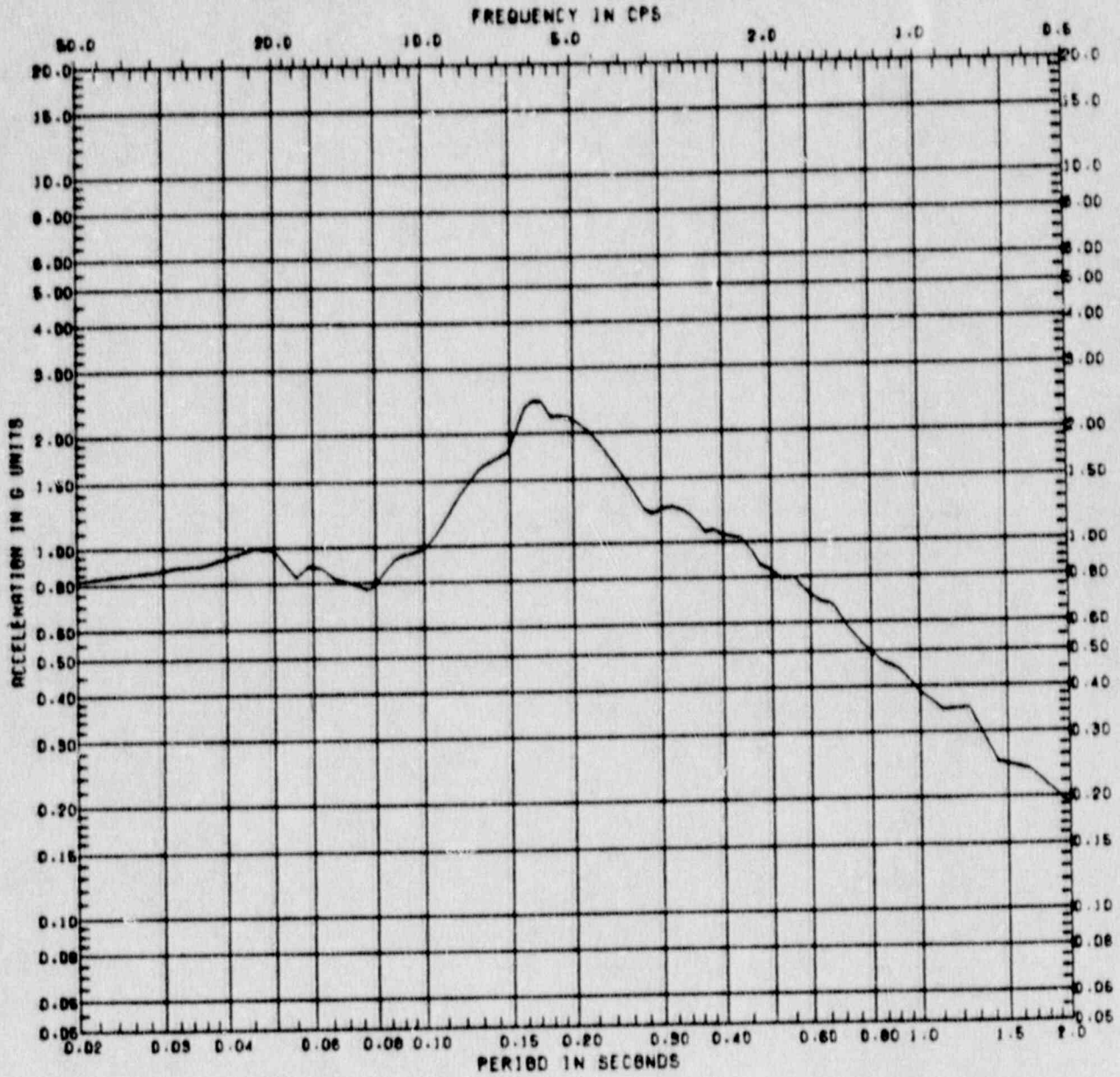

Figure C.4-11 Horizontal Response Spectrum at Sequoyah Model Node 48 (A_H = 0.25g, Damping = 5%, Location = Crane Wall at Elevation 738')

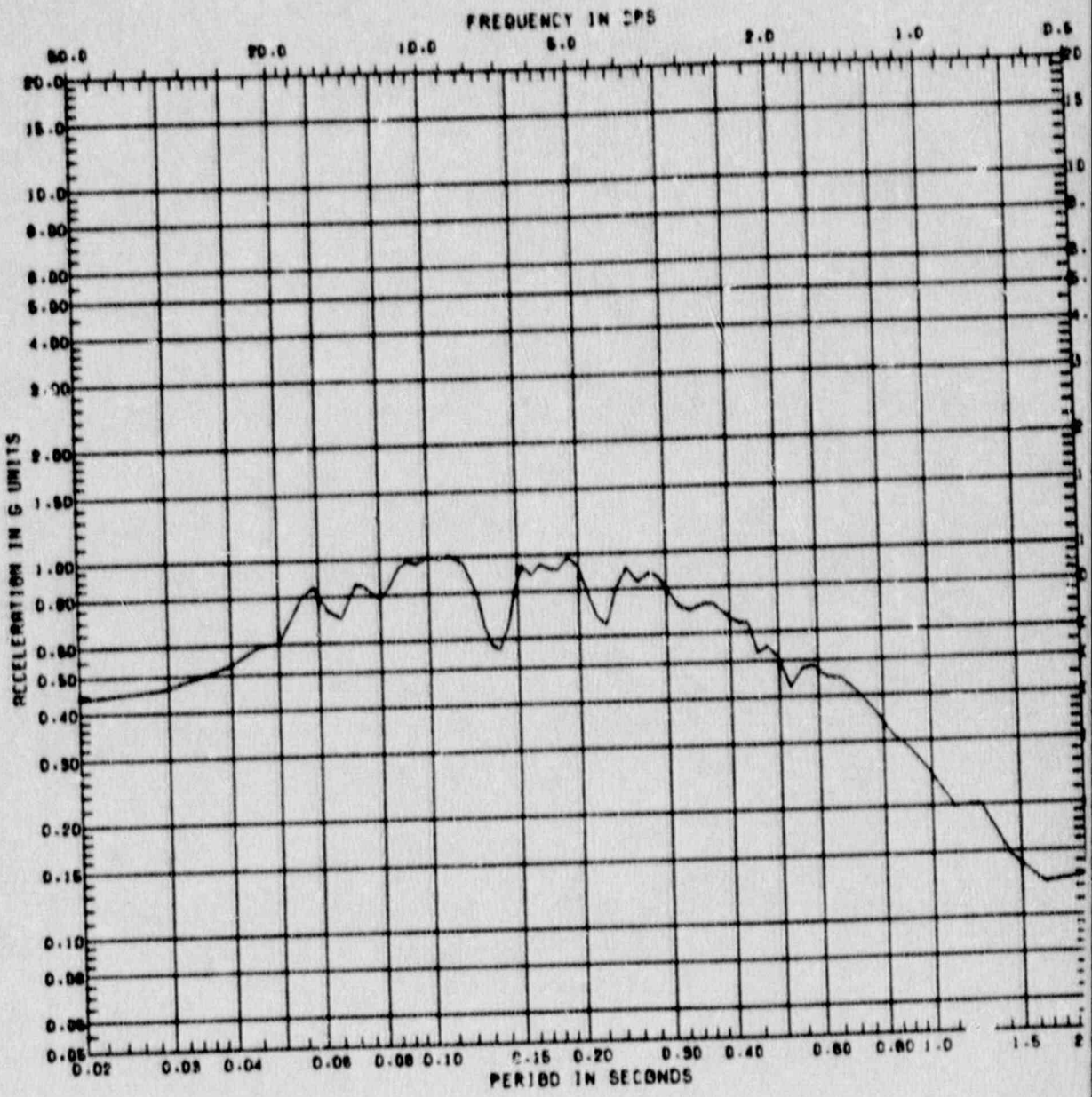

Figure C.4-12 Vertical Response Spectrum at Sequoyah Model N
(A_H = 0.25g, Damping = 5%, Location = Crane Wa
Elevation 738')

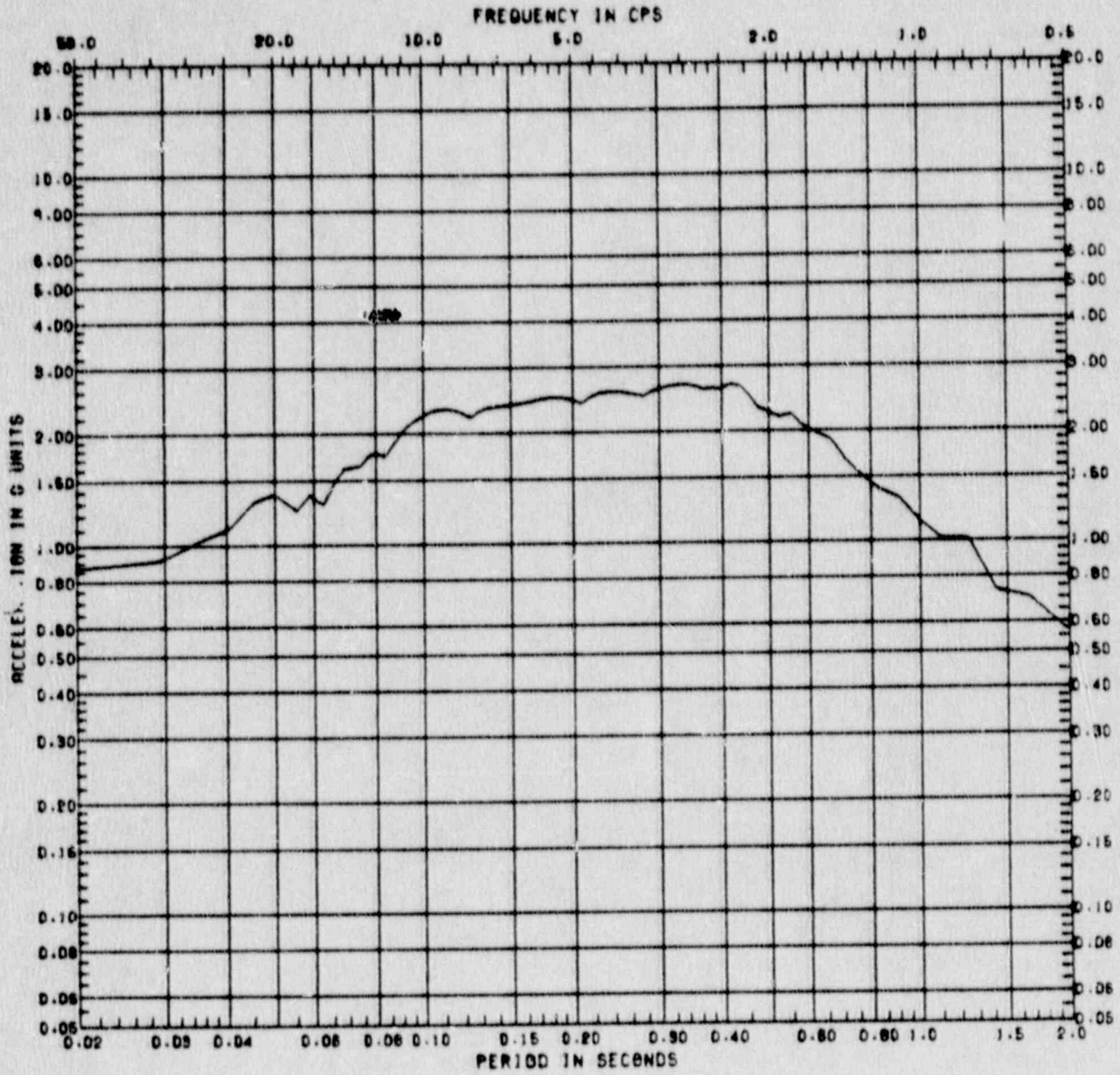

Figure C.4-13 Horizontal Response Spectrum at Sequoyah Model Node 84 (A_H = 0.75g, Damping = 5%, Location = Containment Basemat, Elevation 677')

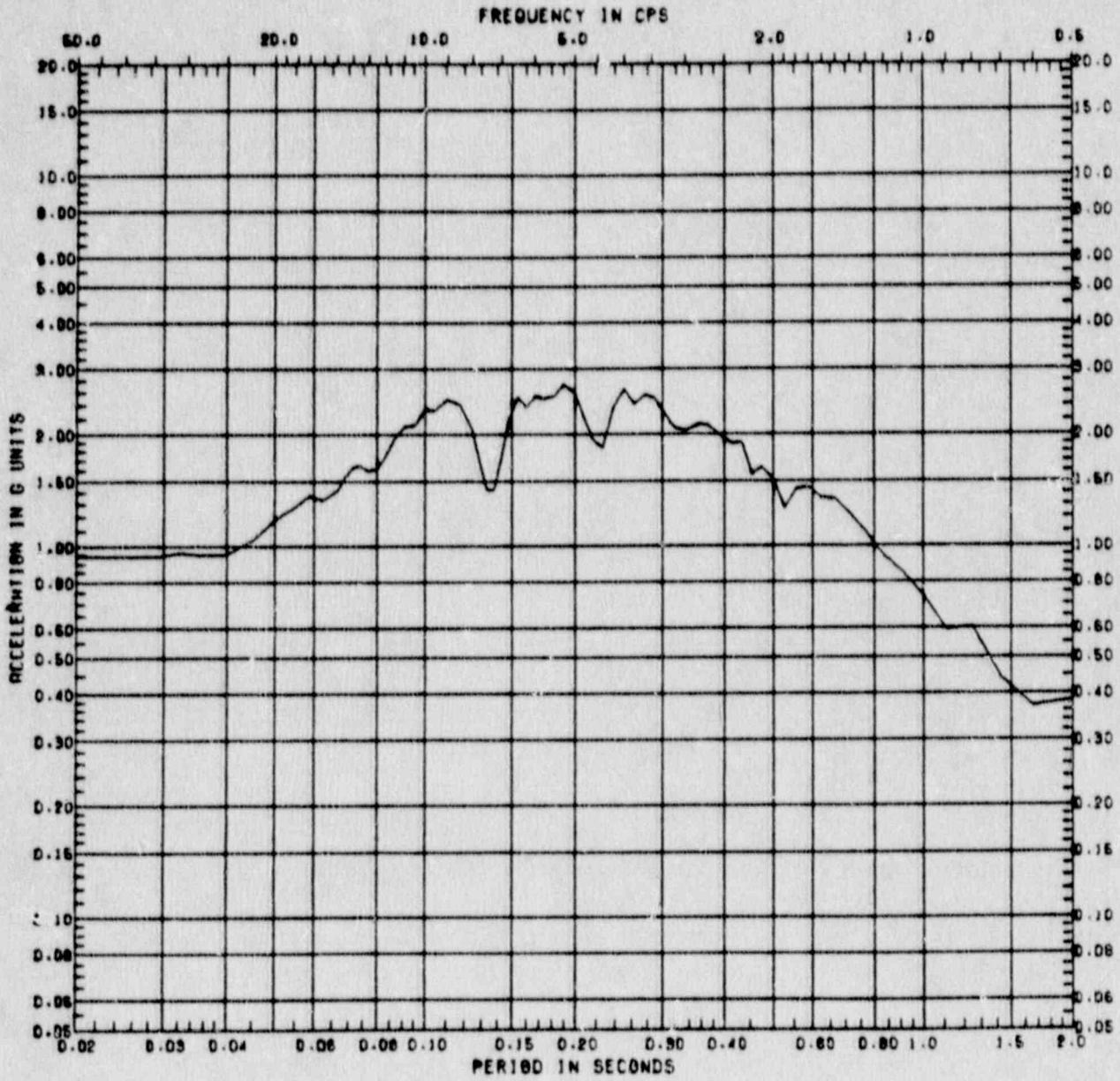

Figure C.4-14 Vertical Response Spectrum at Sequoyah Model Node 84 (A_H = 0.75g, Damping = 5%, Location = Containment Basemat, Elevation 677')

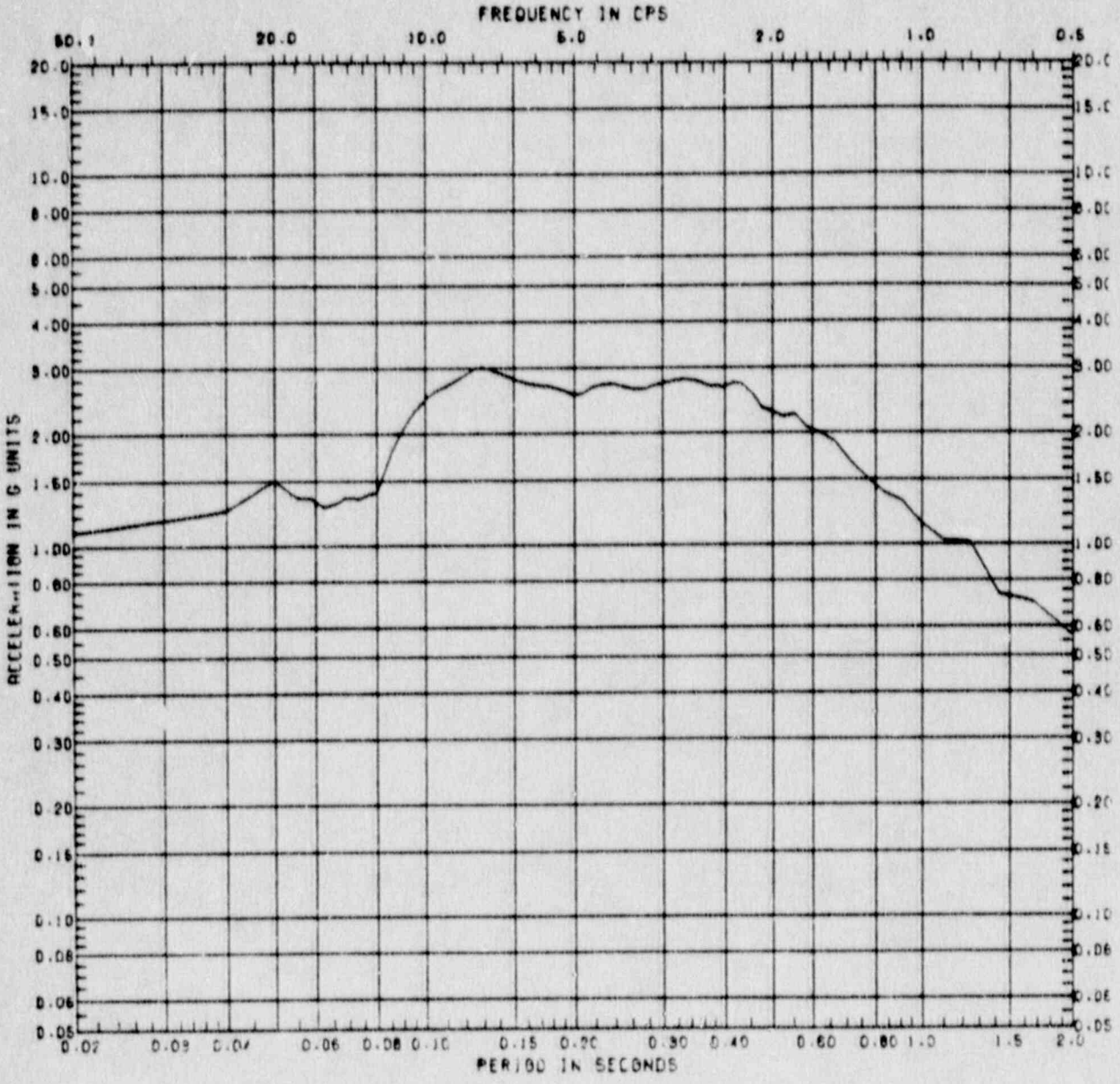

Figure C.4-15 Horizontal Response Spectrum at Sequoyah Model Node 56 (A_H = 0.75g, Damping = 5%, Location = Steel Containment at Elevation 700')

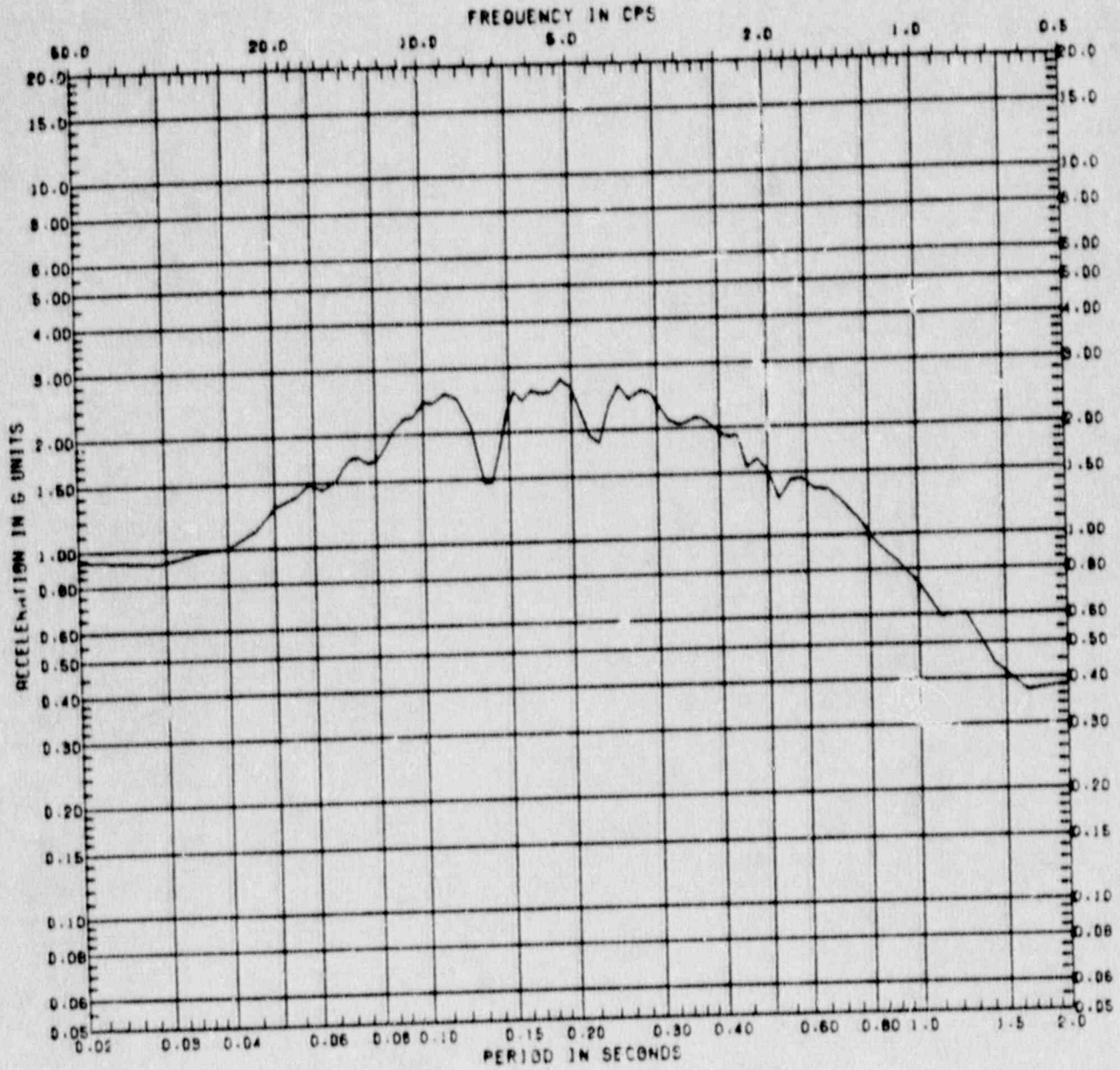

Figure C.4-16 Vertical Response Spectrum at Sequoyah Model Node 56 (A_H = 0.75g, Damping = 5%, Location = Steel Containment at Elevation 700')

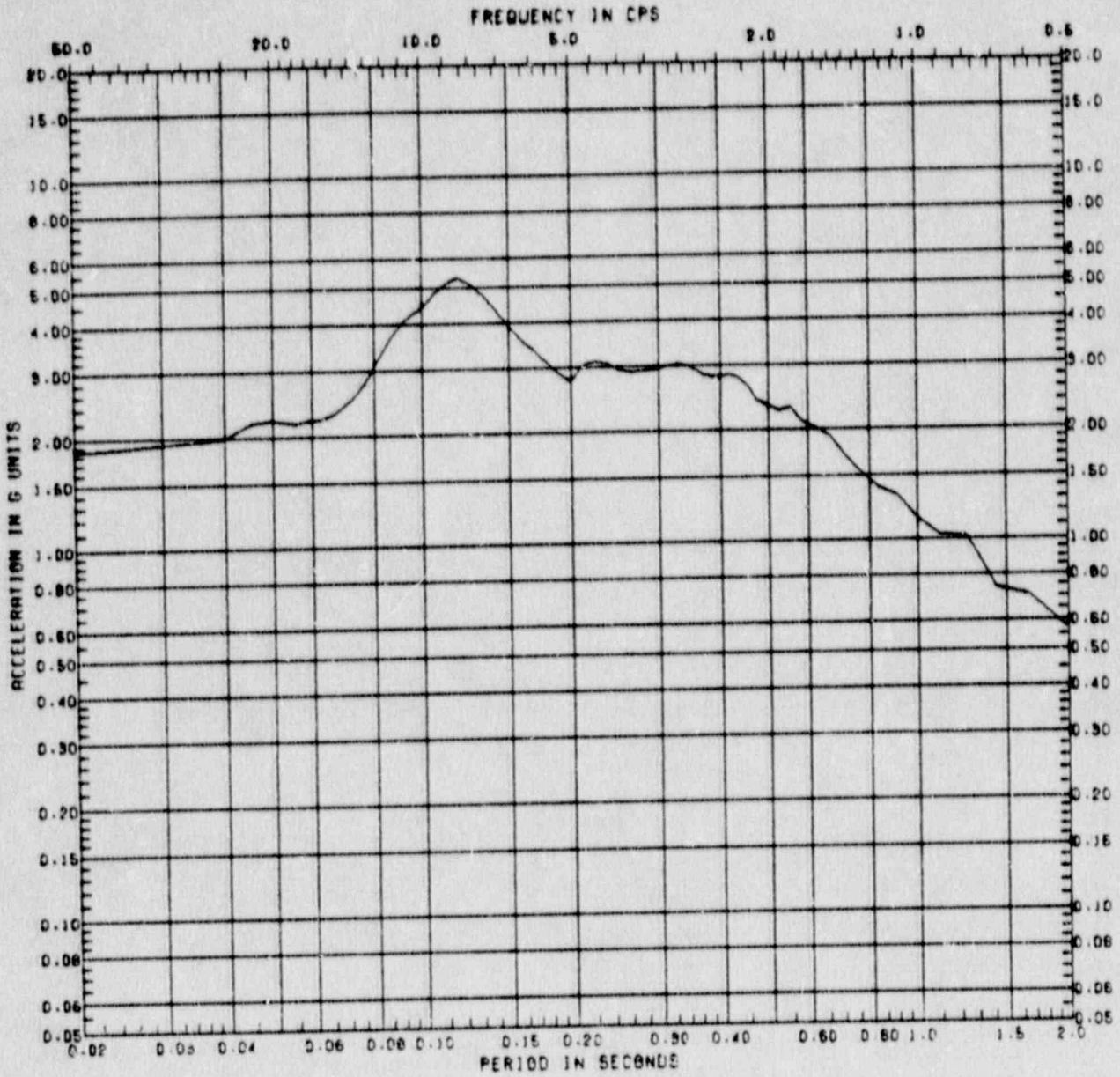

Figure C.4-17 Horizontal Response Spectrum at Sequoyah Model Node 29 (A_H = 0.75g, Damping = 5%, Location = Steel Containment at Elevation 743')

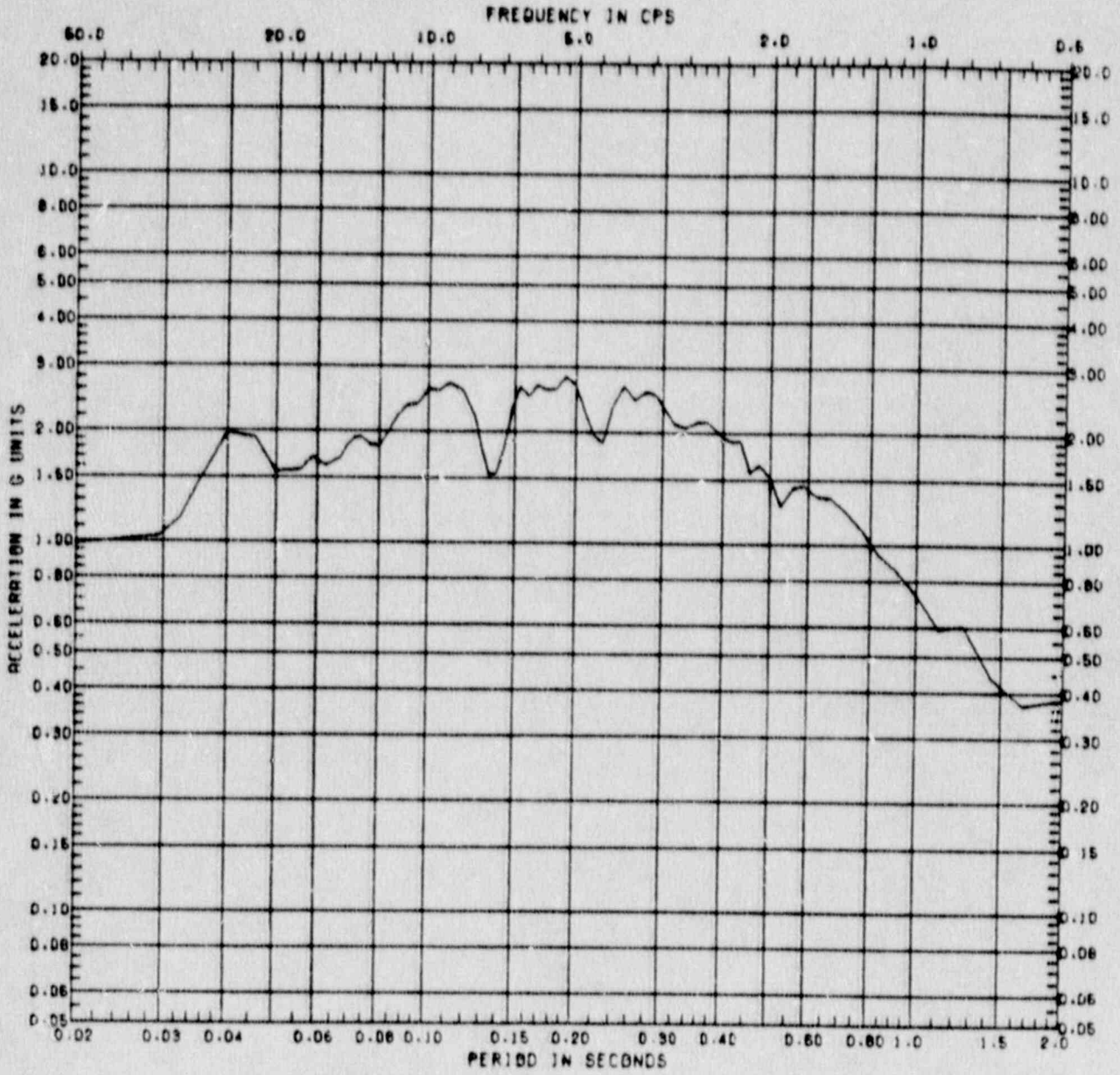

Figure C.4-18 Vertical Response Spectrum at Sequoyah Model Node 29 (A_H = 0.75g, Damping = 5%, Location = Steel Containment Wall at Elevation 743')

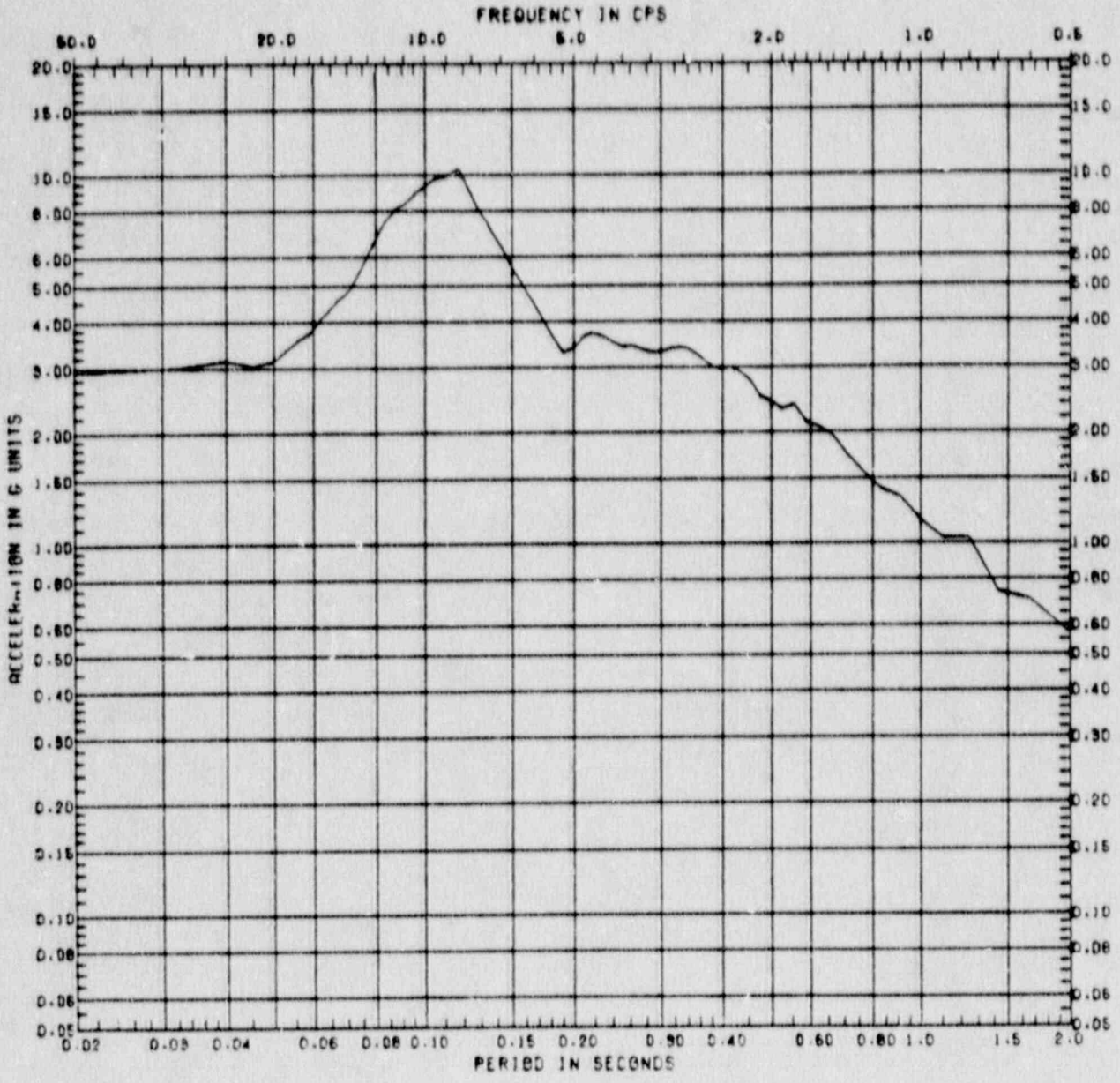

Figure C.4-19 Horizontal Response Spectrum at Sequoyah Model Node 6 (A_H = 0.75g, Damping = 5%, Location = Steel Containment at Elevation 813')

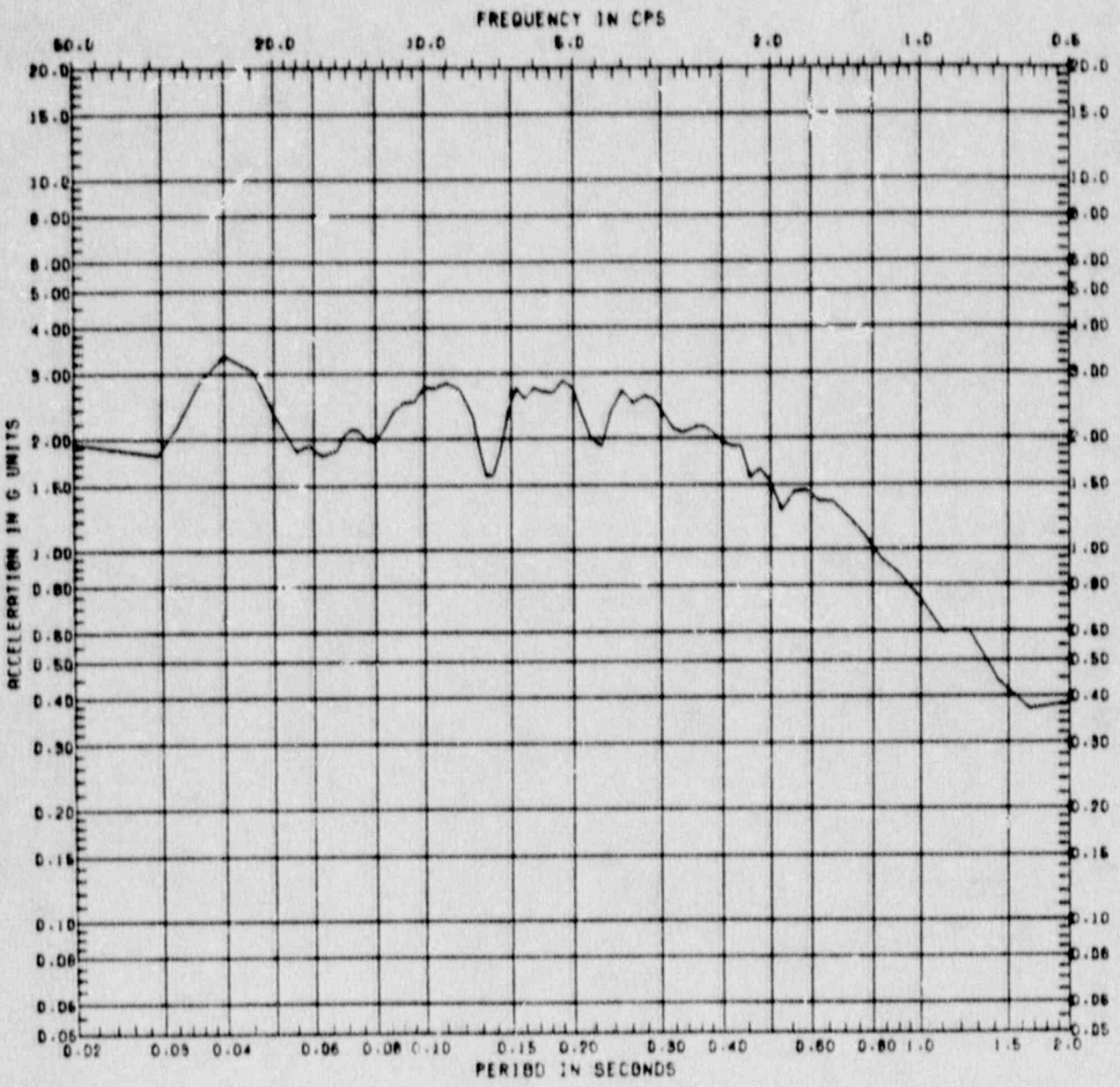

Figure C.4-20 Vertical Response Spectrum at Sequoyah Model Node 6 (A_H = 0.75g, Damping = 5%, Location = Steel Containment at Elevation 813')

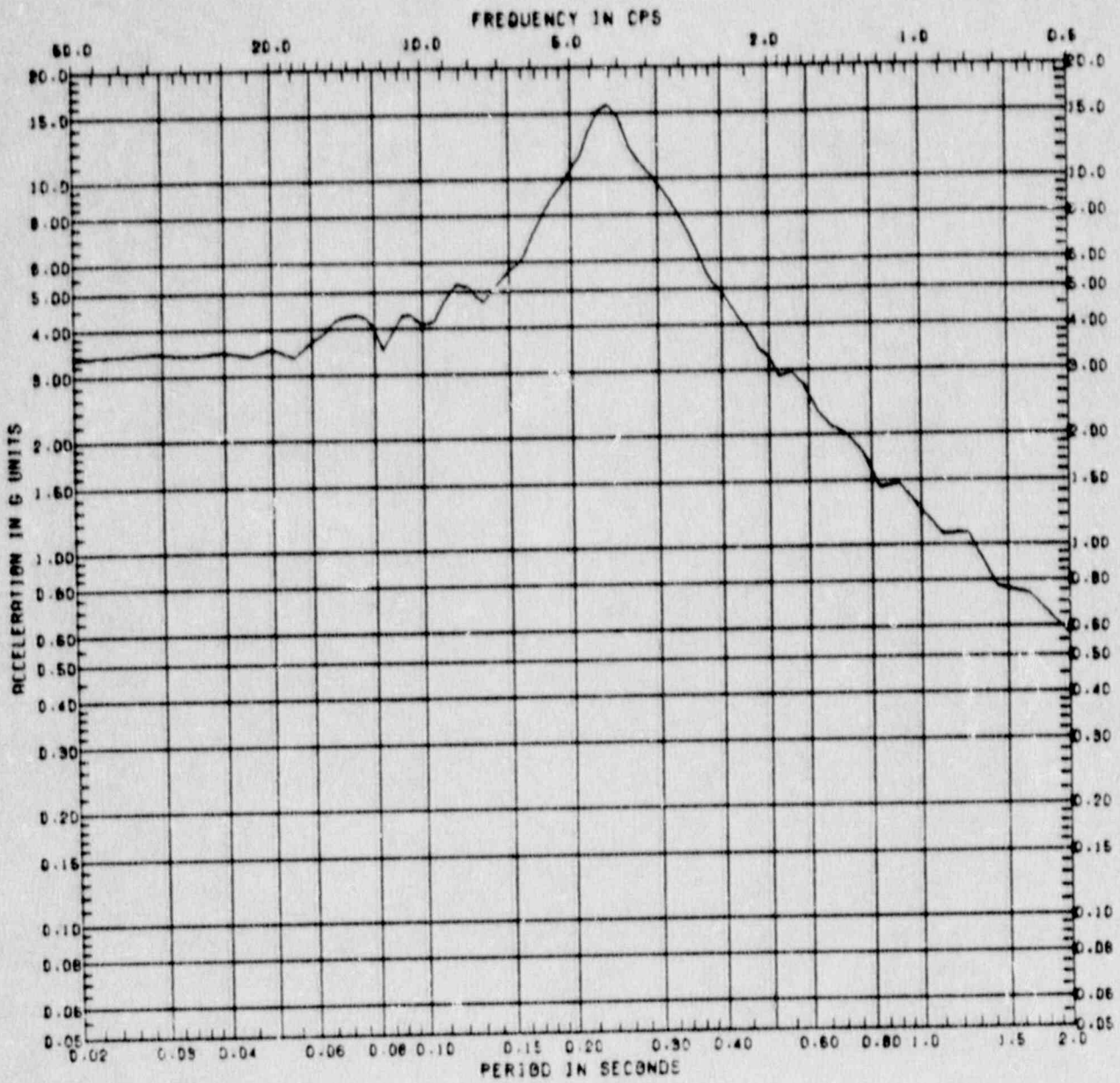

Figure C.4-21 Horizontal Response Spectrum at Sequoyah Model Node 5 (A_H = 0.75g, Damping = 5%, Location = Top of Shield Building, at Elevation 828')

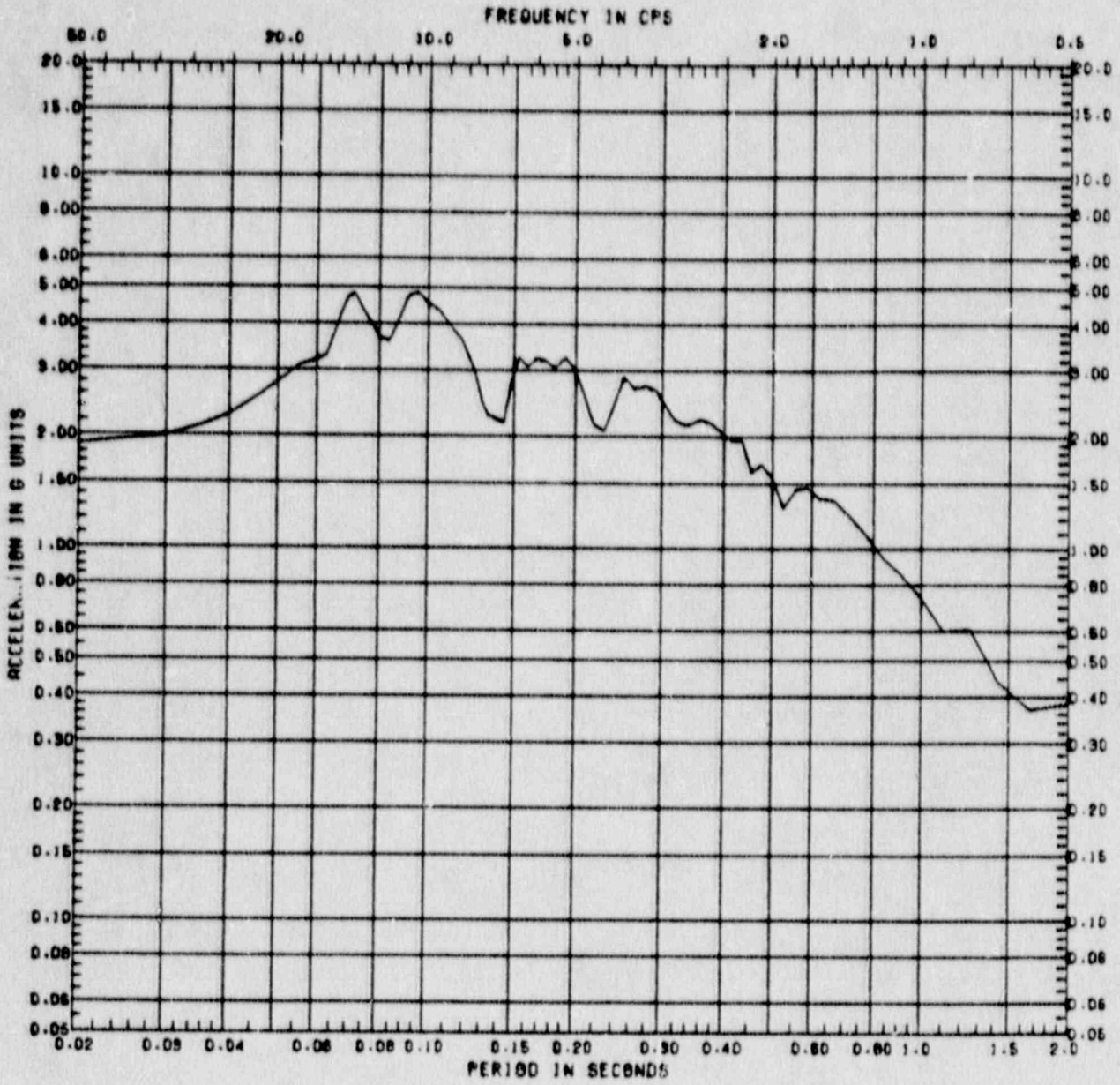

Figure C.4-22 Vertical Response Spectrum at Sequoyah Model Node 5 (A_g = 0.75g, Damping = 5%, Location = Top of Shield Building at Elevation 828')

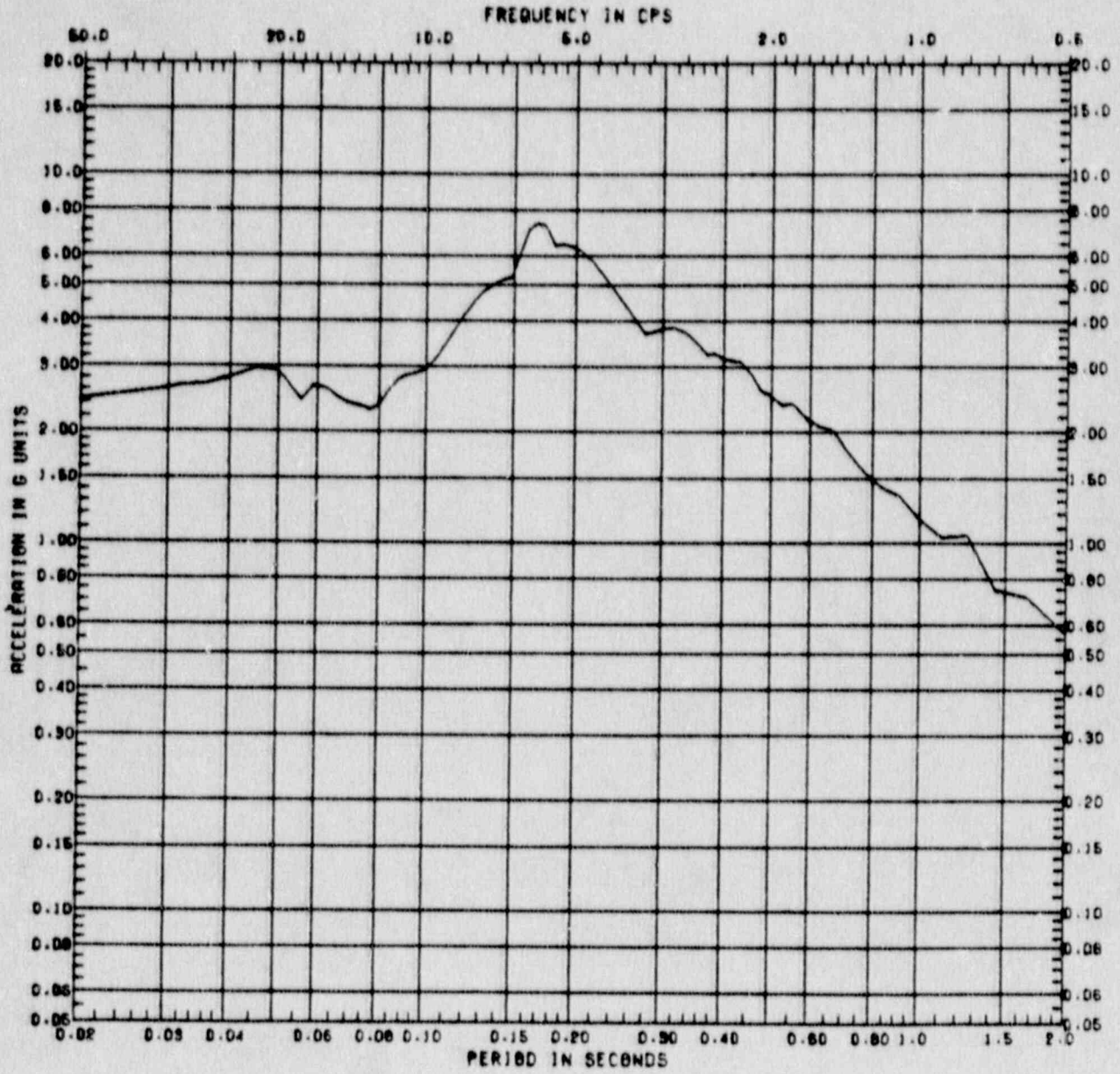

Figure C.4-23 Horizontal Response Spectrum at Sequoyah Model Node 48 (A_H = 0.75g, Damping = 5%, Location = Crane Wall at Elevation 738')

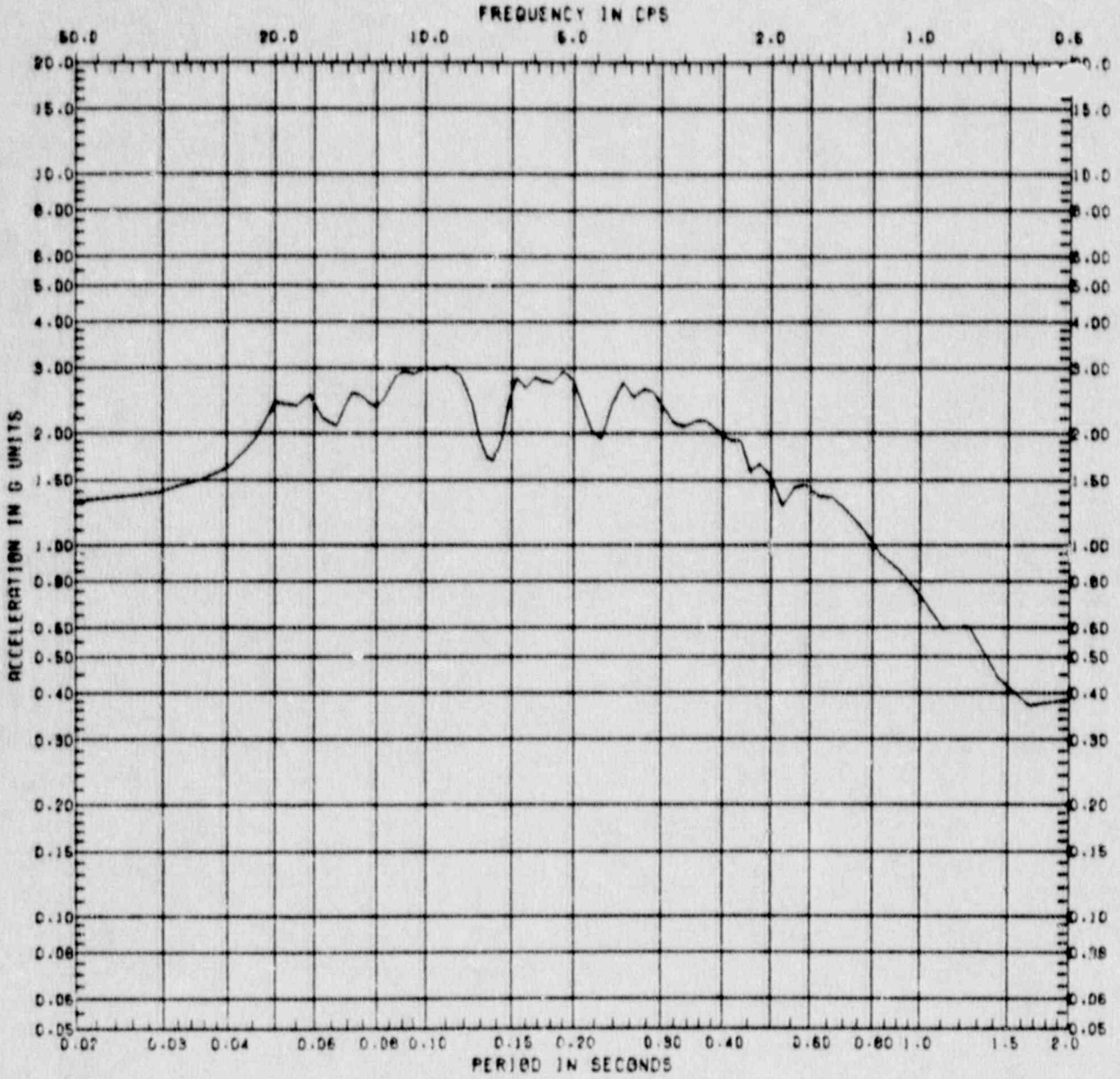

Figure C.4-24 Vertical Response Spectrum at Sequoyah Model Node 48 (A_H = 0.75g, Damping = 5%, Location = Crane Wall at Elevation 738')

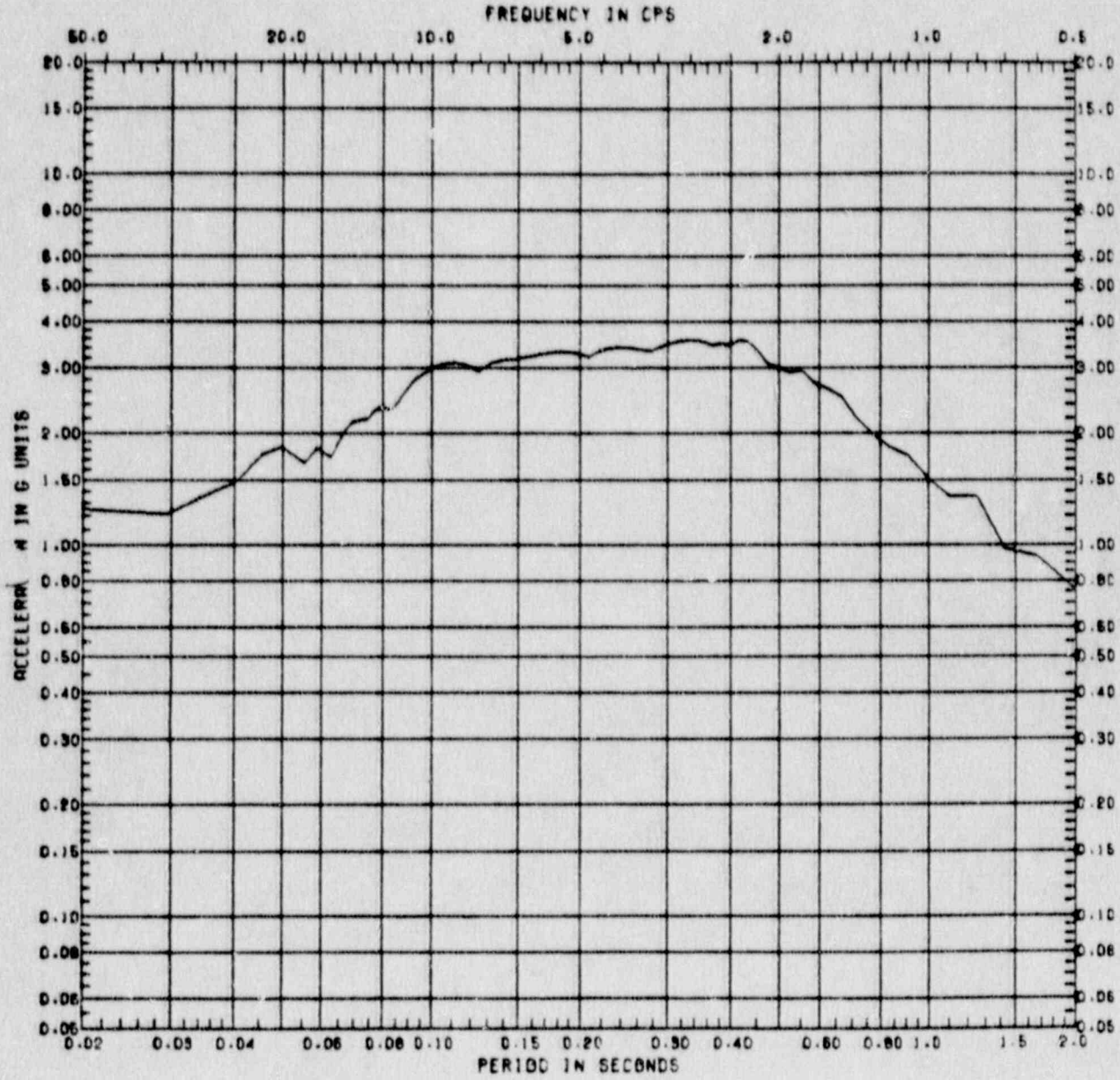

Figure C.4-25 Horizontal Response Spectrum at Sequoyah Model Node 84 (A_H = 1.0g, Damping = 5%, Location = Containment Basemat, Elevation 677')

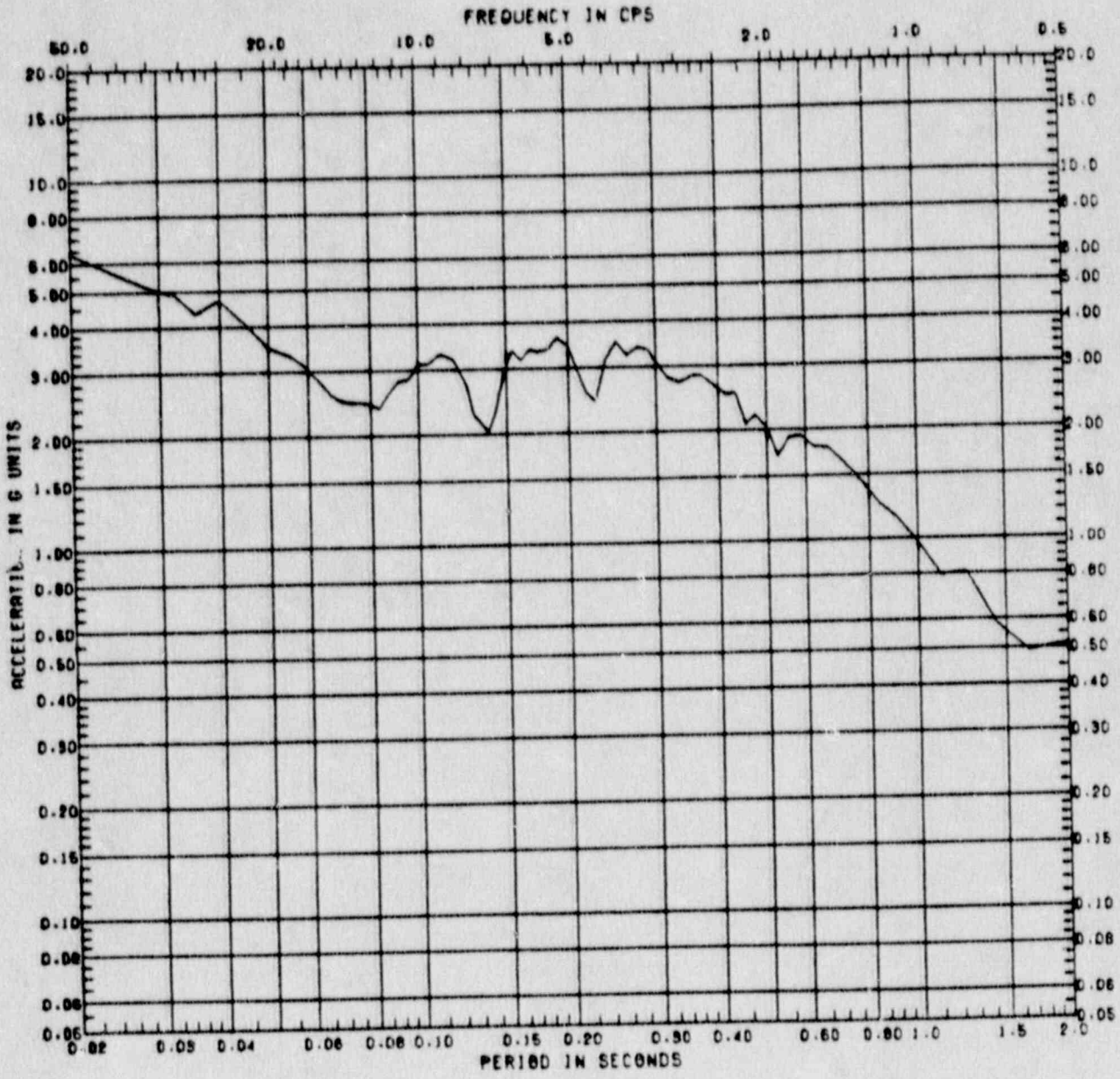

Figure C.4-26 Vertical Response Spectrum at Sequoyah Model Node 84 (A_H = 1.0g, Damping = 5%, Location = Containment Basemat, Elevation 677')

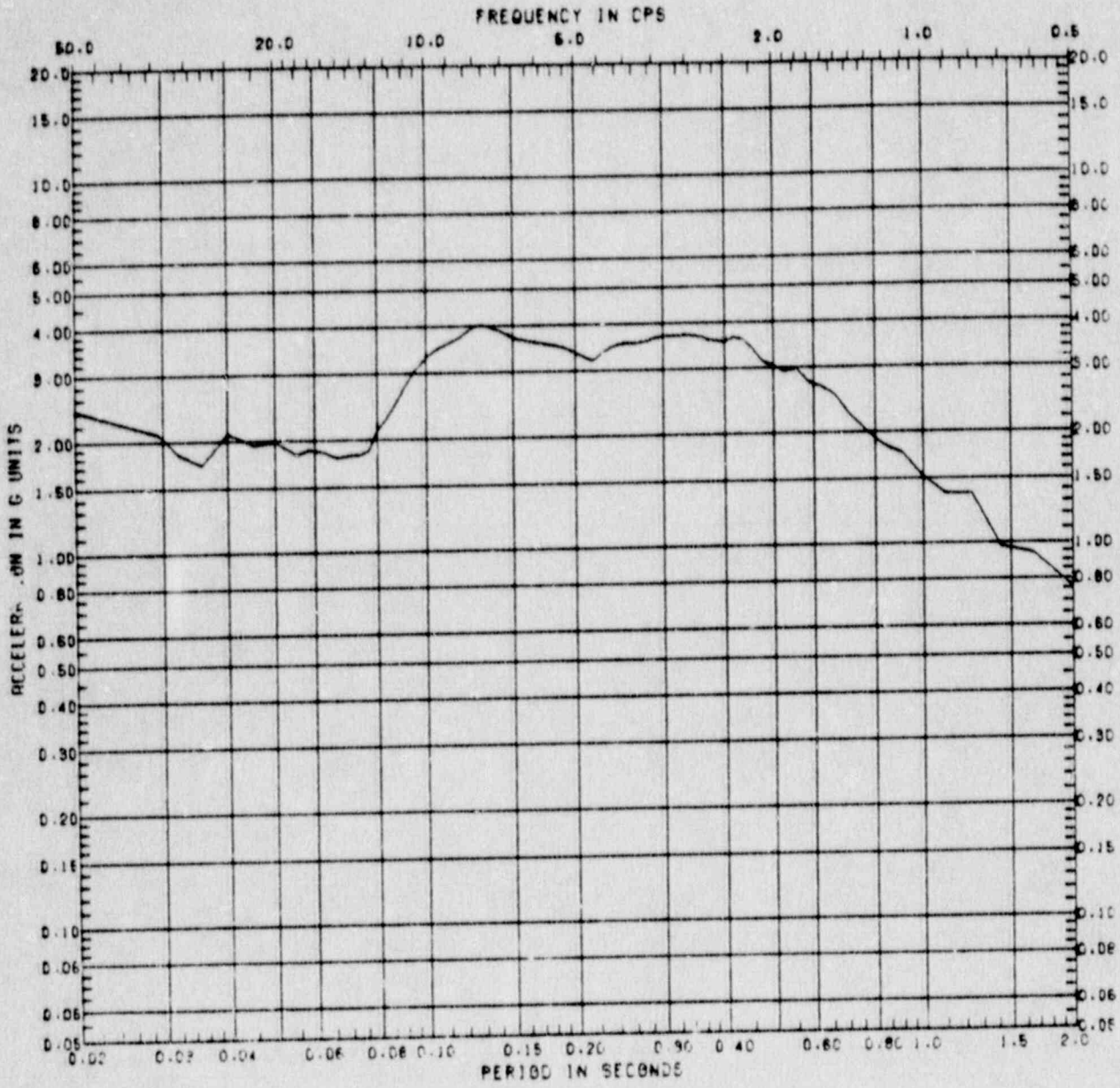

Figure C.4-27 Horizontal Response Spectrum at Sequoyah Model Node 56 (A_H = 1.0g, Damping = 5%, Location = Steel Containment at Elevation 700')

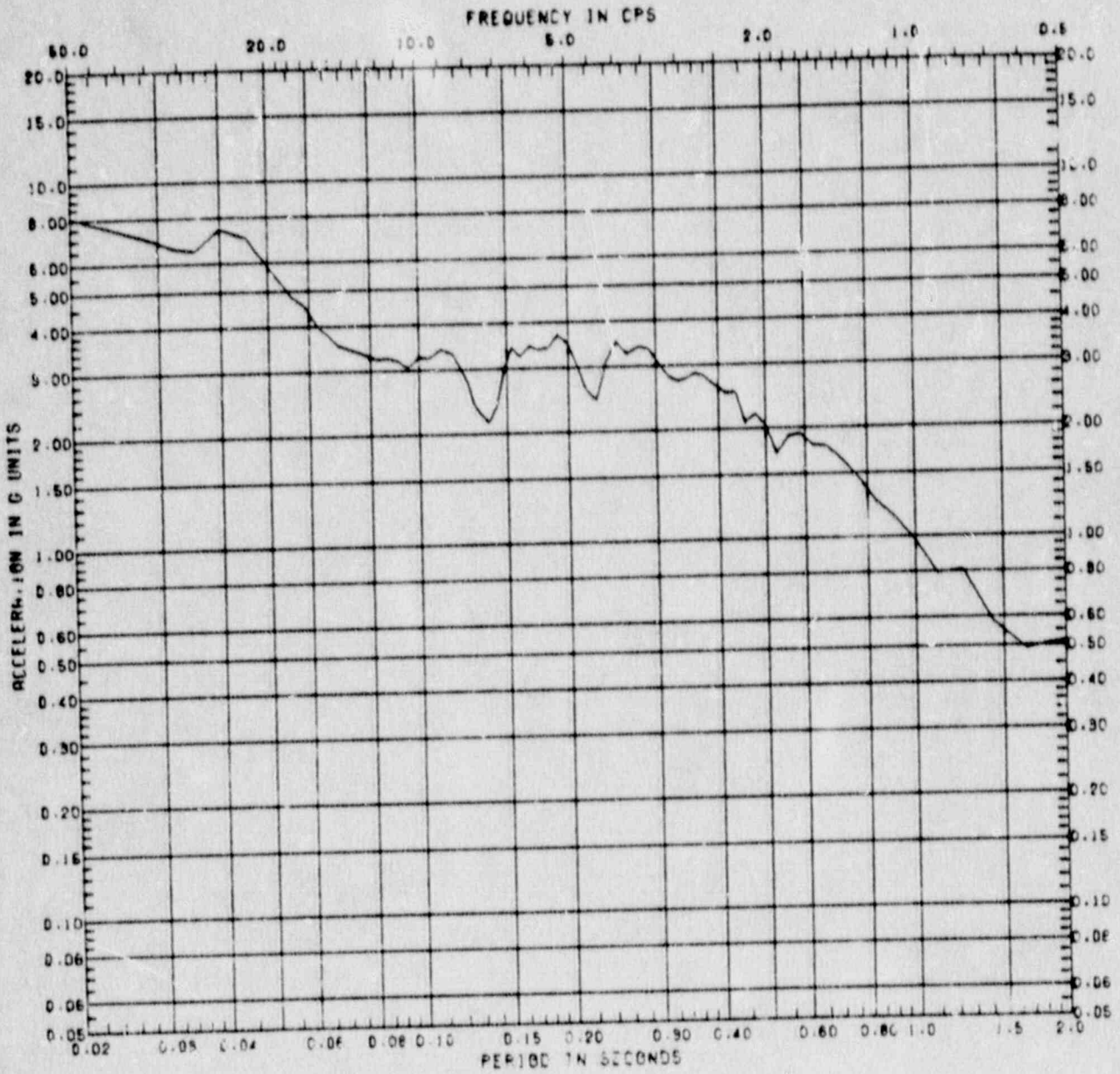

Figure C.4-28 Vertical Response Spectrum at Sequoyah Model Node 56 (A_H = 1.0g, Damping = 5%, Location = Steel Containment at Elevation 700')

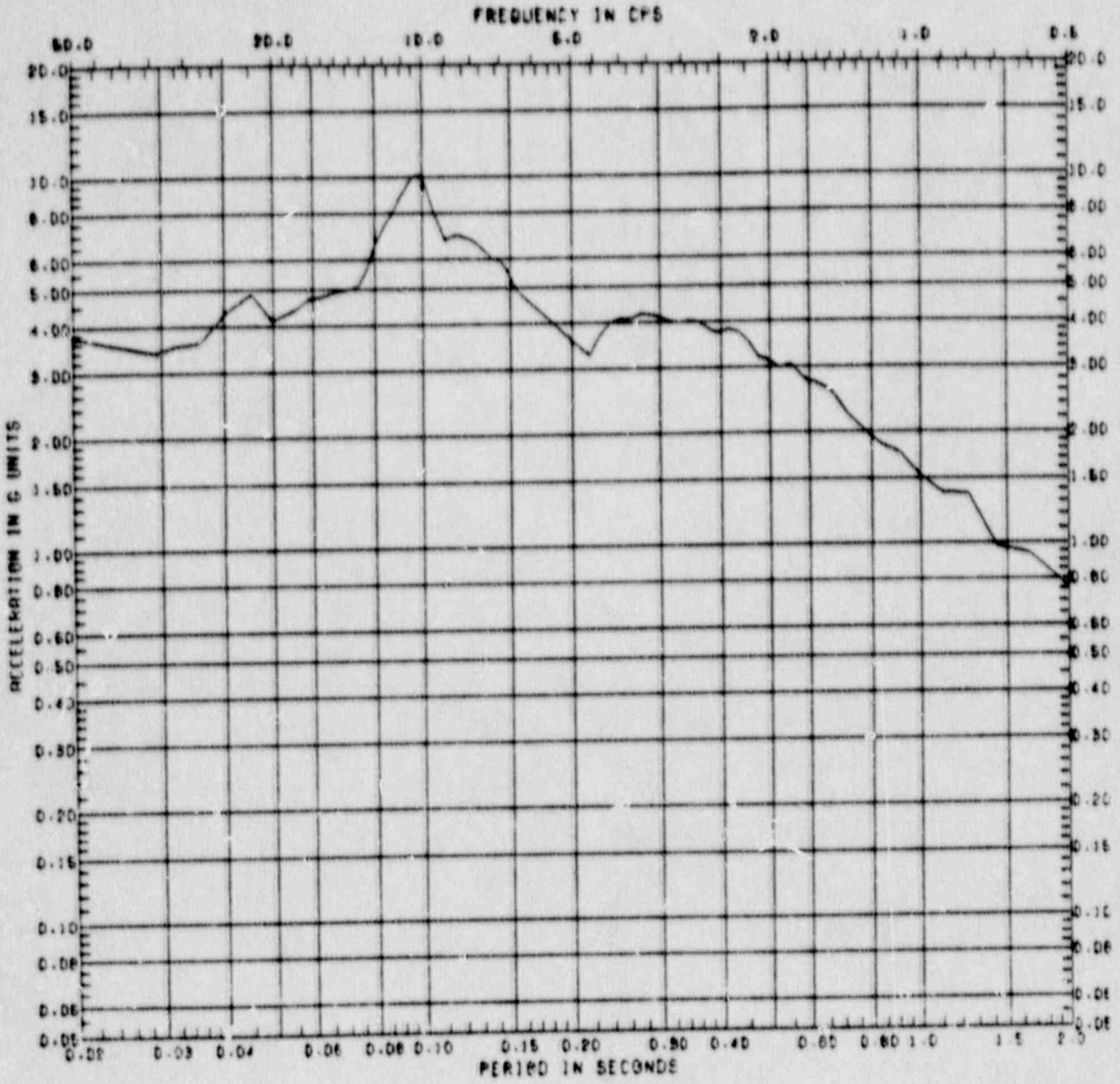

Figure C.4-29 Horizontal Response Spectrum at Sequoyah Model Node 29 (A_H = 1.0g, Damping = 5%, Location = Steel Containment at Elevation 743')

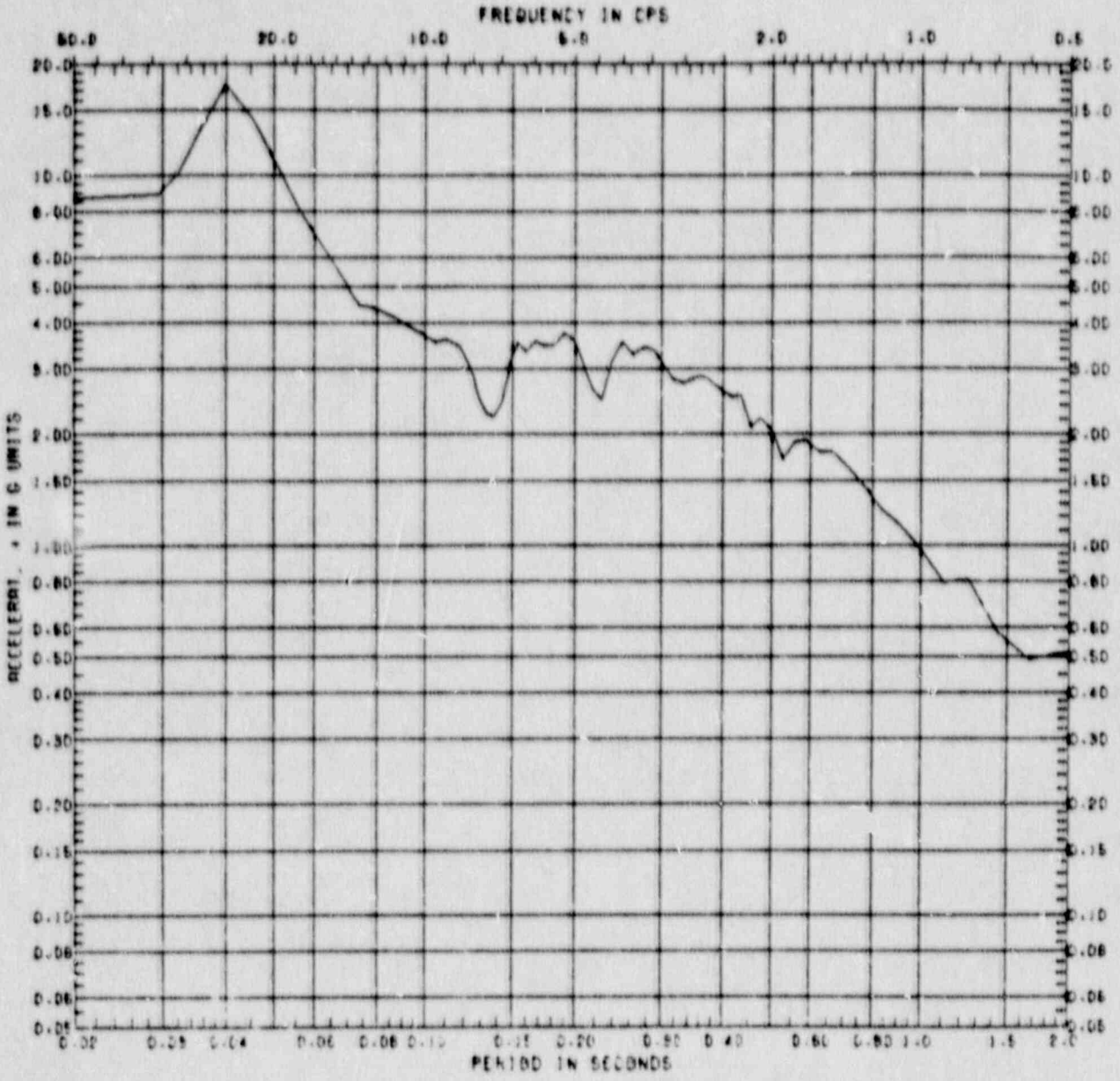

Figure C.4-30 Vertical Response Spectrum at Sequoyah Model Node 29 (A_H = 1.0g, Damping = 5%, Location = Steel Containment Wall at Elevation 743')

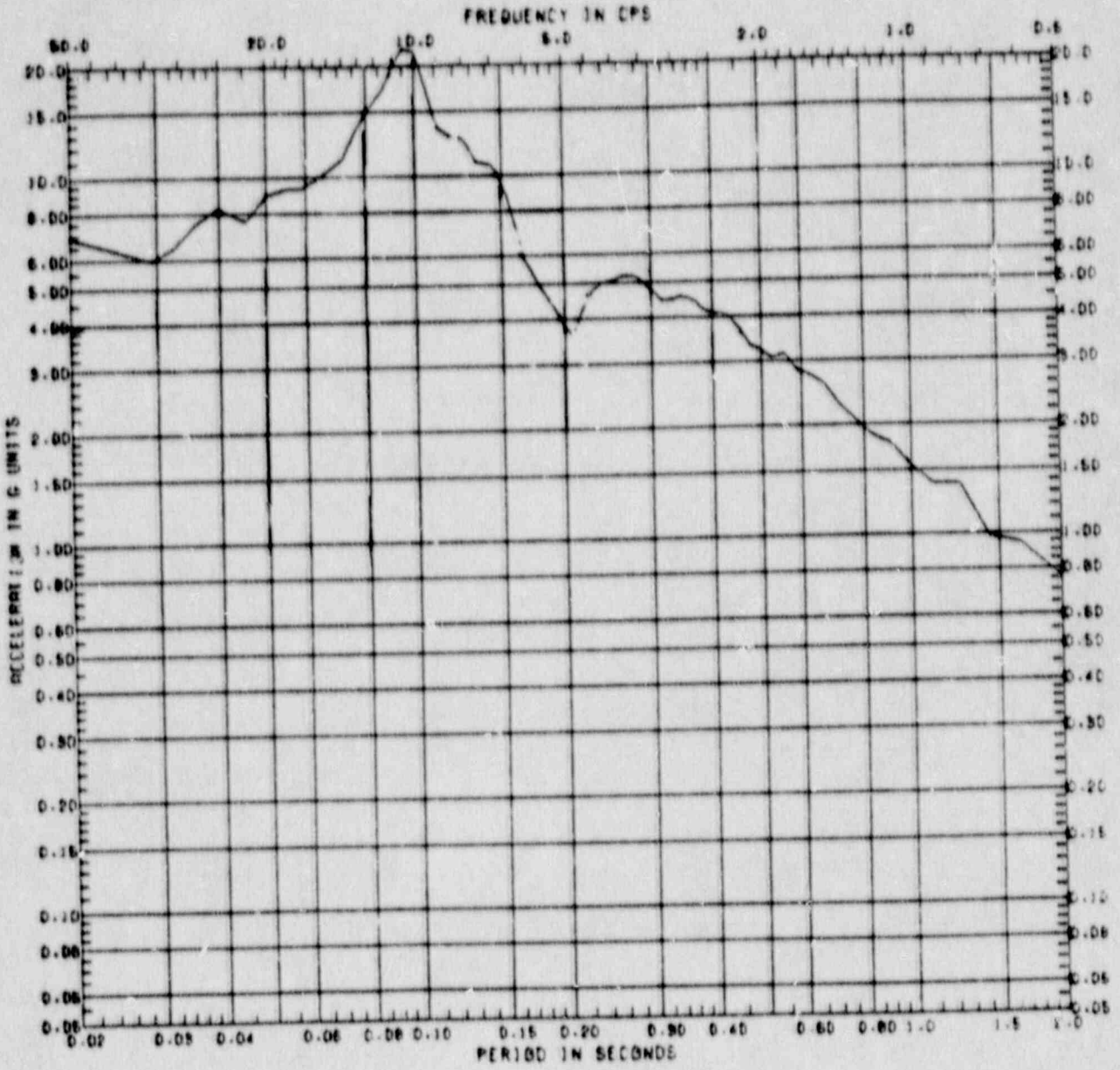

Figure C.4-31 Horizontal Response Spectrum at Sequoyah Model Node 6 (A_H = 1.0g, Damping = 5%, Location = Steel Containment at Elevation 813')

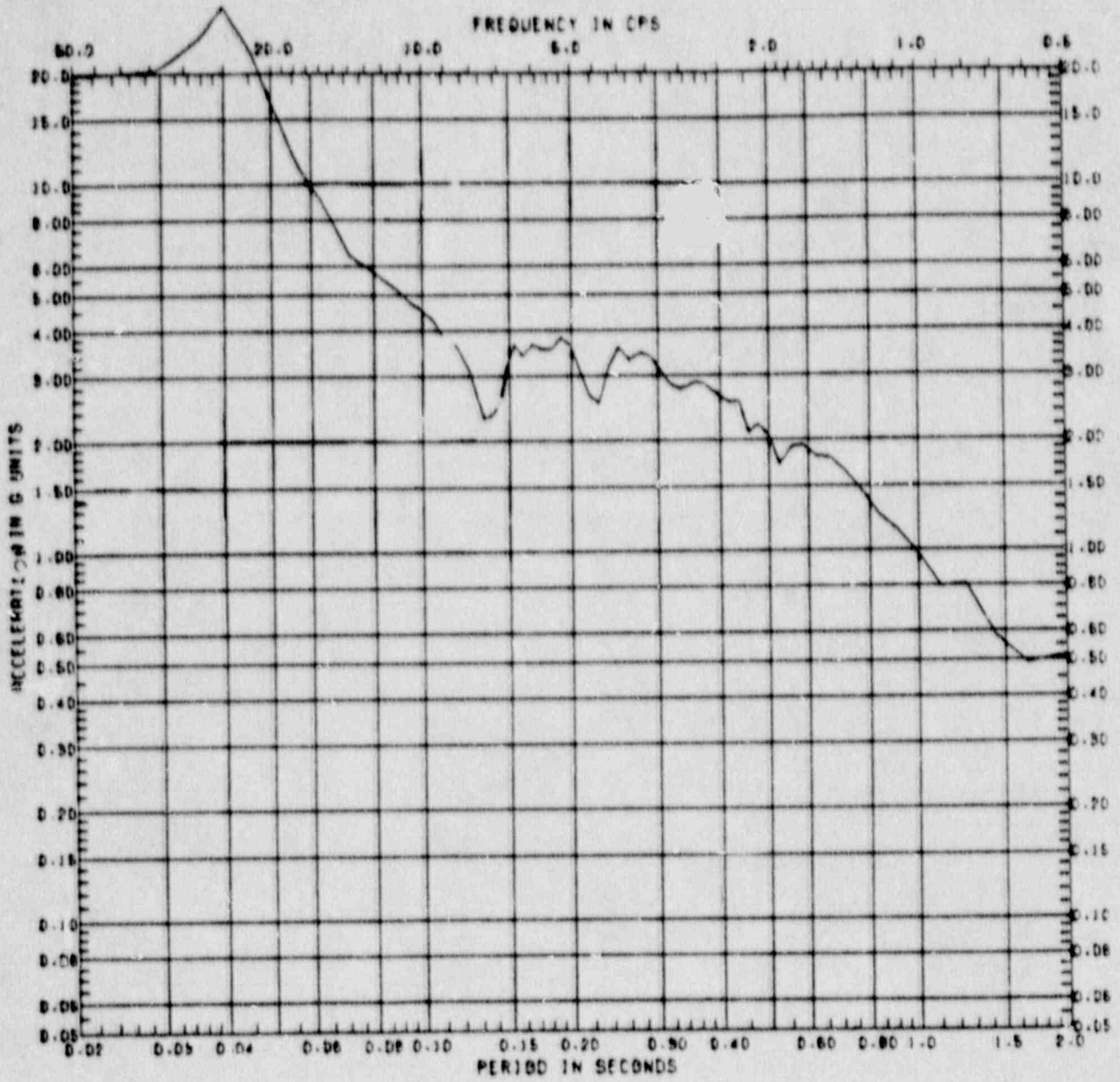

Figure C.4-32 Vertical Response Spectrum at Sequoyah Model Node 6 (A_H = 1.0g, Damping = 5%, Location = Steel Containment at Elevation 813')

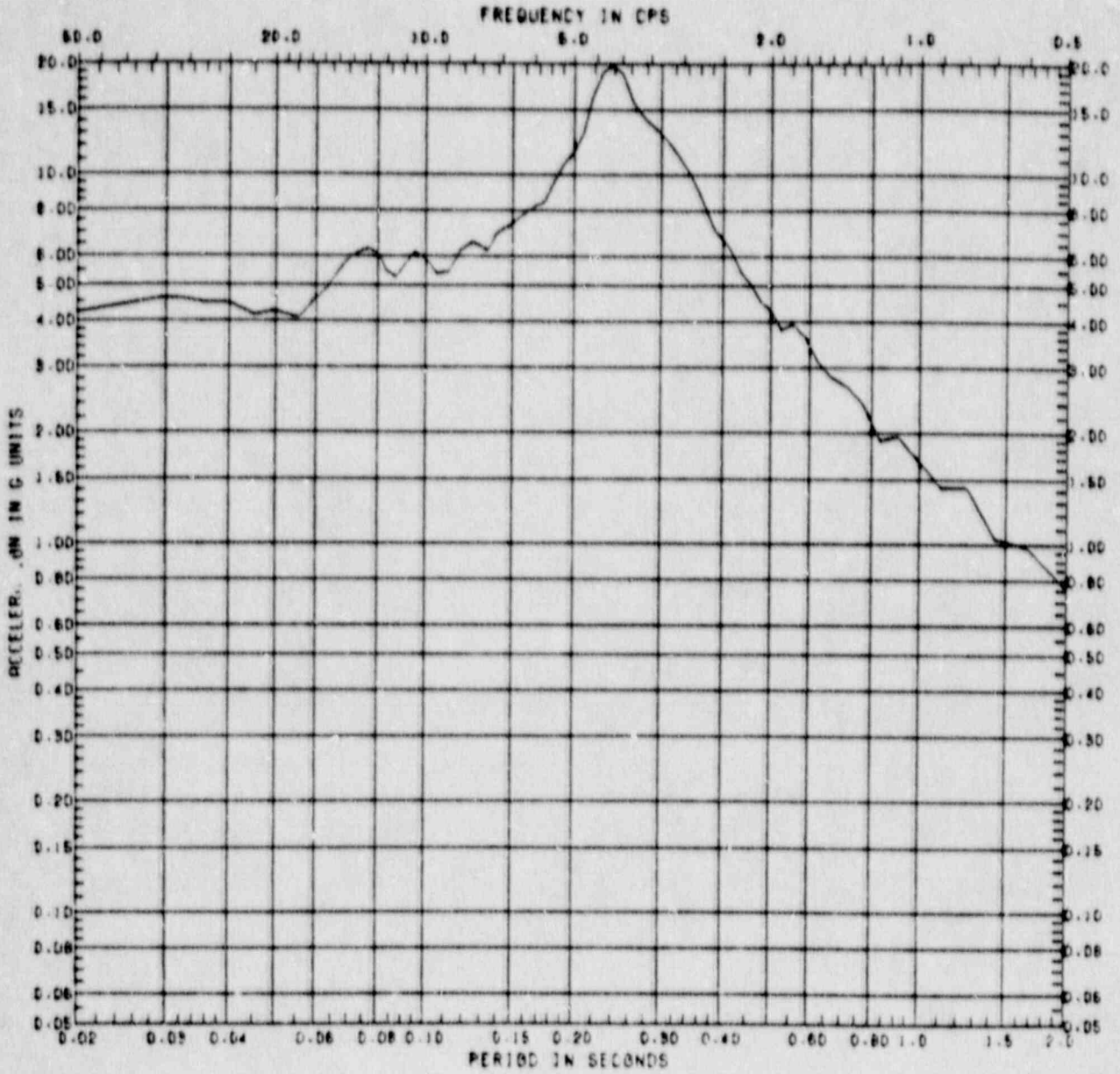

Figure C.4-33 Horizontal Response Spectrum at Sequoyah Model Node 5 (A_H = 1.0g, Damping = 5%, Location = Top of Shield Building, at Elevation 828')

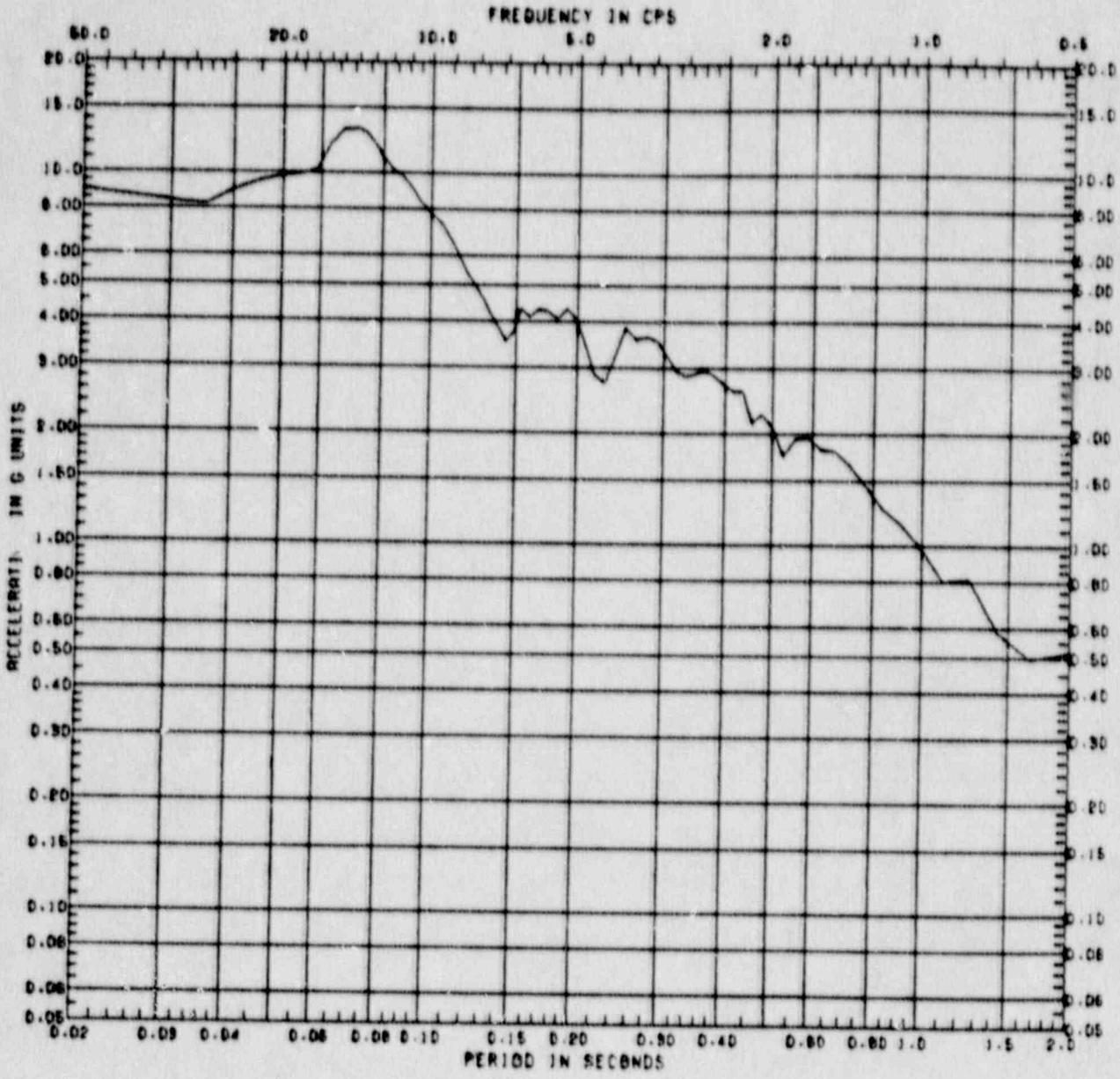

Figure C.4-34 Vertical Response Spectrum at Sequoyah Model Node 5 (A_g = 1.0g, Damping = 5%, Location = Top of Shield Building at Elevation 828')

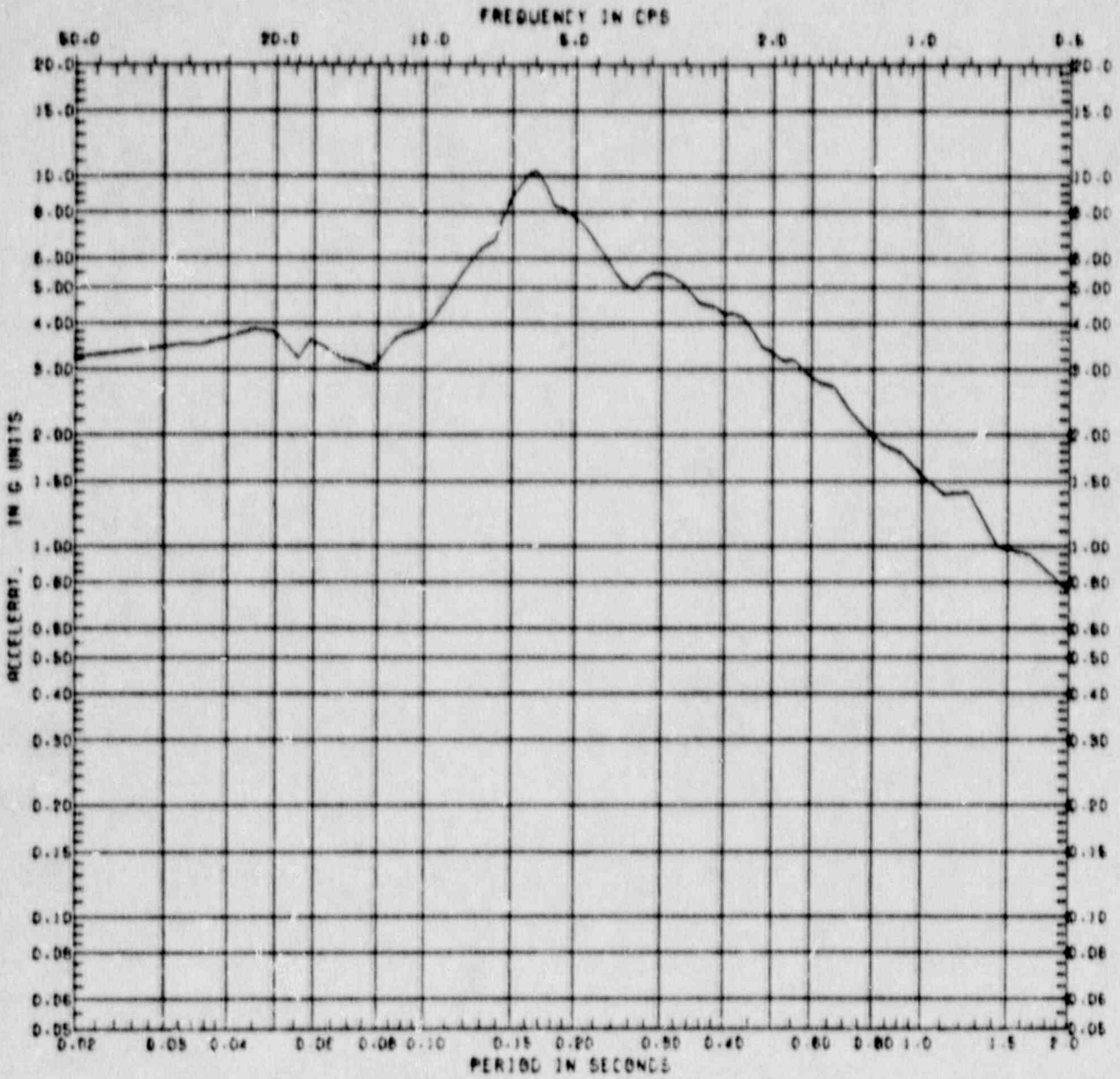

Figure C.4-35 Horizontal Response Spectrum at Sequoyah Model Node 48 (A_H = 1.0g, Damping = 5%, Location = Crane Wall at Elevation 738')

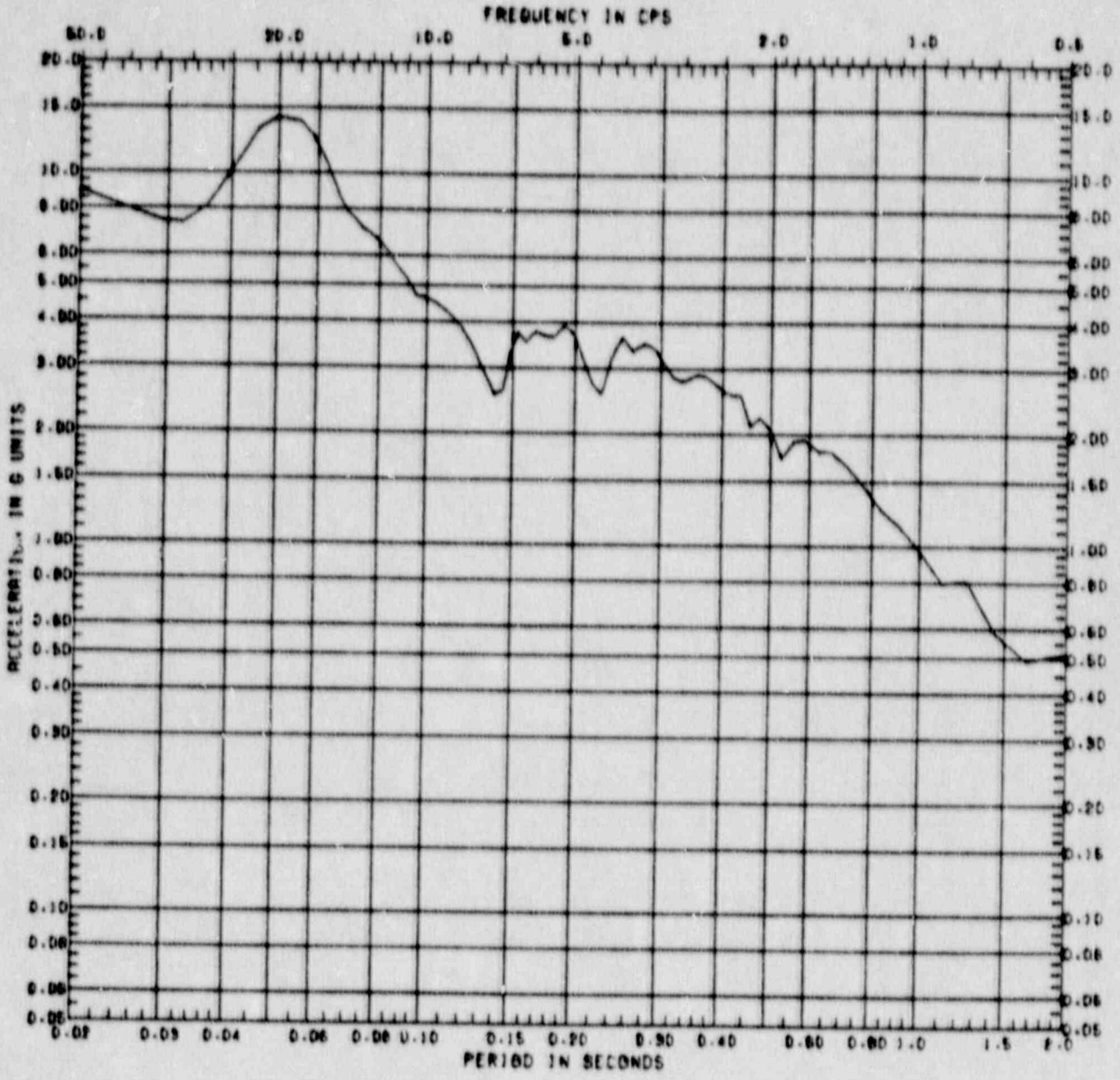

Figure C.4-36 Vertical Response Spectrum at Sequoyah Model Node 48 (A_H = 1.0g, Damping = 5%, Location = Crane Wall at Elevation 738')